

https://dspace.org/

Geochronology and evolution of the Magondi Belt

Glynn, Sarah Maeve

2017

http://hdl.handle.net/10539/23463

Glynn, Sarah Maeve (2017) Geochronology and evolution of the Magondi Belt, University of the Witwatersrand, Johannesburg, <http://hdl.handle.net/10539/23463>

Downloaded from a DSpace repository. https://dspace.org/

GEOCHRONOLOGY AND EVOLUTION OF THE MAGONDI BELT



Sarah Maeve Glynn

A Thesis submitted to the Faculty of Science at the University of the Witwatersrand, in fulfilment of the requirements for the degree of Doctor of Philosophy in Geology

2017



The financial assistance of the South African National Research Foundation (NRF) towards this research is hereby acknowledged. The opinions expressed and conclusions arrived at, are those of the author and are not necessarily to be attributed to the NRF.

Declaration

I, Sarah Glynn, declare that this Thesis is my own, unaided work. It is being submitted for the Degree of Doctor of Philosophy at the University of the Witwatersrand, Johannesburg. It has not been submitted before for any degree or examination at any other University.

_____

Sarah Glynn

On this the____day of_____2017, at Braamfontein, Johannesburg.

Abstract

The Magondi Belt is a NE-trending Palaeoproterozoic mobile belt, composed of a succession of supracrustal metasediments and minor metavolcanics that is subdivided into the Deweras, Lomagundi and Piriwiri Groups. The Magondi Belt is located in north-west Zimbabwe and is bounded on its eastern flank by the Archaean Zimbabwe Craton and the Pan-African Zambezi Belt to the north.

A connection between the Superior and Zimbabwe cratons has previously been made based on similarly aged dyke swarms across the two cratons. This matching magmatic barcode implies that the Superior and Zimbabwe cratons rifted away from one another *circa* 2.26 Ga based on the ages obtained for the Deweras lavas and the Chimbadzi Hill mafic intrusion. It was into this continental rift margin that the Magondi Supergroup sediments were deposited. The majority of the detrital and xenocrystic zircon ages from the Deweras Group are Archaean (2.86 to 2.63 Ga, with some inherited grains as old as 3.34 Ga); although a maximum depositional age of *circa* 2.29 Ga for the Deweras Group sedimentary rocks has been determined. Unconformably overlying these sediments, within an environment gradually transitioning from a passive margin into a back-arc basin environment, is the Lomagundi Group. These shallow marine sediments are then followed by those of the Piriwiri Group, deposited within a deeper water environment. Deposition of these two groups is constrained between 2.20 and 2.16 Ga, but may have continued up until the termination of the Magondi orogeny *circa* 1.99 Ga.

According to the currently accepted model, the Magondi orogeny is the result of the Zimbabwe Craton colliding with an unknown continental mass, “Terra Incognita”, resulting in the formation of a Palaeoproterozoic Andean-type magmatic arc along the western margin of the Zimbabwe Craton (the arc is typified by the 2.06 - 2.02 Ga granites and gneisses of the Dete-Kamativi Inlier), which was subsequently thrust over the margin of the Zimbabwe Craton, the consequence of which was a Himalayan-style collision that resulted in high-grade metamorphism and the formation of collisional granitoids (e.g. the Hurungwe Granite) *circa* 1.99 Ga ago.

It has also been established that the Dete-Kamativi Inlier, which flanks the western margin of the Zimbabwe Craton, is an extension of the Magondi Belt. Detrital zircons from paragneisses of the Malaputese Formation have ages ranging from 2.8 to 2.5 Ga, with the youngest grains constraining the maximum depositional age to be around 2.3 Ga. Thus, in terms of age and lithology, the correlation of the Malaputese Formation with the Deweras Group (maximum age of 2.29 Ga) is permissible. A south westward extension of 2.06 - 2.02 Ga granitoids – emplaced during the Magondi orogeny – is indicated by a number of localities in north-eastern Botswana and is believed to also be related to the Palaeoproterozoic magmatic arc. This study has recorded the first evidence of Archaean-aged basement within the Dete-Kamativi Inlier. Two orthogneisses with ages of 2.76 and 2.69 Ga provide strong evidence to suggest that the western margin of the Zimbabwe Craton may extend further to the west than previously recognised. It has also been confirmed, based on the recurrence of ~2.64 Ga aged zircons, in addition to older inherited grains ranging from 3.34 to 2.72 Ga, that the crust below the Magondi Belt is Archaean in age. This is not so, however, for the high-grade gneisses in the northern reaches of the Magondi Belt. It has been previously suggested that these supposed basement granites and gneisses represent an Archaean orogeny, but they are in fact Palaeoproterozoic in age, as represented by the syn-to-post-tectonic 2.02 Ga Hurungwe orthogneiss and the 1.95 Ga Kariba Granite. Additionally, a second, 1.96 Ga, orthogneiss contains zircons with younger metamorphic overgrowth rims that are Pan-African in age (545 Ma) and are attributed to the collision between the Kalahari and Congo cratons in the Neoproterozoic. It is therefore apparent that there is not enough evidence to support the existence of an Archaean “Hurungwe orogeny”.

The Magondi orogeny was the heat source for a widespread mineralisation and metamorphic event between 2.15 and 2.03 Ga, based on titanite and apatite ages from samples of the Archaean Copper King and Copper Queen Domes within the Magondi Belt. There is also evidence of a second, younger, mineralisation event, which primarily affected both the Dete-Kamativi Inlier and the Choma-Kalomo Block (south east Zambia). U-Pb data on columbite-tantalite grains (corroborated by ^{40}Ar-^{39}Ar dating of mica separates) from tin-bearing pegmatites within both the Choma-Kalomo Block and the Dete-Kamativi Inlier indicates that mineralisation occurred simultaneously within these two terranes between 1.06 and 0.98 Ga. The similarities (particularly with regards to mineralisation), between the Choma-Kalomo

Block and the Dete-Kamativi Inlier imply that these two terranes had a shared history, potentially as far back as the Palaeoproterozoic, but were certainly juxtaposed by 1.06 Ga when the pegmatites were emplaced.

The previously undated metasediments of the Choma-Kalomo Block have revealed an abundant Palaeoproterozoic component (2.04 - 1.86 Ga), contradicting the prevailing understanding that the Choma-Kalomo Block is solely Mesoproterozoic in age (on account of the granitoids, which were previously dated at 1.37 and 1.18 Ga). The Choma-Kalomo Block was also thought to constitute an exotic terrane with respect to the neighbouring Dete-Kamativi Inlier and Archaean Zimbabwe Craton. Based on the geochronology presented here, a new model is proposed whereby the thinner lithosphere beneath the Choma-Kalomo Block is either a primary feature or one that resulted from subduction erosion and delamination processes associated with the formation of multiple continental margin magmatic arcs.

Acknowledgements

First and foremost, I would like to acknowledge financial support from the South African National Research Foundation, the Geological Society of South Africa (Kent Fund), the Society of Economic Geologists (Tim Nutt Memorial Fund) as well as funding through the Jim and Gladys Taylor Trust and Carnegie (for the large research grant awarded to Dr. Sharad Master). I also thank the Centre of Excellence for Integrated Mineral and Energy Resource Analysis (CIMERA) for analytical and conference support. Without this support, the project would not have been possible. I would also like to thank the German Ministry for Education and Research as well as the University of the Witwatersrand (and in particular Professor Roger Gibson and Professor Alexander Ziegler for their help in obtaining aid from the University) for additional financial support as part of a Helmholtz-South Africa SIMS initiative; this funding in addition to a contribution made by Professor Maarten de Wit (AEON), allowed me to study in Potsdam for two years.

A special thank you to Dr. Sharad Master for supervising this project, your amazing insight into African Geology always gives me new things to think about. I am also indebted to you for your generosity and for giving me so much of your time.

A massive thank you to my colleagues at the GFZ, who not only hosted my stay in Potsdam, but made me feel welcome from day one. To Abiel Kidane, Frédéric Couffignal, Dr. Alexander Rocholl, and Dr. Robert Trumbull, thank you for your willingness to help whenever I needed it, for all your guidance and expertise and your friendship. I am especially indebted to Dr. Michael Wiedenbeck, who I adopted as a mentor during my stay in Potsdam. Thank you for introducing me to SIMS and for giving me the opportunity to learn so much more about it. I really appreciate all the time and effort you put into helping me over the course of my PhD, your opinions and advice have been invaluable. Special thanks also to you and your wife Dr. Sushma Prasad, as well as your wonderful family for making me feel so at home, when I was so far away from mine.

To all those at the GFZ who aided me in some way, in particular Professor Jörg Erzinger for approving my appointment in the SIMS lab; to Uwe Dittmann, Dr. Johannes Glodny and Juliane Herwig for their help with mineral separation and sample preparation; to Ilona Schäpan and Dr. Dieter Rhede for their help on the SEM and Electron Probe – thank you.

Thank you also to the many staff and fellow post-graduate students within the Wits School of Geosciences who have helped me along the way - particularly Joe Aphane and everyone at the Earth Lab for their analytical expertise as well as Dr. Mary Evans and Dr. Trishya Owen-Smith for their support and advice.

I am particularly grateful to Dr. Martin Whitehouse (NordSIM, Stockholm) for his patient instruction concerning data reduction as well as to Dr. Richard Armstrong (Australian National University) and Professor Dirk Frei (Stellenbosch University) for allowing me to visit their labs and learn so much from them. Thank you also to my other co-authors, Professor Jan Kramers, Professor Donald Davis and Dr. Tomas Oberthür for your contributions and help in editing the various manuscripts; it has been a wonderful experience to work with each of you.

Lastly, and most importantly I would like to thank my family and friends for their love and support, each one of you has helped me in some way to just keep going, and I will be eternally grateful for that. Mom, Dad thank you for encouraging my love of rocks from an early age and for helping to make it possible for me to study something I love.

Table of Contents

Declaration iii
Abstract iii
Acknowledgements vii
Table of Contents ix
List of Figures xiii
List of Tables xxiii
List of Abbreviations xxv

CHAPTER 1: INTRODUCTION

1.1 Regional geology of the Magondi Belt 1
1.1.1 The Magondi Belt and Basement
1.1.2 The Dete-Kamativi Inlier
1.1.3 The Choma-Kalomo Block
1.2 Initial scope of this thesis 3
1.2.1 Subsequent objectives
1.3 Approach 5
1.4 Summary of scientific contributions 6
1.4.1 The Magondi Belt
1.4.2 The Magondi Basement
1.4.3 The Dete-Kamativi Inlier
1.4.4 The Choma-Kalomo Block
1.4.5 Research outputs

CHAPTER 2: ANALYTICAL METHODS

2.1 Why zircon? 13
2.2 The U-Pb system 13
2.3 Instrumentation 15
2.3.1 Laser Ablation – Inductively Coupled Plasma Mass Spectrometry (LA-ICPMS)
2.3.2 Secondary Ion Mass Spectrometry (SIMS)
2.4 Data acquisition 21
2.4.1 Reference materials
2.4.2 Defining an analysis
2.5 Data evaluation and presentation 23
2.5.1 Processing the raw data
2.5.2 Data representation

2.6 Analytical methods.....30

2.6.1 SHRIMP-RG

2.6.2 SIMS

2.6.3 LA-ICPMS

2.6.4 ID-TIMS

2.6.5 ^{40}Ar-^{39}Ar

CHAPTER 3: NEW U-Pb AGES FOR THE LATE PALAEOPROTEROZOIC MAGONDI SUPERGROUP, ZIMBABWE

3.1 Introduction.....37

3.2 Regional geology.....37

3.2.1 Deweras Group

3.2.2 Lomagundi Group

3.2.3 Piriwiri Group

3.2.4 Volcanic Centres

3.3 Field and petrographic descriptions.....43

3.3.1 Deweras Group

3.3.2 Lomagundi Group

3.3.3 Piriwiri Group

3.4 Geochemistry.....47

3.5 Geochronology.....48

3.5.1 Primary volcanic features

3.5.2 Epiclastic volcanic deposits

3.6 Discussion and conclusions.....52

3.6.1 The Zimbabwe-Superior Craton connection

3.6.2 The Zimbabwe Craton in the Palaeoproterozoic

CHAPTER 4: THE VANISHED OROGENY: GEOCHRONOLOGY OF PALAEOPROTEROZOIC "BASEMENT" GNEISSES OF THE KARIBA AREA, WESTERN MAGONDI BELT (ZIMBABWE AND ZAMBIA)

4.1 Introduction.....59

4.2 Regional geological setting.....59

4.2.1 The Kariba and Chipisa Paragneisses

4.2.2 The Urungwe Paragneiss

4.2.3 The Hurungwe orogeny

4.2.4 The Copper King and Copper Queen Domes

4.3 Analytical methods.....63

4.4 Results.....63

4.4.1 Biotite-rich Chiroti Paragneiss, Sample Z MB 13/5

4.4.2 Chiroti Paragneiss, Sample Z MB 13/6

4.4.3 Hurungwe Orthogneiss, Sample Z MB 13/8b

4.4.4 Kariba Granite, Sample Z MB 13/10

4.4.5 Sillimanite Quartzite, Sample Z MB 13/11

4.4.6 Manchinchi Bay Migmatitic Orthogneiss, Sample Z MB 13/12

4.4.7 Copper King and Copper Queen Domes

4.5 Discussion....72

4.6 Conclusion....74

CHAPTER 5: U-Pb ZIRCON GEOCHRONOLOGY FROM THE DETE-KAMATIVI INLIER, NW ZIMBABWE WITH IMPLICATIONS FOR THE WESTERN MARGIN OF THE ARCHAEAN ZIMBABWE CRATON

5.1 Introduction....75

5.2 Geological setting of the Dete-Kamativi Inlier....76

5.2.1 Malaputese Formation

5.2.2 Inyantue Formation

5.2.3 Tshontanda Formation

5.2.4 Kamativi Formation

5.2.5 Granitic Gneisses

5.2.6 Structure and mineralisation

5.4 Results....80

5.4.1 Analytical methods

5.4.2 Evidence for the formation of an arc

5.4.3 Age and petrography of the supracrustal metasediments

5.4.4 Age and petrography of the Granitic Gneisses

5.5 Discussion....93

5.5.1 Supracrustal metasediments – age of deposition and correlation with the Magondi Belt

5.5.2 Granitic Gneisses – defining the extent of the Archaean Zimbabwe Craton and Palaeoproterozoic arc

5.6 Conclusions....99

CHAPTER 6: THE PROTEROZOIC CHOMA-KALOMO BLOCK, SE ZAMBIA: EXOTIC TERRANE OR A REWORKED SEGMENT OF THE ZIMBABWE CRATON?

6.1 Introduction....100

6.2 Regional geology....101

6.2.1 Metasedimentary Sequence

6.2.2 Choma-Kalomo Batholith

6.2.3 Muscovite and tin-bearing pegmatites

6.3 Analytical methods....106

6.4 Results....107

6.4.1 Intrusives of the Choma-Kalomo Batholith

6.4.2 The Metasedimentary Sequence

6.4.3 Pegmatites in the Choma-Kalomo Block and Dete-Kamativi Inlier

6.5 Discussion.....117

6.5.1 The Choma-Kalomo, Dete-Kamativi link

6.5.2 Proposed model for the formation of the Choma-Kalomo Block

6.6 Conclusions.....121

CHAPTER 7: SUMMARY

7.1 Proposed model for the formation of the Magondi Belt.....123

7.1.1 Development of the Magondi Belt from the Neoarchaean through to the Mesoproterozoic

7.1.2 Meso-Neoproterozoic evolution of the Choma-Kalomo Block

7.2 Limitations and recommendations – where to from here.....129

REFERENCES.....131

APPENDICES

Appendix A: Data Tables.....158

A.1 Full CAF LA-ICPMS U-Th-Pb zircon dating methodology

A.2 Magondi Belt

A.3 Magondi Basement

A.4 Dete-Kamativi Inlier

A.5 Choma-Kalomo Block

Appendix B: Sample Preparation.....203

B.1 Mineral separation

B.2 Grain mounts

B.3 Imaging

Appendix C: Analytical Methods.....212

C.1 SIMS design features which aid U-Pb zircon geochronology

C.2 Deciding which calibration curve to use, and the factors which can affect it

Appendix D: Research Outputs.....220

D.1 Sijarira Manuscript

D.2 Thesis-related Conference Abstracts

D.3 SIMS-related Conference Abstracts

List of Figures

Figure 1.1: Geological and geographical maps of central Africa depicting the location of the Choma-Kalomo Block, Magondi Belt and Dete-Kamativi Inlier; after Hanson et al. (1988a); Wikipedia (2016) and Wikimedia commons (2015).....1

Figure 1.2: Detailed map of the Magondi Belt and some of the so-called 'basement' gneisses to the north. The map is after Master (1991a) and McCourt et al. (2001).....2

Figure 2.1: Graphic representation of the three decay chains for ^{238}U, ^{235}U and ^{232}Th (Schoene, 2014). The rate of radioactive decay for each isotope is indicated by a number of alpha and beta decays, before reaching the stable daughter product.…….....15

Figure 2.2: Photograph showing the LA-SF-ICPMS setup at the University of Stellenbosch's Central Analytical Facility, which consists of a Thermo Element 2 Sector Field-ICPMS equipped with a New Wave UP 213 Laser Ablation system. Spot sizes using this instrument were typically on the order of 30 µm in diameter and 20 µm deep. Photo supplied by Prof. Dirk Frei.....16

Figure 2.3: Sketch (after Arlinghaus, 2014) depicting how the sputtering process works: a collision cascade is initiated when the primary beam interacts with the sample; because of this, ions of the primary beam can become implanted in the sample surface or extracted along with the secondary ions and other particles such as electrons (e) and photons (hv). Molecules can become broken up (either into their constituent atoms or into molecular fragments) only when the binding energy is overcome by the kinetic energy of the primary beam.….....17

Figure 2.4: Photograph showing the configuration of the Reverse Geometry SHRIMP housed at the ANU (note the placement of the magnet before the electrostatic analyser); photo is author's own.....18

Figure 2.5: Photograph of the Potsdam CAMECA 1280-HR (photo supplied by the author).....19

Figure 2.6: Ion optics of the Potsdam CAMECA 1280-HR. (CAMECA).....20

Figure 2.7: The top left plot depicts the various shapes a calibration curve can have based on the type of correlation used, while the remaining plots demonstrate how consistent the relationship is between the respective secondary ion ratios. The slope of the line of best fit through the data points is defined by the exponent value. The figure is after Williams (1998); Jeon and Whitehouse (2015).....24

Figure 2.8: Sketch of how to use the calibration curve to calculate the age for a zircon of unknown age (after Ireland and Williams, 2003).....25

Figure 2.9: Wetherill (Figure 2.9a) and Tera-Wasserburg (Figure 2.9b) concordia plots which can be used to display U/Pb isotopic data. The respective pattern made by zircons experiencing recent lead loss and isotopic disturbances are illustrated in the diagrams (Williams, 1998). LI = lower intercept, whereas UI = upper intercept.....29

Figure 3.1: Simplified geological map of Zimbabwe, from Master (1991a) indicating the location of the Magondi Belt, and its position relative to the Zimbabwe Craton, the Zambezi Belt and the younger cover, which together bound it on all sides. The area delineated by the rectangle is represented in more detail in Figure 3.12, and indicates the approximate location of the Chimbadzi Hill Intrusion.....38

Figure 3.2: Geological map of the Magondi Belt, after McCourt et al. (2001). Ugr = Hurungwe granite, Ugn = Hurungwe gneiss, U = Hurungwe klippe. The sampling localities are indicated by the symbols.....39

Figure 3.3: Sketch depicting the depositional environments in which the Magondi Supergroup formed (Leyshon and Tennick, 1988).....40

Figure 3.4: Hand specimen of sample DV 11/1 (Figure 3.4a), the left-hand side of the

photomicrograph in (Figure 3.4b) was taken under XPL, while the right-hand side is in PPL. XPL photomicrographs of the andesitic agglomerates NC 1 (Figure 3.4c) and GD Z 11/3 (Figure 3.4d) from the Nyamakari and Godzi volcanic centres respectively.....46

Figure 3.5: Sample DV11/ 2 seen under PPL (Figure 3.5a), is from the Deweras Group, while samples Z 11/C – SKR 2B (Figure 3.5b; XPL) and SKG Z11/1 (Figure 3.5c; PPL) originate from the Lomagundi Group. Sample GD Z11/ 2A (Figure 3.5d; XPL) is found within the Piriwiri Group and is related to the Godzi volcanic centre.....47

Figure 3.6: Plot of Total Alkalis vs. Silica (Figure 3.6a) to discriminate between the various samples. 1=Foidite; 2=Tephrite (Ol<10%), Basanite (Ol>10%); 3=Picrobasalt; 4=Trachybasalt; 5=Basalt; 6=Phonotephrite; 7=Basaltic trachyandesite; 8=Basaltic andesite; 9=Tephriphonolite; 10=Trachyandesite; 11=Andesite; 12=Phonolite; 13=Trachyte (Q<20%), Trachydacite (Q>20%); 14=Dacite; 15=Rhyolite. Figure 3.6b is a bivariate plot of Ti vs. V, the data are normalised according to the values from Taylor and McLennan (1981) for the average upper crust.....48

Figure 3.7: CL images of zircons typical of the samples analysed. Several grains can be seen to be inherited, due to their rounded morphology and truncated oscillatory zoning within the grain interior.....49

Figure 3.8 Concordia plots of the SHRIMP data for samples DV 11/1 (Figure 3.8a) and NC 1 (Figure 3.8b), in addition to the LA-ICPMS data for sample GD Z 11/ 3 (Figure 3.8c).....50

Figure 3.9: Concordia plots of the SHRIMP data for samples DV 11/ 2 (Figure 3.8a), Z 11/C – SKR 2B (Figure 3.8b) and GD Z 11/ 2A (Figure 3.8c).....52

Figure 3.10: Compilation of age data for the Magondi Belt. The ages in brackets represent the maximum depositional ages, whereas those not in brackets are magmatic ages, after Master et al. (2010).....54

Figure 3.11: Barcode pattern of mafic intrusions which have occurred on the Zimbabwe,

Kaapvaal and Superior Cratons, after Söderlund et al. (2010).....55

Figure 3.12: Geological setting for the Chimbadzi Hill Intrusion (after Sithole, 1977).....57

Figure 4.1: Simplified geological map of the northern half of the Magondi Belt; sample localities are indicated by stars. The black square indicates the approximate location of the Copper King and Copper Queen Domes, whereas ages in bold represent inheritance, those in plain text are magmatic ages and those in italics relate to a period of metamorphism. The map is after Treloar and Kramers (1989) and Broderick (1976).....…….....….60

Figure 4.2: Thin section photomicrographs and concordia plots for samples Z MB 13/5 (Figure 4.2a, b), Z MB 13/6 (Figure 4.2c, d), and Z MB 13/8b (Figure 4.2e, f). Blue ellipses indicate measurements made on cores while black represent rims.....…..65

Figure 4.3: BSE and CL images of selected zircons from samples Z MB 13/5, 13/6 and 13/8b, indicating the spots analysed and the ages obtained, as well as the U concentration.....66

Figure 4.4: Sample Z MB 13/10 in hand specimen (Figure 4.4a) and thin section photomicrograph under XPL in Figure 4.4b. T he Kariba Heights sillimanite quartzite (Figures 4.4 c and d) and Manchinchi Bay Gneiss field sample and thin section photomicrograph are presented likewise in Figures 4.4e and f.....…….....…..68

Figure 4.5: Concordia plots for the SIMS analyses done on s amples Z MB 13/10 (Figure 4.5a), Z MB 13/11 (Figure 4.5b) and Z MB 13/12 (Figure 4.5c)....…….....…69

Figure 4.6: CL images of selected zircons from samples Z MB 13/10 (Figure 4.6a), Z MB 13/11 (Figure 4.6b) and Z MB 13/12 (Figure 4.6c)…….....….69

Figure 4.7: The map in Figure 4.7a is after Leyson (1969), while the concordia plots in Figures 4.7b through f show the U-Pb, LA-ICPMS and ID-TIMS results, for the Copper King and Copper Queen Dome samples. Sample CQD-4 (Figure 4.7c) is a strongly foliated,

coarse-grained porphyroblastic granite in the core of the Copper Queen Dome. Sample CQD-5 (Figure 4.7c), a weakly foliated, coarse-grained K-feldspar granite, constitutes the greatest part of the Copper Queen Dome; however, due to its poor yield of altered zircons none could be dated; while sample CQD-6 (Figure 4.7c) is a coarse-grained gneiss that occurs at the margin of the Copper Queen Dome. Sample CQD-8 (Figure 4.7d) is an unfoliated granite from the Copper Queen Dome and sample CQD-10 (Figure 4.7e) a metapelitic schist, in the vicinity of the Copper Queen Dome, consists predominantly of Palaeoproterozoic zircon grains ranging from 2.46 to 2.15 Ga; with the exception of one (3023 ± 1 Ma), there are no late Archaean grains within this sample. Finally, sample CQD-11 (Figure 4.7f) is a tonalitic gneiss from the Copper King Dome.....71

Figure 4.8: The mechanism by which Leyshon (1973) proposed the basement was reactivated.....73

Figure 5.1: Simplified geological map of Zimbabwe, indicating the locations of both the Magondi Belt and Dete-Kamativi Inlier (after Master, 1991a). The area covered by the map in Figure 5.2 is indicated by the rectangle. 76

Figure 5.2: Simplified geological map of the Dete-Kamativi Inlier (after Lockett, 1979a, b, 1981). Teardrop shapes mark those locations where samples from the first field season were collected (and as a result, were analysed using LA-ICPMS). The stars mark the locations of samples collected as part of the later fieldwork and were analysed using SIMS.....77

Figure 5.3: Sketch of the depositional environment under which the Malaputese Formation is believed to have developed (after Lockett, 1979b).....77

Figure 5.4: Quartz-Alkali-Plagioclase Streckeisen diagram based on normative analyses of the granitoids samples (Figure 5.4a). *Figure* 5.4b is an AFM diagram *for all the samples* (*where geochemistry is available*). The major element data can be found in Table 5.3 (Appendix A4).....81

Figure 5.5: Hand specimen of Z DK 9C, with its 'salt and pepper' appearance (Figure 5.5a), contrasted with the more pinkish Z DK 10 (Figure 5.5b). In the thin section photomicrograph

of sample Z DK 9C in Figure 5.5c the alteration of hornblende to chlorite is visible as well as the apatite inclusions found in the titanite. Figure 5.5d depicts how sample Z DK 13/8A appears in outcrop, with the leucocratic phase being prominent on an outcrop scale. In thin section however, phenocrysts such as the large orthoclase grain are rare in comparison with the smaller almost completely sericitised feldspars (Figure 5.5e). Sample Z DK 13/5 contains poikiloblastic garnets (Figure 5.5f), which show evidence for having been rotated slightly due to the surrounding biotite and fibrolite laths flowing around the garnets (Figure 5.5g).....84

Figure 5.6: Concordia plots of the LA-ICPMS data for samples Z DK 9C (Figure 5.6a) and Z DK 10 (Figure 5.6b), belonging to the Malaputese Formation. The SIMS data for Z DK 13/8A (Inyantue Formation) and Z DK 13/5 (Tshontanda Formation) appear in Figures 5.6c and d. In the SIMS concordia plots, the blue ellipses represent measurements made on cores and those which are black represent rims, the LA-ICPMS concordia plots however, were not constructed in such a manner.....85

Figure 5.7: Figures 5.7a and b illustrate what samples Z DK 11 and Z DK 13/2 looks like in outcrop. Thin section photomicrograph of sample Z DK 11 clearly shows recrystallised pockets of fine-grained quartz, feldspar and biotite ± muscovite; also indicated in the inset of Figure 5.7c are zircon grains, which tend to occur in these recrystallised pockets. The photomicrograph of sample Z DK 13/2 (Figure 5.7d), indicates that this sample has been affected by retrograde metamorphism, which has resulted in the formation of significant amounts of chlorite. Sample Z DK 1 consists of abundant quartz in addition to large grains of muscovite and microcline feldspar, lending it a pinkish tinge (Figure 5.7 e and f).....87

Figure 5.8: Concordia plot of the LA-ICPMS data for sample Z DK 11 (Figure 5.8a), and the SIMS data for Z DK 13/2 (Figure 5.8b) and Z DK 1 (Figure 5.8c).....88

Figure 5.9: Thin bands of biotite in Z DK 13/6 define its foliation (Figure 5.9a). Mafic xenoliths within Z DK 12 have been observed in outcrop (Figure 5.9b), while in thin section (Figure 5.9c) it is possible to see alteration in the form of myrmekitic textures and altered biotite grains. The three units which constitute sample Z DK 13/7B can be distinguished in (Figure 5.9d): an altered supracrustal component (i), a pegmatitic component (ii) and a

foliated biotite-rich gneiss (iii). The thin section photomicrograph of sample Z DK 13/7B in Figure 5.9e shows how the relict microcline phenocryst (itself with a cryptoperthitic texture) has been affected by brittle deformation, resulting in fracture filling of the twin lamellae by recrystallised quartz. Sample Z DK 2 is clearly porphyritic and aplitic veins can be seen on an outcrop scale (Figure 5.9f), while the photomicrograph in Figure 5.9g illustrates how heavily sericitised the relict microcline phenocrysts are. Sample Z DK 13/10 consists of microcline phenocrysts which have been transformed into augen via shearing; this has been accompanied by recrystallisation of the surrounding quartz and biotite matrix (Figure 5.9h).....90

Figure 5.10: Concordia plots of the SIMS data for samples Z DK 13/6 (Figure 5.10a), Z DK 13/7B (Figure 5.10c) and Z DK 13/10 (Figure 5.10e), as well as the LA-ICPMS data for samples Z DK 12 (Figure 5.10b) and Z DK 2 (Figure 5.10d).....93

Figure 5.11: Sketch map depicting the proposed new extent of the Archaean Zimbabwe Craton and Palaeoproterozoic magmatic arc (after Majaule et al., 2001; McCourt et al., 2001; Mapeo et al., 2004; Kramers et al., 2006; Jacobs et al., 2008; Eglington et al., 2009; Naydenov et al., 2014; Lehmann et al., 2015).....95

Figure 6.1: Simplified regional tectonic map for southern Africa indicating the localities of interest, the area demarcated by the rectangle appears in detail in Figure 6.2 (from Hanson et al., 1988a, and modified after Hanson, 2003). HG = Hurungwe Granite, MG = Makuti Group, MDZ = Mwembeshi Dislocation Zone.....101

Figure 6.2: Simplified geological map of the Choma-Kalomo Block (after Hanson et al., 1988a; Newton, 1963b). Stars indicate sampling localities from this study and correspond with the data in Tables 6.1 and 6.2 (Appendix A5).....102

Figure 6.3: Field photograph (Figure 6.3a) and photomicrograph of the granite sample Z CK 13/3 under cross-polarised light where medium-grained biotite frequently plays host to zircon, and interstitial fine-grained muscovite is associated with recrystallised quartz (Figure 6.3b). Photomicrographs of the leuconorite (sample Z CK 13/2) under cross-polarised and plane-polarised light are shown in Figure 6.3c and d respectively. It is evident from these images that the sample consists of pyroxene (augite and hypersthene), plagioclase and quartz,

which together form a granoblastic texture; there is also evidence of retrograde metamorphism in the form of hornblende which is locally replacing the pyroxene.....108

Figure 6.4: Concordia plots of the SIMS data for the samples Z CK 13/2 (Figure 6.4a) and Z CK 13/3 (Figure 6.4b) as well as the quartz-muscovite schist sample Z CK 13/4C (Figure 6.4c), and quartzite sample Z CK 13/6 (Figure 6.4d). The number of detrital zircons analysed for samples Z CK 13/4C and Z CK 13/6 are, respectively, 10 grains each.....110

Figure 6.5: Field photograph of the Ndonde schist (sample Z CK 13/4C) in outcrop (Figure 6.5a). Photomicrograph under cross-polarised light (Figure 6.5b) illustrating the crenulation cleavage in the schist. The inset of Figure 6.5b, confirms the presence of tourmaline in the sample, whereas the inset to Figure 6.5c demonstrates the heavy mineral-rich foreset laminae in quartzite sample Z CK 13/6. Under plane polarised light the cubic pseudomorphs of haematite after magnetite can be seen to be concentrated in thin irregular bands (Figure 6.5c). Outcrop of schist (sample Z9), showing strong subhorizontal foliation and jointing (Figure 6.5d)……111

Figure 6.6: Concordia plot of the SIMS data collected for sample Z CK 13/1 (Figure 6.6a), where N=9. Figures 6.6b through d are the concordia and relative probability plots for the quartz-biotite-muscovite schist sample Z9. Approximately 120 detrital zircons from this sample were dated using LA-ICPMS.....113

Figure 6.7: U-Pb and Pb-Pb ID-TIMS ages for the various coltan fragments from Chisuki Mine: 12R04B (Figure 6.7a), 12R07 (Figure 6.7b) and 10631 (Figure 6.7c). The Pb-Pb isochron in Figure 6.7d incorporates both coltan and plagioclase fragments from sample 786, which was collected from Kamativi Mine in the Dete-Kamativi Inlier.....115

Figure 6.8: ^{40}Ar-^{39}Ar data obtained on biotite and muscovite separates from samples Z DK 12 and Z DK 13/5, from the Dete-Kamativi Inlier. A Pseudoplateau can indicate that more ^{30}Ar was released or that the errors do not overlap by more than 70%.....116

Figure 6.9: Comparison of the mineralisation ages obtained for the Choma-Kalomo Block and Dete-Kamativi Inlier. Figure 6.9a is a histogram indicating the overlap in ages, while

Figure 6.9b indicates how the various techniques used compare with one another. The ^{40}Ar-^{39}Ar and Pb-Pb data are from this study, while the K-Ar and Rb-Sr data are taken from Priem et al. (1971), Snelling et al. (1972) and Cahen et al. (1984).....119

Figure 7.1: Location and extent of Archaean aged crust within the Magondi Belt (MB), Dete-Kamativi Inlier (DKI) and Zimbabwe Craton. The lettering in bold represents inherited zircon ages and those which are underlined are crystallisation ages.
1 = Makaha, 2 = Mt. Darwin-Dindi, 3 = Chinhoyi-Guruve, 4 = Harare-Shamva, 5 = Norton, 6 = Chegutu, 7 = Midlands, 8 = Gweru-Mvuma, 9 = Shurugwi, 10 = Beatrice, 11 = Mwanesi, 12 = Felixburg, 13 = Bubi, 14 = Bulawayo, 15 = Filabusi, 16 = Shangani, 17 = Gwanda, 18 = Antelope-Lower Gwanda, 19 = Mweza, 20 = Buchwa, 21 = Belingwe, 22 = Masvingo, 23 = Odzi-Mutare-Manica, 24 = Matsitama, 25 = Vumba, 26 = Tati, CKB = Choma-Kalomo Block, C = Choma, K = Kalomo, Ka = Kariba, H = Harare, D = Dett, B = Bulawayo, F = Francistown, KI = Kubu Island and G = Gweta (after, Hanson et al., 1988a; Jelsma et al., 1996, 2004; Jelsma and Dirks, 2002; Lockett, 1979a, 1981; McCourt et al., 2001; Rollinson and Whitehouse, 2011).....124

Figure 7.2: Proposed geological model for the formation of the Magondi Belt. Ages in bold lettering are emplacement ages, whereas those which are underlined represent an older component and finally the ages in plain script represent maximum ages of sedimentation. CKB = Choma-Kalomo Block, DKI = Dete-Kamativi Inlier and MB = Magondi Belt.....125

Figure B1: Depicts the design of a typical Wilfley table (after Grewal, 2016).....205

Figure B2: Demonstrates the component features of a (Charles Cook and Sons) Frantz Magnetic Separator.....206

Figure B3: Illustrating the apparatus used for heavy liquid separations.....207

Figure B4: Grain mount preparation using epoxy as a base.....208

Figure B5: Preferred grain mount geometry for SIMS analyses. By mounting the grains within the inner ring, the edge effect observed in isotopic analyses is greatly reduced. Figure B5a is taken from Andersson (2015).....209

Figure C1: Sketch illustrating how ionisation is improved with oxygen flooding, where E_V: Vacuum level and E_i: Ionisation level (after Arlinghaus, 2014).....214

Figure C2: Sketch of how the secondary ions are separated according to their mass-to-charge ratio (after CAMECA).....215

Figure C3: Simple schematic of how the two types of ion detectors (Electron Multiplier (Figure C3a) and (Figure C3b) Faraday Cup) commonly used in ion probe instruments operate. Images sourced from Wiedenbeck (2012) and Busch (2011) respectively.....216

Figure C4: Secondary ion energy scan with a 50 eV wide energy window, where the signals have been normalised so as to all have the same peak heights. This image illustrates how distinct the ^{238}U energy spectrum is from its molecular counterparts, while in comparison the curve for ^{206}Pb is very similar to that of $^{238}U^{16}O_2$. The curve shape for the latter is also significantly more robust than that of ^{238}U. Figure is after Jeon and Whitehouse (2015).....218

Figure C5: An example of a calibration where the primary beam intensity varied over the course of the session. Both the pressure in the sample chamber and oxygen source remained constant over the course of this session at 2×10^{-5} mbar and 5.4×10^{-5} mbar, respectively.....218

List of Tables

Table 2.1: Decay constants and corresponding half-lives for the U-Pb decay series.....14
Table 2.2: The various reference materials used over the course of this project.....21
Table 2.3: The peak stepping sequence measured during a typical Potsdam 1280-HR analysis.....23
Table 2.4: Full CAF LA-ICPMS U-Th-Pb zircon dating methodology.....A1

Table 3.1: Major and selected trace element analyses for samples from the Magondi Belt....A2
Table 3.2: SHRIMP U-Pb zircon data for samples from the Magondi Belt.....A2
Table 3.3: LA-ICPMS U-Pb zircon data for a sample from the Godzi Volcanic Centre (Magondi Belt).....A2

Table 4.1: SIMS U-Pb zircon data for samples which make up the Magondi Basement.....A3
Table 4.2: ID-TIMS U-Pb data on zircon, apatite, titanite and rutile in samples from the Copper King and Copper Queen Domes.....A3
Table 4.3: ID-TIMS U-Pb data on samples in table 4.2 which contain significant initial Pb.....A3
Table 4.4: LA-ICPMS U-Pb zircon data for the Copper King Dome.....A3

Table 5.1: LA-ICPMS U-Pb zircon data for various rocks within the Dete-Kamativi Inlier.....A4
Table 5.2: SIMS U-Pb zircon data for various rocks within the Dete-Kamativi Inlier.....A4
Table 5.3: Major element analyses for selected samples from the Dete-Kamativi Inlier.....A4

Table 6.1: SIMS U-Pb zircon data from the various rocks within the Choma-Kalomo Block.....A5
Table 6.2: LA-ICPMS U-Pb zircon data for sample Z9, Choma-Kalomo Block.....A5

Table 6.3: ID-TIMS U-Pb coltan data on fragments from the Dete-Kamativi Inlier and Choma-Kalomo Block.....A5
Table 6.4: ID-TIMS Pb-Pb data on coltan and plagioclase fragments from the Dete-Kamativi Inlier.....A5
Table 6.5: ^{40}Ar-^{39}Ar data on mica separates from the Dete-Kamativi Inlier.....A5

List of Abbreviations

GENERAL TERMS

U-Pb: Uranium-Lead

$\delta^{13}C$: Deviation in the carbon isotopic ratio (relative to a reference material)

Ga: Giga-annum (equivalent to 1 billion years)

Ma: Mega-annum (equivalent to 1 million years)

SHRIMP RG: Reverse Geometry, Sensitive High Resolution Ion MicroProbe

LA-SF-ICPMS: Sector Field – Laser Ablation – Inductively coupled Mass Spectrometry

SIMS: Secondary Ion Mass Spectrometry

ID-TIMS: Isotope Dilution – Thermal Ionisation Mass Spectrometry

MB: Magondi Belt

DKI: Dete-Kamativi Inlier

CKB: Choma-Kalomo Block

μm: micro metre (micron)

e: electron

hν: photon

ESA: Electrostatic Analyser

PBMF: Primary Beam Mass Filter

Φ: work function

E_F: fermi level

E_V: vacuum level

E_i: ionisation level

amu: atomic mass unit

RAE: Resistive Anode Encoder

FC: Faraday Cup

EM: Electron Multiplier

RM: Reference Material

sd: standard deviation

RSF: Relative Sensitivity Factor

eV: electron Volts

nA: nano Amps

U^+: Uranium Ion ($^+$ refers to secondary ions generated as a result of sputtering)

IUGS: International Union of Geological Sciences

CL: Cathodoluminescence

BSE: Back Scattered Electron

REE: Rare Earth Element

XPL: Cross polarised illumination

PPL: Plane polarised illumination

TAS: Total Alkalis vs. Silica diagram

AFM: Alkalis-Iron-Magnesium ternary plot

TERMS USED IN THE EQUATIONS

D: number of daughter atoms produced

t: time

P_0: number of parent atoms originally present

λ: decay constant value

P: number of parent atoms remaining

$t_{1/2}$: half-life

M: mass

ΔM: difference in mass

at: atomic weight percent

UNK: unknown

f: fraction of the total ^{206}Pb which consists of the initial lead component

*: radiogenic component

Chapter 1: Introduction

The structure of this thesis is such that the scope of the project is outlined here in Chapter 1, along with a brief description of the regional geology. Chapter 2 is an introduction to U-Pb zircon geochronology and contains detailed descriptions of the various analytical methods employed. Chapters 3 through 6 contain a series of manuscripts, each one focussing on a particular region of interest. The outcomes of these manuscripts have been summarised and are discussed in Chapter 7.

1.1 REGIONAL GEOLOGY OF THE MAGONDI BELT

As can be seen in Figure 1.1, the area of interest is primarily in north-western Zimbabwe, but extends into the south-eastern portion of Zambia. A significant fraction of this area is obscured by younger Karoo and Kalahari aged sediments, providing added complexity in determining how these terrains are related to one another.

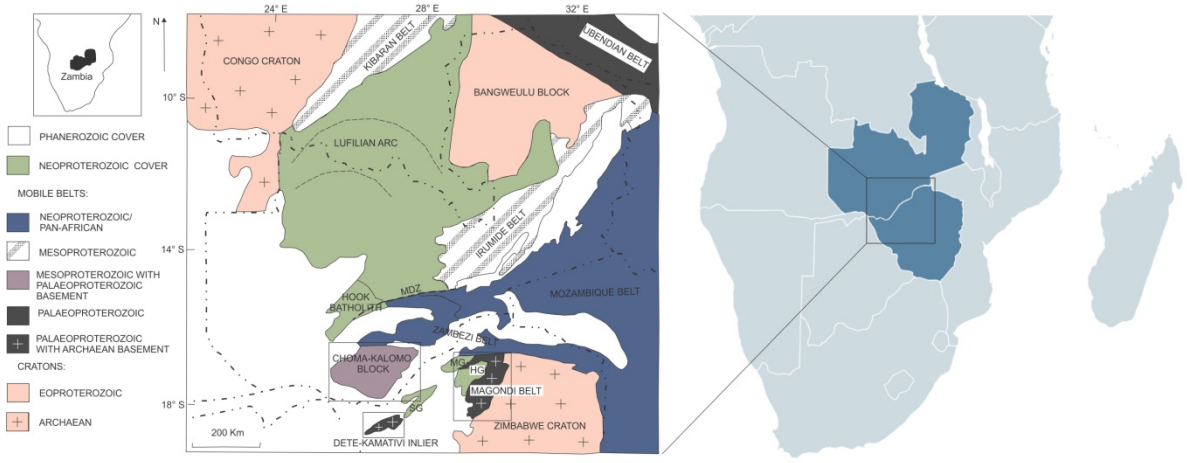

Figure 1.1: Geological and geographical maps of central Africa depicting the location of the Choma-Kalomo Block, Magondi Belt and Dete-Kamativi Inlier; after Hanson et al. (1988a); Wikipedia (2016) and Wikimedia commons (2015).

1.1.1 The Magondi Belt and Basement

The Magondi Belt is a Palaeoproterozoic NE-trending mobile belt, approximately 250 km in

length and 50 km wide (Leyshon and Tennick, 1988), and it is bounded on its eastern flank by the Archaean Zimbabwe Craton and the Pan-African Zambezi Belt to the north. The Magondi Belt is composed of a succession of supracrustal metasediments and minor metavolcanics, and is subdivided into the Deweras, Lomagundi and Piriwiri Groups – these can be found within the greenschist to amphibolite-grade facies part of the belt. High-grade intrusive granitoids like the Hurungwe Gneiss (Figure 1.2) are located in the more northern reaches of the belt and are associated with allochthonous units (such as the Makuti Group), which are in unconformable contact with the Zimbabwe Craton. Some of these units and other high-grade intrusives were initially thought by Master (1991b, 1996) to represent Archaean basement, and were therefore interpreted to be a precursor to the Magondi orogeny (Leyshon and Tennick, 1988; Master et al., 2010; McCourt et al., 2001).

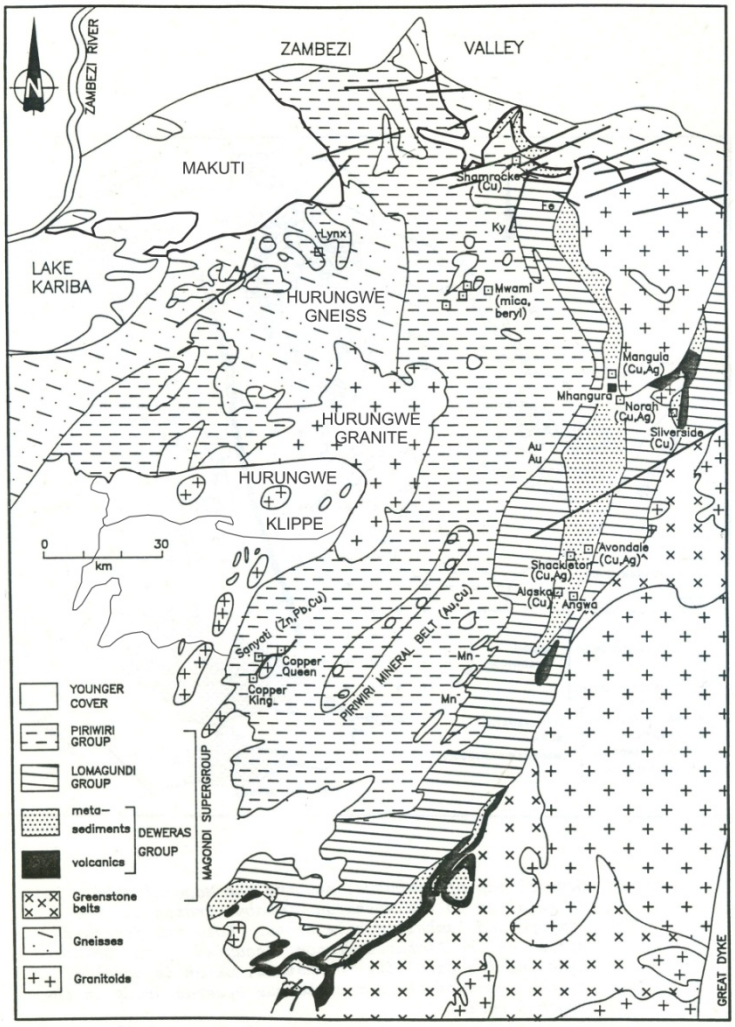

Figure 1.2: Detailed map of the Magondi Belt and some of the so-called 'basement' gneisses to the north. The map is after Master (1991a) and McCourt et al. (2001).

The high-grade rocks in the northern parts of the Magondi Belt consist of a series of variable para - and orthogneisses, some of which belong to the Zambezi Belt, while others were considered older (Broderick, 1976, 1981). The Magondi Supergroup on the other hand consists of the Deweras Group, which is in general known to be unconformable with the underlying granite-greenstone basement; while the Lomagundi and Piriwiri Groups represent a marine transgression over the Deweras Group sediments, as a result of protracted subsidence. Deposition of the Magondi Supergroup was terminated *circa* 2.0 Ga ago due to the Magondi orogeny as evidenced by the emplacement of collisional granitoids between 1.99 and 1.96 Ga (Treloar, 1988; Master et al., 2010; McCourt et al., 2001).

1.1.2 The Dete-Kamativi Inlier

The Dete-Kamativi Inlier is a window of Precambrian rocks surrounded by late Palaeozoic sediments exposed in north-west Zimbabwe. The Inlier consists of a set of four NE-trending supracrustal units: namely the Malaputese, Inyantue, Kamativi and Tshontanda Formations. Each is composed of deformed and metamorphosed supracrustal sediments separated from one another by granitic gneisses (Lockett, 1979a, b). The various protoliths for the rocks within the four units have been interpreted by Lockett (1979a, b) and Master et al. (2010) to vary from a shallow marine environment to a deep water environment, in a manner similar to the units within the neighbouring Magondi Belt. In addition to this, the Tshontanda and Kamativi Formations are known to host abundant tin pegmatites (Lockett, 1979a, b).

1.1.3 The Chomo-Kalomo Block

The Choma-Kalomo Block is a NE-trending, predominantly Mesoproterozoic terrane, located in southern Zambia. It consists of a sequence of metasediments sandwiched between younger granitic rocks of the Choma-Kalomo Batholith and the Karoo-aged sediments to the south-east which separate it from the Magondi Belt (Bulambo et al., 2004, 2006; Matheson, 1969). The intrusive Choma-Kalomo Batholith, dated by Bulambo et al. (2004, 2006) and Hanson et al. (1988a) is composed of several discrete granitic plutons, the ages of which represent two phases of emplacement and coeval deformation at 1.37 and 1.18 Ga. The older metasediments of the Choma-Kalomo Block, much like the Dete-Kamativi Inlier, have been intruded by numerous tin-bearing pegmatites (Matheson, 1969).

1.2 INITIAL SCOPE OF THIS THESIS

The initial aim of this project was limited to using U-Pb geochronology to date (both detrital and igneous) zircons from Magondi Supergroup samples in order to provide more accurate constraints on the timing of deposition for these sediments. The Magondi Supergroup was chosen because amongst the three stratigraphic units which make up the Supergroup, the Lomagundi Group is significant – as it records a global, positive $\delta^{13}C$ marine carbonate excursion first defined by Schidlowski et al. (1976). The carbonates in the Lomagundi Group have since been described as the type locality for this excursion, which occurred sometime between 2.2 and 2.1 Ga, after the rise in atmospheric oxygen, during the Palaeoproterozoic glacial epoch between 2.45 and 2.32 Ga (Master et al., 2010). Properly constraining the timing of the "Lomagundi Excursion" would prove to be hugely beneficial, as there are several excursions of this age worldwide, implying that there was widespread burial of organic carbon as a result of an oxygen-rich atmosphere. This information could therefore be used to gain insight into past ocean circulation patterns and redox states (Master et al., 2010; Schröder, et al., 2008).

The results obtained on the Magondi Supergroup samples (those presented in Chapter 3) prompted further research, as it was possible to make new and important inferences about tectonic events which affected not only the Magondi Belt, but some of the adjacent terrains. Hence, the scope of the project then expanded to encompass the evolution of the Magondi Belt, which entailed obtaining ages for the basement rocks to the north-west of the main Magondi Belt, the Dete-Kamativi Inlier to the west and the Choma-Kalomo Block in south-east Zambia (refer to Figure 1.1, for locations).

1.2.1 Subsequent objectives

Magondi Basement

Exposed granites and gneisses in the northern, high-grade part of the Magondi Belt as well as on the Zambian side of Lake Kariba (also believed to reflect basement to the Magondi Belt), were collected for dating to ascertain the extent of this late Archaean Hurungwe orogeny. These granitoids according to Master (1991b, 1996) were believed to predate the Palaeoproterozoic Magondi orogeny, and would therefore provide valuable information relating to the early evolution of the Magondi Belt at the western margin of the Zimbabwe Craton.

Dete-Kamativi Inlier

As noted above, within the Dete-Kamativi Inlier are four metasedimentary units, believed to be correlatives of the Magondi Belt (Master et al., 2010). The goal here was to confirm this, and if successful, it would then mean that the Dete-Kamativi Inlier could be considered as an extension of the Magondi Belt. Additionally, according to Lockett (1979a, b) the granitic gneisses which make up over half the Inlier are simply considered to be of various ages; thus, a number of these were also sampled in order to confirm their exact ages.

Choma-Kalomo Block

The Choma-Kalomo Block could potentially be considered a possible correlative of the Dete-Kamativi Inlier – primarily due to similarities in the nature of their respective tin pegmatite deposits (Lockett, 1979a, b). Studies by workers such as Hanson et al. (1988a) and Bulambo et al. (2004, 2006) focussed primarily on dating the granitic units which make up the Choma-Kalomo Batholith, and as a result there had not been any direct dating of the basal metasediments which host the mineralisation.

1.3 APPROACH

This project initially started out as an MSc Dissertation, and thus sample collection was ultimately split over two field seasons, as it was necessary to return at a later date and collect additional samples for dating. The first field season took place over two weeks in mid 2011. The primary focus at the time was to collect samples from the Magondi Belt. Five of these first samples were chosen to be dated using the Sensitive High Resolution Ion MicroProbe (SHRIMP) at the Research School for Earth Sciences at the Australian National University in Canberra, while the nine remaining samples were subsequently dated using Laser Ablation – Inductively Coupled Mass Spectrometry (LA-ICPMS) at the University of Stellenbosch's Central Analytical Facility. The samples were prepared according to the standard mineral separation methods outlined in Appendix B1 at the Earth Lab (University of the Witwatersrand). During this time small reserves of the individual samples were used to prepare thin sections as well as perform major and trace element analyses on selected samples.

The project was approved to be upgraded to PhD status in early 2013, roughly around the same time that an application to study in Potsdam, Germany, at the Deutsches GeoForschungsZentrum (GFZ), was accepted. This guest scientist position entailed receiving

two years of training on Ion Probe instrumentation – specifically the newly acquired CAMECA 1280-HR. The decision was made to work part-time on the thesis, while based in Potsdam, as this afforded the unique possibility to receive hands-on training analysing the very samples collected during the second field season (carried out in late 2013) using the Secondary Ion Mass Spectrometer (SIMS) 1280-HR. The seventeen samples collected during the second field season were all prepared and analysed at the GFZ. Sample preparation was much the same as previously; with some exceptions regarding the preparation of grain mounts (refer to Appendices B2 and B3 for details). An additional three samples of columbite-tantalite (coltan) from pegmatites within the Choma-Kalomo Block were analysed at the Earth Sciences Centre of the University of Toronto in Canada, by Isotope Dilution – Thermal Mass Spectrometry (ID-TIMS), and the results combined with unpublished data of D.W. Davis for a further seven samples. The ^{40}Ar-^{39}Ar dating (conducted at the University of Johannesburg) comes from two samples which were collected during the first field season but were only dated in 2015.

1.4 SUMMARY OF SCIENTIFIC CONTRIBUTIONS

Chapters 3 through 6 contain manuscripts in various stages of assessment: Chapters 5 and 6 respectively are being prepared for and submitted to *Precambrian Research*, whereas Chapters 3 and 4 are intended for two well respected local geoscientific journals – *South African Journal of Geology* and the *Journal of African Earth Sciences* respectively.

1.4.1 The Magondi Belt

Chapter 3 contains the most recent geochronology available for the Magondi Supergroup. It has been well documented that the Zimbabwe and Superior Cratons have a similar record of mafic intrusive events between 2.5 and 2.4 Ga, with rifting believed to have initiated sometime around 2.26 Ga. However, the ages for the Deweras Group samples collected are primarily Archaean in age (2.86 and 2.64-2.63 Ga), but this has been attributed to the zircons being primarily derived from the Archaean granite-greenstone basement of the Zimbabwe Craton. It is also uncertain whether the volcanic centres (found almost exclusively within the Piriwiri Group) represent an extensive volcanic event or localised intrusions. The Nyamakari and Godzi centres likewise reflect inheritance from the granite-greenstone basement but are believed to have erupted sometime around 2.25 Ga. The Lomagundi Group was deposited between 2204 and 2071 Ma, and the Piriwiri Group between 2163 and 1997 Ga. The

recurrence of ages between 2.8 and 2.6 Ga, in addition to inherited zircon grains (as old as 3.34 Ga), supports the general notion that the basement below the Magondi Belt is Archaean.

1.4.2 The Magondi Basement

Chapter 4 is titled "The vanished orogeny" as it was suggested by Master (1991b) that an Archaean orogeny was represented by the high-grade gneisses in the northern part of the Magondi Belt. In actual fact, these supposed basement granites and gneisses are Palaeoproterozoic in age, being syn - to post-tectonic with the Palaeoproterozoic Magondi orogeny, which occurred between 2.2 and 2.0 Ga. Our results indicate the presence of both late syn - tectonic intrusives (the 2020 Ma Hurungwe orthogneiss), as well as 1967 and 1952 Ma post-tectonic intrusives within the northern reaches of the Magondi Belt, in the form of a Zambian migmatitic orthogneiss in Manchinchi Bay and the sample of Kariba Granite. Additionally, the migmatitic orthogneiss was shown to have zircons with younger metamorphic overgrowth rims that are Pan-African in age (545 Ma) – a result of the collision between the Kalahari and Congo Cratons in the Neoproterozoic.

The Magondi orogeny was also the heat source for a mineralisation and metamorphic event which affected a wide area, including the Copper King and Copper Queen Domes between 2.15 and 2.03 Ga.

Author Contributions - Chapter 4

Master, S., Glynn, S.M., Davis, D.W., Wiedenbeck, M. and Frei, D. (In Preparation). The vanished orogeny: Geochronology of Palaeoproterozoic "basement" gneisses of the Kariba area, western Magondi Belt (Zimbabwe and Zambia).

Glynn – **45%**: collected and processed the SIMS data, produced the figures, wrote the manuscript

Master – 20%: reviewed the manuscript

Davis – 20%: collected the ID-TIMS data, contributed to the analytical methods section

Wiedenbeck – 10%: assisted S.M Glynn in collecting and interpreting the SIMS data

Frei – 5%: collected the LA-ICPMS data for one of the samples

1.4.3 The Dete-Kamativi Inlier

The focus of Chapter 5 is the Dete-Kamativi Inlier – which for many years has been suspected of being a continuation of the Magondi Belt. Dating done on a number of samples collected from the Inlier confirms that the metasediments within the Dete-Kamativi Inlier are

similar in age to units within the Magondi Belt. Detrital zircons from paragneisses within the Malaputese Formation (Dete-Kamativi Inlier) have ages ranging from 2.8 to 2.5 Ga, with the youngest grains constraining deposition to be *circa* 2.3 Ga. In terms of age and lithology it is therefore possible to correlate the Malaputese Group with the Deweras Group (maximum sedimentation age of approximately 2.29 Ga). Additionally, the first recorded Archaean ages within the Dete-Kamativi Inlier of 2769 and 2694 Ma provide strong evidence that the basement in the vicinity of the Dete-Kamativi Inlier is Archaean in age. Thus we propose that the Archaean Zimbabwe Craton extends as far west as the Dete-Kamativi Inlier. The Dete-Kamativi Inlier also contains evidence for the existence of a Palaeoproterozoic arc along the western margin of the Zimbabwe Craton, as various granites and gneisses within the Dete-Kamativi Inlier (in addition to a number of localities in Botswana) have crystallisation ages between 2.06 and 2.02 Ga.

Author Contributions - Chapter 5

Glynn, S.M., Master, S., Frei, D. and Wiedenbeck, M. (In Preparation). U-Pb zircon geochronology from the Dete-Kamativi Inlier, NW Zimbabwe with implications for the western margin of the Archaean Zimbabwe Craton.

Glynn – **50%**: collected the SIMS data, produced the figures, wrote the manuscript

Master – 25%: reviewed the manuscript

Frei – 15%: assisted S.M Glynn in collecting the LA-ICPMS data, processed the data, wrote part of the analytical methods section

Wiedenbeck – 10%: assisted S.M Glynn in collecting and interpreting the SIMS data, reviewed the manuscript

1.4.4 The Choma-Kalomo Block

Chapter 6 focuses on the Choma-Kalomo Block and in particular its ties to the Dete-Kamativi Inlier. Previously considered to be solely Mesoproterozoic, our new detrital zircon ages reveal an abundant Palaeoproterozoic component (2049 - 1861 Ma) within the metasedimentary sequence; thus the protoliths of these older units were derived from the Magondi Belt. Also ^{40}Ar-^{39}Ar and Pb-Pb data on tin pegmatites, common to both terranes, implies that the style and timing of mineralisation was concurrent, and that the Choma-Kalomo Block and Dete-Kamativi Inlier were certainly juxtaposed by 1060 Ma when the pegmatites were emplaced.

Some previous models for the formation of the Choma-Kalomo Block have it as an exotic terrane with respect to the Archaean Zimbabwe Craton and Palaeoproterozoic Magondi Belt. However our new ages contest this, and instead a new model is proposed whereby the thinner lithosphere beneath the Choma-Kalomo Block is either a primary feature or it resulted from subduction erosion, and delamination processes associated with the formation of continental margin magmatic arcs.

Author Contributions - Chapter 6

Glynn, S.M., Master, S., Wiedenbeck, M., Davis, D.W., Kramers, J.D., Belyanin, G.A., Frei, D. and Oberthür, T. (Under Review). The Proterozoic Choma-Kalomo Block, SE Zambia: exotic terrane or a reworked segment of the Zimbabwe Craton?

Glynn – **30%**: collected the SIMS data, produced the figures, co-wrote the manuscript

Master – 25%: co-wrote and reviewed the manuscript

Wiedenbeck – 10%: assisted S.M Glynn in collecting and interpreting the SIMS data as well as wrote part of the analytical methods section, reviewed the manuscript

Davis – 10%: collected the ID-TIMS data, wrote part of the analytical methods section

Kramers and Belyanin – 10%: collected the Ar-Ar data and interpreted the results, wrote part of the analytical methods section

Oberthür – 10%: reviewed the manuscript, collected the ID-TIMS data

Frei – 5%: collected and processed the LA-ICPMS data for one sample

1.4.5 Research outputs

Over the course of this project, the candidate has produced several research products that are comprised of two manuscripts (which have been submitted for peer review), and a further two which are in preparation, as well as eleven conference abstracts related to this PhD Thesis.

The following manuscript (located in appendix D1); resulted from the unexpected ages obtained from a quartzite of the Sijarira Group, and has been submitted to the *International Journal of Earth Sciences*.

Author Contributions

Master, S., Glynn, S.M. and Wiedenbeck, M. (Under Review). U-Pb ages and provenance of zircons from the Neoproterozoic Sijarira Group, Western Zimbabwe – an Antarctica connection?

Master – 70%: wrote the manuscript
Glynn – **20%**: collected the SIMS data, produced some figures, reviewed the manuscript
Wiedenbeck – 10%: assisted S.M Glynn in collecting the SIMS data, reviewed the manuscript

The conference abstracts listed below are included as appendix D2.

- Sharad Master, Sarah M. Glynn, Michael Wiedenbeck. (2016). New age constraints on the Neoproterozoic Sijarira Group, in the Chizarira Hills, western Zimbabwe, with implications for regional correlations. 26th Colloquium of African Geology, Ibadan, Nigeria.
- S.M. Glynn, S. Master, M. Wiedenbeck, D. Davis, D. Frei, T. Oberthür. (2016). New U-Pb SIMS zircon geochronology on the Dete-Kamativi Inlier (NW Zimbabwe) and the Choma-Kalomo Block, of SE Zambia. Igneous and Metamorphic Studies Group Meeting, Cape Town, South Africa.
- S.M. Glynn, S. Master, M. Wiedenbeck, D. Davis, D. Frei, T. Oberthür. (2015). Implications for the extent of the Zimbabwe Craton, from U-Pb zircon geochronology of the Dete-Kamativi Inlier (NW Zimbabwe) and the Choma-Kalomo Block, of SE Zambia. Geological Society of Zimbabwe Annual Summer Symposium, Kariba, Zimbabwe.
- S. Master, S. Glynn, D. Frei, M. Wiedenbeck. (2015). The Choma-Kalomo Block, SE Zambia: exotic terrane, or a metacratonic segment of the Zimbabwe Craton? 14th South African Geophysical Association Biennial Technical Meeting and Exhibition, Drakensburg, South Africa.
- Glynn, S.M, Wiedenbeck, M, Master, S, Frei, D. (2015). New U-Pb zircon geochronology of the Choma-Kalomo Block (Zambia) and the Dete-Kamativi Inlier (Zimbabwe), with implications for the extent of the Zimbabwe Craton. European Geosciences Union Meeting, Vienna, Austria.
- S. Master, S. Glynn, D. Frei, D. Davis and T. Oberthür. (2013). New U-Pb and Pb-Pb geochronology of rocks and minerals from the Proterozoic Dete-Kamativi Inlier (Zimbabwe) and Choma-Kalomo Block (Zambia): regional implications. Geological Society of Zimbabwe Annual Summer Symposium, Victoria Falls, Zimbabwe.
- Glynn, S.M, Master, S, Armstrong, R.A, Hofmann, A and Bekker, A. (2013). New U-Pb (SHRIMP) ages for the Palaeoproterozoic Magondi Supergroup, Zimbabwe. 7th Biennial Geo-SIMS Workshop, Potsdam, Germany.

- Glynn, S.M Master, S and Frei, D. (2013). Refining the Margin of the Zimbabwe Craton: New U-Pb Zircon ages from the Dete-Kamativi Inlier, NW Zimbabwe. Deutsche Mineralogische Gesellschaft Meeting, Tübingen, Germany.
- Sharad Master, Sarah Glynn and Dirk Frei. (2013). New U-Pb zircon geochronology of the Palaeoproterozoic Dete-Kamativi Inlier, Magondi Belt, Zimbabwe, and implications for the western boundary of the Archaean Zimbabwe Craton. 24th Colloquium of African Geology, Johannesburg, South Africa.
- Glynn, S.M, Master, S, Armstrong, R.A, Hofmann, A and Bekker, A. (2012). New U-Pb ages for the Palaeoproterozoic Magondi Supergroup, Zimbabwe. Craton Formation and Destruction Workshop, Johannesburg, South Africa.
- Glynn, S.M, Master, S, Armstrong, R.A, Hofmann, A and Bekker, A. (2012). New U-Pb (SHRIMP) ages for the Palaeoproterozoic Magondi Supergroup, Zimbabwe. Igneous and Metamorphic Studies Group Meeting, Johannesburg, South Africa.

An additional three peer reviewed conference abstracts highlight the candidate's involvement in the establishment of the 1280-HR laboratory during her stay as a guest scientist at the GFZ, Potsdam in Germany. The abstracts are included as appendix D3.

- Sarah Glynn, Michael Wiedenbeck, Frédéric Couffignal, Abiel Kidane, Alexander Rocholl, Robert Trumbull (2016). Performance capabilities of the Cameca 1280-HR SIMS instrument and its role in a virtual SIMS network. Mineralogical Analytical Techniques Workshop, Johannesburg, South Africa.
- Wiedenbeck, M, Couffignal, F, Glynn, S, Kidane, A, Rocholl, A, Trumbull, R. (2015). Performance capabilities of the Cameca 1280-HR SIMS instrument. Geoanalysis, Leoben, Austria.
- Rocholl, A, Wiedenbeck, M, Couffignal, F, Glynn, S, Kidane, A, Alonso-Perez, R. (2015). The microanalytical Reference Material programme at the Potsdam SIMS Laboratory. Geoanalysis, Leoben, Austria.

During her stay at the GFZ, the candidate was also involved in a number of projects utilising her experience in dating zircons with the 1280-HR. Below is a list of manuscripts which mark her involvement in the projects.

- Zhu, J, Zhang, Z, Glynn, S, Jin, Z, Wiedenbeck, M, Ye, J. and Hou, T. (In preparation). The Emeishan flood basalts of SW China and their role in the two Permian mass extinctions: New evidence from volcanic tuffs.
- Słodczyk, E, Pietranik, A, Glynn, S, Wiedenbeck, M, Breitkreuz, C and Duime, B. (Submitted to *Lithos* for review). Contrasting sources of late Paleozoic rhyolite magma in the Polish Lowlands: evidence from U-Pb zircon ages, Hf and O isotopic composition.

Chapter 2: Analytical Methods

2.1 WHY ZIRCON?

Zircon is widely used in geochronology for three main reasons:

- When zircon crystallises, it preferentially excludes large Pb^{2+} ions from the crystal lattice in favour of the smaller U^{4+} and Th^{4+}, and thus Pb in general is prevented from entering the crystal lattice. The end result is high initial U/Pb and Th/Pb ratios at the time of crystallisation (Faure and Mensing, 2005).
- Zircon is a common accessory mineral (particularly in silicate rocks), and is abundant enough to be extracted with minimal effort.
- Zircon is a robust mineral, capable of withstanding high temperature and pressure conditions as well as sedimentary transport over long distances. This robustness plays a key role in zircon's usefulness as a geochronometer because the radiogenic lead which has been generated cannot easily escape the crystal lattice, unless the lattice becomes damaged.

The reasons outlined above give zircon a distinct advantage and popularity over other minerals such as monazite, titanite, xenotime and baddeleyite which are also commonly used for U-Pb geochronology (e.g. Li et al., 2013; Stern and Berman, 2000), and naturally each has its own pitfalls which must be overcome.

2.2 THE U-Pb SYSTEM

The concept behind radioactive decay is simply that some elements have isotopes (atoms with the same atomic number, but a different mass number) which are naturally radioactive; that is, the nucleus is unstable and breaks down or decays at a characteristic rate to the isotope of a different element. This process continues until an element with a stable nucleus is formed (Williams, 1998).

$$D = P_0 (1 - e^{-\lambda t}) \quad (1)$$

The above expression describes the equation fundamental to radioactive decay: where the number of daughter atoms produced (D) within a unit of time (t) is exponential to the number of parent atoms originally present (P_0). The characteristic rate at which an element breaks down is represented by (λ) the decay constant.

Equation 1, written more conventionally to express the ratio between the number of daughter atoms produced and the number of parent atoms remaining (P) is:

$$\frac{D}{P} = e^{\lambda t} - 1 \qquad (2)$$

In order for an isotopic system to be suitable for geochronology it should ideally cover a long time span, and this is dependent on the rate of decay. The rate of decay is more easily represented as the half-life ($t_{1/2}$) of a radio isotope (refer to Table 2.1 for the U-Th-Pb system half-lives); this is defined as the time it takes for half the parent isotope to decay to the stable daughter product.

Table 2.1: Decay constants and corresponding half-lives for the U-Pb decay series

Decay Series	λ Decay Constant (years^{-1})	Half-Life
$^{238}U \rightarrow {}^{206}Pb$	1. 1.55125 x 10^{-10}	4446 Ma
$^{235}U \rightarrow {}^{207}Pb$	9. 9.8485 x 10^{-10}	704 Ma
$^{232}Th \rightarrow {}^{208}Pb$	9. 49475 x 10^{-11}	14.045 Ga

The decay constants are taken from Steiger and Jäger (1977) and the half-lives for the uranium species are quoted in Jaffey et al. (1971) and for ^{232}Th in Browne et al. (1986).

The half-life is defined by the decay constant used, and is calculated by means of the following formula:

$$t_{1/2} = \frac{\ln 2}{\lambda} \qquad (3)$$

The U-Pb decay series is made up of three decay chains: ^{238}U to ^{206}Pb, ^{235}U to ^{207}Pb and ^{232}Th to ^{208}Pb as illustrated in Figure 2.1. T here are, however, four stable isotopes of lead; the

remaining isotope ^{204}Pb is non-radiogenic. Non-radiogenic lead (often referred to as common lead) encompasses (1) initial lead, which has existed inside the mineral since the time it crystallised and (2) lead as a result of contamination, commonly introduced by way of sample preparation, but can occur naturally prior to sampling, and is commonly found either in cracks or inclusions within grains.

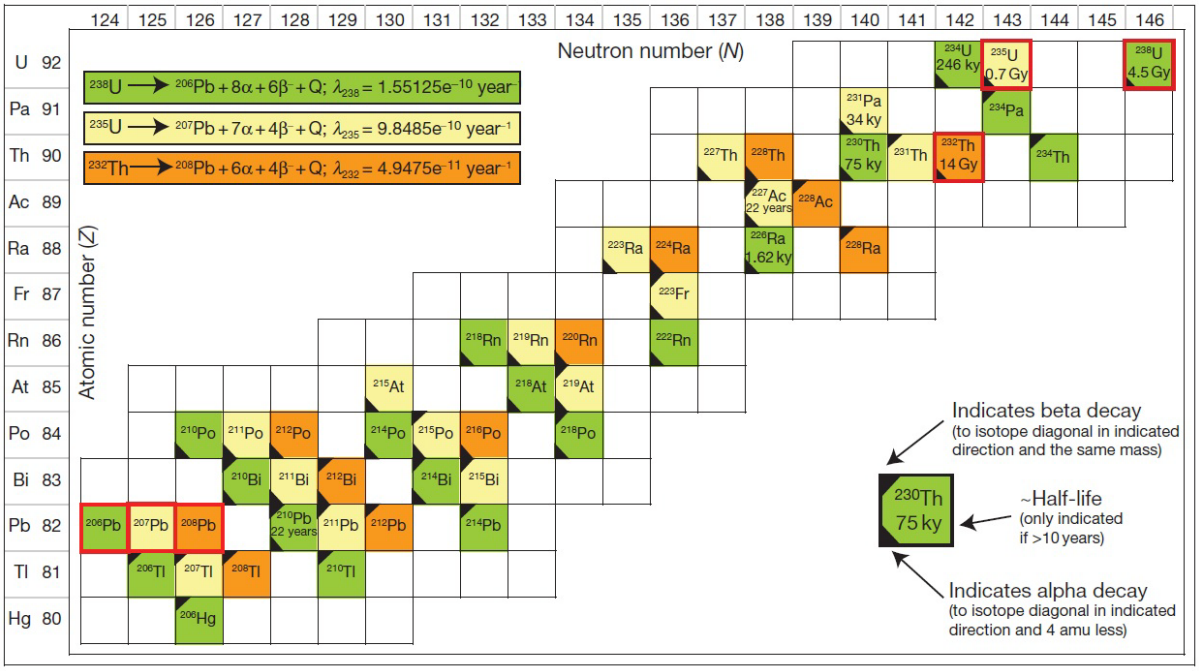

Figure 2.1: Graphic representation of the three decay chains for ^{238}U, ^{235}U and ^{232}Th (Schoene, 2014). The rate of radioactive decay for each isotope is indicated by a number of alpha and beta decays, before reaching the stable daughter product.

2.3 INSTRUMENTATION

2.3.1 Laser Ablation - Inductively Coupled Plasma Mass Spectrometry (LA-ICPMS)

The principle of laser ablation was first applied to U-Pb geochronology in the 1990s (Schoene, 2014). This simple addition to an ICPMS allowed solid samples to be analysed with the use of a high-powered laser that ablates the surface of a sample. Ablation, as defined by Thomas (2004), involves aerosolising a small area of a solid's surface by converting the photons generated by the laser into heat energy.

LA-ICPMS units – such as the one in Figure 2.2 – typically consist of two main parts: (1) the laser ablation system which includes the sample cell and (2) the ICPMS, which consists of the plasma interface and mass spectrometer. The sample is placed within the sample cell and targeted with the laser. The now ablated (aerosolised) sample is swept into the ICPMS via a gas stream. The aerosolised material is first ionised using a high temperature argon plasma torch, and the resulting positive ions are then transferred to the mass spectrometer where they are separated according to their mass-to-charge ratio (Thomas, 2004).

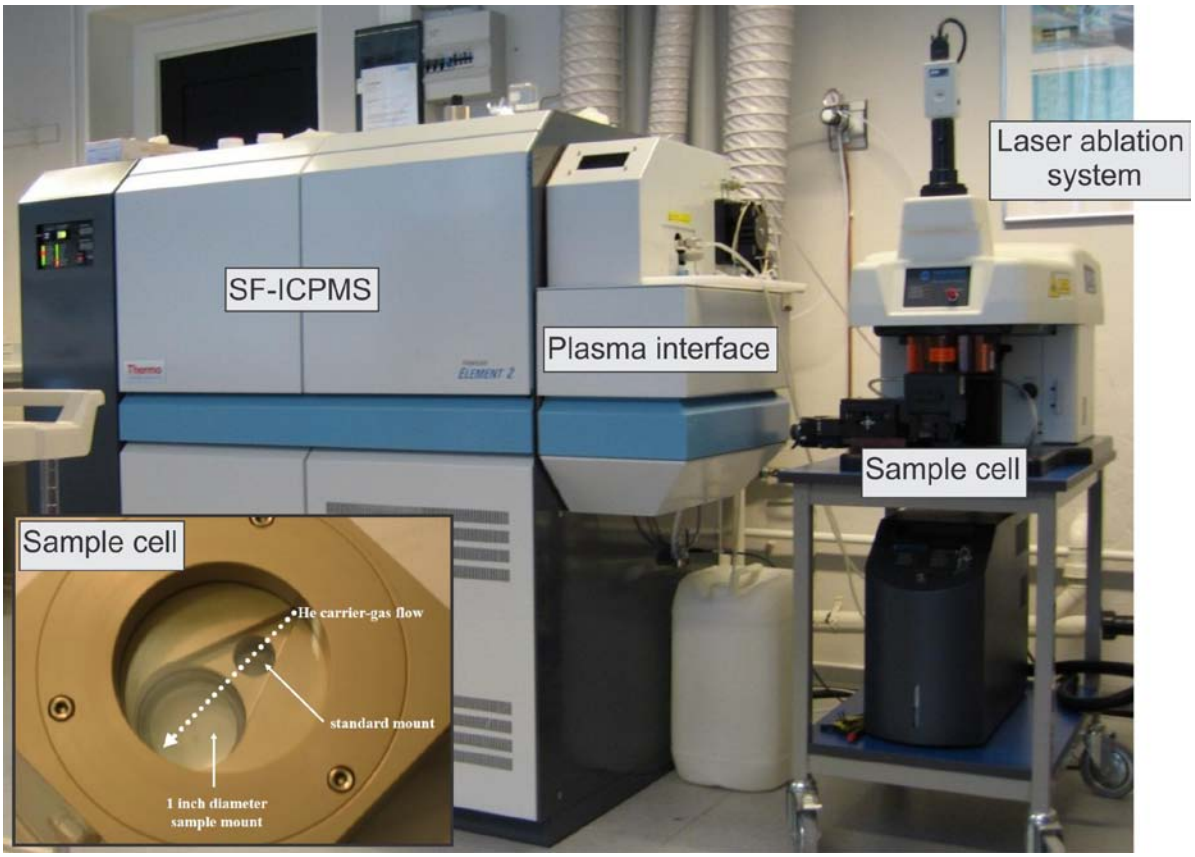

Figure 2.2: Photograph showing the LA-SF-ICPMS setup at the University of Stellenbosch's Central Analytical Facility, which consists of a Thermo Element 2 Sector Field-ICPMS equipped with a New Wave UP 213 Laser Ablation system. Spot sizes using this instrument were typically on the order of 30 µm in diameter and 20 µm deep. Photo supplied by Prof. Dirk Frei.

2.3.2 Secondary Ion Mass Spectrometry (SIMS)

Secondary Ion Mass Spectrometry, as the name suggests, involves analysing the secondary ions generated by the impact of a primary ion beam with the sample surface. This process –

which is referred to as sputtering – is demonstrated in Figure 2.3. For geological applications the primary beam used can consist of either oxygen ($^{16}O^-$ / $^{16}O_2^-$) or cesium ($^{133}Cs^+$) ions, depending on the polarity of the secondary ions which are to be measured – for zircon measurements a primary $^{16}O_2^-$ beam is used. The use of $^{16}O_2^-$ is just one parameter which can be adjusted in order to improve the useful ion yield. By just using an oxygen species with a higher mass for example, it will strike the sample surface with more force, thus sputtering more material. It is also possible to alter the current (i.e. number of primary ions produced), energy (speed at which the ions hit the surface) or angle of incidence of the primary ion beam (Arlinghaus, 2014). The resulting sputtered material consists primarily of neutral particles, and to a lesser degree electrons, photons and atoms belonging to both the sample and primary beam (Arlinghaus, 2014; Stern, 2009; Wiedenbeck, 2012).

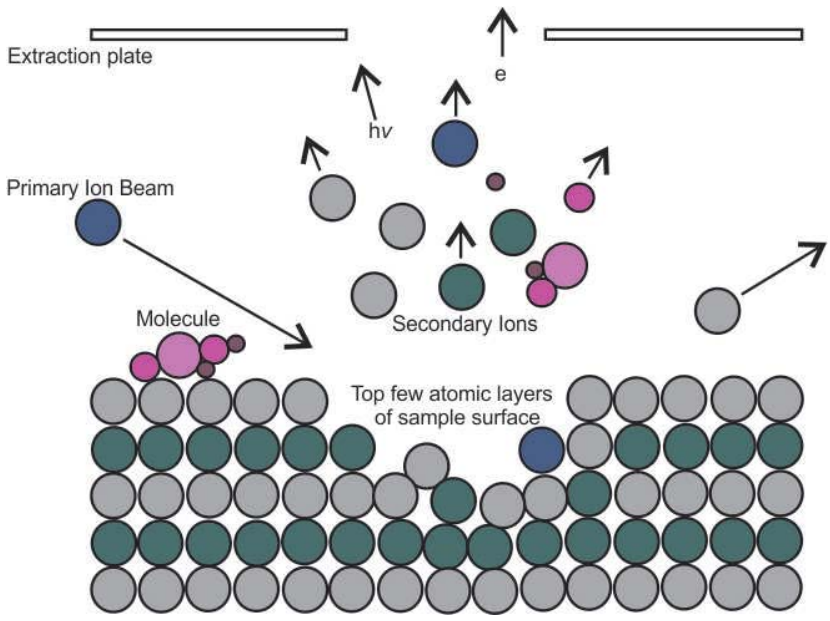

Figure 2.3: Sketch (after Arlinghaus, 2014) depicting how the sputtering process works: a collision cascade is initiated when the primary beam interacts with the sample; because of this, ions of the primary beam can become implanted in the sample surface or extracted along with the secondary ions and other particles such as electrons (e) and photons (hv). Molecules can become broken up (either into their constituent atoms or into molecular fragments) only when the binding energy is overcome by the kinetic energy of the primary beam.

The secondary ions are then extracted, and directed via the transfer section (refer to Figure 2.6 for a schematic view of the ion optics), into an Electrostatic Analyser (ESA) and magnet due to a potential applied to the sample holder. The ESA and magnet are responsible for

separating the ions according to their mass-to-charge ratio (Wiedenbeck, 2012; Williams, 1998). This is accomplished via a double focusing effect which is explained in more detail in Appendix C1, in addition to several other design features of SIMS instrumentation which aid U-Pb measurements.

Australian Scientific: Sensitive High Resolution Ion MicroProbe (SHRIMP)

The SHRIMP I was designed and built in the 1970s, by Dr. Steve Clement and Prof. William Compston. Further modifications eventually led to the development of the SHRIMP II and SHRIMP RG (ANU, 2014). The Reverse Geometry SHRIMP design, pictured in Figure 2.4 and housed at the Research School of Earth Sciences at the Australian National University in Canberra makes use of a modified optical design, whereby the position of the magnet and the ESA are reversed. This configuration was meant to improve on t he mass resolution capabilities of the instrument, while still maintaining high transmission. The reverse geometry design is no longer in use in the currently available SHRIMP IV.

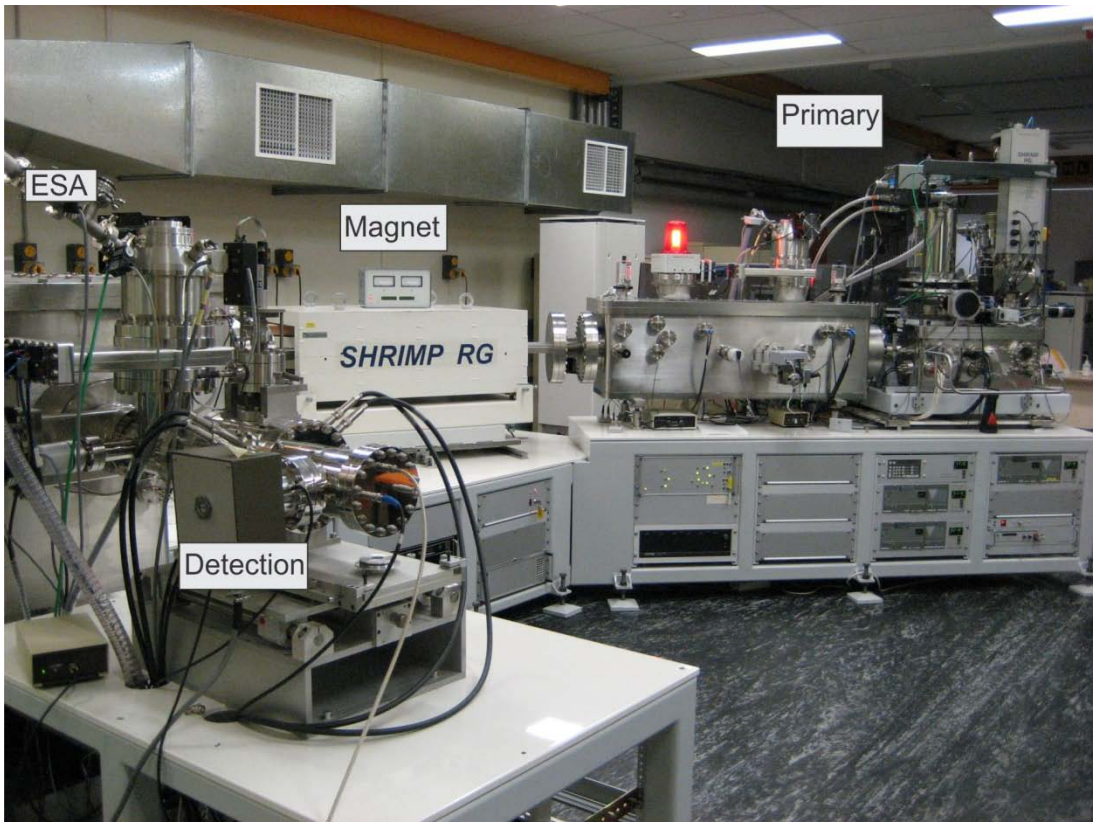

Figure 2.4: Photograph showing the configuration of the Reverse Geometry SHRIMP housed at the ANU (note the placement of the magnet before the electrostatic analyser); photo is author's own.

CAMECA: 1280-HR

The first SIMS instruments were being developed as early as the 1940s before either CAMECA or Australian Scientific were established (in 1978 and 1989 respectively). According to de Chambost (2011), in the 1960s Georges Slodzian and Raimond Castaing began work on the first small geometry ion probes. The first in the series was the IMS 3F, and this was followed up by the 5F, 6F and 7F before moving onto the large geometry instruments: the 1270 and 1280-HR, pictured in Figure 2.5.

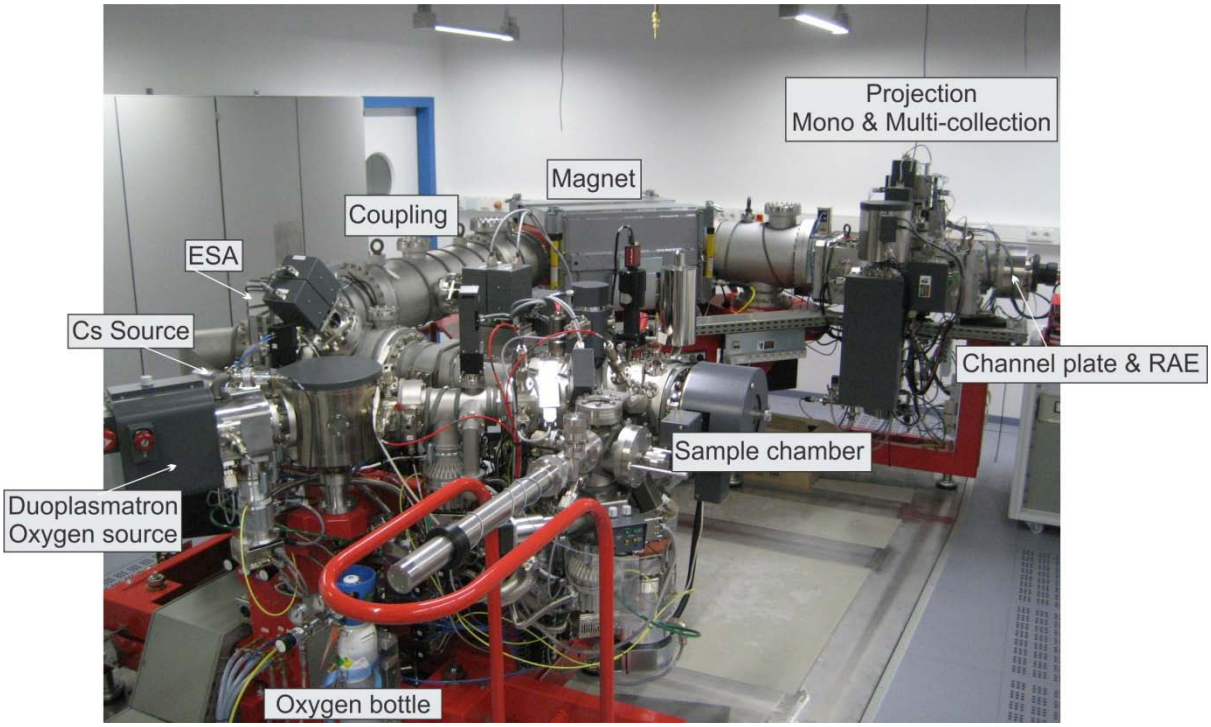

Figure 2.5: Photograph of the Potsdam CAMECA 1280-HR (photo supplied by the author).

The 1280-HR, like the SHRIMP IV, are ion probes capable of operating at high mass resolving powers, while still retaining their ability to have many ions reaching the detector (i.e. high transmission). While the SHRIMP was uniquely designed with geochronology in mind, the 1280-HR has the advantage of also being well suited for high precision isotopic analyses (Schoene, 2014; Wiedenbeck, 2012).

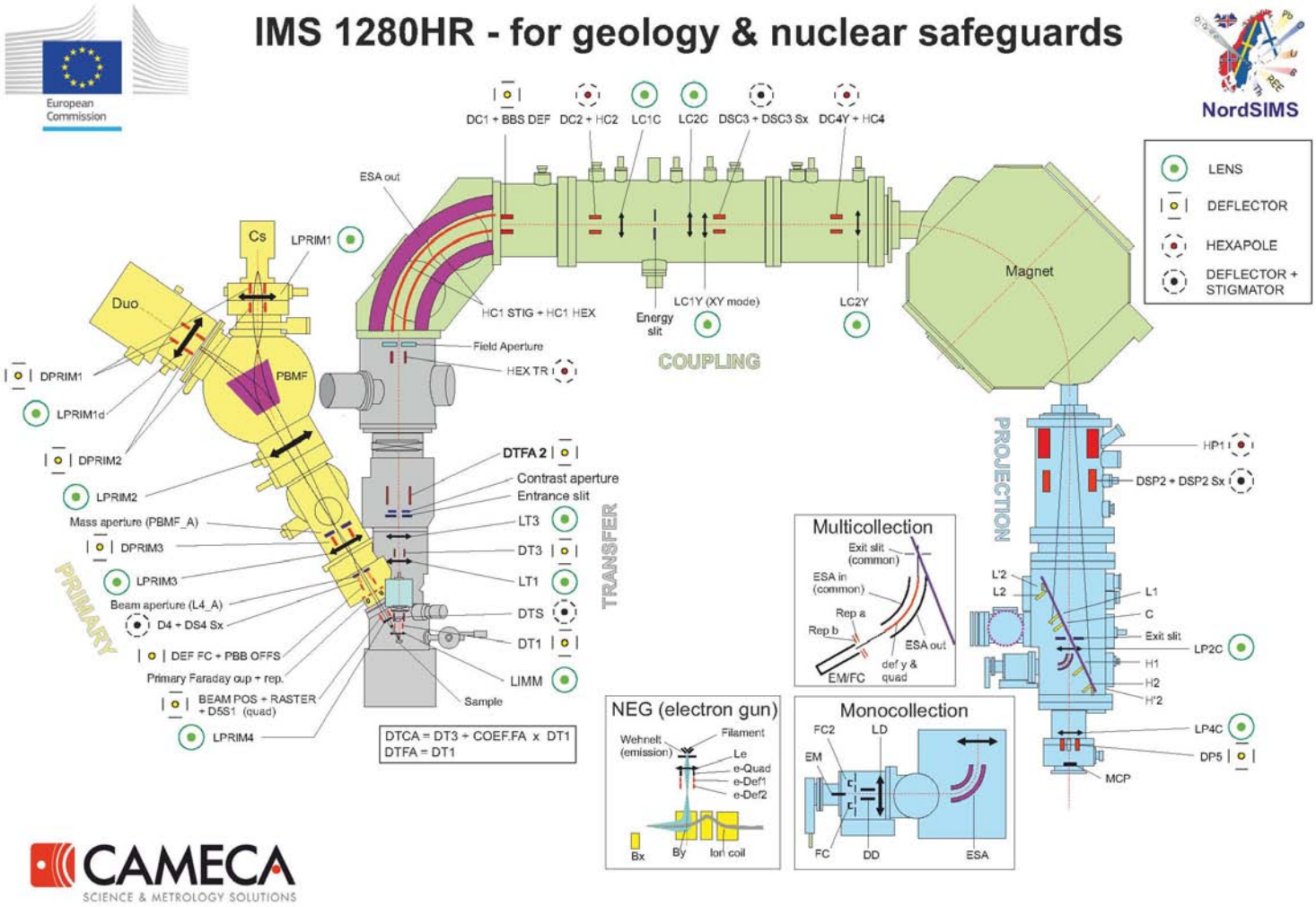

Figure 2.6: Ion optics of the Potsdam CAMECA 1280-HR. (CAMECA).

2.4 DATA AQUISITION

2.4.1 Reference materials

Having a well characterised, matrix-matched reference material (RM) is the principal limitation in acquiring ion probe data; without a suitable reference material, it is not possible to quantify the results. A reference material is defined as a material which has a known composition closely similar to the mineral to be analysed (i.e. it is matrix-matched), and it should also be homogeneous; additionally, in the case of zircon, the age should be accurately known (Faure and Mensing, 2005; Schoene, 2014; Williams, 1998). It is good practice to make use of at least two reference materials during an analytical session and regularly intersperse measurements on them among those on the unknown mineral being analysed. A distinction is made between a primary reference material, defined as the principal U-Pb age when calibrating the instrument and a quality control material which is used to evaluate the accuracy and stability of the U-Pb calibration.

The zircon reference materials used over the course of this project (as either a primary or quality control material) are listed in Table 2.2.

Table 2.2: The various reference materials used over the course of this project

Zircon RM	$^{207}Pb/^{206}Pb$ age (Ma)	$^{206}Pb/^{238}U$ age (Ma)	Reference	Instrument
91500	1065.4 ± 0.3	1062.4 ± 0.4	Wiedenbeck et al., 1995a	1280-HR
Temora 2		416.78 ± 0.33	Black et al., 2004	1280-HR, SHRIMP
Plešovice		337.13 ± 0.3	Sláma et al., 2008	1280-HR, LA-ICPMS
SL 13			Claoué-Long et al., 1995	SHRIMP
FC 1	1099.0 ± 0.6 Ma	1099.9 ± 1.1 Ma	Paces and Miller, 1993	SHRIMP
GJ 1	608.5 ± 0.4 Ma		Jackson et al., 2004	LA-ICPMS

The uncertainties in the age are quoted at 1 standard deviation (sd).

It is essential to use reference materials, as it is not possible to directly measure the absolute elemental concentration using an ion probe. One is obliged to indirectly measure the concentration by making use of the fundamental SIMS equation. The left-hand side term of equation 4 is referred to as the Relative Sensitivity Factor (RSF), and is assumed to remain constant under stable analytical conditions. The RSF allows for the conversion of the secondary ion intensity of the element of interest into a concentration by directly relating it to

the same ratio recorded in the unknown (Van der Heide, 2014). Hence it is important to ensure that the reference material is analysed in the same session as the unknown, in order for it to be used to correct for any matrix effects.

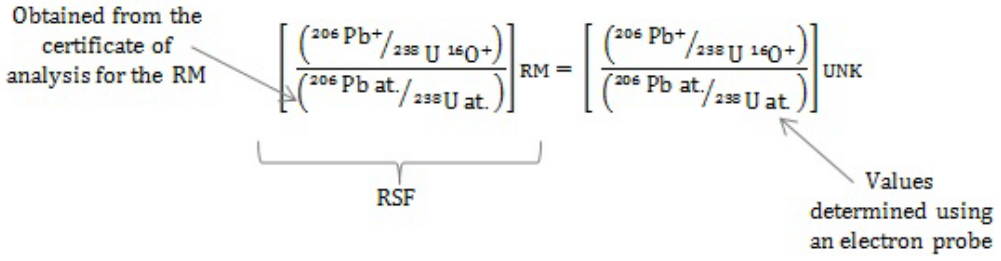

(4)

In equation 4 the top term on either side is determined by the measurements made using the ion probe. In the case of the reference material, these values are obtained by averaging all the measurements done on it, for the unknown (UNK) however, these are the values for a single measurement.

Matrix effects are due to inherent features in the material of interest – such as compositional variations – which affect how efficiently secondary ions are produced, and often make quantification problematic. Matrix effects tend to occur during sputtering and can include adsorption, implantation and primary ion beam induced damage to the crystal lattice (Van der Heide, 2014).

2.4.2 Defining an analysis

The exact 'recipe' for the various sessions varies; however, in the case of the Potsdam 1280-HR measurements, the U-Pb data were acquired using an electron multiplier operating in mono-collection mode, and the data were filtered at the 3sd level between each cycle. A single analysis consisted of 12 cycles of the peak stepping sequence listed in Table 2.3. Thus, including pre-sputtering, a single such analysis lasted approximately 15 minutes.

Table 2.3: The peak stepping sequence measured during a typical Potsdam 1280-HR analysis

Species	Measurement time per integration (s)	Comment
$^{90}Zr_2\ ^{16}O$	1	This mass station is used to correct for any secondary magnetic field drift of the secondary ion beam This peak is also used to confirm that the mineral is indeed zircon.
$^{92}Zr_2\ ^{16}O$	1	
200.5	4	Measures the background on the Electron Multiplier. Uses $^{92}Zr_2\ ^{16}O$ as its reference mass.
$^{94}Zr_2\ ^{16}O$	1	
^{204}Pb	6	Monitors the presence of common lead in the sample. Uses $^{94}Zr_2\ ^{16}O$ as its reference mass.
^{206}Pb	4	
^{207}Pb	6	
^{208}Pb	2	
$^{177}Hf\ ^{16}O_2$	1	Used to estimate the hafnium content of the zircon.
^{232}Th	2	
^{238}U	2	
$^{232}Th\ ^{16}O$	2	
$^{238}U\ ^{16}O$	2	
$^{238}U\ ^{16}O_2$	2	The energy distribution for U behaves differently to Pb, However $^{238}U\ ^{16}O_2$ as a similar energy distribution to Pb and is used to calibrate for U.

2.5 DATA EVALUATION AND PRESENTATION

2.5.1 Processing the raw data

The details pertaining to data reduction procedures for the SHRIMP and LA-ICPMS data in the ensuing chapters are from correspondence with Dr. Richard Armstrong and Professor Dirk Frei who respectively, completed the data reduction. The raw SHRIMP data were processed using the "SQUID I" Excel Macro of Ludwig (2001), whereas "GLITTER", an online interactive data reduction software, was used for the LA-ICPMS data. The steps involved in processing the raw 1280-HR data using "NordAge" – an excel-based geochronology program written by Dr. Martin Whitehouse (NORDSIM facility, Stockholm; Whitehouse et al., 1999) – are discussed below in more detail as a means of describing the basic procedure.

U-Pb calibration

It is commonly observed that the ionisation yield of sputtered material is not uniform; this results in differences in the 'true' ($^{206}Pb/^{238}U$) and 'measured' ratios. The measured secondary ion ratios ($^{206}Pb^{+}/^{238}U^{+}$) are not constant from spot to spot or from session to session even for reference materials, and this can be owing to a number of factors which commonly include changes in the sample chamber pressure or primary beam intensity (Jeon and Whitehouse, 2015; Van der Heide, 2014). Early users saw that a way to deal with the problem of differences in the true and measured ratios was to use the measured secondary ion ratios to correct for this inter-element fractionation, based on the assumption that sputtering affects ionisation efficiency the same way in both a reference material and an unknown (Williams, 1998). Hinthorne et al. (1979) observed that the secondary ion ratios of Pb^{+}/U^{+} (or Pb^{+}/UO^{+}) correlated with the secondary ion ratios for the oxide and metal species of U (i.e. UO^{+}/U^{+}, UO_2^{+}/UO^{+} and UO_2^{+}/U^{+}). This correlation seen in Figure 2.7 is extraordinarily consistent, thus making it possible to use this relationship to convert measured secondary ion ratios into true elemental ratios (Jeon and Whitehouse, 2015).

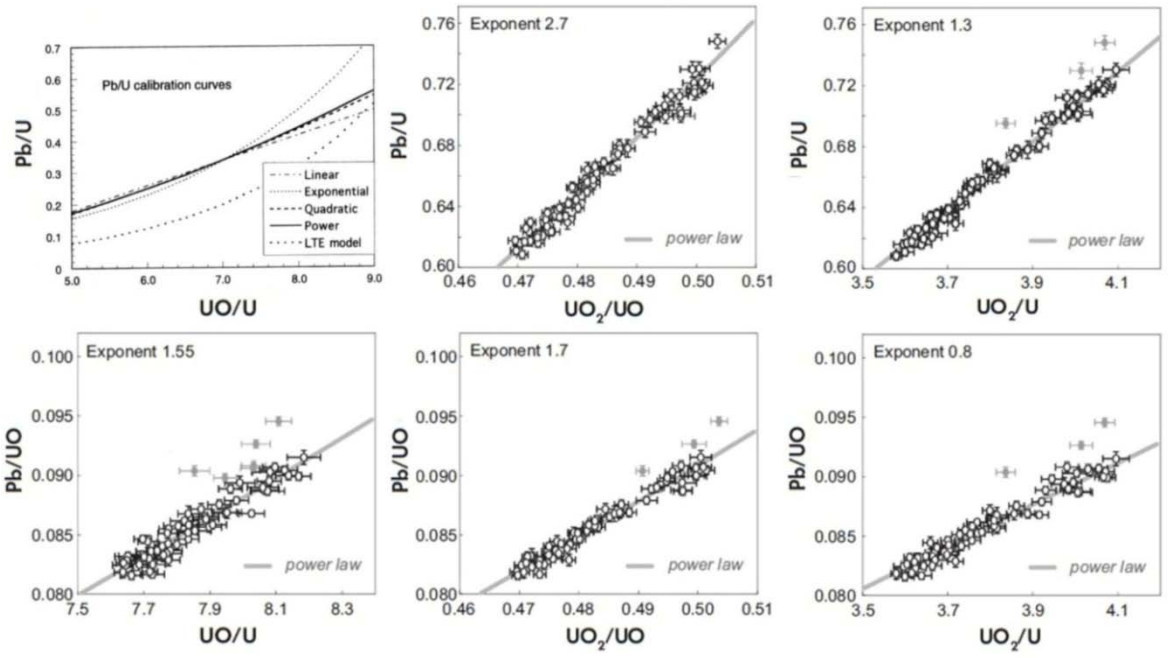

Figure 2.7: The top left plot depicts the various shapes a calibration curve can have based on the type of correlation used, while the remaining plots demonstrate how consistent the relationship is between the respective secondary ion ratios. The slope of the line of best fit through the data points is defined by the exponent value. The figure is after Williams (1998); Jeon and Whitehouse (2015).

What is also apparent in the plot on the top left of Figure 2.7 are the various shapes this calibration curve can have. Initially the correlation was shown to be linear, but over time it became evident that this was only over a limited range, because at high UO^+/U^+ values the calibration no l onger fitted adequately (Williams, 1998). Exponential and quadratic calibrations were for a time used before Claoué-Long et al. (1995) showed that using a power law function (equation 5; Jeon and Whitehouse, 2015) provided the best fit with the data over a wider range.

$$Pb^+/ UO^+_x = a\,[UO^+_y/ UO^+_z]^{\,b} \qquad (5)$$

Where x = 0, 1 or 2; y = 1 or 2; z = 0 or 1 ($y \neq z$); a = a constant (0.0069) and b = the exponent

Information on factors which can affect the type of calibration curve used can be found in Appendix C2.

Calculating an age via this method

In order to calculate the age for an unknown zircon, the 'true' isotopic ratio of the analysed spot must be determined from the measured secondary ion ratio. To do this, measurements must be made on the reference material under the same conditions as the unknown, which allows for a calibration curve to be made. The data for the unknowns, with their own measured secondary ion ratios, are then plotted relative to this curve – any variations in the ratios will result in the unknowns moving either up/down or left/right relative to the calibration curve (Figure 2.8).

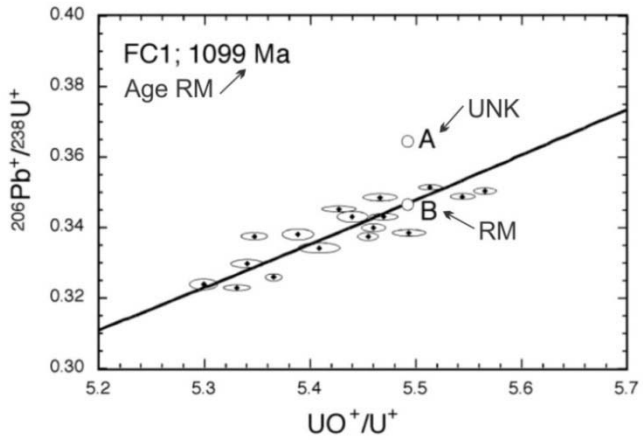

Figure 2.8: Sketch of how to use the calibration curve to calculate the age for a zircon of unknown age (after Ireland and Williams, 2003).

In order to calculate the age of an unknown zircon at point A (i.e. the true $^{206}Pb/^{238}U$ ratio) in figure 2.8, equation 6 from Ireland and Williams, (2003) is used.

$$Age_{UNK} = [Age_{RM}] \times [(Pb^+/U^+)_{UNK} / (Pb^+/U^+)_{RM}] \quad (6)$$

The term $(Pb^+/U^+)_{RM}$ represents the Pb^+/U^+ ratio of the reference material at the corresponding UO^+/U^+ ratio of the unknown A (Ireland and Williams, 2003).

Correcting for Initial Pb

A small component of the total amount of lead within a zircon is made up of non-radiogenic lead, and it should be as little as <1 % in unaltered zircon, but can increase to more than 50 % if a grain was subjected to alteration. For this reason it is particularly important to account for the presence of the initial lead component in order for an age to be truly meaningful. Initial lead can be present as mineral inclusions within a zircon grain, and can also be trapped in micro-fractures, but is more commonly found to either build up naturally after a grain has been altered. Initial lead can also be introduced as 'laboratory derived initial lead' from polishing compounds etc. during sample preparation (Ireland and Williams, 2003). Initial lead is generally referred to either as "common lead" or "non-radiogenic lead". However, the term initial lead has been used here purposefully to make use of the distinction of Schoene (2014), whereby initial lead does not include any lead introduced either through contamination or from a blank.

The most commonly used method of estimating the amount of initial lead present is to measure the ^{204}Pb content directly. This information is then used to subtract the non-radiogenic (i.e. initial) lead component from the measured total lead signal by way of equations 7 and 8 (Ireland and Williams, 2003).

$$f = {}^{206}Pb_{initial} / {}^{206}Pb_{total} \quad (7)$$

f is the fraction of the measured ^{206}Pb component which is initial, and is calculated using the measured $^{204}Pb/^{206}Pb$ ratio in equation 8.

$$f = \frac{(^{204}\mathrm{Pb}/\,^{206}\mathrm{Pb})_{total}}{(^{204}\mathrm{Pb}/\,^{206}\mathrm{Pb})_{initial}} \quad (8)$$

Cogenetic minerals (often K-feldspar) containing lead are occasionally measured in place of zircon to obtain the initial lead component (Ireland and Williams, 2003). But where it is not feasible to directly measure the ^{204}Pb component – as is typically the case for LA-ICPMS where there is an unresolvable isobaric interference between ^{204}Pb and ^{204}Hg (Schoene, 2014) – it is possible to estimate the initial lead value. There is also another shortcoming, which is that ^{204}Pb (being the least abundant lead isotope) can also introduce analytical uncertainties, particularly for young and/or low-U zircons. In situations such as this, sometimes a correction using ^{208}Pb/^{206}Pb and the measured ^{232}Th/^{238}U ratio is advisable (equation 9 from Ireland and Williams, (2003).

$$f = \frac{(^{208}\mathrm{Pb}/\,^{206}\mathrm{Pb})_{total} - (^{208}\mathrm{Pb}/\,^{206}\mathrm{Pb})^{*}}{(^{208}\mathrm{Pb}/\,^{206}\mathrm{Pb})_{initial} - (^{208}\mathrm{Pb}/\,^{206}\mathrm{Pb})^{*}} \quad (9)$$

This method of correcting for initial lead requires the assumption that the ^{232}Th/^{238}U, nor the radiogenic ^{208}Pb/^{206}Pb* ratio has been disturbed; thus any discrepancies between the radiogenic and measured ratios can be attributed to the presence of initial lead. This method also works well for low Th/U zircons, but becomes less precise for those rich in Th. One significant drawback is that this method is prone to underestimate the initial lead composition due to ^{208}Pb being more readily lost from altered zircons than ^{206}Pb (Ireland and Williams, 2003).

A third strategy for young (Phanerozoic aged) zircons, which contain low levels of initial lead (because the range of radiogenic lead in the Phanerozoic is small), is to make use of the measured ^{207}Pb/^{206}Pb ratio because even that small component of initial lead makes them susceptible to over-correction. Thus a ^{207}Pb corrected age (derived by using the assumed initial lead composition to anchor a line, projected through the uncorrected ^{238}U/^{206}Pb and ^{207}Pb/^{206}Pb ratios onto concordia; Ludwig (2003)) is seldom used, except for samples which are known or expected to be concordant (Ireland and Williams, 2003; Yaseen et al., 2013).

$$f = \frac{(^{207}Pb/\,^{206}Pb)_{total} - (^{207}Pb/\,^{206}Pb)^*}{(^{207}Pb/\,^{206}Pb)_{initial} - (^{207}Pb/\,^{206}Pb)^*} \quad (10)$$

This calculation is iterative, requiring a value for f to be determined using equation 10, which gives a corrected $^{206}Pb/^{238}U$ age; this is then used to calculate a revised f value and age (Ireland and Williams, 2003).

More conventional age calculations

The following equations (11-13) have been simplified, and can be used to calculate a model age provided that the initial lead composition when the zircon crystallised is know or is small enough so as to be negligible once the other common lead components have been accounted for.

$$\frac{^{206}Pb^*}{^{238}U} = e^{\lambda_{238}t} - 1 \quad (11)$$

$$\frac{^{207}Pb^*}{^{235}U} = e^{\lambda_{235}t} - 1 \quad (12)$$

$$\frac{^{208}Pb^*}{^{232}Th} = e^{\lambda_{232}t} - 1 \quad (13)$$

Where t is the time since the mineral crystallised, λ denotes the relevant decay constant and * indicates a radiogenic component (Schoene, 2014).

The advantage of using equations 11-13 to calculate ages is that the focus is less on the absolute concentration of U and Pb, but rather the ratio, which can be measured with more precision. Also the dual decay system allows for a fourth isochron equation to be constructed by dividing equation (12) by (13) to give the Pb-Pb age:

$$\frac{\left(\frac{^{207}Pb}{^{204}Pb}\right) - \left(\frac{^{207}Pb}{^{204}Pb}\right)_{initial}}{\left(\frac{^{206}Pb}{^{204}Pb}\right) - \left(\frac{^{206}Pb}{^{204}Pb}\right)_{initial}} = \left(\frac{^{235}U}{^{238}U}\right)\frac{(e^{\lambda_{235}t} - 1)}{(e^{\lambda_{238}t} - 1)} = \left(\frac{^{207}Pb}{^{206}Pb}\right)^* \quad (14)$$

The present day $^{238}U/^{235}U$ ratio according to Steiger and Jäger (1977) is 137.88, t hus eliminating the need to measure U. An age can therefore be calculated by constructing an isochron in $^{206}Pb/^{204}Pb$ - $^{207}Pb/^{204}Pb$ space, and in the case of negligible initial lead, the measured radiogenic $(^{207}Pb/^{206}Pb)^*$ ratio can be used to directly determine an age (Schoene, 2014).

2.5.2 Data representation

The software package Isoplot (Ludwig, 2003, 2012) is used to plot the data as either Wetherill (1956) or Tera-Wasserberg (1972) Concordia plots (Figure 2.9) using the decay constants recommended by the IUGS sub-commission on geochronology (Steiger and Jäger, 1977).

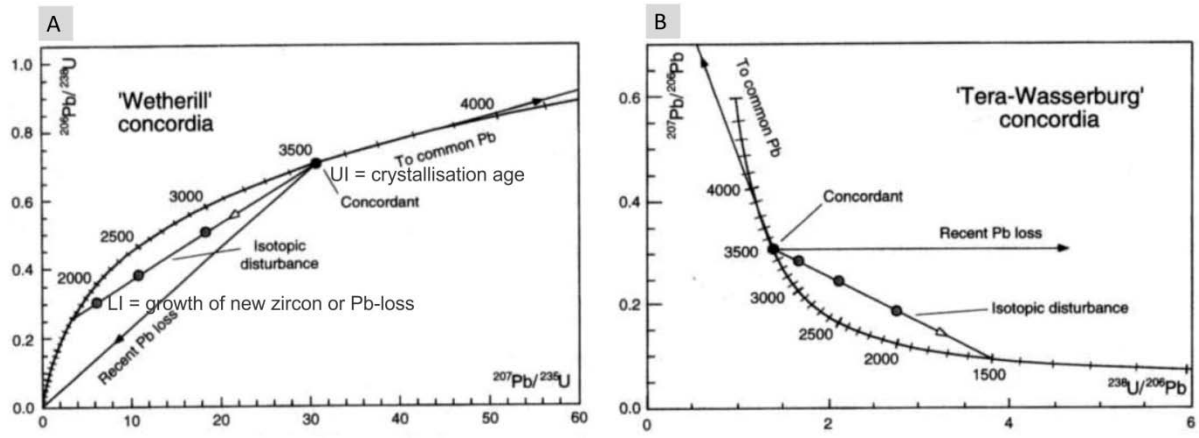

Figure 2.9: Wetherill (Figure 2.9a) and Tera-Wasserburg (Figure 2.9b) concordia plots which can be used to display U/Pb isotopic data. The respective pattern made by zircons experiencing recent lead loss and isotopic disturbances are illustrated in the diagrams (Williams, 1998). LI = lower intercept, whereas UI = upper intercept.

Concordia plots are a means of graphically representing the behaviour of a system by monitoring the change in the isotopic ratios of uranium and lead over time (ANU, 2014; Faure and Mensing, 2005; Williams, 1998). It is possible to construct these concordia diagrams because the U-Pb system is paired. This relates to the fact that ^{238}U and ^{235}U decay at different rates to produce ^{206}Pb and ^{207}Pb respectively. ^{235}U decays the fastest, and as a result was more abundant in the past, which resulted in a high ^{207}Pb concentration. Thus when constructing a concordia line, this difference in abundance, results in the line actually forming a curve within this paired U-Pb space. The change in the lead abundance over time

also provides an internal check on whether the system has remained closed or not (Williams, 1998).

Closed vs. open system behaviour refers to disturbances in the Pb and/or U composition. In the case of a closed system, in order for an analysis to be considered concordant and plot on the concordia curve, it should have $^{206}Pb/^{238}U$ and $^{207}Pb/^{235}U$ ages, which are equal (Williams, 1998; Schoene, 2014). In order to achieve this: (1) the isotopic system must have remained undisturbed, meaning that U and Pb were not mobilised, (2) the correct initial Pb value was used and (3) the uncertainty on the decay constant was taken into account (Faure and Mensing, 2005). If any of these criteria are not met, then the analysis will fall off of the concordia curve and form a discordia line. Within an open system, the most common feature is that the Pb has become mobilised due to damage caused by radioactive decay, which allows it to escape from the crystal structure (Faure and Mensing, 2005). In order to minimise the effect of this lead loss, a $^{207}Pb/^{206}Pb$ age is often calculated because it is insensitive to such processes, particularly if the disturbance took place during recent weathering (Faure and Mensing, 2005). It is also possible for U to become mobilised, in which case analyses can become reversely discordant; plotting above the Concordia curve due to the increase in uranium (Wiedenbeck, 1995b).

As noted in Figure 2.9, a wealth of information can be extracted from a concordia diagram, the upper and lower intercepts respectively of an isotopic disturbance can give an indication of when a grain crystallised as well as of when the disturbance occured (Williams, 1998; Schoene, 2014). Either style of concordia diagram can be used, however the Tera-Wasserburg plot has some advantages over the Wetherill plot when it comes to ion probe data, in that the initial lead isotopic composition can be read off the $^{207}Pb/^{206}Pb$ axis at the point where the upper intercept intersects the concordia curve, and the true age of the sample is represented by the lower intercept (Schoene, 2014).

2.6 ANALYTICAL METHODS

The zircons dated by SHRIMP, SIMS and LA-ICPMS were extracted from the samples using conventional crushing and separation methods, before being embedded into epoxy grain mounts. Where possible the relevant reference materials were placed alongside the unknowns, the only exception being the samples analysed using LA-ICPMS, where the

reference materials were embedded within a separate grain mount, which is maintained inside the instrument.

After embedding, the zircon grains were sectioned by polishing, prior to being investigated optically using a petrographic microscope as well as with Back Scattered Electron (BSE) and Cathodoluminescence (CL) imaging to identify any zonation or other internal structures within the grains. These images are then used to select the appropriate sites to analyse.

2.6.1 SHRIMP-RG

The SHRIMP-RG dating was done at the Research School for Earth Sciences at the Australian National University in Canberra. Three different reference materials were used for these analyses: SL 13, with a uranium concentration of 238 μg/g (Claoué-Long et al., 1995) was used to calibrate the U, Th and Pb concentrations for each session while Temora 2 (416.8 ± 1.3 Ma; Black et al., 2004) and FC 1 (1099.1 ± 0.5 Ma; Paces and Miller, 1993) were used to perform the primary U-Pb age calibration and monitor the $^{207}Pb/^{206}Pb$ compositions in the older zircons respectively.

The analytical methods and data reduction were performed using the methods described by Compston et al. (1984); Williams (1998) and references therein. Briefly, this entailed using a 25 μm diameter primary O_2^- beam with a current of 2-3 nA. In order to optimize the number of grains analyzed, the ion intensity for the various species were measured over only four cycles per spot; this yielded somewhat lower precision for each grain, but allowed for the analysis of a l arge number of grains. Due to the low number of cycles, our analytical uncertainty is higher than normally expected.

The data were reduced using the SQUID 1 Excel Macro of Ludwig (2001), followed by the calculation of the ages in Isoplot/Ex 3.0 (Ludwig, 2003), using the decay constants recommended by the IUGS sub-commission on geochronology in Steiger and Jäger (1977) and corrected for common lead using the measured ^{204}Pb and the relevant common lead compositions from the model of Stacey and Kramers (1975).

2.6.2 SIMS

All of the U-Pb zircon determinations by SIMS were obtained using the CAMECA 1280-HR at the GFZ in Potsdam, Germany. Each of the prepared grain mounts contained the zircon reference material 91500 in addition to grains of either Plešovice or Temora 2 alongside the unknowns. Prior to analysis the mounts were cleaned with high-purity ethanol for five

minutes in an ultrasonic bath, after which they were argon sputter coated with a 35 nm thick film of high-purity gold. The mounts were then placed into holders using tension springs, and imaged in reflected light using the stitching software on a Nikon Eclipse LVDIA-N microscope, thereby generating a map which was used to assist with navigation during data acquisition by using the SIMS instrument's point-logger software.

The SIMS analyses employed a 7 nA, $^{16}O_2^-$ primary ion beam (operated in Köhler mode) with a total impact energy of 23 keV, resulting in a beam diameter of approximately 25 µm on the sample's surface. Positive secondary ions were extracted using a +10 kV potential applied to the sample holder. Each analysis was preceded by a 7 nA, pre-sputtering lasting 120 seconds and employed a 25 µm raster, which locally removed the gold coat, suppressed surface contamination and helped establish equilibrium sputtering conditions. Oxygen flooding was used to enhance lead sensitivity, with the total pressure in the sample chamber maintained around 1.5 x 10^{-3} Pa throughout the analytical session.

After completing the pre-sputtering, centring routines were applied to the secondary beam that automatically scanned (1) the sample high voltage to centre the secondary ions 5 V above maximum within our 50 eV wide energy window, (2) the field aperture in both the X and Y directions and (3) corrected for any secondary magnetic field drift using the $^{90}Zr_2{}^{16}O$ mass station. Data were acquired using an ETP electron multiplier operating in mono-collection mode. A single analysis consisted of 12 cycles of the peak stepping sequence: $^{90}Zr_2{}^{16}O$ (1 second integration time per cycle), $^{92}Zr_2{}^{16}O$ (1s), 200.5 (4s), $^{94}Zr_2{}^{16}O$ (1s), ^{204}Pb (6s), ^{206}Pb (4s), ^{207}Pb (6s), ^{208}Pb (2s), $^{177}Hf^{16}O_2$ (1s), ^{232}Th (2s), ^{238}U (2s), $^{232}Th^{16}O$ (2s), $^{238}U^{16}O$ (2s) and $^{238}U^{16}O_2$ (2s). Thus, including pre-sputtering, a single such analysis lasted approximately 12 minutes. Data were filtered at the 3 sd level within each run. The mass resolution of the instrument was set at approximately $M/\Delta M \approx 5400$. The typical count rate for $^{90}Zr_2{}^{16}O$ under these conditions was between 3 and 7 x 10^{+4} counts per second, to which a 46.2 ns dead time correction was applied, as defined by a delay line in the electron multiplier's pre-amplifier circuitry.

The U-Pb inter-element calibration for the analytical session was based on the zircon reference material 91500 ($^{206}Pb/^{238}U$ age: 1062.4 ± 0.4 Ma; $^{207}Pb/^{206}Pb$ age: 1065.4 ± 0.3 Ma; Wiedenbeck et al., 1995a) with the Plešovice ($^{206}Pb/^{238}U$ age: 337.13 ± 0.37 Ma; Sláma et al., 2008) and Temora 2 ($^{206}Pb/^{238}U$ age: 416.78 ± 0.33 Ma; Black et al., 2004) reference materials used as quality control materials to evaluate the accuracy and stability of the U-Pb calibration measurements. Data collection employed a series of regularly interspersed

analyses of the reference materials between multiple analyses (typically 4) of the "unknown" sample grains.

Data reduction employed the Excel-based program "NordAge" (M. Whitehouse, NORDSIM facility, Stockholm) where the measurements done on the primary reference material 91500 were used to establish the U-Pb inter-element fractionation against which the unknowns were calibrated. Using a Pb/UO vs. UO_2/UO calibration fitted with a power law function, individual best-fit lines were determined. As an additional means of verifying the robustness of our calibration approach – $^{206}Pb/^{238}U$ ages of 1063.3 ± 1.4 Ma (1 sd, N = 70) were calculated for 91500 by calibrating it against itself; whereas for Plešovice and Temora 2 respectively $^{206}Pb/^{238}U$ ages of 343.1 ± 1.8 Ma (1 sd, N = 7) and 418.4 ± 1.5 Ma (1 sd, N = 10) were obtained. Therefore, both 91500 and Temora 2 are within uncertainty of their published $^{206}Pb/^{238}U$ ages of 1062.4 and 416.78 Ma whereas our Plešovice results are slightly older than its published age of 337.13 Ma.

The Excel program Isoplot (Ludwig, 2012), was used to plot the data using the decay constants recommended by the IUGS Sub-commission on Geochronology (Steiger and Jäger, 1977). A correction for common lead was based on the observed ^{204}Pb counts in conjunction with the modern common lead compositions from the model of Stacey and Kramers (1975). Only those results that were > 95 % concordant were used in age calculations.

2.6.3 LA-ICPMS

The LA-ICPMS data were acquired at the University of Stellenbosch's Central Analytical Facility. The LA-SF-ICP-MS instrument utilizes a Thermo Finnigan Element2 mass spectrometer, which is coupled to a NewWave UP213 laser ablation system. All age data were recorded in spot mode with a beam diameter of 30 µm, the resulting crater depth being approximately 15–20 µm. The methods employed for analysis and data processing are described in detail by Frei and Gerdes (2009), and the references therein; whereas the full analytical details, as well as the results for the primary reference material (Plešovice) and quality control materials (GJ 1 and M127) analysed, are reported within Table 2.4 (Appendix A1). The primary and quality control reference materials were analysed alongside the unknowns, and the results were in agreement with the published ID-TIMS age. The calculation of concordia ages and plotting of concordia diagrams were performed using Isoplot/Ex 3.0 (Ludwig, 2003).

2.6.4 ID-TIMS

The U-Pb and Pb-Pb ID-TIMS dating was done at the Jack Satterly Geochronology Laboratory, in the Earth Sciences Centre of the University of Toronto, Canada, where the samples were first crushed and milled following standard operating procedures, and the powders subjected to the conventional methods of mineral separation in order to concentrate the heavy minerals. Portions of the light fractions from some samples were processed with a liquid of specific gravity 2.60 (made by diluting bromoform with acetone) in order to isolate a pure K-feldspar fraction, because under these conditions plagioclase and quartz sink while K-feldspar floats.

The zircon, titanite, rutile and apatite were recovered from the heavy mineral concentrate of the various samples, and the mineral grains and fragments were handpicked in alcohol using a binocular microscope. The samples chosen were judged, by surface reflectance, to be as fresh as possible. The picked fraction was then leached following a procedure recommended by Romer and Wright (1992). Leaching was carried out using 15% HF in 3 ml Savillex capsules heated to about 100 °C for 30 minutes, followed by ultrasonic agitation for 10 minutes. Grains with the highest reflectance were then selected for analysis and sub-divided into groups representing different visible levels of attack. Weights were estimated from photomicrographs (Matthews and Davis, 1999); this affects only U and Pb concentrations, not age information, which depends only on isotope ratio measurements.

Samples were washed briefly in HNO_3 prior to dissolution in Savillex Teflon capsules. A ^{205}Pb-^{235}U-^{238}U spike (Earthtime spike ET535) was added to the dissolution capsules during sample loading. The apatite and feldspar were dissolved overnight using concentrated HF at 100 °C, while the titanite was attacked by HF in Savillex capsules before being dissolved in 3N HCL. Zircon solutions were redissolved in HCl and loaded directly onto mass spectrometer filaments, if the grains weighed less than 5 µg. These loads produced strong, stable Pb signals, despite the presence of only a small amount of zirconium. Ta and Nb strongly suppress Pb emission in the mass spectrometer and must therefore be completely removed from the samples. For larger zircon grains as well as the titanite, rutile, and apatite solutions, U and Pb were purified using HCL, HBr and HNO_3. The chemical procedures followed were those adapted from those of Romer and Smeds (1994) and Romer and Wright (1992) where: the sample HF solutions were first taken to dryness. The dry samples were

then wetted with one or two drops of concentrated HF followed by the addition of 10 drops 1N HBr. No residues were observed. The vials were then capped and warmed on a hot plate for several minutes, taking care that condensation on the walls did not reduce the samples to dryness. Two sets of 50 µl anion exchange columns (Bio-Rad AG-1 resin) were prepared and cleaned by alternate washes with 6N HCl, 7N HNO_3 and H_2O. The HBr solutions were loaded into one set of cleaned columns, which strongly and preferentially adsorb Pb.

The vials were then placed beneath their respective columns to collect all of the solutions, which contain the U as well as Ta and Nb. These solutions were dried and redissolved in 10 drops 7N HNO_3. The Pb fractions were washed on the columns with 1N HBr followed by 3N HCl. They were then eluted into clean PMP beakers in 6N HCl, dried and redissolved in 10 drops 1N HBr. The U solutions were re-loaded into the columns and washed using 7N HNO_3, which removes Ta and Nb, followed by 6N HCl. The U was then eluted back into the Savillex vials in H_2O, dried and redissolved in 7N HNO_3. The Pb HBr solutions were re-loaded into the second set of columns, washed with 1N HBr followed by 3N HCl and eluted back into the PMP beakers in 6N HCl. Two drops of 0.05N H_3PO_4 were added before drying the solution, which was held for analysis. The H_3PO_4 is hygroscopic and allows the sample to be identified by a small drop in the beaker. The U solutions were re-loaded into this second set of columns, washed with 7N HNO_3 and eluted into the rinsed Savillex vials with H_2O. Two drops of 0.05N H_3PO_4 were added, but the solutions were not dried down at this stage. The Pb samples were loaded onto Re filaments using silica gel and analyzed with a MM354 mass spectrometer in multi-collector mode. Thermal mass discrimination corrections are 0.10% /AMU. Collector efficiencies were monitored using the SRM981 Pb standard. Pb signals were stable with no evidence of suppression by Ta and Nb and were sufficiently strong to allow precise multi-collector analyses where isotope ratio precision is essentially limited by variability of thermal fractionation throughout the run. After loading the Pb samples, the U solutions were transferred into the PMP beakers that held their corresponding Pb samples. This frees up the Savillex vials, which can then be put through cleaning cycles. Following Pb analysis, the U samples were dried and transferred in Si-gel solution onto the Re filaments used to analyze the corresponding Pb samples. U and Pb were analyzed separately in order to minimize blank from the complex chemistry, but the same filaments are used to minimize cleaning. The U is significantly more refractory than Pb. The highest U signals were generally achieved at about 50-100 °C higher than for Pb. U decay constants are from Jaffey et al. (1971), while common Pb in excess of the 1 pg laboratory blank was

corrected for using the isotopic composition of Pb on the Stacey and Kramers (1975) growth curve. Ages from minerals which appeared to be Proterozoic in age were corrected for using the isotopic values of Pb in ore minerals determined by Höhndorf and Vetter (1999). Regressions and plotting were carried out using the Isoplot program of Ludwig (2003).

2.6.5 ^{40}Ar-^{39}Ar

The separated mica grains (analysed at Spectrum, the Central Analytical Facility of the Faculty of Science at the University of Johannesburg) were wrapped in aluminum foil and packed in a silica glass tube which has a 1 cm outer diameter; 50 samples together make up an approximately 4 cm high stack. A set of three fluence monitors were packed at the bottom and top of the stack. These are McClure Mountain amphibole (523.1 ± 1 Ma, Renne et al., 1998), Hb3GR amphibole (1080.4 ± 1.1 Ma, Renne et al., 2010) and Fish Canyon sanidine (28.3 ± 0.4 Ma, Renne et al., 2010). The tube was then vacuum sealed and irradiated at NTP Radioisotopes' SAFARI 1 nuclear reactor at Pelindaba, Pretoria (a subsidiary of the South African Nuclear Energy Corporation, NECSA). The samples were irradiated for 20 hours in position B2W with the reactor running at 20 MW.

The irradiated samples were then loaded into an aluminum disc sample holder and placed in an ultrahigh vacuum laser port fitted with a silica glass window, and baked for 4 hours at about 220 °C. The analyses were done by stepwise heating, using a defocused beam from a SPECTRON® continuous Nd-YAG 1064 nm laser, capable of producing up to 9 W in T_{oo} mode. The heating time for each lasing step was set to 5 minutes; temperatures were increased from approximately 600 °C to fusion at around 1300 °C. The gas released was purified using two SAES APG10 getters (one at room temperature and one at 400 °C) before it was introduced to the MAP 215-50 mass spectrometer. The argon isotopes were measured in seven cycles using a Johnston electron multiplier detector operated in analogue mode. Blank measurements were taken at four step intervals, and corrections made using the regression analysis for the measured data. Necessary corrections and calculation of the ages were done using software developed in-house, which includes full error propagation by Monte Carlo simulations. J-values, identical within error for the three monitors, were interpolated between the top and bottom of the 40 mm sample stack.

Chapter 3: New U-Pb ages for the late Palaeoproterozoic Magondi Supergroup, Zimbabwe

3.1. INTRODUCTION

The review paper by Master et al. (2010) on the Magondi Belt highlights the need for a renewed focus in obtaining ages for the Magondi Belt and the surrounding areas. Earlier studies by Höhndorf et al. (1989), Höhndorf and Vetter (1999) and Schidlowski and Todt (1998), although comprehensive, only published Pb-Pb and Rb-Sr whole rock data for the Magondi Belt with uncertainties at times as much as ± 100 Ma. Here new U-Pb zircon age data are presented for a select number of volcanic units within the Magondi Supergroup to better constrain depositional ages for some of the sedimentary units.

3.2. REGIONAL GEOLOGY

The Magondi Belt, as indicated in Figure 3.1, is a Palaeoproterozoic mobile belt located along the north-western margin of the Zimbabwe Craton in southern Africa. The belt is approximately 250 km in length and 50 km wide, with a north-easterly trend (Leyshon and Tennick, 1988). The western margin of the belt, and likewise the Zimbabwe Craton, is largely undefined due to a large expanse of Mesozoic and Cenozoic to recent Kalahari cover (Majaule et al., 2001; Master, 1994; Master et al., 2010). To the north, the Magondi Belt has been truncated by the E-W trending Pan-African Zambezi Belt, resulting in an overprinting of the original N-S trending structures. Due to this oblique over-thrusting from the north-west, the metamorphic grade along the length of the belt varies from prehnite-pumpellyite facies in the south, gradually increasing to greenschist facies; while in the more northern parts, the rocks are at amphibolite facies, even reaching granulite facies in some places (Leyshon and Tennick, 1988; Master et al., 2010; Mekonnen, 2008; Treloar, 1988).

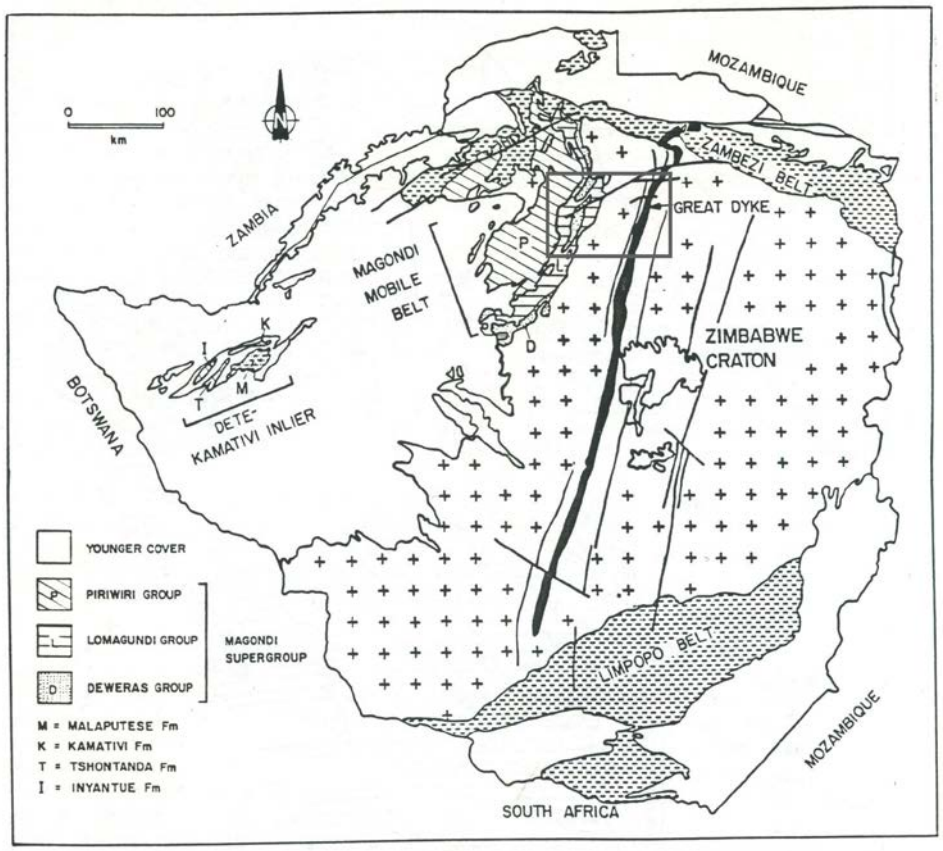

Figure 3.1: Simplified geological map of Zimbabwe, from Master (1991a) indicating the location of the Magondi Belt, and its position relative to the Zimbabwe Craton, the Zambezi Belt and the younger cover, which together bound it on all sides. The area delineated by the rectangle is represented in more detail in Figure 3.12, and indicates the approximate location of the Chimbadzi Hill Intrusion.

Master et al. (2010) and references therein provide a comprehensive review of the geology of the Magondi Supergroup, and thus the following section is simply meant to provide a brief description of the regional geology. The Magondi Supergroup is composed of a supracrustal succession of metasediments including minor metavolcanics, and is subdivided into three groups. They are from oldest to youngest: the Deweras, Lomagundi and Piriwiri Groups (Leyshon and Tennick, 1988; Master, 1994; Master et al., 2010; McCourt et al., 2001). Figure 3.2 is a more detailed geological map of the Magondi Belt.

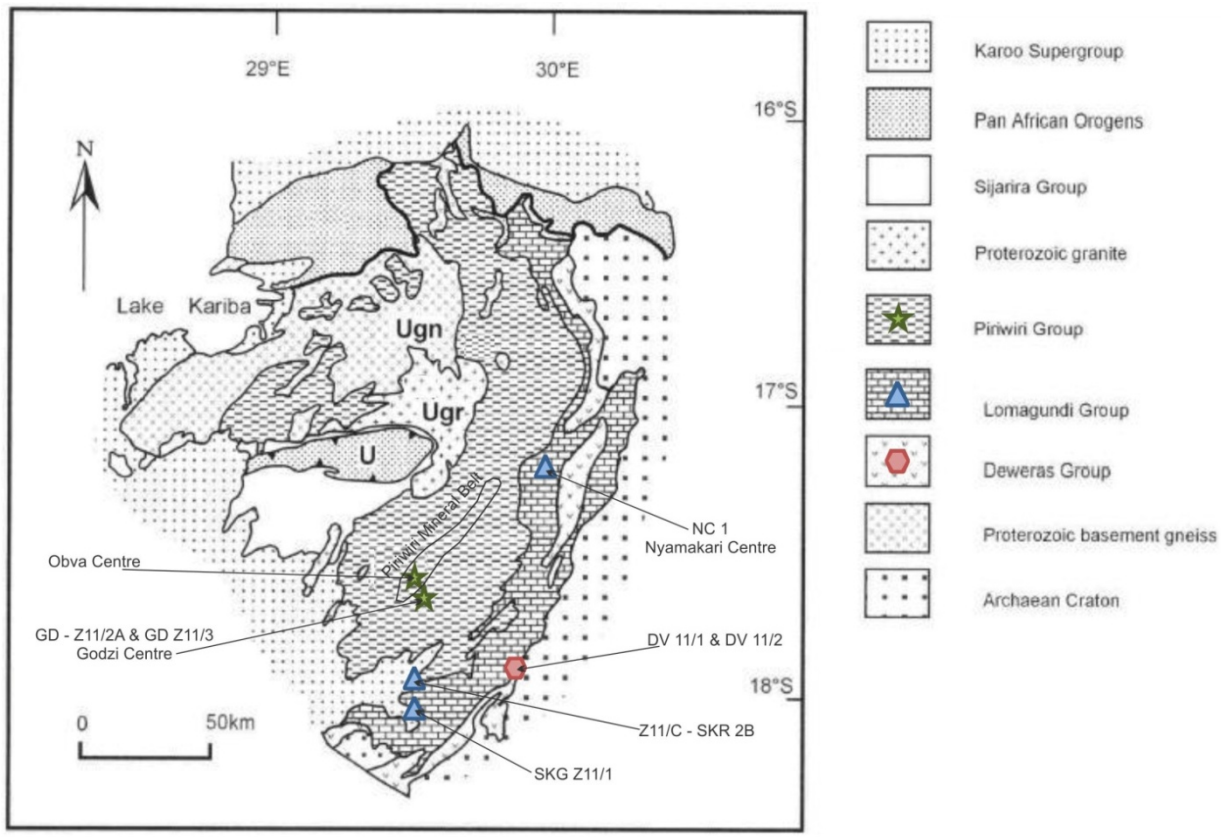

Figure 3.2: Geological map of the Magondi Belt, after McCourt et al. (2001). Ugr = Hurungwe granite, Ugn = Hurungwe gneiss, U = Hurungwe klippe. The sampling localities are indicated by the symbols.

3.2.1 Deweras Group

The now metamorphosed Deweras sediments consist of arenaceous red beds, conglomerates, mudstones, dolomites, greywackes and evaporites, and as Master et al. (2010) explain were deposited in a passive continental margin setting, within what was initially a strike-slip basin (Figure 3.3a). Extension and rotation resulted in the fragmentation of the basin into various sub-basins, separated by en-echelon faults, thereby providing the means for introducing the comparatively minor basaltic lavas (Figure 3.3b). As a result of the formation of these sub-basins, the Deweras Group consists of both a northern and southern facies. The Deweras lavas are fine-grained, basaltic greenstone lavas, which are either massive or amygdaloidal. Tennick and Phaup (1976) cited evidence of pillow lava at the base of the main flow, and described a poorly developed agglomerate unit at the top. These lava flows have since been altered and now consist predominantly of epidote, tremolite and chlorite – including pseudomorphs after the original phenocrysts (Tennick and Phaup, 1976).

A minimum age for the Deweras Group was constrained by Leyshon and Tennick (1988)

who stated that the Deweras Group could be no older than the 2.6 Ga granite-greenstone basement on which it unconformably lies; and a possible constraint on the maximum age – between 2050 ± 100 Ma and 2170 ± 100 Ma – was obtained by directly dating the Deweras lavas using Rb-Sr whole rock geochronology (Treloar 1988; Höhndorf et al., 1989) although these results clearly must be viewed with caution.

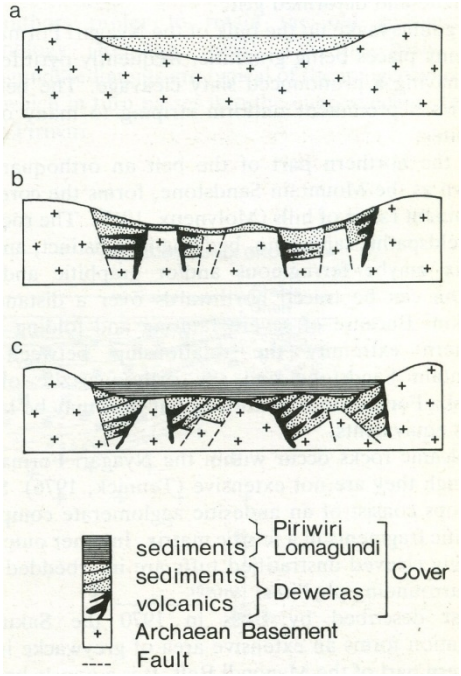

Figure 3.3: Sketch depicting the depositional environments in which the Magondi Supergroup formed (Leyshon and Tennick, 1988).

3.2.2 Lomagundi Group

The Lomagundi and Piriwiri Groups are closely linked, in the sense that they record the change from a passive to an active continental margin (Master et al., 2010). The Lomagundi Group was deposited unconformably, as a result of a marine transgression, over the Deweras Group (Figure 3.3c). Accordingly, the Lomagundi Group consists predominantly of a carbonate platform which formed in a continental shelf environment (Leyshon and Tennick, 1988; Master et al., 2010; McCourt et al., 2001). The lithologies also depict a gradual change in sea level from marginal marine, to subtidal and shallow continental shelf environments; as the rocks transition from dolomite with stromatolites and oolites, to arenite and conglomerate and then to graphitic phyllites along with banded iron formations (Leyshon and Tennick, 1988; Master, 1994; Master et al., 2010; Stagman, 1978). The presence of tuff units and felsic volcanics in the upper parts of the Lomagundi Group further indicate that a shift from a

passive to a more active continental margin occurred around this time period (Master et al., 2010; Stagman, 1978).

Ages for the Lomagundi Group are scarce, with only Schidlowski and Todt (1998) reporting a Pb-Pb age for the dolomites of 2150 ± 50 Ma, while Vail et al. (1968) reported K-Ar whole rock ages of 1905 ± 70 and 1974 ± 70 Ma from two slate samples.

3.2.3 Piriwiri Group

The Piriwiri Group sediments are composed of an upward coarsening trend of graphitic or pyritic schists and argillites, phyllite, chert, dolomite and immature greywacke (Leyshon and Tennick, 1988; Master et al., 2010; McCourt et al., 2001; Stagman, 1978) – these distal, deep water lithologies were deposited in both a continental slope environment and back-arc basin setting. The increase in volcanic activity (andesitic to felsic lavas and minor tuffs associated with the sediments) is seen as an indication that the Piriwiri Group was deposited largely within an active continental margin setting (Master, 1994; Master et al., 2010).

McCourt et al. (2001) obtained a U-Pb zircon age of 1997.5 ± 2.6 Ma for the Hurungwe Granite (refer to Figure 3.2 for its location), which due to its intrusive nature and lack of internal foliation has been interpreted to represent the final stages of the Magondi orogeny; which therefore aids in constraining the maximum age of the Piriwiri Group. Vail et al. (1968) had previously dated phyllites using K-Ar whole rock geochronology, which yielded much younger ages of 1753 ± 65 and 1659 ± 50 Ma.

3.2.4 Volcanic Centres

A number of volcanic centres have been recognised within the sedimentary units of the Magondi Belt, namely: Obva (sometimes referred to as Hova), Godzi, Piriwiri, Montana, Cresent, Kameno and Nyamakari. Leyshon (1969) was the first to describe the Godzi and Obva volcanic centres and Kirkpatrick (1976) the Crescent, Kameno and Nyamakari centres. The term volcanic centre is somewhat deceptive in that the volcanic rocks generally occur discontinuously over large distances (in the case of Godzi, the units occur along strike for over 12 km). The centres consist primarily of felsite (interbedded with chert), as well as tuffs and volcanic breccia or agglomerate. Agglomerate is defined as a specific variety of pyroclastic breccia, where the clasts are dominated by volcanic bombs and are therefore more commonly associated with vents or fissures (ICL, 2013a). In the past, however, the term was used more commonly to refer to any pyroclastic breccia, so the context in the literature is at times unclear whether the agglomerate outcrops represent the remnants of a volcanic vent, or

a volcanic unit (Leyshon, 1969).

The majority of the centres can be found within the Piriwiri Group, along a strike length of approximately 100 km, parallel to the north-east Magondi regional trend. (Leyshon, 1969; Munyanyiwa et al., 1999), which could imply a structural control is involved in their formation.

The age relationships for the various volcanic centres based on field relationships are unclear; Kirkpatrick (1976) believed the centres to be younger than the surrounding country rocks, citing that the agglomerate consists of fragments of tuff, felsite and other country rock fragments (some of which were supposedly unaffected by deformation related to the Magondi orogeny). Leyshon (1969) considered the volcanic centres to be of a similar age to the country rock, and Master et al. (2010), propose that the volcanic centres may not actually represent vent breccias; instead they consider the centres to simply be exposed sections of a fairly continuous volcanic unit termed the "Piriwiri Mineral Belt" (Figure 3.2), interbedded with the country rock.

Godzi

Two varieties of tuff have been described by Leyshon (1969) within Godzi: a more abundant crystal tuff (which forms the bulk of the agglomerate matrix) and a finer-grained variety. Both are yellowish-brown in colour, although in the latter, banding is better defined (Leyshon, 1969). The felsites are fine-grained, light olive-grey rocks, while the interbedded chert is usually black in colour. Pyrite is a common accessory mineral in the felsite, and thus has a tendency to make the felsites appear gossan-like when very weathered (Leyshon, 1969). Leyshon (1969) also postulated that the majority of the felsites have an extrusive origin and were deposited under sub-aerial conditions. Additionally, based on the presence of bedding and large, angular, poorly sorted grains within the crystal tuffs, a mechanism of air-fall aggregation was also put forward for the formation of the crystal tuffs.

Obva (Hova)

The Obva volcanic centre is not as extensive as Godzi, but it does occur as three scattered outcrops. The crystal tuffs at Obva are more varied and extensive when compared to those at Godzi, and in the vicinity of the volcanic centre there is a fairly large outcrop of volcanic breccia, which Leyshon (1969) described as a finer-grained version of the agglomerate at Godzi. The breccia is composed of clasts of a more quartz-rich variety of crystal tuff as well as some felsite fragments, with accessory amounts of haematite, rutile and tourmaline.

Descriptions of the breccia state that it has greyish-orange fragments within a reddish-purple matrix which is similar to the matrix of the Nyamakari agglomerate (Kirkpatrick, 1976).

Nyamakari

The Nyamakari centre, although lithologically similar to the other volcanic centres, is an exception as it is the only centre which is found within the Lomagundi Group (Kirkpatrick, 1976; Master et al., 2010). The main body is roughly oval in shape, its dimensions being approximately 400m by 700m (Kirkpatrick, 1976). The agglomerate unit here appears to be more extensive and contains fragments of tuff, felsite, and country rock as well xenoliths of chloritic schist or granite, all within a coarse-grained matrix of feldspar and magnesian carbonate. These rocks also appear quite altered due to the presence of ubiquitous calcite, goethite and sericite. Both Leyshon (1969) and Kirkpatrick (1976) have respectively indicated that this secondary calcite at Obva and Nyamakari has generated a pseudo-brecciated appearance, as a result of the calcite forming in an irregular, fragmentary-like pattern. Secondary tourmaline is also common to both the Obva and Nyamakari centres.

3.3. FIELD AND PETROGRAPHIC DESCRIPTIONS

According to Fisher and Schmincke (1984), pyroclastic fragments are produced by processes directly related to volcanic eruptions, while epiclastic fragments are either the result of the weathering and erosion of older volcanic rocks or are non-volcanic in origin (like the calcite fragments in sample Z 11/C – SKR 2B). In general epiclastic deposits also consist of at most only a small proportion of glass shards or pumice fragments which readily alter to metastable glass, clays and zeolites (Fisher and Schmincke, 1984).

3.3.1 Deweras Group

DV 11/ 1: Mafic Lava

Samples DV 11/ 1 and DV 11/ 2 were collected within 50 m of one another along the banks of the Mupfure River. The Munyati Formation which sits at the base of the Deweras Group's southern facies is predominantly made up o f mafic volcanics, and sample DV 11/ 1 is believed to represent these lavas. In hand specimen, DV 11/ 1 consists of light (fine-grained) and dark (coarser-grained) green patches (Figure 3.4a), which may be the preservation of an original flow texture. In photomicrographs (Figure 3.4b), it is possible to see that small needles of chlorite make up a significant percentage of the matrix in addition to forming

veins and small clumps. Microphenocrysts of enstatite and augite are also abundant in addition to quartz; the latter is associated with chlorite in the matrix, a common alteration product of olivine. Irregularly shaped titanite and an opaque mineral phase are also common accessory minerals.

DV 11/ 2: Epiclastic volcanic sandstone

The hand specimen of sample DV 11/ 2 exhibits what appears to be some degree of layering, although faint, which as a result lends the sample a similar appearance to that of a fine to medium-grained, grey-green sandstone. Given sample DV 11/ 2's proximity to sample DV 11/ 1, it is likely derived (at least in part) from the former; and from photomicrographs it is evident that there are some similarities, particularly with regards to the matrix composition of the two samples. Sample DV 11/ 2 consists of angular, poorly sorted fragments sitting within a fine-grained matrix consisting of quartz, plagioclase, chlorite and muscovite (Figure 3.5a). The fragments are made up largely of polycrystalline quartz, with sutured grain boundaries, other fragments are plagioclase, chlorite in addition to some smaller grains of muscovite and calcite.

3.3.2 Lomagundi Group

NC 1: Andesitic agglomerate (Nyamakari volcanic centre)

It is possible to identify clasts within the hand specimen of sample NC 1, which are quite clearly irregularly shaped. The sample is also visibly pinkish, due to a combination of the potassic alteration of both plagioclase and orthoclase, as well as abundant interstitial calcite (Figure 3.4c). Tourmaline has also been observed as a common accessory mineral phase (insert to Figure 3.4c).

Z 11/ C – SKR 2B: Epiclastic volcanic sandstone

Sample Z11/ C – SKR 2B was collected along the Sakugwe River, and likely belongs to the volcanic member of the Nyagari Formation within the Lomagundi Group. The larger lithic fragments seen in outcrop range from 1 to approximately 5cm in size, and less than a kilometre upstream, to the north-west, the fragments are larger and more abundant. On an outcrop scale the unit is a light grey colour. Photomicrographs indicate that the more prominent lithic fragments are sub-rounded polycrystalline, equigranular calcite fragments, which are variably affected by haematite staining (Figure 3.5b). There are also sub-rounded

fragments of polycrystalline quartz within a fine-grained matrix of quartz, plagioclase, chlorite and muscovite.

SKG Z11/ 1: Epiclastic volcanic sandstone

Sample SKG Z11/ 1 (18° 06' 12.0" S; 29° 29' 28.0" E), dated as part of an earlier study using LA-ICPMS to be approximately 2.15 Ga in age (Axel Hofmann and Andrey Bekker, personal communication), has been included in this work as it gives more insight into the age of deposition for the Lomagundi Group sediments. As can be seen in Figure 3.5c, the matrix is chiefly composed of interstitial Fe-rich chlorite and muscovite. Overall the fragments of polycrystalline sutured quartz, muscovite, plagioclase and calcite tend to be angular to sub-rounded. In hand specimen the fragments are generally no larger than 0.5 mm in size, and the rock in general has a grey-green appearance which is distinctive on an outcrop scale.

3.3.3 Piriwiri Group

GD – Z11/ 2A Epiclastic volcanic siltstone

The Godzi samples (GD – Z11/ 2A and GD – Z11/ 3) were collected from two NE-trending parallel ridges about a kilometre apart, where the ridges intersect the Mupfure River. Sample GD – Z11/ 2A is fine-grained and grey in colour, and on an outcrop scale layering is evident in the form of alternating light and dark bands. Photomicrographs show that these contacts are neither regular, nor particularly well defined, but that they occur as alternating layers of fine to slightly coarser-grained quartz (Figure 3.5d). Rutile is seen as an accessory mineral phase.

GD – Z11/ 3: Andesitic agglomerate (Godzi volcanic centre)

GD – Z11/ 3, like NC 1, is somewhat pinkish in colour due to the effects of potassic alteration, and again there is abundant interstitial calcite (Figure 3.4d), which seems to heighten the brecciated appearance of the sample. The plagioclase and orthoclase grains are more euhedral in sample GD – Z11/ 3 a nd there is less evidence of recrystallisation, muscovite is also more abundant, while tourmaline is less so.

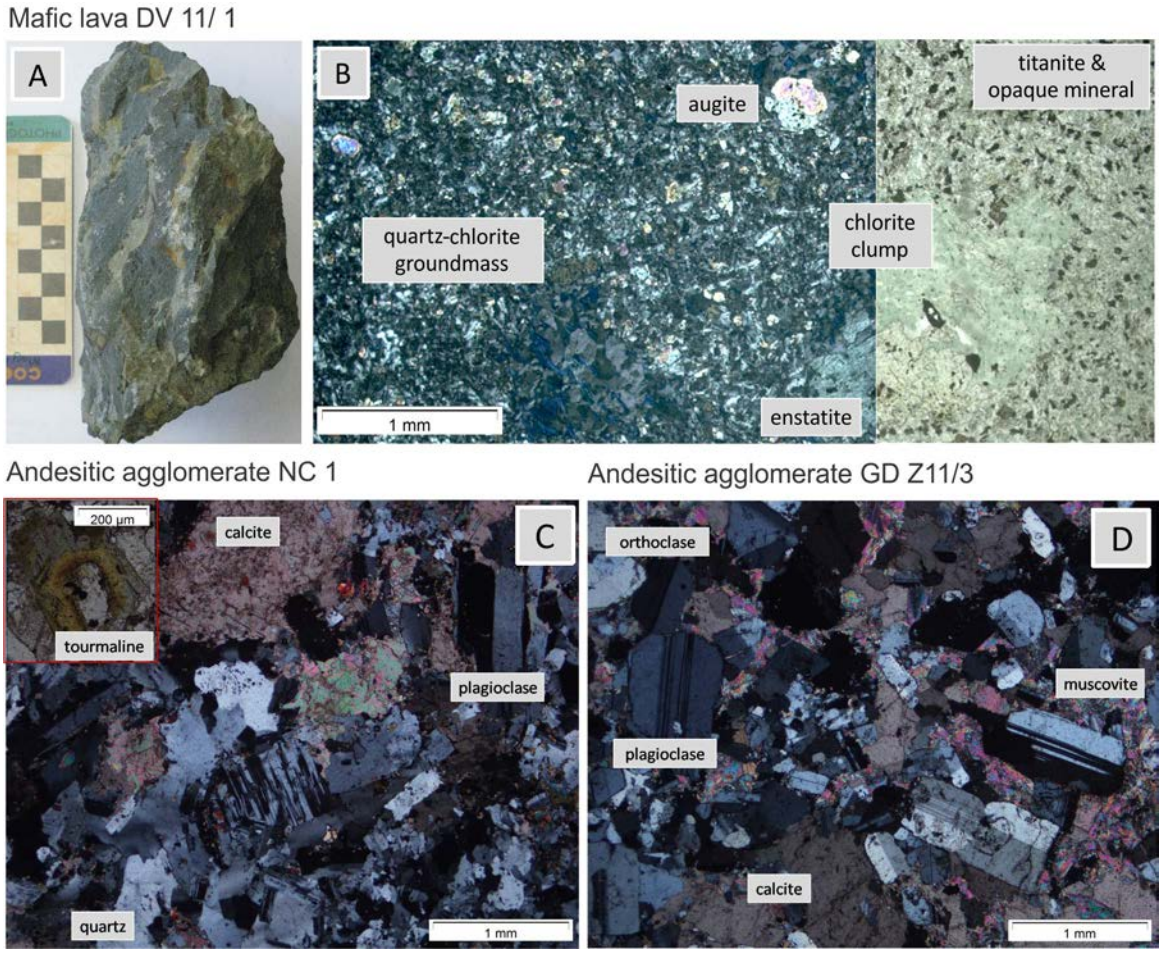

Figure 3.4: Hand specimen of sample DV 11/1 (Figure 3.4a), the left-hand side of the photomicrograph in (Figure 3.4b) was taken under XPL, while the right-hand side is in PPL. XPL photomicrographs of the andesitic agglomerates NC 1 (Figure 3.4c) and GD Z 11/3 (Figure 3.4d) from the Nyamakari and Godzi volcanic centres respectively.

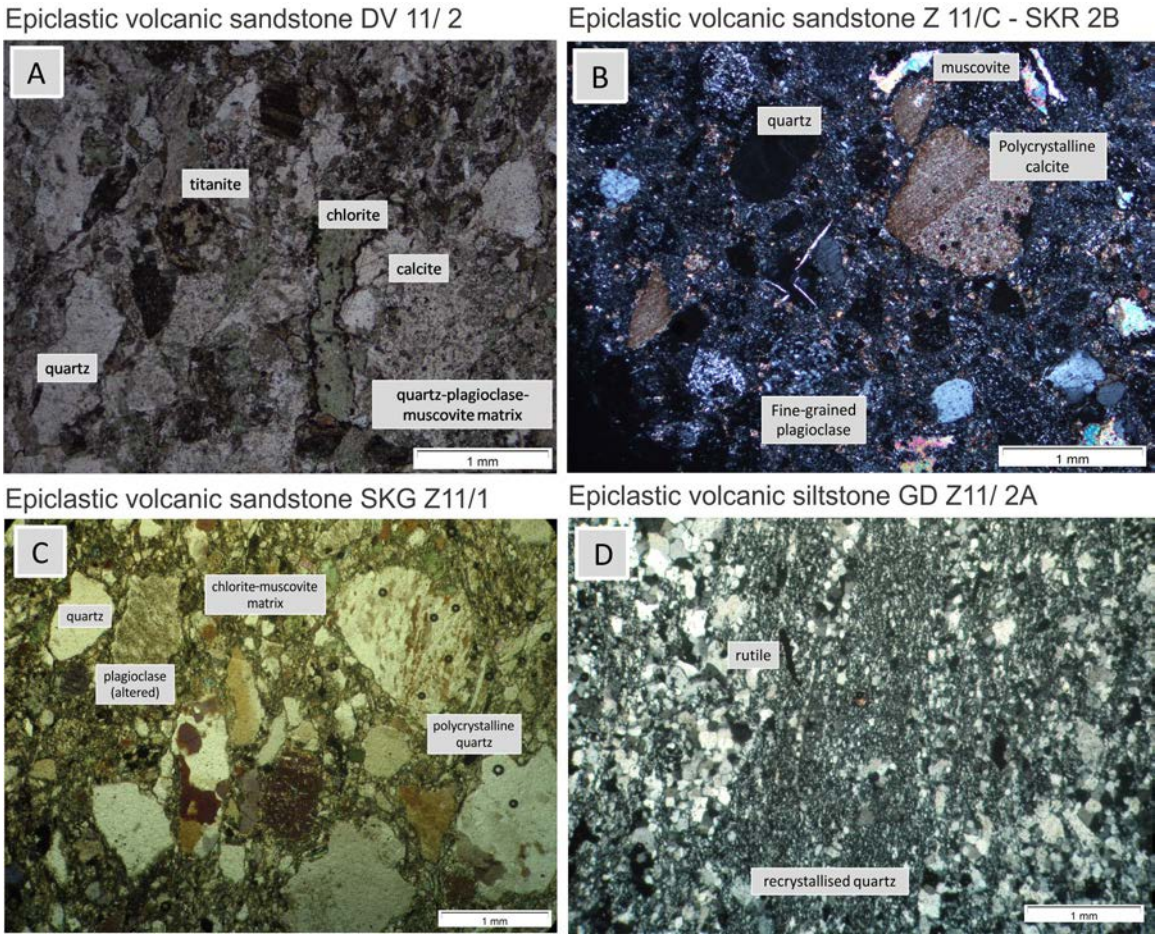

Figure 3.5: Sample DV11/ 2 seen under PPL (Figure 3.5a), is from the Deweras Group, while samples Z 11/C – SKR 2B (Figure 3.5b; XPL) and SKG Z11/1 (Figure 3.5c; PPL) originate from the Lomagundi Group. Sample GD Z11/ 2A (Figure 3.5d; XPL) is found within the Piriwiri Group and is related to the Godzi volcanic centre.

3.4. GEOCHEMISTRY

It is evident that GD Z11/ 2A, NC 1 and GD Z11/ 3 have elevated Na_2O and K_2O values in Figure 3.6a, and the data in Table 3.1 (Appendix A2) show that the latter two have high LOI values, all of which imply that these samples have been affected to some degree by alteration (already confirmed petrographically). For this reason little emphasis is being placed on the results in Figure 3.6a, however the bivaritate plot of Ti vs. V in Figure 3.6b has been used in an attempt to work around the problem of alteration within the samples. Ti and V are incompatible elements, and are therefore less mobile and the fact that all the samples (with the exception of DV 11/ 1) plot quite close together indicates that these samples all have a component within them which has a similar composition. DV 11/ 1 has already been

established as having a more mafic composition (classified as a basaltic andesite in Figure 3.6a) and understandably plots differently, but the other primary volcanic features (NC 1 and GD Z 11/ 3 which represent the volcanic centres) plot alongside the epiclastic deposits. It is therefore likely that the volcanic component found within the epiclastic deposits is that of a similar composition to the andesitic agglomerates.

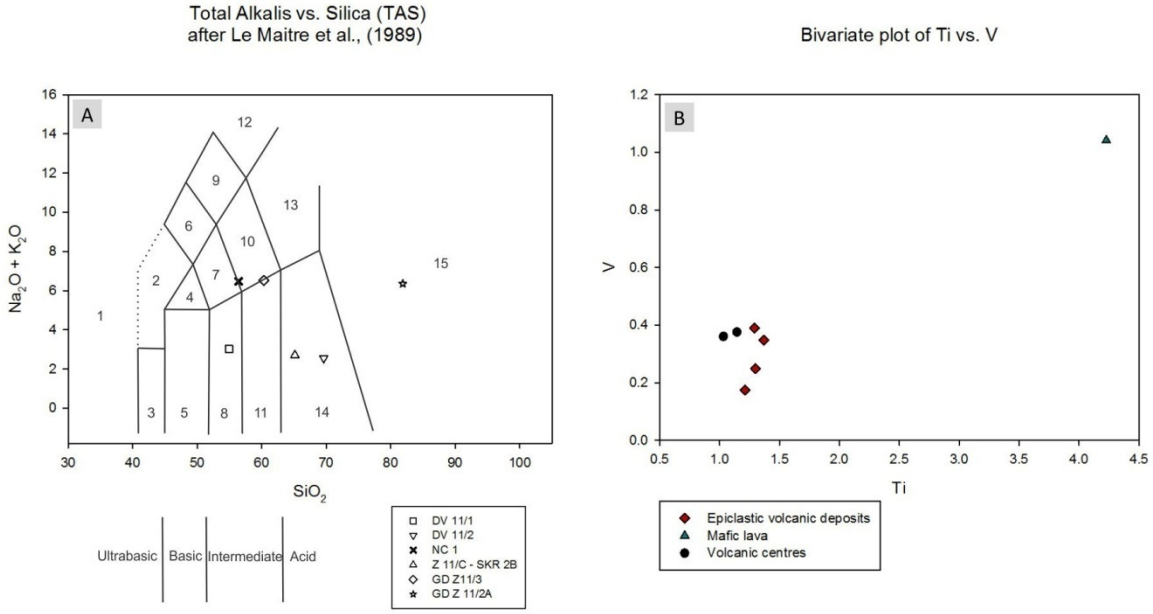

Figure 3.6: Plot of Total Alkalis vs. Silica (Figure 3.6a) to discriminate between the various samples. 1=Foidite; 2=Tephrite (Ol<10%), Basanite (Ol>10%); 3=Picrobasalt; 4=Trachybasalt; 5=Basalt; 6=Phonotephrite; 7=Basaltic trachyandesite; 8=Basaltic andesite; 9=Tephriphonolite; 10=Trachyandesite; 11=Andesite; 12=Phonolite; 13=Trachyte (Q<20%), Trachydacite (Q>20%); 14=Dacite; 15=Rhyolite. Figure 3.6b is a bivariate plot of Ti vs. V, the data are normalised according to the values from Taylor and McLennan (1981) for the average upper crust.

Munyanyiwa et al. (1999) had previously done a geochemical study of the felsic pyroclastic deposits associated with the volcanic centres, and they too recorded significant evidence for alteration, mainly in the form of secondary calcite, siderite and tourmaline replacing the primary feldspars, which they attributed to circulating CO_2 and boron-rich fluids.

3.5. GEOCHRONOLOGY

Five of the six samples discussed were analysed using the SHRIMP-RG, the sixth sample

(GD Z11/ 3) was dated using LA-ICPMS. Detailed information on the methodology followed can be found in sections 2.6.1 and 2.6.3 on page 31. The individual $^{207}Pb/^{206}Pb$ ratios and ages quoted in Tables 3.2 and 3.3 (Appendix A2) have an analytical uncertainty of 1 and 2sd respectively.

The concordia plots in the following section show all the zircons considered in our age evaluations. In some instances the maximum depositional age (i.e. the age defined by the youngest concordant zircon) has been poorly constrained by only a small number of grains, and in such cases we acknowledge that more measurements would result in a more meaningful interpretation.

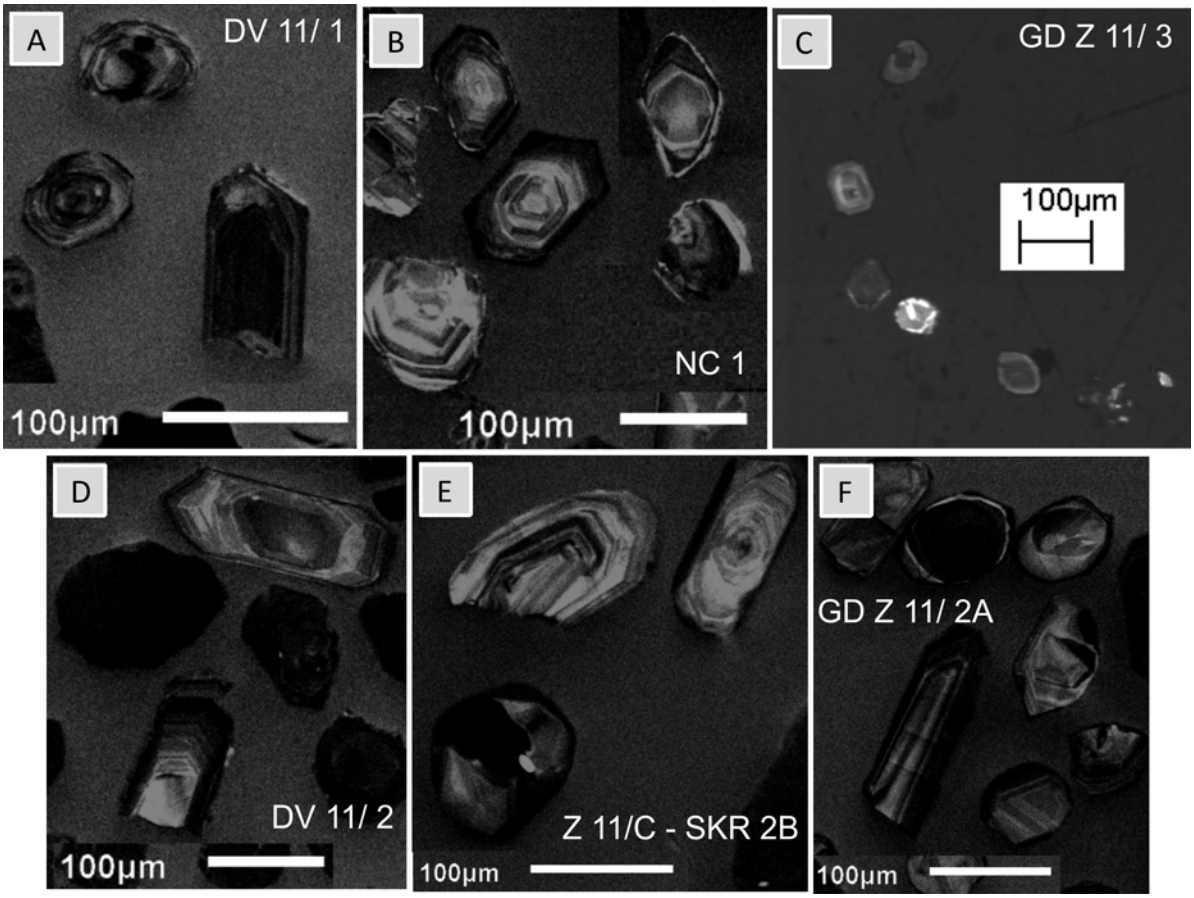

Figure 3.7: CL images of zircons typical of the samples analysed. Several grains can be seen to be inherited, due to their rounded morphology and truncated oscillatory zoning within the grain interior.

3.5.1 Primary volcanic features

Samples DV 11/ 1 (Figure 3.7a), NC 1 (Figure 3.7b) and GD Z11/3 (Figure 3.7c) contain

many semi-rounded grains which have a distinct magmatic zonation pattern and are believed to be inherited. Other grains have a more euhedral appearance; these are fewer in number, but are still magmatic in appearance.

The majority of the twenty two zircons extracted from sample DV 11/ 1 yielded near concordant results, with the six youngest zircons forming a discordia line. From the eleven most concordant zircons an inherited population with an age of 2637 ± 13 Ma (MSWD = 1.9) has been calculated. An age of 2297 ± 970 Ma (MSWD = 19, N = 4) for the upper intercept of the discordia line can also be seen in Figure 3.8a.

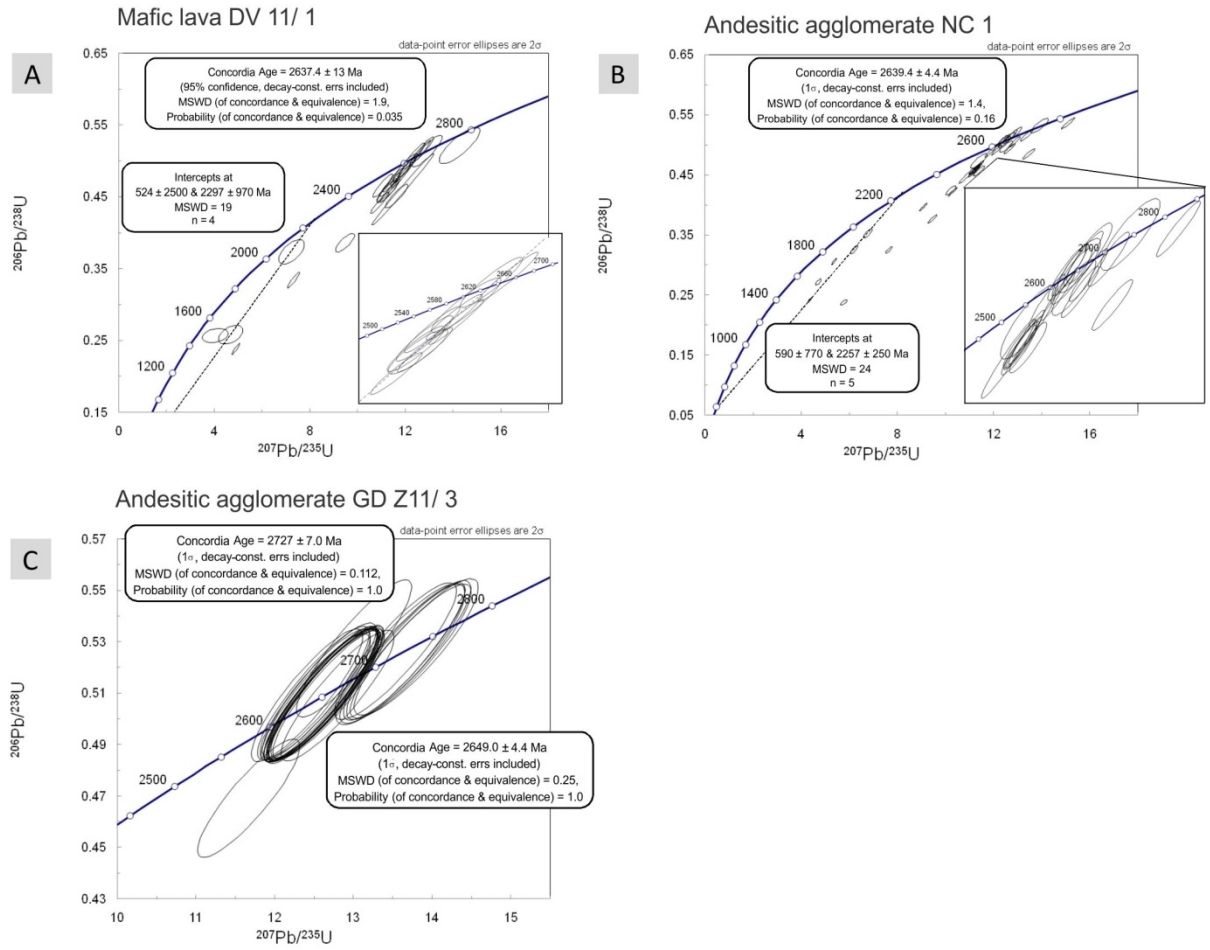

Figure 3.8 Concordia plots of the SHRIMP data for samples DV 11/1 (Figure 3.8a) and NC 1 (Figure 3.8b), in addition to the LA-ICPMS data for sample GD Z 11/ 3 (Figure 3.8c).

Petrographically the samples from the Nyamakari and Godzi centres (located within the Lomagundi and Piriwiri Groups respectively) are very similar (Figures 3.4c and d), so it is unsurprising that the ages for the two volcanic centres are so closely related, with both having inherited populations with ages of 2639 ± 4 (MSWD = 1.4, N = 7) and 2649 ± 4 Ma (MSWD

= 0.25, N = 23) respectively for samples NC 1 and GD Z 11/3 (Figures 3.8b and c). Sample GD Z 11/3 additionally has a slightly older inherited population of zircons dated at 2727 ± 7 Ma (MSWD = 0.11, N = 7), while NC 1 has a discordia line generated by a number of younger zircons with the upper intercept age of 2257 ± 250 Ma (MSWD = 24, N = 5).

3.5.2 Epiclastic volcanic deposits

The zircon grains in sample DV 11/ 2 (Figure 3.7d) consist of a mixture of euhedral prismatic grains and rounded grains. Measurements made on a mixture of both cores and rims, reveal that sample DV 11/ 2 exhibits a clearly bimodal distribution of zircon ages (Figure 3.9a), and is therefore composed of two discrete populations of inherited zircon dated at 2641 ± 4 (MSWD = 1.17, N = 23) and 2865 ± 3 Ma (MSWD = 1.4, N = 34). The two individual zircon grains with ages *circa* 2.42 and 2.17 Ga poorly constrain possible sedimentation ages for this sample and the Deweras Group in general. Unfortunately it is not possible to constrain an age with any real certainty due to the age being defined by only a single zircon in each case.

Samples Z 11/C – SKR 2B and GD Z 11/2A together contain significantly more Palaeoproterozoic zircons than the previous samples combined. The zircon grains in both are a mixture of rounded inherited grains as well as more euhedral prismatic grains, all of which are magmatically zoned (Figures 3.7e and f).

Data from sample Z 11/C – SKR 2B in Figure 3.9b, shows a cluster of inherited Archaean zircons at 2647 ± 30 Ma (MSWD = 1.1, N = 4), and a second, slightly larger, group of zircons forming a discordia line which has an upper intercept of 2204 ± 22 Ma (MSWD = 1.3, N = 9). The two youngest concordant zircons define a maximum sedimentation age of 2071 ± 13 Ma (MSWD = 0.34).

Sample GD Z 11/ 2A consists of inherited zircon grains which range in age from approximately 3.3 to 2.4 Ga. The youngest zircon grain (dated at 2051 ± 9 Ma) would ordinarily define the maximum sedimentation age; it is however, only a single discordant zircon, and a better approximation is afforded by the slightly older group of six concordant grains seen in Figure 3.9c, which have been dated at 2163 ± 5 Ma (MSWD = 1.2).

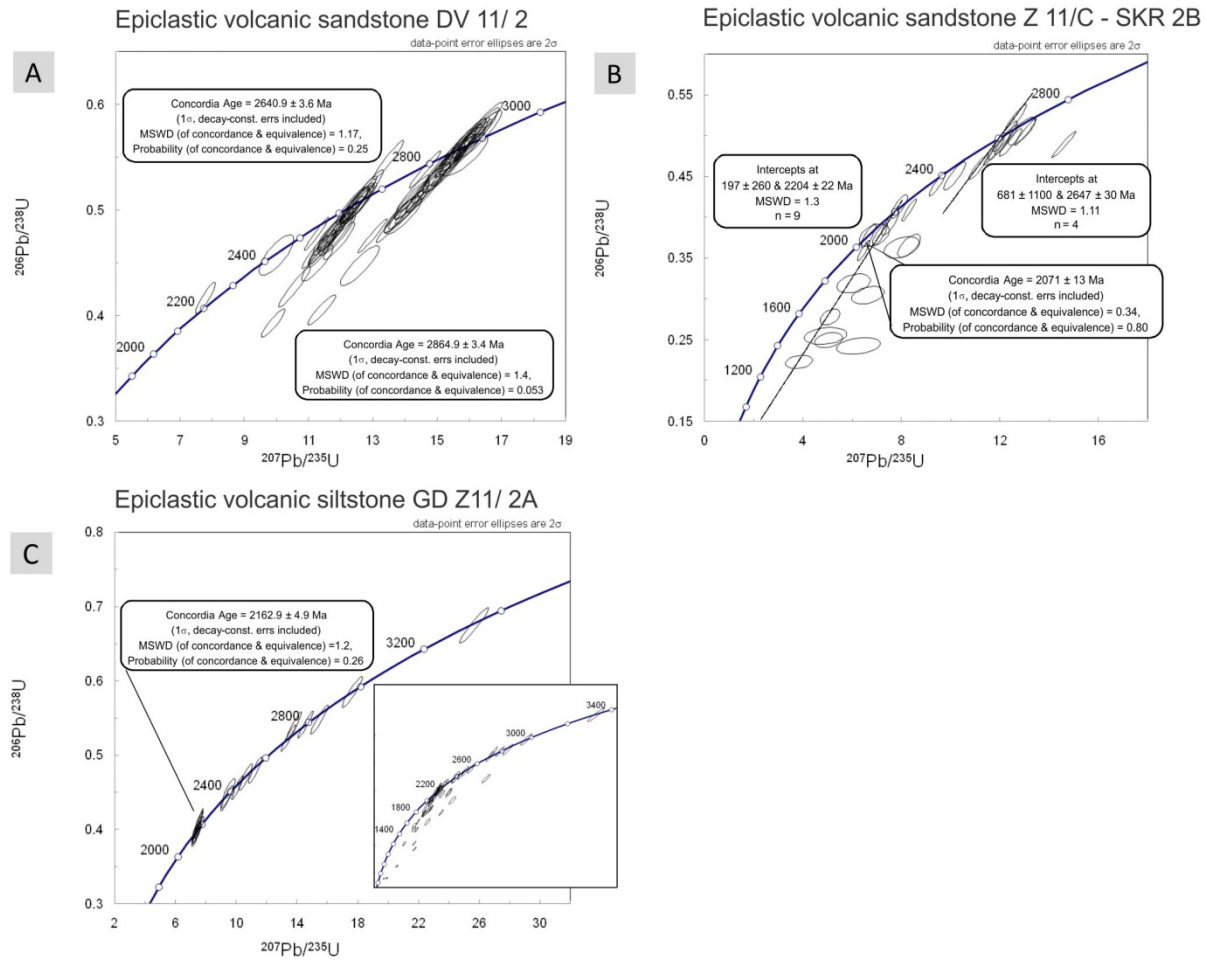

Figure 3.9: Concordia plots of the SHRIMP data for samples DV 11/ 2 (Figure 3.8a), Z 11/C – SKR 2B (Figure 3.8b) and GD Z 11/ 2A (Figure 3.8c).

3.6. DISCUSSION AND CONCLUSIONS

The ages obtained for samples DV 11/ 1 (2637 Ma and 2.29 Ga) and DV 11/ 2 (2865, 2641 Ma and 2.17 Ga) from the Deweras Group confirm that these two samples contain basement derived material, likely originating from the nearby granite-greenstone belts. The 2.29 Ga upper intercept age for the mafic lava DV 11/ 1 places some constraints on the age of the Deweras lavas, while the single youngest zircon in sample DV 11/ 2 (2.17 Ga) is a best estimate at the maximum sedimentation age for the Deweras Group. Samples NC 1 and GD Z 11/ 3 which represent the Nyamakari and Godzi volcanic centres, also reflect inheritance from the granite-greenstone basement dated at 2639 and 2649 Ma respectively. Only the Nyamakari centre (NC 1) gives some indication as to the age of the agglomerate eruption - sometime around 2.25 Ga. The epiclastic volcanic deposits Z 11/C – SKR 2B and GD Z 11/ 2A which originate from the Lomagundi and Piriwiri Groups contain a significant proportion

of both Archaean and Palaeoproterozoic aged zircons. Sample Z 11/C – SKR 2B contains inherited material (between 2647 and 2204 Ma) and has a maximum sedimentation age of 2071 Ma. The depositional age obtained from sample SKG Z 11/ 1 overlaps with the age obtained by Schidlowski and Todt (1998) for the Lomagundi dolomites which they dated, and indicates that the sediments appear to be older than the volcanic unit. The maximum sedimentation age obtained for GD Z 11/ 2A (2163 Ma) is very different from any previously dated samples within the Piriwiri Group, as it is older than one would expect, unless the age of the single youngest zircon (2051 Ma) is considered.

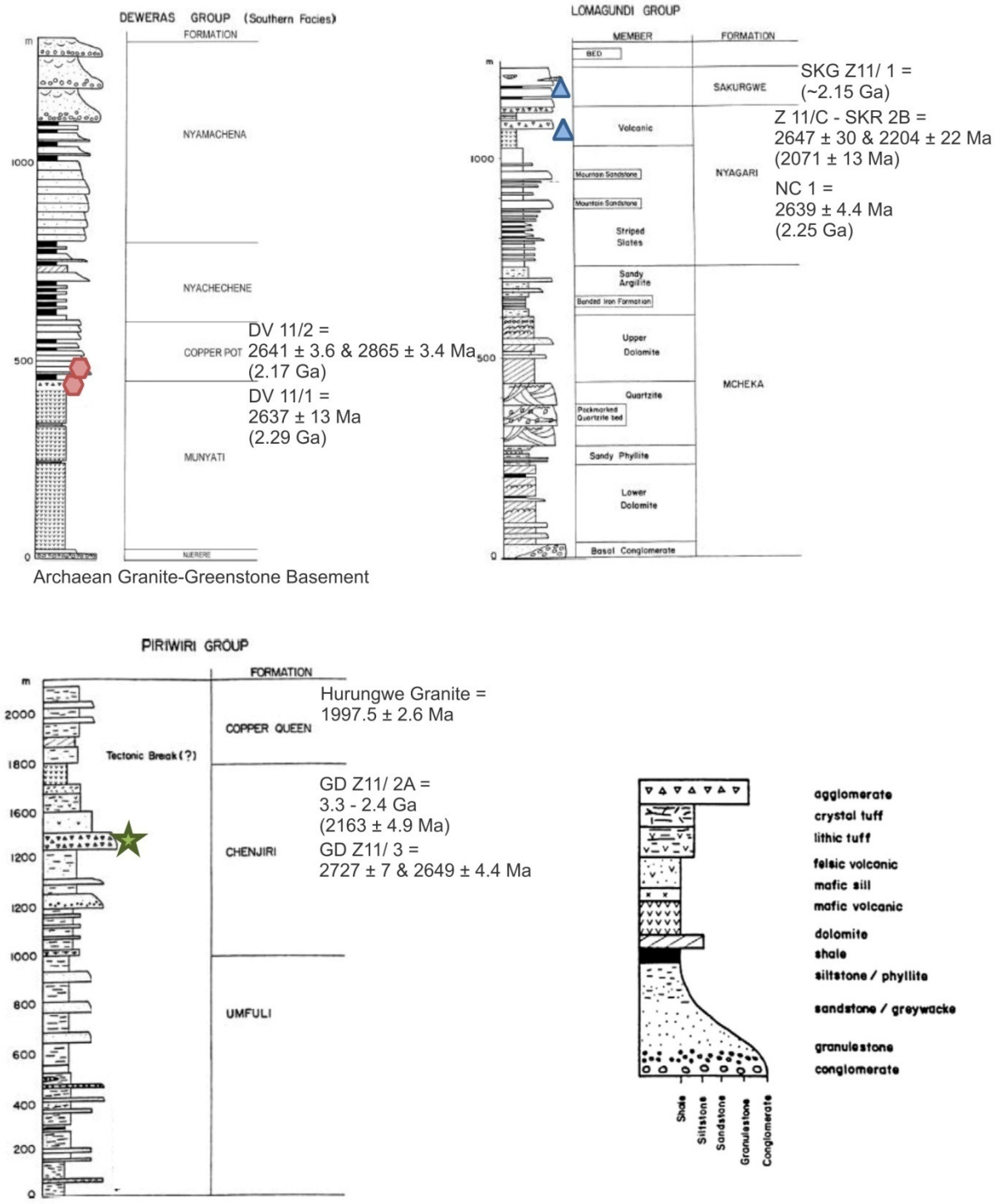

Figure 3.10: Compilation of age data for the Magondi Belt. The ages in brackets represent the maximum depositional ages, whereas those not in brackets are magmatic ages, after Master et al. (2010).

3.6.1 The Zimbabwe-Superior Craton connection

The Kaapvaal and Pilbara Cratons have long been considered to have once formed the supercontinent Vaalbara (Cheney, 1996). According to Bleeker (2003), these two cratons

may have rifted away from one another *circa* 2.77 Ga, just prior to the deposition of the Transvaal and Hamersley basin cover sequences, while the Zimbabwe Craton alternatively, may have been connected to either the Superior or the Slave Craton. The discrepancy arises in part, because workers like Bleeker (2003) have stated that the Kaapvaal and Superior Cratons are radically different from the Slave Craton, and that the latter bears some resemblance to the Zimbabwe Craton, and may therefore have been its nearest neighbour within the Sclavia Supercraton. In comparing the ages of various mafic intrusions side-by-side, a pattern much like that of a barcode emerges, this pattern can then indicate when events of the same age occurred on the respective cratons. Both Master et al. (2010) and Söderlund et al. (2010) have made an association between the Superior and Zimbabwe Cratons based on the magmatic barcode seen in Figure 3.11, which is the result of a series of similarly aged dyke swarms on the Zimbabwe and Superior Cratons.

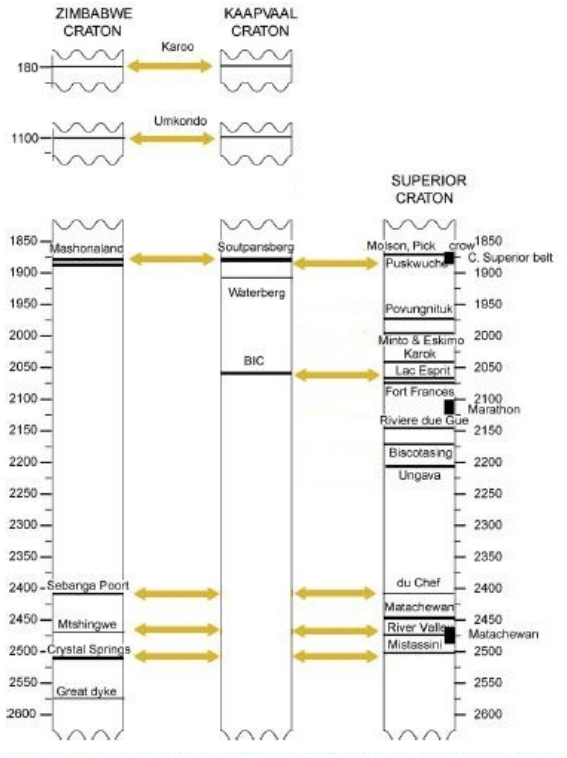

Figure 3.11: Barcode pattern of mafic intrusions which have occurred on the Zimbabwe, Kaapvaal and Superior Cratons, after Söderlund et al. (2010).

The existence of the extensive Chilimanzi Granite Suite dated to be between 2.60 and 2.54 Ga (Rollinson and Whitehouse, 2011) within the Zimbabwe Craton is perhaps the strongest evidence proponents have in favour of the Zimbabwe-Slave Craton connection, as the Slave

and several of its other nearest neighbours also contain a late Archaean granitoid suite culminating at ~2.6 Ga. Bleeker (2003, 2004) also stated that the break-up of the Superior and Slave's respective supercratons occurred approximately 200 Ma apart (2.45 and 2.23 Ga respectively). The 2.40 Ga Sebanga Poort dyke swarm on the Zimbabwe Craton (Figure 3.11), is the youngest of the dyke swarms which bear any relation to the Superior Craton, and thus best represents when the Zimbabwe and Superior Cratons began rifting apart. There is however, the as yet undated Plumtree dyke swarm which is believed to be a possible feeder to the Deweras Group lavas (Wilson et al., 1987). If this is true, the Plumtree dyke swarm would therefore be placed sometime around 2.29 Ga (this work; Söderlund et al., 2010). It is therefore possible that one of the dyke swarms recorded on the Superior Craton within that time period would then correspond with the Plumtree dyke swarm. This would then constrain rifting of the Superior Craton from the Zimbabwe Craton to have occurred around the same time as what is recorded for the Slave Craton (~2.2 Ga).

The magmatic events which the Zimbabwe and Superior Cratons have in common make for a compelling reason as to why it is more likely that the Zimbabwe Craton was the nearest neighbour to the Superior Craton, rather than the Slave Craton. Additionally rifting within the Labrador trough (Superior Craton) between 2210 and 2220 Ma resulted in the formation of the Mistassini and Otish Basins (Master et al., 2010; Söderlund et al., 2010), and both basins contain carbonate successions with high, positive carbon isotope signatures similar to those recorded within the Lomagundi Group (Bekker et al., 2003). Thus it is plausible that the Zimbabwe Craton was situated along the eastern margin of the Superior Craton until approximately 2.29-2.17 Ga (Master et al., 2010).

It is still hotly debated at what point the Zimbabwe and Kaapvaal Cratons collided, with proponents like Kramers et al. (2006, 2011) suggesting that the two were juxtaposed as far back as the Neoarchaean. However it is clear from the work of Söderlund et al. (2010) that the Kaapvaal and Zimbabwe Cratons had very little in common until ~ 1.8-1.9 Ga (Figure 3.11). Bleeker (2003, 2004) moreover states that there is no evidence of Bushveld Complex aged magmatism (2057 - 2054 Ma; Olsson et al., 2010; Scoates and Friedman, 2008) on the Zimbabwe Craton; and likewise the Kaapvaal Craton is lacking evidence of the craton-wide 2.6 Ga Chilimanzi Granite Suite as well as Great Dyke magmatism recorded at 2575 ± 0.7 Ma (Oberthür et al., 2002). Thus we suggest that the collision between the Zimbabwe and Kaapvaal Cratons occurred *circa* 2.0 Ga during the Magondi orogeny.

3.6.2 The Zimbabwe Craton in the Palaeoproterozoic

The Chimbadzi Hill Intrusion – an ultra-mafic dyke, dated at 2262 ± 2 Ma by Manyeruke et al. (2004) – was originally thought to be of a similar age to the Great Dyke based on its proximity and parallel orientation (Figure 3.12). Given its age however, it is reasonable to assume that the Chimbadzi Hill Intrusion could represent the period of rifting related to the break-up of Superia and the initiation of the formation of the Magondi Supergroup within a passive margin setting. Manyeruke et al. (2004) had also concluded that the Chimbadzi Hill Intrusion did not correlate with any other tectono-thermal events within the Zimbabwe Craton; thus we believe it could correlate with one of the similarly aged dyke swarms indicated in figure 3.11 on the Superior Craton.

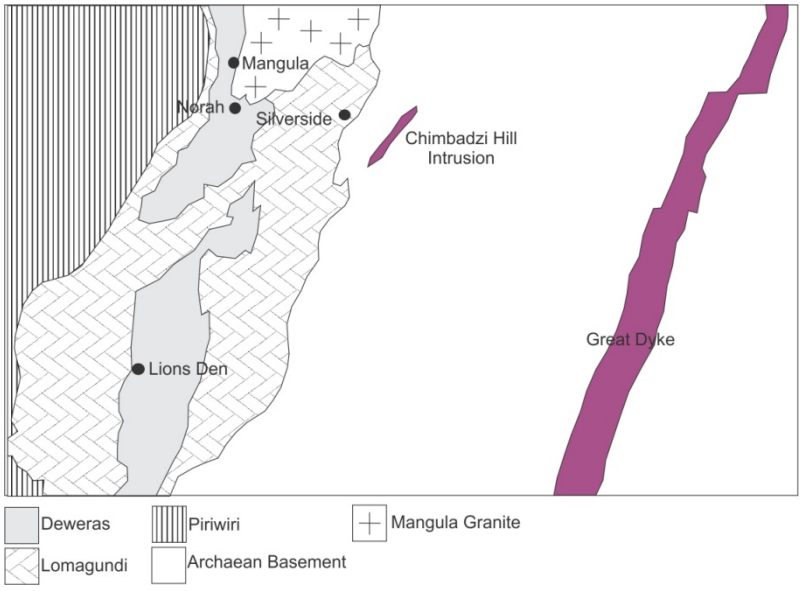

Figure 3.12: Geological setting for the Chimbadzi Hill Intrusion (after Sithole, 1977).

After rifting was initiated and the Deweras lavas were introduced, sedimentation resulting in the Deweras Group took place. The majority of the ages coming out of the Deweras Group samples, however, are Archaean in age (2.86 and 2.64 Ga), indicating that it is largely the underlying granite-greenstone basement which has been sampled.

The lower Lomagundi and Piriwiri Group sediments were deposited within a passive margin environment as the Zimbabwe Craton rifted away from the Superior Craton (Master et al., 2010) between 2.16 and 2.07 Ga. The age McCourt et al. (2001) obtained for the Hurungwe granite (1997.5 ± 2.6 Ma), is believed to constrain the maximum age for the Piriwiri Group, as it intrudes the metasediments and coincides closely with the Magondi orogeny and the formation of a proposed Andean-type magmatic arc along the western margin of the proto

Kalahari Craton. The orogeny and the formation of the Magondi Belt are proposed to be the result of the convergence of an unknown continental mass and the Zimbabwe Craton, and is associated with the deposition of the upper Lomagundi and Piriwiri Group sediments and pyroclastic rocks within an active continental margin (Master et al., 2010, 2013; Glynn et al., 2015).

Chapter 4: The vanished orogeny: Geochronology of Palaeoproterozoic "basement" gneisses of the Kariba area, western Magondi Belt (Zimbabwe and Zambia)

4.1 INTRODUCTION

The Magondi Belt is a Palaeoproterozoic mobile belt situated on the western margin of the Archaean Zimbabwe Craton, extending from north-west Zimbabwe into north-east Botswana, and consists of deformed rocks of the Palaeoproterozoic Magondi Supergroup. In the low-grade (greenschist to amphibolite facies) part of the Magondi Belt are the Deweras, Lomagundi and Piriwiri Groups; while in the high-grade parts of the belt (particularly in the north), are granulites, and intrusive granitoids previously dated to be between 2.5 and 2.2 Ga (Leyshon and Tennick, 1988; Master et al., 2010). New U-Pb zircon ages for these granitoids, belonging to the proposed "Hurungwe orogeny" (Master, 1991b, 1996), believed to predate the Palaeoproterozoic Magondi orogeny (and thus reflect the basement to the Magondi Belt), are outlined in this chapter.

4.2 REGIONAL GEOLOGICAL SETTING

In the northern reaches of the Magondi Belt, the crystalline basement consists of a series of para - and orthogneisses, some of which have been considered part of the Zambezi Belt (Thole, 1976; Broderick, 1976, 1981), while others are thought to be older. These gneisses – depicted in Figure 4.1 – include, but are not limited to, the Urungwe as well as the Chiroti, Chipisa and Kariba gneisses, and are extremely variable in texture and composition, varying from foliated granitic leucogneisses to biotite gneisses and migmatites.

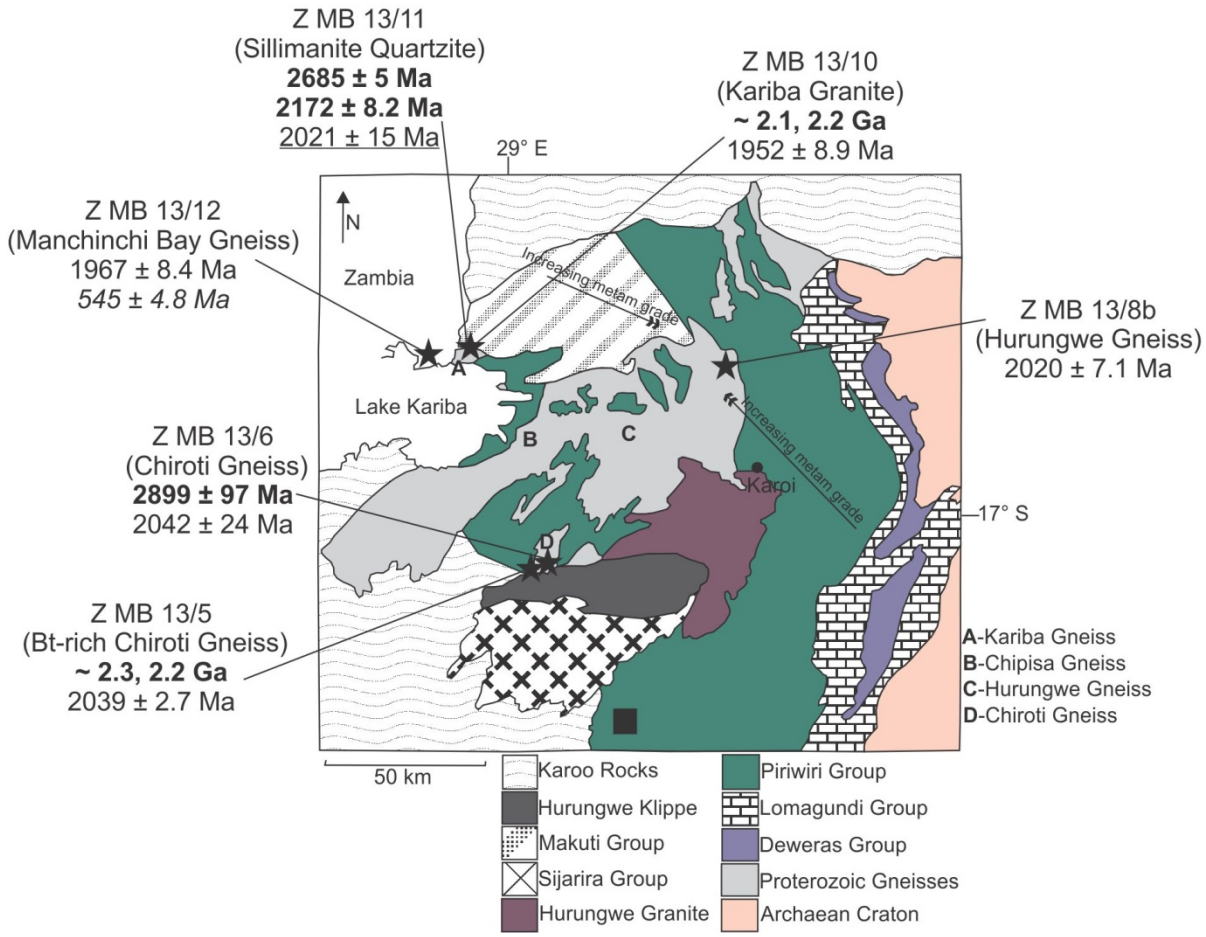

Figure 4.1: Simplified geological map of the northern half of the Magondi Belt; sample localities are indicated by stars. The black square indicates the approximate location of the Copper King and Copper Queen Domes, whereas ages in bold represent inheritance, those in plain text are magmatic ages and those in italics relate to a period of metamorphism. The map is after Treloar and Kramers (1989) and Broderick (1976).

4.2.1 The Kariba and Chipisa Paragneisses

The Kariba paragneiss is the northern continuation of the Chipisa paragneiss, and thus also consists of foliated biotite paragneisses with calc-silicate bands and thin leucogneisses (Hitchon, 1958a; Loney, 1969; Kirkpatrick and Robertson, 1987; Broderick, 1976), with the exception that the Kariba paragneisses are interbedded with sillimanite quartzite which is regarded as an arenaceous facies within the gneiss. Loney (1969) described dark, fine-grained xenoliths within the Kariba paragneiss, and we see similar features within the sample of Kariba Granite (sample Z MB 13/10). These biotite-rich inclusions can often be found within non-to-weakly foliated granitoids, reinforcing the supposition that they are xenoliths. Master (1996) regarded the thick sequences of fairly uniform biotite gneiss within the Chipisa

paragneiss to represent meta-turbidites, which may have been deposited in a deep-sea fan environment. Loney (1969) obtained a whole-rock Rb-Sr age of 2360 ± 90 Ma for the Kariba paragneiss, which Master (1991b) regarded as a minimum age, stating that the age of the protolith was most probably late Archaean or early Palaeoproterozoic. Loney (1969) also dated a meta-granite which intrudes the Kariba paragneisses to be 2050 ± 32 Ma (recalculated Rb-Sr whole rock age), while Dirks et al. (1999) obtained Pb-Pb evaporation ages of 1920 ± 0.4 and 1963 ± 0.4 Ma for the Kariba gneisses; in addition to an age of 2704 ± 0.3 Ma for a felsic biotite gneiss located just below what Dirks et al. (1999) believed to be the unconformable contact of the Makuti Group and the basement rocks. This Archaean gneiss as well as the 2443 ± 90 Ma age Loney (1969) obtained for the Chipisa paragneiss led Master (1991b, 1996) to interpret that these ages indicated a late Archaean to early Proterozoic metamorphic age for these rocks.

4.2.2 The Urungwe Paragneiss

Master (1991b) believes the biotite-rich and quartzo-feldspathic leucogneisses of the Urungwe paragneiss, were potentially derived from arkosic and greywacke-type protoliths. Additionally these gneisses are intercalated with metamorphosed marls, which hint at deposition within a shallow marine setting, whereas the younger, overlying Kariba and Chipisa paragneisses lack an abundance of coarse clastic material, as well as any major carbonate or arenite units, all of which indicate a deeper marine depository.

Clifford et al. (1967) and McCourt et al. (2001) obtained Rb-Sr and U-Pb ages for the Hurungwe Granite of 1980 ± 32 Ma and 1997 ± 2.6 Ma respectively, thereby confirming that this unit is intrusive into both the Piriwiri Group metasediments and the Urungwe paragneiss (Kirkpatrick, 1976; Treloar, 1988).

4.2.3 The Hurungwe orogeny

The gneisses and associated intrusives mentioned previously were proposed by Master (1991b, 1996) to record a major orogenic cycle, which although imprecisely dated, appeared to predate the *circa* 2.0 Ga Palaeoproterozoic Magondi orogeny. Because most of the gneisses in question occur in the Hurunge District, and occupy an area that had been termed the ‘Urungwe Subprovince’ by Stowe et al. (1984), Master (1991b) referred to this earlier orogenic cycle as the “Hurungwe orogeny”.

Due to the fact that the age constraints for this Hurungwe orogeny were poorly defined by the Rb-Sr whole-rock data of Loney (1969) to be between 2.3 and 2.8 Ga, Master (1991b, 1996)

believed that if the gneisses around the Hurungwe District could be correlated with those in the Guruve (Sipolilo) District to the north-east, it would help confirm that the former were late Archaean in age. Based on the mapping of Hahn et al. (1990) it appeared probable that there was some correlation between the two areas, as the Guruve gneisses were known to be intruded by the 2575.8 ± 1 Ma old Great Dyke (Worst, 1960; Wiles, 1968; Prost, 1982, Oberthür et al., 2002), meaning they would have to be Archaean in age.

Master (1991b, 1996) further reasoned that if the protoliths of the Hurungwe paragneisses were late Archaean (2.8 Ga; Loney, 1969), then they may have been contemporaneous with the calc-alkaline rocks of the Bulawayan Upper Greenstones in the western part of the Zimbabwe Craton, for which a subduction related origin had been proposed by Condie and Harrison (1976), Wilson et al. (1978) and Watkeys (1984). Thus the Hurungwe orogeny may then have involved the eastward oblique subduction of oceanic crust beneath the Zimbabwe Craton, as it moved to the south-west, before colliding with the Kaapvaal Craton. This would have resulted in the formation of an Andean-type arc (Watkeys, 1984), represented by the greenstone belts, while the Hurungwe orogeny would have represented a fore-arc trench complex, formed along the leading edge of the Zimbabwe Craton *circa* 2.3 Ga, which according to Loney (1969) is when the high-grade metamorphism occurred (Master, 1991b).

4.2.4 The Copper King and Copper Queen Domes

South of the Hurungwe Klippe (represented in Figure 4.1 by the black square), are what Leyshon (1973) described as pre-Magondi granite-gneiss basement inliers – namely the Copper King and Copper Queen Domes. Leyson (1973) described the Copper Queen dome as being composed of a suite of gneisses, which have been intruded by younger granites leaving exposures of foliated biotite-gneisses around the margins; whereas the Copper King Dome he explained, is composed largely of gneissic material bearing a resemblance to that of Copper Queen. The Copper Queen Dome granites are coarse-grained microcline-albite-plagioclase rocks that are generally poorly foliated and lack micas. As is illustrated in Figure 4.7a, the Copper Queen Dome is encircled by amphibolite and quartzite, which Leyson (1973) noted are not discordant with the overall structural trend in the area; this observation then led him to suggest that the gneisses were deformed together with the overlying Piriwiri sediments.

The Copper King Dome, some 70 km to the south-west of Copper Queen, is approximately five times larger, but has limited surface exposures suitable for dating.

4.3 ANALYTICAL METHODS

The individual $^{207}Pb/^{206}Pb$ ratios and ages for the six samples reported in Table 4.1 (Appendix A3), relating to the SIMS data, have an analytical uncertainty of 1 sd whereas the error ellipses in the concordia plots are at the 2 sd level. A detailed description of the SIMS methodology can be found within section 2.6.2 (31 pp).

Results (corrected for blank and initial common Pb) from the six samples where either the zircon, titanite, apatite or rutile fractions were analysed by ID-TIMS are given in Table 4.2 (Appendix A3), with errors for calculated ages at the 2 sd level. The isotopic results on minerals which contain significant initial Pb are given in Table 4.3 (Appendix A3). The methodology used to carry out the various ID-TIMS analyses has been outlined in detail in section 2.6.4 (34 pp).

The data relating to the single sample dated by LA-ICPMS (CKD – Z11/3) are represented in Table 4.4 (Appendix A3), and the methodology which was applied can be found in section 2.6.3 (33 pp).

4.4 RESULTS

The samples presented here were collected along a traverse through the northern Magondi Belt in both Zimbabwe, as well as in the Siavonga area of Zambia along the shores of Lake Kariba.

4.4.1 Biotite-rich Chiroti Paragneiss, Sample Z MB 13/5

Petrographically this sample consists of quartz, plagioclase, microcline and biotite. It has a gneissic fabric, marked by a preferred alignment of elongated quartz and feldspar grains. The biotite tends to form around, and enclose, larger grains of sericitised K-feldspar – microcline in particular (Figure 4.2a). Some quartz grains are recrystallised, with lobate to straight intergrain boundaries, and undulose extinction. The biotite grains are poikiloblastic, and are full of inclusions of quartz, apatite, zircon, titanite and epidote; there is additionally some tourmaline present, which is pleochroic from pale to dark green. Zircon grains are found enclosed within the biotite, where they are surrounded by pleochroic haloes (inset to Figure 4.2a).

The zircons are for the most part euhedral, magmatically zoned, prismatic grains, often containing inclusions and cracks (Figure 4.3a). As indicated in figure 4.2b the maximum

sedimentation age for this sample is 2039 ± 3 Ma (MSWD = 0.82, N = 26), with hints of somewhat older inherited ages of 2.15 and 2.25 Ga which reflect the provenance of the source material.

4.4.2 Chiroti Paragneiss, Sample Z MB 13/6

This second sample of Chiroti paragneiss contains large orthoclase and microcline grains surrounded by recrystallised quartz, sericitized K-feldspar, biotite (partly retrograded to chlorite), as well as accessory muscovite (Figure 4.2c). The larger feldspar grains give the rock the appearance of having a micro-porphyritic texture, while muscovite can be found along fractures within the more altered phenocrysts. The biotite grains do not show any preferred orientation, but some can be seen surrounding the phenocrysts.

While the majority of the zircons are euhedral, they are considerably more pyramidal in shape when compared to those in sample Z MB 13/5. In addition to this they are almost all broken, and it is rare to find an intact grain. Magmatic zoning is evident (such as in figure 4.3b), but is not particularly strong. Despite this, the zircons yielded upper intercept ages of 2042 ± 24 Ma (MSWD = 8.4, N = 10) and 2899 ± 97 Ma (MSWD = 4.1, N = 3), the latter indicating inheritance from an Archaean source, while the maximum sedimentation age is regarded to be 2042 Ma (Figure 4.2d).

4.4.3 Hurungwe Orthogneiss, Sample Z MB 13/8b

This sample, collected along a road cut in the northern part of the Hurungwe gneisses, is made up of exposures of deformed garnetiferous quartzofeldspathic gneisses. The biotite laths, which are concentrated in narrow bands, give this sample its gneissic appearance; while recrystallised quartz, plagioclase and microcline feldspar are strong evidence for deformation (Figure 4.2e). This particular sample is not very garnetiferous, but does contain relatively large cordierite grains.

The zircons in sample Z MB 13/8b are a mixture of euhedral prismatic and pyramidal crystals (although the latter is perhaps more abundant), which exhibit fairly complex magmatic zonation patterns. While it is possible in some grains to make out what looks like an older core surrounded by new growth, everything is in actual fact very similar in age, as evidenced by the zircon grain in Figure 4.3c and the concordia curve in Figure 4.2f, where the zircons are all derived from one very localised source dated to be 2020 ± 7 Ma (MSWD = 1.6, N = 24) with no evidence for inheritance.

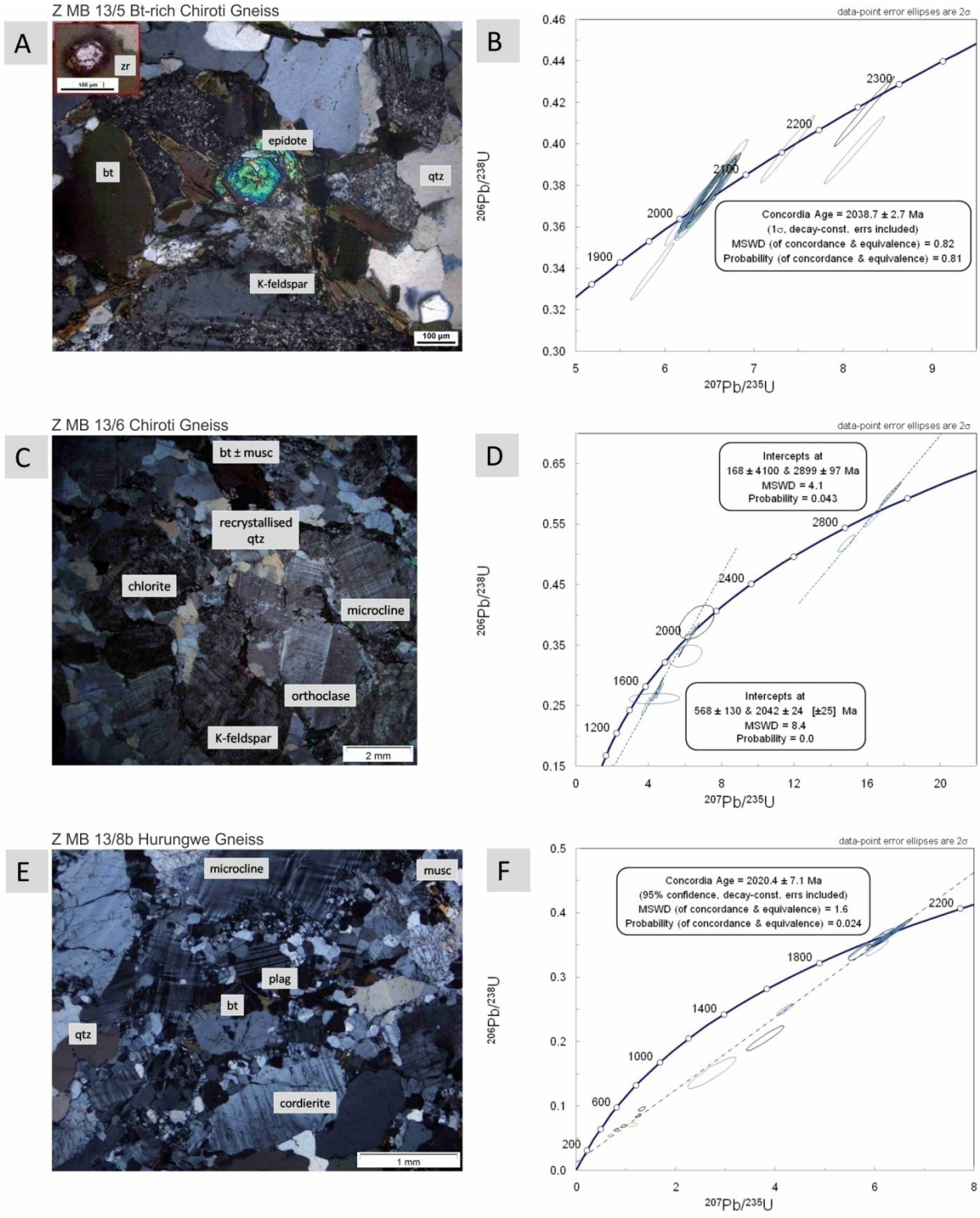

Figure 4.2: Thin section photomicrographs and concordia plots for samples Z MB 13/5 (Figure 4.2a, b), Z MB 13/6 (Figure 4.2c, d), and Z MB 13/8b (Figure 4.2e, f). Blue ellipses indicate measurements made on cores while black represent rims.

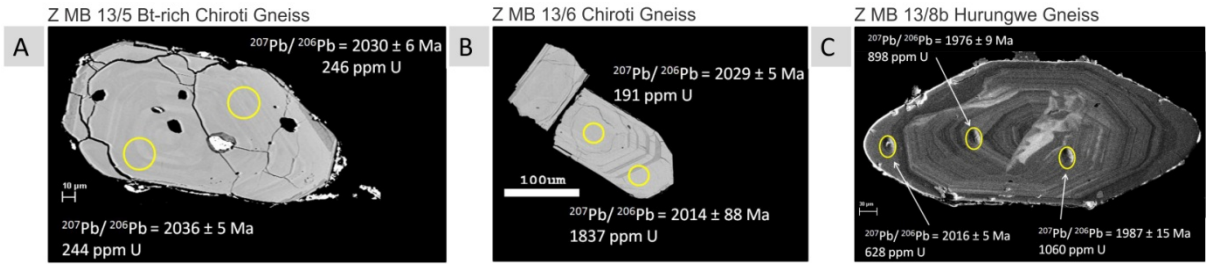

Figure 4.3: BSE and CL images of selected zircons from samples Z MB 13/5, 13/6 and 13/8b, indicating the spots analysed and the ages obtained, as well as the U concentration.

4.4.4 Kariba Granite, Sample Z MB 13/10

Sample Z MB 13/10 is a porphyritic granite, found 10 km east of the town of Kariba. Large phenocrysts of microcline seen in Figures 4.4a and b give it its porphyritic appearance; these grains are surrounded by a finer-grained matrix of recrystallised quartz, plagioclase and muscovite. Abundant biotite (partially retrograded to chlorite) is also present.

The zircons in this sample are fairly large, with some reaching ~ 500 µm. They are all noticeably rounded and have a rather convoluted zonation pattern, the likes of which can be seen in Figure 4.6a, which according to Corfu et al. (2003) is attributed to the migration of trace elements during late to post-magmatic recrystallisation. This post-magmatic event is believed to be represented by the overgrowth rims which lend the zircons their rounded morphology. Some evidence of inheritance can be seen in zircons which yielded ages between 2.2 and 2.1 Ga, however the majority of the grains record an upper intercept age of 1952 ± 9 M a (MSWD = 0.7, N = 22), and can be regarded as representing when recrystallisation and the growth of new zircon occurred, while the two older zircons reflect the ages of the cores (Figure 4.5a), although the effects of recrystallisation have made distinctions between core and rim difficult.

4.4.5 Sillimanite Quartzite, Sample Z MB 13/11

Sample Z MB 13/11 is a sillimanite quartzite from Kariba Heights (in the town of Kariba) and is clearly folded as Figure 4.4c shows. This quartzite is one of several which are interbedded with the Kariba paragneisses, and is made up largely of coarse-grained quartz. Fine needles of sillimanite appear as felted masses and small laths of muscovite occur along grain boundaries, such as indicated in Figure 4.4d.

These detrital zircons are clearly rounded (Figure 4.6b), but may have been derived from a proximal source, owing to the fact that the original euhedral morphology in some grains is

still preserved. Magmatic zoning, thin overgrowth rims and inclusions are also apparent in many grains.

As indicated in Figure 4.5b, the zircons fall under three main groupings: 2685 ± 5 Ma (MSWD = 0, N = 2) and 2172 ± 8 Ma (MSWD = 0.7, N = 2) with the majority at 2021 ± 15 Ma (MSWD = 11.1, N = 21). The youngest detrital zircons constrain the maximum age of the quartzite to be 2021 Ma, while the older zircons reflect provenance from a Palaeoproterozoic to Neoarchaean source.

4.4.6 Manchinchi Bay Migmatitic Orthogneiss, Sample Z MB 13/12

Across the border in the town of Siavonga (Zambia), located along the north-eastern shore of Lake Kariba is the quartzo-feldspathic biotite migmatitic orthogneiss from Manchinchi Bay. On an outcrop scale this migmatite is highly deformed, as evidenced by the fine, alternating, light and dark bands which have been refolded (Figure 4.4e). The leucosome consist of a granular intergrowth of quartz and plagioclase feldspar, whereas the paleosome are made up of coarse-grained hornblende and biotite. The latter are also host to abundant titanite and zircon inclusions (Figure 4.4f).

The zircons in sample Z MB 13/12 are rounded with some more irregularly shaped, magmatic as well as convoluted zonation patterns are also evident. A CL image of one of these grains in Figure 4.6c shows a thin, bright rim which surrounds many of the grains; where this rim was thick enough to date; it revealed that it is the result of a younger metamorphic event at 545 ± 5 Ma (MSWD = 0.4, N = 3), which corresponds with the peak of the Pan-African Zambezi orogeny. The cores yielded an age of 1967 ± 8 Ma (MSWD = 1.8, N = 17) giving the initial intrusive age (Figure 4.5c).

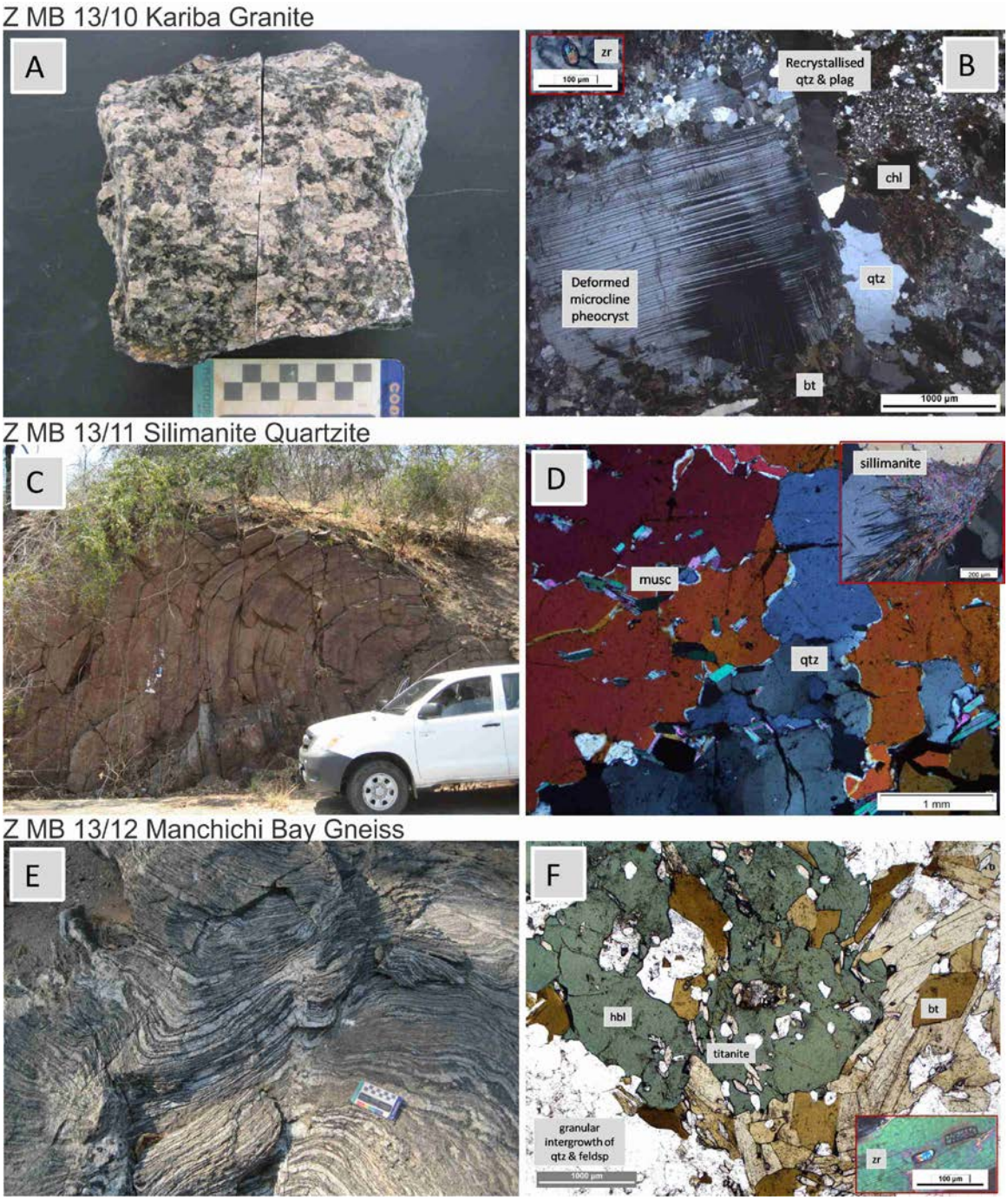

Figure 4.4: Sample Z MB 13/10 in hand specimen (Figure 4.4a) and thin section photomicrograph under XPL in Figure 4.4b. The Kariba Heights sillimanite quartzite (Figures 4.4 c and d) and Manchinchi Bay Gneiss field sample and thin section photomicrograph are presented likewise in Figures 4.4e and f.

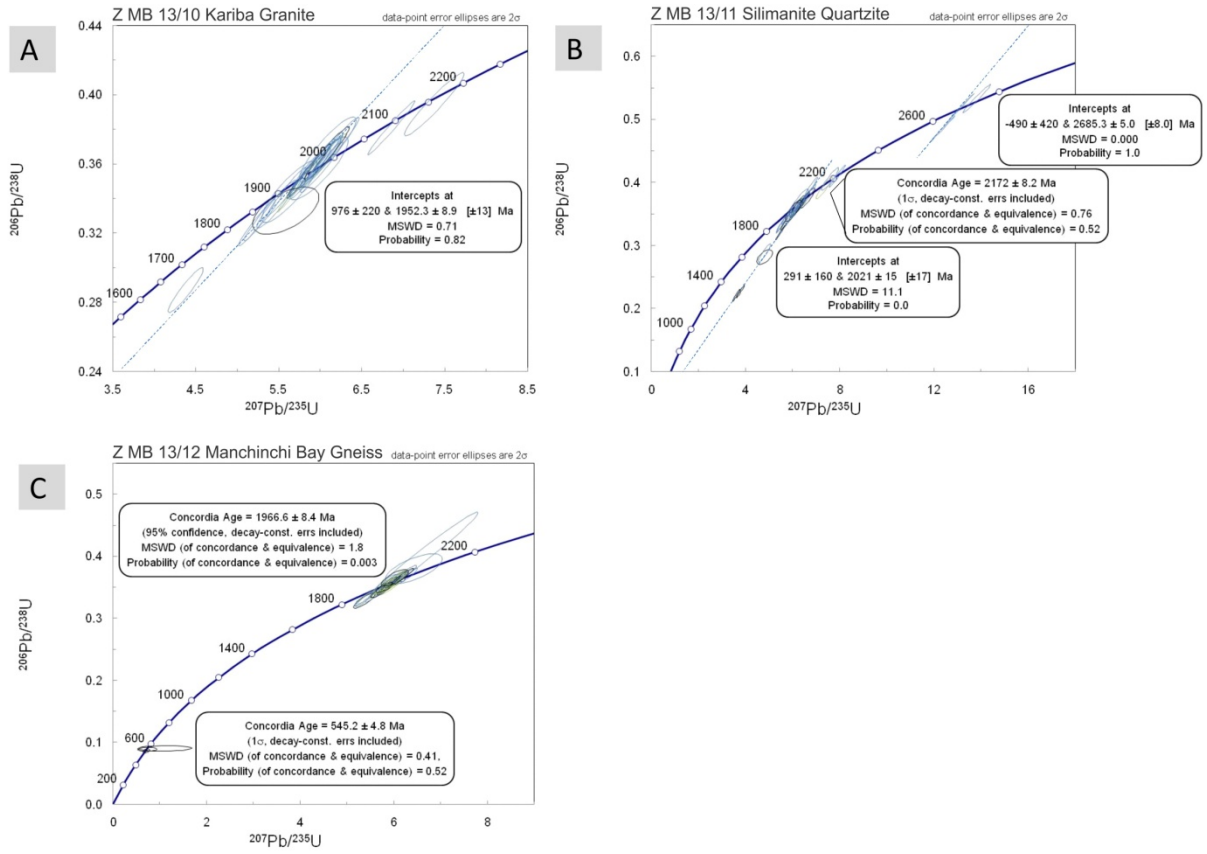

Figure 4.5: Concordia plots for the SIMS analyses done on samples Z MB 13/10 (Figure 4.5a), Z MB 13/11 (Figure 4.5b) and Z MB 13/12 (Figure 4.5c).

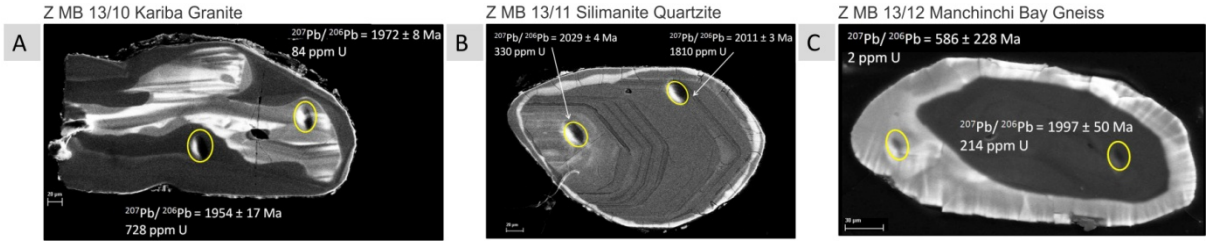

Figure 4.6: CL images of selected zircons from samples Z MB 13/10 (Figure 4.6a), Z MB 13/11 (Figure 4.6b) and Z MB 13/12 (Figure 4.6c).

4.4.7 Copper King and Copper Queen Domes

Five samples from the Copper Queen Dome (CQD-4, -5, -6, CQD-8, and CQD-10) in addition to two from the Copper King Dome (CQD-11 and CKD Z11/3) were dated as part of this study, and the results obtained can be summarised as follows:

The gneisses within the Copper King Dome crystallised between 2651 ± 5 Ma (MSWD = 0.3, N = 12) and 2653 ± 2 Ma (Figures 4.7b and f). A lower intercept age of 986 Ma also coincides with ^{40}Ar-^{39}Ar and Pb-Pb ages obtained for tin pegmatites within the Dete-

Kamativi Inlier (Zimbabwe) and Choma-Kalomo Block (Zambia), implying that this was a widespread mineralisation event that also affected the Magondi Belt (Glynn et al., Under Review).

The Copper Queen Dome has a more complex record of the regional geological history – beginning with crystallisation ages similar to the Copper King Dome between 2648 ± 5 Ma and 2621 ± 3 Ma (Figures 4.7d and 4.7c where the ages were obtained on magmatic titanite and zircon in sample CQD-4). Mineralisation, followed by peak metamorphism, is bracketed between the maximum age for the host sediments (metapelitic schist, CQD-10, dated at 2152 ± 1 Ma; Figure 4.7e) and the cooling ages obtained on metamorphic titanite and apatite at approximately 2.03 Ga (figure 4.7d). This is consistent with Pb-Pb model ages of 2.1 Ga measured by Höhndorf and Vetter (1999) on ore-related sulphides. The 1942 ± 19 Ma age obtained on rutile from CQD-6 (figure 4.7c), most likely represents post-peak metamorphic cooling. It is also clear from the lower intercept ages of 549 ± 4 and 551 ± 4 Ma respectively for samples CQD-4 and CQD-8 (Figures 4.7c and 4.7d) that they record the much younger period of metamorphism related to the Pan-African collision between the Kalahari and Congo Cratons.

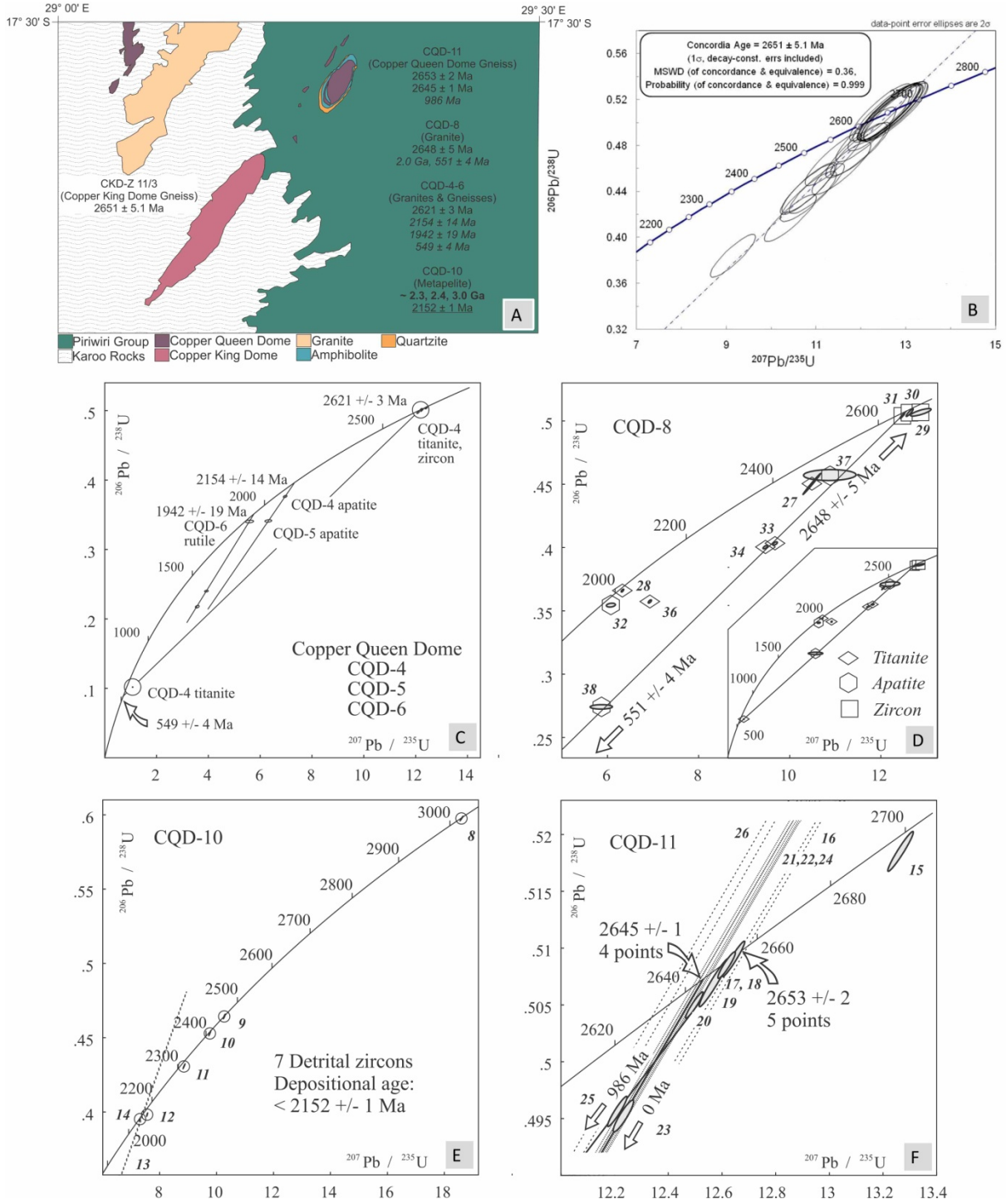

Figure 4.7: The map in Figure 4.7a is after Leyson (1969), while the concordia plots in Figures 4.7b through f show the U-Pb, LA-ICPMS and ID-TIMS results, for the Copper King and Copper Queen Dome samples. Sample CQD-4 (Figure 4.7c) is a strongly foliated, coarse-grained porphyroblastic granite in the core of the Copper Queen Dome. Sample CQD-5 (Figure 4.7c), a weakly foliated, coarse-grained K-feldspar granite, constitutes the greatest part of the Copper Queen Dome; however, due to its poor yield of altered zircons none could be dated; while sample CQD-6 (Figure 4.7c) is a co arse-grained gneiss that occurs at the

margin of the Copper Queen Dome. Sample CQD-8 (Figure 4.7d) is an unfoliated granite from the Copper Queen Dome and sample CQD-10 (Figure 4.7e) a metapelitic schist, in the vicinity of the Copper Queen Dome, consists predominantly of Palaeoproterozoic zircon grains ranging from 2.46 to 2.15 Ga; with the exception of one (3023 ± 1 Ma), there are no late Archaean grains within this sample. Finally, sample CQD-11 (Figure 4.7f) is a tonalitic gneiss from the Copper King Dome.

4.5 DISCUSSION

It has been established that the Copper Queen and Copper King Domes represent 2.6 Ga Archaean basement, confirming Leyshon's (1973) statement that the domes are pre-Piriwiri in age. Given their age, Archaean granitioids, like the domes, could not have been the heat source responsible for the mineralisation and peak metamorphism which occurred between 2.1 and 2.0 Ga. Rather, the heat generated during the Magondi orogeny is responsible.

From his observations in the Copper Queen district, Leyshon (1973) proposed that during the Magondi orogeny the Archaean basement became reactivated – in a manner similar to what is depicted in Figure 4.8 – whereby the sediments of the Magondi Supergroup were deformed together with the basement, during the main NW-SE compressive phase of the orogeny; this, in combination with the intrusion of younger granitoids, resulted in a doming of the basement, as it was forced upwards by the rising granitic magmas.

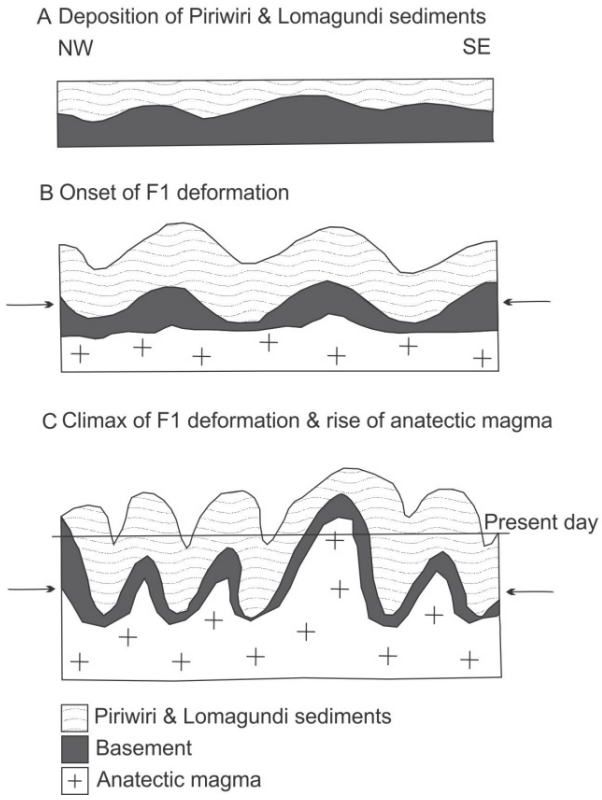

Figure 4.8: The mechanism by which Leyshon (1973) proposed the basement was reactivated.

The ages obtained from the dated samples seem to confirm that the metasediments were deformed along with the basement samples (e.g. CKD Z 11/ 3), considering the two Chiroti paragneiss samples (Z MB 13/5 and Z MB 13/6), and the Kariba sillimanite quartzite (sample Z MB 13/11) all contain a mixture of basement derived Archaean aged zircons and Magondi Supergroup aged zircons, which range from 2899 and 2685 to 2172 Ma. The subsequent doming, however, is likely little more than exposures of the post-tectonic granites and orthogneisses (such as the Kariba Granite samples Z MB 13/10 and Zambian gneiss, Z MB 13/12) dated at 1952 and 1967 Ma respectively.

Mineralisation and metamorphic events within these basement rocks have been shown to have occurred on a number of occasions, most notably between 2.15 and 1.94 Ga as a result of the Magondi orogeny, and again at approximately 1 Ga (a mineralisation event which strongly affected the nearby Dete-Kamativi Inlier and Choma-Kalomo Block). Clifford et al. (1967) and Vail et al. (1968) had previously recorded this later event within the Hurungwe District, but believed its extent to be largely masked by the younger, high-grade metamorphic events. One such event, is the Pan-African overprint (represented by the metamorphic

overgrowth rim in sample Z MB 13/12), which was dated at 545 Ma; and coincides with the lower intercept ages of titanite extracted from a granite of the Copper Queen Dome.

4.6 CONCLUSION

From the ages presented here, in addition to the sequence of events outlined in the previous sections, it is apparent that there was no Palaeoproterozoic (Hurungwe orogeny) prior to the Magondi orogeny. Thus with these newer results, it is clear that the granites and gneisses within the high-grade portion of the Magondi Belt were syntectonic with the Palaeoproterozoic Magondi orogeny, and may have been overprinted by the Pan-African Zambezi orogeny.

Chapter 5: U-Pb zircon geochronology from the Dete-Kamativi Inlier, NW Zimbabwe, with implications for the western margin of the Archaean Zimbabwe Craton

5.1 INTRODUCTION

The first comprehensive documentation of the Kamativi region was undertaken by Watson (1962), followed by Lockett (1979a) who mapped the Dete-Kamativi Inlier as part of his PhD thesis. Subsequent to this, only a modest amount of research has occurred in the area. Treloar (1988) and Master (1991a) are among the subsequent workers who revived the notion that the Dete-Kamativi Inlier is an extension of the Palaeoproterozoic Magondi Belt, situated along the NW-margin of the Zimbabwe Craton (see Figure 5.1). With the aid of more modern analytical techniques – SIMS and LA-ICPMS – we present new U-Pb zircon ages for the Dete-Kamativi Inlier, as a means of testing the links between the Dete-Kamativi Inlier and Magondi Belt.

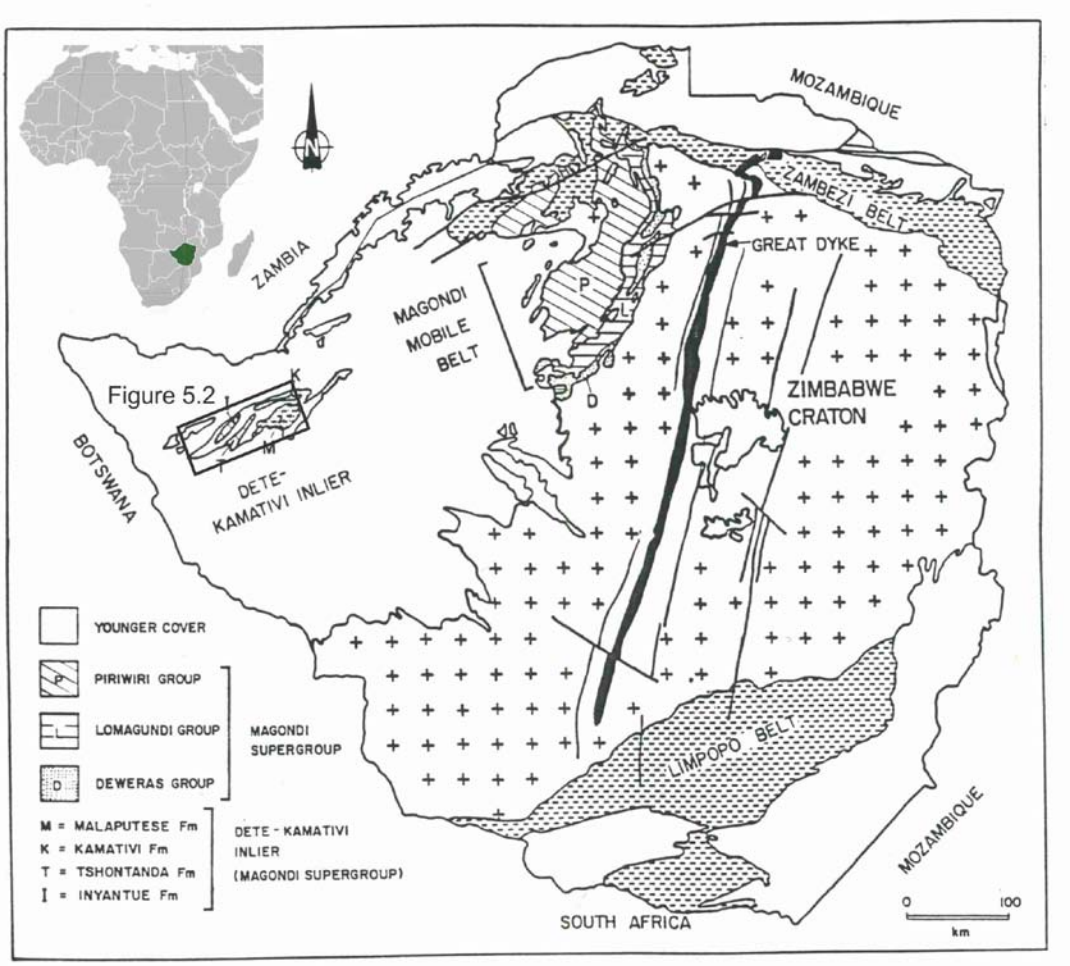

Figure 5.1: Simplified geological map of Zimbabwe, indicating the locations of both the Magondi Belt and Dete-Kamativi Inlier (after Master, 1991a). The area covered by the map in Figure 5.2 is indicated by the rectangle.

5.2 GEOLOGICAL SETTING OF THE DETE-KAMATIVI INLIER

The Dete-Kamativi Inlier is located in western Zimbabwe, near the border with eastern Botswana and south-western Zambia (Figure 5.1). The Inlier is bounded to the north-west and north-east, respectively, by Mesozoic Karoo and Neoproterozoic Sijarira Group sediments, while younger Cenozoic Kalahari sands cover the area to the south. Stratigraphically the Dete-Kamativi Inlier is composed of a set of four NE-trending Formations, namely the Malaputese, Inyantue, Kamativi and Tshontanda (Figure 5.2). Associated with these supracrustal sediments are various granites and gneisses, which are thought to be syn - to post-depositional (Lockett, 1979a, b; Master et al., 2010).

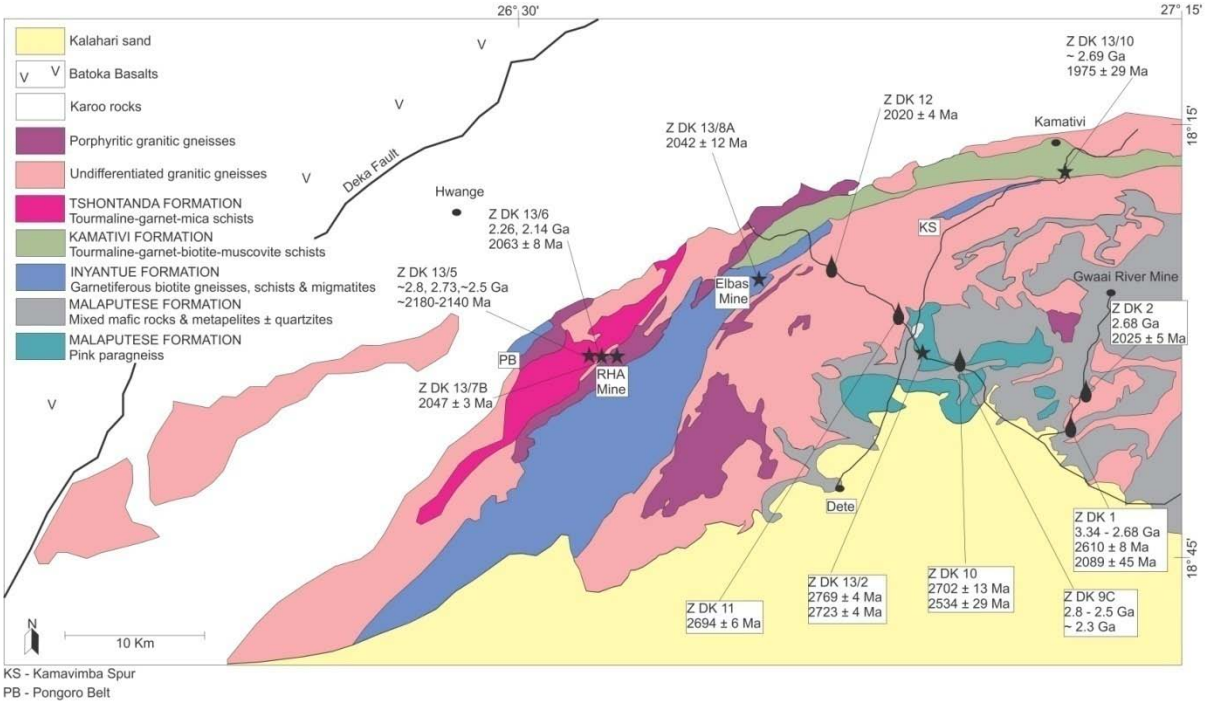

Figure 5.2: Simplified geological map of the Dete-Kamativi Inlier (after Lockett, 1979a, b, 1981). Teardrop shapes mark those locations where samples from the first field season were collected (and as a result, were analysed using LA-ICPMS). The stars mark the locations of samples collected as part of the later fieldwork and were analysed using SIMS.

5.2.1 Malaputese Formation

The Malaputese Formation, which makes up a significant portion of the Inlier, has been divided into five sub-units, with each assigned into either an eastern marine shelf domain or a western sub-aerial domain (Lockett, 1979a, b) in a manner not dissimilar to Figure 5.3.

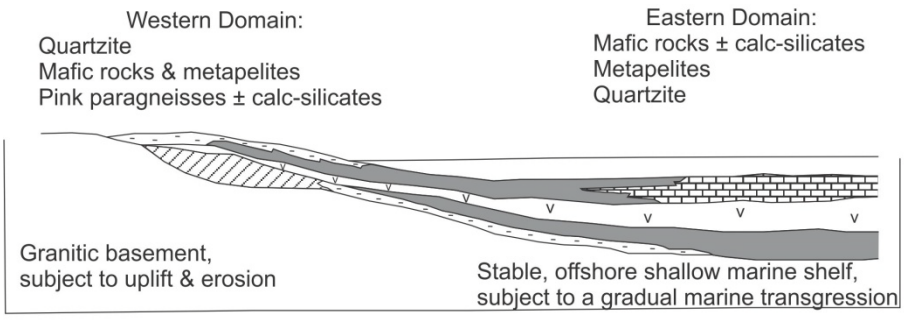

Figure 5.3: Sketch of the depositional environment under which the Malaputese Formation is believed to have developed (after Lockett, 1979b).

The pink paragneisses, which are locally developed in the west, are intercalated with minor calc-silicate and pyroxene-bearing leucogneisses, and were likely previously arkoses (Lockett, 1979b; Master et al., 2010). The mafic rocks, according to Lockett (1979a) can be classified as subalkaline basalts, while the sericite and muscovite-rich quartzite represents quartz-rich arenite units that may have formed in a shallow-marine setting. The metapelites consist of two varieties: a garnetiferous sillimanite-cordierite-andalusite bearing biotite gneiss (dominant in the east), and a low-grade quartz-chlorite-sericite schist, which is a retrograde derivative of the former (Lockett, 1979a, b, 1981).

5.2.2 Inyantue Formation

The Inyantue Formation outcrops in three principle localities: the 'Kamavimba Spur', the 'Pongoro Belt' and the Main Belt, before merging with the Kamativi Belt. Garnetiferous sillimanite-cordierite gneisses intercalated with calc-silicate rocks, graphitic schist, quartzite and talc-chlorite schists make up the largest part of this formation (Lockett, 1979a, b, 1981). Protoliths such as carbonaceous shales, limestone and dolomite interbedded with sandstone and quartz arenite, all point towards deposition within a shallow marine environment (Lockett, 1979a, b; Master et al., 2010).

5.2.3 Tshontanda Formation

According to Lockett (1979a, b, 1981), the Tshontanda Formation consists of tightly folded garnetiferous mica schist and locally preserved, subordinate garnetiferous sillimanite and cordierite-bearing gneisses. The schist is medium - to coarse-grained and varies in colour based on the ratio of biotite to muscovite, and is best developed along a zone of intense tourmaline-mica pegmatite injection in the south-eastern portion of the formation. Conversely, the gneisses (underlying the central and north-western regions) are medium-grained and have a 'salt and pepper' appearance. A distinctive feature in these two units is the garnet morphology: in the gneisses the garnets have a tendency to be poikiloblastic, whereas those in the mica schist are smaller (~ 2 mm in size) single crystals (Lockett, 1979a).

5.2.4 Kamativi Formation

The Kamativi Formation, like the Tshontanda, is a narrow, elongated schist belt consisting of tightly folded muscovite schist, subordinate fine-grained biotite schist and intercalated impure quartzite. Lockett (1979a, b) describes several pegmatite deposits within the Kamativi Formation, these include garnet-tourmaline-veined pegmatites (which are temporally

unrelated to the large, shallow dipping, discordant sheets of lithium and tin bearing pegmatites), as well as the smaller, steeply dipping tin pegmatites and wolframite-cassiterite quartz veins. The country rock schists in general are composed mainly of quartz, muscovite, sericite, biotite and chlorite, with garnet, apatite, titanite, zircon and ilmenite being common accessory minerals (Lockett, 1979a).

Master et al. (2010) suggested protoliths of micaceous shale for both the Tshontanda and Kamativi Formations, which, in combination with the lack of associated arenites and calcareous rocks, would point towards deposition within a deeper-water environment. Such a depositional setting corresponds with that of the Piriwiri Group in the Magondi Belt, while units from the aforementioned Malaputese and Inyantue Formations are likewise broad correlatives with the Deweras and Lomagundi Groups of the Magondi Belt (Lockett, 1979b; Master et al., 2010; Watson, 1962).

5.2.5 Granitic Gneisses

Granitic gneisses encompass roughly 60 % of the Inlier, and are preferentially concentrated towards its centre, varying in composition from quartz monzonite to granodiorite grading into gneisses near the contacts with the supracrustals (Lockett, 1979a, b). The granitoids in general, are all composed of quartz, plagioclase and alkali feldspar, with varying amounts of biotite, muscovite, sericite, chlorite and epidote. Accessory minerals such as zircon and apatite are common, while titanite and iron oxides are rarer (Lockett, 1979a). Lockett (1979a) classified the granitic gneisses into four broad categories: (i) nebulitic (i.e. migmatitic) gneisses and non-foliated granites, (ii) foliated biotite gneisses, (iii) porphyritic gneisses, and finally (iv) mixed biotite gneisses and migmatites. Although the contacts with the metasediments are often deformed or diffuse, there is still strong evidence that they are intrusive in nature (Locket, 1979a, b). Matters are, however, further complicated by the fact that exact age relationships are essentially unknown, as the only geochronology available from the Dete-Kamativi Inlier is from Priem et al. (1971) who obtained (recalculated) Rb-Sr whole-rock ages on some of these units. From this it was then concluded that the granitoids were syn - to postkinematic, having intruded *circa* 2150 ± 100 Ma (Priem et al., 1971). Lockett (1979b) and Master et al. (2010) then proposed these granitoids represented part of a calc-alkaline magmatic arc which may have existed along the western margin of the Zimbabwe Craton.

5.2.6 Structure and mineralisation

Lockett (1979b; 1981) recognised three phases of deformation within the Dete-Kamativi Inlier – the first and third phases both resulted in NE-SW trending folds, whereas the second phase resulted in NW-SE orientated folds. This perpendicular intersection of the two fold axial traces produced a slight dome and basin effect, particularly in the south-east. Conversely, in the north-west, the formations are more linear NE-SW orientated structures, as this is the result of some major fractures which formed due to movement along prominent shear zones (Lockett, 1979b). Lockett (1979b; 1981) proposed that the granitoids were emplaced and partially solidified around the time of the second deformation event, as they show evidence of being deformed along with the metasediments.

The youngest deformation event (i.e. the least pervasive, at low amphibolite to greenschist facies) appears to be related to a period of mineralisation, as pegmatites (which are sources of tin, lithium, wolframite, copper, mica and lead) have been discovered to be preferentially concentrated within these low-grade units rather than in the older, medium to high-grade rocks of amphibolite and granulite facies (Lockett, 1979b, 1981; Master et al., 2010). Mineral separates from these pegmatites yielded recalculated Rb-Sr ages of 954.4 ± 20 Ma and 956 ± 20 Ma, respectively, while muscovite and biotite, from the same pegmatites, gave recalculated K-Ar ages of 1006 ± 20 Ma and between 997 and 991 Ma (Priem et al., 1971). New Ar-Ar ages obtained by Glynn et al. (Under Review) on biotite and muscovite from both granitoids and metasediments within the Dete-Kamativi Inlier are also within a similar range (983 ± 4 Ma to 1016 ± 6 Ma). These ages therefore confirm a widespread mineralisation event occurred between 1030 and 954 Ma.

5.4 RESULTS

Of the twelve samples described in detail below, only those samples collected during the first field season have been analysed geochemically, nevertheless a detailed description of the petrography and age data for each sample is discussed in this section.

5.4.1 Analytical methods

The LA-ICPMS data for six of the samples are reported in Table 5.1 (Appendix A4), whereas the SIMS data for the remaining six samples are reported in Table 5.2 (Appendix A4). The ratios and ages have an analytical uncertainty of 2 sd and 1 sd respectively, whereas the error

ellipses in the concordia plots are at the 2 sd level. Detailed information on the methodology followed can be found in sections 2.6.3 (33 pp) and 2.6.2 (31 pp).

5.4.2 Evidence for the formation of an arc

In terms of geochemistry, the average plutonic and volcanic rocks within a continental arc environment range between andesite and dacite and those which form above a subduction zone contain significant amounts of volatiles, have a large range in silica content, are calc-alkaline and can have distinctive trace element patterns (Ducea et al., 2015).

The geochemical information available for the Dete-Kamativi Inlier indicates that samples Z DK 2, Z DK 11 and Z DK 12 all plot within the granite-granodiorite field on a standard Streckeisen diagram (Figure 5.4a). Granodiorites are commonly related to orogenic magmatism, and are usually calc-alkaline magmas (ICL, 2013b) as evidenced by all the samples plotting within the calc-alkaline field on the AFM diagram in Figure 5.4b.

This serves to reaffirm the assertion put forward by Master et al. (2010) that intrusives within the Dete-Kamativi Inlier belong to a magmatic arc.

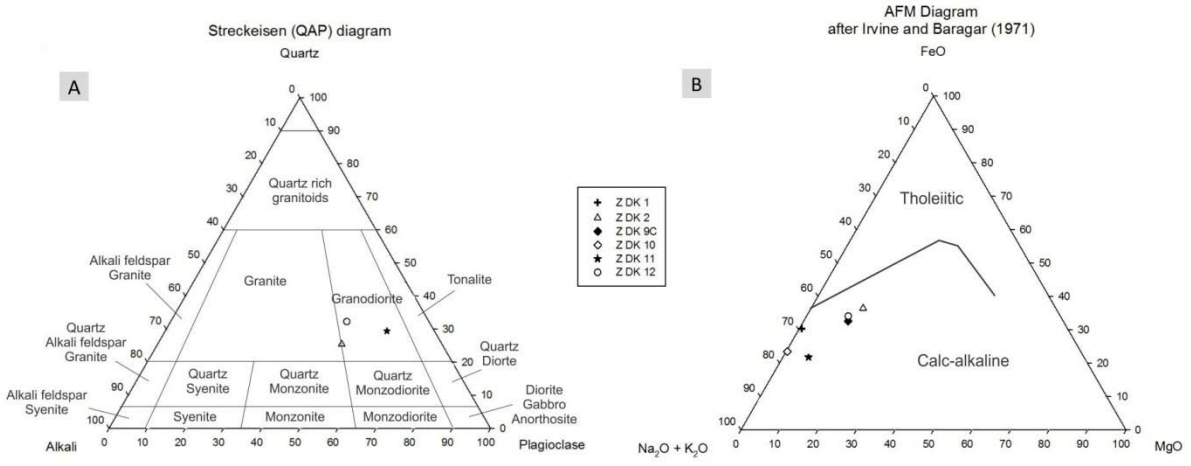

Figure 5.4: Quartz-Alkali-Plagioclase Streckeisen diagram based on normative analyses of the granitoids samples (Figure 5.4a). Figure 5.4b is an AFM diagram for all the samples (where geochemistry is available). The major element data can be found in Table 5.3 (Appendix A4).

While the geochemistry may prove somewhat inconclusive in supporting an arc origin for the Dete-Kamativi Inlier samples, there is petrographic information available which corroborates the proposal that a Palaeoproterozoic arc formed along the western margin of the Zimbabwe Craton. It is well known that continental magmatic arcs form above subduction zones and

that periods of crustal and lithospheric thickening can occur as a result (Ducea et al. (2015). Evidence presented in Chapter 3 confirmed deposition of the Magondi Supergroup within a back-arc basin environment; this was also accompanied by volcanism and the emplacement of granitoid intrusives. Additionally granulites within the Magondi Belt, studied by Munyanyiwa and Maaskant (1998), are proposed to be the result of crustal thickening within an active continental margin setting; this therefore means that the age of the granulite-facies metamorphism could constrain the time interval when subduction occurred. Thermobarometry studies by Munyanyiwa et al., (1993) indicate that the emplacement of enderbites within the Piriwiri Group (Magondi Belt) are contemporaneous with peak metamorphism, and these same enderbites were dated by Munyanyiwa et al., (1995), using Pb-Pb evaporation techniques, to be between 1.96 and 1.93 Ga. These results roughly coincide with the age McCourt et al. (2001) obtained for the Hurungwe granite (1997.5 ± 2.6 Ma), and suggests that subduction along the western margin of the Zimbabwe Craton likely culminated sometime between 1.99 and 1.93 Ga with the emplacement of post-tectonic intrusives which mark the final stages of the Magondi orogeny.

5.4.3 Age and petrography of the supracrustal metasediments

Malaputese Formation

Samples Z DK 9C and Z DK 10 consist of roughly equal proportions of quartz and feldspar, which are intergrown to form a granophyric texture. Sample Z DK 9C has a distinct 'salt and pepper' appearance due to the presence of hornblende, which has largely been retrogressed to chlorite (Figure 5.5a and c). Based on the description of Lockett (1979a), sample Z DK 9C is an example of the more leucocratic variety of the pink paragneisses, which make up the bulk of the Malaputese Formation. Samples Z DK 10 likewise is a paragneiss from the same formation and occurs in very close proximity to sample Z DK 9C. The feldspar in sample Z DK 10 is roughly an equal mixture of perthitic microcline and plagioclase, lending it a more pinkish tinge (Figure 5.5b), while the plagioclase in sample Z DK 9C makes it paler in comparison.

CL images of the zircon grains in sample Z DK 9C show them to be irregularly shaped fragments, with very little magmatic zoning – the zonation is in fact rather patchy and convoluted which implies the migration of trace elements subsequent to crystallisation (Corfu et al., 2003). Likewise the zircons in sample Z DK 10 also exhibit convoluted zonation, but appear to be more metamict, with higher average concentrations of uranium. Figures 5.6a and b show that samples, Z DK 9C and Z DK 10 consist largely of inherited Archaean and

Palaeoproterozoic aged zircons (between 2.8 and 2.3 Ga) spread along the concordia curve, putting the maximum sedimentation ages at approximately 2.3 Ga and 2.5 Ga respectively for samples Z DK 9C and Z DK 10. The prevalence of zircons aged between 2.8 and 2.6 Ga implies the erosion of an older Archaean terrane. The number of zircons analysed for the respective samples is 99 and 107.

Inyantue Formation

Sample Z DK 13/8A collected near Elbas Mine is a paragneiss with a leucocratic phase. The sample consists of medium to coarse grained recrystallised quartz which flows around phenocrysts of plagioclase and orthoclase (Figure 5.5e). Some of these phenocrysts contain secondary minerals such as chlorite, but the majority are heavily affected by sericite. Biotite is a common accessory mineral along with muscovite and apatite. Garnet was not observed in thin section. However, according to Lockett (1979a) garnet is more commonly concentrated in the leucocratic phase, which can be seen in Figure 5.5d, and occurs as either veins or irregular patches, but is in general concordant with the gneissic foliation. Some of the veins have been refolded in places, and could coincide with mineralisation, given that tourmaline is also abundant in this phase.

BSE images of the zircons in this sample highlight the oscillatory zoning within these grains, and are consistent with a magmatic origin. The rounded edges on the grains appear to be the result of hydrothermal replacement resulting in the formation of new rims; which not only exist as simple overgrowths, but as embayments into the cores. Dating of several of these cores (Figure 5.6c), gives a well defined maximum sedimentation age of 2042 ± 12 Ma (MSWD = 2.5, N = 4).

Tshontanda Formation

The sillimanite-garnet paragneiss sample Z DK 13/5 was collected from inside an addit of the RHA Mine, located within the Tshontanda Formation. The sample contains quartz, biotite and sillimanite (both bladed crystals and fibrolite forms), all of which flow around poikiloblastic garnets (Figure 5.5g). There is evidence for rotation of these garnets within the fine grained fibrolite groundmass (Figure 5.5f), indicating that the garnets may have formed prior to being subjected to any deformation. Tourmaline, titanite, iron ore and apatite are other common accessory minerals.

The zircons in this sample are sub-rounded, four inherited grains (with ages of ~2.8, 2.73 and ~2.5 Ga) coming from an older source region. The grains are almost all rimmed by a patchy

textured overgrowth (Figure 5.6d), likely a result of the rock being subjected to a high degree of metamorphism. Core and rim measurements on the more discordant, younger population of five zircons give an approximate maximum sedimentation age between 2180 and 2140 Ma.

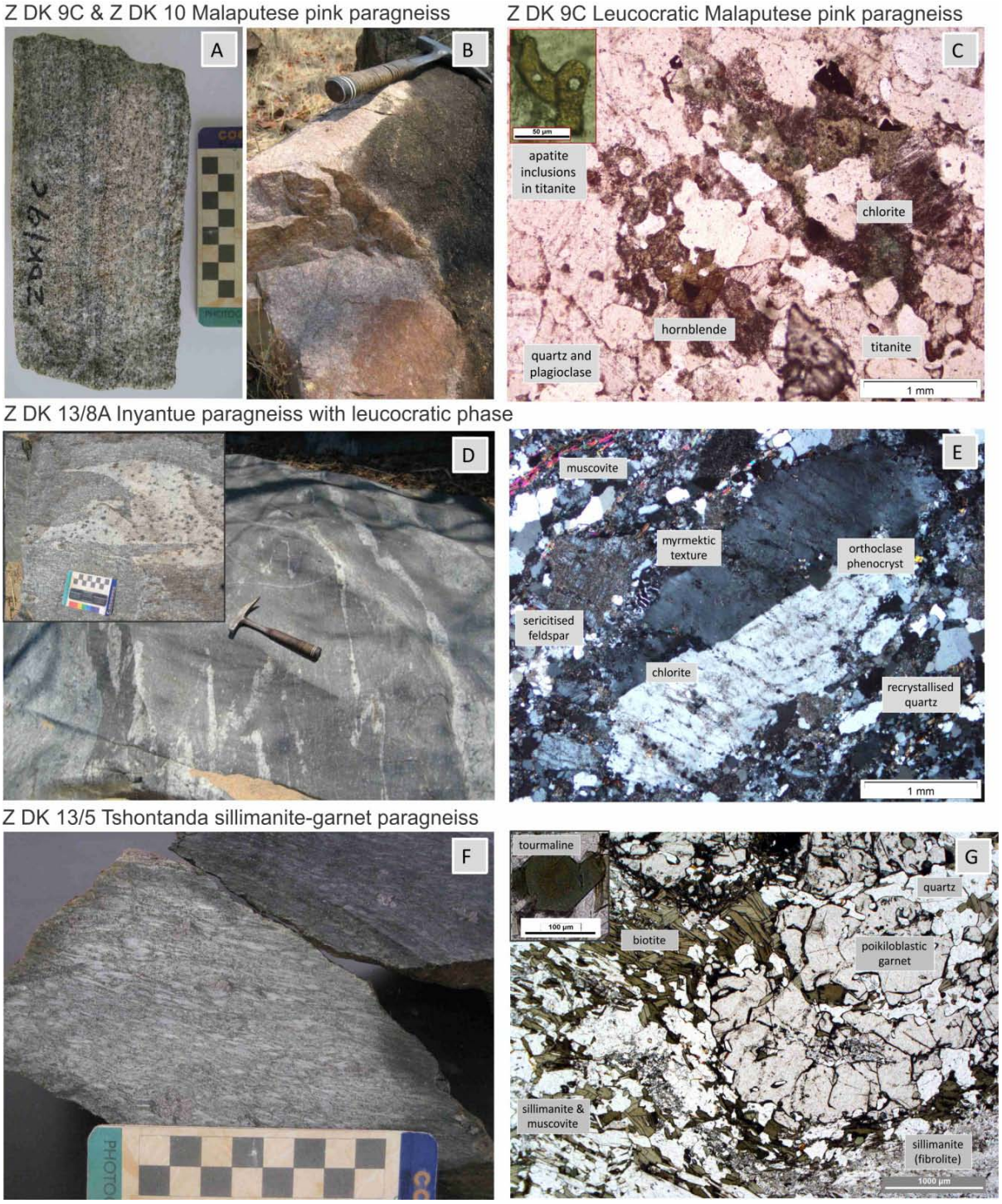

Figure 5.5: Hand specimen of Z DK 9C, with its 'salt and pepper' appearance (Figure 5.5a), contrasted with the more pinkish Z DK 10 (Figure 5.5b). In the thin section photomicrograph of sample Z DK 9C in Figure 5.5c the alteration of hornblende to chlorite is visible as well as

the apatite inclusions found in the titanite. Figure 5.5d depicts how sample Z DK 13/8A appears in outcrop, with the leucocratic phase being prominent on an outcrop scale. In thin section however, phenocrysts such as the large orthoclase grain are rare in comparison with the smaller almost completely sericitised feldspars (Figure 5.5e). Sample Z DK 13/5 contains poikiloblastic garnets (Figure 5.5f), which show evidence for having been rotated slightly due to the surrounding biotite and fibrolite laths flowing around the garnets (Figure 5.5g).

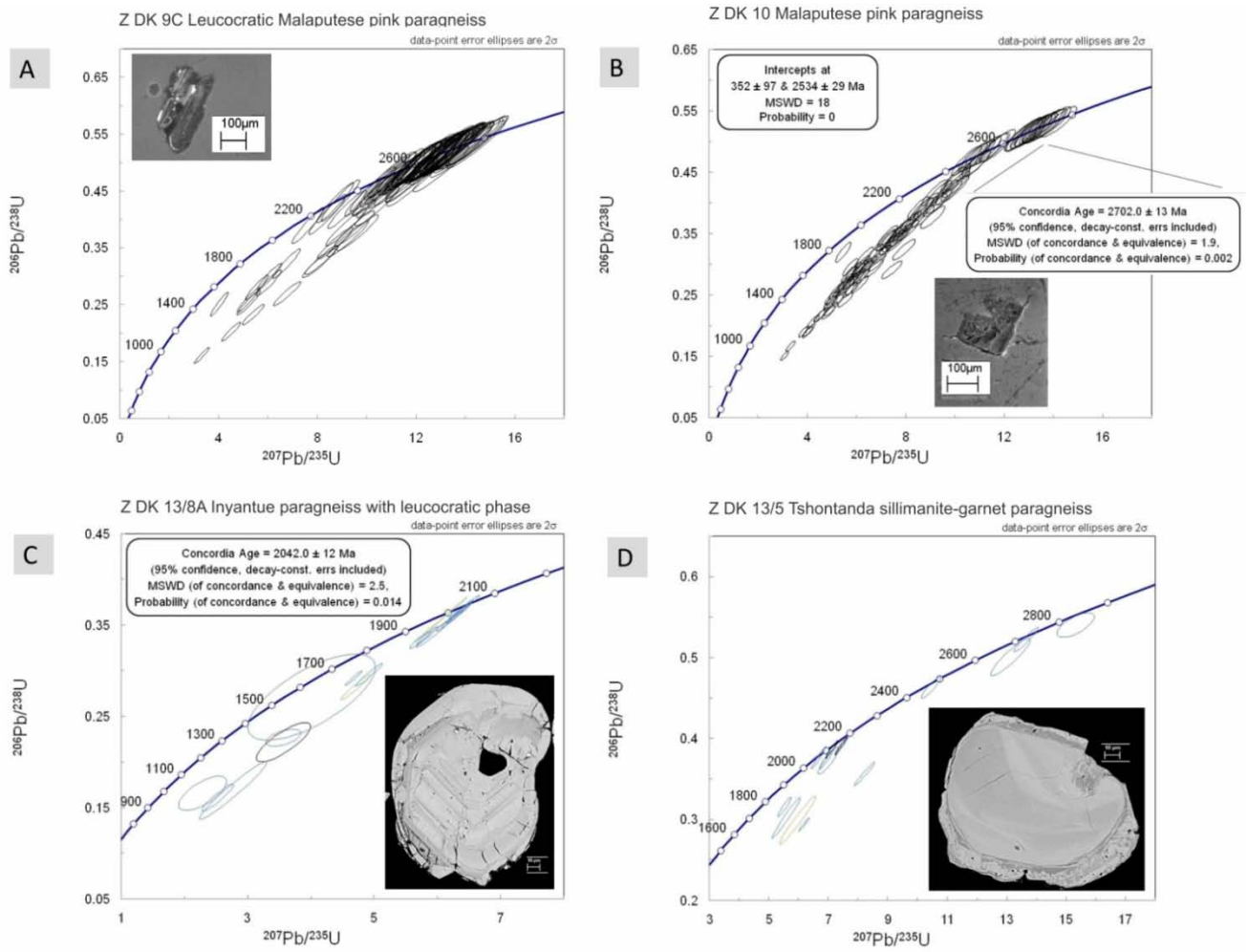

Figure 5.6: Concordia plots of the LA-ICPMS data for samples Z DK 9C (Figure 5.6a) and Z DK 10 (Figure 5.6b), belonging to the Malaputese Formation. The SIMS data for Z DK 13/8A (Inyantue Formation) and Z DK 13/5 (Tshontanda Formation) appear in Figures 5.6c and d. In the SIMS concordia plots, the blue ellipses represent measurements made on cores and those which are black represent rims, the LA-ICPMS concordia plots however, were not constructed in such a manner.

5.4.4 Age and petrography of the Granitic Gneisses

These samples have been grouped according to their respective age relationships, as there is evidence of both Archaean aged basement as well as Palaeoproterozoic granitoids.

Archaean basement

Samples Z DK 11 and Z DK 13/2 are the first evidence of Archaean aged crust identified within the Dete-Kamativi Inlier, and the ages are within the range of the granite-greenstone basement found within the Zimbabwe Craton, located just to the east.

Petrography

Sample Z DK 11 is a medium-grained orthogneiss which has a relatively well defined foliation resulting from alternating bands of felsic-rich and biotite-rich bands (Figure 5.7a), while the orthogneiss Z DK 13/2 is cut by aplitic veins and has a more subtle mineral lineation (Figure 5.7b). Despite only being approximately 5 km apart, sample Z DK 13/2 appears to have suffered retrograde metamorphism – given the large amount of chlorite present – and sample Z DK 11, only shows the effects of recrystallisation (Figures 5.7d and c respectively).

Sample Z DK 1 is a non-foliated, quartz-rich, pink leucogranite, which the orthogneisses grade into, in the less deformed regions of the Dete-Kamativi Inlier (Lockett, 1979a). The pinkish tinge is owing to the presence of microcline (Figures 5.7e and f).

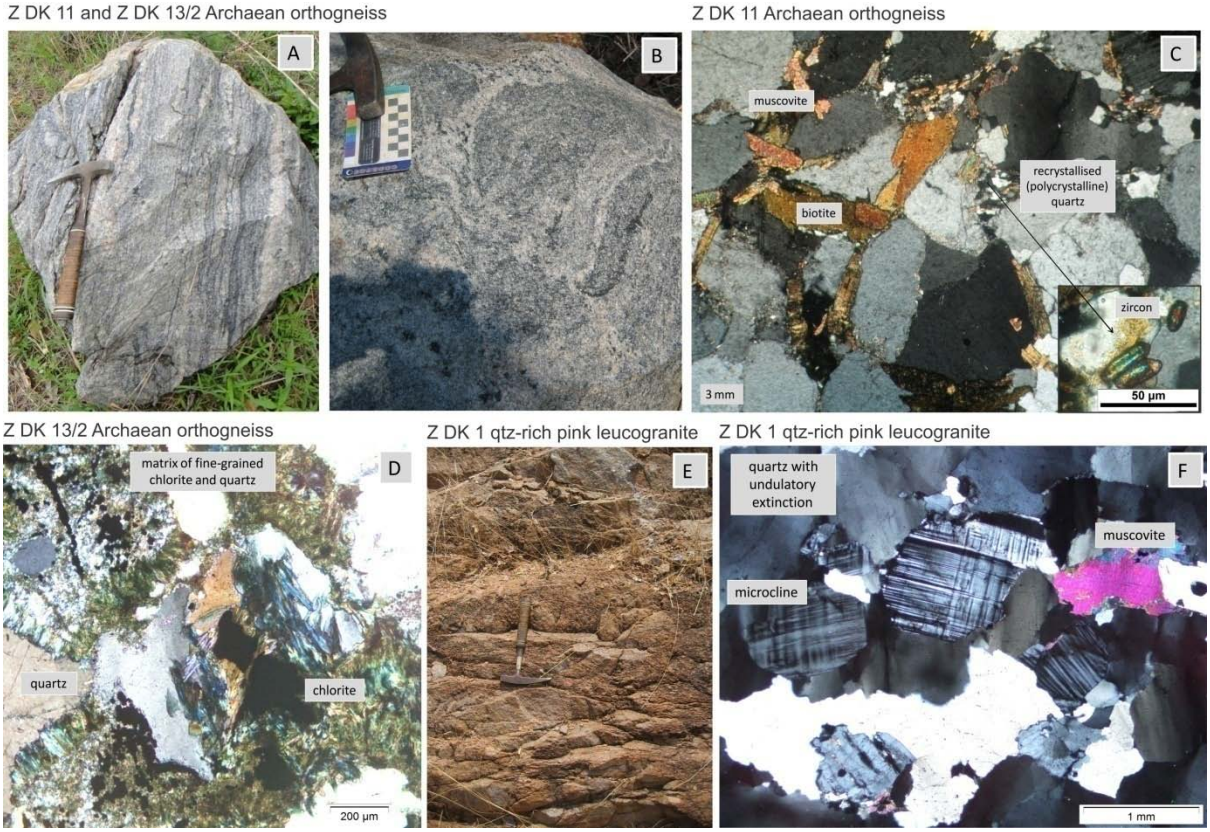

Figure 5.7: Figures 5.7a and b illustrate what samples Z DK 11 and Z DK 13/2 looks like in outcrop. Thin section photomicrograph of sample Z DK 11 clearly shows recrystallised pockets of fine-grained quartz, feldspar and biotite ± muscovite; also indicated in the inset of Figure 5.7c are zircon grains, which tend to occur in these recrystallised pockets. The photomicrograph of sample Z DK 13/2 (Figure 5.7d), indicates that this sample has been affected by retrograde metamorphism, which has resulted in the formation of significant amounts of chlorite. Sample Z DK 1 consists of abundant quartz in addition to large grains of muscovite and microcline feldspar, lending it a pinkish tinge (Figure 5.7 e and f).

Geochronology

Figure 5.8a shows that a well defined magmatic age for sample Z DK 11 of 2694 ± 6 Ma (MSWD = 0.2, N = 16) was obtained. CL imagery shows that these zircons are for the most part long, narrow and euhedral prismatic crystals with clear magmatic zoning. The zircons in sample Z DK 13/2 on the other hand are a mixture of prismatic and pyramidal grains, again with evidence for magmatic zonation. A large grain (depicted in Figure 5.8b) with a well developed overgrowth rim was dated at 2723 ± 4 Ma (MSWD = 1.6, N = 6); the core was only marginally older at 2769 ± 3 Ma (MSWD = 0.9, N = 6) – the latter therefore defines the

age of this orthogneiss, while the slightly younger rim, likely relates to some degree of in-situ partial melting.

CL images of the zircons in the granite Z DK 1 indicate that the vast majority of the grains are euhedral, and magmatically zoned. The rims, dated at 2089 ± 45 Ma (MSWD = 2.4, N = 13) enclose a large number of Archaean cores. The ages of these inherited zircons range from 3.34 to 2610 ± 8 Ma (MSWD = 0.1, N = 7), with the majority coming from the 2.6 Ga source (Figure 5.8c). This Palaeoproterozoic granite therefore entrained a significant number of xenocrystic zircons during its emplacement.

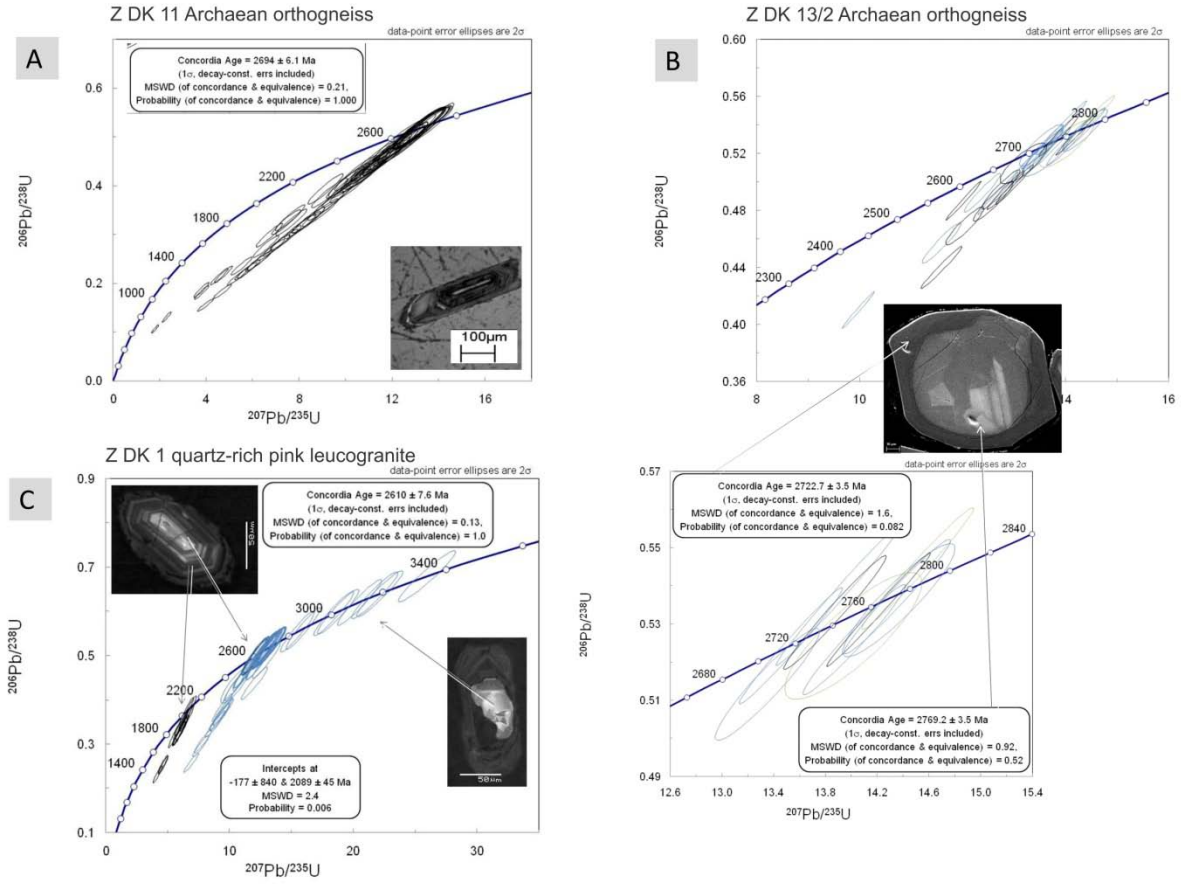

Figure 5.8: Concordia plot of the LA-ICPMS data for sample Z DK 11 (Figure 5.8a), and the SIMS data for Z DK 13/2 (Figure 5.8b) and Z DK 1 (Figure 5.8c).

Palaeoproterozoic Granitoids

Petrography

Samples Z DK 13/6 and Z DK 12 are both foliated biotite orthogneisses. Sample Z DK 12 was collected along the main Victoria Falls-Bulawayo road and has been affected by

retrograde metamorphism, as evidenced by the biotite which has been largely replaced by Fe-rich chlorite. Figure 5.9c illustrates how late stage fluids have produced myrmekitic textures along many of the feldspar grain boundaries. Mafic xenoliths (like those seen in outcrop in Figure 5.9b) are also common. Sample Z DK 13/6 which occurs right along the southern margin of the Tshontanda Formation has a strong foliation, very likely due to its proximity to this boundary. The foliation is also evident in thin section where the biotite grains are arranged in narrow bands (Figure 5.9a).

Sample Z DK 13/7B could be said to fall under the classification scheme of Lockett (1979a), as a 'zone of biotite-rich gneiss and migmatite' where the following three rock units, can usually be seen occurring together: (i) an altered supracrustal rock, veined by pegmatite and containing feldspar porphyroblasts, (ii) a pegmatitic component containing mafic minerals (that forms veins within the supracrustals, and varies from only a few mafic minerals to a banded gneiss dominated by pegmatoid material); and (iii) a foliated biotite-rich gneiss which encloses all the other components. Sample Z DK 13/7B, overall has a texture which is clearly that of an orthogneiss, and certainly seems to be made up of units which fit these descriptions, and have been annotated within Figure 5.9d.

Lockett (1979a) originally used the term 'megacryst' in reference to the size of the microcline phenocrysts within this porphyritic orthogneiss. Sample Z DK 2 was collected roughly 6 km off of the main Victoria Falls-Bulawayo road in close proximity to sample Z DK 1, and the single inherited Archaean zircon in sample Z DK 2 may have been derived from the same source as those inherited zircons which were so abundant in Z DK 1. In general the feldspar grains have no specific orientation and are also affected by sericitisation (Figures 5.9f and g), both biotite and muscovite are present as accessory phases.

Sample Z DK 13/10 collected on the road to Kamativi is a fine-grained augen orthogneiss. It is made up of microcline phenocrysts surrounded by fine-grained recrystallised quartz, feldspar and biotite (Figure 5.9h); accessory amounts of muscovite and garnet are also present. This sample appears to be somewhat deformed, which is unsurprising given its proximity to the contact with the Kamativi Formation, where shearing appears to have resulted in the rounding of the feldspar grains, while the quartz and biotite became recrystallised.

Z DK 13/6 foliated biotite orthogneiss

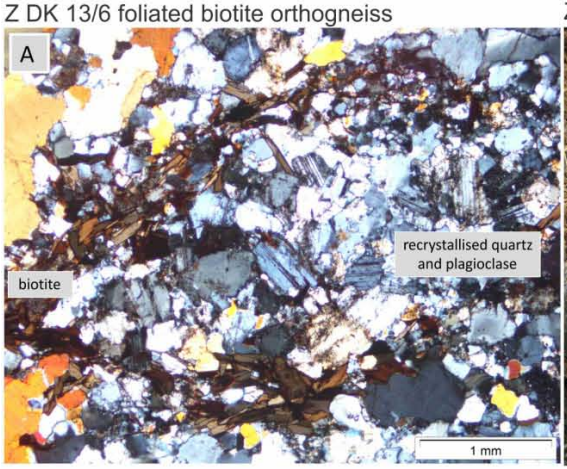

Z DK 12 biotite orthogneiss



Z DK 12 biotite orthogneiss

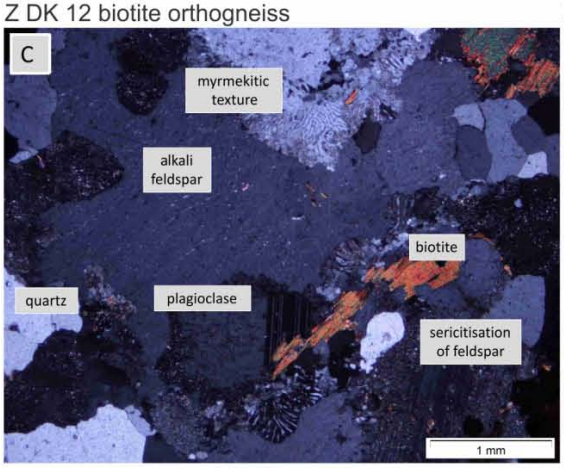

Z DK13/7B biotite orthogneiss



Z DK13/7B biotite orthogneiss

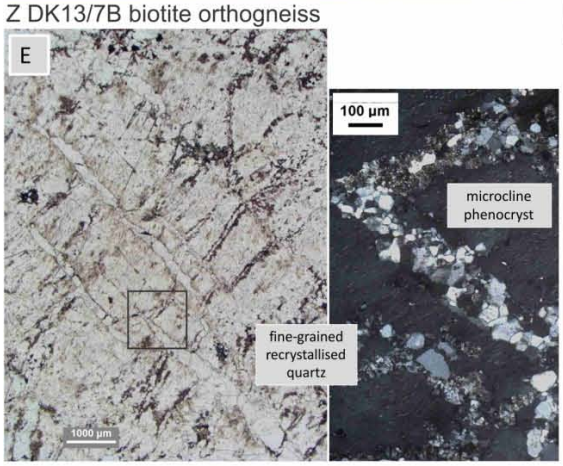

Z DK 2 porphyritic orthogneiss



Z DK 2 porphyritic orthogneiss

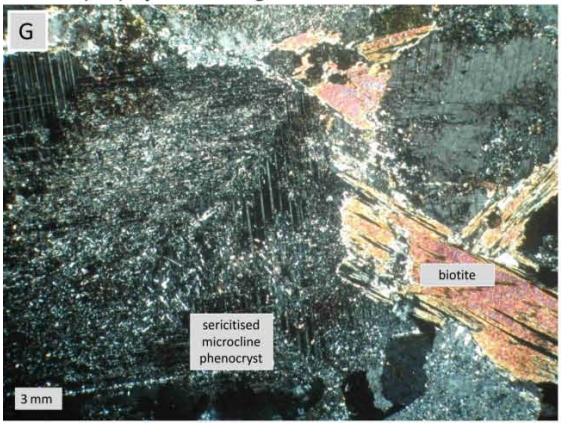

Z DK 13/10 augen orthogneiss

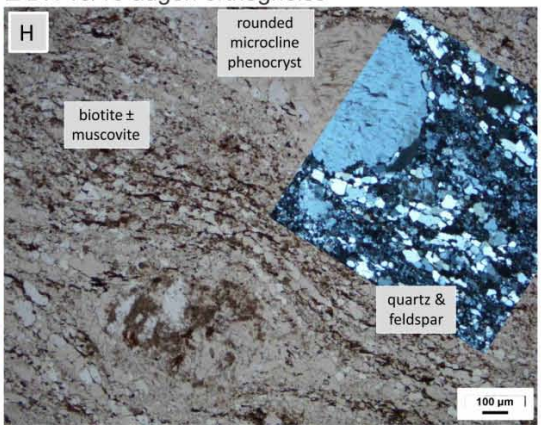

Figure 5.9: Thin bands of biotite in Z DK 13/6 define its foliation (Figure 5.9a). Mafic xenoliths within Z DK 12 have been observed in outcrop (Figure 5.9b), while in thin section (Figure 5.9c) it is possible to see alteration in the form of myrmekitic textures and altered biotite grains. The three units which constitute sample Z DK 13/7B can be distinguished in (Figure 5.9d): an altered supracrustal component (i), a pegmatitic component (ii) and a foliated biotite-rich gneiss (iii). The thin section photomicrograph of sample Z DK 13/7B in Figure 5.9e shows how the relict microcline phenocryst (itself with a cryptoperthitic texture) has been affected by brittle deformation, resulting in fracture filling of the twin lamellae by recrystallised quartz. Sample Z DK 2 is clearly porphyritic and aplitic veins can be seen on an outcrop scale (Figure 5.9f), while the photomicrograph in Figure 5.9g illustrates how heavily sericitised the relict microcline phenocrysts are. Sample Z DK 13/10 consists of microcline phenocrysts which have been transformed into augen via shearing; this has been accompanied by recrystallisation of the surrounding quartz and biotite matrix (Figure 5.9h).

Geochronology

BSE images of the zircons from sample Z DK 13/6 indicate they are a mixture of euhedral prismatic and pyramidal grains, which are magmatically zoned but contain a number of inclusions (Figure 5.10a). An age of 2063 ± 8 Ma (MSWD = 2, N = 11) was derived for this sample, while two older somewhat concordant grains give ages of 2.26 and 2.14 Ga respectively. The zircon grains in sample Z DK 12 (Figure 5.10b) are predominantly magmatic, euhedral, prismatic grains which tend to be rectangular in shape and record a well defined age for the protolith of 2020 ± 4 Ma (MSWD = 0.8, N = 32).

The zircons from sample Z DK 13/7B, seen in Figure 5.10c, are predominantly euhedral, magmatically zoned, pyramidal grains and BSE images indicate the presence of a number of small cracks, implying that these grains may have been deformed in a manner not dissimilar to the microcline phenocrysts. A well constrained age of 2047 ± 3 Ma (MSWD = 1.3, N = 4) was obtained, and indicates the crystallisation age for the sample.

The zircons in sample Z DK 2 are for the most part euhedral and magmatically zoned, but in some cases the zonation was more convoluted, and indicates recrystallisation; the effects of this can be seen by the discordance in most grains. Despite this measurements on both cores and rims give an age of 2025 ± 5 Ma (MSWD = 0.2, N = 68), with the exception of one inherited grain at 2.68 Ga (Figure 5.10d).

BSE images of the zircons in sample Z DK 13/10 indicate that the majority of the grains have been subjected to recrystallisation, thus there has been some migration of trace elements – the result of which is patchy or spongy textured zircon which has magmatic to convoluted zonation. Zircons like those in Figure 5.10e, with a patchy textured core are generated when a low uranium core is metasomatically replaced by zircon higher in uranium (Corfu et al., 2003; Hoskin, 2005). A magmatic age of 1975 ± 29 Ma (MSWD = 4.1, N = 3) was calculated from a number of cores and rims for this sample, and three inherited grains, which are mostly discordant but indicate ages of *circa* 2.6 Ga, were also identified.

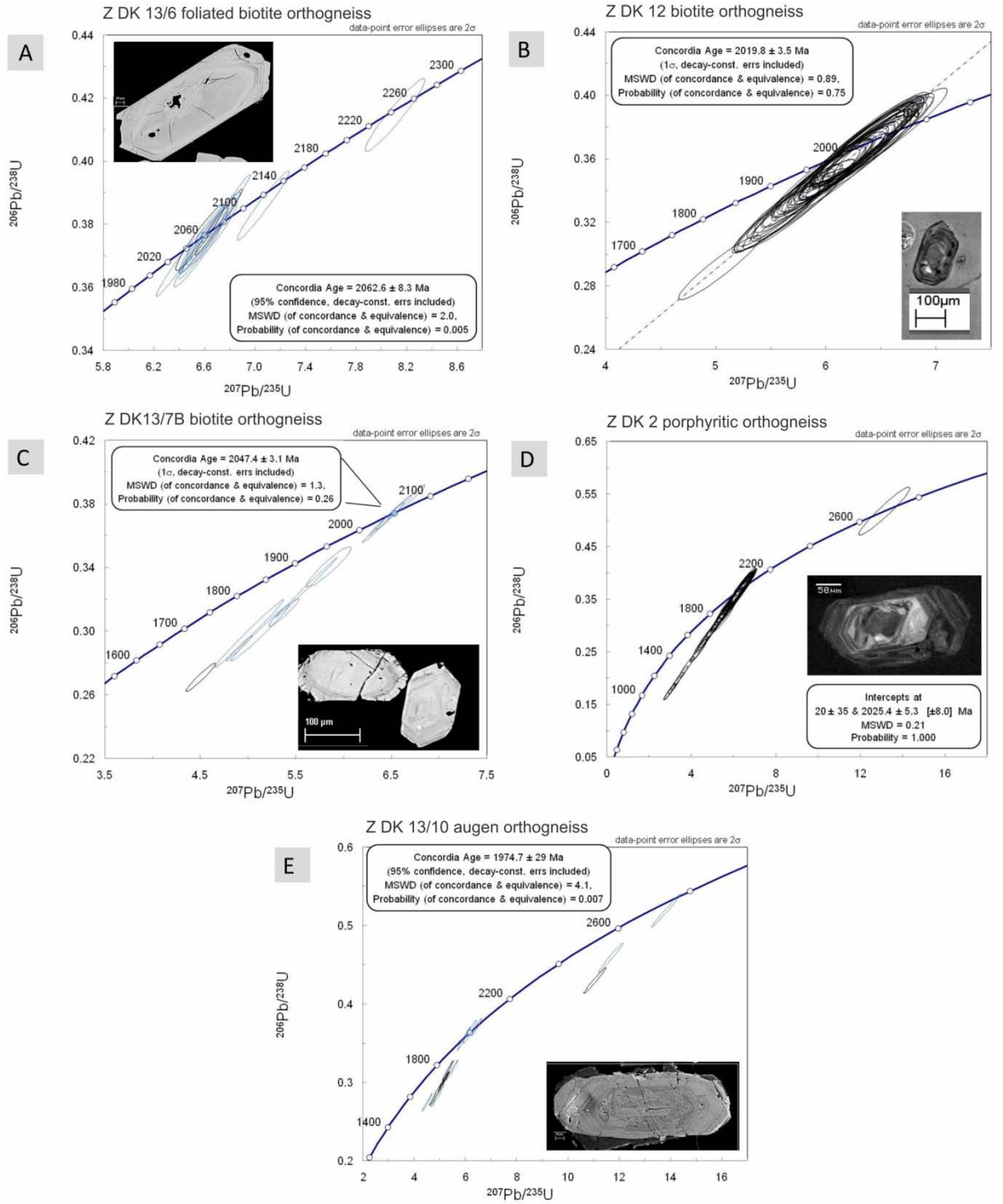

Figure 5.10: Concordia plots of the SIMS data for samples Z DK 13/6 (Figure 5.10a), Z DK 13/7B (Figure 5.10c) and Z DK 13/10 (Figure 5.10e), as well as the LA-ICPMS data for samples Z DK 12 (Figure 5.10b) and Z DK 2 (Figure 5.10d).

5.5 DISCUSSION

5.5.1 Supracrustal metasediments – age of deposition and correlation with the Magondi Belt

The Magondi Belt samples are largely derived from Archaean aged rocks, however sedimentation ages for the Deweras, Lomagundi and Piriwiri Groups are loosely constrained at 2.29, 2.07 and 2.16 Ga respectively (although late stage granitoids, which intrude the Piriwiri Group, constrain a maximum age of 1.99 Ga for the Piriwiri Group).

Ages obtained from almost all the Dete-Kamativi supracrustal samples contain an Archaean component between 2.8 and 2.6 Ga. Samples Z DK 9C and Z DK 10 are paragneisses of the Malaputese Formation, deposited at 2.3 and 2.5 Ga respectively, and can be considered arkosic protoliths derived from weathered granites of the Zimbabwe Craton. Thus, in terms of age and lithology, the correlation of the Malaputese Formation with the Deweras Group (maximum sedimentation age of 2.29 Ga; Glynn et al., 2012), as suggested by Master et al. (2010), can now be confirmed based on similarities in sedimentation age as well as lithology. Sample Z DK 13/5 from the Tshontanda Formation is the second oldest unit, deposited *circa* 2.1 Ga; this is then followed by the Inyantue Formation (sample Z DK 13/8A), at 2.04 Ga which broadly correlates with the sedimentation ages obtained for the Lomagundi and Piriwiri Groups of the Magondi Belt between 2.16 and 2.07 Ga (Glynn et al., 2012).

5.5.2 Granitic Gneisses – defining the extent of the Archaean Zimbabwe Craton and Palaeoproterozoic arc

Lockett (1979a, b) argued that the four different varieties of granitic gneisses formed during a single episode, which he based on the observation that most of the contacts between the various units are gradational, and that the textural differences could simply reflect the intensity of deformation. From the data presented here it is clear, however, that there are two distinct episodes – which respectively resulted in the formation of Archaean and Palaeoproterozoic granitic gneisses.

The two orthogneiss samples (Z DK 11 and Z DK 13/2), are Archaean in age, and represent the first direct evidence for Archaean aged crust within the Dete-Kamativi Inlier. There is also additional evidence from the sample of non-foliated granite (Z DK 1) which contains a significant proportion of inherited Archaean-aged zircons, that these grains were presumably entrained by the granite when it intruded. Based on this, it is highly probable that the Dete-Kamativi Inlier is part of the Archaean Zimbabwe Craton, and that the latter extends much

further to the west than previously supposed. We therefore propose that the western margin of the Zimbabwe Craton extends as far as the Dete-Kamativi Inlier (Figure 5.11).

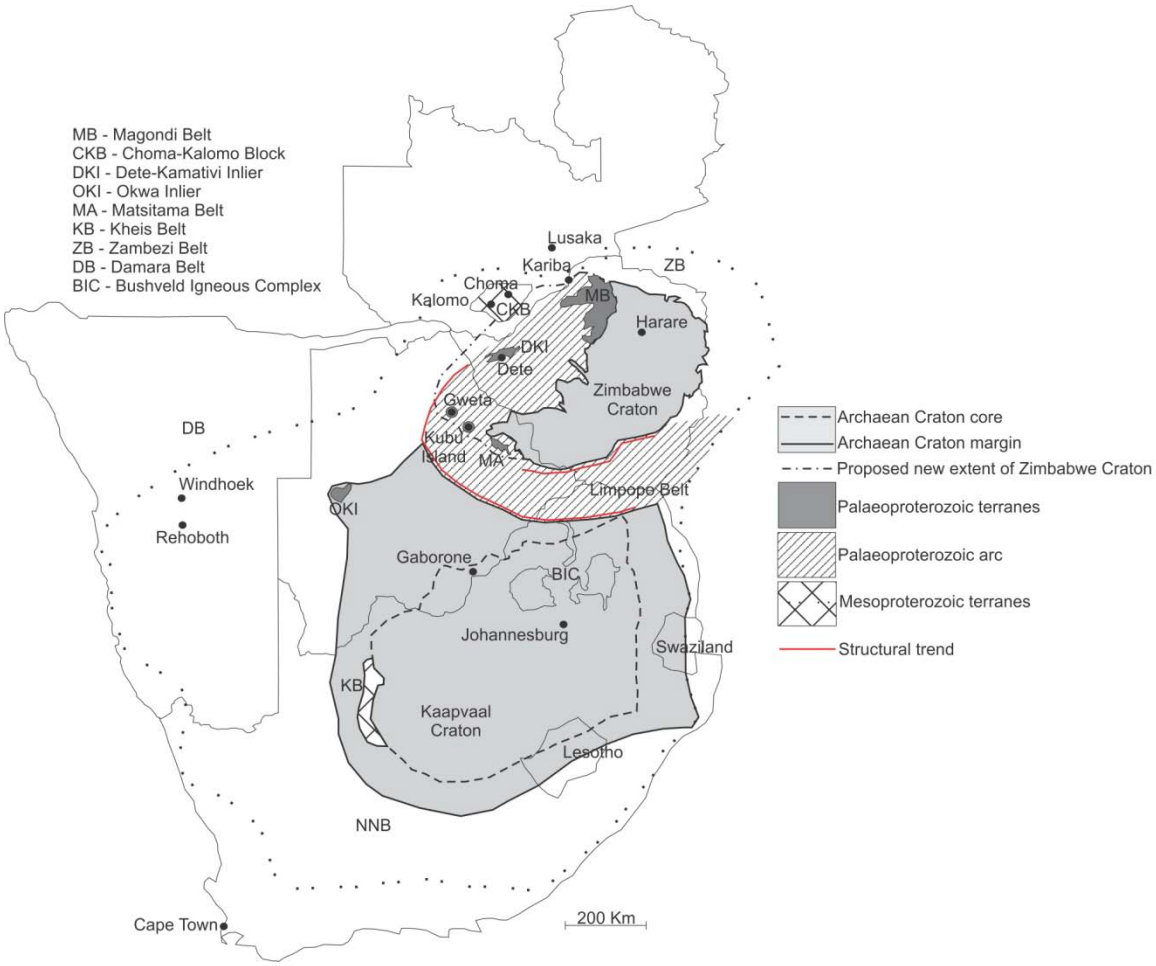

Figure 5.11: Sketch map depicting the proposed new extent of the Archaean Zimbabwe Craton and Palaeoproterozoic magmatic arc (after Majaule et al., 2001; McCourt et al., 2001; Mapeo et al., 2004; Kramers et al., 2006; Jacobs et al., 2008; Eglington et al., 2009; Naydenov et al., 2014; Lehmann et al., 2015).

Samples Z DK 13/6, Z DK 12, Z DK 13/7B and Z DK 2 represent a suite of orthogneisses dated between 2.06 and 2.02 Ga, and are indicative of the formation of a Palaeoproterozoic Andean-type magmatic arc along the western edge of the Zimbabwe Craton. The arc therefore began developing approximately 100 Ma prior to the height of the Magondi orogeny at around 1.9 Ga (Treloar, 1988; Master et al., 2010), which is marked by syn - orogenic granitoids like the Hurungwe Granite within the Magondi Belt (1997.5 ± 2.6 Ma; McCourt et al., 2001) and the orthogneiss sample Z DK 13/10 dated at 1975 Ma. There is also evidence that this Palaeoproterozoic arc existed as far afield as eastern Botswana based

on lithological similarities, geophysical trends and any available geochronology. The following potential extensions to the arc are discussed below; and their respective localities are depicted in figure 5.11.

Gweta (20° 16' 19"S; 25° 13' 25"E)

Stowe et al. (1984) and Carney and Dowsett (1991) favoured the idea that the Gweta Basement Complex correlates with the Dete-Kamativi Inlier, on the basis of a series of similarly orientated magnetic anomalies which lead from the Dete-Kamativi Inlier and extend all the way to Gweta in north-east Botswana. This unexposed basement complex had been identified by the Geological Survey of Botswana – as part of their project to map below the Kalahari cover – after discovering a positive aeromagnetic and gravity anomaly, approximately 20 km wide and 500 m thick. The borehole drilled intersected a garnet-sillimanite paragneiss which bears some resemblance to high-grade rocks of the Magondi Belt (Carney and Dowsett, 1991; Mapeo et al., 2001) and the Dete-Kamativi Inlier (Aldiss and Carney, 1992; Lockett, 1979a, b; this work). An age of 2027 ± 8 Ma was calculated, using SHRIMP U-Pb dating of zircons from the paragneiss, as the onset of granulite facies metamorphism from a number of overgrowth rims, and the maximum age of sedimentation was fixed at 2125 ± 6 Ma, based on a group of the youngest concordant detrital zircons by Mapeo et al. (2001). The Gweta sample also contained numerous inherited Archaean (3.01, 2.69 Ga) and Palaeoproterozoic grains (2.45 to 2.12 Ga). The Archaean grains were likely sourced from the exposed Zimbabwe Craton in eastern Botswana; however, the source region for the bulk of the Palaeoproterozoic zircons is still at present unknown, as rocks approximately 2.4 Ga in age are not common within the Zimbabwe Craton (Mapeo et al., 2001).

Kubu Island (20° 53' 17"S; 25° 49' 48"E)

Kubu Island is one of several isolated exposures of basement granite within the Sua Pan area of north-east Botswana. The granite is porphyritic, medium-grained and well-jointed; additionally it is intruded by pegmatite veins which crosscut the foliation. The foliation is defined by thin seams of muscovite, recrystallised quartz and biotite (altered to chlorite and epidote under greenschist facies metamorphism) which wrap around the alkali feldspar phenocrysts. Titanite, apatite and zircon are common accessory minerals (Majaule et al., 2001).

The Kubu Island granite had, prior to the TIMS dating carried out by Majaule et al. (2001), been considered to constitute part of the Archaean Zimbabwe Craton; however it is now known to be Palaeoproterozoic in age, having a crystallisation age of 2039.2 ± 1.4 Ma. A xenocrystic zircon aged 2673 Ma and a depleted mantle Sm-Nd model age of 2682 Ma are consistent with the granite sampling Archaean material, either from the Zimbabwe Craton or the Limpopo Belt (Majaule et al., 2001). McCourt et al. (2004) proposed that the presence of Archaean crust – coeval with the Matsitama and Limpopo Belts – indicates that the Zimbabwe Craton in north-east Botswana could be extended as far west as Kubu Island.

Matsitama Belt

The Matsitama Belt is described as one of four granite-greenstone terranes which constitute the portion of the Zimbabwe Craton which is exposed in north-east Botswana (Bagai et al., 2002). Majaule and Davis (1998) obtained conventional single zircon U-Pb ages between 2.71 and 2.64 Ga for granitoids enclosing the Matsitama Belt, and similarly Bagai et al. (2002) obtained U-Pb SHRIMP ages between 2.69 and 2.64 Ga for granitoids in the neighbouring Vumba granite-greenstone terrane. It is also known from the work of Wilson et al. (1995) that the Upper Bulawayan rocks in the Zimbabwe Craton are within a similar age range, as well as those of the Limpopo Belt (Bagai et al., 2002). The Matsitama Belt however, is mainly composed of metasedimentary rocks (siliclastic and carbonate mostly), with the more felsic lavas being absent, and the mafic-ultramafic rocks less common. This is exactly the reverse of the majority of the other granite-greenstone terrains, where the metasediments only make up a small component (Bagai et al., 2002).

Slight discrepancies, such as this difference in lithology between the various greenstone belts, prompted Master (1994) to propose that the Matsitama Belt is a continuation of the Magondi Belt. Roberts (1965) was perhaps the first to have considered that the Matsitama Belt was Palaeoproterozoic, stating that it overlay granitic basement. Coomer et al. (1977) did not find any field evidence to support this, owing to the fact that the granites and metasediments have been deformed together; they do however state that among one of the oldest units is a conglomerate containing granitic clasts, not dissimilar to the main conglomerate of the Copper Pot Formation (Deweras Group) said to contain clasts of Archaean basement material, in addition to those of the Deweras lavas (Master et al., 2010). Coomer et al. (1977), also after proposing a shallow water environment in which the Matsitama sediments were deposited (given the lithologies of conglomerate, quartzite and shales topped by limestone), concluded that the Matsitama Belt is fundamentally different from the other granite-

greenstone terranes. Barton et al. (1994) and Coomer et al. (1977) also noted that deformation and mineralisation within the Bushman Shear Zone and Thakadu Shear Zone was Magondian in age, with ages of 1.92 and 2.2 Ga obtained for the respective shear zones (Rb-Sr ages from muscovite and Pb-Pb isotopic results on pyrite and chalcopyrite). Furthermore Coward (1976) subdivided the Limpopo Belt into different sub-domains based on the dominant structural trend observed, and from his map, in the northern-most domain, it is clear that in the west the foliation is NW-trending, but curves to become more NE-trending in the south and east. This NW-trend was also picked up in early geophysical studies by Coward and Fairhead (1980) and Ranganai et al. (2002), who interpret the Shashe Belt (adjacent to the Matsitama Belt) as being an extension of the Limpopo Belt – thus forming an arcuate belt along the south-western margin of the Zimbabwe Craton. They also claimed that the Magondi Belt truncated the western margin of the Limpopo Belt, but the evidence discussed above, rather supports the model of a single orogenic belt which includes both the Matsitama and Magondi Belts (Bagai et al., 2002; Majaule et al., 2001; McCourt et al., 2004; Stowe et al., 1984).

Kheis Belt (Northern Cape)

Workers such as Carney and Dowsett (1991) and Aldiss and Carney (1992) have previously linked the Magondi and Kheis Belts to form a single orogenic belt; and while there is geophysical evidence to trace the Kheis Belt northward (along the Kalahari Suture Zone; Key and Ayres, 2000) and the Magondi Belt to the south-west as far as Gweta, it is difficult to say whether the two terranes actually join. For one, there is strong evidence to suggest that the Magondi Belt wraps around the Zimbabwe Craton to join with the Limpopo Belt, and added to this is the dating done by Moen and Armstrong (2008) on both volcanic and sedimentary rocks of the Kheis Belt, which has since shown that the Kheis Belt is predominantly Mesoproterozoic in age. Of the samples analysed, a number of detrital zircons were Archaean to Palaeoproterozoic in age, and were likely derived from the Kaapvaal Craton, while sedimentation ages calculated for several units confirm that these units are younger than 1.8 Ga and are therefore not related to either the Magondi Belt or the Okwa Inlier. Rb-Sr ages on muscovite in various schistose rocks further indicate that metamorphism occurred *circa* 1.2 Ga, further disproving the Palaeoproterozoic connection between the Kheis Belt and the Magondi Belt. Ultimately, this lead Moen and Armstrong (2008) to include the Kheis Belt as part of the Mesoproterozoic Namaqua-Natal Belt.

Okwa Inlier

The Okwa Inlier is a window of Precambrian basement within the Kalahari Desert, and consists of four main lithologies according to Mapeo et al. (2006). The oldest is a meta-rhyolite, which is accompanied by two monzogranite units which grade into one another – an augen gneiss and K-spar rich monzogranite – while the fourth unit is an aplitic microgranite. The dating done on all four units confirms that the Okwa Inlier formed as a single intrusive event at 2056 ± 2 Ma; while a single inherited grain (2101 ± 4 Ma) hints at a possible Palaeoproterozoic basement (Mapeo et al., 2006). The Okwa Inlier, although similar in age to the other Palaeoproterozoic arc rocks, does not fit particularly well with our current understanding of the Limpopo-Magondi orogenic belt outlined above. Additionally, previous models which had the Okwa Inlier at the centre of an orogenic belt linking the Magondi Belt and the Kheis Belt, have since been shown to no longer be realistic. However Mapeo et al. (2004) has previously hinted at the possibility that the Okwa Inlier is coeval with the Bushveld Complex, given the very close similarity in age, and this is perhaps the most feasible scenario.

5.6 CONCLUSIONS

Based on the ages presented here, we propose that the Dete-Kamativi Inlier is likely an extension of the Magondi Belt, due to the similar lithologies and depositional ages for the respective metasediments; and the second, rather more significant finding is that of Archaean crust within the Dete-Kamativi Inlier, as this implies that the Zimbabwe Craton is in fact continuous below the younger sedimentary cover that exists between the Magondi Belt and the Dete-Kamativi Inlier. The prevalence of ages between 2.06 and 2.02 Ga, derived from a number of orthogneisses within the Inlier, indicates the presence of a Palaeoproterozoic arc along the western margin of the Zimbabwe Craton. It is also possible to suggest that this arc (based on geophysical evidence and various age relationships extends as far south as north-east Botswana, and may even form a single arcuate orogenic belt which consists particularly of the north-western parts of the Northern Marginal Zone and Central Zone of the Limpopo Belt, the Matsitama Belt, and the Kubu Island granites; it then curves round towards the north, to include the Gweta Basement Complex, the Dete-Kamativi Inlier and finally the Magondi Belt.

Chapter 6: The Proterozoic Choma-Kalomo Block, SE Zambia: exotic terrane or a reworked segment of the Zimbabwe Craton?

6.1. INTRODUCTION

The Choma-Kalomo Block, a NE-SW trending, Precambrian terrane located in south-eastern Zambia, consists of a sequence of high-grade metasedimentary gneisses and schists, intruded by Mesoproterozoic granites and granitic gneisses of the Choma-Kalomo Batholith. Several tectonic models have been proposed in the past to account for the formation of the Choma-Kalomo Block. Hanson et al. (1988a) proposed that the Choma-Kalomo Block was part of the Mesoproterozoic Irumide Belt of eastern Zambia, separated from it by the Neoproterozoic Zambezi Belt. Unrug (1992) considered both the Choma-Kalomo Block and Dete-Kamativi Inlier as exotic terranes, whereas Bulambo et al. (2004, 2006) considered the Choma-Kalomo Block alone as an exotic terrane, with respect to the neighbouring Archaean Zimbabwe Craton and Palaeoproterozoic Magondi Belt.

Previous studies by Hanson et al. (1988a) and Bulambo et al. (2004, 2006) focussed primarily on dating the granitic units, and as a result there had not yet been any direct dating of the metasedimentary rocks. In this study, samples of the Main Granite as well as a leuconorite within the Choma-Kalomo Batholith were dated to constrain the magmatic record within the block. Additionally, coltan fragments from tin-bearing granite pegmatites in both the Choma-Kalomo Block and the Dete-Kamativi Inlier were dated using ID-TIMS, as a way to potentially aid the SIMS U-Pb zircon data in testing the validity of the tectonic models proposed for the formation of the Choma-Kalomo Block. In order to also assess these links between the Choma-Kalomo Block and the Dete-Kamativi Inlier, ^{40}Ar-^{39}Ar data reflecting a period of mineralisation within the latter was compared with the coltan results from the Choma-Kalomo Block.

6.2. REGIONAL GEOLOGY

The Choma-Kalomo Block is flanked to the north-west by the late Neoproterozoic to Cambrian Hook Batholith, to the north by the Neoproterozoic Zambezi Belt, and to the south-east and south-west by sedimentary and volcanic rocks of the Permo-Triassic to Lower-Jurassic Karoo Supergroup of the Mid-Zambezi Basin (Figure 6.1), which separates it from the Palaeoproterozoic Magondi Belt and Dete-Kamativi Inlier (Matheson, 1969; Hanson et al., 1988a; Master et al., 2010).

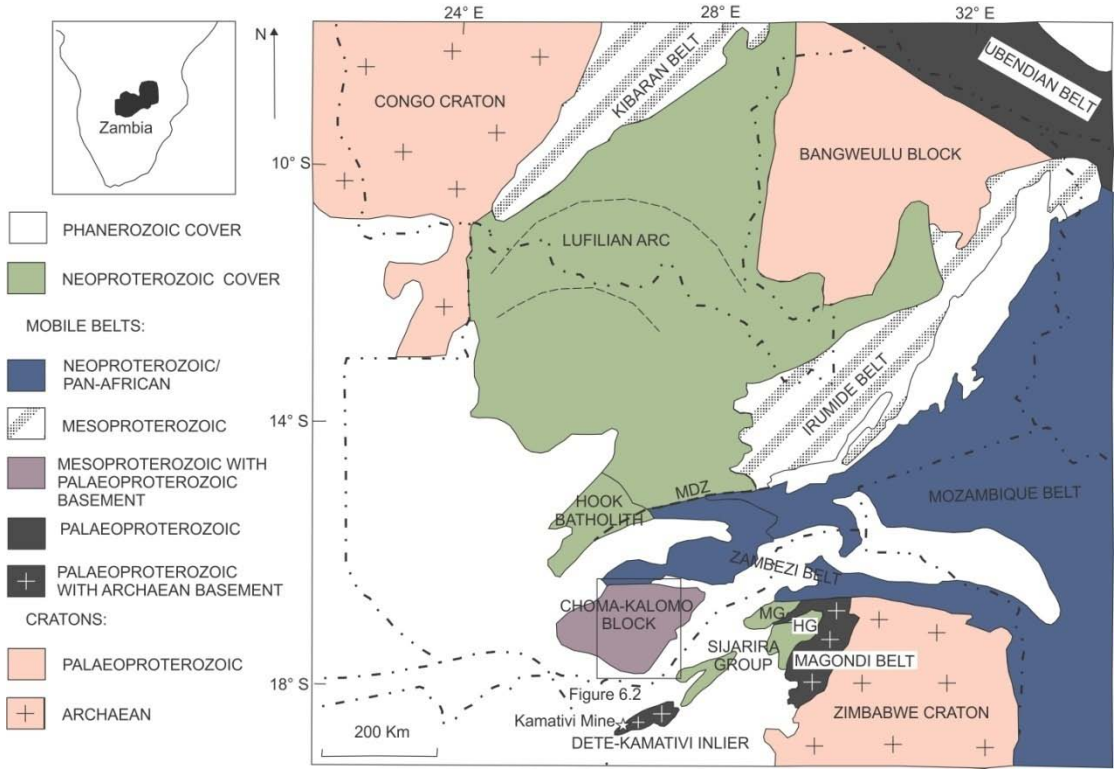

Figure 6.1: Simplified regional tectonic map for southern Africa indicating the localities of interest, the area demarcated by the rectangle appears in detail in Figure 6.2 (from Hanson et al., 1988a, and modified after Hanson, 2003). HG = Hurungwe Granite, MG = Makuti Group, MDZ = Mwembeshi Dislocation Zone.

Detailed mapping of the Choma-Kalomo Block and its surrounding areas was initiated by the Geological Survey of Zambia (formerly Northern Rhodesia) in the 1950's, this resulted in a number of publications containing descriptions of the geology and detailed geological maps at a published scale of 1: 100,000 (Hays, 1955, 1956a, 1957, 1958a,b; Hitchon, 1958b; Tavener-Smith, 1958, 1961; Newton, 1960a,b,c,d, 1961, 1963a,b; Brown, 1966; Matheson,

1969, 1974; Johns, 1995; Zikmund, 1995; Liyungu, 1998). We have consolidated much of this early mapping information into the simplified map of the Choma-Kalomo Block in Figure 6.2.

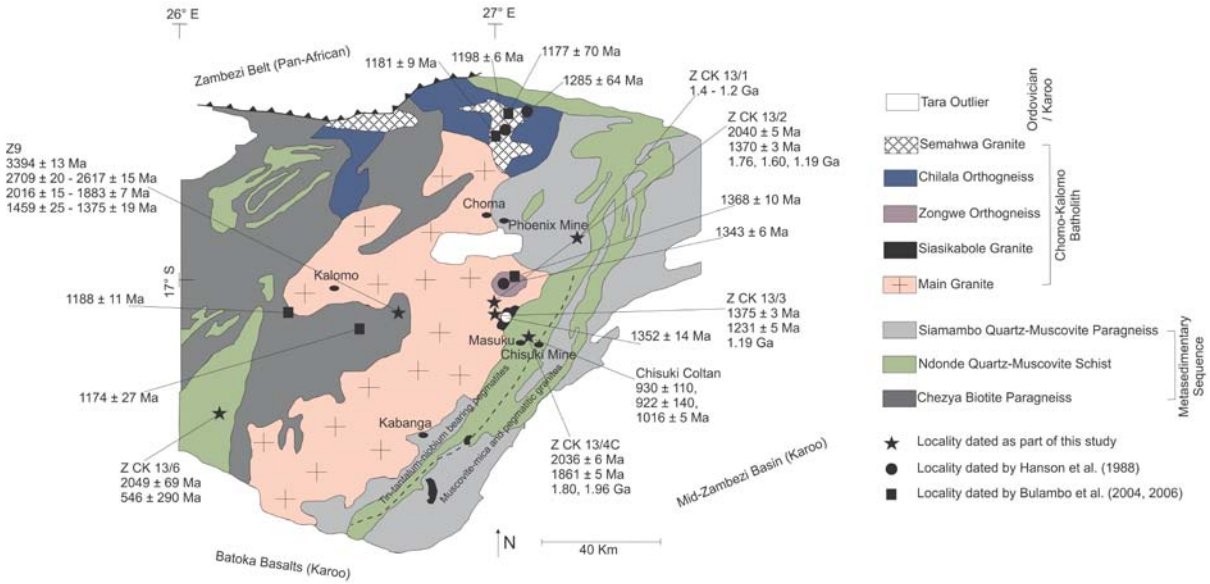

Figure 6.2: Simplified geological map of the Choma-Kalomo Block (after Hanson et al., 1988a; Newton, 1963b). Stars indicate sampling localities from this study and correspond with the data in Tables 6.1 and 6.2 (Appendix A5).

6.2.1 Metasedimentary Sequence

The rocks which make up this older sequence consist of three major units: the Chezya biotite paragneiss at the base (with some minor basic intrusions), which is overlain by, and interfolded with the Ndonde quartz-muscovite schist and Siamambo quartz-muscovite paragneiss. These units are structurally separated from an overlying series of quartz-biotite gneisses and schists of the Nadongo Group, which is the basal part of the WNW-ESE-trending Neoproterozoic Zambezi Belt (Newton, 1960a; Tavener-Smith, 1961; Brown, 1966; Hanson et al., 1994; Loughlin, 1998).

The Chezya and Siamambo paragneisses, and Ndonde schist were polydeformed after being subjected to amphibolite-grade metamorphism, thus making sillimanite, kyanite and garnet the common metamorphic index minerals (Matheson, 1969, 1974; Newton, 1960a,b, 1963b; Brown, 1966; Johns, 1995; Zikmund, 1995; Liyungu, 1998). In general the metasedimentary rocks strike NE-SW, which is parallel to the line of the escarpment of the Mid-Zambezi Valley where the rift touches the eastern margin of the Main Granite (Hays, 1955; Hanson et al., 1988a).

Chezya Biotite Paragneiss

Hays (1955) first referred to the Chezya biotite paragneiss as an "injection gneiss", because the rocks were so invaded by pegmatites and strongly folded. He also considered them to be the oldest exposed metasedimentary rocks. The paragneiss is quite variable, ranging from migmatitic biotite granite, to alternating biotite-rich and quartz-microcline rich bands, all of which contain accessory amounts of apatite, iron oxide and epidote (Newton, 1963b). Hays (1955) also recognised two different types of pegmatite that were injected into these rocks – an earlier phase with quartz and pink and white feldspar, often epidotised, and a later, less common type consisting of quartz, white feldspar, muscovite and tourmaline, which is related to the tin and muscovite pegmatites cutting the overlying schists.

Ndonde Quartz-Muscovite Schist

The Ndonde quartz-muscovite schist consists of quartz and muscovite with varying proportions of garnet, biotite, sillimanite, plagioclase and chlorite (Newton, 1963b; Matheson, 1969), in addition to tourmaline, occurring as grains with green cores and brown rims. Other lithologies found associated with the Ndonde schist, include micaceous and haematitic quartzites, as well as folded bands of marble, which can be found in the southeast and occurs as intercalations within the schist (Hays, 1956c; Matheson, 1969, 1974).

Siamambo Quartz-Muscovite Paragneiss

Newton (1963b) proposed that the Siamambo paragneiss is a metasomatic equivalent of the Ndonde schist, given the similar quartz-muscovite mineralogy with varying proportions of porphyritic plagioclase and microcline, in addition to garnet. Matheson (1969) split this unit into granulitic gneisses (on the eastern-most edge) and migmatitic gneisses, which are in contact with the Ndonde schist. The granulitic gneisses are commonly quartzo-feldspathic, fine grained, and of a granular appearance.

Basic intrusions

Small basic intrusions, such as the (4.0 x 0.8 km) arcuate Kala Hill Gabbro, found intruded into a tight antiform between the basement gneisses and schists (Newton, 1961), and the Chinkozia Norite have been mapped within the metasediments. The latter is a 14.4 x 3.2 km noritic intrusion, surrounded by schists and gneisses (Newton, 1963a) and consists of hypersthene, augite, and plagioclase of labradorite to bytownite composition (Hitchon, 1957,

Newton, 1963a). Aside from these small intrusions and the mafic, hornblende-biotite schists interfolded with the Chezya paragneiss, there are no other Proterozoic basic rocks in the Choma-Kalomo Block (Hays, 1955; Newton, 1960d). Some of these mafic schists represent dykes, sills and mafic lava flows that have since been metamorphosed, but there are also some much younger, unmetamorphosed mafic dykes which trend NE-SW, and are part of the Karoo Dyke Swarm as feeders to the 180 Ma Batoka Basalts (Jones et al., 2001), which cover the southern part of the Choma-Kalomo Block (Hays, 1955; Zikmund, 1995).

6.2.2 Choma-Kalomo Batholith

Detailed mapping of the Choma-Kalomo Batholith (Matheson, 1969, 1974; Mapani, 1986; Johns, 1995) revealed that it is composed of a number of discrete granite and granite-gneiss plutons that together form a composite batholith, which makes up a significant portion of the Choma-Kalomo Block. Hitchon (1958b) and Newton (1963b) describe the granitic units within the batholith as having compositions of biotite-rich quartz monzonites and granodiorites, with a typical granodiorite consisting of quartz, phenocrysts of microcline and plagioclase, and biotite ± hornblende, with accessory epidote, apatite, iron oxides and rarely, allanite (Newton, 1963b).

As part of an earlier study, five samples from the Choma-Kalomo Batholith were dated by Bulambo et al. (2004, 2006) who only presented these results in abstracts. More details were provided by Johnson et al. (2005) and de Waele et al. (2006), the ages and localities however are depicted in Figure 6.2. Four samples gave ages between 1188 ± 11 Ma and 1174 ± 27 Ma, while the remaining sample was dated at 1368 ± 10 Ma. These ages, obtained from U-Pb SHRIMP dating of single zircon grains, broadly reproduce the results of Hanson et al. (1988a), which were obtained by dating bulk zircon fractions (ID-TIMS), and range from 1352 ± 14 Ma to 1198 ± 6 Ma. Both Hanson et al. (1988a) and Bulambo et al. (2004, 2006) were therefore able to demonstrate that there are two periods of granitoid emplacement *circa* 1.37 Ga and 1.19-1.18 Ga respectively.

As outlined below, the batholith was subdivided according to a scheme put forward by Hanson et al. (1988a).

Zongwe Orthogneiss

The Zongwe orthogneiss, a strongly deformed augen granitic gneiss, with its orientated microcline phenocrysts, was first described by Matheson (1974), although it was not differentiated on his map due to poor exposure.

Main Granite

The main granite (a medium-grained hypidiomorphic biotite granite), contains sparse microcline megacrysts (Hanson et al., 1988a), as well as foliated gneissic inclusions and hornfels xenoliths (Tavener-Smith, 1961; Newton, 1963b). The presence of such inclusions within unfoliated granite, in addition to the progressive shearing observed at the granite margins led Hanson et al. (1988a) to conclude that the main granite was intruded syntectonically, around the time the foliation within the country rocks was produced.

Siasikabole Granite

The Siasikabole granite is a small body of fine-grained, hornblende granite, occurring within both the main granite and the surrounding country rocks (Matheson, 1969, 1974; Mapani, 1986; Hanson et al., 1988a; Zikmund, 1995). Petrographically the granite consists of equigranular quartz, hornblende ± biotite, muscovite, plagioclase and microcline (Matheson, 1969, 1974). The contacts with the surrounding rocks are sharp; however a weak NE-SW foliation is evident at the margins (Matheson, 1969; Hanson et al., 1988a).

Chilala Orthogneiss

The Chilala orthogneiss, a migmatitic, biotite orthogneiss containing variable amounts of microcline augen, is found around the northern margins of the main granite (Hanson et al., 1988a), and includes areas originally mapped as the Kabumbwe gneiss (Tavener-Smith, 1961) and Chezya paragneiss (Newton, 1963b), Hanson et al. (1988a) had also noted some similarities between the Chilala and Zongwe orthogneisses.

Semahwa Granite

The Semahwa granite is a hornblende-biotite granite with abundant microcline phenocrysts, and unlike the Chilala orthogneiss, into which it intrudes, the Semahwa granite lacks a pre-Zambezi foliation. Thus it likely post-dates the regional NE-SW fabric seen in the country rock metasediments (Hanson et al., 1988a).

6.2.3 Muscovite and tin-bearing pegmatites

A number of different pegmatites can be found intruding the metasediments. The first variety is a set of muscovite-mica pegmatites, which intrude the Ndonde schist, following its regional NNE strike (Hays, 1956b). Tin (tantalum-niobium) bearing quartz-muscovite pegmatites are

also found intruding the metasedimentary sequence along strike (NE-SW), in a narrow band about 7 km wide and 100 km long, and do not appear to be spatially associated with any granitic intrusions (Legg, 1972; Legg and Namateba, 1982; Matheson, 1969).

Muscovite bearing pegmatites trending NNE

Muscovite from Phoenix Mine (situated at 16°49'S, 27°02'E, in the north of the map area 1727 NW (Hays, 1956c)), was dated using both the Rb-Sr and K-Ar systems, by Snelling et al. (1964). The ages were originally reported as 1040 ± 40 Ma and 1050 ± 40 Ma, but were recalculated using updated decay constants by Snelling et al. (1972) and Cahen et al. (1984), to be 1080 ± 31 Ma (Rb/Sr, R_i = 0.705), and 1060 ± 40 Ma (K/Ar). The muscovite at the mine occurs in quartz-microcline veins, which were injected along vertical fractures and fissures, while the pegmatite veins vary in thickness from 30 cm to as much as 17 m (Hays, 1956c).

Tin-(tantalum-niobium)-bearing pegmatites

The tin-bearing pegmatite belt of the Choma-Kalomo Block is associated with regional NE-trending shear zones, which are parallel to the strike of the older metasediments and eastern margin of the Choma-Kalomo Batholith (Hays, 1956b; Nash, 1960; Newman and Drysdall, 1964; Drysdall, 1967, Matheson, 1969). Three types of pegmatite are recognised within the metasedimentary sequence of the Choma-Kalomo Block: (1) quartz-muscovite pegmatites, (2) quartz-muscovite-biotite-feldspar-tourmaline pegmatites, and (3) cassiterite-bearing quartz-muscovite ± feldspar pegmatites (Drysdall, 1967), the latter were further divided into either Sn-Ta or Ta-Nb varieties by Legg and Namateba (1982) based on mineralogical, textural and geochemical variations, and are generally composed of quartz, muscovite ± biotite, microcline and plagioclase (Hays, 1956b; Newman and Drysdall, 1964; Drysdall, 1967; Legg, 1972; Legg and Namateba, 1982). Accessory minerals vary but include cassiterite, tourmaline, columbite-tantalite, beryl, garnet, and rare wolframite (Matheson, 1969; Legg and Namateba, 1982). Legg and Namateba (1982) proposed that the various pegmatites formed roughly simultaneously, but owing to differing distances from the source of the fluids as well as water content, and pressure and temperature conditions, formed the various types observed.

6.3. ANALYTICAL METHODS

In the course of this study a total of six samples from the Choma-Kalomo Block were dated using U-Pb zircon geochronology, the SIMS data from five of these samples are recorded in Table 6.1 (Appendix A5), where the analytical uncertainty for the ratios and ages is at 1 sd. Sample Z9 was dated, on a separate occasion, using LA-ICPMS, and the U-Pb zircon age data is presented in Table 6.2 (Appendix A5). An additional four samples of coltan fragments collected from pegmatites in both the Choma-Kalomo Block as well as the Dete-Kamativi Inlier were dated using ID-TIMS; the results of the isotopic analyses (corrected for blank and initial common Pb) are given in Table 6.3, while coltan and plagioclase analyses uncorrected for common Pb are given in Table 6.4 (Appendix A5). Mica separates from two samples in the Dete-Kamativi Inlier were also dated using ^{40}Ar-^{39}Ar geochronology, and the results are listed in Table 6.5 (Appendix A4). The methodologies adopted for the various analyses are detailed in Section 2.6 (pp 30).

6.4. RESULTS

6.4.1 Intrusives of the Choma-Kalomo Batholith

Exposures within the Choma-Kalomo Block are poor, as the topography is in general very flat. Nonetheless sample Z CK 13/3, a medium-grained granite crosscut by pegmatitic veins, was observed in the field as a small expanse of pavement (figure 6.3a). As already noted by Hanson et al. (1988a), the main granite is unfoliated in the interior of the pluton and no contacts were visible within the outcrop, it is therefore not possible to say with any real certainty how the quartz-plagioclase-pyroxene leuconorite (sample Z CK 13/2) is related to the granite, although it is likely that the leuconorite is a xenolith within the granite (Tavener-Smith, 1961; Newton, 1963b).

Z CK 13/2 is a quartz-plagioclase-augite-hypersthene leuconorite, forming low resistant outcrops. No contacts with the nearby granite (Z CK 13/3), which outcrops less than a km away, are exposed. This leuconorite could be a xenolith within the granite batholith, or it could represent a roof pendant, as suggested by Hays (1956a) for similar country rock fragments within the Choma-Kalomo Batholith.

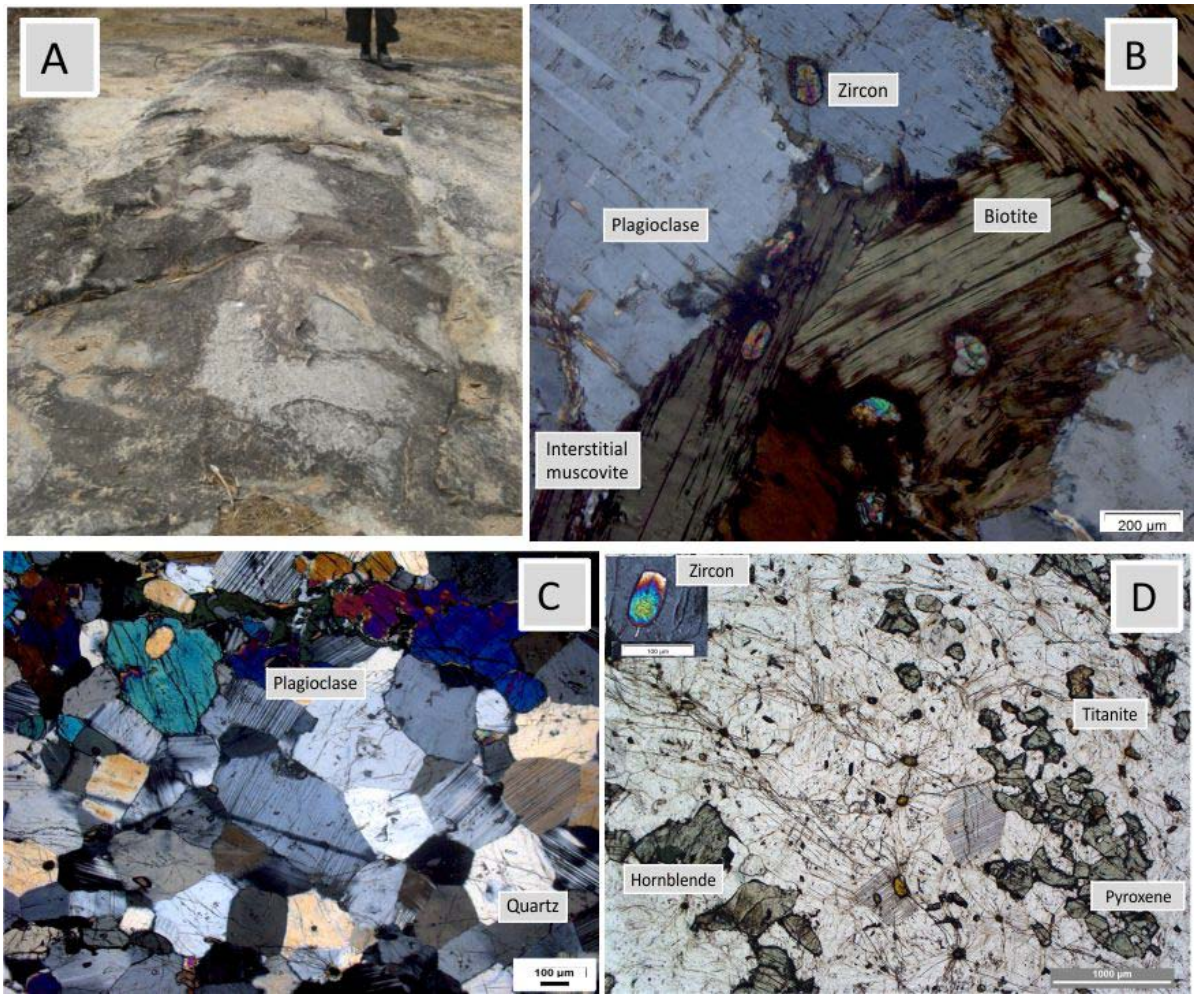

Figure 6.3: Field photograph (Figure 6.3a) and photomicrograph of the granite sample Z CK 13/3 under cross-polarised light where medium-grained biotite frequently plays host to zircon, and interstitial fine-grained muscovite is associated with recrystallised quartz (Figure 6.3b). Photomicrographs of the leuconorite (sample Z CK 13/2) under cross-polarised and plane-polarised light are shown in Figure 6.3c and d respectively. It is evident from these images that the sample consists of pyroxene (augite and hypersthene), plagioclase and quartz, which together form a granoblastic texture; there is also evidence of retrograde metamorphism in the form of hornblende which is locally replacing the pyroxene.

As expected from its mafic composition, only a few zircon grains were present in sample Z CK 13/2. Nine cores and four rims were analysed from thirteen zircon grains, and reveal that the zircons extracted from sample Z CK 13/2 (Figure 6.4a) are predominantly confined to two populations. The cores from the three oldest, more rounded, concordant grains gave an age of 2040 ± 5 Ma (MSWD = 0.6), and have good oscillatory zoning revealing their igneous crystallization origin. The cores from the four youngest, more euhedral, zircons were dated at

1370 ± 3 Ma (MSWD = 1.7), which is interpreted to represent the age of the leuconorite intrusion, and implies that it was incorporated into the Choma-Kalomo Batholith roughly around the same time as the first generation of granitoids were being emplaced. The remaining single zircons which lie along the concordia curve were measurements made on cores of various ages, and therefore reflect inheritance, and together with the 2.04 Ga zircons, represent a xenocrystic component within the leuconorite derived from an older Palaeoproterozoic source region.
The four rim analyses yielded ages of between 1380 and 1349 Ma (with the youngest at 1194 Ma), and are interpreted to be overgrowth rims.

The zircon grains collected from sample Z CK 13/3 have a fairly distinct euhedral morphology, which in some cases has been completely mantled by a patchy-textured overgrowth. Fifteen measurements were made on fourteen grains, and of the nine most concordant measurements made on zircon cores, an age of 1375 ± 3 Ma (MSWD = 1.3) was obtained. This emplacement age coincides with the age of the first generation of plutons in the Choma-Kalomo Batholith, from around 1370 to 1350 Ma (Hanson et al., 1988a; Bulambo et al., 2004, 2006).
The overgrowth rims are dated at 1231 ± 5 Ma (MSWD = 0.3, N = 2), while a second, slightly younger rim (seen in Figure 6.4b as having formed an embayment into the grain) is dated to be 1197 ± 12 Ma. The measurements made on the patchy-textured overgrowths coincide with the intrusion of the second, younger phase of granitoids within the batholith. This patchy texture observed may be attributed to the zircon having been affected by metasomatic fluids, associated with the second intrusive phase of the Choma-Kalomo Batholith, before being partially resorbed (Corfu et al., 2003; Harlov et al., 2012, 2014).

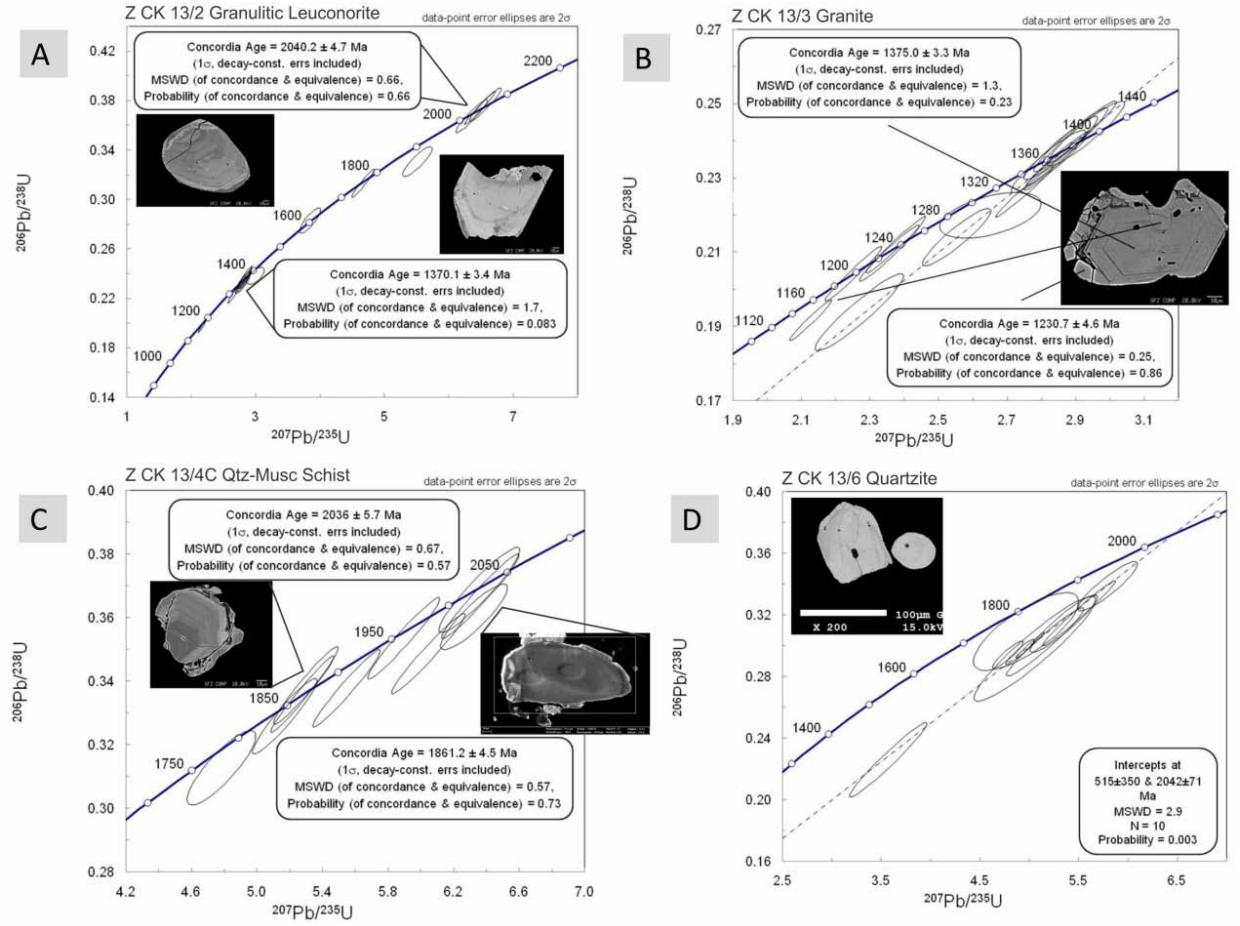

Figure 6.4: Concordia plots of the SIMS data for the samples Z CK 13/2 (Figure 6.4a) and Z CK 13/3 (Figure 6.4b) as well as the quartz-muscovite schist sample Z CK 13/4C (Figure 6.4c), and quartzite sample Z CK 13/6 (Figure 6.4d). The number of detrital zircons analysed for samples Z CK 13/4C and Z CK 13/6 are, respectively, 10 grains each.

6.4.2 The Metasedimentary Sequence

A semi-pelitic, quartz-muscovite-tourmaline schist (sample Z CK 13/4C, Figure 6.5a) represents the country rock at the Starfield Tin Mine, near Masuku Mission (Figure 6.2). A well defined crenulation cleavage is evident in thin section, where coarse-grained muscovite laths bend around grains of quartz and tourmaline (Figure 6.5b).

Sample Z CK 13/6, a heavy mineral-rich medium to coarse-grained quartzite (Figure 6.5c), is one of several, 100 m-wide, discontinuous quartzite bands which are interbedded within the Ndonde schist.

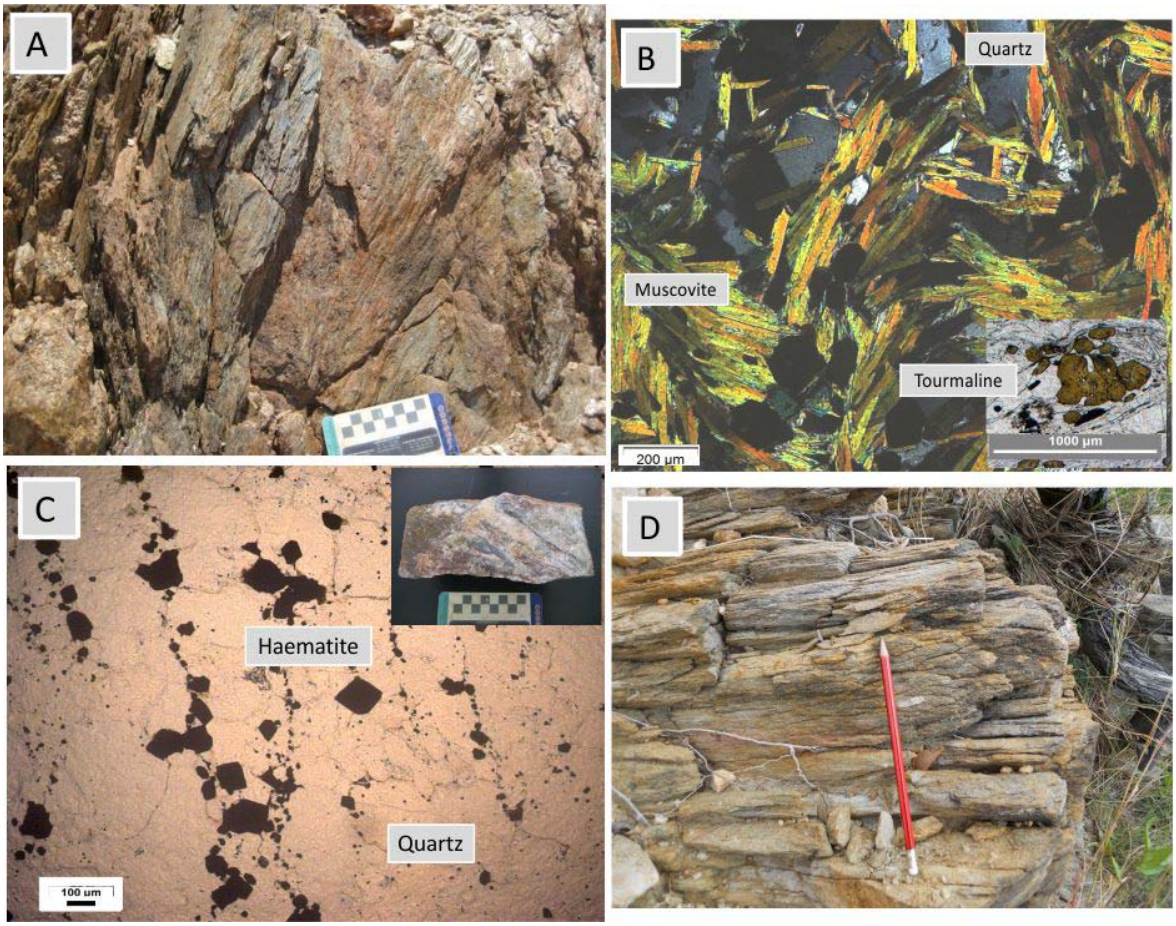

Figure 6.5: Field photograph of the Ndonde schist (sample Z CK 13/4C) in outcrop (Figure 6.5a). Photomicrograph under cross-polarised light (Figure 6.5b) illustrating the crenulation cleavage in the schist. The inset of Figure 6.5b, confirms the presence of tourmaline in the sample, whereas the inset to Figure 6.5c demonstrates the heavy mineral-rich foreset laminae in quartzite sample Z CK 13/6. Under plane polarised light the cubic pseudomorphs of haematite after magnetite can be seen to be concentrated in thin irregular bands (Figure 6.5c). Outcrop of schist (sample Z9), showing strong subhorizontal foliation and jointing (Figure 6.5d).

The ten zircon grains in sample Z CK 13/4C are predominantly fragments, however faint traces of magmatic zoning are evident in addition to thin, patchy-textured overgrowth rims, similar to those observed in sample Z CK 13/3. The age data obtained for sample Z CK 13/4C (Figure 6.4c) reveal Palaeoproterozoic aged zircons, ranging in age from 2036 ± 6 to 1861 ± 5 Ma (MSWD of 0.7 [N = 2] and 0.6 [N = 3] respectively).

The quartzite (Z CK 13/6) yielded relatively poor quality zircons for analysis – hence the high degree of discordance seen in Figure 6.4d. The grains have distinctly rounded edges, but the original oscillatory zonation pattern in many of the grains is still preserved. An upper

intercept age, based on the 10 measurements made, of 2042 ± 71 Ma (MSWD = 2.9) was calculated.

Z CK 13/4C and Z CK 13/6 thus both record maximum detrital zircon ages within uncertainty of one another, at 2036 ± 6 Ma and 2042 ± 71 Ma respectively. The maximum sedimentation age for sample Z CK 13/4C, defined by the youngest detrital zircon, is 1.81 Ga. However the cluster of three detrital zircons in this sample defines a mean age of 1861 ± 5 Ma, which provides a more robust maximum age for sedimentation of the protolith. Zircons within this age range are an indication that they were sourced from an exposed Palaeoproterozoic source, and reflect the development of an evolving sedimentary basin which contains material probably derived from the adjacent Magondi Belt on the western side of the Zimbabwe Craton prior to the emplacement of the Choma-Kalomo Batholith.

A strongly weathered quartzofeldspathic paragneiss (sample Z CK 13/1) consisting largely of recrystallised quartz and plagioclase, along with muscovite and minor amounts of biotite yielded zircons of poor quality for analysis. BSE images of these grains revealed some cores with overgrowth rims; however, the morphology indicated that many of the grains are fragments, often containing large cracks. Figure 6.6a shows large uncertainties on the error ellipses suggesting that the cracks in the grains acted as access points for common lead. The sampled unit with zircons between 1.4 and 1.2 Ga, is therefore at best either synchronous with, or postdates the intrusion of the first phase of the Choma-Kalomo Batholith at 1.37 Ga.

Sample Z9 (a semi-pelitic quartz-biotite-muscovite schist) is quite deformed, with a strong sub-horizontal foliation expressed by the preferential alignment of mica; the outcrop is also severely jointed (Figure 6.5d). CL images of zircons from sample Z9 reveal that most grains are euhedral with some form of igneous oscillatory zoning, while some have distinctly inherited cores surrounded by an overgrowth rim (Figure 6.6b). The concordia and relative probability plots of ages in Figures 6.6b through d show that the zircons fall into four groupings: 3394 ± 13 Ma, 2709 ± 20 to 2617 ± 11 Ma, 2016 ± 15 to 1883 ± 7 Ma and 1459 ± 25 to 1375 ± 19 Ma. Although the bulk of these detrital zircon ages are Palaeoproterozoic, at 1883 ± 7 Ma (MSWD = 0.8, N = 39), and fall within the large peak between 2.01 and 1.88 Ga the protolith is constrained to have a maximum depositional age of around 1256 ± 18 Ma (MSWD = 0.08) based on the three youngest detrital zircons. Some of the older Palaeoproterozoic ages (2016 ± 15 Ma; MSWD = 0.68, N = 7) correspond to ages of igneous events within the Magondi Belt of western Zimbabwe (Glynn et al., 2012; Master et al.,

2013), while the large peak of 1883 Ma corresponds to the age of metamorphism in the Magondi Belt between 2.0 and 1.8 Ga (Treloar and Kramers, 1989; Munyanyiwa et al., 1995). The oldest zircons, of Mesoarchaean (3394 ± 13 Ma) and Neoarchaean (2709 ± 20 - 2617 ± 11 Ma) age, match closely the ages of Archaean rocks from the adjacent Zimbabwe Craton, where the Sebakwe protocraton has ages between 3.45 to 3.35 Ga (Horstwood et al., 1999), and the Upper Bulawayan greenstones have ages between 2.7 and 2.6 Ga (Blenkinsop et al., 1997). Thus the presence of so many similarly aged Palaeoproterozoic and Archaean aged detrital zircons gives rise to the possibility that the zircons in sample Z9 were derived from units within the adjacent Zimbabwe Craton.

The zircons dated between 1.45 and 1.37 Ga are primarily of unknown provenance as ages of ~1.4 Ga are not typical of the Magondi Belt. It is likely however that the 1.37 Ga zircons originate from the Choma-Kalomo Batholith, as they are within error of the age calculated for the initial phase of granitoids.

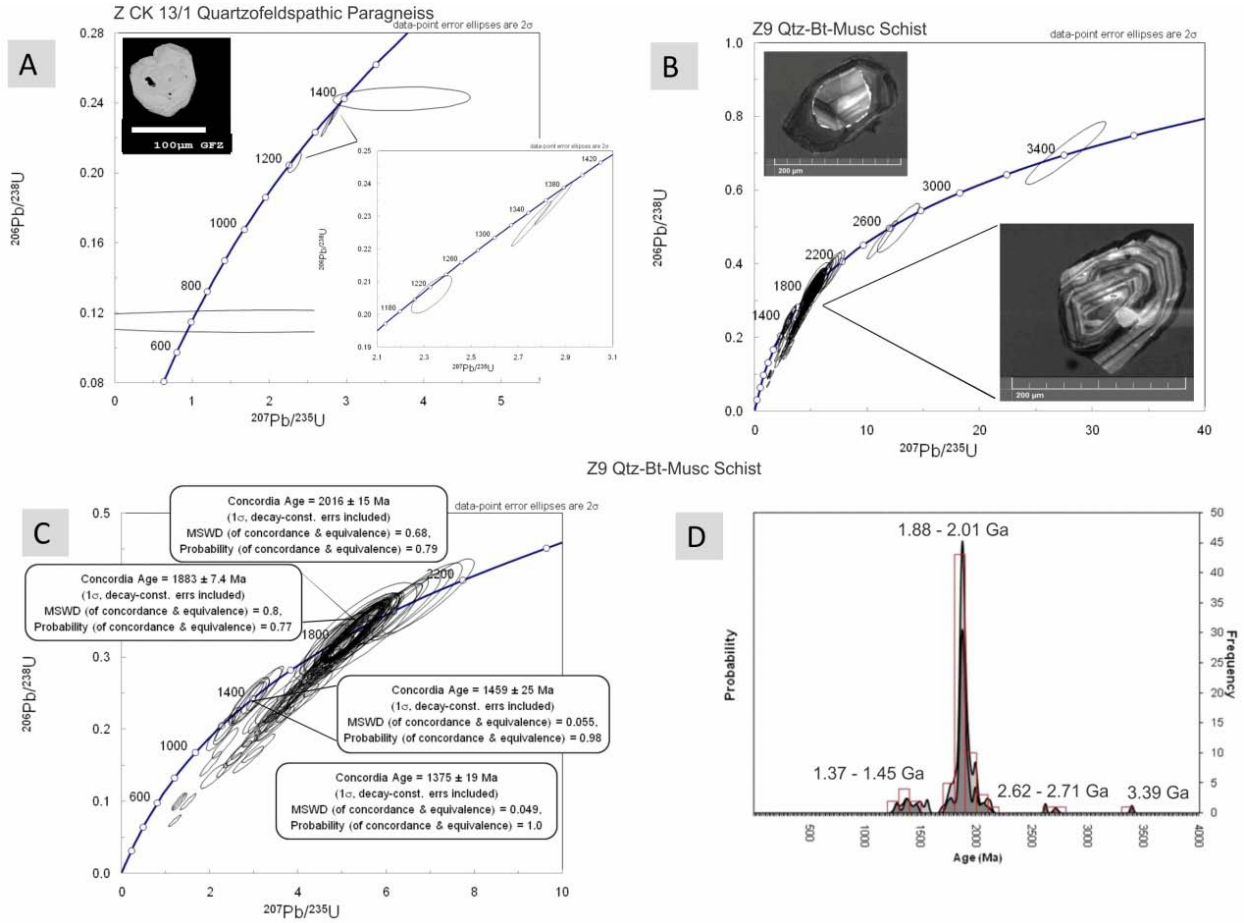

Figure 6.6: Concordia plot of the SIMS data collected for sample Z CK 13/1 (Figure 6.6a), where N=9. Figures 6.6b through d are the concordia and relative probability plots for the

quartz-biotite-muscovite schist sample Z9. Approximately 120 de trital zircons from this sample were dated using LA-ICPMS.

6.4.3 Pegmatites in the Choma-Kalomo Block and Dete-Kamativi Inlier

Coltan U-Pb and Pb-Pb ages

Coltan concentrates were obtained from tin pegmatites in the Choma-Kalomo Block, as well as in the Dete-Kamativi Inlier. Fragments from samples 12R04B, 12R07 and 10631 (Figures 6.7a through c) were collected from Chisuki Mine (~4 km SSE of sample Z CK 13/4C, within the Choma-Kalomo Block). Coltan and plagioclase fragments from sample 786 (Figure 6.7d) were obtained from the Kamativi Tin Mine in the Dete-Kamativi Inlier for comparison. The coltan fragments 12R04B, 12R07 and 10631 from Chisuki Mine yielded Pb/Pb model ages of 930 ± 110 Ma (MSWD = 5.2), 922 ± 140 Ma (MSWD = 34) and 1016 ± 5 Ma (MSWD = 0.03) respectively, whereas the coltan fragments from Kamativi Mine yielded a Pb/Pb age of 1037 ± 5 Ma when plotting only the coltan data (corrected for laboratory blank). However, the coltan contains relatively high proportions of common lead, which can influence the precision of the common lead correction. For this reason the Pb isotopes for plagioclase, intergrown with the coltan, were analysed in order to better constrain the isotopic composition of the common lead component, and the result is a Pb/Pb age of 1030 ± 8 Ma (MSWD = 3.1).

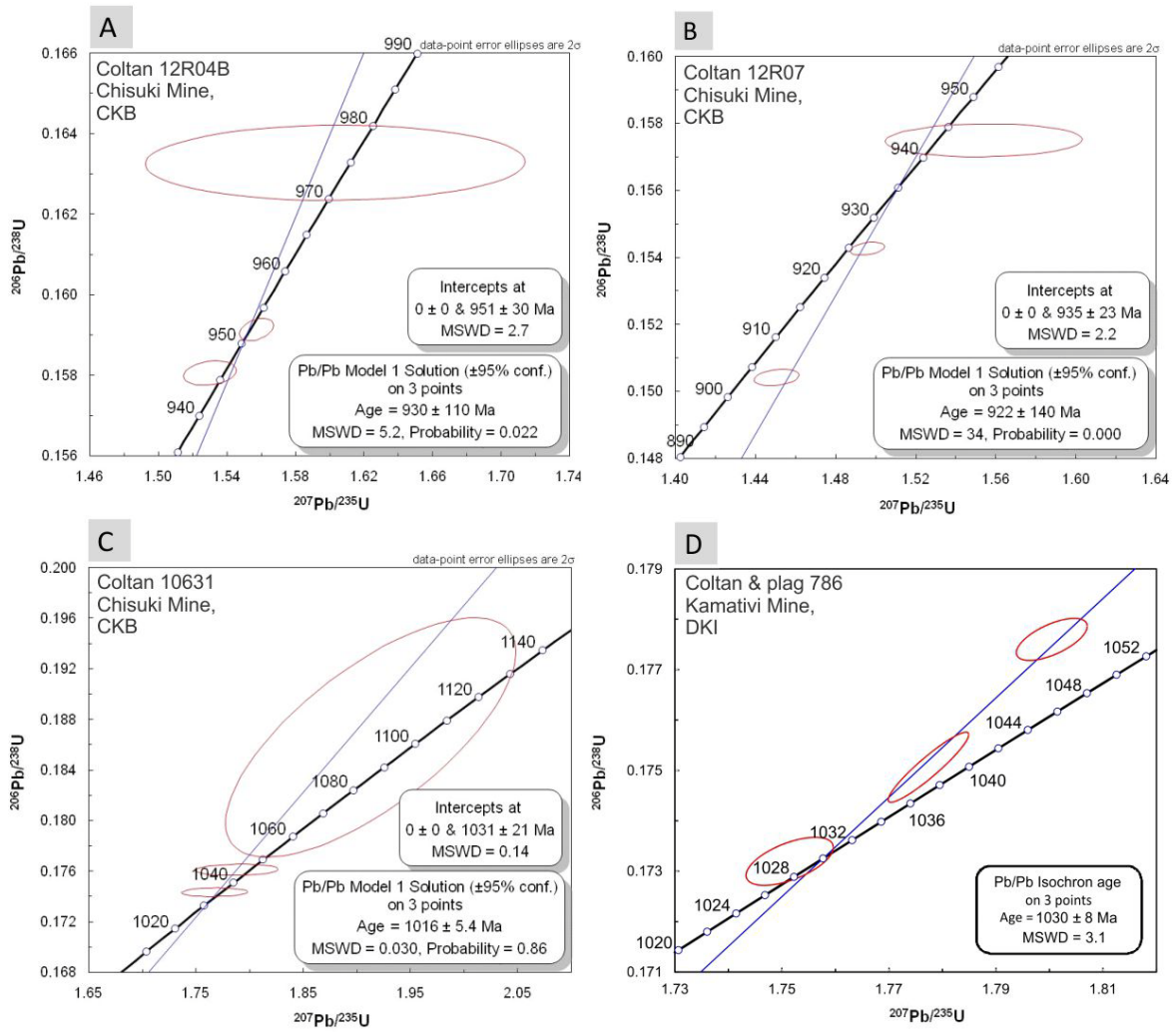

Figure 6.7: U-Pb and Pb-Pb ID-TIMS ages for the various coltan fragments from Chisuki Mine: 12R04B (Figure 6.7a), 12R07 (Figure 6.7b) and 10631 (Figure 6.7c). The Pb-Pb isochron in Figure 6.7d incorporates both coltan and plagioclase fragments from sample 786, which was collected from Kamativi Mine in the Dete-Kamativi Inlier.

^{40}Ar-^{39}Ar ages

The Ar-Ar data was obtained on bi otite and muscovite from two units within the Dete-Kamativi Inlier, the results are presented in Figure 6.8 and the sample locations are shown in Figure 5.2 (pp 77). Sample Z DK 12 (Figures 6.8a and b) is a biotite-rich orthogneiss (collected at 18°25’59”S; 26°50’50”E), ~40 km SE of the town of Hwange (Watson, 1962; Lockett, 1979a,b), while sample Z DK 13/5 (Figures 6.8c and d) is a micaceous schist from the Tshontanda Formation (Lockett, 1979a,b; Master et al., 2010), and was collected from RHA Mine at the following location: 18°30’44.3”S, 26°37’59.8”E.

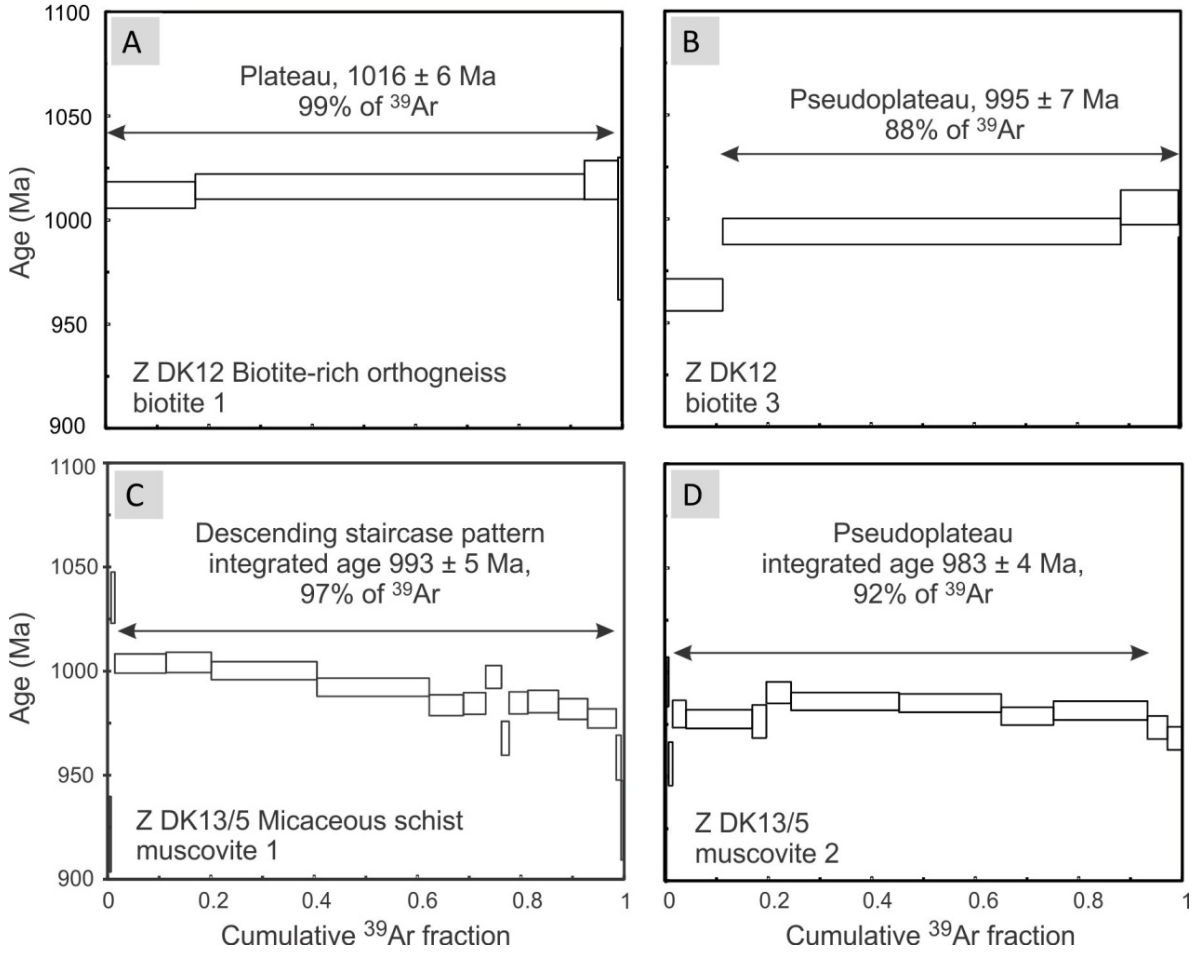

Figure 6.8: ^{40}Ar-^{39}Ar data obtained on biotite and muscovite separates from samples Z DK 12 and Z DK 13/5, from the Dete-Kamativi Inlier. A Pseudoplateau can indicate that more ^{30}Ar was released or that the errors do not overlap by more than 70%.

The Z DK 12 biotite samples were small grains, and were therefore analysed in only a few steps, whereas the muscovite from sample Z DK 13/5 was larger and allowed for multistep analyses. Disturbed age patterns like those in Figure 6.8 can either be caused by surface weathering in a tropical climate, partial resetting, or by subsequent recrystallisation. However, the plateau age on biotite from sample Z DK 12 (Figure 6.8a) which is 1016 ± 6 Ma; and the staircase pattern in Figure 6.8b, with its pseudoplateau age of 995 ± 7 Ma may both indicate surface weathering. A descending staircase pattern (like that in Figure 6.8c), with an integrated age of 993 ± 5 Ma cannot be explained by weathering, and rather indicates late partial recrystallisation (i.e. a mixture of two age populations); while the irregular pattern seen in Figure 6.8d (with an integrated age of 983 ± 4 M a), also suggests partial recrystallisation.

6.5. DISCUSSION

6.5.1 The Choma-Kalomo, Dete-Kamativi link

Based on geophysical data, outcrop and drill core samples, the seemingly continuous structural trends on either side of the younger, cross-cutting Zambezi Belt (Snelling et al., 1964; Shackleton, 1973; Hanson et al., 1988a; Singletary et al., 2003) would suggest that the Choma-Kalomo Block was a continuation of the Irumide Belt (refer to Figure 6.1), implying that the Zambezi Belt was the result of the closure of a narrow, Red Sea-type ocean. However, de Waele et al. (2003, 2009) and Johnson et al. (2007) have demonstrated that there is a complete mismatch in the ages of magmatic events between the Irumide Belt and the Choma-Kalomo Block. The 1.37 and 1.18 Ga ages of granitoid magmatism within the Choma-Kalomo Block are absent from the Southern Irumide Belt, where the magmatic events are between 1.1 and 0.9 Ga. Furthermore, there are granitoids between 1.6 and 1.5 Ga in the Southern Irumide Belt, which are not found in the Choma-Kalomo Block, in addition to the discovery of eclogites and kyanite-talc white schists in the Zambezi Belt which led John et al. (2003, 2004) to suggest that the Zambezi Belt and Lufilian Arc represented the closure of a much larger ocean, at least 2,000 km wide. Thus, the former continuity of the Choma-Kalomo Block with the Irumide Belt is not upheld as they have different histories, and were part of the Kalahari and Congo Cratons respectively, prior to their Neoproterozoic collision.

Unrug (1992) alternatively had proposed that the Choma-Kalomo Block, the Dete Kamativi Inlier, and the Kibara Belt in the DRC (refer to Figure 6.1), were once connected, and were displaced through 150-200 km of sinistral movement along the Mwembeshi Dislocation Zone. The idea that the Choma-Kalomo Block was part of the Kibara Belt was revived again by Bulambo et al. (2004, 2006) who suggested that only the Choma-Kalomo Block was an exotic terrane, derived by rifting from the Kibara Belt during the breakup of Rodinia, and was then caught up between the Hook Batholith and the Magondi Belt during the Pan-African Damara-Lufilian-Zambezi orogenic event. In Unrug's (1992) model the Choma-Kalomo Block and the Dete-Kamativi Inlier would both need to be considered as exotic terranes with respect to the neighbouring Zimbabwe Craton (and Magondi Belt), as well as the Lufilian Arc to the north-west. It would also imply Pan-African tectonism occurred in both the Choma-Kalomo Block and Dete-Kamativi Inlier to account for their present positions. However, geochronological investigations of the Choma-Kalomo Block by Snelling et al.

(1964), Hanson et al. (1988a), and Bulambo et al. (2004, 2006), and of the Dete-Kamativi Inlier by Priem et al. (1971) and Master et al. (2013) show almost no Pan-African metamorphism in these terranes. Furthermore, the Dete-Kamativi Inlier has since been shown to have ties with both the Magondi Belt and Archaean Zimbabwe Craton (Master et al., 2013, 2015; Glynn et al., 2012, 2015). Since the Dete-Kamativi Inlier cannot be thought of as an exotic terrane, but rather an integral part of the Zimbabwe Craton, Unrug's (1992) model is therefore contentious. The model by Bulambo et al. (2004, 2006) which regarded only the Choma-Kalomo Block as an exotic terrane therefore implies no links between the Choma-Kalomo Block and the Dete-Kamativi Inlier prior to the Pan-African. However, as pointed out already there is a strong similarity in terms of the nature and age of pegmatites in both the Choma-Kalomo Block and the Dete-Kamativi Inlier (Drysdall, 1967; Unrug, 1992), which is a strong indication that the two terranes were already juxtaposed *circa* 1 Ga, countering the model of Bulambo et al. (2004, 2006). Additionally with regards to the Kibara – Choma-Kalomo link, Kokonyangi et al. (2007) have shown that the bulk of the Kibaran detrital zircons have ages between 2.34 and 1.69 Ga, with peaks at 2.05 and 1.85 Ga, as well as a significant Mesoproterozoic population (1.49 to 1.32 Ga). The Kibaran detrital zircon population (Kokonyangi et al., 2007) lacks zircons as old as 3394 ± 13 Ma, or as young as 1256 ± 18 Ma (which are present in the schist sample Z9 from the Choma-Kalomo Block), and it has age peaks, such as at 2.05 Ga, which are lacking in the Z9 population. It is therefore unlikely that the Choma-Kalomo Block is derived from the Kibrara Belt.

Mineralisation in the Choma-Kalomo Block vs. Dete-Kamativi Inlier

There is a distinct overlap in the mineralisation episodes recorded within the Choma-Kalomo Block and the Dete-Kamativi Inlier, with the majority of ages coinciding between ~ 1050 and 950 Ma (Figure 6.9a). This regional thermal event is responsible for the intrusion of the quartz-muscovite-tourmaline and tin-(tantalum-niobium-tungsten-lithium-beryllium) pegmatites as well as the resetting of mica ages in regional granites and schists (Figure 6.9b).

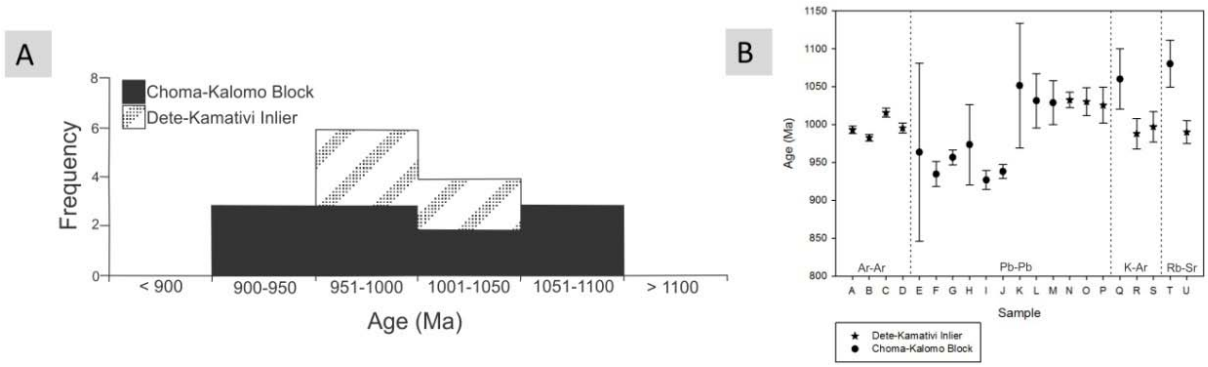

Figure 6.9: Comparison of the mineralisation ages obtained for the Choma-Kalomo Block and Dete-Kamativi Inlier. Figure 6.9a is a histogram indicating the overlap in ages, while Figure 6.9b indicates how the various techniques used compare with one another. The ^{40}Ar-^{39}Ar and Pb-Pb data are from this study, while the K-Ar and Rb-Sr data are taken from Priem et al. (1971), Snelling et al. (1972) and Cahen et al. (1984).

The late Mesoproterozoic to early Neoproterozoic ages obtained from the Chisuki coltan samples (1016 ± 5, 930 ± 100 and 922 ± 140 Ma), as well as the coltan and ^{40}Ar-^{39}Ar ages from the Dete-Kamativi Inlier (1030 ± 8, 995 ± 7 Ma, 993 ± 5 and 983 ± 4) correspond to the metamorphic event first noted by Priem et al. (1971), who recorded that muscovite from an older deformed tourmaline pegmatite in the Dete-Kamativi Inlier yielded a recalculated Rb-Sr age (using decay constants recommended by Steiger and Jäger, 1977) of 1022 ± 20 Ma, while biotite from a deformed basement granite (also in the Dete-Kamativi Inlier) yielded recalculated Rb-Sr ages of between 989 and 959 ± 30 Ma (2-point model ages assuming $^{87}Sr/^{86}Sr_i = 0.705$). The tourmaline pegmatite gave a recalculated muscovite K-Ar age of 981 Ma, while the biotite from the biotite granite gave recalculated K-Ar ages of between 981 and 972 Ma. A younger cross-cutting undeformed tin pegmatite, yielded a muscovite-albite Rb-Sr age of 1032 ± 20 Ma ($^{87}Sr/^{86}Sr_i = 0.848$), while muscovite from the same pegmatite gave a recalculated K-Ar age of 990 ± 20 Ma (Priem et al., 1971). Additionally muscovite from the Phoenix Mine in the Choma-Kalomo Block yielded late Mesoproterozoic recalculated ages of 1080 ± 31 Ma (Rb-Sr) and 1060 ± 40 Ma (K-Ar) (Snelling et al., 1964, 1972; Cahen et al., 1984). Thus both the Choma-Kalomo Block and the Dete-Kamativi Inlier contain muscovite and tin-(tantalum-niobium-tungsten-lithium-beryllium) pegmatites of late Mesoproterozoic to early Neoproterozoic age (*circa* 1060-920 Ma), together with ^{40}Ar-^{39}Ar evidence for a regional thermal event that reset muscovite and biotite from older granites and pegmatites, and accompanied the intrusion of the tin pegmatites.

6.5.2 Proposed model for the formation of the Choma-Kalomo Block

It has been established that the Choma-Kalomo Block (either by itself or together with the Dete-Kamativi Inlier) is not an exotic terrane, and instead we propose a new model for the evolution of the Choma-Kalomo Block, which presents the Choma-Kalomo Block as a terrain which developed along the western margin of the proto-Kalahari Craton, and consists of, in part, an undated crystalline basement overlain by a metasedimentary succession, which was in turn intruded by two generations of Mesoproterozoic plutons, and covered by younger sedimentary basins.

The metasedimentary succession contains previously undocumented Palaeoproterozoic zircons (*circa* 2049-1861 Ma, from samples Z CK 13/4C and Z CK 13/6,) which are potentially derived from the adjacent Magondi Belt (and Dete-Kamativi Inlier) on the western edge of the Zimbabwe Craton. These sediments were deposited *circa* 1.8 Ga, thus the Choma-Kalomo Block may have been part of the Zimbabwe Craton by this time, based on the presence of this previously undocumented Palaeoproterozoic component, which contests the earlier models of Unrug (1992) and Bulambo et al. (2004, 2006), that considered the Choma-Kalomo Block as solely Mesoproterozoic in age, and thus an exotic terrane.

In the late Mesoproterozoic era, the proto-Kalahari Craton (consisting of the amalgamated Zimbabwe and Kaapvaal Cratons), was surrounded by accreted terrains and subduction-related active margins, including in the Namaqua-Natal, Rehoboth and Ngamiland Belts (Jacobs et al., 2008; van Schijndel et al., 2011; 2014; Lehmann et al., 2015). The Mesoproterozoic magmatism in the Choma-Kalomo Block, represented by two phases of intrusives within the Choma-Kalomo Batholith at 1.37 and 1.18 Ga (Hanson et al., 1988a; Bulambo et al., 2004, 2006), may have formed during this time in a similar manner. The protolith of the schist, Z9, was deposited after 1256 Ma in a younger sedimentary basin, and records some Archaean ages in addition to a strong Palaeoproterozoic component, most likely derived from the Zimbabwe Craton and Magondi Belt.

The Choma-Kalomo Block and the Dete-Kamativi Inlier may have been juxtaposed as early as the Palaeoproterozoic but were certainly joined in the late Mesoproterozoic, as evidenced by the *circa* 1060-980 Ma quartz-muscovite-tourmaline and tin-(tantalum-niobium-tungsten-lithium-beryllium) pegmatite deposits which are common to both terrains, coinciding with a regional thermal event documented in the Dete-Kamativi Inlier. The regional thermal event characterised by the emplacement of the tin pegmatites, within the Choma-Kalomo Block and

Dete-Kamativi Inlier, is not associated with any granites, and may have been facilitated by a significant difference in lithospheric mantle thickness between the Zimbabwe Craton and Choma-Kalomo Block (Begg et al., 2009).

During the subsequent Pan-African Zambezi orogeny resulting from the collision between the Congo and the Kalahari Cratons, the northern margin of the Choma-Kalomo Block was strongly deformed, and a second generation of pegmatites (parallel to the new Pan-African fabric) were intruded, and mineral ages were reset – evidence that the Choma-Kalomo Block had a different rheological response to the adjacent Dete-Kamativi Inlier, because it behaved more like a mobile belt. The Himalayan-style collision transformed the Zambezi Belt into an allochthonous terrane by thrusting it over the northern parts of the Choma-Kalomo Block and Magondi Belt, and relicts of this event are observed in the form of the overthrust nappes of the Makuti Group and the Hurungwe Klippe (Hanson et al., 1988b, 1994; Wilson et al., 1985; Wilson and Hanson, 1987; Gibson, 1989; Munyanyiwa et al., 1997; John et al., 2003, 2004). Granitic magmatism also accompanied the collision, and resulted in the formation of the granitic Hook Batholith, located in western Zambia (Milani et al., 2015; Naydenov et al., 2014).

The Palaeozoic to Mesozoic Mid-Zambezi Rift, formed on t he boundary between the Zimbabwe Craton and the Choma-Kalomo Block, is filled with sedimentary rocks of the late Carboniferous to Early Jurassic Karoo Supergroup, and is capped by a thick succession of continental flood basalts, the Batoka Basalts, dated at 180 M a (Jones et al., 2001). An extensive NE-trending dyke swarm, of presumed Karoo age and regarded as a feeder to the Batoka Basalts, is present in the Choma-Kalomo Block (Zikmund, 1995), but is not found in the Dete-Kamativi Inlier (Tavener-Smith, 1958, 1961; Nyambe, 1999). All these lines of evidence as well as the study by Miensopust et al. (2011) who recorded that the lithosphere below the Choma-Kalomo Block is approximately 180 km thick (40 km thinner than the lithosphere below the Zimbabwe Craton), all serve to highlight the lithospheric differences between the Choma-Kalomo Block and the Zimbabwe Craton.

6.6. CONCLUSIONS

The results presented here show that the Choma-Kalomo Block is not an exotic terrane; rather it shares some similarities with the Dete-Kamativi Inlier, Magondi Belt and Zimbabwe Craton. For these reasons the models proposed by Unrug (1992) and Bulambo et al. (2004,

2006) appear to no longer be applicable. In the model outlined above, the thinner lithosphere beneath the Choma-Kalomo Block could be a primary feature or it may have resulted from subduction erosion and delamination processes associated with the formation of continental margin magmatic arcs (Yang et al., 2008). The presence of 2040 Ma xenocrystic zircons in the leuconorite Z CK 13/2 shows that the Choma-Kalomo Block contains evidence of an older basement, and is not a Mesoproterozoic juvenile terrain, while the deformed metasedimentary sequences, with their Palaeoproterozoic components, were probably derived from the Magondi Belt. Thus it is possible that the Choma-Kalomo Block may have originated as the western edge of the Dete-Kamativi Inlier (underlain by Archaean rocks of the Zimbabwe Craton), but has subsequently been reworked. Currently however, there is not enough age data to conclusively show that the Choma-Kalomo Block was originally an integral part of the Zimbabwe Craton, unless evidence of Archaean aged crust within the Choma-Kalomo Block is discovered.

Chapter 7: Summary

A detailed history of events associated with the formation of the Magondi Belt has been presented in the preceding chapters, each of which has focussed on a particular region of interest associated with the Magondi Belt. In this chapter, a summary of these events is provided and forms the basis of a new model for the formation of the Magondi Belt.

7.1 PROPOSED MODEL FOR THE FORMATION OF THE MAGONDI BELT

7.1.1 Development of the Magondi Belt from the Neoarchaean through to the Mesoproterozoic

During the late Archaean, the Zimbabwe Craton is believed to have been connected to the eastern margin of the Superior Craton (Söderlund et al., 2010). Although there is no direct evidence for when these two cratons began rifting away from one another, it is estimated that the mafic Chimbadzi Hill Intrusion, alleged to be a precursor to the Deweras lavas (2262 ± 2 Ma; Manyeruke et al., 2004) and the undated Plumtree dyke swarm, believed to be a possible feeder to the Deweras lavas (Wilson et al., 1987), suggest that rifting was initiated sometime around 2.2 Ga. In addition to this Bekker et al. (2003) and Master et al. (2010) confirm that carbonates within the Labrador Trough as well as those of the Lomagundi Group both contain high, positive carbon isotopic signatures, confirming that the carbonates in the two localities formed during the Lomagundi Carbon Isotope Excursion.

The majority of the detrital and xenocrystic zircon ages obtained from the Magondi Supergroup samples are Archaean (broadly between 3.34 and 2.63 Ga) and thus reflect the underlying granite-greenstone basement of the Zimbabwe Craton (Blenkinsop et al., 1997). Likewise for the Dete-Kamativi Inlier the two orthogneisses dated at 2.76 and 2.69 Ga respectively, are the first evidence of Archaean crustal material within the Inlier and suggest that the Zimbabwe Craton may extend further to the west than previously thought. These and some other Archaean ages obtained as part of this study are represented in Figure 7.1 to highlight the extent of the proposed new craton margin.

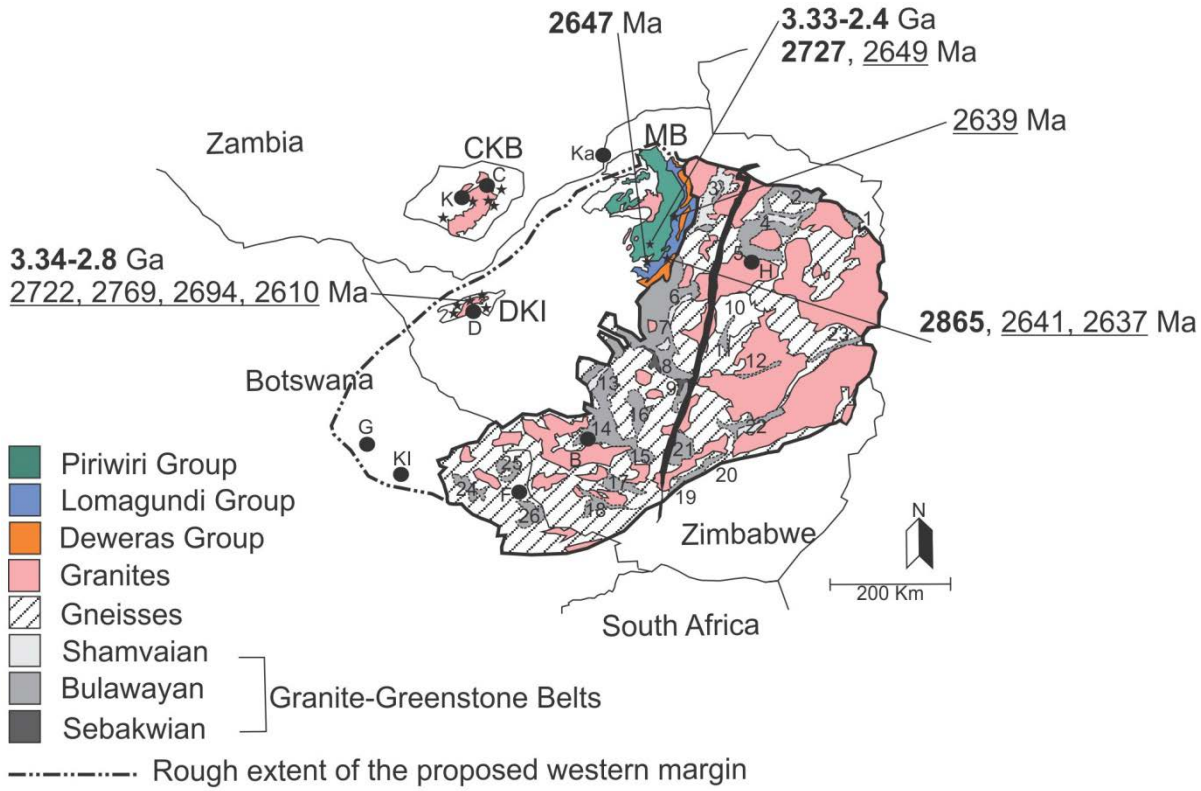

Figure 7.1: Location and extent of Archaean aged crust within the Magondi Belt (MB), Dete-Kamativi Inlier (DKI) and Zimbabwe Craton. The lettering in bold represents inherited zircon ages and those which are underlined are crystallisation ages.
1 = Makaha, 2 = Mt. Darwin-Dindi, 3 = Chinhoyi-Guruve, 4 = Harare-Shamva, 5 = Norton, 6 = Chegutu, 7 = Midlands, 8 = Gweru-Mvuma, 9 = Shurugwi, 10 = Beatrice, 11 = Mwanesi, 12 = Felixburg, 13 = Bubi, 14 = Bulawayo, 15 = Filabusi, 16 = Shangani, 17 = Gwanda, 18 = Antelope-Lower Gwanda, 19 = Mweza, 20 = Buchwa, 21 = Belingwe, 22 = Masvingo, 23 = Odzi-Mutare-Manica, 24 = Matsitama, 25 = Vumba, 26 = Tati, CKB = Choma-Kalomo Block, C = Choma, K = Kalomo, Ka = Kariba, H = Harare, D = Dett, B = Bulawayo, F = Francistown, KI = Kubu Island and G = Gweta (after, Hanson et al., 1988a; Jelsma et al., 1996, 2004; Jelsma and Dirks, 2002; Lockett, 1979a, 1981; McCourt et al., 2001; Rollinson and Whitehouse, 2011).

Figure 7.2 depicts a series of time-steps (T) which briefly outline a series of events which ultimately led to the formation of the Magondi Belt. The subsequent development of the Choma-Kalomo Block (T6) has also been described.

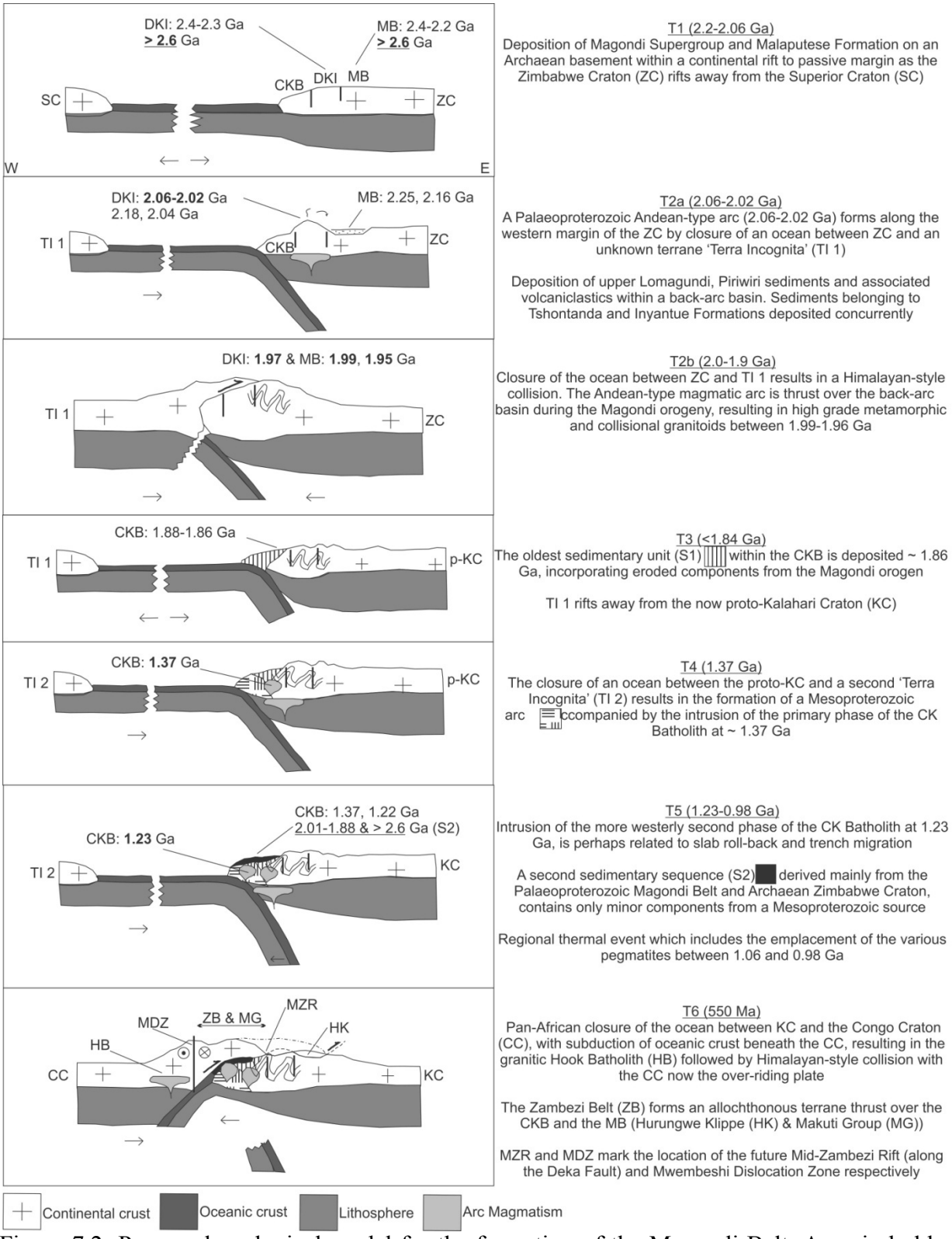

Figure 7.2: Proposed geological model for the formation of the Magondi Belt. Ages in bold lettering are emplacement ages, whereas those which are underlined represent an older component and finally the ages in plain script represent maximum ages of sedimentation. CKB = Choma-Kalomo Block, DKI = Dete-Kamativi Inlier and MB = Magondi Belt.

T1. 2.3-2.06 Ga

As is depicted in Figure 7.2, the continental rift between the Superior and Zimbabwe Cratons gradually opened into a passive margin in accordance with the model proposed by Master et al. (2010). The Deweras lavas then intruded, and are thus unconformable with the Archaean basement within the opening rift. The shallow marine sediments of the Lomagundi Group, together with the deeper water sediments of the Piriwiri Group record the gradual transition from rift to passive margin.

The pink paragneisses of the Malaputese Formation in the Dete-Kamativi Inlier have a maximum sedimentation age of 2.3 Ga, which loosely correlates with its Deweras Group counterpart (2.29 Ga). It therefore is possible that the Deweras Group was deposited within the same sedimentary basin.

T2a. 2.06-2.02 Ga

The convergence and closure of an ocean, between an unknown continental mass "Terra Incognita 1" and the Zimbabwe Craton, resulted in the formation of granitic intrusives, which constitute a Palaeoproterozoic Andean-type magmatic arc (typified by the 2.06 - 2.02 Ga granites and orthogneisses of the Dete-Kamativi Inlier) along the western margin of the Zimbabwe Craton (Master et al., 2010, 2013; Glynn et al., 2015). This Palaeoproterozoic arc extends to the south-west, into north-eastern Botswana and is represented by 2.03 - 2.02 Ga granitoids, such as those at Gweta and Kubu Island.

Deposition of the upper Lomagundi and Piriwiri Group sediments occurred within a back-arc basin setting. Moreover the andesitic agglomerates which punctuate the sediment record, at 2.25 Ga, are indicative of explosive volcanism during deposition (Master, 1994, 1996; Master et al., 2010), a feature typical of magmatic arcs. Maximum sedimentation ages for the Tshontanda and Inyantue Formations (2.14 and 2.04 Ga) are broadly similar to units within the Magondi Supergroup at 2.07 and 2.16 Ga.

T2b. 2.0-1.9 Ga

The Himalayan-style collision between the Zimbabwe Craton and Terra Incognita 1 marks the commencement of the Magondi orogeny (Master et al., 2010). During the collision, the Palaeoproterozoic magmatic arc was thrust over the Magondi Supergroup, resulting in the formation of high-grade metamorphic and collisional granitoids (Treloar and Kramers, 1989; Munyanyiwa et al., 1995; McCourt et al., 2001; Master et al., 2015). Several of these granitoids, the high-grade gneisses in the Hurungwe District in particular, were previously

considered pre-Magondian in age – imprecisely dated by Loney (1969) to be approximately 2.4 Ga. However it has since been shown that the granitoids in the northern reaches of the Magondi Belt are related to the Palaeoproterozoic Magondi orogeny, with some having a Pan-African overprint. Those in the Hurungwe District therefore can no longer be ascribed to the existence of a major Archaean orogenic cycle, "the Hurungwe orogeny", which probably predated the Magondi orogeny (Master, 1991b). Rather they are syn-to-post tectonic (2.04 - 1.95 Ga) Palaeoproterozoic granitoids emplaced during the Magondi orogeny. The Hurungwe Granite – one of the more prominent granitoids, dated to be 1997.5 ± 2.6 Ma (McCourt et al., 2001) – intrudes the Piriwiri Group sediments and thus provides a more definitive depositional age.

The formation of the proto-Kalahari Craton (formed by the episodic accretion of mobile belts around an Archaean core (Jacobs et al., 2008), i.e. around the Zimbabwe and Kaapvaal Cratons) occurred concurrently with the Magondi orogeny. While there is still much debate as to when exactly the Zimbabwe and Kaapvaal Cratons collided, the work by Söderlund et al. (2010), Bleeker (2003, 2004), Olsson et al. (2010) and Oberthür et al. (2002) all shows that there is very little the two cratons have in common until ~1.9 Ga.

T3. <1.84 Ga

Following the events of the Magondi orogeny Terra Incognita 1 is believed to have rifted away from the newly formed proto-Kalahari Craton (details regarding the mode and timing of rifting remain unconstrained).

The protoliths of the Ndonde schist, Chezya and Siamambo paragneiss, which constitute sedimentary unit "S1" within the Choma-Kalomo Block, are deposited sometime between 1.88 and 1.86 G a, and represent sedimentation of eroded material derived from the Palaeoproterozoic Magondi Belt.

7.1.2 Meso-Neoproterozoic evolution of the Choma-Kalomo Block

T4. 1.37 Ga

As a result of the closure of an ocean between a second Terra Incognita "TI 2", and the proto-Kalahari Craton, a Mesoproterozoic Andean-type magmatic arc developed along the craton margin (van Schijndel et al., 2011, 2014; Lehmann et al., 2015). This resulted in the emplacement of granitic intrusives, the first of which (dated at 1.37 G a), is considered the

older or primary phase of the composite Choma-Kalomo Batholith (Hanson et al., 1988a; Bulambo et al., 2004, 2006).

T5. 1.23- 0.98 Ga

A second sedimentary sequence "S2" was deposited around the same time as the second, younger phase of the Choma-Kalomo Batholith was intruded (1.23 Ga). The bulk of the zircons in this cover sequence are derived from the Palaeoproterozoic Magondi Belt (2.01 - 1.88 Ga) as well as the Archaean Zimbabwe Craton (2.71 - 2.62 Ga), with some from a Mesoproterozoic source.

A regional thermal event occurring between 1.06 and 0.98 Ga results in the intrusion of the various pegmatites in both the Choma-Kalomo Block and the Dete-Kamativi Inlier.

T6. 550 Ma

During the Pan-African Zambezi orogeny, closure of the ocean between the Congo and Kalahari Cratons resulted in the Himalayan-style collision where the rocks of the Congo Craton overrode those of the Kalahari Craton (Hanson et al., 1994; John et al., 2003, 2004). The Zambezi Belt, Makuti Group and the Hurungwe Klippe, therefore form allochthonous terranes thrust over the Choma-Kalomo Block, Dete-Kamativi Inlier and northern part of the Magondi Belt (Wilson et al., 1985; Wilson and Hanson, 1987; Gibson, 1989). This also resulted in the formation of the granitic Hook Batholith within the Congo Craton, as the Kalahari Craton is now the down-going slab (Milani et al., 2015; Naydenov et al., 2014). As a result of this Pan-African orogeny the rocks within the Choma-Kalomo Block were strongly deformed.

The final phase of this model for the development of the Choma-Kalomo Block invokes the possibility that the regional thermal event, as well as events related to the Pan-African Zambezi orogeny, were facilitated by a difference in lithospheric mantle thickness between the Zimbabwe Craton and Choma-Kalomo Block (Begg et al., 2009). It is possible therefore that the Choma-Kalomo Block was originally an integral part of the Zimbabwe Craton, but has subsequently been reworked due to the formation of multiple magmatic arcs along the western margin of the Zimbabwe Craton (Yang et al., 2008). However, unless evidence of Archaean aged crust within the Choma-Kalomo Block is discovered it is not possible to say if this is true or not.

7.2 LIMITATIONS AND RECOMMENDATIONS – WHERE TO FROM HERE...

When this project was first initiated the primary aim was to try and constrain depositional ages within the Magondi Supergroup, in particular the Lomagundi Group, as it is the type locality for a positive $\delta^{13}C$ excursion. However, we were unable to precisely constrain deposition of the Lomagundi Group sediments better than between 2.20 and 2.07 Ga. It was therefore not possible to precisely constrain the timing of the Lomagundi excursion as a result. A more focussed study on the Lomagundi Group would be necessary in order to solve the question of the "Lomagundi Puzzle". However, a detailed carbon isotope study has already been initiated by S. Master and will hopefully shed more light on the extent and nature of this isotope excursion. The topics discussed in Chapter 3 (regarding the Magondi Supergroup) are to be split into two manuscripts. The first of these papers will focus on the sedimentation ages and therefore form the basis for a provenance study, while the second will cover aspects relating to the tectonic setting based on the information obtained from the volcanic rocks.

Another recommendation is to conduct a detailed study of the Choma-Kalomo Block which should include some mapping to more fully characterise the region. It was clear from reading up on the regional geology that many of the previous workers were not consistent with naming and mapping out the units, and as a result it was difficult to make clear distinctions between units. With regards to the proposed model, some evidence of Archaean aged crust within the Choma-Kalomo Block would be invaluable in confirming the series of events. Additionally, geophysical methods (such as gravity and geomagnetics) applied to the Choma-Kalomo Block would also be beneficial in determining whether or not the lithospheric mantle in this region really is thinned.

A single sandstone sample from the Sijarira Group, which unconformably overlies the Magondi Belt, has resulted in a publication of its own (Master et al., (Under Review) which is included as Appendix D1), as the age obtained for a population of zircons within this sample (1035 ± 2.8 Ma) is inconsistent with any intrusives and other sedimentary units which would have been the most likely source regions. Therefore we believe it may be possible that the zircons were derived from either the southern Mozambique Belt and/or the Maud Belt of Dronning Maud Land in Antarctica where there are gneisses of that age range. The maximum

depositional age *circa* 632 Ma however, correlates with other late Neoproterozoic to Palaeozoic molasse basins covering the Kalahari Craton, while there is a general lack of Pan-African aged magmatism in the southern Mozambique Belt and Dronning Maud Land. Until the source of these zircons can be confirmed, a more detailed study of the Sijarira Group would be necessary in order to ascertain provenance.

References

Aldiss, D.T. and Carney, J.N. (1992). The geology and regional correlation of the Proterozoic Okwa Inlier, western Botswana. *Precambrian Research*, **56**, 255-274.

Andersson, P. (2015). NORDSIM User Information. [WWW]. http://www.nrm.se/english/researchandcollections/geosciences/nordsim/userinformation.91111_en.html. (April 2016).

Arlinghaus, H. (2014). Ion/Matter Interaction. *In*: *Nanobeams PhD School: Nanoanalysis using finely focussed Ion and Electron beams.* Centre de Recherche Public Gabriel Lippmann, Belvaux, Luxembourg.

ANU: Australian National University. (2014). SHRIMP sensitive high resolution ion microprobe. [WWW]. http://shrimp.anu.edu.au/shrimp_home.htm. (January 2014).

Bagai, Z., Armstrong, R.A. and Kampunzu, A.B. (2002). U-Pb single zircon geochronology of granitoids in the Vumba granite-greenstone terrain (NE Botswana): Implications for the evolution of the Archaean Zimbabwe Craton. *Precambrian Research*, **118**, 149-168.

Barton, J.M., Blaine, J.L., Doig, R. and Byron, C.L. (1994). The geological setting and style of copper mineralisation at the Bushman group of deposits, northeastern Botswana. *Journal of African Earth Sciences*, **18**(2), 87-97.

Begg, G.C., Griffin, W.L., Natapov, L.M., O'Reilly, S.Y., Grand, S.P., O'Neill, C.J., Hronsky, J.M.A., Poudjom Djomani, Y., Swain, C.J., Deen, T., Bowden, P. (2009). The lithospheric architecture of Africa: Seismic tomography, mantle petrology, and tectonic evolution. *Geosphere*, **5**(1), 23-50.

Bekker, A., Karhu, J.A., Eriksson, K.A. and Kaufmann, A.J. (2003). Chemostratigraphy of Palaeoproterozoic carbonate successions of the Wyoming Craton: tectonic forcing of biochemical change? *Precambrian Research*, **120**, 279-325.

Black, L.P., Kamo, S.L., Allen, C.M., Davis, D.W., Aleinikoff, J.N., Valley, J.W., Mundil, R., Campbell, I.H., Korch, R.J., Williams, I.S. and Foudoulis, C. (2004). Improved $^{206}Pb/^{238}U$ microprobe geochronology by monitoring of a trace-element-related matrix effect; SHRIMP, ID-TIMS, ELA-ICP-MS and oxygen isotope documentation for a series of zircon standards. *Chemical Geology*, **205**, 115-140.

Bleeker, W. (2003). The late Archaean record: a puzzle in ca. 35 pieces. *In*: Jones, A.G., Carlson, R.W. and Grutter, H. (Eds.), *A tale of two cratons: the Slave – Kaapvaal workshop*. Lithos, **71**, 99-134.

Bleeker, W. (2004). Taking the pulse of planet earth: A proposal for a new multi-disciplinary flag-ship project in Canadian soild earth sciences. *Geoscience Canada*, **31**, 179-190.

Blenkinsop, T.G., Martin, A., Jelsma, H.A. and Vinyu, M.L. (1997). The Zimbabwe Craton. *In*: de Wit, M.J. and Ashwal, L.D. (Eds.), *Greenstone Belts*. Oxford University Press, Oxford, 567-580.

Broderick, T.J. (1976). Explanation to the geological map of the country east of Kariba. Geological Survey of Rhodesia, Short Report, **43**, 98 pp.

Broderick, T.J. (1981). The Zambezi Metamorphic Belt in Zimbabwe. *In*: Hunter, D.R. (Ed.), *Precambrian of the Southern Hemisphere*. Elsevier, Amsterdam, 822 pp.

Brown, A.G. (1966). The geology of the Monze area. Explanation of Degree Sheet 1627, NW Quarter. Geological Survey of Zambia, Report, **17**, 38 pp.

Browne, E., Firestone, R.B. and Shirley, V.S. (1986). *Table of Radioactive Isotopes*, John Wiley and Sons, New York.

Bulambo, M., de Waele, B., Kampunzu, A.B. and Tembo, F. (2004). SHRIMP U-Pb geochronology of the Choma-Kalomo block (Zambia) and geological implications. Abstracts volume, 20th Colloquium of African Geology, Orléans, France.

Bulambo, M., de Waele, B., Kokonyangi, J., Johnson, S.P., Kampunzu, A.B. and Tembo, F. (2006). SHRIMP zircon U-Pb geochronology and geochemistry of the Choma-Kalomo Block granitoids (Zambia): geological implications. Abstracts volume, 21st Colloquium of African Geology, Maputo, Mozambique.

Busch, K.L. (2011). Detecting Ions in Mass Spectrometers with the Faraday Cup. *Spectroscopy*, **26**(11) found at spectroscopyonline [WWW] http://www.spectroscopyonline.com/detecting-ions-mass-spectrometers-faraday-cup. (March 2016).

Cahen, L., Snelling, N.J., Delhal, J., Vail, J.R. Bonhomme, M. and Ledent, D. (1984). *The Geochronology and Evolution of Africa*. Clarendon Press, Oxford, 512pp.

CAMECA, CAMECA instrumentation manuals

Carney, J.N. and Dowsett, J.S. (1991). Lithological information from a borehole cored through cover and basement rocks near Gweta and its bearing on the distribution of major crustal boundaries in Botswana. *The Botswana Journal of Earth Sciences*, **1**, 1-13.

Cheney, E.S. (1996). Sequence stratigraphy and plate tectonic significance of the Transvaal succession of southern Africa and its equivalent in Western Australia. *Precambrian Research*, **79**, 3-24.

Claoué-Long, J.C., Compston, W., Roberts, J. and Fanning, C.M. (1995). Two Carboniferous ages: a comparison of SHRIMP zircon dating with conventional zircon ages and $^{40}Ar/^{39}Ar$ analysis. *In*: Berggen, W.A., Kent, D.V., Aubry, M.P. and Hardenbol, J. (Eds.), *Geochronology, Time Scales and Global Stratigraphic Correlation*. SEPM (Society for Sedimentary Geology) Special Publication **54**, 3-21.

Clifford. T.N., Rex, D.C. and Snelling, N.J. (1967). Radiometric age data for the Urungwe and Miami granites of Rhodesia. *Earth and Planetary Science Letters*, **2**, 5-12.

Compston, W., Williams, I.S. and Meyer, C. (1984). U-Pb Geochronology of Zircons from Lunar Breccia 73217 using a Sensitive High Mass-Resolution Ion Microprobe. *In: Proceedings of the fourteenth Lunar and Planetary Science Conference, part 2*. Journal of Geophysical Research, **89**, supplementary pages B525-B534.

Condie, K.C. and Harrison, N.M. (1976). Geochemistry of the Archean Bulawayan Group, Midlands greenstone belt, Rhodesia. *Precambrian Research*, **3**, 252-271.

Coomer, P.G., Coward, M.P. and Lintern, B.C. (1977). Stratigraphy, structure and geochronology of ore leads in the Matsitama Belt of northern Botswana. *Precambrian Research*, **5**, 23-41.

Corfu, F., Hanchar, J.M., Hoskin, P.W.O. and Kinny, P. (2003). Atlas of Zircon Textures. *In*: Hanchar, J.M. and Hoskin, P.W.O. (Eds.), *Zircon*. Reviews in Mineralogy and Geochemistry, **53**, 469-500.

Coward, M.P. (1976). Archaean deformation patterns in southern Africa. *Philosophical Transactions of the Royal Society London*, **283**, 313-331.

Coward, M.P. and Fairhead, J.D. (1980). Gravity and structural evidence for the deep structure of the Limpopo Belt, southern Africa. *Tectonophysics*, **68**, 31-43.

de Chambost, E. (2011). A History of Cameca (1954–2009). *Advances in Imaging and Electron Physics*, Academic Press-Elsevier, pp.1–119.

de Waele, B., Wingate, M.T.D., Mapani, B. and Fitzsimons, I.C.W. (2003). Untying the Kibaran knot: a reassessment of Mesoproterozoic correlations in southern Africa based on SHRIMP U–Pb data from the Irumide belt. *Geology*, **31**(6), 509–512.

de Waele, B., Kampunzu, A.B., Mapani, B.S.E. and Tembo, F. (2006). The Mesoproterozoic Irumide belt of Zambia. *Journal of African Earth Sciences*, **46**, 36-70.

de Waele, B., Fitzsimons, I., Wingate, M., Tembo, F., Mapani, B. and Belousova, E. (2009). The geochronological framework of the Irumide Belt: A prolonged crustal history along the margin of the Bangweulu Craton. *American Journal of Science*, **309**, 132-187.

Dirks, P.H.G.M., Kröner, A., Jelsma, H.A., Sithole, T.A. and Vinyu, M.L. (1999). Structural relations and Pb-Pb zircon ages for the Makuti gneisses: evidence for a crustal-scale Pan-African shear zone in the Zambezi Belt, northwest Zimbabwe. *Journal of African Earth Sciences*, **28**(2), 427-442.

Drysdall, A.R. (1967). The tin belt of the Southern Province, a summary report. Geological Survey Department Zambia, Economic Report, **1**, 29pp.

Ducea, M.N. Saleeby, J.B. and Bergantz, G. (2015). The Architecture, Chemistry, and Evolution of Continental Magmatic Arcs. *The Annual Review of Earth and Planetary Sciences*. 10.1146/annurev-earth-060614-105049.

Eglington, B.M., Reddy, S.M. and Evans, D.A.D. (2009). The IGCP 509 da tabase system: design and application of a tool to capture and illustrate litho – and chrono – stratigraphic information for Paleoproterozoic tectonic domains, large igneous provinces and ore deposits; with examples from Southern Africa. *In*: Reddy, S.M., Mazumder, R., Evans, D.A.D. and Collins, A.S. (Eds.), *Palaeoproterozoic Supercontinents and Global Evolution*. Geological Society London, Special Publications, **323**, 27-47.

Faure, G. and Mensing, T.M. (2005). *Isotopes, principles and applications* (3rd edition). John Wiley and Sons, New Jersey, 928pp.

Fisher, R.V. and Schmincke, H.U. (1984). *Pyroclastic Rocks*, Springer-Verlag, Berlin, 472pp.

Frei, D. and Gerdes, A. (2009). Precise and accurate in situ U–Pb dating of zircon with high sample throughput by automated LA-SF-ICPMS. *Chemical Geology*, **261**, 261–270.

Gibson, M.T. (1989). Microstructural analysis of polydeformed schists from the southern margin of the Pan-African Zambezi Belt, Africa. Unpublished Dissertation, Ohio State University, USA, 51 pp.

Glynn, S.M., Master, S., Armstrong, R.A., Hofmann, A. and Bekker, A. (2012). New U-Pb (SHRIMP) ages for the Palaeoproterozoic Magondi Supergroup, Zimbabwe. Abstracts volume, 4th Annual Meeting of the Igneous and Metamorphic Studies Group, Johannesburg, South Africa.

Glynn, S.M., Wiedenbeck, M., Master, S. and Frei, D. (2015). New U-Pb zircon geochronology of the Choma-Kalomo Block (Zambia) and the Dete-Kamativi Inlier (Zimbabwe), with implications for the extent of the Zimbabwe Craton. Abstracts volume, European Geosciences Union Annual Meeting, Vienna, Austria.

Glynn, S.M., Master, S., Wiedenbeck, M., Davis, D.W., Kramers, J.D., Belyanin, G.A., Frei, D. and Oberthür, T. (Under Review). The Proterozoic Choma-Kalomo Block, SE Zambia: exotic terrane or a reworked segment of the Zimbabwe Craton? *Precambrian Research*.

Grewal, I. (2016). Introduction to mineral processing. [WWW]. http://met-solvelabs.com/library/articles/mineral-processing-introduction. (May 2016).

Hahn, L., Steiner, L., Bosum, W., Damaske, D., Höhndorf, A., Kreuzer, H., Ott, G., and Resch, M. (1990). Geology and mineral prospecting in the Makonde and Guruve Districts, Zimbabwe. Bundesanstalt für Geo-wissenschaften und R ohstoffe (BGR), Hannover, Technical Cooperation Project No. 8421703, File No. 106842, 295 pp.

Hanchar, J.M. and Miller, C.F. (1993). Zircon zonation patterns as revealed by cathodoluminescence and backscattered electron images: Implications for interpretation of complex crustal histories. *Chemical Geology*, **110**, 1-13.

Hanson, R.E., Wilson, T.J., Brueckner, H.K., Onstott, T.C., Wardlaw, M.S., Johns, C.C. and Hardcastle, K.C. (1988a). Reconnaissance geochronology, tectonothermal evolution, and

regional significance of the middle Proterozoic Choma-Kalomo Block, Southern Zambia. *Precambrian Research*, **42**, 39-61.

Hanson, R.E., Wilson, T.J. and Wardlaw, M.S. (1988b). Deformed batholiths in the Pan-African Zambezi belt, Zambia: Age and implications for regional Proterozoic tectonics. *Geology*, **16**, 1134-1137.

Hanson, R.E., Wilson, T.J. and Munyanyiwa, H. (1994). Geologic evolution of the Neoproterozoic Zambezi Orogenic Belt in Zambia. *Journal of African Earth Sciences*, **18**, 135–150.

Hanson, R.E. (2003). Proterozoic geochronology and tectonic evolution of southern Africa. *In*: Yoshida, M., Windley, B.F. and Dasgupta, S. (Eds.), *Proterozoic East Gondwana: Supercontinent Assembly and Breakup*. Geological Society, London, Special Publications, **206**, 427–463.

Harlov, D.E. and Dunkley, D. (2012). Experimental high-grade alteration of zircon using alkali- and Ca-bearing solutions: resetting the zircon geochronometer during metasomatism. Abstracts volume, Conference on Mechanisms of Mineral Replacement Reactions, Oviedo, Spain.

Harlov, D.E., Anczkiewicz, R., Lewerentz, A., Dunkley, D.J. and Schersten, A. (2014). Experimental high-grade alteration of zircon using alkali-bearing and Ca-bearing solutions: Nature and experiment. *In*: Baginski, B., Grafka, O., Matyszczak, W. and MacDonald, A. (Eds.), Abstracts volume, Workshop on Accessory Minerals, Warsaw, Poland.

Hays, J. (1955). Notes on a section of the mid-Zambezi rift valley. Records of the Geological Survey of Northern Rhodesia (for 1953), 6-7.

Hays, J. (1956a). The Basement system in the Choma District. Records of the Geological Survey of Northern Rhodesia (for 1954), 3-6.

Hays, J. (1956b). Some notes on the tin deposits of the Choma District. Records of the Geological Survey of Northern Rhodesia (for 1954), 12pp.

Hays, J. (1956c). Phoenix Mica Mine. Geological Survey of Northern Rhodesia, Technical Report, **41**, 2 pp.

Hays, J. (1957). Progress in fieldwork, Masuku Sheet 1727 NW and Kalomo Sheet 1726 NE. Records of the Geological Survey of Northern Rhodesia (for 1955), 5-7.

Hays, J. (1958a). The Zhima River catchment area, Kalomo (Sheet 1726, N E. Quarter). Records of the Geological Survey of Northern Rhodesia (for 1956), 19-23.

Hays, J. (1958b). Some notes on the history of the mid-Zambezi valley. Records of the Geological Survey of Northern Rhodesia (for 1956), 29-35.

Hinthorne, J.R., Andersen, C.A., Conrad, R.L. and Lovering, J.F. (1979). Single-grain $^{207}Pb/^{206}Pb$ and U/Pb age determinations with a 10 μm spatial resolution using the ion microprobe mass analyser (IMMA). *Chemical Geology*, **25**, 271-303.

Hitchon, B. (1957). Preliminary report on the Ngwezi norite complex. Geological Survey of Northern Rhodesia, Technical Report, **50**.

Hitchon, B. (1958a). The geology of the Kariba area. Geological Survey of Northern Rhodesia, Report, **3,** 41pp.

Hitchon, B. (1958b). Notes on a reconnaissance of the Zimba-Kalomo area. Records of the Geological Survey of Northern Rhodesia (for 1956), 23-25.

Höhndorf, A., Broderick, T.J., Kramers, J.D., Besang, C. and Carl, C. (1989). Age determination of the Proterozoic Deweras lavas, Zimbabwe: another case of too old Sm–Nd ages. Bundesanstalt für Geowissenschaften und Rohstoffe (BGR), Hannover, Unpublished Report.

Höhndorf, A. and Vetter, U. (1999). The Sanyati ore deposits in Zimbabwe: Pb-isotopic investigation of sulfide and oxide ores. *Zeitschrift für Angewandte Geologie,* **45**, 11–13.

Horstwood, M.S.A., Nesbitt, R.W., Noble, S.R., Wilson, J.F. (1999). U-Pb zircon evidence for an extensive early Archaean craton in Zimbabwe: A reassessment of the timing of craton formation, stabilization, and growth. *Geology,* **27**, 707-710.

Hoskin, P.W.O. (2005). Trace-element composition of hydrothermal zircon and the alteration of Hadean zircon from the Jack Hills, Australia. *Geochimica et Cosmochimica Acta*, **69**(3), 637-648.

ICL: Imperial College London (2013a). Agglomerate [WWW]. https://wwwf.imperial.ac.uk/earthscienceandengineering/rocklibrary/viewglossrecord.php?Term=agglomerate. (26/04/2016).

ICL: Imperial College London (2013b). Granodiorite [WWW]. https://wwwf.imperial.ac.uk/earthscienceandengineering/rocklibrary/viewglossrecord.php?Term=granodiorite. (19/05/2017).

Ireland, T.R. and Williams, I.S. (2003). Considerations in zircon geochronology by SIMS. *Reviews in Mineralogy and Geochemistry*, **53**(1), 215-241.

Irvine, T.N. and Baragar, W.R.A. (1971). A guide to the chemical classification of the common volcanic rocks. *Canadian Journal of Earth Sciences*, **8**, 523-548.

Jackson, S., Pearson, N.J., Griffin, W.L. and Belousova, E.A. (2004). The application of laser ablation – inductively coupled plasma – mass spectrometry to in situ U–Pb zircon geochronology. *Chemical Geology*, **211**, 47–69.

Jacobs, J., Pisarevsky, S., Thomas, R.J. and Becker, T. (2008). The Kalahari Craton during the assembly and dispersal of Rodinia. *Precambrian Research*, **160**, 142-158.

Jaffey, A.H., Flynn, K.F., Glendenin, L.E., Bentley, W.C. and Essling, A.M. (1971). Precision measurement of half-lives and specific activities of ^{235}U and ^{238}U. *Physical Review,* **4**, 1889-1906.

Jelsma, H.A., Vinyu, M.L., Valbracht, P.J., Davies, G.R., Wijbrans, J.R. and Verdurmen, A.T. (1996). Constraints on A rchaean crustal evolution of the Zimbabwe craton: a U-Pb zircon, Sm-Nd and Pb-Pb whole-rock isotope study. *Contributions to Mineralogy and Petrology*, **124**, 55-70.

Jelsma, H.A. and Dirks, P.H.G.M. (2002). Neoarchaean tectonic evolution of the Zimbabwe Craton, *In*: Fowler, C.M.R., Ebinger, C.J. and Hawkesworth, C.J. (Eds.), *The Early Earth: Physical, Chemical and Biological Development*. Geological Society, London, Special Publications, **199**, 183-211.

Jelsma, H., Kröner, A., Bozhko, N. and Stowe, C. (2004). Single zircon ages for two Archean banded migmatitic gneisses from central Zimbabwe. *South African Journal of Geology*, **107**, 577-586.

Jeon, H. and Whitehouse, M.J. (2015). A Critical Evaluation of U-Pb Calibration Schemes Used in SIMS Zircon Geochronology. *Geostandards and Geoanalytical Research*, **39**(4), 443-452.

John, T., Schenk, V., Haase, K., Scherer, R. and Tembo, F. (2003). Evidence for a Neoproterozoic ocean in South-central Africa from mid-oceanic ridge-type geochemical signatures and pressure–temperature estimates of Zambian eclogites. *Geology*, **31**(3), 243–246.

John, T., Schenk, V., Mezger, K. and Tembo, F. (2004). Timing and PT evolution of whiteschist metamorphism in the Lufilian arc-Zambezi belt orogen (Zambia): implications for the assembly of Gondwana. *Journal of Geology*, **112**, 71–90.

Johns, C.C. (1995). The geology of the Choma area, Explanation of Degree Sheet 1626, SE Quarter. Geological Survey of Zambia, Report, **94**, 40 pp.

Johnson, S.P. Rivers, T. and de Waele, B. (2005). A review of the Mesoproterozoic to early Palaeozoic magmatic and tectonothermal history of south-central Africa: implications for Rodinia and Gondwana. *Journal of the Geological Society London*, **162**, 433–450.

Johnson S. P., de Waele, B., Evans, D., Banda, W., Tembo, F., Milton, J.A. and Tani, K. (2007). Geochronology of the Zambezi supracrustal sequence, southern Zambia: a record of Neoproterozoic divergent processes along the southern margin of the Congo craton. *Journal of Geology*, **115**, 355-374.

Jones, D.L., Duncan, R.A., Briden, J.C., Randall, D.E. and MacNiocaill, C. (2001). Age of the Batoka basalts, northern Zimbabwe, and the duration of the Karoo Large Igneous Province magmatism. *Geochemistry, Geophysics, Geosystems* (G^3), **2**, Paper No. 2000GC000110.

Key, R.M. and Ayres, N. (2000). The 1998 edition of the National Geological Map of Botswana. *Journal of African Earth Sciences*, **30**(3), 427-451.

Kirkpatrick, I.M. (1976). The Geology of the Country around Tengwe, Lomagundi District. Geological Survey of Rhodesia, Bulletin, **75,** 176pp.

Kirkpatrick, I.M and Robertson, I.D.M. (1987). A geological reconnaissance of the Makuti-Kariba road. Annals of the Geological Survey of Zimbabwe, **XII**, 1-7.

Kokonyangi, J.W., Kampunzu, A.B., Armstrong, R., Arima, M., Yoshida, M. and Okudaira, T. (2007). U-Pb SHRIMP dating of detrital zircons from the Nzilo Group (Kibaran Belt): Implications for the source of sediments and Mesoproterozoic evolution of Central Africa. *Journal of Geology*, **115**, 99-113.

Kramers, J.D., McCourt, S. and van Reenen, D.D. (2006). The Limpopo Belt. *In*: Johnson, M.R., Anhaeusser, C.R. and Thomas, R.J. (Eds.), *The Geology of South Africa*. Geological Society of South Africa, Council for Geosciences, Pretoria, 209-236.

Kramers, J.D., McCourt, S., Roering, C., Smit, C.A. and van Reenen, D.D. (2011). Tectonic models proposed for the Limpopo complex: Mutual compatibilities and constraints. *In*: van Reenen, D.D., Kramers, J.D., McCourt, S. and Perchuk, L.L. (Eds.), *Origin and evolution of Precambrian high-grade gneiss terranes, with special emphasis on the Limpopo complex of Southern Africa*. Geological Society of America Memoir, **207**, 311-324.

Legg, C.A. (1972) The tin belt of the Southern Province. Geological Survey of Zambia, Economic Report, **29**, 58pp.

Legg, C.A. and Namateba, C. (1982). Regional Zoning of Tin-tantalum-niobium Pegmatites in the Masuku Area, Southern Province, Zambia. *In*: Evans. A.M. (Ed.), *Metallization Associated with Acid Magmatism*, John Wiley & Sons, Chichester, 181-190.

Lehmann, J., Master, S., Rankin, W., Milani, L., Kinnaird, J.A., Naydenov, K.V., Saalmann, K. and Kumar, M. (2015). Regional aeromagnetic and stratigraphic correlations of the Kalahari Copperbelt in Namibia and Botswana. *Ore Geology Reviews*, **71**, 169-190.

Le Maitre, R.W., Bateman, P., Dudek, A., Keller, J., Lameyre, J., Le Bas, M.J., Sabine, P.A., Schmid, R., Sorensen, H., Streckeisen, A., Woolley, A.R. and Zanettin, B. (1989). *A Classification of Igneous Rocks and Glossary of Terms*, Blackwell, Oxford, 193pp.

Leyshon, P.R. (1969). The Geology of the Country around the Copper Queen. Geological Survey of Rhodesia, Bulletin, **66,** 174pp.

Leyshon, P.R. (1973). Two granite-gneiss domes in the Copper Queen area, Rhodesia. *Geological Society of South Africa, Special Publication*, **3**, 97-109.

Leyshon, P.R. and Tennick, F.P. (1988). The Proterozoic Magondi mobile belt in Zimbabwe – a review. *South African Journal of Geology,* **91**, 114-131.

Li, Q.L., Li, X.H., Lan, Z.W., Guo, C.L., Yang. Y.N., Liu, Y. and Tang, G.Q. (2013). Monazite and xenotime U-Th-Pb geochronology by ion microprobe: dating highly fractionated granites at Xihuashan tungsten mine, SE China. *Contributions to Mineralogy*

and Petrology, **166**, 65-80.

Liyungu, A.K. (1998). Geology of the Nyawa Area, Explanation of Degree Sheet 1725, NE Quarter. Geological Survey of Zambia, Report, **99**, 26 pp.

Lockett, N.H. (1979a). The Metamorphism and Structural Geology of the Dett-Kamativi Area, Rhodesia. Unpublished PhD Thesis, University of Rhodesia, 194pp.

Lockett, N.H. (1979b). The geology of the country around Dett. Geological Survey of Rhodesia, Bulletin, **85**, 198 pp.

Lockett, N.H. (1981). The Dete-Kamativi Inlier. *In*: Hunter, D.R. (Ed.), *Precambrian of the Southern Hemisphere*, Elsevier, Amsterdam, 717-721.

Loney, P.E. (1969). The geology of the Kariba District, Rhodesia, with special reference to geochemistry and amphibolite petrochemistry. Unpublished PhD Thesis, Leeds University.

Loughlin, W.P. (1998). The Geology of the Idiamala Pool area, Explanation of Degree Sheet 1626, NW Quarter. Geological Survey of Zambia, Report, **87**, 14 pp.

Ludwig, K.R. (2001). *SQUID 1.03, A User's Manual*. Berkeley Geochronology Centre, Special Publication, **2**, 19 pp.

Ludwig, K.R. (2003). *Isoplot/ Ex version 3: A Geochronological toolkit for Microsoft Excel.* Berkeley Geochronology Centre, Special Publication, **4**, 71 pp.

Ludwig, K.R. (2012). *Isoplot/ Ex version 3.75: A Geochronological Toolkit for Microsoft Excel*. Berkeley Geochronology Centre, Special Publication, **5**, 75 pp.

Majaule, T. and Davis, D. (1998). U-Pb zircon dating and geochemistry of granitoids in the Mosetse area, northeast Botswana – tectonic implications. Abstracts volume, International conference on t he role of a National Geological Survey in sustainable development, Gaborone, Botswana.

Majaule, T., Hanson, R.E., Key, R.M., Singletary, S.J., Martin, M.W. and Bowring, S.A. (2001). The Magondi Belt in northeastern Botswana: regional relations and new geochronological data from the Sua Pan area. *Journal of African Earth Sciences*, **32**(2), 257-267.

Manyeruke, T.D., Blenkinsop, T.G., Buchholz, P., Love, D., Oberthür, T., Vetter, U.K. and Davis, D.W. (2004). The age and petrology of the Chimbadzi Hill Intrusion, NW Zimbabwe: first evidence for early Palaeoproterozoic magmatism in Zimbabwe. *Journal of African Earth Sciences*, **40**, 281-292.

Mapani, B.S.E. (1986). The Geology of Siasikabole Area. Unpublished Dissertation, University of Zambia, Zambia, 70 pp.

Mapeo, R.B.M., Armstrong, R.A. and Kampunzu, A.B. (2001). SHRIMP U-Pb zircon geochronology of gneisses from the Gweta borehole, northeast Botswana: implications for the Palaeoproterozoic Magondi Belt in southern Africa. *Geological Magazine*, **138**(3), 299-308.

Mapeo, R.B.M., Kampunzu, A.B., Ramokate, L.V., Corfu, F. and Key, R.M. (2004). Bushveld-age magmatism in southeastern Botswana: evidence from U-Pb zircon and titanite geochronology of the Moshaneng Complex. *South African Journal of Geology*, **107**, 219-232.

Mapeo, R.B.M., Ramokate, L.V., Corfu, F., Davis, D.W. and Kampunzu, A.B. (2006). The Okwa basement complex, western Botswana: U-Pb zircon geochronology and implications for Eburnean processes in southern Africa. *Journal of African Earth Sciences*, **46**, 253-262.

Master, S. (1991a). Stratigraphy, tectonic setting, and mineralisation of the early Proterozoic Magondi Supergroup, Zimbabwe: A review. Economic Geology Research Unit (EGRU), Information Circular, **238**, 75pp.

Master, S. (1991b). The origin and controls on the distribution of copper and precious-metal mineralization at the Mangula and Norah mines, Mhangura, Zimbabwe. Unpublished PhD Thesis, University of the Witwatersrand, Johannesburg, 385 pp.

Master, S. (1994). Geodynamic evolution and correlation of the Magondi Belt (Zimbabwe): Implications for the Palaeoproterozoic history of Botswana. *The Botswana Journal of Earth Sciences*, **2**, 25-32.

Master, S. (1996). The Palaeoproterozoic Magondi Mobile Belt, NW Zimbabwe. *In:* Master, S. (Ed.), *Excursion Guidebook, Palaeo-proterozoic of Zambia and Zimbabwe. IGCP Project 363: Lower Proterozoic of Sub-Equatorial Africa, First Field Conference, Zambia and Zimbabwe, 14-30 September, 1996*. Economic Geology Research Unit (EGRU), Information Circular, **302**, 27-65.

Master, S., Bekker, A. and Hofmann, A. (2010). A review of the stratigraphy and geological setting of the Palaeoproterozoic Magondi Supergroup, Zimbabwe: type locality for the "Lomagundi" global carbon isotope excursion. *In:* Karhu, J.A., Sial, A.N. and Ferreira, V.P. (Eds.), *Precambrian Isotope Stratigraphy*. Precambrian Research, **182**(4), 254-273.

Master, S., Glynn, S.M., Frei, D., Davis, D. and Oberthür, T. (2013). New U-Pb and Pb-Pb geochronology of rocks and minerals from the Proterozoic Dete-Kamativi Inlier (Zimbabwe) and Choma-Kalomo Block (Zambia): regional implications. Abstracts volume, Geological Society of Zimbabwe Annual Summer Symposium, Victoria Falls, Zimbabwe.

Master, S., Glynn, S.M. and Wiedenbeck, M. (2015). The vanished orogeny: Geochronology of Palaeoproterozoic "basement" gneisses of the Kariba and adjacent areas, western Magondi Belt (Zimbabwe and Zambia). Abstracts volume, Geological Society of Zimbabwe Annual Summer Symposium, Kariba, Zimbabwe.

Master, S., Glynn, S.M. and Wiedenbeck, M. (Under Review). U-Pb ages and provenance of zircons from the Neoproterozoic Sijarira Group, Western Zimbabwe – an Antarctica connection?

Matheson, G.D. (1969). The Pre-Katangan basement geology of the Masuku-Kabanga Area, southern Province, Zambia. Unpublished PhD Thesis, Leeds University, 110pp.

Matheson, G.D. (1974). The geology of the Masuku-Kabanga area, Explanation of Degree Sheets 1726, SE Quarter, and 1727, NW and SW Quarters. Geological Survey of Zambia, Report, **37**, 96 pp.

Matthews, W. and Davis, W.J. (1999). A practical image analysis technique for estimating the weight of abraded mineral fractions used in U-Pb dating. *In:* van Breemen, O. (Ed.), *Radiogenic Age and Isotopic Studies: Report 12*. Geological Survey of Canada, Current Research, 1-7.

Mattinson, J.M. (2010). Analysis of the relative decay constants of ^{235}U and ^{238}U by multi-step CA-TIMS measurements of closed-system natural zircon samples. *Chemical Geology*, **275**, 186–198.

McCourt, S., Hilliard, P., Armstrong, R.A. and Munyanyiwa, H. (2001). SHRIMP U-Pb zircon geochronology of the Hurungwe granite northwestern Zimbabwe: Age constraints on the timing of the Magondi orogeny and implications for the correlation between the Kheis and Magondi Belts. *South African Journal of Geology*, **104**, 39-46.

McCourt, S., Kampunzu, A.B., Bagai, Z. and Armstrong, R.A. (2004). The crustal architecture of Archaean terranes in Northeastern Botswana. *South African Journal of Geology*, **107**, 146-158.

Mekonnen, S.Z. (2008). Geological and Mineral Potential Mapping by Geoscience Data Integration. Unpublished MSc Thesis. International Institute for Geo-Information Science and Earth Observation, Enschede, The Netherlands, 112pp.

Miensopust, M.P., Jones, A.G., Muller, M.R., Garcia, X., Evans, R.L. (2011). Lithospheric structures and Precambrian terrane boundaries in northeastern Botswana revealed through magnetotelluric profiling as part of the Southern African Magnetotelluric Experiment. *Journal of Geophysical Research,* **116**, B02401.

Milani, L., Lehmann, J., Naydenov, K.V., Saalmann, K., Kinnaird, J.A., Daly, J.S., Frei, D. and Lobo-Guerrero Sanz, A. (2015). A-type magmatism in a syn-collisional setting: The case of the Pan-African Hook Batholith in Central Zambia. *Lithos*, **216-217**, 48-72.

Moen, H.F.G. and Armstrong, R.A. (2008). New age constraints on the tectogenesis of the Kheis Subprovince and the evolution of the eastern Namaqua Province. *South African Journal of Geology*, **111**, 79-88.

Munyanyiwa, H., Touret, J.L.R. and Jelsma, H.A. (1993). Thermobarometry and fluid evolution of enderbites within the Magondi Mobile Belt, northern Zimbabwe. *Lithos*, **29**, 163-176.

Munyanyiwa, H., Kröner, A. and Jaeckel, P. (1995). U–Pb and Pb–Pb single zircon ages for charno-enderbites from the Magondi mobile belt, northwest Zimbabwe. *South African Journal of Geology*, **98**, 52–57.

Munyanyiwa, H., Hanson, R.E., Blenkinsop, T.G. and Treloar, P.J. (1997). Geochemistry of amphibolites and quartzofeldspathic gneisses in the Pan-African Zambezi belt, NW Zimbabwe: evidence for bimodal magmatism in a continental rift setting. *Precambrian Research*, **81**, 179–196.

Munyanyiwa, H. and Maaskant, P. (1998). Metamorphism of the Palaeoproterozoic Magondi mobile belt north of Karoi, Zimbabwe. *Journal of African Earth Sciences*, **27**(2), 223-240.

Munyanyiwa, H., Manyanhaire, M., Mapani, B., Dube, J. and Nyarufuro, B. (1999). Geochemistry of felsic volcanics in the Magondi basin (northwestern Zimbabwe): evidence for regional carbonate and boron alteration. *In*: Frimmel, H.E. (Ed.), 11th International Conference of the Geological Society of Africa, Earth Resources For Africa. *Journal of African Earth Sciences*, **28**(4), 56 pp.

Nasdala, L., Zhang, M., Kempe, U., Panczer, G., Gaft, M., Andrut, M. and Plötze, M. (2003). Spectroscopic methods applied to zircon. *In*: Hanchar, J.M. and Hoskin, P.W.O. (Eds.), *Zircon*. Reviews in mineralogy and geochemistry, 53, 429-434pp.

Nasdala, L., Hofmeister, W., Norberg, N., Mattinson, J.M., Corfu, F., Dörr, W., Kamo, S.L., Kennedy, A.K., Kronz, A., Reiners, P.W., Frei, D., Košler, J., Wan, Y., Götze, J., Häger, T., Kröner, A. and Valley, J.W. (2008). Zircon M257 – a homogeneous natural reference material for the ion microprobe U-Pb analysis of zircon. *Geostandards and Geoanalytical Research*, **32**, 247–265.

Nash, R.A. (1960). The geology and mineralogy of some North Rhodesian pegmatites. Unpublished PhD Thesis, University of London, UK.

NPL: National Physical Laboratory. (2015). Tables of Physical and Chemical Constants. [WWW]. http://www.kayelaby.npl.co.uk/atomic_and_nuclear_physics/4_3/4_3.html. (March 2016).

Naydenov, K.V., Lehmann, J., Saalmann, K., Milani, L., Kinnaird, J.A., Charlesworth, G., Frei, D. and Rankin, W. (2014). New constraints on the Pan-African Orogeny in Central Zambia: A structural and geochronological study of the Hook Batholith and the Mwembeshi Zone. *Tectonophysics*, **637**, 80-105.

Newman, D. and Drysdall, A.R. (1964). Tin mineralisation of Chimwami Mine, Choma District. Geological Survey of Zambia, Economic Report, **2**.

Newton, A.R. (1960a). The Geology of the Country between Magoye and Gwembe, Explanation of Degree Sheet 1627, NE. Quarter. Geological Survey of Northern Rhodesia Report, **7**.

Newton, A.R. (1960b). A preliminary account of the geology of the Muzoka area, Sheet 1627 SE. and SW. Quarters. Records of the Geological Survey of Northern Rhodesia (for 1959), 12-13.

Newton, A.R. (1960c). The geology of the Siamambo Forest Plantation, Sheet 1627, S W. Quarter. Records of the Geological Survey of Northern Rhodesia (for 1959), 14-16.

Newton, A.R. (1960d). On some amphibolites from the Southern Province. Records of the Geological Survey of Northern Rhodesia (for 1958), 46-48.

Newton, A.R. (1961). An unusual gabbroic intrusion from Northern Rhodesia. *Geological Magazine*, **98**, 417-422.

Newton, A.R. (1963a). An outline of the geology of the Chinkozia norite. Records of the Geological Survey of Northern Rhodesia, **9**, 24-27.

Newton, A.R. (1963b). The geology of the country between Choma and Gwembe, Explanation of Degree Sheet 1627, S W. and SE. Quarters. Geological Survey of Northern Rhodesia, Report, **8**, 33pp.

Nyambe, I.A. (1999). Tectonic and climatic controls on sedimentation during deposition of the Sinakumbe Group and Karoo Supergroup, in the mid-Zambezi Valley Basin, southern Zambia. *Journal of African Earth Sciences*, **28**(2), 443-463.

Oberthür, T., Davis, D.W., Blenkinsop, T.G. and Höhndorf, A. (2002). Precise U-Pb mineral ages, Rb-Sr and Sm-Nd systematic for the Great Dyke, Zimbabwe – constraints on l ate Archean events in the Zimbabwe craton and Limpopo belt. *Precambrian Research*, **113**(3-4), 293-305.

Olsson, J.R., Söderlund, U., Klausen, M.B. and Ernst, R.E. (2010). U-Pb Baddeleyite ages linking major Archean dyke swarms to volcanic-rift forming events in the Kaapvaal craton (South Africa), and a precise age for the Bushveld Complex. *In*: Srivastava, R.K., Ernst, R.E., Bleeker, W. and Hamilton, M.A. (Eds.), *Precambrian Large Igneous Provinces (LIPs) and their dyke swarms: New insights from high-precision geochronology integrated with paleomagnetism and geochemistry*. Precambrian Research, **183**(3), 490-500.

Paces, J.B. and Miller, J.D. (1993). Precise U-Pb age of Duluth Complex and related mafic

intrusions, north-eastern Minnesota: Geochronological insights to physical, petrogenetic, paleomagnetic, and tectonomagnetic processes associated with the 1.1 Ga mid-continent rift system. *Journal of Geophysical Research*, **98**, 13997-14013.

Pagal, M., Barbin, V., Blanc, P. and Ohnenstetter, D. (2000). Cathodoluminescence in Geosciences: An Introduction. *In*: Pagal, M., Barbin, V., Blanc, P. and Ohnenstetter, D. (Eds.), *Cathodoluminescence in Geosciences*, Springer Verlag, Berlin, 1, 4, 12-14pp.

Priem, H.N.A., Boelrijk, N.A.I.M., Hebeda, E.H., Verdurmen, E.A Th. and Verschure, R.H. (1971). Isotopic dating in the Kamativi tin belt, southern Rhodesia. *Geologie en Mijnbouw*, **50**, 619-624.

Prost, A.E. (1982). A preliminary report on the geology of the country north of Centenary. Annals of the Geological Survey of Zimbabwe, **VII**, 20-27.

Ranganai, R.T., Kampunzu, A.B., Atekwana, E.A., Paya, B.K., King, J.G., Koosimile, D.I. and Stettler, E.H. (2002). Gravity evidence for a larger Limpopo belt in southern Africa and geodynamic implications. *Geophysics Journal International*, **149**, 9-14.

Renne P. R., Swisher C. C., Deino A. L., Karner D. B., Owens T. and DePaolo D. J. (1998). Intercalibration of standards, absolute ages and uncertainties in $^{40}Ar/^{39}Ar$ dating. *Chemical Geology (Isotope Geoscience Section)*, **145**, 117–152.

Renne, P.R., Mundil, R., Balco, G., Min, K. and Ludwig, K.R. (2010). Joint determination of ^{40}K decay constants and $^{40}Ar^*/^{40}K$ for the Fish Canyon sanidine standard, and improved accuracy for $^{40}Ar/^{39}Ar$ geochronology. *Geochimica et Cosmochimica Acta*, **74**, 5349–5367.

Roberts, A.E. (1965). An Investigation into some Copper-bearing beds in North-Eastern Bechuanaland. Unpublished PhD Thesis, University of Natal, South Africa.

Rollinson, H.R. and Whitehouse, M. (2011). The growth of the Zimbabwe Craton during the late Archaean: an ion microprobe U-Pb zircon study. *Journal of the Geological Society, London*, **168**, 941-952.

Romer, R.L. and Wright, J. E. (1992). U-Pb dating of columbites: a geochronologic tool to date magmatism and ore deposits. *Geochimica et Cosmochimica Acta,* **56**, 2137-2142.

Romer, R.L. and Smeds, S-A. (1994). Implications of U-Pb ages of columbite-tantalites from granitic pegmatites for the Paleoproterozoic accretion of 1.90-1.85 Ga magmatic arcs to the Baltic Shield. *Precambrian Research,* **67**, 141-158.

Rubatto, D. and Gebauer, D. (2000). Use of cathodoluminescence for U-Pb zircon dating by Ion Microprobe: some examples from the western Alps. *In*: Pagal, M., Barbin, V., Blanc, P. and Ohnenstetter, D. (Eds), *Cathodoluminescence in Geosciences*. Springer Verlag, Berlin, 373-400pp.

Schidlowski, M., Eichmann, R. and Junge, C.E. (1976). Carbon isotope geochemistry of the Precambrian Lomagundi carbonate province, Rhodesia. *Geochimica et Cosmochimica Acta,* **40**, 449-455.

Schidlowski, M. and Todt, W. (1998). The Proterozoic Lomagundi carbonate province as a paragon of a ^{13}C-enriched carbonate facies: Geology, radiometric age and geochemical significance. *Chinese Science Bulletin*, **43,** 114.

Schoene, B. (2014). U-Th-Pb Geochronology. *In*: Holland, H. and Turekian, K. (Eds.), *Treatise on Geochemistry, second edition*. Elsevier, London, 341-378.

Schröder, S., Bekker, A., Beukes, N.J., Strauss, H. and van Niekerk, H.S. (2008). Rise in seawater sulphate concentration associated with the Palaeoproterozoic positive carbon isotope excursion: evidence from sulphate evaporites in the ~2.2-2.1 Gyr shallow marine Lucknow Formation, South Africa. *Terra Nova*, **20**, 108-117.

Schuhmacher, M., deChambost, E., McKeegan, K.D., Harrison, T.M. and Migeon, H.N. (1993). In situ U/Pb dating of zircon with the CAMECA ims 1270. *In*: Benninghoven, A., Nihei, Y., Shimizu, R. and Werner, H.W. (Eds.), *Secondary ion mass spectrometry SIMS IX*. John Wiley, New York, 919-922.

Scoates, J.S. and Friedman, R.M. (2008). Precise age of the platiniferous Merensky Reef, Bushveld Complex, South Africa, by the U-Pb zircon chemical abrasion ID-TIMS technique. *Economic Geology*, **103**(3), 465-471.

Shackleton, R.M., (1973). Correlation of structures across Precambrian orogenic belts in Africa. *In*: Tarling, D.H. and Runcorn, S.K. (Eds.), *Implications of Continental Drift to the Earth Sciences*. Academic press, London, 1091–1095.

Singletary, S.J., Hanson, R.E., Martin, M.W., Crowley, J.L., Bowring, S.A., Key, R.M., Ramokate, L.V., Direng, B.B. and Krol, M.A. (2003). Geochronology of basement rocks in the Kalahari Desert, Botswana, and implications for regional Proterozoic tectonics. *Precambrian Research*, **121**, 47-71.

Sithole, R.T. (1977). 1:1000 000 Geological map of Zimbabwe, Seventh edition. Zimbabwe Geological Survey, Harare.

Sláma, J., Košler, J., Condon, D.J., Crowley, J.L., Gerdes, A., Hanchar, J.M., Horstwood, M.S.A., Morris, G.A., Nasdala, L., Norberg, N., Schaltegger, U., Schoene, B., Tubrett, M.N. and Whitehouse, M.J. (2008). Plešovice zircon - a new natural reference material for U–Pb and Hf isotopic microanalysis. *Chemical Geology,* **249**, 1–35.

Snelling, N.J., Hamilton, E.I., Drysdall, A.R. and Stillman, C.J. (1964). A review of age determinations from Northern Rhodesia. *Economic Geology*, **59**, 961-981.

Snelling, N.J., Johnson, R.L. and Drysdall, A.R. (1972). The geochronology of Zambia. Records of the Geological Survey of Zambia, **12**, 19-30.

Söderlund, U., Hofmann, A., Klausen, M.B., Olsson, J.R, Ernst, R.E. and Persson, P.O. (2010). Towards a complete magmatic barcode for the Zimbabwe craton: Baddeleyite U-Pb dating of regional dolerite dyke swarms and sill complexes. *In*: Srivastava, R.K., Ernst, R.E., Bleeker, W. and Hamilton, M.A. (Eds.), *Precambrian Large Igneous Provinces (LIPs) and their dyke swarms: New insights from high-precision geochronology integrated with*

paleomagnetism and geochemistry. Precambrian Research, **183**(3), 388-398.

Stacey, J.S. and Kramers, J.D. (1975). Approximation of terrestrial lead isotope evolution by a two-stage model. *Earth and Planetary Science Letters*, **26**, 207-221.

Stagman, J.G. (1978). An Outline of the geology of Rhodesia. Rhodesia Geological Survey Bulletin, **80**, 126pp.

Steiger, R.H. and Jäger, E. (1977). Subcommission on geochronology: convention on the use of decay constants in geo- and cosmochronology. *Earth and Planetary Science Letters*, **36**, 359-362.

Stern, R.A. and Berman, R.G. (2000). Monazite U-Pb and Th-Pb geochronology by ion microprobe, with an application to in situ dating of an Archean metasedimentary rock. *Chemical Geology*, **172**, 113-130.

Stern, R.A. (2009). An introduction to Secondary Ion Mass Spectrometry (SIMS) in geology. *In*: Fayek, M. (Ed.). *Secondary Ion Mass Spectrometry in the Earth Sciences: Gleaning the big picture from a small spot*. Mineralogical Association of Canada Short Course Series, **41**, 1-19.

Stowe, C.W., Hartnady, C.J.H. and Joubert, P. (1984). Proterozoic tectonic provinces of Southern Africa. *Precambrian Research*, **25**, 229-231.

Tavener-Smith, R. (1958). The development of the Mid-Zambezi Valley in Northern Rhodesia since early Karroo times. *Geological Magazine*, **95**(2), 105-118.

Tavener-Smith, R. (1961). The geology of the Mapanza Mission area: explanation of Degree Sheet 1626, N.E. Quarter. Geological Survey of Northern Rhodesia, Report, **10**, 41pp.

Taylor, S. R. and McLennan, S. M. (1981). The composition and evolution of the continental crust: rare earth element evidence from sedimentary rocks. *Phillospohical Transactions of the Royal Society*, **A301**, 381-399.

Tennick, F.P. and Phaup, A.E. (1976). The Geology of the Country around Magondi, Lomagundi, Hartley and Gatooma Districts, Rhodesia Geological Survey, Bulletin, **65**.

Tera, F. and Wasserburg, G.J. (1972). U/Th/Pb systematic in three Apollo 14 basalts and the problems of initial Pb in lunar rocks. *Earth and Planetary Science Letters*, **14**, 281-304.

Thole, R.H. (1976). The geology of the Shamrocke Mine, Rhodesia: a stratiform copper deposit. *Economic Geology*, **71**, 202-208.

Thomas, R. (2004). *Practical guide to ICP-MS*. Marcel Dekker, New York, 1-7, 47, 61-71, 118, 162, 179-187pp.

Treloar, P.J. (1988). The geological evolution of the Magondi mobile belt, Zimbabwe. *Precambrian Research*, **38**, 55-73.

Treloar, P.J. and Kramers, J.D. (1989). Metamorphism and geochronology of granulites and migmatitic granulites from the Magondi Mobile Belt, Zimbabwe. *Precambrian Research*, **45**, 277-289.

Unrug, R. (1992). Kibaran terranes with cassiterite mineralization in the Zambezi belt, Zambia and Zimbabwe. *In*: *IGCP Project No. 255, Metallogeny of the Kibara Belt, Central Africa*. Bulletin-Newsletter, **4**, 121-124.

Vail, J.R., Snelling, N.J. and Rex, D.C. (1968). Pre-Katangan geochronology of Zambia and adjacent parts of Central Africa. *Canadian Journal of Earth Science*, **5**, 621–628.

Van der Heide, P. (2014). *Secondary Ion Mass Spectrometry, an Introduction to Principles and Practices*. Wiley and Sons, New Jersey, 365pp.

Van Schijndel, V., Cornell, D.H., Hoffmann, K.H. and Frei, D. (2011). Three episodes of crustal development in the Rehoboth Province, Namibia. *In*: Van Hinsbergen, D.J.J., Butter, S.J.H., Torsvik, T.H., Gaina, C. and Webb, S.J. (Eds.). *The Formation and Evolution of*

Africa: A Synopsis of 3.8 Ga of Earth History. Geological Society, London, Special Publications, **357**, 27-47.

Van Schijndel, V., Cornell, D.H., Frei, D., Simonsen, SL. and Whitehouse, M.J. (2014). Crustal evolution of the Rehoboth Province from Archaean to Mesoproterozoic times: Insights from the Rehoboth Basement Inlier. *Precambrian Research*, **240**, 22-36.

Vermeesch, P. (2004). How many grains are needed for a provenance study? *Earth and Planetary Science Letters*, **224**, 441-451.

Watkeys, M.K. (1984). The Precambrian geology of the Limpopo Belt north and west of Messina. Unpublished PhD Thesis, University of the Witwatersrand, Johannesburg, 349 pp.

Watson, R.L.A. (1962). The Geology of the Kamativi and Lubimbi areas. Geological Survey of Southern Rhodesia, Bulletin, **57**, 42pp.

Wetherill, G.W. (1956). Discordant uranium-lead ages. *Transactions of the American Geophysical Union*, **37**, 320-326.

Whitehouse, M.J., Claesson, S., Sunde, T. and Vestin, J. (1997). U-Pb geochronology of the Lewisian Complex at Gruinard Bay, *Geochimica et Cosmochimica Acta*, **61**(20), 4429-4438.

Whitehouse, M.J., Kamber, B.S. and Moorbath, S. (1999). Age significance of U-Th-Pb zircon data from early Archaean rocks of west Greenland – a reassessment based on combined ion-microprobe and imaging studies. *Chemical Geology*, **160**(3), 201-224.

Wiedenbeck, M., Allé, P., Corfu, F., Griffin, W.L., Meier, M., Oberli, F., Von Quadt, A., Roddick, J.C and Spiegel, W. (1995a). Three Natural Zircon Standards for U-Th-Pb, Lu-Hf, Trace Element and REE Analysis. *Geostandards Newsletter*, **19**, 1-23.

Wiedenbeck, M. (1995b). An example of reverse discordance during ion microprobe zircon dating: An artifact of enhanced ion yields from a radiogenic labile Pb. *Chemical Geology*, **125**, 197-218.

Wiedenbeck, M. (2012). *An Introduction to Secondary Ion Mass Spectrometry in the Earth and Material Sciences*. Short course handout, 79pp.

Wikimedia Commons. (2015). Zambia map image search. [WWW]. https://commons.wikimedia.org/wiki/File:Location_Zambia_AU_Africa.svg. (February 2016).

Wikipedia. (2016). Zimbabwe map image search. [WWW]. https://en.wikipedia.org/wiki/Zimbabwe. (February 2016).

Wiles, J.W. (1968). Some aspects of the metamorphism of the Basement Complex in the Sipolilo District. *Transactions of the Geological Society of South Africa (Annexure)*, **71**, 79-88.

Williams, I.S. (1998). U-Th-Pb geochronology by ion microprobe, *In*: McKibben, M.A., Shanks III, W.C., Ridley, W.I. (Eds.), *Reviews of microanalytical techniques to understanding mineralising processes*. Reviews in Economic Geology, **7**, 1- 35.

Wilson, J.F., Bickle, M.J., Hawkesworth, R.J., Martin, A., Nisbet, E.G. and Orpen, J.L. (1978). The granite-greenstone terrains of the Rhodesian Archaean craton. *Nature*, **271**, 23-27.

Wilson, J.F., Jones, D.L. and Kramers, J.D. (1987). Mafic dike swarms in Zimbabwe. *In*: Halls, H.C. and Fahrig, W.F. (Eds.), *Mafic Dike Swarms*. Geological Association of Canada, Special Paper, **34**, 433-444.

Wilson, J.F., Nesbitt, R.W. and Fanning, C.M. (1995). Zircon geochronology of Archaean felsic sequences in the Zimbabwe craton: a review of greenstone stratigraphy and a model for crustal growth. *In*: Coward, M.P. and Ries, A.C. (Eds.), *Early Precambrian Processes*. Geological Society of London Special Publications, **95**, 109-126.

Wilson, T.J., Hanson, R.E and Brueckner, H.K. (1985). Transposition, ductile shearing, and noncylindrical folding of remobilized gneisses along the junction between two Proterozoic mobile belts in southern Zambia. *Abstracts Programmes Geological Society America*, **17**, 752.

Wilson, T.J. and Hanson, R.E. (1987). Structural evolution of the southern margin of the Pan-African Zambezi mobile belt in Zambia. *Abstracts Programmes Geological Society America*, **19**, 252.

Wirtz, T. (2014). Instrumentation: geometrical and charged particle optics. *In*: *Nanobeams PhD School: Nanoanalysis using finely focussed Ion and Electron beams*. Centre de Recherche Public Gabriel Lippmann, Belvaux, Luxembourg.

WolframAlpha. (2011a). Bromoform. [WWW]. http://www.wolframalpha.com/entities/chemicals/bromoform/sz/ym/kb/. (July 2012).

WolframAlpha. (2011b). Diiodomethane. [WWW]. http://www.wolframalpha.com/input/?i=diiodomethane. (July 2012).

Worst, B.G. (1960). The Great Dyke of Southern Rhodesia. Geological Survey of Southern Rhodesia, Bulletin, **47**.

Yang, J-H., Wu, F-Y., Wilde, S.A., Belousova, E. and Griffin, W.L. (2008). Mesozoic decratonization of the North China block. *Geology*, **36**(6), 467-470.

Yaseen, N., Pease, V., Jarrar, G.H. and Whitehouse, M. (2013). U-Pb detrital zircon provenance of the Saramuj Conglomerate, Jordan, and implications for the Neoproterozoic evolution of the Red Sea region. *In*: Jarrar, G.H., Kadi, K., Pease, V., and Shalaby, M.H. (Eds.), *JEBEL*. Precambrian Research, **239**, 6-23.

Zikmund, J. (1995). Geology of the Zimba-Makwela area, Explanation of Degree Sheet 1726, NW and NE Quarters. Geological Survey of Zambia, Report, **73**, 36 pp.

Appendix A: Data Tables

A.1 FULL CAF LA-ICPMS U-Th-Pb ZIRCON DATING METHODOLOGY

Table 2.4: Full CAF LA-ICPMS U-Th-Pb zircon dating methodology

Laboratory & Sample Preparation	
Laboratory name	Central Analytical Facility, Stellenbosch University
Sample type / mineral	Igneous and detrital zircons
Sample preparation	Conventional mineral separation, 1 inch resin mount, 1 µm polish to finish
Laser ablation system	
Make, Model & type	ESI/New Wave Research, UP213, Nd:YAG
Ablation cell & volume	Custom build low volume cell, dead-volume ca.3 cm^3
Laser wavelength	213 nm
Pulse width	3 ns
Fluence	2.5 J/cm^{-2} (as determined by build-in energy meter)
Repetition rate	10 Hz
Spot size	30 µm
Sampling mode / pattern	30 µm single spot analyses
Carrier gas	100% He, Ar make-up gas combined using a T-connector close to sample cell
Pre-ablation laser warm-up (background collection)	40 seconds
Ablation duration	20 seconds
Wash-out delay	30 seconds
Cell carrier gas flow	0.3 l/min He
ICP-MS Instrument	
Make, Model & type	Thermo Finnigan Element2 single collector HR-SF-ICP-MS
Sample introduction	Via tygon tubing
RF power	1100 W
Make-up gas flow	1000 ml/min Ar
Detection system	Single collector secondary electron multiplier
Masses measured	202, 204, 206, 207, 208, 232, 233, 235, 238
Integration time per peak	4 ms
Total integration time per reading	0.1 sec *(represents the time resolution of the data)*
Sensitvity	20000 cps/ppm Pb
Dead time	6 ns
Data Processing	
Gas blank	40 second on-peak
Calibration strategy	Plešovice used as primary reference material, GJ-1 & M127 used as secondary reference material (Quality Control)
Reference Material info	Plešovice (Sláma et al. 2008) GJ-1 (Jackson et al. 2004) M127 (Nasdala et al. 2008; Mattinson, 2010)
Data processing package used / Correction for LIEF	In-house spreadsheet data processing using intercept method for LIEF correction
Mass discrimination	Standard-sample bracketing with $^{207}Pb/^{206}Pb$ and $^{206}Pb/^{238}U$ normalized to reference material GJ-1
Common-Pb correction, composition and uncertainty	^{204}Pb-method, Stacey & Kramers (1975) composition at the projected age of the mineral, 5% uncertainty assigned
Uncertainty level & propagation	Ages are quoted at 2 sigma absolute, propagation is by quadratic addition. Reproducibility and age uncertainty of reference material and common-Pb composition uncertainty are propagated.
Quality control / Validation	Plešovice: Wtd ave $^{206}Pb/^{238}U$ age = 338 ± 4 (2SD, MSWD = 0.52) GJ-1: Wtd ave $^{207}Pb/^{206}Pb$ age = 608.5 ± 0.4 (95% conf., MSWD = 0.59) M127: Wtd ave $^{206}Pb/^{238}U$ age = 528 ± 5 (2SD, MSWD = 0.91)
Other information	For detailed method description see Frei & Gerdes (2009)

A.2 MAGONDI BELT

Table 3.1: Major and selected trace element analyses for samples from the Magondi Belt

Sample name	DV 11/ 1	DV 11/ 2	NC 1	GD - Z11/ 2A	GD - Z11/ 3	Z11/ C - SKR 2B	SKG - Z11/ 1
Major Elements							
SiO2	54.94	69.6	56.41	81.85	60.34	65.14	74.69
Al2O3	16.33	11.76	12.65	10.85	12.35	14.69	12.41
Fe2O3	1.3	0.57	0.48	0.01	0.26	0.85	0.52
FeO	10.5	4.61	3.93	0.1	2.11	6.92	4.19
MnO	0.16	0.11	0.11	0.01	0.07	0.25	0.09
MgO	3.15	2.25	10.23	0.01	17.35	5.18	1.97
CaO	8.29	7.51	8.42	0.14	0.2	3.92	1.73
Na2O	2.63	1.42	6.42	6.33	6.47	0.71	2.45
K2O	0.38	1.14	0.05	0.02	0.04	1.99	1.95
TiO2	1.89	0.65	0.61	0.55	0.57	0.68	0.58
P2O5	0.21	0.11	0.08	0.09	0.12	0.08	0.11
Cr2O3	0.023	0.027	0.021	0.017	0.025	0.025	0.019
NiO	0.009	0.009	0.001	-0.001	0.004	0.009	0.008
LOI	2.69	3.82	15.99	0.1	14.73	7.76	3.3
TOTAL	99.8	99.77	99.41	99.98	99.9	100.46	100.73
Trace Elements							
Ti	10145.38	3100.03	2476.47	2910.51	2748.03	3286.87	3118.79
V	305.02	114.09	105.63	51.09	110.08	101.89	73.09

Table 3.2: SHRIMP U-Pb zircon data for samples from the Magondi Belt

Spot	% $^{206}Pb_c$	µg/g U	µg/g Th	µg/g $^{*206}Pb$	$^{232}Th/^{238}U$ Meas	$^{207}Pb/^{206}Pb$ age (1)	± 1sd	$^{206}Pb/^{238}U$ age (1)	± 1sd	% Disc (2sd)	$^{*207}Pb/^{*206}Pb$	± 1sd	$^{*207}Pb/^{235}Pb$	± 1sd	$^{*206}Pb/^{238}Pb$	± 1sd	Error Correlation
DV 11/1: Mafic lava (17°52'16.5" S; 29°51'15.3" E)																	
1.1	1.97	466	464	158	1.03	2635	±17	2105	±25	20	0.178	1	9.48	1.7	0.3862	1.4	.795
2.1	0.28	748	248	153	0.34	2340.8	± 8.2	1377	±17	41	0.14955	0.48	4.91	1.4	0.2381	1.3	.941
3.1	0.16	293	253	120	0.89	2614.3	± 7.6	2498	±29	4	0.17587	0.46	11.48	1.5	0.4734	1.4	.952
4.1	0.02	356	269	156	0.78	2643.5	± 6	2662	±31	-1	0.17898	0.36	12.62	1.5	0.5112	1.4	.969
5.1	0.02	430	245	177	0.59	2646.6	± 5.7	2523	±29	5	0.17932	0.34	11.84	1.4	0.4789	1.4	.971
6.1	0.18	236	156	103	0.68	2622.8	± 9	2645	±31	-1	0.17677	0.54	12.36	1.5	0.5072	1.4	.936
7.1	0.08	303	135	126	0.46	2630.7	± 7.2	2537	±29	4	0.17761	0.44	11.81	1.4	0.4822	1.4	.954
8.1	0.75	229	74	90.6	0.34	2639	±13	2430	±29	8	0.1785	0.76	11.27	1.6	0.4577	1.4	.884
8.2	0.03	206	195	81.4	0.98	2719	± 8.4	2443	±90	10	0.18734	0.51	11.9	4.4	0.461	4.4	.993
9.1	0.10	924	21	266	0.02	2445	± 8.6	1858	±21	24	0.159	0.51	7.32	1.4	0.3341	1.3	.934
9.2	0.05	56	21	24.7	0.38	2674	±15	2674	±38	0	0.1823	0.92	12.92	2	0.514	1.7	.885
10.1	0.01	257	140	101	0.56	2650.6	± 7.3	2434	±29	8	0.17975	0.44	11.37	1.5	0.4588	1.4	.955
11.1	0.12	208	124	92.3	0.61	2643.2	± 8.6	2681	±31	-1	0.17895	0.52	12.72	1.5	0.5157	1.4	.940
12.1	0.04	344	191	146	0.57	2634.7	± 6.1	2584	±29	2	0.17804	0.37	12.1	1.4	0.493	1.4	.966
13.1	0.24	271	113	109	0.43	2619.7	± 8.9	2471	±29	6	0.17645	0.54	11.37	1.5	0.4672	1.4	.936
14.1	6.33	481	207	113	0.45	1869	±95	1474	±21	21	0.1143	5.3	4.05	5.5	0.2569	1.6	.287
15.1	0.11	185	119	73	0.67	2628.1	± 9.8	2438	±29	7	0.1773	0.59	11.24	1.6	0.4596	1.4	.926
16.1	--	348	248	132	0.74	2649	± 7.1	2359	±27	11	0.17958	0.43	10.94	1.4	0.4419	1.4	.956
17.1	0.24	254	130	102	0.53	2579.7	± 9.7	2464	±29	4	0.1723	0.58	11.06	1.5	0.4656	1.4	.924
18.1	0.08	145	56	56.1	0.40	2717	±12	2401	±30	12	0.1871	0.71	11.64	1.7	0.4512	1.5	.903
19.1	1.44	426	249	95.8	0.60	2124	±69	1480	±27	30	0.1319	3.9	4.69	4.4	0.258	2.1	.467
20.1	0.72	86	35	27.7	0.42	2235	±42	2046	±32	8	0.1406	2.4	7.24	3	0.3736	1.8	.610
21.1	0.51	131	38	58.9	0.30	2813	±23	2707	±44	4	0.1984	1.4	14.28	2.4	0.522	2	.812
23.1	0.22	177	72	74.8	0.42	2626	±12	2574	±34	2	0.1772	0.7	11.99	1.8	0.4908	1.6	.919
DV 11/2: Epiclastic volcanic sandstone (17°52'17.0" S; 29°51'13.6" E)																	
1.1	0.05	160	85	78.5	0.55	2872.9	± 8.1	2916	±34	-2	0.2058	0.5	16.24	1.6	0.5721	1.5	.947
3.1	0.04	458	263	212	0.59	2800.5	± 4.8	2776	±30	1	0.19688	0.29	14.61	1.4	0.5383	1.3	.977
4.1	0.02	176	115	77.7	0.68	2637.2	± 8.1	2675	±31	-1	0.17831	0.49	12.64	1.5	0.5142	1.4	.947
5.1	--	228	157	98.8	0.71	2643.4	± 7.4	2633	±30	0	0.17897	0.45	12.45	1.5	0.5045	1.4	.953
6.1	0.04	139	103	62.3	0.76	2644	± 9.1	2698	±32	-2	0.17904	0.55	12.83	1.6	0.5196	1.5	.936
7.1	0.02	147	80	64	0.56	2646	±14	2636	±32	0	0.1792	0.82	12.49	1.7	0.5052	1.5	.873
8.1	0.14	115	56	47.4	0.51	2637	±12	2525	±32	4	0.1783	0.69	11.78	1.7	0.4794	1.5	.911
8.2	0.01	577	46	237	0.08	2564.7	± 5.2	2516	±28	2	0.17072	0.31	11.24	1.4	0.4775	1.3	.974
9.1	0.03	114	44	55.4	0.40	2856.3	± 8.9	2887	±37	-1	0.2037	0.54	15.87	1.7	0.5651	1.6	.945
10.1	--	143	60	66.5	0.43	2855.4	± 8.6	2796	±35	2	0.2036	0.53	15.24	1.6	0.543	1.5	.946
11.1	--	214	87	103	0.42	2858.2	± 6.8	2874	±33	-1	0.20396	0.41	15.8	1.5	0.5618	1.4	.960
12.1	0.12	97	43	42.2	0.46	2647	±12	2641	±34	0	0.1793	0.72	12.52	1.7	0.5063	1.6	.908
13.1	--	156	75	73.9	0.50	2889	±19	2835	±34	2	0.2079	1.1	15.84	1.9	0.5525	1.5	.793
14.1	0.11	74	24	34.1	0.34	2866	±12	2771	±36	3	0.205	0.72	15.18	1.7	0.5371	1.6	.911
15.1	0.05	178	82	86.4	0.48	2878.1	± 7	2892	±33	0	0.20648	0.43	16.12	1.5	0.5663	1.4	.957
16.1	0.00	63	29	29.6	0.47	2856	±12	2802	±38	2	0.2037	0.76	15.29	1.8	0.5445	1.7	.910
17.1	0.05	168	108	67.2	0.66	2636.5	± 8.8	2463	±30	7	0.17823	0.53	11.43	1.5	0.4652	1.4	.938
18.1	0.02	148	69	68.2	0.48	2856.5	± 8.3	2769	±39	3	0.2038	0.51	15.07	1.8	0.5365	1.7	.960
19.1	--	219	104	97.1	0.49	2864	± 6.9	2682	±32	6	0.2047	0.42	14.56	1.5	0.516	1.4	.960
20.1	0.02	109	93	43.9	0.89	2688	±11	2487	±31	7	0.1839	0.64	11.94	1.7	0.4708	1.5	.922
21.1	0.05	211	120	92.1	0.59	2846.6	± 7.1	2652	±32	7	0.20251	0.44	14.21	1.5	0.5089	1.5	.958
22.1	0.41	132	68	51.2	0.53	2669	±14	2394	±31	10	0.1817	0.85	11.27	1.8	0.4498	1.5	.877

23.1	0.01	204	70	99.4	0.35	2864.6	± 6.8	2902	±33	-1	0.20478	0.42	16.05	1.5	0.5685	1.4	.959
24.1	0.04	188	88	91	0.49	2869.4	± 7.1	2881	±34	0	0.20538	0.44	15.96	1.5	0.5635	1.5	.958
25.1	0.06	151	67	71.8	0.46	2859.9	± 8.3	2832	±35	1	0.2042	0.51	15.53	1.6	0.5516	1.5	.948
26.1	0.00	149	63	74.4	0.44	2863.5	± 7.8	2952	±36	-3	0.20463	0.48	16.39	1.6	0.5809	1.5	.953
27.1	0.00	187	134	68.6	0.74	2646.2	± 9.4	2292	±35	13	0.1793	0.57	10.55	1.9	0.4269	1.8	.955
28.1	0.02	175	85	80.4	0.51	2865.1	± 9.3	2766	±33	3	0.2048	0.57	15.13	1.6	0.5359	1.5	.933
29.1	0.10	120	53	49.1	0.45	2626	±11	2504	±31	5	0.1771	0.65	11.59	1.6	0.4746	1.5	.918
30.1	0.05	67	29	27.5	0.44	2658	±15	2516	±37	5	0.1805	0.88	11.89	2	0.4775	1.8	.895
31.1	0.08	253	180	99.9	0.74	2619.7	± 7.7	2440	±28	7	0.17645	0.46	11.2	1.5	0.4602	1.4	.948
32.1	0.02	158	72	67	0.47	2859	±15	2593	±31	9	0.204	0.93	13.93	1.7	0.4951	1.5	.843
33.1	0.05	119	41	53.6	0.35	2859.1	± 9.8	2725	±34	5	0.2041	0.6	14.8	1.6	0.5261	1.5	.929
34.1	0.03	244	180	97.5	0.76	2633.9	± 8.2	2459	±30	7	0.17796	0.5	11.39	1.5	0.4643	1.4	.946
35.1	--	134	84	55.1	0.65	2661.1	± 9.2	2517	±32	5	0.1809	0.56	11.91	1.6	0.4776	1.5	.940
36.1	0.25	145	125	63.9	0.89	2843	±10	2656	±32	7	0.202	0.62	14.2	1.6	0.5099	1.5	.920
37.1	--	62	23	23.8	0.38	2859	±15	2383	±35	17	0.204	0.92	12.58	2	0.4473	1.7	.883
38.1	0.13	212	110	73.8	0.54	2858.2	± 9.3	2194	±27	23	0.204	0.57	11.4	1.5	0.4054	1.4	.928
39.1	0.05	122	71	54.3	0.60	2864.8	± 9.6	2689	±34	6	0.2048	0.59	14.62	1.7	0.5177	1.6	.936
40.1	0.00	137	102	49.1	0.77	2171	±11	2245	±28	-3	0.13553	0.66	7.79	1.6	0.4167	1.5	.911
41.1	0.03	69	32	34	0.47	2881	±11	2914	±38	-1	0.2068	0.7	16.29	1.8	0.5714	1.6	.920
42.1	0.01	147	49	73.1	0.35	2867.4	± 7.6	2936	±34	-2	0.20512	0.47	16.31	1.5	0.5768	1.4	.951
43.1	0.03	180	133	78.1	0.76	2637.9	± 7.9	2636	±31	0	0.17838	0.48	12.42	1.5	0.5051	1.4	.948
44.1	0.06	135	89	65.1	0.68	2851.7	± 8.3	2862	±33	0	0.2032	0.51	15.66	1.5	0.5589	1.4	.943
45.1	0.03	221	138	92	0.65	2642.6	± 7.6	2552	±30	3	0.17889	0.46	11.98	1.5	0.4856	1.4	.951
46.1	0.06	171	75	83.4	0.45	2856	± 7.6	2898	±33	-1	0.20369	0.47	15.94	1.5	0.5675	1.4	.950
47.1	0.04	167	119	73	0.74	2658.2	± 8.5	2648	±31	0	0.18058	0.51	12.65	1.5	0.508	1.4	.942
48.1	0.08	158	140	68.6	0.92	2632	±12	2631	±31	0	0.1778	0.71	12.36	1.6	0.5041	1.4	.898
49.1	0.28	146	166	62.3	1.17	2850	±11	2597	±31	9	0.2029	0.65	13.88	1.6	0.4961	1.4	.913
50.1	0.04	380	180	159	0.49	2848.3	± 6.1	2551	±29	10	0.20273	0.38	13.57	1.4	0.4854	1.4	.965
51.1	--	147	93	63.4	0.65	2652.3	± 8.8	2622	±31	1	0.17994	0.53	12.45	1.5	0.5019	1.4	.939
52.1	0.04	124	59	59.4	0.49	2870	±12	2861	±35	0	0.2055	0.75	15.83	1.7	0.5586	1.5	.895
53.1	0.00	186	139	76.3	0.77	2635.9	± 9.6	2514	±31	5	0.1782	0.58	11.72	1.6	0.477	1.5	.930
54.1	0.19	256	127	109	0.51	2846.8	± 7	2594	±29	9	0.20254	0.43	13.84	1.4	0.4954	1.4	.954
55.1	0.55	291	113	98.7	0.40	2676	±10	2137	±25	20	0.1825	0.61	9.89	1.5	0.3931	1.4	.916
56.1	0.02	190	108	90.4	0.59	2866.7	± 6.4	2837	±33	1	0.20503	0.39	15.63	1.5	0.5528	1.4	.964
57.1	0.02	247	120	115	0.50	2873.9	± 6.3	2788	±31	3	0.20595	0.39	15.36	1.4	0.541	1.4	.964
58.1	0.02	243	149	104	0.63	2646.7	± 6.9	2597	±30	2	0.17934	0.42	12.27	1.4	0.4961	1.4	.958
59.1	0.25	192	91	91.8	0.49	2858.2	± 8	2848	±33	0	0.204	0.49	15.62	1.5	0.5554	1.4	.945
60.1	0.11	499	169	204	0.35	2810.2	± 5.1	2508	±29	11	0.19805	0.32	12.99	1.4	0.4757	1.4	.975
61.1	0.10	178	68	76.6	0.40	2852.7	± 8.5	2616	±32	8	0.2033	0.52	14.03	1.6	0.5004	1.5	.944
62.1	0.10	161	95	63.9	0.61	2645.5	± 9.1	2451	±29	7	0.1792	0.55	11.43	1.5	0.4627	1.4	.935
63.1	0.03	415	288	176	0.72	2638.8	± 5.6	2580	±29	2	0.17848	0.34	12.11	1.4	0.4921	1.4	.970
64.1	0.01	446	238	197	0.55	2643.4	± 5.1	2669	±29	-1	0.17898	0.31	12.66	1.4	0.513	1.3	.975
65.1	0.25	234	77	104	0.34	2829.5	± 7.5	2680	±31	5	0.2004	0.46	14.25	1.5	0.5156	1.4	.951
66.1	0.01	267	147	126	0.57	2861.9	± 5.8	2825	±33	1	0.20443	0.36	15.5	1.5	0.55	1.4	.970
67.1	0.10	53	38	21	0.73	2439	±23	2428	±35	0	0.1584	1.4	9.99	2.2	0.4574	1.7	.778
68.1	0.03	239	139	104	0.60	2862.7	± 7.3	2630	±31	8	0.20453	0.45	14.21	1.5	0.5038	1.4	.954
69.1	0.06	201	167	82.8	0.86	2626.2	± 8.8	2524	±30	4	0.17713	0.53	11.71	1.5	0.4793	1.4	.937
70.1	0.04	244	144	115	0.61	2639	± 6.7	2815	±32	-7	0.17851	0.4	13.48	1.4	0.5476	1.4	.960
GD Z 11/2A: Epiclastic volcanic siltstone (17° 38' 30.9" S; 29° 30' 42.4" E)																	
1.1	1.24	890	315	96.6	0.37	2412	±25	757.8	± 9.7	69	0.1559	1.5	2.682	2	0.1247	1.4	.679

2.1	0.06	386	60	180	0.16	2787	± 6	2788	±31	0	0.19526	0.37	14.57	1.4	0.5412	1.4	.966
3.1	0.23	149	81	40.4	0.56	2153	±16	1771	±23	18	0.1342	0.93	5.85	1.7	0.3161	1.5	.845
4.1	0.46	229	126	72	0.57	2663	±14	2000	±25	25	0.1811	0.83	9.08	1.7	0.3637	1.5	.871
5.1	0.02	140	60	57.8	0.44	2558	±10	2527	±31	1	0.17	0.62	11.25	1.6	0.48	1.5	.924
6.1	0.07	240	107	64.9	0.46	2169	±13	1763	±22	19	0.1354	0.73	5.873	1.6	0.3146	1.4	.892
7.1	0.07	439	182	136	0.43	2127.3	± 7.6	1983	±23	7	0.13219	0.44	6.564	1.4	0.3602	1.3	.951
8.1	0.04	217	183	67.7	0.87	2103	±10	1998	±25	5	0.1304	0.57	6.53	1.6	0.3632	1.4	.929
9.1	0.67	352	196	79.1	0.57	2098	±20	1487	±19	29	0.13	1.1	4.649	1.8	0.2594	1.4	.775
10.1	0.04	146	65	68.8	0.46	2864.5	± 7.9	2818	±33	2	0.20476	0.48	15.48	1.5	0.5482	1.5	.949
11.1	0.39	396	242	88	0.63	2223	±12	1477	±18	34	0.13965	0.69	4.959	1.5	0.2575	1.4	.893
12.1	0.26	121	78	28.2	0.67	2030	±22	1546	±22	24	0.1251	1.2	4.673	2	0.271	1.6	.783
13.1	0.16	170	72	51.8	0.44	2162	±13	1958	±25	9	0.1348	0.77	6.6	1.6	0.355	1.5	.883
14.1	0.22	397	143	131	0.37	2152.1	± 8.6	2086	±25	3	0.13408	0.49	7.06	1.5	0.382	1.4	.942
15.1	0.12	60	44	23.1	0.76	2377	±16	2390	±36	-1	0.1528	0.96	9.46	2	0.4489	1.8	.884
16.1	0.25	560	295	154	0.54	2625.4	± 6.6	1786	±21	32	0.17704	0.4	7.79	1.4	0.3191	1.4	.961
17.1	--	209	81	71	0.40	2170	±11	2150	±26	1	0.13544	0.61	7.39	1.6	0.3958	1.4	.919
18.1	0.25	295	202	52.6	0.71	2496	±11	1215	±16	51	0.1639	0.68	4.686	1.6	0.2073	1.4	.901
19.1	0.31	360	383	123	1.10	2452.9	± 9.1	2146	±25	13	0.15974	0.54	8.7	1.5	0.395	1.4	.932
20.1	0.21	255	143	73.1	0.58	2246	±13	1851	±22	18	0.1415	0.73	6.49	1.6	0.3325	1.4	.884
21.1	0.22	218	24	83.1	0.12	2924	± 7.9	2364	±28	19	0.2124	0.49	12.97	1.5	0.4429	1.4	.945
22.1	0.03	173	113	87	0.67	2970.8	± 8.7	2970	±34	0	0.2187	0.54	17.64	1.5	0.5851	1.4	.936
23.1	0.14	199	165	69.3	0.86	2218	±11	2196	±27	1	0.13925	0.66	7.79	1.6	0.4058	1.4	.909
24.1	0.02	118	143	45	1.25	2390	±12	2360	±31	1	0.1539	0.7	9.38	1.7	0.4422	1.6	.913
25.1	0.10	113	48	39.2	0.44	2177	±13	2183	±28	0	0.136	0.74	7.56	1.7	0.4031	1.5	.897
26.1	0.52	1072	477	173	0.46	2681	± 6.9	1107	±14	59	0.18309	0.42	4.729	1.4	0.1873	1.3	.955
27.1	0.01	185	121	62	0.68	2184	±11	2127	±26	3	0.13654	0.63	7.36	1.6	0.3909	1.4	.916
28.1	0.05	153	222	60.1	1.49	2456.9	± 9.8	2423	±29	1	0.16012	0.58	10.07	1.5	0.4562	1.4	.928
29.1	0.12	546	130	134	0.25	2092.2	± 8	1622	±19	22	0.12957	0.45	5.113	1.4	0.2862	1.4	.948
30.1	0.21	316	151	85.9	0.49	2126	±11	1767	±22	17	0.13213	0.62	5.743	1.5	0.3153	1.4	.915
31.1	0.05	322	65	103	0.21	2193.1	± 9	2037	±24	7	0.13727	0.52	7.04	1.5	0.3717	1.4	.935
32.1	0.02	195	80	87.6	0.42	2709.5	± 7.4	2713	±31	0	0.18627	0.45	13.44	1.5	0.5232	1.4	.953
33.1	2.30	585	432	40.9	0.76	1776	±49	493.3	± 7	72	0.1086	2.7	1.191	3.1	0.0795	1.5	.480
34.1	0.13	341	91	105	0.28	2051.2	± 9.3	1972	±23	4	0.12659	0.53	6.246	1.5	0.3578	1.4	.933
35.1	0.18	105	55	29.6	0.54	2227	±16	1820	±24	18	0.14	0.92	6.3	1.8	0.3263	1.5	.854
36.1	0.14	102	64	34.4	0.65	2464	±14	2125	±29	14	0.1608	0.8	8.66	1.8	0.3904	1.6	.892
37.1	0.02	121	93	70.2	0.79	3339.4	± 6.7	3324	±38	0	0.2758	0.43	25.66	1.5	0.6748	1.5	.960
38.1	0.05	141	68	44.5	0.50	2121	±13	2023	±27	5	0.13174	0.72	6.69	1.7	0.3685	1.5	.904
39.1	0.59	157	105	38.9	0.69	2434	±18	1621	±26	33	0.1579	1	6.23	2.1	0.2859	1.8	.865
40.1	0.06	119	70	40.4	0.61	2171	±13	2146	±28	1	0.1355	0.76	7.38	1.7	0.395	1.5	.897
41.1	0.11	153	112	50.7	0.76	2326	±11	2106	±26	9	0.14828	0.66	7.9	1.6	0.3863	1.4	.910
42.1	0.02	262	106	89	0.42	2246.7	± 8.2	2146	±26	4	0.14159	0.48	7.71	1.5	0.3951	1.4	.947
43.1	2.01	289	206	20.6	0.74	2191	±37	503.2	± 7.5	77	0.1371	2.2	1.535	2.6	0.0812	1.5	.584
44.1	0.06	412	182	118	0.46	2276.8	± 7	1859	±22	18	0.14408	0.4	6.639	1.4	0.3342	1.4	.959
45.1	0.32	283	139	80.3	0.51	2079	±14	1836	±23	12	0.12858	0.77	5.841	1.6	0.3295	1.4	.879
46.1	0.00	80	73	27.6	0.94	2145	±15	2181	±29	-2	0.1336	0.84	7.41	1.8	0.4026	1.5	.880
47.1	0.00	260	117	88.9	0.46	2147.9	± 8.7	2159	±25	-1	0.13376	0.5	7.34	1.5	0.3978	1.4	.941
48.1	0.05	85	72	31.2	0.87	2234	±15	2286	±30	-2	0.1406	0.84	8.25	1.8	0.4256	1.5	.878
49.1	0.61	246	133	43.7	0.56	2013	±21	1208	±15	40	0.1239	1.2	3.521	1.8	0.2061	1.4	.761
50.1	0.25	347	119	105	0.36	2155.6	± 9.5	1945	±23	10	0.13435	0.55	6.524	1.5	0.3522	1.4	.930
51.1	0.01	434	58	155	0.14	2128.6	± 6.5	2233	±27	-5	0.13229	0.37	7.55	1.5	0.4141	1.4	.967

52.1	0.00	116	75	39.5	0.67	2105	±13	2157	±27	-2	0.13053	0.72	7.15	1.6	0.3974	1.5	.899
53.1	0.00	253	100	89.4	0.41	2140	± 8.6	2218	±26	-4	0.13315	0.49	7.54	1.5	0.4107	1.4	.942
54.1	0.00	184	142	85.5	0.80	2702.6	± 7	2782	±32	-3	0.1855	0.42	13.8	1.5	0.5396	1.4	.958
55.1	0.02	113	145	40.7	1.33	2227	±12	2259	±28	-1	0.13999	0.7	8.1	1.6	0.4197	1.5	.904
56.1	0.07	81	28	32.6	0.35	2492	±13	2486	±32	0	0.1635	0.76	10.61	1.7	0.4705	1.6	.899
NC 1: Andesitic agglomerate (17° 10' 25.0" S; 29° 57' 50.0" E)																	
1.1	0.09	567	207	206	0.38	2625.2	± 4.9	2269	±27	14	0.17702	0.3	10.3	1.4	0.422	1.4	.978
2.1	0.11	328	283	130	0.89	2632	± 6.4	2446	±28	7	0.17775	0.38	11.31	1.5	0.4615	1.4	.964
3.1	0.57	667	698	108	1.08	2586.7	± 9.6	1107	±19	57	0.17298	0.57	4.467	2	0.1873	1.9	.956
4.1	0.19	164	124	68.5	0.78	2836.3	± 8.3	2550	±30	10	0.2012	0.51	13.46	1.5	0.4851	1.4	.942
5.1	0.12	122	58	53	0.50	2622.9	± 9.8	2642	±32	-1	0.1768	0.59	12.35	1.6	0.5065	1.5	.929
6.1	0.27	185	320	71.4	1.79	2615	±10	2392	±48	9	0.1759	0.62	10.9	2.5	0.449	2.4	.969
7.1	0.26	79	37	35.6	0.48	2652	±13	2699	±35	-2	0.1799	0.79	12.9	1.8	0.5199	1.6	.894
8.1	0.21	150	85	66.8	0.59	2726	± 9.1	2681	±32	2	0.1881	0.55	13.38	1.5	0.5157	1.4	.934
9.1	0.10	205	117	81	0.59	2632.9	± 7.7	2433	±29	8	0.17785	0.46	11.24	1.5	0.4585	1.4	.950
10.1	0.14	337	264	135	0.81	2626.5	± 6.3	2466	±28	6	0.17717	0.38	11.39	1.4	0.4661	1.4	.964
11.1	0.14	102	50	44.1	0.51	2645	±11	2632	±33	0	0.1791	0.68	12.46	1.7	0.5043	1.5	.911
12.1	0.03	382	149	160	0.40	2617.1	± 7.9	2563	±31	2	0.17617	0.47	11.86	1.5	0.4883	1.5	.951
13.1	0.03	326	352	128	1.12	2627.8	± 7.1	2430	±29	8	0.1773	0.42	11.19	1.5	0.4578	1.4	.958
14.1	0.03	221	167	93.7	0.78	2707.4	± 7.6	2587	±30	4	0.18604	0.46	12.67	1.5	0.4939	1.4	.951
15.1	0.16	285	378	104	1.37	2603	±14	2281	±28	12	0.1747	0.85	10.22	1.7	0.4244	1.4	.859
16.1	0.00	247	206	100	0.86	2600	±21	2499	±44	4	0.1744	1.2	11.39	2.5	0.473	2.1	.862
17.1	0.34	86	89	26.3	1.07	2216	±21	1949	±29	12	0.1391	1.2	6.77	2.1	0.3531	1.7	.809
18.1	0.20	46	15	20.8	0.33	2738	±18	2751	±41	0	0.1895	1.1	13.91	2.1	0.5323	1.8	.858
19.1	0.10	248	336	80.4	1.40	2670.8	± 8.9	2061	±25	23	0.18196	0.54	9.45	1.5	0.3767	1.4	.937
20.1	0.24	78	83	21.8	1.11	2202	±19	1818	±28	17	0.138	1.1	6.2	2.1	0.3259	1.7	.846
21.1	0.06	175	80	77.5	0.48	2644.8	± 9	2683	±32	-1	0.17913	0.54	12.75	1.6	0.5161	1.5	.937
22.1	1.02	389	752	80.3	2.00	2615	±19	1376	±19	47	0.176	1.2	5.77	1.9	0.2379	1.5	.798
23.1	0.62	418	629	117	1.56	2563	±10	1814	±21	29	0.1705	0.62	7.64	1.5	0.3251	1.4	.909
24.1	0.07	253	224	116	0.92	2860.2	± 6.8	2767	±32	3	0.20422	0.42	15.09	1.5	0.536	1.4	.960
25.1	0.06	689	474	235	0.71	2517.6	± 5.2	2153	±25	14	0.16599	0.31	9.07	1.4	0.3964	1.4	.975
26.1	1.09	1073	1242	133	1.20	2464	±14	862	±11	65	0.1608	0.84	3.171	1.6	0.143	1.4	.850
27.1	0.57	202	181	47.5	0.93	2039	±22	1550	±21	24	0.1257	1.2	4.709	2	0.2717	1.5	.786
28.1	0.06	168	67	65.6	0.41	2633.5	± 9.5	2418	±30	8	0.1779	0.57	11.16	1.6	0.4551	1.5	.934
29.1	0.03	264	23	116	0.09	2626.8	± 7.5	2651	±31	-1	0.1772	0.45	12.43	1.5	0.5086	1.4	.953
30.1	0.00	115	50	49.1	0.45	2677	±14	2601	±33	3	0.1826	0.85	12.52	1.8	0.497	1.5	.876
31.1	0.12	154	88	60.6	0.59	2661	±11	2425	±31	9	0.1808	0.65	11.39	1.6	0.4566	1.5	.919
32.1	0.27	1357	474	283	0.36	2106	±11	1395	±17	34	0.13063	0.6	4.352	1.5	0.2416	1.3	.910
33.1	0.05	222	79	96.6	0.37	2696.8	± 7.7	2636	±31	2	0.18485	0.47	12.88	1.5	0.5052	1.4	.950
34.1	0.07	359	177	152	0.51	2643.5	± 6.3	2577	±29	3	0.17899	0.38	12.13	1.4	0.4915	1.4	.964
35.1	0.12	193	98	76.1	0.53	2623	± 9.1	2435	±29	7	0.17679	0.55	11.19	1.5	0.459	1.4	.933
36.1	0.23	441	124	116	0.29	2059	±10	1720	±21	16	0.12718	0.59	5.364	1.5	0.3059	1.4	.920
37.1	0.14	172	113	75.6	0.68	2645	±15	2663	±32	-1	0.1792	0.91	12.64	1.7	0.5115	1.4	.848
Z 11/ C - SKR 2B: Epiclastic volcanic sandstone (17° 57' 30.4" S; 29° 30' 24.0" E)																	
1.1	0.40	308	290	117	0.97	2408.7	± 9.6	2354	±27	2	0.15563	0.57	9.46	1.5	0.4408	1.4	.922
3.1	--	451	332	196	0.76	2718.9	± 5.8	2634	±29	3	0.18734	0.35	13.04	1.4	0.5048	1.3	.966
4.1	12.65	682	194	163	0.29	2714	± 91	1400	±21	48	0.187	5.5	6.25	5.8	0.2426	1.7	.294
5.1	0.16	94	43	30.6	0.47	2180	± 17	2072	±26	5	0.1363	0.97	7.12	1.8	0.3791	1.5	.837
6.1	0.09	355	225	141	0.66	2604.4	± 9.3	2449	±28	6	0.17482	0.56	11.14	1.5	0.462	1.4	.925
7.1	0.08	73	38	24.8	0.54	2216	± 18	2138	±29	4	0.1391	1.1	7.54	1.9	0.3933	1.6	.834

8.1	8.16	503	162	105	0.33	2024	±100	1298	±18	36	0.1247	5.6	3.83	5.8	0.223	1.5	.256
9.1	7.60	500	338	142	0.70	2433	± 64	1714	±22	30	0.1579	3.8	6.63	4	0.3046	1.4	.357
10.1	0.00	74	48	24.2	0.66	2070	± 17	2065	±28	0	0.128	0.97	6.66	1.9	0.3777	1.6	.853
11.1	0.00	147	114	65.7	0.80	2613.1	± 8.4	2701	±31	-3	0.17575	0.5	12.61	1.5	0.5204	1.4	.941
12.1	0.23	184	120	65.4	0.67	2213	± 18	2230	±27	-1	0.1389	1	7.91	1.7	0.4134	1.4	.809
13.1	0.07	297	309	104	1.08	2315.4	± 8.5	2209	±25	5	0.14735	0.5	8.3	1.4	0.4087	1.4	.939
14.1	0.12	223	133	94.4	0.62	2683.8	± 9	2578	±30	4	0.1834	0.55	12.43	1.5	0.4917	1.4	.932
15.1	0.05	154	162	65.6	1.09	2646.8	± 9.1	2595	±32	2	0.17934	0.55	12.26	1.6	0.4956	1.5	.939
16.1	4.46	221	253	75.3	1.18	2128	± 58	2067	±27	3	0.1323	3.3	6.89	3.6	0.378	1.5	.414
17.1	0.18	564	178	237	0.33	2954.1	± 4.8	2568	±28	13	0.2164	0.3	14.6	1.4	0.4894	1.3	.976
18.1	0.15	207	73	64.1	0.37	2103	± 12	1979	±24	6	0.1304	0.68	6.46	1.6	0.3593	1.4	.904
19.1	6.87	334	365	112	1.13	2453	± 57	1997	±25	19	0.1598	3.4	8	3.7	0.3632	1.5	.396
20.1	7.54	274	323	81.1	1.22	2198	± 76	1785	±23	19	0.1376	4.4	6.05	4.6	0.319	1.5	.324
21.1	1.63	74	66	23.7	0.91	2507	± 28	2007	±27	20	0.1649	1.7	8.3	2.3	0.3653	1.6	.689
22.1	--	81	58	31.3	0.75	2492	± 14	2399	±31	4	0.1635	0.82	10.16	1.8	0.4508	1.6	.885
23.1	0.31	413	304	171	0.76	2629	± 6.8	2529	±29	4	0.17743	0.41	11.75	1.5	0.4804	1.4	.959
24.1	4.08	303	420	75.5	1.43	2138	± 51	1581	±20	26	0.133	2.9	5.1	3.2	0.278	1.4	.444
25.1	1.79	241	101	107	0.43	2696	± 18	2637	±30	2	0.1848	1.1	12.88	1.7	0.5054	1.4	.784
26.1	0.00	206	116	86	0.58	2638.2	± 8.7	2557	±29	3	0.17842	0.52	11.97	1.5	0.4868	1.4	.935
27.1	0.03	108	103	46.4	0.98	2627	± 11	2611	±33	1	0.1772	0.67	12.2	1.7	0.4993	1.5	.915
28.1	8.44	349	306	83.5	0.91	2223	±120	1463	±22	34	0.1397	7	4.91	7.2	0.2548	1.7	.230
29.1	7.94	398	260	92.8	0.67	2303	± 75	1437	±19	38	0.1463	4.4	5.04	4.6	0.2497	1.5	.323

Pb_c and Pb* indicate the common and radiogenic proportions respectively

(1) Corrected for common Pb, using measured ^{204}Pb

Errors are 1 sd

Error in Standard calibration was 0.31% (not included in above errors but required when comparing data from different mounts).

Table 3.3: LA-ICPMS U-Pb zircon data for a sample from the Godzi Volcanic Centre (Magondi Belt)

Spot	µg/g U[a]	µg/g ^{*206}Pb[a]	^{232}Th/ ^{238}U Meas[a]	^{207}Pb/ ^{206}Pb age (1)	± 2sd	^{206}Pb/ ^{238}U age (1)	± 2sd	% Conc (2sd)	^{*207}Pb/ ^{*206}Pb[e]	± 2sd[d]	^{*207}Pb/ ^{235}Pb[b]	± 2sd[d]	^{*206}Pb/ ^{238}Pb[b]	± 2sd[d]	Error Correlation[c]
GD - Z 11/3: Andesitic agglomerate (17° 38' 21.1'' S; 29° 30' 04.5'' E)															
11	126	66	0.80	2725	35	2723	47	100	0.1880	0.0040	13.62	0.32	0.526	0.011	0.89
12	251	128	0.61	2652	34	2657	46	100	0.1799	0.0037	12.65	0.30	0.510	0.011	0.90
13	114	58	0.72	2653	34	2656	46	100	0.1800	0.0038	12.65	0.30	0.510	0.011	0.90
14	146	75	0.63	2651	34	2652	46	100	0.1798	0.0037	12.62	0.30	0.509	0.011	0.90
15	101	51	0.67	2645	34	2656	46	100	0.1791	0.0037	12.59	0.30	0.510	0.011	0.90
46	122	62	0.93	2644	34	2655	46	100	0.1790	0.0037	12.58	0.29	0.510	0.011	0.90
20	67	34	0.60	2637	35	2662	46	101	0.1783	0.0038	12.56	0.29	0.511	0.011	0.89
21	123	63	0.56	2653	34	2655	45	100	0.1800	0.0037	12.65	0.29	0.510	0.011	0.90
22	107	55	0.69	2646	34	2653	45	100	0.1792	0.0037	12.58	0.29	0.509	0.011	0.89
23	110	56	0.46	2645	34	2653	45	100	0.1791	0.0037	12.58	0.29	0.509	0.011	0.89
24	140	72	0.91	2631	34	2657	45	101	0.1776	0.0037	12.49	0.29	0.510	0.011	0.90
25	122	62	0.49	2651	34	2653	45	100	0.1798	0.0037	12.62	0.29	0.509	0.011	0.90
26	60	32	0.30	2730	35	2728	47	100	0.1886	0.0041	13.70	0.32	0.527	0.011	0.89
27	193	102	0.78	2642	34	2731	46	103	0.1788	0.0036	13.01	0.30	0.527	0.011	0.90
33	55	28	0.57	2623	35	2654	45	101	0.1768	0.0038	12.41	0.29	0.509	0.011	0.89
34	99	50	0.48	2649	34	2653	45	100	0.1796	0.0037	12.61	0.29	0.509	0.010	0.89
35	67	35	0.66	2726	34	2725	46	100	0.1881	0.0039	13.64	0.31	0.526	0.011	0.89
36	115	59	0.57	2674	34	2653	44	99	0.1823	0.0038	12.80	0.29	0.509	0.010	0.89
37	130	66	0.87	2636	35	2655	44	101	0.1781	0.0037	12.51	0.29	0.510	0.010	0.89
38	63	33	0.47	2711	36	2726	46	101	0.1865	0.0041	13.53	0.32	0.526	0.011	0.88
39	156	79	0.63	2647	34	2657	44	100	0.1794	0.0037	12.61	0.29	0.510	0.010	0.89
40	17	9	0.22	2722	40	2721	47	100	0.1877	0.0046	13.59	0.33	0.525	0.011	0.87
41	104	53	0.92	2647	35	2655	44	100	0.1794	0.0038	12.60	0.29	0.510	0.010	0.89
42	119	61	0.36	2658	34	2655	44	100	0.1805	0.0038	12.68	0.29	0.510	0.010	0.89
46	47	25	0.36	2738	37	2733	46	100	0.1895	0.0042	13.80	0.32	0.528	0.011	0.88
47	62	33	0.48	2735	35	2726	45	100	0.1891	0.0040	13.73	0.31	0.526	0.011	0.89
48	77	39	0.72	2651	35	2653	44	100	0.1798	0.0038	12.62	0.29	0.509	0.010	0.89
53	145	74	0.24	2641	35	2650	43	100	0.1787	0.0038	12.52	0.28	0.508	0.010	0.88
54	83	43	0.47	2653	35	2655	43	100	0.1801	0.0038	12.65	0.29	0.510	0.010	0.88
55	121	57	0.54	2657	35	2480	41	93	0.1804	0.0039	11.67	0.26	0.469	0.009	0.88

[a]U and Pb concentrations and Th/U ratios are calculated relative to GJ-1 reference zircon

[b]Corrected for background and within-run Pb/U fractionation and normalised to reference zircon GJ-1 (ID-TIMS values/measured value); ^{207}Pb/^{235}U calculated using (^{207}Pb/^{206}Pb)/(^{238}U/^{206}Pb * 1/137.88)

[c] Is the error correlation defined as the quotient of the propagated errors of the ^{206}Pb/^{238}U and the ^{207}/^{235}U ra

[d]Quadratic addition of within-run errors (2 SD) and daily reproducibility of GJ-1 (2 SD)

[e]Corrected for mass-bias by normalising to GJ-1 reference zircon (~0.6 per atomic mass unit) and common Pb using the model Pb composition of Stacey & Kramers (1975)

Pb_c and Pb* indicate the common and radiogenic proportions respectively

(1) Corrected for common Pb

A.3 MAGONDI BASEMENT

Table 4.1: SIMS U-Pb zircon data for samples which make up the Magondi Basement

Spot	Comment	% $^{206}Pb_c$	µg/g U	µg/g Th	µg/g $^{*206}Pb$	$^{232}Th/^{238}U$ Meas	$^{207}Pb/^{206}Pb$ age (1)	± 1sd	$^{206}Pb/^{238}U$ age (1)	± 1sd	% Disc (2sd)	$^{*207}Pb/^{*206}Pb$	± 1sd	$^{*207}Pb/^{235}Pb$	± 1sd	$^{*206}Pb/^{238}Pb$	± 1sd	Error Correlation
Z MB 13/5: Biotite-rich Chiroti Paragneiss (17°6'13.0"S, 29°01'06.1"E)																		
MB 13-5@1	core	0.03	202	148	106	0.731	2027.5	6.0	2106.0	30.3	4.5	0.12491	0.34	6.65446	1.72	0.3864	1.68	0.98035
MB 13-5@2	rim	{0.02}	138	83	68	0.604	2033.5	5.9	2056.7	29.5	1.3	0.12533	0.33	6.49438	1.70	0.3758	1.67	0.98055
MB 13-5@3	c	0.02	298	295	155	0.989	2035.7	5.5	2047.4	29.4	0.7	0.12549	0.31	6.46815	1.70	0.3738	1.67	0.98284
MB 13-5@4	c	0.40	533	532	255	0.998	2036.1	4.2	1879.8	27.3	-8.8	0.12552	0.24	5.85953	1.69	0.3386	1.67	0.98995
MB 13-5@5	c	0.02	213	167	107	0.782	2031.2	7.2	2057.4	29.5	1.5	0.12517	0.41	6.48856	1.72	0.3760	1.67	0.97127
MB 13-5@6	c	0.02	244	205	126	0.840	2036.0	5.1	2074.4	29.7	2.2	0.12551	0.29	6.56914	1.70	0.3796	1.67	0.98567
MB 13-5@7	c	0.02	246	162	119	0.656	2030.4	5.8	2026.5	29.1	-0.2	0.12511	0.33	6.37189	1.70	0.3694	1.67	0.98142
MB 13-5@8		{0.01}	211	184	108	0.874	2037.1	5.5	2058.9	29.5	1.2	0.12559	0.31	6.51563	1.70	0.3763	1.67	0.98289
MB 13-5@9	c	{0.02}	188	177	98	0.945	2037.8	5.7	2068.3	29.7	1.8	0.12564	0.32	6.55326	1.70	0.3783	1.67	0.98217
MB 13-5@10	r	0.02	235	159	117	0.675	2029.1	6.1	2073.0	29.7	2.5	0.12502	0.34	6.53832	1.70	0.3793	1.67	0.97950
MB 13-5@11	c	{0.01}	204	250	111	1.224	2028.6	5.4	2038.8	29.3	0.6	0.12499	0.31	6.41072	1.70	0.3720	1.67	0.98359
MB 13-5@12	c	{0.02}	199	168	102	0.842	2035.2	5.5	2064.1	29.7	1.7	0.12545	0.31	6.52799	1.71	0.3774	1.68	0.98302
MB 13-5@13	c	{0.02}	271	306	146	1.130	2040.8	4.9	2054.5	29.4	0.8	0.12585	0.28	6.51318	1.69	0.3753	1.67	0.98658
MB 13-5@14	r	0.01	373	251	181	0.674	2030.2	4.1	2039.0	29.2	0.5	0.12510	0.23	6.41720	1.69	0.3720	1.67	0.99043
MB 13-5@15	r	0.02	303	234	154	0.773	2037.1	4.7	2077.3	29.8	2.3	0.12559	0.27	6.58372	1.69	0.3802	1.67	0.98767
MB 13-5@16		{0.01}	211	188	107	0.890	2036.4	5.5	2043.0	29.3	0.4	0.12554	0.31	6.45434	1.70	0.3729	1.67	0.98300
MB 13-5@17	r	0.24	458	101	229	0.221	2272.9	3.6	2240.9	31.7	-1.7	0.14375	0.21	8.23935	1.68	0.4157	1.67	0.99224
MB 13-5@18	c	0.41	435	131	214	0.301	2328.2	4.2	2155.7	30.7	-8.7	0.14845	0.24	8.12803	1.69	0.3971	1.67	0.98957
MB 13-5@19		{0.01}	192	183	101	0.952	2031.8	5.8	2072.0	29.7	2.3	0.12521	0.33	6.54461	1.70	0.3791	1.67	0.98139
MB 13-5@20		{0.01}	263	299	143	1.138	2034.4	4.9	2074.0	29.7	2.3	0.12540	0.28	6.56184	1.69	0.3795	1.67	0.98651
MB 13-5@21	r	{0.02}	228	199	116	0.873	2024.7	6.1	2052.2	29.4	1.6	0.12471	0.35	6.44566	1.71	0.3748	1.67	0.97911
MB 13-5@22	r	{0.02}	183	157	93	0.858	2043.6	6.3	2051.3	29.5	0.4	0.12605	0.35	6.51142	1.71	0.3747	1.67	0.97823
MB 13-5@23	r	0.03	235	251	125	1.068	2035.5	6.7	2063.7	29.8	1.6	0.12547	0.38	6.52758	1.72	0.3773	1.68	0.97579
MB 13-5@24	c	0.04	405	334	217	0.825	2158.8	4.6	2157.9	30.7	-0.1	0.13460	0.26	7.37847	1.69	0.3976	1.67	0.98773
MB 13-5@25	c	{0.02}	212	179	108	0.844	2035.0	6.0	2057.7	29.5	1.3	0.12544	0.34	6.50360	1.70	0.3760	1.67	0.97963
MB 13-5@26	c	0.02	265	248	135	0.935	2041.1	7.7	2028.8	29.1	-0.7	0.12587	0.43	6.41903	1.73	0.3699	1.67	0.96783
MB 13-5@27	c	{0.02}	234	222	118	0.950	2039.3	6.5	2022.8	29.1	-0.9	0.12574	0.37	6.39054	1.71	0.3686	1.67	0.97631
MB 13-5@28	c	0.12	322	419	172	1.299	2016.8	6.6	2010.2	28.9	-0.4	0.12416	0.37	6.26419	1.71	0.3659	1.67	0.97620
MB 13-5@29	c	{0.00}	417	329	207	0.789	2031.5	6.9	2047.2	29.4	0.9	0.12519	0.39	6.45208	1.72	0.3738	1.67	0.97333
MB 13-5@30	c	0.03	329	268	165	0.813	2035.3	5.7	2059.7	29.5	1.4	0.12546	0.32	6.51216	1.70	0.3765	1.67	0.98202
Z MB 13/6: Chiroti Paragneiss (17°05'52.2"S; 29°01'38.0"E)																		
MB13-6@1	c	{0.04}	41	14	28	0.334	2888.2	8.9	2693.1	25.0	-8.3	0.20777	0.55	14.85551	1.26	0.5186	1.13	0.90050
MB13-6@2	c	9.86	1954	1426	602	0.730	1952.8	216.5	1500.3	17.9	-25.9	0.11977	13.05	4.32737	13.12	0.2620	1.34	0.10183
MB13-6@3	r	11.94	1837	239	821	0.130	2013.6	88.4	2114.9	53.7	5.9	0.12393	5.14	6.63500	5.93	0.3883	2.97	0.50021
MB13-6@4		0.01	1130	49	459	0.043	2028.5	2.5	1970.3	19.2	-3.3	0.12498	0.14	6.16059	1.14	0.3575	1.13	0.99206
MB13-6@5	c	0.70	1467	354	461	0.241	1980.2	3.5	1566.1	26.1	-23.5	0.12163	0.20	4.61153	1.89	0.2750	1.87	0.99459
MB13-6@6	c	0.04	1536	215	491	0.140	1938.6	6.1	1568.3	17.7	-21.5	0.11882	0.34	4.51244	1.31	0.2754	1.27	0.96585
MB13-6@7	c	{0.01}	315	101	145	0.322	2057.3	3.3	2061.0	20.0	0.2	0.12703	0.19	6.59870	1.15	0.3767	1.13	0.98642
MB13-6@8	r	0.01	1327	25	511	0.019	2011.2	2.1	1890.1	19.4	-6.9	0.12376	0.12	5.81403	1.19	0.3407	1.18	0.99514
MB13-6@9	r	0.06	2322	72	750	0.031	1924.5	3.6	1625.7	20.8	-17.5	0.11789	0.20	4.66248	1.46	0.2868	1.45	0.99058
MB13-6@10	c	0.04	1174	97	331	0.083	1840.7	13.6	1432.2	32.2	-24.7	0.11253	0.75	3.86032	2.61	0.2488	2.50	0.95757
MB13-6@11	c	0.05	191	153	95	0.799	2029.2	4.9	2019.7	26.1	-0.5	0.12503	0.28	6.34283	1.53	0.3679	1.50	0.98354
MB13-6@12	r	0.27	2080	74	624	0.036	1917.2	12.3	1520.3	15.4	-23.2	0.11741	0.69	4.30574	1.33	0.2660	1.14	0.85563
MB13-6@13	c	2.45	159	91	66	0.573	2122.2	94.6	1849.5	36.0	-14.8	0.13181	5.58	6.03879	6.01	0.3323	2.23	0.37126
MB13-6@14	r	0.01	692	215	535	0.311	2896.9	3.2	3029.9	31.9	5.8	0.20888	0.20	17.28083	1.33	0.6000	1.32	0.98863
MB13-6@15	c	{0.05}	38	16	28	0.409	2908.6	6.3	2871.4	26.7	-1.6	0.21039	0.39	16.27868	1.21	0.5612	1.15	0.94719
MB13-6@16		0.02	296	174	142	0.589	2029.8	3.8	2035.9	20.1	0.4	0.12507	0.22	6.40442	1.17	0.3714	1.15	0.98289
Z MB 13/8B: Hurungwe Orthogneiss (16°32'33.7"S, 29°32'48.1"E)																		
MB13-8B@1	c	0.07	563	245	394	0.435	1978.8	4.0	2883.0	32.9	57.0	0.12153	0.23	9.45031	1.43	0.5640	1.41	0.98751
MB13-8B@2	c	{0.01}	687	198	425	0.289	1979.4	4.9	2664.0	30.8	42.4	0.12157	0.27	8.57799	1.43	0.5117	1.41	0.98146
MB13-8B@3	r	1.07	989	246	455	0.249	1963.2	11.6	2191.1	26.6	13.7	0.12047	0.65	6.72371	1.57	0.4048	1.43	0.90903
MB13-8B@4	c	0.42	250	142	109	0.569	2059.6	9.4	1911.6	23.3	-8.3	0.12719	0.53	6.05389	1.50	0.3452	1.40	0.93452

MB13-8B@5	r	12.57	2740	229	219	0.084	1618.3	34.6	428.6	5.9	-75.9	0.09969	1.88	0.94482	2.35	0.0687	1.42	0.60185
MB13-8B@6	c	0.01	1047	272	463	0.260	2017.3	3.2	2028.0	24.5	0.6	0.12419	0.18	6.33061	1.42	0.3697	1.41	0.99160
MB13-8B@7	c	{0.01}	497	147	218	0.296	2015.7	4.4	2000.5	24.5	-0.9	0.12408	0.25	6.22509	1.44	0.3639	1.42	0.98494
MB13-8B@8	c	0.02	551	187	250	0.340	2027.6	5.3	2034.0	24.6	0.4	0.12491	0.30	6.38935	1.44	0.3710	1.41	0.97799
MB13-8B@9	c	{0.01}	534	83	226	0.156	2018.7	6.0	1988.2	25.2	-1.8	0.12429	0.34	6.19137	1.51	0.3613	1.47	0.97471
MB13-8B@10	c	{0.01}	352	104	152	0.296	2021.2	6.3	1975.3	23.9	-2.6	0.12447	0.36	6.15330	1.45	0.3586	1.40	0.96949
MB13-8B@11	c	{0.01}	486	230	225	0.473	2022.9	7.3	2018.7	24.4	-0.2	0.12458	0.41	6.31647	1.46	0.3677	1.40	0.95963
MB13-8B@12	c	{0.01}	560	154	229	0.276	1955.5	4.6	1899.3	23.2	-3.3	0.11995	0.26	5.66661	1.43	0.3426	1.40	0.98342
MB13-8B@13	c	{0.01}	998	344	446	0.345	2021.0	3.7	2011.9	24.4	-0.5	0.12445	0.21	6.28520	1.42	0.3663	1.41	0.98920
MB13-8B@14	r	10.31	2553	184	250	0.072	1725.1	15.6	526.6	7.1	-72.3	0.10562	0.85	1.23953	1.64	0.0851	1.40	0.85474
MB13-8B@15	c	1.60	935	521	299	0.557	1993.4	8.1	1438.9	18.2	-31.0	0.12253	0.46	4.22482	1.48	0.2501	1.41	0.95138
MB13-8B@16	r	0.04	809	441	377	0.545	2026.1	6.2	2001.6	24.2	-1.4	0.12481	0.35	6.26583	1.45	0.3641	1.41	0.97017
MB13-8B@17	c	{0.00}	691	313	326	0.453	2029.4	4.8	2059.5	24.9	1.7	0.12504	0.27	6.48988	1.43	0.3764	1.41	0.98171
MB13-8B@18	r	15.85	2639	569	197	0.216	1463.4	31.6	395.3	5.4	-75.2	0.09181	1.68	0.80050	2.20	0.0632	1.42	0.64462
MB13-8B@19	c	0.05	519	174	228	0.336	2009.0	4.7	1982.4	24.1	-1.5	0.12361	0.27	6.13626	1.43	0.3600	1.41	0.98256
MB13-8B@20	c	{0.01}	420	142	186	0.339	2018.8	7.2	1998.6	24.4	-1.2	0.12430	0.41	6.22907	1.48	0.3635	1.42	0.96109
MB13-8B@23	c	0.18	736	250	333	0.339	2024.5	4.3	2025.6	24.5	0.1	0.12470	0.24	6.34752	1.43	0.3692	1.41	0.98537
MB13-8B@24	r	{0.00}	635	218	295	0.344	2028.7	4.8	2071.1	24.9	2.4	0.12499	0.27	6.52970	1.43	0.3789	1.40	0.98182
MB13-8B@27	c	22.91	2396	1576	172	0.658	1477.7	45.3	337.5	4.8	-79.1	0.09250	2.43	0.68551	2.84	0.0537	1.47	0.51798
MB13-8B@29	c	0.14	594	282	267	0.474	2025.1	4.0	2013.6	24.7	-0.7	0.12474	0.23	6.30627	1.44	0.3667	1.42	0.98750
MB13-8B@33	r	0.06	718	34	294	0.047	2002.6	14.7	1987.3	28.3	-0.9	0.12317	0.83	6.13208	1.85	0.3611	1.65	0.89258
MB13-8B@34	c	{0.01}	702	337	330	0.480	2032.2	4.6	2047.5	24.9	0.9	0.12524	0.26	6.45546	1.44	0.3738	1.42	0.98352
MB13-8B@35	r	{0.01}	628	329	288	0.524	2015.7	4.9	1981.0	24.0	-2.0	0.12408	0.28	6.15461	1.43	0.3598	1.41	0.98118
MB13-8B@36	c	1.98	898	514	287	0.572	1975.6	8.9	1439.2	18.2	-30.2	0.12131	0.50	4.18386	1.50	0.2501	1.41	0.94202
MB13-8B@37	r	0.25	1060	62	409	0.058	1986.9	14.6	1882.2	24.4	-6.1	0.12208	0.83	5.70767	1.70	0.3391	1.49	0.87462
MB13-8B@38	c	{0.01}	631	227	285	0.359	2031.6	6.5	2025.5	24.6	-0.3	0.12520	0.37	6.37262	1.46	0.3692	1.41	0.96804
MB13-8B@39	c	0.02	860	314	374	0.365	2002.7	4.3	1955.8	23.8	-2.7	0.12317	0.24	6.01966	1.43	0.3544	1.41	0.98538
MB13-8B@40	c	{0.01}	574	232	263	0.404	2017.1	4.7	2035.8	24.6	1.1	0.12418	0.27	6.35828	1.43	0.3714	1.41	0.98231
MB13-8B@41		17.56	2606	3001	261	1.151	1862.5	68.8	441.0	6.8	-78.9	0.11390	3.90	1.11191	4.22	0.0708	1.61	0.38099
MB13-8B@42	r	14.64	2177	1706	245	0.784	1626.4	29.7	588.7	8.0	-66.7	0.10012	1.61	1.32007	2.15	0.0956	1.41	0.65901
MB13-8B@43	c	0.01	755	307	346	0.406	2025.1	5.1	2028.5	24.5	0.2	0.12474	0.29	6.36041	1.44	0.3698	1.41	0.97955
MB13-8B@44	c	3.65	2736	266	483	0.097	2102.3	51.9	910.3	55.9	-60.7	0.13033	3.01	2.72527	7.21	0.1517	6.56	0.90889
MB13-8B@45	r	2.31	1872	179	447	0.096	2152.5	21.7	1204.6	42.5	-48.2	0.13411	1.25	3.79912	4.05	0.2055	3.86	0.95108
Z MB 13/10: Kariba Granite (16°30'40.6"S, 28°50'30.3"E)																		
MB 13-10@1	c	0.05	325	233	156	0.717	1966.6	6.7	1991.1	28.8	1.5	0.12070	0.37	6.02268	1.72	0.3619	1.68	0.97593
MB 13-10@02	c	0.04	298	173	137	0.580	1962.4	4.8	1986.9	28.6	1.4	0.12042	0.27	5.99356	1.69	0.3610	1.67	0.98702
MB 13-10@03	c	{0.01}	312	153	139	0.489	1959.3	8.0	1956.1	28.7	-0.2	0.12020	0.45	5.87552	1.76	0.3545	1.70	0.96688
MB 13-10@04		{0.02}	211	264	113	1.252	1972.7	5.7	1995.5	28.8	1.3	0.12112	0.32	6.05875	1.70	0.3628	1.67	0.98230
MB 13-10@05	c	0.49	310	318	142	1.028	1903.4	7.7	1820.1	26.5	-5.0	0.11651	0.43	5.24071	1.72	0.3262	1.67	0.96836
MB 13-10@06	c	{0.01}	206	81	87	0.391	1925.5	6.2	1905.8	27.8	-1.2	0.11795	0.35	5.59432	1.72	0.3440	1.68	0.97915
MB 13-10@07	c	{0.01}	231	92	109	0.400	2105.9	4.9	2080.7	29.8	-1.4	0.13059	0.28	6.85929	1.69	0.3810	1.67	0.98605
MB 13-10@08	c	{0.02}	205	307	114	1.498	1968.6	8.3	1981.9	28.6	0.8	0.12084	0.47	5.99705	1.73	0.3599	1.67	0.96319
MB 13-10@09	c	{0.00}	385	36	158	0.094	1978.8	20.9	1970.5	35.5	-0.5	0.12153	1.18	5.99110	2.39	0.3575	2.08	0.86986
MB 13-10@10	r	{0.00}	468	41	191	0.087	1948.0	5.5	1963.0	30.8	0.9	0.11945	0.31	5.86245	1.84	0.3560	1.81	0.98598
MB 13-10@11	r	0.65	211	126	77	0.597	1992.1	42.7	1668.1	24.7	-18.4	0.12244	2.44	4.98576	2.96	0.2953	1.68	0.56646
MB 13-10@12		{0.25}	312	78	116	0.248	2008.1	21.9	1776.3	27.2	-13.2	0.12355	1.24	5.40443	2.15	0.3173	1.75	0.81518
MB 13-10@13	c	0.16	624	410	287	0.657	2157.4	13.8	1995.1	28.9	-8.7	0.13449	0.80	6.72627	1.86	0.3627	1.68	0.90364
MB 13-10@14	r	0.15	604	130	217	0.216	1904.2	22.1	1750.6	25.9	-9.2	0.11656	1.24	5.01456	2.09	0.3120	1.68	0.80482
MB 13-10@15		0.41	455	70	172	0.154	1965.3	19.6	1828.8	26.7	-8.0	0.12061	1.11	5.45480	2.01	0.3280	1.67	0.83316
MB 13-10@16	c	8.14	378	151	143	0.400	1931.0	93.2	1804.6	26.8	-7.5	0.11832	5.37	5.26997	5.63	0.3230	1.70	0.30119
MB 13-10@17	r	0.20	463	130	164	0.281	1879.2	15.9	1702.9	25.3	-10.7	0.11496	0.89	4.79223	1.90	0.3023	1.68	0.88452
MB 13-10@18	c	0.25	326	236	131	0.724	1923.0	19.2	1774.4	26.3	-8.8	0.11779	1.08	5.14618	2.00	0.3169	1.69	0.84313
MB 13-10@19	c	{0.04}	680	63	253	0.093	1956.9	10.2	1822.6	26.6	-7.9	0.12004	0.57	5.40814	1.77	0.3267	1.67	0.94563
MB 13-10@20	r	1.59	309	206	123	0.667	1993.2	25.6	1831.0	26.8	-9.3	0.12252	1.45	5.54888	2.22	0.3285	1.68	0.75607
MB 13-10@21	c	{0.04}	397	857	216	2.162	1972.5	12.9	1902.6	27.6	-4.1	0.12110	0.73	5.73257	1.82	0.3433	1.67	0.91646
MB 13-10@22		{0.09}	393	78	162	0.198	1990.7	13.5	1953.7	29.2	-2.2	0.12235	0.76	5.97168	1.89	0.3540	1.73	0.91467

MB 13-10@23	c	{0.05}	231	205	101	0.884	1931.6	15.0	1855.1	27.2	-4.6	0.11836	0.84	5.44167	1.88	0.3334	1.68	0.89455
MB 13-10@24	r	{0.02}	269	359	126	1.333	1974.4	13.3	1835.8	26.9	-8.1	0.12123	0.75	5.50695	1.84	0.3295	1.68	0.91270
MB 13-10@25	c	{0.08}	89	122	42	1.369	1991.8	22.5	1843.4	28.1	-8.6	0.12242	1.27	5.58772	2.16	0.3310	1.75	0.80798
MB 13-10@26	r	0.08	427	138	171	0.323	1956.1	10.6	1866.6	27.2	-5.3	0.11999	0.60	5.55614	1.78	0.3358	1.67	0.94168
MB 13-10@27	c	{0.05}	545	77	203	0.141	1937.2	12.5	1806.1	26.3	-7.8	0.11873	0.70	5.29347	1.81	0.3234	1.67	0.92200
MB 13-10@28	c	{0.10}	150	252	76	1.679	1975.6	16.9	1865.1	27.3	-6.4	0.12131	0.95	5.61219	1.94	0.3355	1.69	0.87043
MB 13-10@29	r	{0.05}	438	88	175	0.200	1961.7	12.5	1901.8	27.9	-3.5	0.12037	0.70	5.69482	1.83	0.3431	1.69	0.92384
MB 13-10@30	c	0.01	4647	516	1875	0.111	1961.7	4.4	1946.4	28.1	-0.9	0.12037	0.25	5.84989	1.69	0.3525	1.67	0.98930
MB 13-10@31	c	{0.11}	205	277	92	1.352	1885.0	16.7	1764.7	25.8	-7.3	0.11533	0.94	5.00712	1.91	0.3149	1.67	0.87258
MB 13-10@32	c	{0.03}	133	297	72	2.226	1934.5	17.7	1853.1	27.8	-4.8	0.11855	0.99	5.44385	1.99	0.3330	1.72	0.86644
MB 13-10@33	c	{0.02}	520	63	210	0.121	1997.8	8.9	1939.8	28.0	-3.4	0.12284	0.50	5.94631	1.74	0.3511	1.67	0.95790
MB 13-10@34	c	0.16	464	91	153	0.196	1818.0	14.8	1619.1	24.1	-12.4	0.11113	0.82	4.37490	1.87	0.2855	1.68	0.89841
MB 13-10@37	r	0.02	255	152	123	0.595	1963.8	8.8	2010.8	30.0	2.8	0.12051	0.49	6.08251	1.80	0.3661	1.73	0.96183
MB 13-10@38	c	{0.04}	77	64	36	0.830	1926.2	10.9	1871.4	27.2	-3.3	0.11800	0.61	5.48029	1.78	0.3368	1.67	0.93892
MB 13-10@39		{0.00}	432	145	184	0.336	1952.9	3.5	1918.4	28.3	-2.0	0.11978	0.20	5.72434	1.71	0.3466	1.70	0.99341
MB 13-10@40	c	{0.02}	159	128	78	0.803	1952.2	6.3	1961.7	28.6	0.6	0.11973	0.35	5.87203	1.73	0.3557	1.69	0.97872
MB 13-10@41	c	{0.01}	274	47	116	0.173	1949.7	5.4	1980.3	29.0	1.8	0.11957	0.30	5.92834	1.72	0.3596	1.70	0.98455
MB 13-10@42	c	{0.01}	199	136	95	0.683	1947.2	6.1	1971.0	30.6	1.4	0.11939	0.34	5.88766	1.83	0.3577	1.80	0.98239
MB 13-10@43	r	5.54	188	156	86	0.831	1980.8	42.1	1853.2	27.0	-7.4	0.12167	2.40	5.58746	2.93	0.3331	1.67	0.57197
MB 13-10@44	c	{0.02}	84	73	42	0.869	1959.1	7.7	1994.0	30.9	2.1	0.12019	0.44	6.00717	1.85	0.3625	1.79	0.97183
MB 13-10@45	c	{0.00}	139	96	54	0.690	1809.9	12.5	1627.2	26.4	-11.4	0.11064	0.69	4.38021	1.96	0.2871	1.83	0.93546
MB 13-10@46	c	{0.03}	85	86	45	1.021	1983.1	7.2	1974.4	28.5	-0.5	0.12182	0.41	6.01949	1.72	0.3584	1.67	0.97151
MB 13-10@47	c	{0.03}	84	161	54	1.909	1972.0	7.9	2035.3	30.4	3.7	0.12106	0.44	6.19706	1.79	0.3713	1.74	0.96878
MB 13-10@48	c	0.01	728	40	305	0.055	1954.0	17.4	2022.3	36.1	4.1	0.11985	0.98	6.08946	2.29	0.3685	2.07	0.90441
MB 13-10@49	c	{0.01}	283	39	113	0.137	1937.0	21.3	1905.9	35.0	-1.9	0.11872	1.20	5.63086	2.43	0.3440	2.11	0.87003
MB 13-10@50	c	0.00	992	273	480	0.275	2171.4	9.8	2144.2	34.6	-1.5	0.13557	0.56	7.37667	1.97	0.3946	1.89	0.95837
MB 13-10@51	c	0.09	134	139	64	1.041	1910.4	7.3	1837.7	28.3	-4.4	0.11696	0.41	5.31972	1.82	0.3299	1.77	0.97413
Z MB 13/11: Silimanite Quartzite (16°31'26.5"S, 28°47'33.6"E)																		
MB 13-11@1	r	2.54	672	302	235	0.450	2009.6	40.3	1600.8	23.8	-22.9	0.12365	2.30	4.80570	2.85	0.2819	1.68	0.58883
MB 13-11@02	r	0.42	2870	528	746	0.184	1926.5	7.2	1288.3	20.4	-36.5	0.11803	0.40	3.59992	1.79	0.2212	1.74	0.97434
MB 13-11@03		{0.02}	87	31	43	0.360	2175.3	11.0	2129.3	32.7	-2.5	0.13588	0.64	7.33273	1.91	0.3914	1.80	0.94263
MB 13-11@04	c	0.20	315	138	113	0.437	1969.2	15.5	1631.7	30.0	-19.4	0.12088	0.87	4.80075	2.25	0.2880	2.07	0.92179
MB 13-11@05	c	0.28	1793	351	763	0.196	2016.3	18.9	1980.6	28.8	-2.1	0.12412	1.07	6.15556	2.00	0.3597	1.68	0.84319
MB 13-11@06	c	0.01	329	102	148	0.312	2004.4	22.5	2021.1	40.9	1.0	0.12329	1.27	6.25982	2.67	0.3682	2.35	0.87901
MB 13-11@07	r	0.02	587	171	260	0.291	2017.6	13.3	1999.9	30.2	-1.0	0.12421	0.75	6.22952	1.91	0.3637	1.75	0.91875
MB 13-11@08	c	0.05	1148	613	753	0.534	2695.6	1.5	2552.0	35.5	-6.4	0.18471	0.09	12.36966	1.68	0.4857	1.68	0.99855
MB 13-11@09	r	{0.01}	271	124	127	0.457	2043.7	9.0	2022.6	32.9	-1.2	0.12606	0.51	6.40572	1.96	0.3685	1.89	0.96570
MB 13-11@10	c	0.09	879	127	342	0.145	1955.3	6.0	1862.5	27.1	-5.5	0.11994	0.34	5.53989	1.70	0.3350	1.67	0.98024
MB 13-11@11	c	{0.01}	330	195	159	0.593	2029.1	4.2	2004.9	30.8	-1.4	0.12502	0.24	6.28852	1.80	0.3648	1.78	0.99131
MB 13-11@12	r	0.19	1810	348	690	0.192	2010.6	3.1	1799.1	26.3	-12.0	0.12373	0.17	5.49189	1.68	0.3219	1.67	0.99468
MB 13-11@13	c	0.02	182	109	80	0.597	1959.9	8.2	1866.9	31.6	-5.5	0.12025	0.46	5.56923	2.00	0.3359	1.95	0.97321
MB 13-11@14	r	0.02	207	111	92	0.538	1999.4	8.7	1888.9	30.8	-6.4	0.12295	0.49	5.77140	1.94	0.3405	1.88	0.96746
MB 13-11@15	c	0.01	354	155	162	0.437	2009.7	4.3	1984.6	28.7	-1.5	0.12366	0.24	6.14711	1.69	0.3605	1.68	0.98967
MB 13-11@16	c	0.03	194	109	89	0.565	2018.8	8.6	1925.1	30.9	-5.4	0.12429	0.49	5.96426	1.91	0.3480	1.85	0.96682
MB 13-11@17	r	0.83	2742	780	740	0.284	1966.5	6.1	1319.2	20.6	-36.3	0.12070	0.34	3.77901	1.76	0.2271	1.73	0.98068
MB 13-11@18	c	0.02	1154	463	788	0.401	2684.4	1.1	2696.7	37.3	0.6	0.18346	0.07	13.13935	1.69	0.5194	1.69	0.99915
MB 13-11@19	c	0.03	97	66	48	0.679	2026.5	7.8	1991.0	29.5	-2.0	0.12484	0.44	6.22862	1.78	0.3619	1.72	0.96863
MB 13-11@20	c	0.03	79	43	57	0.540	2723.5	4.9	2754.7	38.8	1.4	0.18786	0.30	13.80973	1.75	0.5332	1.72	0.98549
MB 13-11@21	r	0.02	349	94	160	0.269	2070.4	15.1	2055.3	30.5	-0.8	0.12798	0.86	6.62624	1.93	0.3755	1.73	0.89471
MB 13-11@22	c	0.02	105	48	51	0.458	2059.0	9.4	2069.7	35.9	0.6	0.12716	0.54	6.63764	2.09	0.3786	2.02	0.96653
MB 13-11@23	r	0.05	724	232	369	0.320	2391.4	4.4	2189.6	32.2	-9.9	0.15406	0.26	8.59150	1.75	0.4045	1.73	0.98914
MB 13-11@24	c	0.03	412	197	215	0.478	2171.5	12.3	2194.7	33.7	1.3	0.13558	0.71	7.58207	1.94	0.4056	1.81	0.93105
MB 13-11@25	r	0.31	648	57	265	0.088	2000.6	21.5	1960.4	32.9	-2.3	0.12303	1.22	6.02892	2.29	0.3554	1.94	0.84724
MB 13-11@26	c	0.03	275	322	172	1.169	2222.3	5.0	2214.9	32.8	-0.4	0.13960	0.29	7.89178	1.77	0.4100	1.74	0.98658
MB 13-11@27	c	0.02	408	184	180	0.452	1962.8	5.7	1925.4	28.1	-2.2	0.12045	0.32	5.78053	1.71	0.3481	1.68	0.98232
MB 13-11@28	c	{0.01}	242	172	128	0.708	2029.6	7.3	2132.8	30.4	6.0	0.12506	0.41	6.76177	1.72	0.3922	1.67	0.97089

Z MB 13/12: Manchichi Bay Migmatitic Orthogneiss (16°32'7.9"S, 28°43'35.7"E)																	
ZMB13-12@1		{0.02}	130	136	63	1.045	1988.0	13.1	1935.8	24.8	-3.0	0.12216	0.74	5.89950	1.65	0.3503	1.48	0.89477
ZMB13-12@2		0.17	772	978	393	1.267	1989.1	7.9	1973.7	25.4	-0.9	0.12223	0.45	6.03731	1.56	0.3582	1.49	0.95758
ZMB13-12@3	r	{0.03}	273	174	122	0.638	1968.9	7.7	1940.1	24.7	-1.7	0.12085	0.44	5.85119	1.53	0.3511	1.47	0.95889
ZMB13-12@4	c	{0.00}	232	95	101	0.411	1955.4	14.4	1981.0	25.9	1.5	0.11994	0.81	5.94942	1.72	0.3597	1.51	0.88222
ZMB13-12@5		{0.01}	731	249	304	0.340	1955.6	4.0	1911.7	24.3	-2.6	0.11996	0.22	5.70977	1.49	0.3452	1.47	0.98864
ZMB13-12@6	c	{0.01}	267	215	127	0.807	1991.0	6.5	1986.7	25.2	-0.3	0.12237	0.36	6.08993	1.52	0.3609	1.47	0.97079
ZMB13-12@7	c	0.03	273	141	112	0.515	1925.8	9.6	1842.2	23.6	-5.0	0.11798	0.54	5.38083	1.56	0.3308	1.47	0.93920
ZMB13-12@8	r	0.39	330	83	128	0.253	1933.1	16.3	1832.1	24.1	-6.0	0.11846	0.92	5.36878	1.76	0.3287	1.51	0.85477
ZMB13-12@9	r	{2.72}	2	0	0	0.008	585.7	228.3	548.9	7.7	-6.6	0.05951	11.31	0.72920	11.41	0.0889	1.47	0.12873
ZMB13-12@10	c	{0.02}	214	102	100	0.478	1997.2	50.2	2075.4	46.3	4.6	0.12279	2.87	6.43050	3.87	0.3798	2.60	0.67093
ZMB13-12@11		{0.01}	222	137	94	0.619	1921.8	10.2	1863.4	23.8	-3.5	0.11771	0.57	5.44010	1.58	0.3352	1.47	0.93228
ZMB13-12@12	c	{0.00}	238	122	118	0.514	1952.4	21.7	2181.5	130.7	13.8	0.11974	1.22	6.64892	7.09	0.4027	6.99	0.98499
ZMB13-12@13	c	{0.04}	235	126	100	0.536	1957.8	9.3	1891.8	28.9	-3.9	0.12011	0.52	5.64823	1.84	0.3411	1.76	0.95862
ZMB13-12@14	r	{0.01}	512	146	216	0.286	1969.0	6.2	1960.3	24.9	-0.5	0.12086	0.35	5.92229	1.51	0.3554	1.47	0.97268
ZMB13-12@15	c	{0.01}	304	156	133	0.513	1962.0	15.8	1951.6	26.4	-0.6	0.12039	0.89	5.86874	1.80	0.3536	1.57	0.86899
ZMB13-12@16	c	{0.03}	218	115	90	0.527	1911.4	9.6	1847.4	23.7	-3.8	0.11703	0.54	5.35498	1.57	0.3319	1.47	0.93967
ZMB13-12@17	r	{0.01}	393	172	174	0.436	1968.8	10.4	1995.2	25.6	1.6	0.12085	0.59	6.04465	1.60	0.3628	1.49	0.93063
ZMB13-12@18	c	{0.02}	288	161	131	0.559	1956.9	11.9	2001.0	25.4	2.6	0.12004	0.67	6.02450	1.62	0.3640	1.47	0.91064
ZMB13-12@19	r	{8.20}	2	0	0	0.062	1390.5	363.3	558.7	10.6	-62.4	0.08837	21.41	1.10305	21.50	0.0905	1.97	0.09164
ZMB13-12@20		{0.04}	300	156	130	0.521	1954.7	20.3	1947.2	25.1	-0.4	0.11990	1.15	5.82961	1.88	0.3526	1.49	0.79295
ZMB13-12@21	r	{0.34}	94	1	9	0.007	581.9	81.1	534.4	7.7	-8.5	0.05940	3.83	0.70787	4.11	0.0864	1.49	0.36287
ZMB13-12@22	r	{0.03}	319	262	147	0.821	1956.9	13.1	1956.0	24.9	-0.1	0.12005	0.74	5.86752	1.65	0.3545	1.47	0.89337
ZMB13-12@23		{0.03}	266	154	119	0.579	1981.3	10.9	1980.5	25.1	0.0	0.12170	0.61	6.03497	1.59	0.3596	1.47	0.92288
ZMB13-12@24	c	{0.01}	348	98	153	0.281	1982.5	9.8	2037.1	26.6	3.2	0.12178	0.55	6.24002	1.62	0.3716	1.52	0.94007
ZMB13-12@25	c	{0.01}	202	109	89	0.539	1929.3	12.0	1971.5	25.1	2.5	0.11820	0.67	5.83056	1.62	0.3577	1.48	0.91056
ZMB13-12@26	r	{0.03}	234	278	112	1.186	1963.0	13.8	1914.4	24.5	-2.9	0.12046	0.78	5.74282	1.67	0.3458	1.48	0.88547
ZMB13-12@27		{0.00}	675	650	325	0.963	1967.2	10.4	2000.5	25.3	2.0	0.12074	0.58	6.05762	1.58	0.3639	1.47	0.92931
ZMB13-12@28	c	{0.04}	320	171	146	0.533	2007.1	10.6	2018.5	25.7	0.7	0.12348	0.60	6.26003	1.60	0.3677	1.48	0.92624
ZMB13-12@29	r	{0.01}	215	114	97	0.528	1949.5	22.7	2006.5	25.7	3.4	0.11955	1.28	6.01890	1.96	0.3651	1.49	0.75779
ZMB13-12@30	r	{0.02}	368	247	171	0.672	1988.1	9.0	2015.7	26.2	1.6	0.12217	0.51	6.18356	1.59	0.3671	1.51	0.94733
ZMB13-12@31		{0.07}	235	109	103	0.465	1963.0	13.1	1975.2	26.8	0.7	0.12046	0.74	5.95449	1.74	0.3585	1.57	0.90492

Pb_c and Pb* indicate the common and radiogenic proportions respectively

{} indicate where no correction has been applied otherwise a value has been calculated using the present-day Stacey & Kramers common Pb value

(1) Corrected for common Pb

Errors are 1 sd

No data indicates that the applied correction resulted in an impossible age

Positive numbers for % Disc, indicate reverse discordance

Table 4.2: ID-TIMS U-Pb data on zircon, apatite, titanite and rutile in samples from the Copper King and Copper Queen Domes

Sample number	Comments	Wt. (mg)	U (µg/g)	Th/U	Pb_C (pg)	$^{207}Pb/^{204}Pb$	$^{206}Pb/^{238}U$	± 2sd	$^{207}Pb/^{235}U$	± 2sd	$^{207}Pb/^{206}Pb$ age	± 2sd	% Disc
CQD-11 Tonalitic Gneiss, Copper King Dome													
dwd3233	pink	0.004	66	0.41	0.24	6879	0.5185	0.0018	13.266	0.047	2703.2	1.6	0.5
dwd3282	brown, cracked	0.008		0.38	3.58	1747					2656.1	1.5	
dwd3293		0.002	51	0.55	0.21	2951	0.5091	0.0016	12.643	0.042	2654.1	1.6	0.1
dwd3232	pink	0.012	44	0.34	0.4	7879	0.5085	0.0012	12.618	0.033	2652.5	1.6	0.1
dwd3294		0.002	43	0.5	0.51	1001	0.507	0.0021	12.571	0.055	2651.3	1.9	0.4
dwd3290	tip, cracked	0.003	109	0.36	0.44	4288	0.505	0.0012	12.497	0.033	2648.1	1.4	0.6
dwd3283	brown	0.002		0.31	0.08	3372					1645.4	2	
dwd3279	tip, cracked, brown	0.004		0.33	0.11	2574					2645.1	1.5	
dwd3292	tip, cracked	0.0005	191	0.32	0.63	882	0.4952	0.0014	12.233	0.038	2645	2.1	2.4
dwd3280	tip	0.0005		0.32	2.5	1250					2643.7	1.9	
dwd3291	tip, cracked	0.0005	267	0.35	0.52	1464	0.4956	0.0013	12.21	0.37	2640.6	1.6	2.1
dwd3281	tip	0.0005		0.32	0.37	779					2633	2.7	
dwd3288	Titanite, brown	0.517	99	1.88	955	237.5	0.4503	0.0082	10.485	0.193	2546.6	3.3	7.1
dwd3289	Titanite, colourless-brown	0.060	31	0.05	112	59.616	0.3663	0.0010	6.332	0.027	2034.3	5.0	1.3
CQD-10 Metapelitic Schist, Copper Queen Dome													
dwd3269		0.0008	109	0.5	0.14	5426	0.5976	0.0017	18.604	0.058	3022.6	1.4	0.1
dwd3270		0.0008	128	0.85	0.35	1416	0.4643	0.0017	10.27	0.04	2460.1	3.1	0.1
dwd3234	pink	0.002	40	0.99	0.29	1284	0.4531	0.0019	9.763	0.043	2415.8	2.6	0.3
dwd3277	brown	0.0005	82	0.55	0.23	740	0.4307	0.0018	8.856	0.041	2335.8	2.8	1.4
dwd3271	brown	0.0008	110	0.62	0.25	1254	0.3982	0.0012	7.561	0.023	2198.4	3.2	2
dwd3278	brown	0.0005		0.52	3.5	813					2162.3	3.4	
dwd3235	pink	0.001	103	0.8	0.2	1743	0.3952	0.0015	7.307	0.03	2152.4	2.2	0.3
CQD-8 Unfoliated Granite, Copper Queen Dome													
dwd3268		0.0005	67	0.28	5.4	52.52	0.5068	0.003	12.876	0.227	2691.6	22	2.2
dwd3266	tip, red-brown	0.0003	88	0.48	0.16	978	0.5066	0.003	12.632	0.077	2660.7	4.3	0.9
dwd3267	red-brown	0.015	73	0.6	0.34	1898	0.504	0.002	12.471	0.052	2647.8	2.3	0.8
dwd3307	Apatite, large, round	0.300	14	1.33	1511	22.271	0.3547	0.0015	6.076	0.100	2018	28	3.5
CQD-6 Gneiss, Copper Queen Dome													
9	Rutile, brown-opaque	0.23	18	0.95	998	21.402	0.2177	18	3.574	74	1942	34	38.1
10	Rutile, green-brown	0.304	20	1.4	3493	19.327	0.3403	20	5.588	157	1943	50	3.2
11	Rutile, yellow	0.197	27	1.36	1339	21.642	0.2401	12	3.927	72	1936	32	31.5
CQD-5 Weakly Foliated Granite, Copper Queen Dome													
8	25 apatite	0.15	25	1.11	1759	20.9	0.3411	18	6.315	131	2154	35	14
CQD-4 Strongly Foliated Granite, Copper Queen Dome													
1	pink, cracked	0.002	162	0.93	1.3	1477	0.504	15	12.425	40	2641.8	2.2	0.5
2	pink	0.002	126	0.52	1.5	737.7	0.5009	21	12.248	52	2628.3	3	0.5
3	pink	0.001	145	0.61	1.4	598.9	0.5041	15	12.394	42	2637.3	2.7	0.3
4	Titanite, brown	0.03	177	3.75	194	145.9	0.4975	18	12.099	52	2619.1	4.4	0.7
5	12 titanite, brown	0.15	147	2.84	610	189.7	0.5018	13	12.217	40	2620.8	3.7	0
6	16 titanite	0.15	7	1.1	47	25.709	0.1018	4	1.078	15	1116	25	46.1
7	Apatite	0.15	28	1.52	910	28.521	0.3764	16	6.965	72	2154	16	5.1

Zircons are colourless, equant and abraded unless noted otherwise

Pb_C - Common Pb, assuming the isotopic composition of the blank

Th/U calculated from radiogenic $^{208}Pb/^{206}Pb$ ratio and $^{207}Pb/^{206}Pb$ age assuming concordance

% Disc - Discordance realtive to $^{207}Pb/^{206}Pb$ age

U decay constants are from Jaffey et al., (1971)

Table 4.3: ID-TIMS U-Pb data on samples in table 4.2 which contain significant initial Pb

Sample number	Comments	Wt. (mg)	U (µg/g)	Pb (µg/g)	$^{207}Pb/^{206}Pb$ (± 1sd)	$^{206}Pb/^{204}Pb$	± 1sd	$^{207}Pb/^{204}Pb$	± 1sd	$^{208}Pb/^{204}Pb$	± 1sd
CQD-11 Tonalitic Gneiss, Copper King Dome											
dwd3288	Titanite, brown	0.517	99	67	0.07	1334.9	0.37	237.86	0.38	720.52	0.41
dwd3289	Titanite, colourless	0.06	31	13	0.18	374.56	0.82	60.342	0.65	39.419	0.22
CQD-8 Unfoliated Granite, Copper Queen Dome											
dwd3307	Apatite, large, round	0.3	14	11	0.05	71.49	0.11	22.275	0.14	56.254	0.18
dwd3306	K-feldspar, fresh	0.1	172	38	0.44	18.722	0.57	15.658	0.38	37.957	0.82

Zircons are colourless, equant and abraded unless noted otherwise

Pb_C - Common Pb, assuming the isotopic composition of the blank

Th/U calculated from radiogenic $^{208}Pb/^{206}Pb$ ratio and $^{207}Pb/^{206}Pb$ age assuming concordance

% Disc - Discordance realtive to $^{207}Pb/^{206}Pb$ age

U decay constants are from Jaffey et al., (1971)

Table 4.4: LA-ICPMS U-Pb zircon data for the Copper King Dome

Spot	µg/g U[a]	µg/g ^{*206}Pb[a]	^{232}Th/ ^{238}U Meas[a]	^{207}Pb/ ^{206}Pb age (1)	± 2sd	^{206}Pb/ ^{238}U age (1)	± 2sd	% Conc (2sd)	^{*207}Pb/ ^{*206}Pb[e]	± 2sd[d]	^{*207}Pb/ ^{235}Pb[b]	± 2sd[d]	^{*206}Pb/ ^{238}Pb[b]	± 2sd[d]	Error Correlation[c]
CKD - Z 11/3: Copper King Dome Gneiss (17°38'11.6"S, 29°12'42.4"E)															
61	124	61	0.22	2647	35	2569	42	97	0.179	0.0038	12.11	0.27	0.490	0.010	0.88
62	217	103	0.33	2673	35	2514	41	94	0.182	0.0038	11.98	0.27	0.477	0.009	0.88
63	155	79	0.37	2653	34	2655	43	100	0.180	0.0038	12.65	0.28	0.510	0.010	0.88
64	166	85	0.29	2650	35	2652	43	100	0.180	0.0038	12.61	0.28	0.509	0.010	0.88
65	93	47	0.28	2651	35	2613	43	99	0.180	0.0038	12.39	0.28	0.500	0.010	0.88
66	150	76	0.26	2661	35	2650	43	100	0.181	0.0038	12.68	0.28	0.508	0.010	0.88
67	218	84	0.24	2585	35	2095	35	81	0.173	0.0036	9.15	0.21	0.384	0.008	0.88
68	176	90	0.20	2649	35	2653	43	100	0.180	0.0038	12.61	0.28	0.509	0.010	0.88
72	199	102	0.25	2660	35	2652	43	100	0.181	0.0038	12.68	0.29	0.509	0.010	0.88
73	184	81	0.24	2629	36	2366	40	90	0.177	0.0039	10.85	0.25	0.443	0.009	0.88
74	348	145	0.34	2666	35	2247	38	84	0.181	0.0039	10.43	0.24	0.417	0.008	0.88
75	223	104	0.25	2620	35	2475	41	94	0.176	0.0037	11.39	0.26	0.468	0.009	0.88
76	156	72	0.24	2673	37	2441	41	91	0.182	0.0041	11.56	0.27	0.460	0.009	0.87
77	309	157	0.34	2626	35	2652	43	101	0.177	0.0037	12.43	0.28	0.509	0.010	0.88
78	152	78	0.31	2651	35	2655	44	100	0.180	0.0038	12.63	0.29	0.510	0.010	0.88
79	200	102	0.32	2659	36	2659	44	100	0.181	0.0039	12.72	0.29	0.511	0.010	0.88
81	262	116	0.29	2657	35	2363	40	89	0.180	0.0039	11.02	0.25	0.443	0.009	0.88
85	213	108	0.35	2671	35	2653	44	99	0.182	0.0039	12.77	0.29	0.509	0.010	0.88
86	192	98	0.26	2666	35	2658	44	100	0.181	0.0039	12.76	0.29	0.510	0.010	0.88
87	172	76	0.16	2629	36	2359	40	90	0.177	0.0038	10.81	0.25	0.442	0.009	0.88
88	196	85	0.30	2656	38	2332	40	88	0.180	0.0042	10.83	0.26	0.436	0.009	0.87
89	236	120	0.36	2651	36	2654	44	100	0.180	0.0039	12.63	0.29	0.509	0.010	0.88
90	231	110	0.33	2666	37	2509	42	94	0.181	0.0041	11.90	0.28	0.476	0.010	0.88
91	168	85	0.41	2642	36	2648	44	100	0.179	0.0039	12.53	0.29	0.508	0.010	0.88

[a]U and Pb concentrations and Th/U ratios are calculated relative to GJ-1 reference zircon

[b]Corrected for background and within-run Pb/U fractionation and normalised to reference zircon GJ-1 (ID-TIMS values/measured value); ^{207}Pb/^{235}U calculated using (^{207}Pb/^{206}Pb)/(^{238}U/^{206}Pb * 1/137.88)

[c] Is the error correlation defined as the quotient of the propagated errors of the ^{206}Pb/^{238}U and the ^{207}/^{235}U ratio

[d]Quadratic addition of within-run errors (2 SD) and daily reproducibility of GJ-1 (2 SD)

[e]Corrected for mass-bias by normalising to GJ-1 reference zircon (~0.6 per atomic mass unit) and common Pb using the model Pb composition of Stacey & Kramers (1975)

Pb_c and Pb* indicate the common and radiogenic proportions respectively

(1) Corrected for common Pb

A.4 DETE-KAMATIVI INLIER

Table 5.1: LA-ICPMS U-Pb zircon data for various rocks within the Dete-Kamativi Inlier

Spot	µg/g U[a]	µg/g *206Pb[a]	232Th/ 238U Meas[a]	207Pb/ 206Pb age (1)	± 2sd	206Pb/ 238U age (1)	± 2sd	% Conc (2sd)	*207Pb/ *206Pb[e]	± 2sd[d]	*207Pb/ 235Pb[b]	± 2sd[d]	*206Pb/ 238Pb[b]	± 2sd[d]	Error Correlation[c]
Z DK 1 - Quartz-rich pink leucogranite (18° 33' 59" S; 27° 03' 18" E)															
7	321	159	0.37	2612	34	2598	70	99	0.1756	0.0036	12.02	0.41	0.496	0.016	0.96
9	100	44	0.61	2612	38	2322	65	89	0.1756	0.0040	10.50	0.37	0.434	0.014	0.95
10	297	138	0.18	2612	34	2454	67	94	0.1756	0.0036	11.21	0.39	0.463	0.015	0.96
11	613	230	0.03	2047	36	2052	58	100	0.1263	0.0026	6.53	0.22	0.375	0.012	0.96
13	68	35	0.52	2702	36	2701	73	100	0.1854	0.0040	13.31	0.46	0.520	0.017	0.95
14	85	54	0.50	3189	33	3189	83	100	0.2506	0.0053	22.12	0.77	0.640	0.021	0.95
16	31	13	0.39	2604	78	2315	74	89	0.1748	0.0083	10.41	0.47	0.432	0.016	0.85
20	146	73	0.59	2610	37	2622	72	100	0.1755	0.0040	12.14	0.43	0.502	0.017	0.95
22	137	71	0.39	2706	37	2692	73	99	0.1858	0.0042	13.28	0.47	0.518	0.017	0.95
23	77	38	0.63	2615	44	2600	73	99	0.1759	0.0047	12.05	0.44	0.497	0.017	0.93
24	488	185	0.03	2084	38	2071	59	99	0.1290	0.0028	6.74	0.24	0.379	0.013	0.95
25	753	240	0.03	2041	37	1782	52	87	0.1259	0.0026	5.53	0.19	0.318	0.011	0.95
27	138	41	0.39	2724	37	1671	49	61	0.1879	0.0043	7.67	0.27	0.296	0.010	0.95
28	193	72	0.30	2698	34	2037	58	76	0.1850	0.0038	9.48	0.33	0.372	0.012	0.95
29	510	165	0.03	2124	38	1809	52	85	0.1319	0.0028	5.89	0.21	0.324	0.011	0.95
34	101	51	0.65	2591	34	2614	71	101	0.1735	0.0036	11.96	0.42	0.500	0.017	0.95
35	48	24	0.47	2607	39	2624	73	101	0.1751	0.0042	12.13	0.43	0.502	0.017	0.94
36	806	309	0.06	2636	36	2090	60	79	0.1781	0.0039	9.40	0.33	0.383	0.013	0.95
37	629	224	0.04	2099	36	1960	56	93	0.1301	0.0026	6.37	0.22	0.355	0.012	0.96
40	508	177	0.04	2048	38	1922	55	94	0.1264	0.0027	6.05	0.21	0.347	0.012	0.95
41	593	151	0.04	2115	38	1461	44	69	0.1313	0.0029	4.60	0.16	0.254	0.009	0.95
42	78	39	0.48	2614	40	2613	73	100	0.1759	0.0043	12.12	0.44	0.500	0.017	0.94
47	1131	262	0.03	2102	41	1344	41	64	0.1303	0.0031	4.17	0.15	0.232	0.008	0.94
48	223	108	0.37	2695	34	2551	70	95	0.1847	0.0038	12.36	0.43	0.485	0.016	0.96
49	136	66	0.41	2700	34	2549	70	94	0.1852	0.0038	12.38	0.43	0.485	0.016	0.96
51	916	232	0.03	2137	36	1453	44	68	0.1329	0.0028	4.63	0.16	0.253	0.008	0.96
52	663	215	0.03	2139	36	1811	53	85	0.1331	0.0027	5.95	0.21	0.324	0.011	0.96
53	186	97	0.44	2701	34	2713	74	100	0.1853	0.0039	13.37	0.47	0.523	0.018	0.95
54	33	21	1.36	3168	34	3175	84	100	0.2474	0.0053	21.71	0.77	0.636	0.021	0.95
55	201	102	0.40	2671	34	2661	73	100	0.1819	0.0038	12.82	0.45	0.511	0.017	0.96
62	50	26	0.40	2669	36	2684	74	101	0.1818	0.0039	12.94	0.46	0.516	0.017	0.95
63	201	103	1.21	2670	34	2674	74	100	0.1819	0.0038	12.89	0.45	0.514	0.017	0.96
64	539	202	0.12	2672	35	2052	59	77	0.1820	0.0038	9.41	0.33	0.375	0.013	0.95
65	612	220	0.07	2125	40	1979	58	93	0.1320	0.0030	6.54	0.23	0.359	0.012	0.95
66	289	124	0.53	2607	34	2298	65	88	0.1751	0.0036	10.34	0.36	0.428	0.014	0.96
67	157	78	0.51	2608	36	2602	72	100	0.1752	0.0038	12.01	0.43	0.497	0.017	0.95
68	742	240	0.03	2124	38	1804	53	85	0.1320	0.0029	5.87	0.21	0.323	0.011	0.95
72	292	76	0.43	2771	34	1482	45	53	0.1934	0.0040	6.89	0.24	0.258	0.009	0.96
73	106	54	0.64	2642	34	2648	73	100	0.1788	0.0037	12.52	0.44	0.508	0.017	0.96
74	228	82	0.47	2699	35	1985	58	74	0.1850	0.0040	9.20	0.33	0.361	0.012	0.95
75	62	32	0.71	2694	35	2683	75	100	0.1845	0.0039	13.13	0.47	0.516	0.018	0.96
76	882	298	0.03	2130	40	1876	55	88	0.1324	0.0030	6.17	0.22	0.338	0.011	0.95
77	324	151	0.10	2619	34	2461	69	94	0.1763	0.0036	11.30	0.40	0.465	0.016	0.96
78	125	57	0.86	2629	34	2435	69	93	0.1774	0.0037	11.23	0.40	0.459	0.016	0.96
79	789	263	0.04	2122	36	1852	54	87	0.1318	0.0027	6.05	0.21	0.333	0.011	0.96

80	70	34	0.20	2759	34	2569	72	93	0.1919	0.0041	12.96	0.46	0.490	0.017	0.95
81	55	28	0.66	2658	35	2671	74	100	0.1806	0.0039	12.78	0.46	0.513	0.017	0.95
85	39	20	0.50	2699	36	2708	76	100	0.1851	0.0040	13.32	0.48	0.522	0.018	0.95
86	41	21	0.25	2677	37	2683	75	100	0.1826	0.0042	13.00	0.47	0.516	0.018	0.95
87	201	103	0.33	2683	34	2669	74	100	0.1833	0.0038	12.96	0.46	0.513	0.017	0.96
88	42	22	0.38	2703	42	2702	76	100	0.1855	0.0048	13.32	0.49	0.521	0.018	0.94
89	834	283	0.03	2076	36	1880	55	91	0.1284	0.0026	5.99	0.21	0.339	0.012	0.96
90	43	24	0.45	2845	36	2846	79	100	0.2023	0.0045	15.48	0.56	0.555	0.019	0.95
91	57	17	0.22	2703	38	1723	52	64	0.1855	0.0043	7.84	0.28	0.306	0.011	0.95
92	52	27	0.60	2709	39	2706	76	100	0.1862	0.0045	13.39	0.49	0.522	0.018	0.94
93	139	78	0.46	2874	33	2873	79	100	0.2059	0.0043	15.94	0.57	0.562	0.019	0.96
94	348	216	0.26	3116	32	3111	84	100	0.2395	0.0049	20.48	0.73	0.620	0.021	0.96
98	85	44	0.54	2681	36	2688	75	100	0.1831	0.0040	13.06	0.47	0.517	0.018	0.95
99	72	37	0.47	2656	35	2662	75	100	0.1804	0.0038	12.72	0.46	0.511	0.017	0.96
100	143	73	0.42	2660	34	2661	75	100	0.1808	0.0038	12.74	0.46	0.511	0.018	0.96
101	77	46	0.63	3030	37	3028	83	100	0.2269	0.0053	18.76	0.68	0.600	0.021	0.95
102	826	268	0.04	2128	37	1811	54	85	0.1323	0.0028	5.92	0.21	0.324	0.011	0.95
103	213	74	0.36	2701	36	1913	57	71	0.1853	0.0041	8.83	0.32	0.345	0.012	0.95
104	22	11	0.35	2707	37	2705	77	100	0.1860	0.0042	13.37	0.49	0.521	0.018	0.95
107	22	11	0.51	2659	38	2651	75	100	0.1807	0.0041	12.67	0.46	0.509	0.018	0.95
114	64	33	0.35	2680	35	2667	75	100	0.1830	0.0039	12.93	0.47	0.513	0.018	0.96
115	319	190	0.32	3011	33	3012	83	100	0.2241	0.0046	18.41	0.66	0.596	0.020	0.96
116	22	11	1.07	2618	38	2610	76	100	0.1763	0.0041	12.13	0.45	0.499	0.018	0.95
118	365	160	0.20	2816	34	2339	67	83	0.1987	0.0041	11.99	0.43	0.437	0.015	0.96
119	191	99	0.42	2708	34	2702	76	100	0.1861	0.0039	13.35	0.48	0.521	0.018	0.96
124	93	63	0.66	3345	33	3344	90	100	0.2768	0.0059	25.94	0.94	0.680	0.023	0.96
127	227	82	0.25	2684	35	1996	59	74	0.1835	0.0039	9.18	0.33	0.363	0.013	0.96
128	222	110	0.46	2615	36	2602	74	100	0.1759	0.0038	12.06	0.44	0.497	0.017	0.95
Z DK 2 - Porphyritic orthogneiss (18° 31’ 53” S; 27° 04’ 29” E)															
7	303	108	0.01	2029	38	1963	60	97	0.1250	0.0027	6.13	0.23	0.356	0.013	0.96
8	177	63	0.54	2028	43	1955	60	96	0.1249	0.0031	6.10	0.23	0.354	0.013	0.94
9	435	153	0.29	2032	36	1946	59	96	0.1252	0.0026	6.08	0.22	0.352	0.012	0.96
10	227	83	0.76	2035	36	2020	61	99	0.1255	0.0026	6.36	0.23	0.368	0.013	0.96
11	736	263	0.39	2031	38	1972	60	97	0.1251	0.0027	6.17	0.23	0.358	0.013	0.96
12	195	64	0.39	2027	49	1829	57	90	0.1249	0.0035	5.65	0.22	0.328	0.012	0.93
13	232	81	0.24	2021	36	1932	59	96	0.1244	0.0026	6.00	0.22	0.349	0.012	0.96
14	437	90	0.49	2019	37	1204	39	60	0.1243	0.0026	3.52	0.13	0.205	0.007	0.96
15	150	54	0.62	2024	39	1991	61	98	0.1247	0.0027	6.22	0.23	0.362	0.013	0.96
16	421	108	0.50	2028	40	1470	47	73	0.1249	0.0029	4.41	0.16	0.256	0.009	0.95
20	222	80	0.22	2028	43	1992	61	98	0.1250	0.0031	6.24	0.24	0.362	0.013	0.95
21	255	87	0.83	2020	37	1897	58	94	0.1244	0.0026	5.87	0.22	0.342	0.012	0.96
22	514	153	0.46	2020	37	1681	52	83	0.1244	0.0026	5.11	0.19	0.298	0.011	0.96
23	214	75	0.52	2022	40	1945	60	96	0.1245	0.0029	6.04	0.23	0.352	0.013	0.95
24	662	116	0.23	2023	41	1036	34	51	0.1246	0.0029	3.00	0.11	0.174	0.006	0.95
25	290	107	0.53	2019	38	2020	62	100	0.1243	0.0027	6.31	0.23	0.368	0.013	0.96
26	635	210	0.47	2007	37	1840	57	92	0.1234	0.0026	5.62	0.21	0.330	0.012	0.96
27	393	145	0.41	2017	36	2022	61	100	0.1241	0.0025	6.31	0.23	0.368	0.013	0.96
28	260	79	0.20	2027	37	1705	53	84	0.1249	0.0026	5.21	0.19	0.303	0.011	0.96

29	197	73	0.46	2029	38	2035	62	100	0.1250	0.0027	6.40	0.24	0.371	0.013	0.96
33	557	200	0.47	2018	38	1976	60	98	0.1243	0.0026	6.15	0.23	0.359	0.013	0.96
34	358	131	0.05	2024	37	2012	61	99	0.1246	0.0026	6.29	0.23	0.366	0.013	0.96
36	242	89	0.32	2025	37	2021	62	100	0.1247	0.0026	6.33	0.23	0.368	0.013	0.96
37	449	127	0.06	2014	37	1604	50	80	0.1240	0.0026	4.83	0.18	0.283	0.010	0.96
38	658	128	0.29	2018	37	1148	37	57	0.1242	0.0026	3.34	0.12	0.195	0.007	0.96
39	130	48	0.53	2029	38	2014	62	99	0.1250	0.0027	6.32	0.23	0.367	0.013	0.96
40	414	148	0.58	2028	38	1974	60	97	0.1249	0.0027	6.17	0.23	0.358	0.013	0.96
46	181	68	0.25	2021	42	2059	63	102	0.1244	0.0030	6.46	0.24	0.376	0.013	0.95
48	233	87	0.45	2038	38	2052	63	101	0.1256	0.0027	6.49	0.24	0.375	0.013	0.96
49	137	49	0.74	2033	44	1954	61	96	0.1253	0.0032	6.12	0.23	0.354	0.013	0.94
50	417	133	0.10	2016	38	1789	56	89	0.1241	0.0027	5.47	0.20	0.320	0.011	0.96
51	493	125	0.50	2028	37	1453	46	72	0.1250	0.0026	4.36	0.16	0.253	0.009	0.96
52	133	48	0.53	2042	37	2000	61	98	0.1259	0.0027	6.32	0.23	0.364	0.013	0.96
53	277	102	0.06	2043	37	2016	62	99	0.1260	0.0026	6.38	0.24	0.367	0.013	0.96
54	364	114	0.27	2028	38	1758	55	87	0.1250	0.0027	5.40	0.20	0.313	0.011	0.96
55	258	93	0.50	2028	39	1985	61	98	0.1250	0.0028	6.21	0.23	0.361	0.013	0.95
59	422	152	0.32	2032	36	1980	61	97	0.1252	0.0026	6.21	0.23	0.359	0.013	0.96
61	471	119	0.69	2029	41	1450	47	71	0.1250	0.0029	4.35	0.16	0.252	0.009	0.95
62	520	144	0.34	2019	37	1580	50	78	0.1243	0.0026	4.76	0.18	0.278	0.010	0.96
63	159	59	0.30	2032	41	2024	62	100	0.1252	0.0029	6.37	0.24	0.369	0.013	0.95
65	499	168	0.50	2018	36	1866	58	92	0.1242	0.0025	5.75	0.21	0.336	0.012	0.96
66	616	178	0.46	2012	37	1639	52	81	0.1238	0.0026	4.94	0.18	0.290	0.010	0.96
67	380	138	0.38	2014	36	1999	61	99	0.1240	0.0025	6.21	0.23	0.363	0.013	0.96
68	163	60	0.56	2033	38	2022	62	99	0.1253	0.0027	6.37	0.24	0.368	0.013	0.96
75	705	190	0.52	1999	37	1535	49	77	0.1229	0.0026	4.56	0.17	0.269	0.010	0.96
76	178	56	0.45	2051	51	1773	57	86	0.1266	0.0037	5.52	0.22	0.317	0.012	0.93
77	298	112	0.41	2035	37	2058	63	101	0.1254	0.0026	6.50	0.24	0.376	0.013	0.96
78	348	129	0.03	2008	36	2030	62	101	0.1235	0.0025	6.31	0.23	0.370	0.013	0.96
79	387	144	0.56	2015	36	2036	62	101	0.1240	0.0026	6.35	0.24	0.371	0.013	0.96
80	552	103	0.52	2029	39	1102	36	54	0.1250	0.0028	3.21	0.12	0.186	0.007	0.95
85	169	63	0.46	2029	38	2038	63	100	0.1250	0.0027	6.41	0.24	0.372	0.013	0.96
86	276	101	0.02	2034	38	2015	62	99	0.1253	0.0027	6.34	0.24	0.367	0.013	0.96
87	394	88	0.51	2013	41	1294	42	64	0.1239	0.0029	3.80	0.14	0.222	0.008	0.95
88	221	81	0.44	2029	38	2022	62	100	0.1250	0.0027	6.35	0.24	0.368	0.013	0.96
89	217	80	0.01	2026	39	2030	63	100	0.1248	0.0027	6.37	0.24	0.370	0.013	0.96
90	211	76	0.53	2020	37	1991	61	99	0.1244	0.0026	6.21	0.23	0.362	0.013	0.96
91	94	33	0.55	2024	38	1957	61	97	0.1247	0.0027	6.10	0.23	0.355	0.013	0.96
92	277	101	0.40	2023	37	2008	62	99	0.1246	0.0026	6.28	0.23	0.365	0.013	0.96
93	87	45	0.36	2690	36	2689	79	100	0.1841	0.0040	13.13	0.49	0.517	0.019	0.96
98	747	130	0.64	2010	37	1034	34	51	0.1237	0.0026	2.97	0.11	0.174	0.006	0.96
99	358	98	0.60	2016	37	1557	50	77	0.1241	0.0026	4.67	0.18	0.273	0.010	0.96
100	186	69	0.02	2025	37	2034	63	100	0.1247	0.0027	6.38	0.24	0.371	0.013	0.96
101	275	88	0.45	2031	37	1781	56	88	0.1252	0.0026	5.49	0.21	0.318	0.011	0.96
102	411	142	0.53	2019	37	1909	59	95	0.1243	0.0026	5.91	0.22	0.345	0.012	0.96
103	442	163	0.59	2009	37	2023	62	101	0.1236	0.0026	6.28	0.24	0.369	0.013	0.96
104	615	207	0.04	2021	38	1871	59	93	0.1245	0.0027	5.78	0.22	0.337	0.012	0.96
105	79	27	0.40	2023	56	1864	60	92	0.1246	0.0040	5.76	0.23	0.335	0.012	0.92

106	222	82	0.02	2031	38	2035	63	100	0.1252	0.0027	6.40	0.24	0.371	0.013	0.96
107	134	50	0.50	2037	39	2041	63	100	0.1256	0.0028	6.45	0.24	0.373	0.013	0.96
Z DK 9C - (Malaputese Formation) Leucocratic pink paragneiss (18° 30’ 46” S; 26° 57’ 51” E)															
7	814	292	0.24	2619	34	1977	54	75	0.176	0.0037	8.72	0.29	0.359	0.011	0.95
8	1209	282	0.25	2544	35	1350	39	53	0.169	0.0035	5.42	0.18	0.233	0.007	0.95
9	1033	340	0.22	2653	34	1833	50	69	0.180	0.0037	8.17	0.27	0.329	0.010	0.95
10	695	334	0.19	2583	34	2529	66	98	0.173	0.0036	11.43	0.38	0.480	0.015	0.95
13	1106	311	0.13	2269	35	1596	45	70	0.143	0.0029	5.56	0.19	0.281	0.009	0.95
14	385	169	0.15	2589	34	2339	62	90	0.173	0.0035	10.45	0.35	0.437	0.014	0.95
15	658	347	0.37	2731	34	2734	71	100	0.189	0.0039	13.74	0.46	0.528	0.017	0.95
16	643	320	0.18	2608	34	2601	68	100	0.175	0.0036	12.00	0.40	0.497	0.016	0.95
20	533	286	0.48	2778	33	2768	72	100	0.194	0.0040	14.36	0.48	0.536	0.017	0.95
21	1237	334	0.24	2674	34	1540	44	58	0.182	0.0037	6.78	0.23	0.270	0.009	0.95
22	1236	357	0.16	2364	38	1637	46	69	0.152	0.0034	6.04	0.21	0.289	0.009	0.94
23	431	213	0.20	2588	34	2590	68	100	0.173	0.0035	11.80	0.40	0.494	0.016	0.95
24	533	277	0.33	2704	34	2700	71	100	0.186	0.0038	13.31	0.45	0.520	0.017	0.95
25	454	226	0.16	2605	34	2609	69	100	0.175	0.0036	12.03	0.40	0.499	0.016	0.95
26	651	346	0.37	2796	34	2751	72	98	0.196	0.0041	14.41	0.49	0.532	0.017	0.95
27	319	162	0.40	2666	34	2651	70	99	0.181	0.0037	12.72	0.43	0.509	0.016	0.95
28	210	106	0.33	2676	34	2642	70	99	0.183	0.0038	12.75	0.43	0.507	0.016	0.95
29	193	91	0.16	2647	34	2505	67	95	0.179	0.0037	11.75	0.40	0.475	0.015	0.95
33	865	280	0.21	2663	35	1807	51	68	0.181	0.0039	8.08	0.27	0.324	0.010	0.95
34	1141	368	0.14	2366	35	1804	51	76	0.152	0.0031	6.75	0.23	0.323	0.010	0.95
35	975	292	0.25	2309	35	1691	48	73	0.147	0.0030	6.07	0.21	0.300	0.010	0.95
36	665	324	0.18	2551	34	2557	68	100	0.169	0.0034	11.36	0.38	0.487	0.016	0.95
37	557	295	0.47	2743	34	2740	72	100	0.190	0.0039	13.89	0.47	0.530	0.017	0.95
38	638	301	0.18	2562	35	2490	67	97	0.170	0.0036	11.08	0.38	0.472	0.015	0.95
40	568	285	0.27	2630	34	2621	70	100	0.177	0.0036	12.28	0.42	0.502	0.016	0.95
41	603	326	0.50	2785	34	2784	73	100	0.195	0.0040	14.52	0.49	0.540	0.018	0.95
42	544	270	0.32	2611	34	2600	69	100	0.175	0.0036	12.02	0.41	0.497	0.016	0.95
46	635	328	0.18	2705	34	2681	71	99	0.186	0.0039	13.20	0.45	0.516	0.017	0.95
47	635	280	0.17	2492	34	2355	64	94	0.163	0.0033	9.94	0.34	0.441	0.014	0.95
48	527	278	0.25	2725	33	2733	72	100	0.188	0.0038	13.68	0.47	0.528	0.017	0.95
49	734	395	0.38	2783	35	2774	74	100	0.195	0.0041	14.44	0.50	0.538	0.018	0.95
50	572	286	0.17	2628	34	2612	70	99	0.177	0.0037	12.22	0.42	0.500	0.016	0.95
51	490	240	0.15	2588	34	2571	69	99	0.173	0.0035	11.70	0.40	0.490	0.016	0.95
60	697	323	0.17	2552	34	2458	67	96	0.169	0.0035	10.84	0.37	0.464	0.015	0.95
62	363	188	0.35	2702	34	2692	72	100	0.185	0.0038	13.26	0.46	0.518	0.017	0.95
63	464	234	0.22	2638	34	2632	71	100	0.178	0.0037	12.40	0.43	0.504	0.017	0.95
64	440	184	0.14	2453	35	2252	63	92	0.160	0.0033	9.21	0.32	0.418	0.014	0.95
65	610	319	0.47	2683	34	2714	73	101	0.183	0.0038	13.23	0.46	0.523	0.017	0.95
67	632	332	0.29	2704	34	2720	73	101	0.186	0.0038	13.43	0.46	0.525	0.017	0.96
68	704	363	0.32	2684	35	2682	73	100	0.183	0.0039	13.05	0.45	0.516	0.017	0.95
72	811	316	0.13	2254	35	2120	60	94	0.142	0.0029	7.63	0.26	0.389	0.013	0.96
73	616	324	0.21	2712	35	2726	74	101	0.187	0.0040	13.53	0.47	0.526	0.018	0.95
74	436	220	0.25	2634	34	2636	72	100	0.178	0.0036	12.40	0.43	0.505	0.017	0.96
75	816	361	0.14	2545	35	2362	66	93	0.169	0.0035	10.30	0.36	0.443	0.015	0.95
76	588	253	0.14	2315	35	2305	64	100	0.147	0.0030	8.73	0.30	0.430	0.014	0.95

79	678	325	0.18	2536	34	2521	69	99	0.168	0.0034	11.08	0.39	0.479	0.016	0.96
80	490	244	0.20	2607	34	2607	71	100	0.175	0.0036	12.03	0.42	0.498	0.017	0.96
81	890	342	0.17	2649	34	2095	60	79	0.180	0.0037	9.50	0.33	0.384	0.013	0.96
85	694	326	0.31	2666	34	2485	69	93	0.181	0.0037	11.76	0.41	0.470	0.016	0.96
86	524	279	0.36	2770	33	2752	75	99	0.193	0.0040	14.18	0.50	0.532	0.018	0.96
87	673	357	0.40	2750	34	2743	75	100	0.191	0.0039	13.96	0.49	0.530	0.018	0.96
89	783	363	0.12	2621	36	2453	69	94	0.177	0.0038	11.28	0.40	0.463	0.016	0.95
90	547	232	0.26	2638	34	2276	64	86	0.178	0.0037	10.42	0.37	0.423	0.014	0.96
91	662	324	0.18	2766	34	2566	71	93	0.193	0.0040	12.99	0.46	0.489	0.016	0.96
92	477	246	0.20	2685	34	2679	74	100	0.184	0.0038	13.04	0.46	0.515	0.017	0.96
93	1687	343	0.22	2470	35	1192	37	48	0.161	0.0034	4.52	0.16	0.203	0.007	0.96
94	706	347	0.38	2598	34	2578	72	99	0.174	0.0036	11.80	0.42	0.492	0.017	0.96
101	403	197	0.30	2601	34	2566	72	99	0.174	0.0036	11.76	0.42	0.489	0.017	0.96
102	533	277	0.45	2715	34	2701	75	99	0.187	0.0039	13.41	0.48	0.520	0.018	0.96
103	639	320	0.25	2618	34	2619	73	100	0.176	0.0036	12.18	0.43	0.501	0.017	0.96
104	879	331	0.16	2703	34	2062	60	76	0.186	0.0038	9.64	0.34	0.377	0.013	0.96
105	1223	317	0.13	2302	35	1485	45	65	0.146	0.0030	5.22	0.19	0.259	0.009	0.96
106	676	344	0.32	2635	34	2649	74	101	0.178	0.0037	12.48	0.44	0.508	0.017	0.96
107	533	253	0.21	2509	34	2506	71	100	0.165	0.0034	10.82	0.38	0.475	0.016	0.96
111	393	205	0.30	2700	34	2701	75	100	0.185	0.0038	13.29	0.47	0.520	0.018	0.96
113	281	143	0.41	2689	34	2652	74	99	0.184	0.0038	12.91	0.46	0.509	0.017	0.96
114	622	323	0.27	2714	34	2694	75	99	0.187	0.0039	13.36	0.48	0.519	0.018	0.96
115	790	363	0.22	2596	36	2436	70	94	0.174	0.0038	11.01	0.40	0.459	0.016	0.95
116	634	275	0.16	2339	35	2323	67	99	0.149	0.0031	8.94	0.32	0.434	0.015	0.96
117	561	284	0.32	2673	34	2642	74	99	0.182	0.0038	12.73	0.46	0.507	0.017	0.96
118	554	288	0.26	2691	34	2695	76	100	0.184	0.0038	13.18	0.47	0.519	0.018	0.96
119	594	285	0.17	2525	35	2523	72	100	0.167	0.0035	11.01	0.40	0.479	0.016	0.96
120	526	270	0.36	2663	34	2669	75	100	0.181	0.0037	12.81	0.46	0.513	0.018	0.96
124	1437	361	0.16	1903	37	1447	45	76	0.116	0.0024	4.04	0.15	0.252	0.009	0.96
125	691	354	0.26	2670	34	2670	75	100	0.182	0.0038	12.86	0.46	0.513	0.018	0.96
126	687	362	0.38	2723	34	2727	77	100	0.188	0.0039	13.64	0.49	0.527	0.018	0.96
127	309	158	0.27	2670	34	2663	75	100	0.182	0.0038	12.83	0.46	0.512	0.018	0.96
128	422	215	0.28	2661	34	2651	75	100	0.181	0.0037	12.68	0.46	0.509	0.018	0.96
129	788	370	0.30	2674	35	2485	71	93	0.182	0.0038	11.82	0.43	0.470	0.016	0.96
130	460	213	0.24	2705	34	2453	71	91	0.186	0.0039	11.86	0.43	0.463	0.016	0.96
131	542	251	0.14	2534	35	2449	71	97	0.168	0.0035	10.68	0.39	0.462	0.016	0.96
132	555	275	0.19	2610	34	2592	74	99	0.175	0.0036	11.97	0.43	0.495	0.017	0.96
133	726	382	0.47	2757	35	2728	77	99	0.192	0.0041	13.92	0.51	0.527	0.018	0.96
137	765	296	0.19	2575	35	2107	63	82	0.172	0.0036	9.16	0.33	0.387	0.013	0.96
140	1298	329	0.12	2339	35	1458	46	62	0.149	0.0031	5.23	0.19	0.254	0.009	0.96
141	679	303	0.23	2544	35	2377	70	93	0.169	0.0035	10.37	0.38	0.446	0.016	0.96
142	710	372	0.33	2721	34	2717	78	100	0.188	0.0039	13.56	0.49	0.524	0.018	0.96
144	716	372	0.29	2767	35	2694	77	97	0.193	0.0041	13.80	0.51	0.519	0.018	0.96
146	691	361	0.19	2720	34	2711	78	100	0.187	0.0039	13.51	0.50	0.523	0.018	0.96
150	680	279	0.12	2337	36	2213	66	95	0.149	0.0031	8.43	0.31	0.410	0.014	0.96
151	973	356	0.23	2679	34	2011	61	75	0.183	0.0038	9.23	0.34	0.366	0.013	0.96
152	455	232	0.15	2658	34	2656	77	100	0.181	0.0038	12.69	0.47	0.510	0.018	0.96
153	722	366	0.16	2668	35	2642	77	99	0.182	0.0039	12.68	0.47	0.507	0.018	0.96

154	386	199	0.39	2682	34	2682	78	100	0.183	0.0038	13.03	0.48	0.516	0.018	0.96
155	603	304	0.36	2700	34	2637	77	98	0.185	0.0039	12.90	0.48	0.505	0.018	0.96
156	2319	374	0.17	2342	35	964	32	41	0.150	0.0031	3.33	0.12	0.161	0.006	0.96
157	675	306	0.17	2498	35	2410	71	96	0.164	0.0034	10.26	0.38	0.453	0.016	0.96
158	477	251	0.38	2714	34	2724	79	100	0.187	0.0039	13.54	0.50	0.526	0.019	0.96
159	769	374	0.21	2605	35	2552	75	98	0.175	0.0037	11.71	0.43	0.486	0.017	0.96
Z DK 10 - (Malaputese Formation) Pink paragneiss (18° 30’ 42” S; 26° 57’ 36” E)															
7	1216	314	0.07	2468	34	1482	25	60	0.1612	0.0033	5.74	0.12	0.258	0.005	0.88
8	579	303	0.23	2712	33	2711	42	100	0.1865	0.0038	13.45	0.29	0.523	0.010	0.88
9	2029	496	0.24	2424	34	1410	24	58	0.1571	0.0032	5.30	0.11	0.245	0.005	0.88
10	2621	496	0.41	2389	34	1118	20	47	0.1538	0.0031	4.01	0.09	0.189	0.004	0.88
11	836	389	0.18	2552	34	2463	39	97	0.1695	0.0034	10.87	0.23	0.465	0.009	0.88
12	1188	422	0.08	2510	34	1961	32	78	0.1653	0.0033	8.10	0.17	0.355	0.007	0.88
13	1630	480	0.06	2356	34	1663	28	71	0.1509	0.0031	6.12	0.13	0.294	0.006	0.88
14	1910	573	0.05	2424	34	1690	28	70	0.1571	0.0032	6.49	0.14	0.300	0.006	0.88
15	1412	560	0.04	2541	34	2152	35	85	0.1683	0.0034	9.20	0.20	0.396	0.008	0.88
16	1008	381	0.11	2526	34	2068	34	82	0.1668	0.0034	8.70	0.19	0.378	0.007	0.88
20	1607	437	0.14	2384	34	1550	26	65	0.1534	0.0031	5.75	0.12	0.272	0.005	0.88
21	1411	551	0.04	2463	34	2126	35	86	0.1607	0.0033	8.65	0.19	0.391	0.008	0.88
22	939	500	0.29	2771	33	2751	43	99	0.1934	0.0039	14.20	0.31	0.532	0.010	0.88
23	1101	313	0.12	2291	35	1611	27	70	0.1453	0.0030	5.69	0.12	0.284	0.005	0.88
24	1480	414	0.06	2466	34	1588	27	64	0.1610	0.0033	6.20	0.14	0.279	0.005	0.88
25	776	413	0.30	2746	33	2749	43	100	0.1905	0.0039	13.96	0.30	0.532	0.010	0.89
26	910	476	0.32	2711	33	2712	43	100	0.1864	0.0038	13.45	0.29	0.523	0.010	0.89
27	2343	446	0.15	2311	35	1124	20	49	0.1470	0.0030	3.86	0.08	0.190	0.004	0.89
28	1109	435	0.08	2432	34	2133	35	88	0.1578	0.0032	8.53	0.19	0.392	0.008	0.89
29	1771	537	0.11	2491	34	1707	29	69	0.1634	0.0033	6.83	0.15	0.303	0.006	0.89
33	1678	411	0.08	2341	35	1413	25	60	0.1496	0.0030	5.06	0.11	0.245	0.005	0.89
34	1479	437	0.07	2243	35	1668	29	74	0.1413	0.0029	5.75	0.13	0.295	0.006	0.88
35	1592	392	0.16	2312	35	1418	25	61	0.1470	0.0030	4.99	0.11	0.246	0.005	0.89
36	1513	436	0.10	2364	34	1631	28	69	0.1516	0.0031	6.02	0.13	0.288	0.006	0.89
37	1567	347	0.25	2448	34	1289	23	53	0.1593	0.0032	4.86	0.11	0.221	0.004	0.89
38	1311	414	0.07	2466	34	1770	30	72	0.1610	0.0033	7.01	0.15	0.316	0.006	0.89
39	1685	487	0.11	2312	35	1638	28	71	0.1471	0.0030	5.87	0.13	0.289	0.006	0.89
40	858	444	0.31	2688	33	2686	43	100	0.1839	0.0037	13.10	0.29	0.517	0.010	0.89
41	839	350	0.30	2554	34	2247	37	88	0.1696	0.0035	9.75	0.22	0.417	0.008	0.89
42	987	397	0.09	2542	34	2181	36	86	0.1684	0.0034	9.35	0.21	0.403	0.008	0.89
46	821	403	0.04	2572	34	2574	42	100	0.1714	0.0035	11.60	0.26	0.491	0.010	0.89
47	620	271	0.06	2508	35	2339	39	93	0.1650	0.0035	9.95	0.22	0.437	0.009	0.88
48	843	434	0.33	2683	34	2674	43	100	0.1833	0.0037	12.99	0.29	0.514	0.010	0.89
49	1927	513	0.06	2357	34	1521	27	65	0.1510	0.0031	5.54	0.12	0.266	0.005	0.89
50	2625	597	0.08	2440	34	1321	24	54	0.1585	0.0032	4.97	0.11	0.227	0.005	0.89
51	858	453	0.28	2738	33	2733	44	100	0.1895	0.0038	13.79	0.31	0.528	0.010	0.89
52	1392	406	0.03	2376	34	1650	29	69	0.1527	0.0031	6.14	0.14	0.292	0.006	0.89
53	1921	457	0.17	2350	35	1375	25	58	0.1503	0.0031	4.93	0.11	0.238	0.005	0.89
54	1419	307	0.16	2360	35	1264	23	54	0.1513	0.0031	4.52	0.10	0.217	0.004	0.89
55	1045	544	0.32	2705	33	2702	44	100	0.1858	0.0038	13.33	0.30	0.521	0.010	0.89
59	1135	428	0.09	2607	34	2062	35	79	0.1751	0.0036	9.10	0.20	0.377	0.008	0.89

60	1947	458	0.08	2373	34	1362	24	57	0.1524	0.0031	4.95	0.11	0.235	0.005	0.89
61	1957	514	0.11	2475	34	1504	27	61	0.1619	0.0033	5.86	0.13	0.263	0.005	0.89
62	3191	482	0.18	2323	35	906	17	39	0.1480	0.0031	3.08	0.07	0.151	0.003	0.89
63	1640	446	0.08	2330	35	1549	28	66	0.1486	0.0030	5.56	0.12	0.272	0.005	0.89
64	893	309	0.14	2373	35	1916	33	81	0.1524	0.0031	7.27	0.16	0.346	0.007	0.89
65	1617	516	0.16	2443	34	1787	31	73	0.1588	0.0032	6.99	0.16	0.319	0.006	0.89
66	863	382	0.05	2512	34	2364	40	94	0.1654	0.0034	10.10	0.23	0.443	0.009	0.89
67	1279	310	0.32	2517	34	1399	25	56	0.1659	0.0034	5.55	0.12	0.242	0.005	0.89
68	1030	300	1.02	2700	34	1648	29	61	0.1853	0.0038	7.44	0.17	0.291	0.006	0.89
75	1760	469	0.75	2329	35	1523	27	65	0.1485	0.0030	5.46	0.12	0.267	0.005	0.89
76	961	462	0.22	2521	34	2529	42	100	0.1664	0.0034	11.02	0.25	0.480	0.010	0.89
77	1348	456	0.08	2401	35	1877	33	78	0.1549	0.0032	7.22	0.16	0.338	0.007	0.89
78	1534	459	0.05	2347	35	1689	30	72	0.1501	0.0031	6.20	0.14	0.300	0.006	0.89
79	2110	589	0.05	2422	34	1588	29	66	0.1568	0.0032	6.04	0.14	0.279	0.006	0.89
80	530	270	0.15	2659	34	2658	44	100	0.1806	0.0037	12.71	0.29	0.510	0.010	0.89
81	1484	639	0.07	2548	34	2309	39	91	0.1691	0.0035	10.04	0.23	0.431	0.009	0.89
85	1494	530	0.04	2442	34	1957	34	80	0.1587	0.0032	7.76	0.18	0.355	0.007	0.89
86	1426	677	0.03	2497	34	2503	42	100	0.1639	0.0034	10.72	0.25	0.474	0.010	0.89
87	2692	449	1.94	2285	35	994	19	44	0.1447	0.0030	3.33	0.08	0.167	0.003	0.89
88	1379	508	0.06	2464	34	2022	36	82	0.1608	0.0033	8.17	0.19	0.368	0.008	0.89
89	674	320	0.07	2509	35	2507	43	100	0.1652	0.0034	10.82	0.25	0.475	0.010	0.89
90	871	451	0.26	2694	34	2690	45	100	0.1845	0.0038	13.18	0.30	0.518	0.011	0.89
91	773	378	0.21	2562	34	2564	43	100	0.1705	0.0035	11.48	0.26	0.489	0.010	0.89
92	1417	591	0.18	2528	34	2246	39	89	0.1670	0.0034	9.60	0.22	0.417	0.009	0.89
93	1707	579	0.13	2380	35	1884	34	79	0.1531	0.0031	7.16	0.16	0.339	0.007	0.89
94	1407	413	0.28	2517	34	1658	30	66	0.1660	0.0034	6.71	0.15	0.293	0.006	0.90
98	1646	449	0.05	2390	35	1555	29	65	0.1539	0.0032	5.79	0.13	0.273	0.006	0.90
99	1231	410	0.05	2458	34	1853	33	75	0.1602	0.0033	7.35	0.17	0.333	0.007	0.90
100	1409	451	0.06	2013	37	1789	32	89	0.1239	0.0026	5.46	0.13	0.320	0.007	0.89
101	1497	394	0.15	2389	35	1504	28	63	0.1539	0.0032	5.58	0.13	0.263	0.005	0.90
102	1586	543	0.10	2472	34	1899	34	77	0.1616	0.0033	7.63	0.18	0.343	0.007	0.90
103	1578	617	0.06	2490	34	2127	38	85	0.1632	0.0033	8.80	0.20	0.391	0.008	0.90
104	948	402	0.07	2569	34	2278	40	89	0.1712	0.0035	10.00	0.23	0.424	0.009	0.90
105	1391	472	0.09	2495	35	1881	34	75	0.1637	0.0034	7.65	0.18	0.339	0.007	0.89
106	1099	566	0.24	2678	34	2677	46	100	0.1827	0.0037	12.97	0.30	0.515	0.011	0.90
107	1075	557	0.29	2695	34	2691	46	100	0.1846	0.0038	13.19	0.31	0.518	0.011	0.90
111	2467	477	1.58	2381	35	1141	22	48	0.1531	0.0031	4.09	0.10	0.194	0.004	0.90
112	1047	550	0.33	2731	34	2724	47	100	0.1887	0.0039	13.68	0.32	0.526	0.011	0.90
113	1335	554	0.17	2488	35	2240	40	90	0.1631	0.0034	9.34	0.22	0.415	0.009	0.90
114	1347	652	0.14	2540	34	2546	44	100	0.1682	0.0035	11.23	0.26	0.484	0.010	0.90
115	1496	400	0.07	2521	34	1526	29	61	0.1663	0.0034	6.13	0.14	0.267	0.006	0.90
116	880	413	0.07	2476	35	2478	43	100	0.1619	0.0033	10.47	0.25	0.469	0.010	0.90
117	1278	592	0.04	2553	34	2454	43	96	0.1695	0.0035	10.82	0.25	0.463	0.010	0.90
118	948	415	0.04	2524	35	2341	41	93	0.1666	0.0035	10.06	0.24	0.438	0.009	0.90
119	972	405	0.09	2454	35	2243	40	91	0.1599	0.0033	9.17	0.22	0.416	0.009	0.90
120	996	346	0.07	2487	35	1925	35	77	0.1630	0.0034	7.82	0.19	0.348	0.007	0.90
124	1286	417	0.08	2630	34	1809	33	69	0.1775	0.0037	7.93	0.19	0.324	0.007	0.90
125	992	507	0.21	2667	34	2660	46	100	0.1816	0.0038	12.79	0.30	0.511	0.011	0.90

126	1045	389	0.12	2489	35	2040	37	82	0.1632	0.0034	8.38	0.20	0.372	0.008	0.90
127	1447	372	0.08	2304	35	1475	28	64	0.1464	0.0030	5.19	0.12	0.257	0.005	0.90
128	1453	515	0.07	2454	35	1956	36	80	0.1598	0.0033	7.81	0.18	0.354	0.008	0.90
129	1779	463	0.07	2339	35	1492	28	64	0.1494	0.0031	5.36	0.13	0.260	0.006	0.90
130	719	368	0.03	2668	35	2667	47	100	0.1816	0.0039	12.83	0.31	0.513	0.011	0.89
131	1591	546	0.04	2415	35	1903	35	79	0.1562	0.0032	7.40	0.18	0.343	0.007	0.90
132	1189	471	0.12	2475	35	2151	39	87	0.1618	0.0034	8.84	0.21	0.396	0.008	0.90
133	873	318	0.09	2457	35	2002	37	82	0.1601	0.0033	8.04	0.19	0.364	0.008	0.90
140	1194	404	0.06	2465	35	1877	35	76	0.1609	0.0033	7.50	0.18	0.338	0.007	0.90
141	1975	408	0.17	2332	36	1210	24	52	0.1488	0.0032	4.24	0.10	0.206	0.004	0.90
142	1100	348	0.06	2386	36	1772	34	74	0.1535	0.0032	6.70	0.16	0.316	0.007	0.90
143	817	403	0.15	2583	36	2586	46	100	0.1726	0.0037	11.75	0.29	0.494	0.011	0.90
144	1711	591	0.12	2446	35	1912	36	78	0.1591	0.0033	7.58	0.18	0.345	0.007	0.90
145	1417	417	0.23	2389	35	1663	32	70	0.1538	0.0032	6.24	0.15	0.294	0.006	0.90
146	1067	560	0.28	2722	34	2720	48	100	0.1877	0.0039	13.58	0.33	0.525	0.011	0.90
150	1415	411	0.15	2418	36	1645	32	68	0.1565	0.0033	6.27	0.15	0.291	0.006	0.90
151	1379	429	0.04	2313	36	1747	33	76	0.1472	0.0031	6.31	0.15	0.311	0.007	0.90
152	2260	493	0.15	2369	35	1272	25	54	0.1520	0.0032	4.57	0.11	0.218	0.005	0.90
Z DK 11 - Archaean orthogneiss (18° 28’ 13” S; 26° 54’ 26” E)															
7	480	251	0.06	2707	33	2709	70	100	0.186	0.0038	13.39	0.44	0.522	0.016	0.95
10	1227	223	0.16	2366	35	1077	31	46	0.152	0.0031	3.81	0.13	0.182	0.006	0.95
11	540	127	0.95	2555	34	1364	39	53	0.170	0.0035	5.51	0.18	0.236	0.007	0.95
12	132	60	0.20	2645	34	2422	64	92	0.179	0.0037	11.27	0.37	0.456	0.014	0.95
13	413	197	0.05	2689	33	2514	66	93	0.184	0.0037	12.10	0.40	0.477	0.015	0.95
14	244	115	0.24	2684	33	2481	65	92	0.183	0.0037	11.87	0.39	0.470	0.015	0.95
15	669	216	0.07	2705	33	1800	50	67	0.186	0.0038	8.25	0.27	0.322	0.010	0.95
20	364	165	0.16	2702	33	2407	64	89	0.185	0.0037	11.57	0.39	0.453	0.014	0.95
21	310	161	0.03	2706	34	2698	70	100	0.186	0.0038	13.32	0.45	0.520	0.017	0.95
22	212	94	0.18	2677	35	2364	63	88	0.183	0.0038	11.15	0.37	0.443	0.014	0.95
24	591	253	0.03	2697	33	2297	61	85	0.185	0.0037	10.91	0.36	0.428	0.014	0.95
25	227	109	0.24	2714	34	2535	67	93	0.187	0.0039	12.41	0.42	0.482	0.015	0.95
26	862	188	0.04	2427	34	1274	37	53	0.157	0.0032	4.74	0.16	0.219	0.007	0.95
27	1136	122	0.05	1991	38	655	20	33	0.122	0.0026	1.80	0.06	0.107	0.003	0.95
28	857	238	0.07	2684	33	1581	45	59	0.183	0.0037	7.03	0.24	0.278	0.009	0.95
33	930	269	0.05	2693	33	1635	46	61	0.184	0.0037	7.34	0.25	0.289	0.009	0.95
34	403	156	0.06	2606	34	2103	57	81	0.175	0.0035	9.30	0.31	0.386	0.012	0.95
36	659	280	0.03	2702	33	2284	62	85	0.185	0.0037	10.87	0.37	0.425	0.014	0.95
38	558	243	0.17	2683	33	2333	63	87	0.183	0.0037	11.02	0.37	0.436	0.014	0.95
39	1117	205	0.05	2702	33	1088	32	40	0.185	0.0038	4.70	0.16	0.184	0.006	0.95
42	503	244	0.04	2719	33	2548	68	94	0.187	0.0038	12.52	0.42	0.485	0.016	0.95
46	723	279	0.06	2689	34	2105	58	78	0.184	0.0038	9.79	0.33	0.386	0.012	0.95
47	310	126	0.20	2638	34	2199	60	83	0.178	0.0037	10.00	0.34	0.406	0.013	0.95
48	548	216	0.08	2541	34	2138	59	84	0.168	0.0034	9.13	0.31	0.393	0.013	0.95
49	323	168	0.07	2692	33	2700	71	100	0.184	0.0037	13.22	0.45	0.520	0.017	0.95
50	758	247	0.03	2514	35	1817	51	72	0.166	0.0035	7.43	0.25	0.326	0.011	0.95
51	336	170	0.07	2683	34	2642	70	98	0.183	0.0038	12.80	0.43	0.507	0.016	0.95
52	345	178	0.03	2687	33	2686	71	100	0.184	0.0037	13.10	0.44	0.517	0.017	0.95
53	1098	235	0.12	2396	34	1251	37	52	0.154	0.0031	4.56	0.15	0.214	0.007	0.95

54	170	88	0.20	2695	35	2694	72	100	0.185	0.0040	13.21	0.45	0.519	0.017	0.95
63	985	210	0.06	2671	33	1248	37	47	0.182	0.0037	5.36	0.18	0.214	0.007	0.95
64	516	251	0.05	2693	33	2554	69	95	0.184	0.0037	12.36	0.42	0.486	0.016	0.95
65	379	196	0.32	2686	34	2693	72	100	0.184	0.0037	13.13	0.45	0.519	0.017	0.95
66	181	74	0.33	2672	35	2202	61	82	0.182	0.0039	10.22	0.35	0.407	0.013	0.95
67	412	188	0.14	2702	34	2429	66	90	0.185	0.0038	11.69	0.40	0.458	0.015	0.95
68	758	240	0.12	2690	33	1773	51	66	0.184	0.0037	8.03	0.27	0.317	0.010	0.96
72	322	168	0.17	2683	34	2698	72	101	0.183	0.0037	13.13	0.45	0.520	0.017	0.95
73	815	225	0.18	2583	34	1571	46	61	0.173	0.0035	6.57	0.22	0.276	0.009	0.96
74	521	271	0.03	2710	34	2695	72	99	0.186	0.0038	13.34	0.46	0.519	0.017	0.95
77	758	250	0.15	2695	33	1839	52	68	0.185	0.0038	8.40	0.29	0.330	0.011	0.95
79	328	110	0.18	2507	35	1860	53	74	0.165	0.0034	7.61	0.26	0.334	0.011	0.95
80	582	156	0.17	2681	33	1535	45	57	0.183	0.0037	6.78	0.23	0.269	0.009	0.96
85	491	253	0.05	2696	33	2682	72	99	0.185	0.0037	13.14	0.45	0.516	0.017	0.96
86	1317	296	0.07	2688	34	1308	39	49	0.184	0.0038	5.70	0.20	0.225	0.007	0.95
87	1582	247	0.04	2694	34	935	29	35	0.185	0.0038	3.97	0.14	0.156	0.005	0.95
89	1070	141	0.06	2059	36	796	25	39	0.127	0.0026	2.30	0.08	0.131	0.004	0.96
90	863	258	0.06	2487	34	1686	49	68	0.163	0.0033	6.72	0.23	0.299	0.010	0.96
92	668	239	0.10	2698	33	1975	56	73	0.185	0.0038	9.14	0.32	0.358	0.012	0.96
93	1156	265	0.06	2690	33	1331	40	49	0.184	0.0037	5.82	0.20	0.229	0.008	0.96
94	882	165	0.12	2315	35	1105	34	48	0.147	0.0030	3.80	0.13	0.187	0.006	0.96
98	828	273	0.09	2694	33	1834	53	68	0.185	0.0038	8.37	0.29	0.329	0.011	0.96
102	571	255	0.06	2687	34	2379	66	89	0.184	0.0037	11.31	0.39	0.446	0.015	0.96
104	53	22	0.11	2691	38	2265	64	84	0.184	0.0043	10.69	0.38	0.421	0.014	0.95
105	1036	253	0.05	2694	34	1408	42	52	0.184	0.0038	6.21	0.22	0.244	0.008	0.96
107	535	274	0.10	2697	34	2668	73	99	0.185	0.0038	13.07	0.46	0.513	0.017	0.96
112	543	267	0.35	2691	33	2575	71	96	0.184	0.0037	12.47	0.44	0.491	0.016	0.96
114	534	281	0.10	2708	33	2725	75	101	0.186	0.0038	13.50	0.47	0.526	0.018	0.96
116	408	189	0.30	2685	35	2457	69	91	0.184	0.0039	11.74	0.41	0.464	0.016	0.95
117	700	241	0.21	2718	33	1911	56	70	0.187	0.0038	8.91	0.31	0.345	0.012	0.96
124	446	205	0.05	2698	34	2442	69	91	0.185	0.0038	11.74	0.41	0.460	0.016	0.96
125	853	211	0.07	2694	34	1425	43	53	0.185	0.0038	6.29	0.22	0.247	0.008	0.96
126	660	244	0.10	2695	33	2027	59	75	0.185	0.0038	9.41	0.33	0.369	0.012	0.96
127	384	158	0.39	2638	36	2224	64	84	0.178	0.0039	10.13	0.36	0.412	0.014	0.95
129	654	213	0.06	2566	34	1816	54	71	0.171	0.0035	7.66	0.27	0.325	0.011	0.96
131	416	216	0.03	2721	34	2697	75	99	0.188	0.0039	13.43	0.48	0.520	0.018	0.96
132	576	281	0.17	2696	34	2565	72	95	0.185	0.0038	12.45	0.44	0.489	0.017	0.96
138	537	241	0.03	2662	34	2389	68	90	0.181	0.0037	11.19	0.40	0.448	0.015	0.96
139	510	266	0.06	2707	34	2705	75	100	0.186	0.0039	13.37	0.48	0.521	0.018	0.96
143	564	239	0.25	2692	34	2280	66	85	0.184	0.0038	10.78	0.38	0.424	0.015	0.96
144	282	137	0.16	2679	34	2548	72	95	0.183	0.0038	12.22	0.44	0.485	0.017	0.96
145	280	145	0.06	2693	34	2690	75	100	0.184	0.0038	13.17	0.47	0.518	0.018	0.96
151	438	191	0.07	2667	34	2330	67	87	0.182	0.0038	10.90	0.39	0.435	0.015	0.96
154	514	219	0.05	2632	35	2288	66	87	0.178	0.0037	10.45	0.38	0.426	0.015	0.96
155	391	192	0.07	2657	34	2580	73	97	0.180	0.0038	12.25	0.44	0.492	0.017	0.96
156	583	280	0.17	2704	34	2527	72	93	0.186	0.0039	12.29	0.44	0.480	0.017	0.96
157	643	189	0.12	2685	34	1659	50	62	0.184	0.0038	7.43	0.27	0.294	0.010	0.96
158	501	260	0.14	2690	34	2691	76	100	0.184	0.0038	13.15	0.47	0.518	0.018	0.96

159	677	270	0.04	2705	35	2165	64	80	0.186	0.0040	10.22	0.37	0.399	0.014	0.96
Z DK 12 - Foliated biotite orthogneiss (18° 25’ 59” S; 26° 50’ 50” E)															
9	452	166	0.42	2051	36	2014	46	98	0.127	0.0026	6.40	0.18	0.367	0.010	0.93
10	660	231	0.26	2028	37	1931	44	95	0.125	0.0026	6.02	0.17	0.349	0.009	0.93
11	695	233	0.29	2021	36	1864	43	92	0.124	0.0025	5.75	0.16	0.335	0.009	0.93
12	509	187	0.71	2021	36	2018	46	100	0.124	0.0026	6.31	0.18	0.368	0.010	0.93
13	799	258	0.55	2027	38	1804	42	89	0.125	0.0027	5.56	0.16	0.323	0.009	0.93
14	504	185	0.24	2031	36	2012	46	99	0.125	0.0026	6.32	0.18	0.366	0.010	0.93
15	840	297	0.78	2031	37	1954	45	96	0.125	0.0026	6.11	0.17	0.354	0.009	0.93
20	759	265	0.19	2022	37	1933	45	96	0.124	0.0026	6.00	0.17	0.350	0.009	0.93
27	534	191	0.32	2025	36	1968	46	97	0.125	0.0026	6.14	0.18	0.357	0.010	0.93
28	515	190	0.29	2016	36	2024	47	100	0.124	0.0026	6.31	0.18	0.369	0.010	0.93
33	234	87	0.23	2041	37	2031	47	100	0.126	0.0026	6.42	0.19	0.370	0.010	0.93
34	677	242	0.22	2036	37	1971	46	97	0.126	0.0026	6.19	0.18	0.358	0.010	0.93
39	571	206	0.19	2038	38	1984	47	97	0.126	0.0027	6.24	0.18	0.360	0.010	0.93
40	424	137	0.16	2032	36	1809	43	89	0.125	0.0026	5.59	0.16	0.324	0.009	0.94
41	550	177	0.17	2027	36	1801	43	89	0.125	0.0026	5.55	0.16	0.322	0.009	0.94
49	838	288	0.19	2030	36	1908	46	94	0.125	0.0026	5.94	0.18	0.344	0.010	0.94
51	568	198	0.14	2024	36	1929	46	95	0.125	0.0025	5.99	0.18	0.349	0.010	0.94
62	690	245	0.33	2026	36	1959	47	97	0.125	0.0026	6.11	0.18	0.355	0.010	0.94
63	677	251	0.22	2047	36	2029	49	99	0.126	0.0026	6.44	0.19	0.370	0.010	0.94
68	489	181	0.40	2026	36	2029	49	100	0.125	0.0026	6.36	0.19	0.370	0.010	0.94
72	641	187	0.20	2032	36	1650	41	81	0.125	0.0026	5.04	0.15	0.292	0.008	0.94
76	743	248	0.40	2019	36	1854	46	92	0.124	0.0025	5.71	0.17	0.333	0.010	0.94
77	470	176	0.16	2038	37	2053	50	101	0.126	0.0026	6.50	0.20	0.375	0.011	0.94
80	595	220	0.28	2020	37	2031	50	101	0.124	0.0026	6.35	0.19	0.370	0.011	0.94
88	762	284	0.13	2027	37	2040	51	101	0.125	0.0026	6.41	0.20	0.372	0.011	0.94
89	676	235	0.35	2011	36	1927	48	96	0.124	0.0026	5.95	0.18	0.348	0.010	0.94
90	192	69	0.41	2051	37	1987	50	97	0.127	0.0027	6.30	0.19	0.361	0.011	0.94
92	460	171	0.28	2025	36	2035	51	101	0.125	0.0026	6.38	0.20	0.371	0.011	0.94
93	399	150	0.28	2023	36	2054	51	102	0.125	0.0026	6.45	0.20	0.375	0.011	0.94
102	519	186	0.60	2035	36	1971	50	97	0.125	0.0026	6.18	0.19	0.358	0.011	0.94
103	902	314	0.11	2020	37	1925	49	95	0.124	0.0026	5.97	0.19	0.348	0.010	0.94
106	702	240	0.27	2021	36	1894	49	94	0.124	0.0026	5.86	0.18	0.341	0.010	0.94
114	629	233	0.42	2026	36	2027	52	100	0.125	0.0026	6.36	0.20	0.370	0.011	0.95
115	787	275	0.21	2023	36	1930	50	95	0.125	0.0026	6.00	0.19	0.349	0.010	0.95
116	230	85	0.29	2029	37	2021	52	100	0.125	0.0026	6.35	0.20	0.368	0.011	0.94
117	694	262	0.16	2054	36	2062	53	100	0.127	0.0026	6.59	0.21	0.377	0.011	0.95
118	946	312	0.24	2018	36	1835	48	91	0.124	0.0026	5.64	0.18	0.329	0.010	0.95
120	783	283	0.42	2035	36	1987	52	98	0.125	0.0026	6.24	0.20	0.361	0.011	0.95
124	415	150	0.25	2038	36	1985	52	97	0.126	0.0026	6.25	0.20	0.361	0.011	0.95
127	944	316	0.28	2038	37	1862	49	91	0.126	0.0027	5.80	0.19	0.335	0.010	0.94
128	768	283	0.16	2017	37	2020	53	100	0.124	0.0026	6.30	0.20	0.368	0.011	0.95
131	880	302	0.23	2022	36	1902	50	94	0.125	0.0026	5.89	0.19	0.343	0.011	0.95
132	820	287	0.63	2049	36	1935	51	94	0.126	0.0026	6.10	0.20	0.350	0.011	0.95
138	780	278	0.40	2027	36	1965	52	97	0.125	0.0026	6.14	0.20	0.356	0.011	0.95
139	777	289	0.44	2016	37	2038	54	101	0.124	0.0026	6.36	0.21	0.372	0.012	0.95
140	789	293	0.71	2047	36	2034	54	99	0.126	0.0026	6.46	0.21	0.371	0.011	0.95

150	698	233	0.35	2040	40	1858	51	91	0.126	0.0029	5.79	0.19	0.334	0.011	0.94
151	553	182	0.54	2044	37	1832	50	90	0.126	0.0027	5.71	0.19	0.329	0.010	0.95
153	643	210	0.45	2028	37	1821	50	90	0.125	0.0026	5.62	0.19	0.326	0.010	0.95
154	710	261	0.35	2018	37	2017	55	100	0.124	0.0026	6.30	0.21	0.367	0.012	0.95
155	751	273	0.34	2035	37	2001	54	98	0.125	0.0026	6.29	0.21	0.364	0.012	0.95
156	762	282	0.17	2024	37	2033	55	100	0.125	0.0026	6.37	0.21	0.371	0.012	0.95
157	841	312	0.25	2025	36	2037	55	101	0.125	0.0026	6.39	0.21	0.372	0.012	0.95
159	554	201	0.21	2035	37	1995	55	98	0.125	0.0026	6.27	0.21	0.363	0.012	0.95

[a]U and Pb concentrations and Th/U ratios are calculated relative to GJ-1 reference zircon

[b]Corrected for background and within-run Pb/U fractionation and normalised to reference zircon GJ-1 (ID-TIMS values/measured value); $^{207}Pb/^{235}U$ calculated using $(^{207}Pb/^{206}Pb)/(^{238}U/^{206}Pb * 1/137.88)$

[c] Is the error correlation defined as the quotient of the propagated errors of the $^{206}Pb/^{238}U$ and the $^{207}/^{235}U$ ratio

[d]Quadratic addition of within-run errors (2 SD) and daily reproducibility of GJ-1 (2 SD)

[e]Corrected for mass-bias by normalising to GJ-1 reference zircon (~0.6 per atomic mass unit) and common Pb using the model Pb composition of Stacey & Kramers (1975)

Pb_c and Pb* indicate the common and radiogenic proportions respectively

(1) Corrected for common Pb

Table 5.2: SIMS U-Pb zircon data for various rocks within the Dete-Kamativi Inlier

Spot	Comment	% $^{206}Pb_c$	µg/g U	µg/g Th	µg/g $^{*206}Pb$	$^{232}Th/^{238}U$ Meas	$^{207}Pb/^{206}Pb$ age (1)	± 1sd	$^{206}Pb/^{238}U$ age (1)	± 1sd	% Disc (2sd)	$^{*207}Pb/^{*206}Pb$	± 1sd	$^{*207}Pb/^{235}Pb$	± 1sd	$^{*206}Pb/^{238}Pb$	± 1sd	Error Correlation
Z DK 13/2 - Archaean orthogneiss (18° 30' 07.7" S; 26° 55' 47.5" E)																		
DK13-2@1	core	{0.00}	144	75	101	0.521	2771.2	4.2	2724.4	25.1		0.19339	0.26	14.02384	1.15	0.5259	1.13	0.97507
DK13-2@02	c	{0.01}	467	142	290	0.305	2674.6	5.1	2581.0	24.3	-1.7	0.18238	0.31	12.38172	1.18	0.4924	1.14	0.96549
DK13-2@03	rim	0.61	668	166	393	0.249	2708.1	8.0	2480.1	23.7	-7.3	0.18611	0.49	12.03997	1.25	0.4692	1.15	0.92090
DK13-2@04	c	{0.01}	82	36	58	0.442	2779.0	8.1	2767.7	25.5		0.19431	0.50	14.36704	1.23	0.5363	1.13	0.91520
DK13-2@05	r	{0.00}	717	56	428	0.078	2713.5	6.4	2591.7	24.2	-2.8	0.18672	0.39	12.74027	1.20	0.4949	1.13	0.94513
DK13-2@06	r	0.13	606	894	472	1.475	2736.2	3.2	2606.2	24.5	-3.5	0.18932	0.20	13.00538	1.16	0.4982	1.14	0.98562
DK13-2@07	c	0.01	550	13	341	0.024	2745.5	11.9	2693.6	25.4		0.19039	0.73	13.61585	1.36	0.5187	1.15	0.84515
DK13-2@08	c	0.10	416	168	277	0.405	2727.7	6.7	2674.5	25.5		0.18834	0.41	13.35234	1.23	0.5142	1.16	0.94309
DK13-2@09	c	0.04	3478	647	887	0.186	2409.3	32.5	1240.7	117.3	-40.5	0.15568	1.93	4.55559	10.48	0.2122	10.30	0.98280
DK13-2@10	c	0.01	1464	485	1001	0.331	2720.5	2.8	2775.1	32.4		0.18752	0.17	13.91059	1.44	0.5380	1.43	0.99317
DK13-2@11	r	0.24	447	145	281	0.324	2727.9	3.9	2589.4	24.0	-3.9	0.18836	0.24	12.83799	1.15	0.4943	1.13	0.97882
DK13-2@12	c	0.09	1490	856	809	0.575	2619.1	2.6	2215.9	24.1	-16.0	0.17638	0.15	9.97581	1.29	0.4102	1.28	0.99281
DK13-2@13	r	0.10	510	391	378	0.768	2768.7	2.3	2757.5	25.7		0.19309	0.14	14.21172	1.15	0.5338	1.14	0.99277
DK13-2@14	c	0.01	816	328	519	0.402	2716.4	2.2	2579.3	26.5	-3.7	0.18705	0.14	12.68881	1.25	0.4920	1.24	0.99415
DK13-2@15		0.01	684	399	500	0.584	2770.3	3.3	2802.5	27.3		0.19328	0.20	14.51226	1.22	0.5446	1.20	0.98640
DK13-2@16	r	0.62	250	91	156	0.365	2722.5	7.1	2556.2	25.0	-4.6	0.18774	0.43	12.59750	1.26	0.4866	1.18	0.93962
DK13-2@17	r	0.28	196	64	110	0.326	2750.7	4.2	2351.0	27.1	-14.8	0.19099	0.26	11.58918	1.39	0.4401	1.37	0.98290
DK13-2@18	c	0.17	298	90	174	0.301	2688.0	6.7	2427.5	25.6	-8.9	0.18386	0.40	11.59202	1.33	0.4573	1.26	0.95257
DK13-2@19	c	0.09	908	364	619	0.401	2717.9	3.3	2717.5	26.4		0.18722	0.20	13.53528	1.20	0.5243	1.19	0.98636
DK13-2@20	r	0.01	1215	26	699	0.022	2643.7	2.6	2556.6	24.3	-1.7	0.17901	0.15	12.01411	1.16	0.4868	1.15	0.99104
DK13-2@21		0.78	500	167	338	0.333	2767.3	13.8	2728.5	28.7		0.19293	0.85	14.01663	1.54	0.5269	1.29	0.83597
DK13-2@22	c	{0.01}	139	48	94	0.347	2740.3	3.9	2713.4	25.7		0.18978	0.24	13.69488	1.18	0.5234	1.16	0.98003
DK13-2@23	c	0.02	138	75	100	0.540	2774.8	3.9	2771.7	25.8		0.19381	0.24	14.35529	1.17	0.5372	1.14	0.97899
DK13-2@24	r	0.03	904	47	581	0.052	2731.6	3.6	2754.2	25.7		0.18878	0.22	13.87450	1.16	0.5330	1.14	0.98255
DK13-2@25	r	0.01	480	44	298	0.091	2710.2	13.2	2669.3	24.9		0.18635	0.81	13.17968	1.39	0.5130	1.14	0.81566
DK13-2@26	c	0.01	533	180	357	0.338	2726.5	5.2	2709.8	25.4		0.18820	0.32	13.55802	1.19	0.5225	1.15	0.96396
DK13-2@27	c	0.01	812	28	511	0.034	2712.7	9.6	2723.4	25.4		0.18663	0.58	13.52866	1.28	0.5257	1.14	0.89072
DK13-2@28	c	0.01	712	425	503	0.597	2722.7	2.7	2712.2	25.2		0.18777	0.17	13.54225	1.15	0.5231	1.14	0.98945
Z DK 13/5 - (Tshontanda Formation) Sillimanite-garnet paragneiss (18° 30' 44.3" S; 26° 37' 59.8" E)																		
DK13-5@1	c	2.31	920	334	227	0.363	2062.5	25.9	1163.2	50.9	-39.2	0.12741	1.48	3.47400	4.99	0.1978	4.77	0.95486
DK13-5@2	c	1.82	266	172	132	0.649	2175.9	16.3	2043.1	31.9	-1.9	0.13592	0.94	6.98891	2.05	0.3729	1.82	0.88793
DK13-5@3	c	0.06	135	64	68	0.473	2198.9	5.0	2133.9	20.5	-1.0	0.13773	0.29	7.45149	1.16	0.3924	1.13	0.96906
DK13-5@4	r	3.91	1868	1001	191	0.536	2054.0	9.6	485.0	7.5	-76.3	0.12680	0.55	1.36610	1.70	0.0781	1.61	0.94671
DK13-5@5	c	0.48	446	94	195	0.212	2529.3	5.4	1964.5	28.2	-23.1	0.16715	0.32	8.21091	1.69	0.3563	1.66	0.98161
DK13-5@6	c	0.09	437	86	298	0.196	2870.5	19.9	2785.3	25.8		0.20551	1.23	15.31388	1.68	0.5404	1.14	0.67934
DK13-5@7	c	0.61	929	243	322	0.261	2372.8	3.8	1661.2	17.0	-32.1	0.15238	0.22	6.17560	1.18	0.2939	1.16	0.98208
DK13-5@8	c	5.61	1920	727	286	0.379	1933.9	37.7	750.8	41.9	-53.4	0.11851	2.13	2.01848	6.26	0.1235	5.89	0.94025
DK13-5@9	r	0.01	356	77	167	0.216	2199.1	3.1	2126.1	20.5	-1.6	0.13775	0.18	7.42051	1.14	0.3907	1.13	0.98735
DK13-5@10		4.43	2126	1912	277	0.900	1985.2	33.1	564.3	30.5	-64.7	0.12197	1.88	1.53850	5.95	0.0915	5.64	0.94872
DK13-5@11	c	0.02	341	68	153	0.201	2158.4	4.6	2051.1	23.5	-3.0	0.13456	0.26	6.95073	1.36	0.3746	1.33	0.98116
DK13-5@12	c	1.34	583	205	157	0.352	2189.4	20.4	1245.4	75.3	-38.6	0.13698	1.18	4.02503	6.71	0.2131	6.61	0.98435
DK13-5@13	c	{0.03}	80	60	56	0.744	2742.7	13.6	2617.4	40.7	-0.7	0.19007	0.83	13.12506	2.06	0.5008	1.89	0.91559
DK13-5@14		4.46	1697	1335	268	0.787	1972.8	44.4	779.2	40.9	-51.3	0.12112	2.53	2.14583	6.11	0.1285	5.56	0.91033
DK13-5@15	c	0.72	147	57	55	0.387	2147.9	11.8	1703.4	51.4	-17.5	0.13376	0.68	5.57785	3.49	0.3024	3.42	0.98085
DK13-5@16	r	3.59	1702	292	[329]	0.171	1964.4	40.5	970.0	46.5	-42.7	0.12055	2.30	2.69894	5.64	0.1624	5.15	0.91304
DK13-5@17	c	0.01	515	115	293	0.224	2493.7	8.4	2453.2	23.8		0.16365	0.50	10.44924	1.27	0.4631	1.17	0.91874
DK13-5@18	c	0.02	194	110	137	0.569	2737.8	5.7	2710.6	26.1		0.18949	0.35	13.65660	1.23	0.5227	1.18	0.95903
DK13-5@19	r	1.78	1398	417	255	0.299	2057.7	19.6	945.2	35.9	-51.8	0.12706	1.12	2.76644	4.23	0.1579	4.08	0.96427
DK13-5@20		1.20	108	91	43	0.846	2280.5	15.9	1688.9	61.0	-22.5	0.14439	0.93	5.96269	4.19	0.2995	4.08	0.97508
DK13-5@21	c	0.65	691	335	271	0.485	2052.8	9.3	1769.3	23.9	-12.3	0.12671	0.53	5.51757	1.63	0.3158	1.54	0.94545
DK13-5@22	r	1.83	1770	382	346	0.216	2318.6	19.5	987.3	17.8	-56.5	0.14763	1.14	3.36883	2.25	0.1655	1.94	0.86113
DK13-5@23	r	0.03	239	72	113	0.301	2141.0	5.1	2108.4	20.5		0.13323	0.29	7.10699	1.17	0.3869	1.14	0.96904

DK13-5@24	r	2.24	1593	290	272	0.182	1995.2	22.0	911.1	13.6	-52.1	0.12266	1.25	2.56751	2.03	0.1518	1.60	0.78757
DK13-5@25	c	{0.01}	327	65	146	0.199	2076.2	5.1	2060.1	26.6		0.12840	0.29	6.66622	1.53	0.3765	1.50	0.98189
Z DK 13/6 - Foliated biotite orthogneiss (18° 30' 49.0" S; 26° 38' 35.8" E)																		
DK13-6@1	c	0.10	107	104	57	0.972	2068.7	9.0	2066.0	20.4		0.12785	0.51	6.65991	1.26	0.3778	1.15	0.91296
DK13-6@2	c	{0.00}	166	101	80	0.606	2073.8	5.8	2031.1	19.6		0.12823	0.33	6.54806	1.17	0.3704	1.13	0.95941
DK13-6@3	c	0.51	284	94	121	0.329	2124.6	6.3	1923.1	22.6	-8.1	0.13199	0.36	6.32583	1.40	0.3476	1.36	0.96641
DK13-6@4	r	0.11	1266	427	506	0.337	2045.8	2.5	1819.7	18.1	-10.6	0.12620	0.14	5.67548	1.15	0.3262	1.14	0.99228
DK13-6@5	c	0.00	2568	292	865	0.114	2017.7	9.0	1648.0	60.6	-13.8	0.12422	0.51	4.98922	4.18	0.2913	4.15	0.99252
DK13-6@6	c	{0.01}	311	151	152	0.484	2134.9	4.7	2104.3	20.9		0.13277	0.27	7.06637	1.20	0.3860	1.16	0.97386
DK13-6@7	r	2.85	1492	338	349	0.226	1965.6	15.3	1154.4	13.9	-40.8	0.12064	0.86	3.26183	1.57	0.1961	1.31	0.83600
DK13-6@8	r	0.24	954	204	312	0.214	2031.1	4.4	1588.9	16.1	-22.5	0.12516	0.25	4.82352	1.17	0.2795	1.14	0.97708
DK13-6@9	c	0.01	279	173	133	0.621	2071.2	6.6	2010.5	26.7	0.0	0.12804	0.37	6.46109	1.59	0.3660	1.54	0.97198
DK13-6@10	c	0.05	1432	171	590	0.120	2057.3	2.6	1960.2	19.8	-3.2	0.12703	0.15	6.22436	1.18	0.3554	1.17	0.99238
DK13-6@11	r	0.02	482	296	239	0.615	2069.6	3.6	2079.7	20.1		0.12792	0.21	6.71527	1.15	0.3807	1.13	0.98363
DK13-6@12	c	{0.00}	353	176	163	0.499	2069.1	5.5	2006.7	19.6	-0.9	0.12788	0.31	6.43908	1.18	0.3652	1.13	0.96421
DK13-6@13	r	{0.01}	396	120	169	0.302	2060.3	3.9	1962.9	19.1	-3.1	0.12725	0.22	6.24486	1.15	0.3559	1.13	0.98165
DK13-6@14	c	0.03	574	610	304	1.062	2066.7	4.0	2054.5	19.9		0.12771	0.22	6.60950	1.15	0.3753	1.13	0.98073
DK13-6@15	r	0.12	1715	101	884	0.059	2654.6	7.1	2312.4	35.2	-11.8	0.18018	0.43	10.71982	1.86	0.4315	1.81	0.97284
DK13-6@16	c	0.01	2142	2133	1109	0.996	2048.7	4.1	2017.0	19.8		0.12641	0.23	6.40317	1.16	0.3674	1.14	0.97966
DK13-6@17	c	0.54	217	114	97	0.524	2059.4	7.5	1927.2	21.7	-4.4	0.12718	0.43	6.11034	1.37	0.3484	1.30	0.95021
DK13-6@18	c	0.10	775	129	314	0.166	2053.8	2.7	1908.2	21.5	-5.7	0.12678	0.15	6.02171	1.31	0.3445	1.30	0.99332
DK13-6@19	c	0.15	316	167	152	0.530	2063.5	4.3	2053.2	20.1		0.12748	0.24	6.59282	1.16	0.3751	1.14	0.97795
DK13-6@20	c	{0.02}	131	88	66	0.672	2068.0	5.7	2074.0	20.4		0.12780	0.32	6.68756	1.19	0.3795	1.15	0.96256
DK13-6@21	c	0.01	386	68	178	0.176	2060.6	4.0	2132.2	20.7	1.5	0.12727	0.23	6.87884	1.16	0.3920	1.14	0.98020
DK13-6@22	c	0.03	404	119	206	0.295	2250.0	6.2	2236.3	21.6		0.14186	0.36	8.11078	1.19	0.4147	1.14	0.95379
DK13-6@23	c	{0.02}	92	36	43	0.388	2064.9	6.8	2052.1	20.0		0.12758	0.38	6.59361	1.20	0.3748	1.14	0.94765
DK13-6@24	c	0.01	447	353	233	0.789	2065.3	3.1	2099.7	20.7		0.12761	0.18	6.77418	1.16	0.3850	1.15	0.98857
DK13-6@25	c	0.03	319	117	147	0.366	2071.7	4.5	2045.0	20.5		0.12807	0.25	6.59238	1.19	0.3733	1.17	0.97717
DK13-6@26	r	0.07	126	49	58	0.388	2052.6	6.3	2056.7	20.1		0.12669	0.36	6.56509	1.20	0.3758	1.14	0.95379
DK13-6@27	c	0.01	1780	243	590	0.136	2013.9	3.4	1613.5	16.7	-20.5	0.12395	0.19	4.86076	1.18	0.2844	1.17	0.98707
DK13-6@28	r	4.01	1379	276	268	0.200	1871.4	38.4	1002.2	43.5	-38.8	0.11446	2.16	2.65461	5.14	0.1682	4.67	0.90777
DK13-6@29	c	0.23	1313	150	409	0.114	2032.7	10.8	1527.7	120.8	-14.9	0.12527	0.61	4.61905	8.82	0.2674	8.80	0.99758
Z DK 13/7B - Biotite orthogneiss (18° 30' 42.7" S; 26° 39' 24.5" E)																		
DK13-7B@2	c	0.22	710	177	270	0.250	2029.4	6.2	1749.8	17.5	-13.3	0.12504	0.35	5.37644	1.19	0.3118	1.14	0.95603
DK13-7B@3	c	0.02	943	84	398	0.089	2048.3	2.2	2009.7	19.5		0.12639	0.12	6.37478	1.13	0.3658	1.13	0.99392
DK13-7B@4	c	0.82	3742	566	814	0.151	1840.8	4.4	1105.4	28.4	-40.0	0.11254	0.24	2.90258	2.80	0.1871	2.79	0.99619
DK13-7B@5	c	0.28	1622	232	624	0.143	2018.5	2.5	1826.6	37.3	-6.7	0.12427	0.14	5.61282	2.34	0.3276	2.34	0.99812
DK13-7B@6	r	0.04	1900	1009	565	0.531	1978.5	7.1	1346.4	13.7	-33.0	0.12151	0.40	3.89146	1.20	0.2323	1.13	0.94316
DK13-7B@7	c	{0.01}	484	322	243	0.665	2051.8	3.8	2083.0	20.6		0.12664	0.22	6.66007	1.17	0.3814	1.15	0.98264
DK13-7B@8	c	0.20	1559	923	599	0.592	1982.6	6.3	1684.1	43.4	-12.0	0.12179	0.35	5.01322	2.94	0.2985	2.92	0.99272
DK13-7B@9	c	0.21	2136	475	514	0.223	1954.8	4.1	1161.9	34.1	-40.5	0.11990	0.23	3.26531	3.20	0.1975	3.19	0.99743
DK13-7B@10	c	0.02	943	607	455	0.644	2046.2	3.1	2032.8	19.7		0.12624	0.18	6.45262	1.14	0.3707	1.13	0.98782
DK13-7B@11	c	0.32	1207	593	445	0.491	1999.7	2.9	1639.1	16.4	-18.5	0.12296	0.16	4.90845	1.14	0.2895	1.13	0.98982
DK13-7B@12	r	0.43	3323	246	691	0.074	1919.0	34.4	1067.7	36.7	-38.2	0.11753	1.94	2.91889	4.19	0.1801	3.72	0.88633
DK13-7B@13	r	0.46	1803	198	533	0.110	1922.1	12.9	1460.6	36.8	-21.6	0.11773	0.72	4.12804	2.90	0.2543	2.81	0.96839
DK13-7B@14	c	0.17	336	118	138	0.352	2021.7	10.3	1889.6	24.9	-3.7	0.12450	0.58	5.84698	1.62	0.3406	1.51	0.93370
DK13-7B@15	r	1.29	960	245	321	0.255	1964.4	6.3	1546.7	18.4	-21.3	0.12055	0.35	4.50729	1.38	0.2712	1.33	0.96703
DK13-7B@16	c	0.55	412	149	155	0.362	2019.9	6.4	1686.6	36.0	-14.5	0.12437	0.36	5.12836	2.44	0.2991	2.42	0.98891
DK13-7B@17	c	{0.00}	520	291	251	0.559	2046.6	3.0	2051.8	20.6		0.12627	0.17	6.52440	1.18	0.3748	1.17	0.98964
DK13-7B@18	r	2.23	3392	80	405	0.024	1367.4	21.5	611.8	8.2	-51.1	0.08731	1.13	1.19848	1.80	0.0996	1.40	0.77978
DK13-7B@19	r	3.10	5688	419	581	0.074	1421.3	109.9	477.5	30.4	-33.7	0.08980	5.97	0.95187	8.89	0.0769	6.59	0.74123
DK13-7B@20	r	0.07	2559	76	490	0.030	1837.5	4.2	1014.2	10.7	-46.7	0.11234	0.23	2.63906	1.17	0.1704	1.14	0.98003
Z DK 13/8A - (Inyantue Formation) Paragneiss with leucocratic phase (18° 26' 32.7" S; 26° 46' 53.8" E)																		
DK13-8A@1	c	0.33	821	336	350	0.410	2029.3	5.4	1881.0	18.6	-5.9	0.12504	0.31	5.84119	1.18	0.3388	1.14	0.96578
DK13-8A@2		0.02	1957	60	787	0.031	2004.9	1.5	1963.2	47.6		0.12333	0.09	6.05348	2.81	0.3560	2.80	0.99954

DK13-8A@3	c	0.11	1133	49	372	0.043	1899.0	4.4	1651.0	16.4	-12.6	0.11623	0.24	4.67766	1.15	0.2919	1.13	0.97748
DK13-8A@4	c	0.01	868	190	345	0.219	2022.8	6.6	1857.4	18.7	-6.7	0.12458	0.38	5.73569	1.22	0.3339	1.16	0.95098
DK13-8A@5	c	0.13	2107	1647	838	0.782	1967.2	7.1	1669.3	25.2	-13.8	0.12074	0.40	4.92063	1.76	0.2956	1.71	0.97368
DK13-8A@6	c	0.76	2326	210	442	0.090	1624.6	88.9	989.2	42.6	-17.2	0.10003	4.93	2.28727	6.76	0.1658	4.63	0.68496
DK13-8A@7	c	0.02	925	365	413	0.394	2054.0	3.2	1968.9	19.4	-2.5	0.12679	0.18	6.24469	1.15	0.3572	1.14	0.98776
DK13-8A@8	c	0.00	1200	658	578	0.548	2047.6	3.2	2041.6	19.9		0.12634	0.18	6.49049	1.15	0.3726	1.13	0.98778
DK13-8A@9	c	1.48	2575	348	679	0.135	1866.2	46.9	1317.3	20.1	-20.2	0.11413	2.64	3.56784	3.13	0.2267	1.68	0.53749
DK13-8A@10	c	0.11	1399	1020	685	0.729	2041.4	2.7	2017.3	20.7		0.12589	0.15	6.37785	1.20	0.3674	1.19	0.99175
DK13-8A@11	r	1.74	1996	117	501	0.059	1905.5	51.4	1291.5	46.6	-21.4	0.11665	2.91	3.56783	4.92	0.2218	3.97	0.80638
DK13-8A@12	c	0.24	1927	385	365	0.200	1860.0	24.9	962.9	34.0	-44.2	0.11374	1.39	2.52662	4.04	0.1611	3.79	0.93865
DK13-8A@13	c	1.19	1812	535	384	0.295	1940.3	34.6	1005.8	71.4	-40.2	0.11894	1.96	2.76917	7.87	0.1689	7.62	0.96851
DK13-8A@14	c	0.08	659	230	287	0.349	2051.1	4.4	1957.7	22.0	-2.6	0.12659	0.25	6.19336	1.33	0.3548	1.30	0.98239
DK13-8A@15	r	27.76	5759	473	1627	0.082	2612.5	890.6	658.2	87.7		0.17568	74.43	2.60399	75.72	0.1075	13.91	0.18374
DK13-8A@16		0.01	2206	41	701	0.019	1973.7	8.4	1601.0	28.3	-17.5	0.12118	0.47	4.71057	2.05	0.2819	2.00	0.97309
DK13-8A@17	c	0.29	802	355	344	0.442	2046.8	7.6	1887.9	27.3	-5.4	0.12628	0.43	5.92451	1.72	0.3403	1.67	0.96824
DK13-8A@18	c	0.01	512	161	227	0.314	2051.6	4.2	2001.5	20.1	-0.3	0.12662	0.24	6.35642	1.19	0.3641	1.17	0.97975
DK13-8A@19	c	0.84	1844	375	589	0.204	1753.6	129.2	1547.3	98.3		0.10727	7.38	4.01230	10.24	0.2713	7.09	0.69301
DK13-8A@20	c	0.01	476	122	207	0.256	2046.9	4.3	1993.9	19.6	-0.6	0.12629	0.24	6.31169	1.16	0.3625	1.14	0.97784
Z DK 13/10 - Augen orthogneiss (18° 20' 31.6" S; 27° 03' 36.6" E)																		
DK 13-10@1	c	0.11	189	73	112	0.386	2690.3	4.3	2435.9	34.0	-8.2	0.18412	0.26	11.65639	1.69	0.4592	1.67	0.98786
DK 13-10@2	c	0.15	424	320	179	0.755	2038.4	4.4	1767.7	25.9	-12.1	0.12568	0.25	5.46699	1.69	0.3155	1.67	0.98920
DK 13-10@3	r	3.35	5119	932	552	0.182	1621.4	121.5	563.4	17.8	-31.6	0.09986	6.80	1.25744	7.55	0.0913	3.29	0.43582
DK 13-10@4	c	3.82	1466	737	386	0.503	1993.7	10.8	1210.0	19.4	-39.6	0.12255	0.61	3.48870	1.86	0.2065	1.75	0.94491
DK 13-10@5	r	1.62	3655	1137	427	0.311	1676.4	26.5	610.3	12.1	-58.7	0.10286	1.45	1.40846	2.53	0.0993	2.08	0.82093
DK 13-10@06	c	0.08	252	141	176	0.560	2768.8	3.3	2695.1	36.9		0.19311	0.20	13.81968	1.68	0.5190	1.67	0.99290
DK 13-10@07	r	1.48	4450	731	493	0.164	1539.3	38.1	595.1	14.6	-52.6	0.09557	2.05	1.27434	3.28	0.0967	2.56	0.78079
DK 13-10@17	c	0.37	1619	403	525	0.249	1940.3	4.5	1564.7	23.9	-18.9	0.11894	0.25	4.50523	1.74	0.2747	1.72	0.98937
DK 13-10@18	r	0.43	1080	440	417	0.407	1988.3	4.1	1765.7	25.9	-9.7	0.12218	0.23	5.30807	1.69	0.3151	1.67	0.99037
DK 13-10@19	c	0.03	898	278	383	0.310	1968.0	4.0	1962.6	28.3		0.12080	0.22	5.92720	1.68	0.3559	1.67	0.99123
DK 13-10@20	c	0.08	222	66	97	0.296	1995.3	7.2	2004.9	28.8		0.12266	0.41	6.16983	1.72	0.3648	1.67	0.97157
DK13-10@10	r	0.12	1577	477	573	0.302	2015.9	4.4	1698.5	25.0	-14.9	0.12410	0.25	5.15805	1.69	0.3015	1.67	0.98894
DK13-10@13	c	0.66	4767	2445	796	0.513	1705.0	45.1	829.7	30.5	-41.6	0.10447	2.49	1.97853	4.64	0.1374	3.91	0.84392
DK13-10@14	c	0.26	3229	1277	657	0.396	1868.9	16.9	956.9	35.2	-46.5	0.11430	0.94	2.52181	4.06	0.1600	3.95	0.97270
DK13-10@21		0.11	2257	1814	707	0.804	1922.7	7.3	1328.1	21.1	-31.2	0.11777	0.41	3.71485	1.80	0.2288	1.76	0.97421
DK13-10@22	r	0.19	1911	529	693	0.277	2008.8	2.0	1703.9	21.2	-14.9	0.12360	0.12	5.15581	1.42	0.3025	1.41	0.99667
DK13-10@23	r	0.39	1730	432	491	0.250	2005.7	8.9	1362.6	48.0	-30.0	0.12338	0.50	4.00407	3.93	0.2354	3.90	0.99179
DK13-10@24	c	0.39	930	560	343	0.602	2038.4	5.9	1605.4	28.4	-20.6	0.12568	0.34	4.90044	2.02	0.2828	1.99	0.98606
DK13-10@25	r	0.20	1165	290	395	0.249	2003.3	6.0	1627.0	33.2	-17.3	0.12322	0.34	4.87743	2.33	0.2871	2.30	0.98919
DK13-10@26	c	0.02	230	76	104	0.332	2042.1	4.7	2031.6	20.9		0.12594	0.26	6.43295	1.23	0.3705	1.20	0.97666
DK13-10@27	r	0.10	1148	403	633	0.351	2709.1	4.7	2305.9	30.0	-14.9	0.18623	0.28	11.04238	1.57	0.4300	1.54	0.98364
DK13-10@28	r	0.99	2842	673	549	0.237	1772.3	33.6	977.9	16.4	-39.0	0.10838	1.86	2.44775	2.59	0.1638	1.80	0.69556
DK13-10@29	c	0.19	2316	341	525	0.147	1871.0	19.3	1154.8	14.9	-36.5	0.11443	1.08	3.09536	1.77	0.1962	1.41	0.79405

Pb_c and Pb* indicate the common and radiogenic proportions respectively

{} indicate where no correction has been applied otherwise a value has been calculated using the present-day Stacey & Kramers common Pb value

(1) Corrected for common Pb

Errors are 1 sd

No data indicates that the applied correction resulted in an impossible age

Positive numbers for % Disc, indicate reverse discordance

Table 5.3: Major element analyses for selected samples from the Dete-Kamativi Inlier

Sample name	Z DK1	Z DK2	Z DK9C	Z DK10	Z DK11	Z DK12
Major Elements						
SiO2	91.71	65.91	75.25	79.81	71.30	65.89
Al2O3	4.39	17.09	12.07	11.22	16.24	17.43
Fe2O3	0.17	0.57	0.34	0.26	0.27	0.57
FeO	1.36	4.59	2.74	2.11	2.16	4.64
MnO	0.01	0.04	0.02	0.02	0.03	0.07
MgO	0.03	1.70	0.97	0.03	0.66	1.47
CaO	0.04	3.91	4.08	0.66	2.78	3.13
Na2O	0.50	3.38	4.51	3.64	5.13	3.81
K2O	2.59	2.91	0.18	3.20	1.94	3.67
TiO2	0.07	0.66	0.87	0.11	0.28	0.74
P2O5	0.02	0.27	0.19	0.01	0.07	0.26
Cr2O3	0.005	0.007	0.006	0.002	0.006	0.011
NiO	0.003	0.003	0.003	0.003	0.003	0.004
LOI	0.02	1.51	0.29	0.27	0.51	1
TOTAL	100.90	101.04	101.22	101.09	100.87	101.71

A.5 CHOMA-KALOMO BLOCK

Table 6.1: SIMS U-Pb zircon data from the various rocks within the Choma-Kalomo Block

Spot	Comment	% $^{206}Pb_c$	µg/g U	µg/g Th	µg/g $^{*206}Pb$	$^{232}Th/^{238}U$ Meas	$^{207}Pb/^{206}Pb$ age (1)	± 1sd	$^{206}Pb/^{238}U$ age (1)	± 1sd	% Disc (2sd)	$^{*207}Pb/^{*206}Pb$	± 1sd	$^{*207}Pb/^{235}Pb$	± 1sd	$^{*206}Pb/^{238}Pb$	± 1sd	Error Correlation
Z CK 13/1 - Quartzofeldspathic paragneiss (16° 52' 04.1" S; 27° 16' 21.2" E)																		
CK13-1@2		6.80	138	103	48	0.746	2217.4	241.2	1430.3	109.4	-39.5	0.13921	15.14	4.76805	17.34	0.2484	8.46	0.48772
CK13-1@3	core	0.01	701	414	209	0.590	1389.8	3.6	1354.7	13.8	-2.8	0.08834	0.19	2.84844	1.15	0.2339	1.13	0.98623
CK13-1@4	rim	0.58	1080	7	241	0.006	1246.4	18.9	1208.0	12.6	-3.4	0.08204	0.97	2.33120	1.50	0.2061	1.15	0.76331
CK13-1@5	c	59.94	5599	1904	665	0.340	393.3	971.7	327.4	7.6	-17.2	0.05454	59.90	0.39178	59.94	0.0521	2.36	0.03944
CK13-1@6	c	30.76	1952	895	145	0.459	1711.6	606.7	365.9	15.0	-80.8	0.10484	40.78	0.84432	40.99	0.0584	4.22	0.10298
CK13-1@7	c	34.34	2320	1188	222	0.512	2033.2	307.4	491.9	12.4	-78.6	0.12531	19.33	1.36988	19.51	0.0793	2.63	0.13459
CK13-1@8	c	0.02	832	399	234	0.479	1377.1	4.4	1322.4	14.8	-4.4	0.08775	0.23	2.75507	1.26	0.2277	1.24	0.98302
CK13-1@9	c	15.00	191	112	59	0.589	1818.4	166.6	1399.3	14.3	-25.6	0.11115	9.72	3.71529	9.78	0.2424	1.14	0.11643
CK13-1@10	c	30.93	2182	507	439	0.233	2102.1	748.1	703.2	14.9	-70.1	0.13031	55.76	2.07075	55.81	0.1153	2.23	0.04003
Z CK 13/2 - Quartz-plagiclase-pyroxene leuconorite (17° 05' 21.0" S; 27° 01' 16.7" E)																		
ZCK13-2@1	c	{0.09}	65	127	27	1.942	1596.4	17.6	1606.9	21.1	0.7	0.09853	0.95	3.84588	1.76	0.2831	1.48	0.84147
ZCK13-2@2	c	{0.01}	353	248	167	0.703	2038.2	5.2	2049.0	25.8	0.6	0.12567	0.29	6.48319	1.50	0.3742	1.47	0.98083
ZCK13-2@3		{0.01}	118	105	56	0.889	2034.2	9.1	2017.2	25.8	-1.0	0.12538	0.52	6.35168	1.57	0.3674	1.49	0.94472
ZCK13-2@4	c	0.03	248	253	101	1.021	1768.0	7.5	1757.0	22.7	-0.7	0.10812	0.41	4.67085	1.53	0.3133	1.47	0.96301
ZCK13-2@5	r	0.03	882	616	255	0.699	1365.0	5.5	1368.2	18.2	0.3	0.08720	0.28	2.84301	1.50	0.2365	1.47	0.98185
ZCK13-2@6	c	{0.02}	281	276	139	0.980	2049.2	8.4	2061.1	26.0	0.7	0.12645	0.48	6.56878	1.54	0.3767	1.47	0.95118
ZCK13-2@7	c	0.07	241	275	74	1.139	1369.3	12.2	1355.7	18.0	-1.1	0.08740	0.64	2.82047	1.60	0.2341	1.47	0.91745
ZCK13-2@8	c	0.11	104	82	30	0.788	1370.1	17.1	1348.5	18.0	-1.7	0.08743	0.90	2.80507	1.73	0.2327	1.48	0.85530
ZCK13-2@9	c	0.19	577	709	181	1.229	1352.8	8.0	1375.0	18.4	1.8	0.08665	0.42	2.84056	1.54	0.2377	1.48	0.96267
CK13-2@23	c	{0.01}	235	184	105	0.786	1969.0	14.7	1842.0	23.7	-7.4	0.12086	0.83	5.51168	1.69	0.3307	1.48	0.87250
CK13-2@25	r	0.01	1467	664	420	0.453	1380.3	3.7	1359.8	15.2	-1.6	0.08790	0.19	2.84608	1.26	0.2348	1.24	0.98808
CK13-2@28c	c	0.31	69	51	22	0.733	1453.0	26.0	1378.2	14.9	-5.7	0.09130	1.38	3.00084	1.83	0.2384	1.20	0.65674
CK13-2@28r	r	0.10	338	76	86	0.225	1349.4	7.5	1294.7	13.4	-4.5	0.08650	0.39	2.65285	1.20	0.2224	1.14	0.94602
CK13-2@29	r	{0.01}	735	8	158	0.010	1193.6	4.9	1164.8	12.1	-2.6	0.07986	0.25	2.18068	1.17	0.1980	1.14	0.97661
Z CK 13/3 - Medium-grained granite (17° 05' 41.1" S; 27° 01' 36.1" E)																		
ZCK13-3@1	c	{0.02}	218	94	63	0.432	1378.3	11.0	1397.1	18.5	1.5	0.08781	0.57	2.92990	1.58	0.2420	1.47	0.93172
ZCK13-3@2	r	0.09	1167	22	268	0.019	1227.8	5.7	1240.1	16.6	1.1	0.08126	0.29	2.37670	1.50	0.2121	1.47	0.98113
ZCK13-3@3	r	0.05	1166	16	258	0.014	1196.7	5.8	1197.9	16.2	0.1	0.07999	0.29	2.25226	1.51	0.2042	1.48	0.98085
ZCK13-3@4	c	0.20	309	127	86	0.411	1366.2	10.5	1357.8	18.1	-0.7	0.08726	0.55	2.82076	1.57	0.2345	1.47	0.93707
ZCK13-3_#6@5	c	0.04	270	147	77	0.543	1361.4	8.9	1376.8	18.2	1.3	0.08704	0.46	2.85752	1.54	0.2381	1.47	0.95345
ZCK13-3@6	r	0.14	1000	32	228	0.032	1233.3	6.7	1227.6	16.4	-0.5	0.08149	0.34	2.35692	1.51	0.2098	1.47	0.97428
ZCK13-3_#6@7	c	0.05	321	133	90	0.415	1362.7	8.2	1388.4	18.4	2.1	0.08710	0.43	2.88615	1.53	0.2403	1.47	0.96047
ZCK13-3_#6@8	c	0.06	439	475	139	1.081	1365.7	7.2	1397.3	18.5	2.6	0.08723	0.38	2.91129	1.52	0.2420	1.47	0.96877
ZCK13-3@9		0.57	273	123	69	0.451	1349.4	11.8	1250.4	16.8	-8.1	0.08650	0.61	2.55296	1.60	0.2141	1.47	0.92303
CK13-3@5	c	0.01	887	584	259	0.658	1385.9	4.1	1315.1	14.7	-5.6	0.08816	0.22	2.75067	1.25	0.2263	1.23	0.98504
CK13-3@7	r	0.01	1057	528	307	0.499	1377.7	4.4	1361.7	15.5	-1.3	0.08778	0.23	2.84683	1.28	0.2352	1.26	0.98389
CK13-3@8c	c	0.05	2361	813	546	0.344	1313.6	15.2	1142.0	23.0	-14.2	0.08491	0.79	2.26920	2.33	0.1938	2.19	0.94093
CK13-3@8r	r	0.03	1748	252	378	0.144	1209.0	4.7	1130.5	12.2	-7.1	0.08049	0.24	2.12737	1.20	0.1917	1.17	0.97987
CK13-3@12	c	0.04	661	300	189	0.453	1382.8	5.1	1355.5	15.6	-2.2	0.08802	0.27	2.83999	1.30	0.2340	1.27	0.97848
CK13-3@18	c	0.38	1323	689	363	0.521	1369.9	37.6	1281.7	13.2	-7.1	0.08742	1.98	2.65153	2.28	0.2200	1.14	0.49855
Z CK 13/4C - Quartz-muscovite-tourmaline schist (17° 11' 29.0" S; 27° 07' 08.8" E)																		
ZCK4c@1	c	{0.13}	55	90	24	1.641	1814.7	16.9	1754.5	23.4	-3.8	0.11093	0.94	4.78434	1.79	0.3128	1.52	0.85198
ZCK4c_#6@2		{0.02}	334	174	150	0.522	2041.3	6.2	2014.1	25.5	-1.5	0.12589	0.35	6.36593	1.52	0.3668	1.47	0.97270
ZCK4c@3	c	0.02	502	639	228	1.272	1863.5	5.4	1867.1	23.9	0.2	0.11396	0.30	5.27847	1.50	0.3359	1.47	0.98008
ZCK4c@4	r	0.04	297	313	132	1.054	1856.2	7.0	1880.5	24.0	1.5	0.11350	0.39	5.30076	1.52	0.3387	1.47	0.96677
ZCK4c@5		0.05	396	162	160	0.409	1943.5	6.4	1875.8	24.0	-4.0	0.11915	0.36	5.54873	1.51	0.3378	1.47	0.97130
ZCK4c@6		0.03	284	137	121	0.482	1970.9	6.6	1951.3	24.9	-1.2	0.12099	0.37	5.89715	1.52	0.3535	1.48	0.96959
ZCK4c@7		0.04	377	162	156	0.430	2039.7	6.2	1928.5	24.7	-6.3	0.12577	0.35	6.04725	1.52	0.3487	1.48	0.97299
ZCK4c@8	r	0.03	265	87	116	0.327	2030.2	9.7	2023.2	25.8	-0.4	0.12510	0.55	6.35939	1.58	0.3687	1.49	0.93791
ZCK4c@9	r	0.07	228	277	99	1.217	1863.8	9.2	1833.5	23.5	-1.9	0.11398	0.51	5.17019	1.56	0.3290	1.47	0.94478
CK13-4C@2	c	{0.04}	106	91	52	0.862	2062.0	10.7	1983.4	20.0	-4.4	0.12737	0.61	6.32680	1.32	0.3603	1.17	0.88657
Z CK 13/6 - Heavy mineral-rich quartzite (17° 23' 15.8" S; 26° 08' 58.3" E)																		
CK13-6@1	c	1.08	1765	54	613	0.030	1904.4	49.7	1736.9	51.1	-10.0	0.11658	2.81	4.97033	4.37	0.3092	3.34	0.76493

CK13-6@2		0.17	988	339	393	0.343	2020.1	8.5	1795.1	42.4	-12.8	0.12438	0.48	5.50682	2.74	0.3211	2.70	0.98443
CK13-6@3	c	0.19	1873	587	513	0.313	1874.6	18.7	1313.0	52.2	-33.1	0.11466	1.04	3.57134	4.50	0.2259	4.37	0.97276
CK13-6@4		0.37	1274	375	486	0.294	2007.0	16.9	1761.9	37.3	-13.9	0.12347	0.96	5.35095	2.59	0.3143	2.41	0.92915
CK13-6@5	c	0.80	1251	106	421	0.085	1960.5	7.2	1670.7	16.8	-16.8	0.12029	0.40	4.90681	1.21	0.2958	1.14	0.94239
CK13-6@6	c	0.38	704	243	260	0.345	2001.9	31.0	1681.3	69.4	-18.2	0.12312	1.76	5.05837	4.99	0.2980	4.66	0.93539
CK13-6@7	r	0.15	1841	759	676	0.413	1971.9	3.4	1692.1	17.0	-16.1	0.12106	0.19	5.01029	1.16	0.3002	1.14	0.98588
CK13-6@8	c	0.70	1381	422	571	0.306	2016.9	16.0	1880.4	31.6	-7.8	0.12416	0.91	5.79840	2.13	0.3387	1.93	0.90525
CK13-6@9		0.05	1144	469	428	0.410	2011.7	14.5	1703.5	44.8	-17.4	0.12380	0.82	5.16291	3.09	0.3025	2.98	0.96413
CK13-6@10		0.16	1748	46	579	0.026	1926.0	9.2	1663.0	18.1	-15.5	0.11799	0.51	4.78783	1.34	0.2943	1.24	0.92311

Pb_c and Pb* indicate the common and radiogenic proportions respectively

{} indicate where no correction has been applied otherwise a value has been calculated using the present-day Stacey & Kramers common Pb value

(1) Corrected for common Pb

Errors are 1 sd

Positive numbers for % Disc, indicate reverse discordance

Table 6.2: LA-ICPMS U-Pb zircon data for sample Z9, Choma-Kalomo Block

Spot	µg/g U[a]	µg/g *^{206}Pb[a]	^{232}Th/ ^{238}U Meas[a]	^{207}Pb/ ^{206}Pb age (1)	± 2sd	^{206}Pb/ ^{238}U age (1)	± 2sd	% Conc (2sd)	*^{207}Pb/ *^{206}Pb[e]	± 2sd[d]	*^{207}Pb/ ^{235}Pb[b]	± 2sd[d]	*^{206}Pb/ ^{238}Pb[b]	± 2sd[d]	Error Correlation[c]
Z9 - Quartz-biotite-muscovite schist (17° 4' 3.21" S; 26° 42' 12.23" E)															
7	935	93	0.29	1799	27	611	27	34	0.1100	0.0017	1.51	0.07	0.099	0.005	0.95
8	244	82	0.53	1868	33	1877	78	100	0.1142	0.0021	5.32	0.27	0.338	0.016	0.93
9	181	61	0.40	1854	31	1862	76	100	0.1134	0.0020	5.23	0.26	0.335	0.016	0.94
10	37	12	0.55	1794	60	1783	87	99	0.1097	0.0037	4.82	0.31	0.319	0.018	0.86
11	213	67	0.47	1744	30	1751	72	100	0.1067	0.0018	4.59	0.23	0.312	0.015	0.94
12	82	31	0.41	2061	40	2049	89	99	0.1273	0.0029	6.57	0.36	0.374	0.019	0.91
13	185	64	0.50	1925	30	1919	78	100	0.1179	0.0020	5.64	0.28	0.347	0.016	0.94
14	277	92	0.47	1892	30	1842	75	97	0.1158	0.0019	5.28	0.26	0.331	0.016	0.94
15	451	106	0.23	1863	27	1361	56	73	0.1139	0.0017	3.69	0.18	0.235	0.011	0.95
16	150	51	0.77	1907	37	1900	81	100	0.1167	0.0024	5.52	0.29	0.343	0.017	0.92
20	80	20	0.42	1444	51	1454	67	101	0.0909	0.0025	3.17	0.18	0.253	0.013	0.88
21	305	98	0.85	1887	26	1803	72	96	0.1155	0.0017	5.14	0.25	0.323	0.015	0.95
22	181	31	0.68	1891	37	1013	46	54	0.1157	0.0024	2.72	0.14	0.170	0.008	0.92
23	365	123	0.53	1890	27	1871	75	99	0.1156	0.0018	5.37	0.26	0.337	0.016	0.95
24	92	33	1.20	1977	40	1975	86	100	0.1214	0.0028	6.00	0.33	0.358	0.018	0.91
25	253	81	0.59	1876	28	1782	73	95	0.1148	0.0018	5.04	0.25	0.318	0.015	0.95
26	198	40	0.52	1326	41	1189	52	90	0.0855	0.0018	2.39	0.13	0.203	0.010	0.92
27	262	88	0.52	1876	29	1870	76	100	0.1147	0.0019	5.32	0.26	0.337	0.016	0.95
28	326	109	0.51	1873	26	1862	75	99	0.1146	0.0017	5.29	0.26	0.335	0.015	0.95
29	219	73	0.14	1862	33	1859	77	100	0.1139	0.0021	5.25	0.27	0.334	0.016	0.93
33	284	59	0.47	1946	30	1217	52	63	0.1193	0.0021	3.42	0.17	0.208	0.010	0.94
34	193	65	0.57	1866	30	1863	76	100	0.1141	0.0019	5.27	0.26	0.335	0.016	0.94
35	651	99	0.47	1554	28	913	39	59	0.0963	0.0015	2.02	0.10	0.152	0.007	0.95
36	511	128	0.66	1884	25	1436	59	76	0.1153	0.0016	3.96	0.19	0.249	0.011	0.96
37	396	132	0.24	1986	25	1853	74	93	0.1220	0.0017	5.60	0.27	0.333	0.015	0.96
38	768	212	0.32	2005	27	1571	65	78	0.1234	0.0019	4.69	0.23	0.276	0.013	0.95
39	811	192	0.35	1880	24	1368	56	73	0.1150	0.0016	3.75	0.18	0.236	0.011	0.96
40	260	62	0.62	1368	61	1388	69	101	0.0874	0.0029	2.89	0.18	0.240	0.013	0.86
41	141	70	0.30	2709	41	2602	116	96	0.1862	0.0047	12.76	0.76	0.497	0.027	0.91
42	169	53	0.56	1885	31	1764	73	94	0.1153	0.0020	5.00	0.25	0.315	0.015	0.94
46	435	90	0.62	1282	32	1218	52	95	0.0835	0.0014	2.39	0.12	0.208	0.010	0.94
47	425	120	0.16	1810	28	1600	66	88	0.1106	0.0017	4.30	0.21	0.282	0.013	0.95
48	351	118	0.20	1857	26	1868	75	101	0.1136	0.0016	5.26	0.25	0.336	0.016	0.96
49	617	102	0.59	1883	30	986	43	52	0.1152	0.0020	2.63	0.13	0.165	0.008	0.94
50	310	42	0.25	1835	48	817	40	45	0.1122	0.0030	2.09	0.12	0.135	0.007	0.89
51	690	209	0.19	1840	24	1703	69	93	0.1125	0.0015	4.69	0.22	0.302	0.014	0.96
52	388	92	0.67	1990	27	1369	58	69	0.1223	0.0019	3.99	0.20	0.237	0.011	0.95
53	278	93	0.41	1867	32	1864	78	100	0.1142	0.0021	5.28	0.27	0.335	0.016	0.94
54	225	77	0.30	1882	32	1889	78	100	0.1151	0.0021	5.41	0.28	0.341	0.016	0.94
55	44	15	0.95	1876	71	1873	102	100	0.1147	0.0046	5.33	0.40	0.337	0.021	0.84
59	91	27	0.59	1896	41	1650	74	87	0.1160	0.0027	4.67	0.26	0.292	0.015	0.91
60	396	87	0.36	1691	34	1280	56	76	0.1037	0.0020	3.14	0.16	0.220	0.011	0.93
61	371	88	0.35	1820	28	1370	58	75	0.1112	0.0017	3.63	0.18	0.237	0.011	0.95
62	492	125	0.33	1869	26	1462	61	78	0.1143	0.0017	4.01	0.20	0.255	0.012	0.95
63	455	212	0.21	2617	22	2464	94	94	0.1762	0.0023	11.31	0.54	0.465	0.021	0.96

64	1421	104	0.19	1956	27	454	20	23	0.1200	0.0018	1.21	0.06	0.073	0.003	0.95
65	77	29	0.58	2065	57	2063	103	100	0.1276	0.0042	6.63	0.44	0.377	0.022	0.87
66	260	87	0.33	1855	28	1859	76	100	0.1134	0.0018	5.23	0.26	0.334	0.016	0.95
67	451	81	0.48	1511	36	1071	47	71	0.0942	0.0018	2.35	0.12	0.181	0.009	0.93
68	993	177	0.94	1870	25	1058	45	57	0.1144	0.0016	2.81	0.14	0.178	0.008	0.96
72	240	71	0.64	1861	30	1675	70	90	0.1138	0.0019	4.65	0.23	0.297	0.014	0.94
73	21	7	0.40	1890	101	1884	126	100	0.1157	0.0067	5.41	0.52	0.339	0.026	0.80
74	290	67	0.41	1818	30	1337	57	74	0.1112	0.0019	3.53	0.18	0.230	0.011	0.94
75	166	56	0.18	1860	31	1874	78	101	0.1138	0.0020	5.29	0.27	0.337	0.016	0.94
76	71	24	0.78	1861	51	1877	89	101	0.1138	0.0033	5.30	0.33	0.338	0.018	0.88
77	324	76	0.60	1855	30	1367	59	74	0.1134	0.0019	3.69	0.19	0.236	0.011	0.94
78	100	33	0.50	1885	37	1842	80	98	0.1153	0.0024	5.26	0.28	0.331	0.016	0.92
79	136	32	0.87	1392	43	1370	61	98	0.0884	0.0020	2.89	0.16	0.237	0.012	0.91
80	78	30	0.33	2111	48	2099	98	99	0.1310	0.0037	6.95	0.43	0.385	0.021	0.89
81	125	87	0.40	3394	27	3425	132	101	0.2857	0.0050	27.63	1.46	0.701	0.035	0.94
85	866	130	0.53	1917	27	905	40	47	0.1174	0.0018	2.44	0.12	0.151	0.007	0.95
86	236	47	0.44	1878	34	1169	52	62	0.1149	0.0022	3.15	0.16	0.199	0.010	0.93
87	1170	117	0.23	1490	29	616	28	41	0.0931	0.0014	1.29	0.06	0.100	0.005	0.95
88	435	148	0.25	1885	29	1886	78	100	0.1153	0.0019	5.40	0.27	0.340	0.016	0.95
89	285	68	0.42	1363	34	1378	59	101	0.0871	0.0016	2.86	0.15	0.238	0.011	0.94
90	325	110	0.14	1854	29	1877	77	101	0.1134	0.0019	5.28	0.27	0.338	0.016	0.95
91	199	71	0.36	1988	32	1980	83	100	0.1222	0.0022	6.06	0.31	0.360	0.017	0.94
92	519	165	0.26	1768	26	1779	73	101	0.1082	0.0016	4.74	0.23	0.318	0.015	0.95
93	92	30	0.56	1835	45	1841	84	100	0.1122	0.0029	5.11	0.30	0.330	0.017	0.90
94	286	99	0.41	1930	28	1925	79	100	0.1182	0.0019	5.67	0.28	0.348	0.016	0.95
98	76	26	0.61	1877	44	1883	85	100	0.1148	0.0028	5.37	0.31	0.339	0.018	0.90
99	150	45	0.69	1898	34	1694	73	89	0.1162	0.0022	4.81	0.25	0.300	0.015	0.93
100	176	39	0.45	1767	36	1289	57	73	0.1081	0.0022	3.30	0.18	0.221	0.011	0.93
101	279	93	0.30	1874	33	1861	79	99	0.1146	0.0021	5.29	0.28	0.335	0.016	0.93
102	759	132	0.78	2095	26	1033	45	49	0.1298	0.0019	3.11	0.15	0.174	0.008	0.95
103	94	33	0.66	1922	41	1921	85	100	0.1177	0.0027	5.63	0.32	0.347	0.018	0.91
104	365	73	0.48	1856	30	1172	51	63	0.1135	0.0019	3.12	0.16	0.199	0.010	0.94
105	428	111	0.44	1945	28	1485	63	76	0.1193	0.0019	4.26	0.21	0.259	0.012	0.95
106	233	78	0.30	1859	44	1870	85	101	0.1137	0.0028	5.27	0.31	0.336	0.018	0.90
107	258	50	0.03	1278	53	1151	55	90	0.0834	0.0023	2.25	0.13	0.196	0.010	0.88
111	88	27	0.76	1917	41	1692	76	88	0.1174	0.0027	4.86	0.27	0.300	0.015	0.91
112	226	67	0.61	1876	31	1667	71	89	0.1147	0.0020	4.67	0.24	0.295	0.014	0.94
113	1077	107	0.62	1556	32	609	28	39	0.0964	0.0017	1.32	0.07	0.099	0.005	0.94
114	467	102	0.22	1881	30	1269	55	67	0.1151	0.0020	3.45	0.18	0.218	0.010	0.94
115	137	42	1.12	1725	37	1735	75	101	0.1056	0.0021	4.50	0.24	0.309	0.015	0.93
116	251	56	0.90	1903	33	1290	57	68	0.1165	0.0021	3.56	0.19	0.222	0.011	0.94
117	223	75	0.56	1862	31	1871	78	100	0.1138	0.0020	5.29	0.27	0.337	0.016	0.94
118	585	122	0.88	1983	27	1216	53	61	0.1218	0.0019	3.49	0.17	0.208	0.010	0.95
119	157	44	0.69	1875	35	1581	69	84	0.1147	0.0023	4.40	0.23	0.278	0.014	0.93
120	76	26	0.34	1870	46	1876	86	100	0.1144	0.0029	5.32	0.31	0.338	0.018	0.90
124	125	39	0.39	1899	36	1749	76	92	0.1163	0.0024	5.00	0.27	0.312	0.016	0.93
125	841	209	0.13	1850	26	1434	61	78	0.1131	0.0017	3.89	0.19	0.249	0.012	0.95
126	366	112	0.21	1892	29	1723	72	91	0.1158	0.0019	4.89	0.25	0.307	0.015	0.95

127	236	79	0.36	1857	30	1856	78	100	0.1136	0.0019	5.22	0.27	0.334	0.016	0.94
128	129	37	0.39	1784	39	1605	72	90	0.1091	0.0024	4.25	0.23	0.283	0.014	0.92
129	920	145	0.36	2123	26	946	42	45	0.1319	0.0020	2.88	0.14	0.158	0.008	0.95
130	415	108	0.18	1859	31	1498	65	81	0.1137	0.0020	4.10	0.21	0.262	0.013	0.94
131	422	119	0.41	1856	29	1602	68	86	0.1135	0.0018	4.41	0.22	0.282	0.013	0.95
132	215	54	0.37	1993	33	1444	64	72	0.1225	0.0023	4.24	0.22	0.251	0.012	0.93
133	220	67	0.43	1928	37	1716	76	89	0.1181	0.0025	4.97	0.27	0.305	0.015	0.92
137	70	23	0.61	1913	51	1830	88	96	0.1172	0.0034	5.30	0.33	0.328	0.018	0.89
138	263	83	0.36	1861	31	1770	75	95	0.1138	0.0020	4.96	0.25	0.316	0.015	0.94
139	586	130	0.35	1964	28	1294	56	66	0.1205	0.0019	3.69	0.19	0.222	0.011	0.95
140	63	21	0.92	1881	58	1892	95	101	0.1151	0.0038	5.41	0.36	0.341	0.020	0.87
141	90	33	0.58	2022	47	2015	94	100	0.1246	0.0033	6.30	0.38	0.367	0.020	0.90
142	419	111	0.32	1916	29	1516	65	79	0.1173	0.0019	4.29	0.22	0.265	0.013	0.95
143	175	61	0.59	1921	34	1922	82	100	0.1177	0.0023	5.63	0.30	0.347	0.017	0.93
144	192	67	0.53	1894	37	1916	83	101	0.1159	0.0024	5.53	0.30	0.346	0.017	0.92
145	216	73	0.75	1875	34	1885	81	101	0.1147	0.0022	5.37	0.28	0.340	0.017	0.93
146	265	68	0.18	1462	35	1475	64	101	0.0918	0.0017	3.25	0.17	0.257	0.013	0.93
150	77	24	0.56	1868	44	1776	81	95	0.1142	0.0028	5.00	0.29	0.317	0.017	0.90
151	277	83	0.88	1854	32	1683	72	91	0.1134	0.0020	4.66	0.24	0.298	0.015	0.94
152	93	22	0.46	1758	47	1380	66	78	0.1075	0.0028	3.54	0.21	0.239	0.013	0.90
153	199	67	0.81	1877	35	1873	81	100	0.1148	0.0023	5.34	0.29	0.337	0.017	0.93
154	584	196	0.60	1864	32	1864	79	100	0.1140	0.0020	5.27	0.27	0.335	0.016	0.94
155	221	80	0.41	1991	39	1996	88	100	0.1223	0.0027	6.12	0.34	0.363	0.019	0.92
156	100	24	0.77	1384	61	1376	69	99	0.0881	0.0029	2.89	0.19	0.238	0.013	0.86
157	130	42	0.51	1786	44	1788	82	100	0.1092	0.0027	4.81	0.28	0.320	0.017	0.91
158	145	44	1.10	1874	36	1725	76	92	0.1146	0.0023	4.85	0.26	0.307	0.015	0.93
159	355	112	0.62	1895	30	1766	75	93	0.1160	0.0020	5.04	0.26	0.315	0.015	0.94

[a]U and Pb concentrations and Th/U ratios are calculated relative to GJ-1 reference zircon

[b]Corrected for background and within-run Pb/U fractionation and normalised to reference zircon GJ-1 (ID-TIMS values/measured value); $^{207}Pb/^{235}U$ calculated using $(^{207}Pb/^{206}Pb)/(^{238}U/^{206}Pb * 1/137.88)$

[c] Is the error correlation defined as the quotient of the propagated errors of the $^{206}Pb/^{238}U$ and the $^{207}/^{235}U$ ratio

[d]Quadratic addition of within-run errors (2 SD) and daily reproducibility of GJ-1 (2 SD)

[e]Corrected for mass-bias by normalising to GJ-1 reference zircon (~0.6 per atomic mass unit) and common Pb using the model Pb composition of Stacey & Kramers (1975)

Pb_c and Pb* indicate the common and radiogenic proportions respectively

(1) Corrected for common Pb

Table 6.3: ID-TIMS U-Pb coltan data on fragments from the Dete-Kamativi Inlier and Choma-Kalomo Block

Analysis	Fraction	Wt. (mg)	U (µg/g)	Pb_C (pg)	$^{207}Pb/^{204}Pb$	$^{207}Pb_C$/%	$^{207}Pb/^{235}U$	± 2sd	$^{206}Pb/^{238}U$	± 2sd	Err. Corr	$^{206}Pb/^{238}U$ age	± 2sd	$^{207}Pb/^{206}Pb$ age	± 2sd	% Disc
Kamativi Coltan (Dete-Kamativi Inlier)																
786																
dwd5779	1 CT frag, shiny	0.044	658	181	141	11	1.778	0.011	0.175	0.001	0.574	1039.9	3.2	1032.4	10.2	-0.8
dwd5780	1 CT frag, dull	0.108	251	311	85	18.3	1.802	0.017	0.178	0.000	0.255	1053.8	2.1	1030.1	18.4	-2.5
dwd5781	1 CT frag, dull	0.0117	182	304	70	22.3	1.753	0.021	0.173	0.000	0.222	1029.6	2.4	1025.5	23.5	-0.4
Chisuki Coltan (Choma-Kalomo Block)																
12R04B																
dwd6004	1 CT frag, sl	0.003	177	39	26	61.4	1.603	0.090	0.163	0.001	0.033	975.0	4.2	963.6	117.5	-1.3
dwd6005	1 CT frag, sl	0.003	259	9	79	20.6	1.530	0.013	0.158	0.0002	0.233	946.0	1.4	934.6	16.4	-1.3
dwd6006	1 CT frag, sl	0.004	191	5	116	14.2	1.557	0.008	0.159	0.0002	0.377	952.0	1.3	956.7	9.9	0.5
12R07B																
dwd6008	B, prism, sl	0.044	22	30	38	41.7	1.554	0.040	0.157	0.0004	0.060	942.8	2.2	973.5	53.0	3.4
dwd6009	B, prism, sl	0.014	117	12	105	15.2	1.451	0.009	0.150	0.0002	0.294	903.3	1.1	926.8	12.4	2.7
dwd6007	CT, 2nd B, prism, sl	0.064	53	17	147	10.7	1.496	0.007	0.154	0.0002	0.358	924.8	0.9	938.1	8.9	1.5
10631																
dwd6010	2nd B, prism, sl	0.37	419	8471	31	50.1	1.913	0.111	0.187	0.008	0.715	1102.8	42.1	1051.4	82.4	-5.3
dwd6011	B, prism, sl	0.061	500	681	51	30.5	1.788	0.032	0.176	0.0004	0.100	1045.6	2.0	1031.4	35.9	-1.5
dwd6012	B, prism, sl	0.026	717	330	59	26.1	1.768	0.025	0.174	0.0003	0.110	1035.9	1.5	1028.8	28.8	-0.7

CT - Columbite-Tantalite, frag - fragment, sl - slightly leached (1/2 hr in 15%HF with ET535 spike), B - Best batch, 2nd B - Second best batch

Pb_C - Common Pb from measured 204Pb assuming the isotopic composition of blank: 206/204 - 18.221; 207/204 - 15.612; 208/204 - 39.36

Err. Corr - Correlation between errors in measured concordia coordinates

% Disc - Discordance realtive to 207Pb/206Pb age

Table 6.4: ID-TIMS Pb-Pb data on coltan and plagioclase fragments from the Dete-Kamativi Inlier

Analysis	Fraction	Wt. (mg)	Pb_C (pg)	$^{207}Pb_C$/%	$^{206}Pb/^{204}Pb$	± 2sd	$^{207}Pb/^{204}Pb$	± 2sd	Err. Corr	$^{208}Pb/^{204}Pb$	± 2sd
Kamativi Coltan (Dete-Kamativi Inlier)											
786											
dwd5779	1 CT frag, shiny	0.04	181	11.0	1733	10	141.9	0.8	0.9856	36.16	0.16
dwd5780	1 CT frag, dull	0.11	311	18.3	960.7	4.3	84.95	0.38	0.9784	36.68	0.16
dwd5781	1 CT frag, dull	0.12	304	22.3	757.4	4.1	69.87	0.37	0.9813	38.17	0.20
dwd5907	2 Feld frag	0.15	897	92.7	32.064	0.080	16.757	0.049	0.9353	37.40	0.14
dwd5908	10 Feld frag	0.23	20580	94.3	29.476	0.048	16.455	0.039	0.9905	35.64	0.11
dwd5909	9 Feld frag	0.21	5438	83.3	58.057	0.096	18.623	0.044	0.9891	36.86	0.11

CT - Columbite-Tantalite, frag - fragment, Feld - Feldspar

$^{207}Pb_C$/% - Percent of ^{207}Pb that is initial or blank

Err. Corr - Correlation between errors in measured concordia coordinates

Table 6.5: ^{40}Ar-^{39}Ar data on mica separates from the Dete-Kamativi Inlier

Biotite 1(41) - Z DK 12 (Dete-Kamativi Inlier; 18° 25' 59" S; 26° 50' 50" E)

Step Nr	Laser power	Temp ˚C	cc stp ^{40}Ar	$^{40}Ar/^{36}Ar$	± 1σ	$^{40}Ar^*/^{39}Ar$	± 1σ	$\%^{39}Ar$	Age Ma	± 95%	Included
1	9.8	700	8.09E-09	15883	504	87.30	0.17	17.4	1012.1	6.3	yes
2	10	950	3.53E-08	43870	1635	87.76	0.12	75.3	1016.1	6.0	yes
3	10.2	1100	3.06E-09	27718	2689	88.11	0.41	6.5	1019.3	9.3	yes
4	10.5	1200	2.92E-10	4822	5041	85.49	2.09	0.6	995.9	34.1	no
5	11	1300	9.49E-11	4362	28054	85.19	4.95	0.2	993.2	89.6	no
J-value: 0.008631 ± 0.000024			**Weighted average of included steps**			**87.70**	**0.10**	**99.2**	**1015.6**	**6.0**	

Biotite 3(29) - Z DK 12 (Dete-Kamativi Inlier)

Step Nr	Laser power	Temp ˚C	cc stp ^{40}Ar	$^{40}Ar/^{36}Ar$	± 1σ	$^{40}Ar^*/^{39}Ar$	± 1σ	$\%^{39}Ar$	Age Ma	± 95%	Included
1	9.8	700	3.88E-09	8498	305	81.06	0.30	11.2	963.4	7.7	0
2	10	1000	2.78E-08	37640	1458	84.40	0.13	77.1	993.9	6.2	yes
3	10.2	1100	4.10E-09	34047	2820	85.69	0.32	11.2	1005.5	8.3	yes
4	10.4	1200	9.24E-11	1901	226	78.82	2.70	0.3	942.7	48.5	no
5	10.7	1300	5.03E-11	1380	297	75.45	4.83	0.2	911.0	92.5	no
J-value: 0.008719 ± 0.000027			**Weighted average of included steps**			**84.57**	**0.12**	**88.4**	**995.4**	**6.5**	

Muscovite 1 - Z DK 13/5 (RHA Mine, Dete-Kamativi Inlier; 18° 30' 44.3" S; 26° 37' 59.8" E)

Step Nr	Laser power	Temp ˚C	cc stp ^{40}Ar	$^{40}Ar/^{36}Ar$	± 1σ	$^{40}Ar^*/^{39}Ar$	± 1σ	$\%^{39}Ar$	Age Ma	± 95%	Included
1	9.98A	550	7.98E-11	680	99	39.69	4.48	0.1	515.8	100.6	no
2	10.16A		1.75E-10	1354	91	62.06	1.50	0.2	752.3	31.9	no
3	10.34A	700	4.15E-10	3132	311	79.97	1.04	0.4	921.6	18.1	no
4	10.52A		8.68E-10	5876	720	92.97	0.70	0.7	1035.3	12.3	no
5	10.70A	850	1.09E-08	25648	784	89.27	0.11	9.9	1003.6	4.6	yes
6	10.88A		9.54E-09	34941	2467	89.33	0.13	8.7	1004.2	4.9	yes
7	11.06A		2.21E-08	80169	5383	88.87	0.06	20.4	1000.2	4.3	yes
8	11.24A	1000	2.32E-08	434874	255957	87.95	0.06	21.7	992.2	4.4	yes
9	11.42A		7.03E-09	57476	7968	86.95	0.17	6.6	983.6	5.0	yes
10	11.60A		4.52E-09	>120000		87.05	0.17	4.3	984.5	5.2	yes
11	11.78A		3.25E-09	>40000		88.52	0.20	3.1	997.2	5.5	yes
12	11.90A	1100	1.55E-09	11174	1185	85.14	0.39	1.5	967.7	8.1	yes

13	12.10A		3.87E-09	29309	3885	87.09	0.18	3.6	984.7	5.3	yes
14	12.30A		6.28E-09	46694	5259	87.16	0.19	5.9	985.4	5.4	yes
15	12.50A	1200	6.01E-09	32286	2071	86.74	0.11	5.7	981.8	5.0	yes
16	12.75A		5.90E-09	15748	454	86.23	0.14	5.5	977.3	4.6	yes
17	13.00A	1250	9.94E-10	6315	720	84.09	0.58	0.9	958.5	10.8	no
18	13.25A		4.02E-10	3617	414	80.72	1.06	0.4	928.4	19.0	no
19	13.50A	1350	2.40E-10	1134	96	64.66	2.17	0.2	777.9	42.6	no
J-value: 0.008349 ± 0.000016			**Weighted average of included steps**			**87.98**	**0.03**	**97.1**	**992.6**	**4.6**	

Muscovite 2 - Z DK 13/5 (RHA Mine, Dete-Kamativi Inlier)

Step Nr	Laser power	Temp ˚C	cc stp ^{40}Ar	^{40}Ar/^{36}Ar	± 1σ	^{40}Ar*/^{39}Ar	± 1σ	%^{39}Ar	Age Ma	± 95%	Included
1	10.25A	550	3.76E-10	>4000		77.97	2.49	0.1	903.6	45.8	no
2	10.48A		2.12E-10	>60000		82.14	3.70	0.1	941.2	64.4	no
3	10.71A	700	1.21E-09	>40000		88.31	0.67	0.4	995.4	11.9	no
4	10.93A		2.50E-09	1430	30	83.81	0.54	0.8	956.0	10.4	no
5	11.16A	800	7.28E-09	4125	100	86.54	0.27	2.6	980.0	6.6	yes
6	11.39A		3.39E-08	23109	710	86.26	0.08	12.8	977.6	4.5	yes
7	11.61A	950	7.61E-09	4819	271	86.13	0.36	2.7	976.4	7.9	yes
8	11.84A		1.30E-08	13292	859	87.71	0.17	4.8	990.2	5.1	yes
9	12.07A	1050	5.54E-08	65348	3271	87.23	0.06	20.9	986.1	4.2	yes
10	12.29A		5.25E-08	70302	3958	87.14	0.07	19.8	985.3	4.4	yes
11	12.52A		2.68E-08	31455	930	86.42	0.06	10.1	979.0	4.2	yes
12	12.75A	1200	4.81E-08	41241	1048	86.73	0.07	18.1	981.7	4.5	yes
13	12.97A		1.02E-08	20746	1993	85.80	0.20	3.9	973.6	5.5	no
14	13.20A	1300	7.55E-09	14900	985	85.21	0.19	2.9	968.3	5.5	no
J-value: 0.008350 ± 0.000015			**Weighted average of included steps**			**86.86**	**0.03**	**91.7**	**982.8**	**4.2**	

Appendix B: Sample Preparation

B.1 MINERAL SEPARATION

Mineral separation occurs in four different stages. Step one involves crushing and milling the rock into a powder, from which the zircons can be extracted in subsequent steps. Steps two and four make use of a Wilfley table and heavy liquids (Figures B1 and B3 respectively) to separate the minerals based on their respective densities. Whereas the third step involves the use of a Frantz magnetic separator (Figure B2) to separate the minerals further, based on their different magnetic susceptibilities. The order of steps three and four are interchangeable – it is often dictated as much by preference, as by the volume of sample, proportion of quartz and feldspar, or the cost of consumables (particularly with regards to the heavy liquids).

1.1 Crushing and milling

This first step involves removing as much of the oxidised rind off of the samples as possible, in order to eliminate any likelihood of contamination. Following that the samples are broken up into pieces small enough to be fed through a jaw crusher, the resulting rock chips are then milled (with either a disk mill or rolling mill) to a powdered consistency which is then sieved through a 1000µm and a 300µm mesh. The material in the pan is then bagged for further separation.

1.2 Density Separation using a Wilfley table

A Wilfley Table – like the one in Figure B1 – combines a vibrating motion with a mineral's specific gravity in order to separate the denser minerals from the lighter material out of a slurry consisting of the powdered rock and running water. Minerals, such as quartz and feldspar as well as the very fine grained (dust-like) material, which have a low specific gravity are entrained in the flow of the water and washed off the table. The riffles on the table are designed to catch and direct the denser minerals to the far end of the table where they are collected (Grewal, 2016).

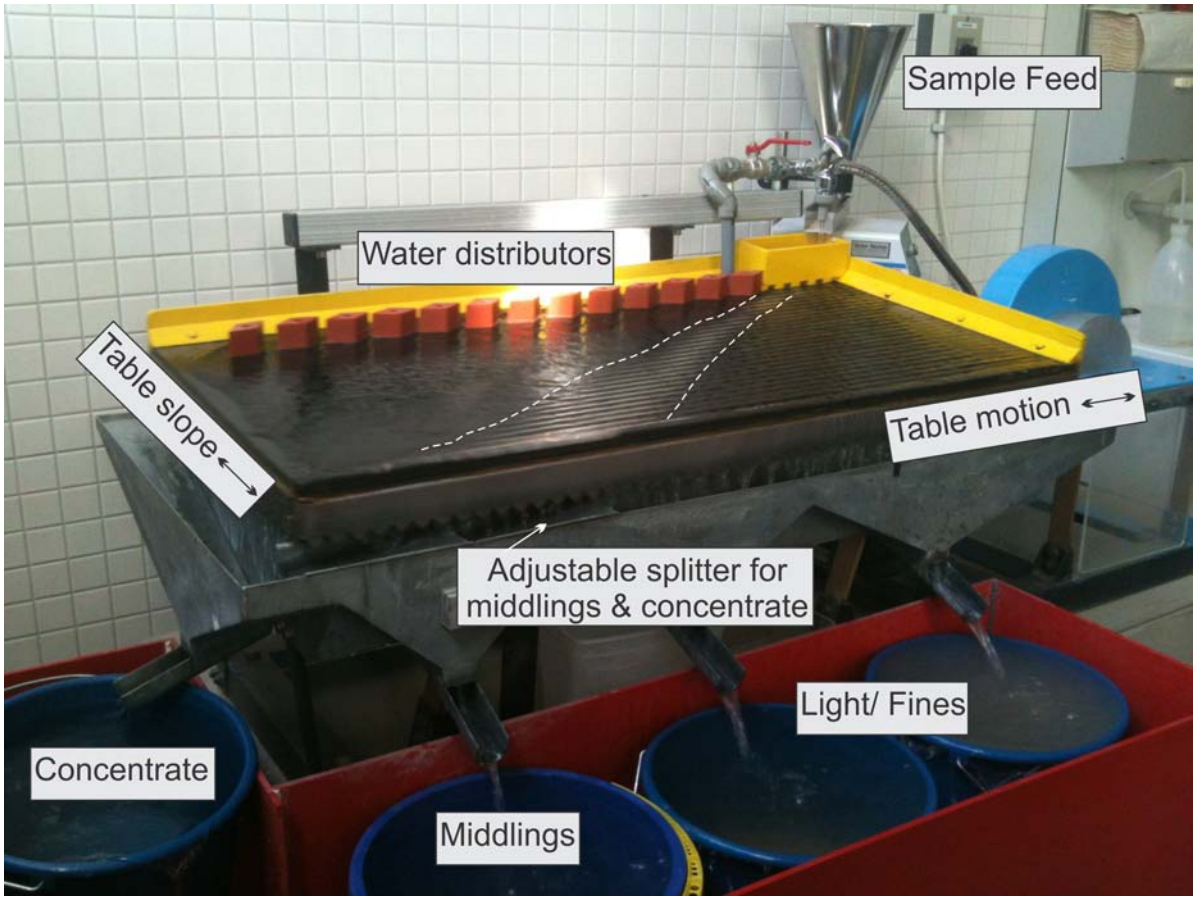

Figure B1: Depicts the design of a typical Wilfley table (after Grewal, 2016).

1.3 Magnetic separation

Once dry, the denser fraction is processed to remove the magnetic component. The material is first passed through an upright magnet (i.e. the coils from a Frantz magnetic separator orientated 90°) at ~ 10 Amps in order to remove any iron fillings which may have been introduced, in addition to the highly magnetic minerals such as magnetite.

The Frantz Magnetic Separator in Figure B2 was set at a 13° forward slope and a 5° sideways tilt, and for each sample passed through it, material was collected at intervals of either 0.3 or 0.6 Amps to start, then between 0.9 and 1.2 Amps (depending on the composition of the sample) and finally at 1.5 Amps. The most magnetic minerals were therefore removed first, with the least magnetic removed last, until only the non-magnetic minerals remain.

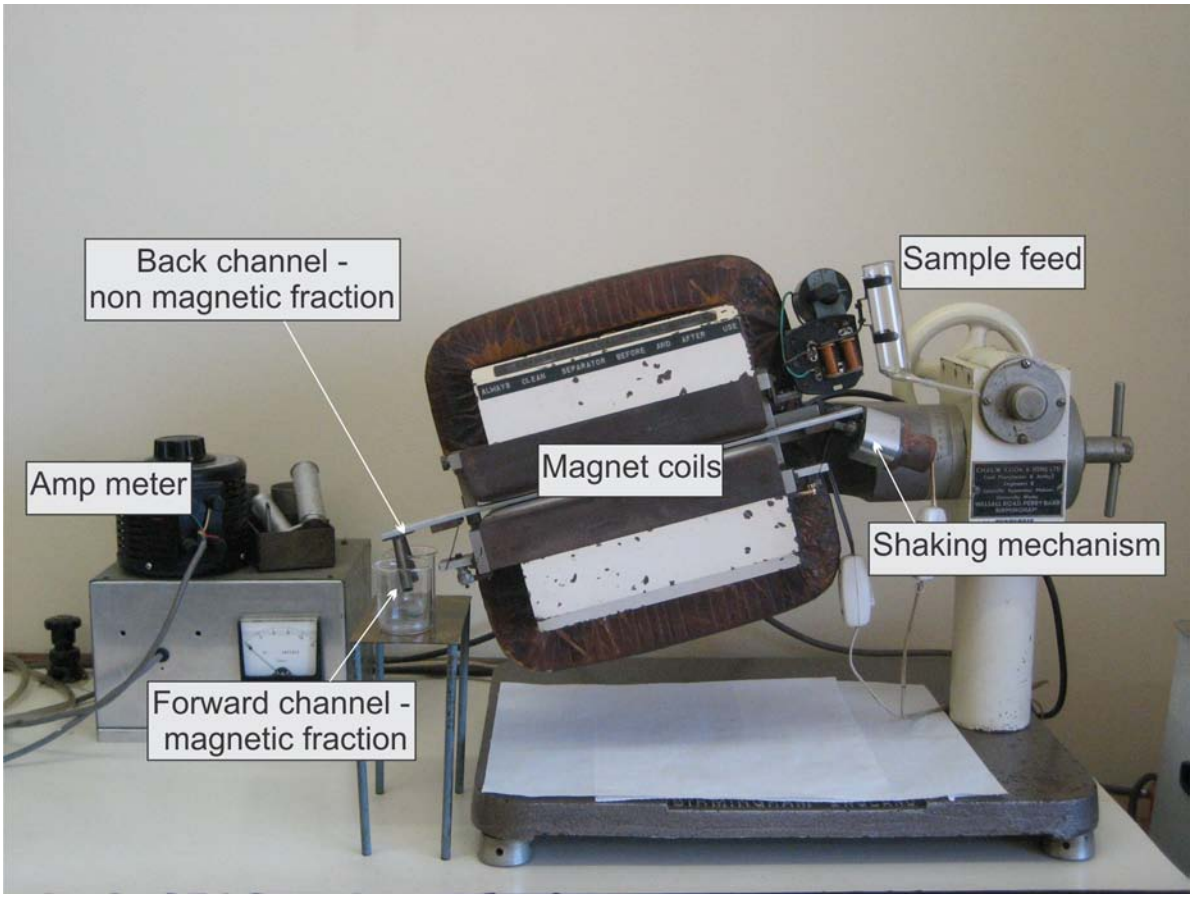

Figure B2: Demonstrates the component features of a (Charles Cook and Sons) Frantz Magnetic Separator.

1.4 Density Separation using Heavy Liquids

The heavy liquids used were Bromoform and Diiodomethane. Bromoform has a density of 2.89 g/cm^3 whereas Diiodomethane has a density of 3.33 g/cm^3 (WolframAlpha, 2011a, b). The latter was used only after the separates had already gone through the Bromoform separation in order to remove minerals such as apatite which tended to remain associated with the zircon.

The heavy liquid separation apparatus shown in Figure B3 consists of a large funnel with a tap at the base, this funnel can be positioned over one of two smaller funnels (each fitted with filter paper to collect the sample material). The two smaller funnels have beakers positioned underneath them to collect the heavy liquid once it has drained through the filter paper.

The concentrate is poured into the large funnel at the top containing the heavy liquid, and stirred gently in order to prevent clumping. The material is then allowed to settle and separate out. Once the material which is denser than the heavy liquid has collected at the bottom of the large funnel, the tap is opened to release that material into the first funnel and beaker set. The

large funnel is then repositioned over the second funnel and beaker set and the tap opened once more to release the less dense material which floats at the top.

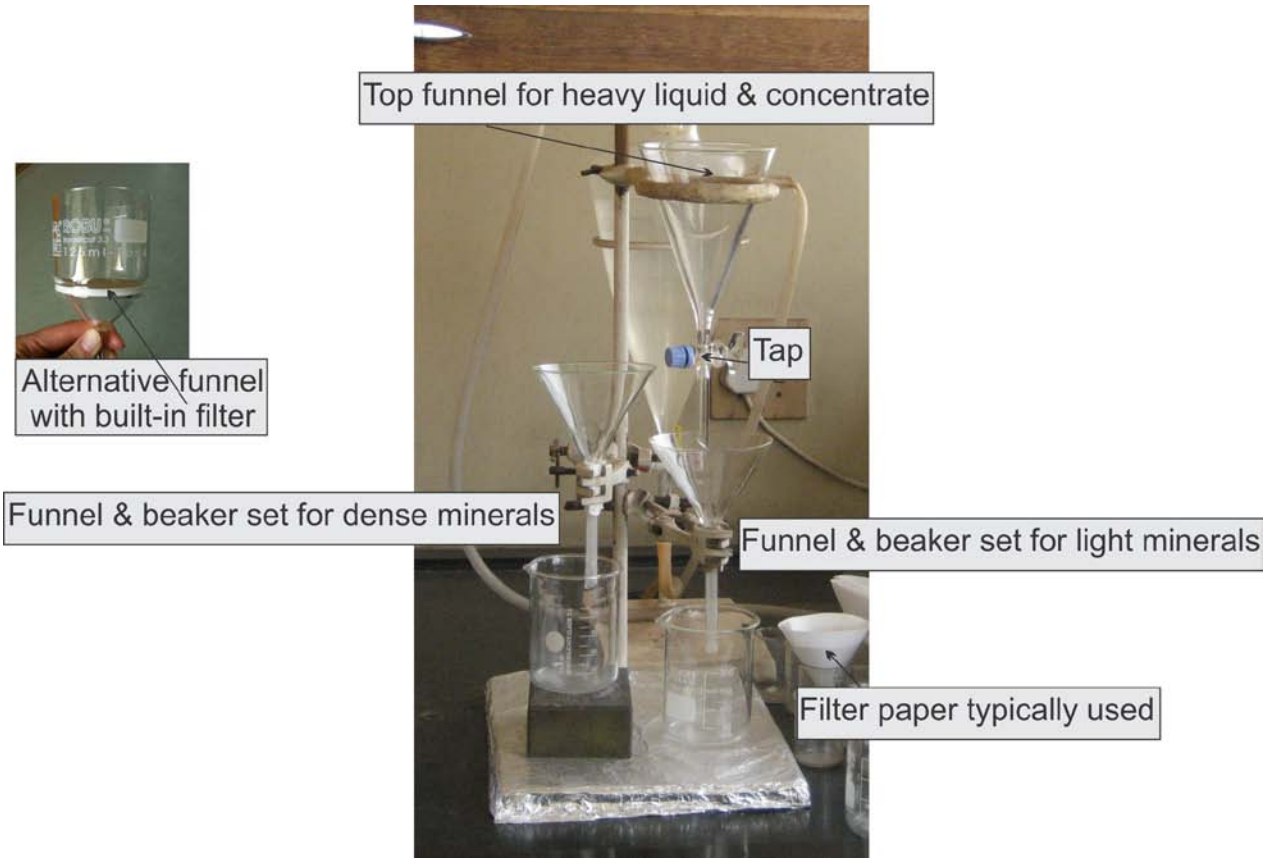

Figure B3: Illustrating the apparatus used for heavy liquid separations.

The filters used can either be standard filter paper, folded into a cone shape and placed inside the funnel, or a funnel with a built-in porous silicate pad. The latter is reusable and has the added advantage of being capable of filtering larger amounts of material more efficiently when connected up to a small roughing pump.

B.2 GRAIN MOUNTS

Subsequent to having separated out the zircon fraction the grains have to then be mounted. There is however a lot of variation in the technique due to preferences in the style and from specifications imposed by the analytical method to be used. Ideally a grain mount should be made up of multiple samples, each consisting of at least 100 grains per sample, mounted alongside the relevant reference materials, this is generally seen as sufficient as only a small number of analyses are generally required in order to determine the age of a rock. If however,

provenance studies are to be carried out – as is the case for detrital samples – then a larger number of grains can be analysed in order to ensure that as many populations as possible within a sample are represented (Vermeesch, 2004).

The grain mounts can be prepared by either using the more conventional method of double-sided tape or by creating a similar effect whereby the grains are embedded in a thin layer of epoxy, effectively replacing the double-sided tape. The advantage of this second method, is that it ensures the grains are completely surrounded by placing them directly into the epoxy, this consequently ensures a smoother surface, unlike the double-sided tape method where the surface is inherently rough due to the glue residue from the tape. One further advantage of using the epoxy base is that there is greater control over the placement of grains, which is ideal if crystallographic orientation is important.

A flat working surface is made by placing a thin film of aluminium foil onto a clean glass plate, using a drop of glycerine to help it adhere (the function of the foil is to help remove the finished grain mount from the glass plate with less difficulty). Any air bubbles in the foil should be smoothed out and the surface cleaned with ethanol to remove any glycerine residue. Using a template (such as the one in Figure B4a, which is the 25 mm ring that functions as the mould for the grain mount), an outline of the mount is drawn directly onto the foil and a drop of epoxy is placed near the outline (Figure B4b). With a clean glass slide, the epoxy is smeared in such a way that there is a thin, even layer of epoxy covering the area of the outline (Figure B4c). The layer must not be too thin in order to avoid it drying too quickly, but it is critical that the layer be even, so that the grains rest directly on the surface of the foil.

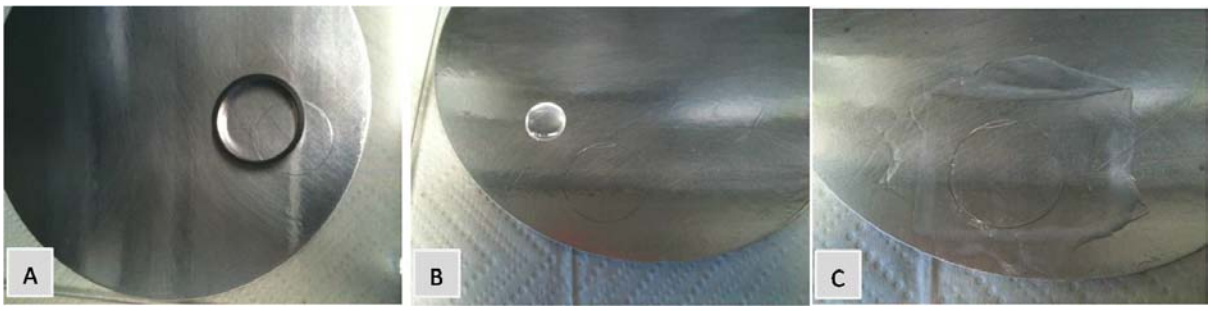

Figure B4: Grain mount preparation using epoxy as a base.

Once the base has been prepared it is then possible to mount the grains. Care must be taken to ensure that the grains mounted together are of a uniform size, so as to prevent losses when polishing. Likewise the grains are placed in close proximity to one another in order to

simplify documentation later. The layout should also be made as unambiguous as possible in order to avoid confusion when it is turned over. An example of a grain mount prepared for SIMS analysis is shown in Figure B5, where the grains were placed within an inner 15 mm diameter ring and a small semi-circle was reserved for the reference material.

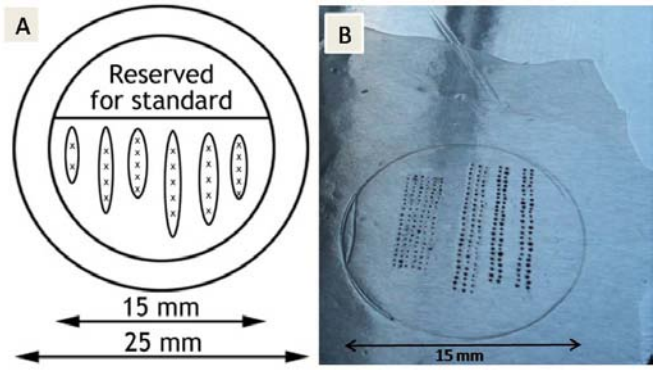

Figure B5: Preferred grain mount geometry for SIMS analyses. By mounting the grains within the inner ring, the edge effect observed in isotopic analyses is greatly reduced. Figure B5a is taken from Andersson (2015).

The grains as well as the mould both need to be fixed in place before the epoxy dries completely. First though the side of the mould which is to make contact with the foil should be polished slightly beforehand in order for it to have a flat surface, which is then level with the grains embedded in the epoxy. Once the epoxy has dried somewhat, it is then possible to finish casting the grain mount. This is done by slowly pouring epoxy down the sides of the mould so that it spread gradually around and over the grains until they are completely covered, care should be taken to avoid making any air bubbles or causing any grains to shift about. The mould is also usually overfilled slightly because as epoxy hardens it contracts slightly.

Polishing should be done gradually, going from 1200 to 2400 and then 4000 grit polishing paper before moving onto 3 µm and ¼ µm diamond paste to achieve the final mirror-like polish. If bubbles around the grains are exposed in the early stages of polishing, the grain mount should be placed within an ultrasonic bath to remove any material from the holes; it should then be wiped clean with ethanol and left to dry overnight before covering the surface again with a thin layer of epoxy. The grain mount can then be placed under vacuum to draw out any air bubbles within the epoxy, when these bubbles appear on the surface they can

simply be burnt off using a lighter. The new layer of epoxy should then be left to harden overnight before resuming polishing.

B.3 IMAGING

The first step is to use reflected and/ or transmitted light to take low magnification images, which when stitched together can be used for navigational purposes. These 'mount maps' aid in taking either CL or BSE images of the grains, which are of vital importance in selecting which grains to measure as imaging is an important step in determining the morphology of the zircon grains.

The CL images were taken at the University of Stellenbosch's Central Analytical Facility, using a LEO 1430VP Scanning Electron Microscope (SEM) fitted with a Centaurus detector, operating with a beam voltage of 20.00 kV and a spot size of 550 µm; while the BSE Images were taken at the GeoForschungsZentrum, Potsdam, using a Zeiss Ultra 55Plus SEM fitted with a angle selective BSE detector, operating with a beam voltage of 20.00 kV and a spot size of 120 µm.

Imaging is practical, non-destructive ways of determining a grain's internal structure, and consequently allows for more informed decisions to be made, as to not only which grain to measure but where. Cracks and inclusions can then be avoided as they introduce unnecessary common lead, as do grains which are highly metamict (i.e. damaged by α-decay and result in anomalously high uranium concentrations). Care should be taken when measuring the rims of grains, as they may have been subjected to a number of events: re-crystallisation, hydrothermal alteration or dissolution and re-precipitation; all of which can affect the age.

CL and BSE images are the result of secondary electrons becoming activated by the interaction of a primary electron beam with the trace elements which exist within a sample (Nasdala et al., 2003; Pagel et al., 2000; Rubatto and Gebauer, 2000). Colour CL images (produced by a CL-detector fitted to an optical microscope) are particularly good at representing the energy spectrum produced by this interaction, because the individual minerals have a unique spectrum of elemental peaks which are represented by specific colours (Nasdala et al., 2003). Conventional CL images however, are taken using a CL-detector fitted to a Scanning Electron Microscope, and like BSE images produce black and white images. This type of imaging is particularly useful in identifying areas where the crystalinity of a grain has been affected by radioactive decay and has effectively become

metamict, it also easily picks up on a ny zonation within grains and can therefore reflect processes such as trace element migration (Corfu et al., 2003; Hanchar and Miller, 1993; Nasdala et al., 2003; Rubatto and Gebauer, 2000).

Appendix C: Analytical Methods

C.1 SIMS DESIGN FEATURES WHICH AID U-Pb ZIRCON GEOCHRONOLOGY

1.1 Primary beam configuration

In order to perform U-Pb measurements, the instrument must first be tuned correctly – this involves firstly selecting the appropriate primary ion beam – in the case of U-Pb measurements a $^{16}O_2^-$ beam is used, in order to generate positive secondary ions. Köhler or Aperture illumination is used to evenly illuminate the Primary Beam Mass Filter (PBMF) aperture in order to produce a spot size of 20-25 μm in diameter on the sample surface (Whitehouse et al., 1997). This spot size is attainable because this type of illumination results in the formation of a more diffuse ion beam, which produces a flat-bottomed pit. Another advantage to working in Köhler mode is that the secondary ion yield is more constant and reproducible, due to contamination from the edges being reduced (Williams, 1998).

1.2 Oxygen flooding

The sputtering process is in reality inefficient, with only a small percentage of the sputtered material becoming ionised. Studies have shown that the secondary ion yield of Pb species is generally very poor; thus for U-Pb measurements, this unique feature of CAMECA ion probes is used to enhance Pb sensitivity (Schuhmacher et al., 1993; Whitehouse et al., 1999). Oxygen flooding entails opening a leak valve (from the same oxygen supply as the primary beam) into the sample chamber; this increases the pressure in the chamber typically to ~2.0 x 10^5 mbar. The increase in pressure has a reciprocal effect on the work function – i.e. the energy required to release an electron from the highest filled Fermi (or electron energy) level (NPL, 2015). As illustrated in Figure C1, by increasing the work function (Φ), the probability of ionisation becomes greater because electrons which are below the Fermi level (E_F) are more readily donated; this means that species such as Pb and U become oxidised to Pb^+ and U^+, which are better ionised (Arlinghaus, 2014). As a result the counts per second on Pb using $^{16}O_2^-$ with oxygen flooding on a CAMECA instrument is approximately 4 times that compared to when used without flooding.

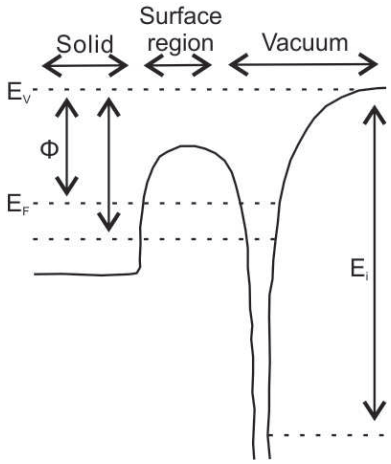

Figure C1: Sketch illustrating how ionisation is improved with oxygen flooding, where E_V: Vacuum level and E_i: Ionisation level (after Arlinghaus, 2014).

1.3 Mass resolution

The Potsdam 1280-HR is tuned to have a mass resolution of approximately 5400 atomic mass units (amu) for zircon measurements. This is calculated by dividing the mass (M) by the difference in mass (ΔM) at 10% of the peak's intensity.

$$M/\Delta M \qquad (C1)$$

The large geometry design of the 1280-HR allows for higher mass resolutions to be obtained relatively easily. In order to maintain high transmission at the higher mass resolutions required for U-Pb analyses, a number of apertures and slits must be tuned to be as open as possible to allow as many ions as possible to reach the detector(s), while at the same time limiting the number of aberrations this causes. Attaining a sufficiently high enough mass resolution is crucial for resolving all key isobaric interferences caused by molecules of similar mass. These interferences occur when the secondary ions of different elements and/ or molecules have effectively the same nominal mass-to-charge ratio. For example the mass resolution required to resolve ^{208}Pb from $^{176}Hf\ ^{16}O_2$ is 4529 – this can be determined using equation C1.

^{208}Pb = 207.976641 amu

$^{176}Hf\ ^{16}O_2$ = 207.9312493 amu [which is 175.941420 + (15.99491464 x 2)]

Therefore ΔM = 0.0453917 amu (207.976641 - 207.9312493)

And the mass resolution necessary is therefore 4529 (207.976641/ 0.0453917).

The most common isobaric interferences for the Pb species are generally a number of hafnium silicates, hafnium oxides and zirconium oxides.

The double focussing effect accomplished by the ESA and the Magnet

The ESA is responsible for generating an energy dispersion, whereby the ions are split according to how much energy they have going into the ESA. Ions with more energy will take a path with a slightly wider trajectory compared to ions of lower energy (see Figure C2). By adjusting the position of the energy slit after the ESA, it is possible to select whether only the high energy ions or the low energy ions should be allowed to pass through. The ions – which are of differing mass, but now all have the same energy – are directed into the magnet, which has an energy and mass dispersive effect. The heavier ions travel along a wider arc, and can be found on the outside edge of the exit slit, while the lighter ions can be found on the inside edge. The ions now all have approximately the same energy as well as mass (CAMECA; Wirtz, 2014).

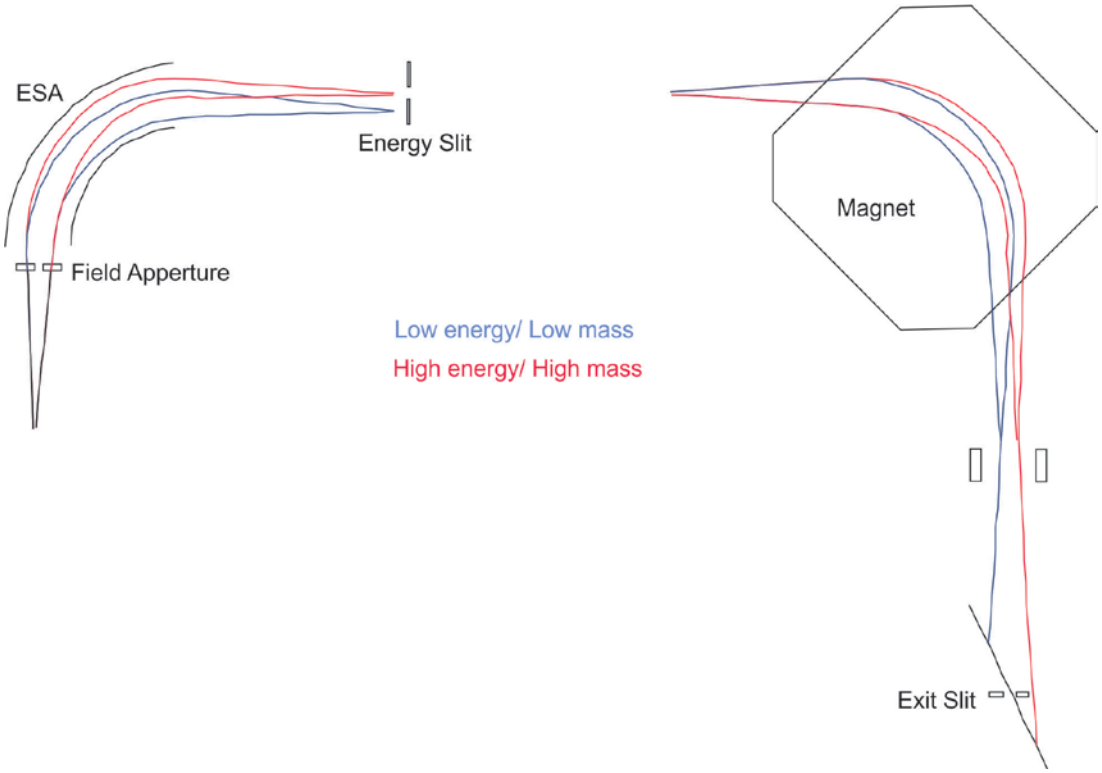

Figure C2: Sketch of how the secondary ions are separated according to their mass-to-charge ratio (after CAMECA).

1.4 Ion detection

There are three ion detection systems on the 1280-HR: mono-collection, multi-collection and ion imaging systems, such as the micro-channel plate and Resistive Anode Encoder (RAE). The latter two pieces of instrumentation can be used to generate qualitative elemental distribution maps with the instrument operating in ion microscope mode. The RAE can digitally record the x: y co-ordinates of ions which hit the surface of a silicon wafer, and each ion is then assigned as a pixel on a screen. The micro-channel plate generates a pul se of electrons when an ion strikes it; this pulse of electrons is then directed to a phosphorescent screen connected to the micro-channel plate which converts the signal to a pulse of photons that are then detected by a CCD camera. The spatial resolution of these two methods is comparable; however the micro-channel plate requires much higher count rates to be as effective, due to its lower sensitivity (Wiedenbeck, 2012).

The mono-collection system consists of two faraday cups (FC) and a single electron multiplier (EM), while the multi-collection system consists of 5 trolleys – each of which can carry either an EM or FC. Currently the Potsdam instrument is set up with 5 EM's and 2 FC's as its multi-collector system.

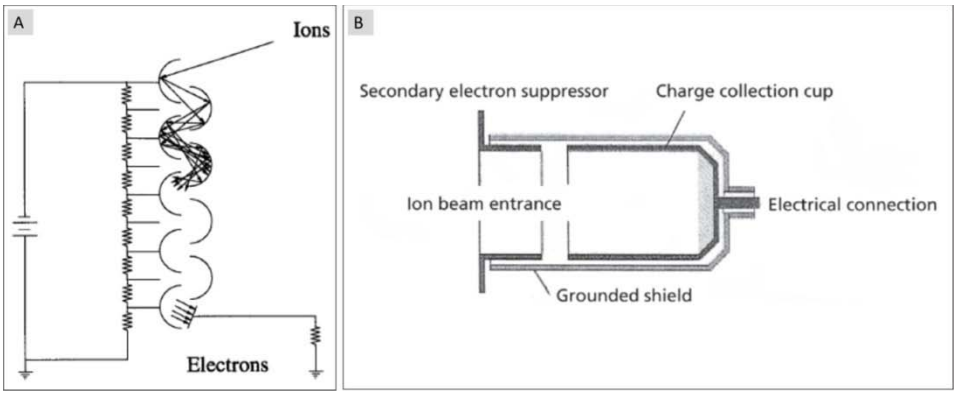

Figure C3: Simple schematic of how the two types of ion detectors (Electron Multiplier (Figure C3a) and (Figure C3b) Faraday Cup) commonly used in ion probe instruments operate. Images sourced from Wiedenbeck (2012) and Busch (2011) respectively.

An electron multiplier (Figure C3a) is designed to detect and count individual ions. When an ion strikes the first dynode of the multiplier it produces a number of secondary electrons; this cascade of electrons eventually hits the collector at the back, which then converts the electrons into a pulse; large enough for the electronics to detect. The EM operates at lower

count rates (<500 000 ions per second) compared to the FC, which operates at count rates of ~ 1 million or more (Wiedenbeck, 2012). A FC (Figure C3b) is a hollowed out metal cup which traps charged particles, and can be considered as a component of a circuit, so when an ion touches the inside surface of the cup its charge is converted to a current which flows through the circuit. This current can be accurately measured, and is directly proportional to the number of ions within the cup (Busch, 2011).

C.2 DECIDING WHICH CALLIBRATION CURVE TO USE, AND THE FACTORS WHICH CAN AFFECT IT

By calibrating in the manner outlined in section 2.5.1, the uncertainty measured for each spot is eventually propagated onto the age; hence a consensus on the type of calibration used is important, as this has implications for the precision and accuracy on the age of the unknown zircon (Jeon and Whitehouse, 2015). SHRIMP users have a tendency to favour a Pb^+/U^+ vs. UO^+/U^+ calibration (Compston et al., 1984), while Whitehouse et al. (1997) observed a better correlation between Pb^+/U^+ and UO_2^+/U^+. Recently however, Jeon and Whitehouse (2015) conducted a study comparing various calibrations in order to determine which was statistically the most reliable. Based on the results, it was concluded that a Pb^+/UO^+ vs. UO_2^+/UO^+ calibration in conjunction with a power law function consistently produced curves with the best fit.

Other factors which could affect the calibration were also considered by Jeon and Whitehouse (2015). Firstly they stated that atomic species generally have stronger secondary ion intensities (counts per second) than their molecular counterparts. However in the case of U and either UO or UO_2, the oxides in particular, have much higher intensities, which translates to better counting statistics and thus better repeatability for the individual measurements. The second factor relates to the energy distribution of atomic vs. molecular species. A calibration involving a UO_2 species is preferable due to the similarity between the UO_2^+ and Pb^+ energy spectra (Schuhmacher et al., 1993); also the shape of the $^{238}U^+$ energy spectrum (Figure C4) makes it less desirable for calibrating with, because the rounded peak which forms is more susceptible to sample charging (Jeon and Whitehouse, 2015).

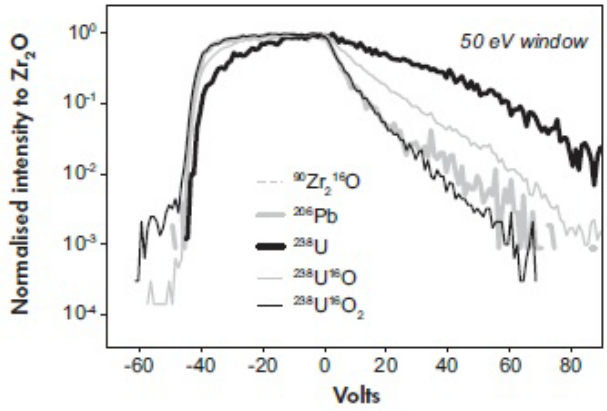

Figure C4: Secondary ion energy scan with a 50 eV wide energy window, where the signals have been normalised so as to all have the same peak heights. This image illustrates how distinct the ^{238}U energy spectrum is from its molecular counterparts, while in comparison the curve for ^{206}Pb is very similar to that of $^{238}U^{16}O_2$. The curve shape for the latter is also significantly more robust than that of ^{238}U. Figure is after Jeon and Whitehouse (2015).

Under stable operating conditions the U-species tend to disperse little (i.e. shift position along the x-axis in a calibration curve plot). If, however, dispersion had occurred it would be either an indication of inhomogeneity and/ or a change in the sputtering conditions during a session (Ireland and Williams, 2003). With regards to the latter, Jeon and Whitehouse (2015) did not observe changes in the sample chamber pressure as having an effect on a calibration. However, as part of our analyses, it was observed that changes in the primary beam current may have an effect, and could be particularly noticeable in some instances, such as the case in Figure C5.

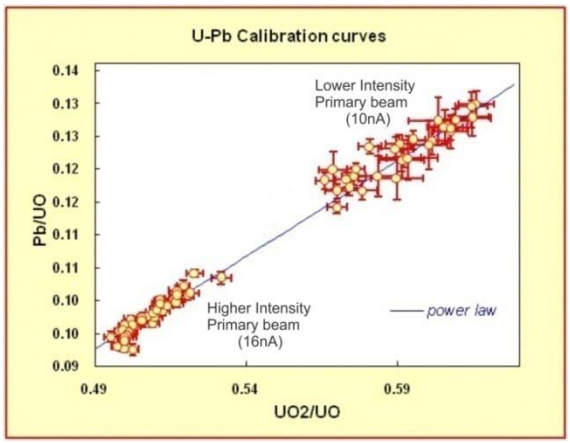

Figure C5: An example of a calibration where the primary beam intensity varied over the course of the session. Both the pressure in the sample chamber and oxygen source remained constant over the course of this session at 2 x 10^{-5} mbar and 5.4 x10^{-5} mbar, respectively.

In this situation where the primary beam intensity is so varied, it was unclear whether to proceed performing the data reduction using a single calibration curve (i.e. use all the measurements, regardless of intensity) or split the data, and generate two curves – one for the samples measured using the lower primary beam current, and another for the those made with a higher current. This problem was tested by using the Plešovice zircon reference material (337.13 ± 0.37 Ma; Sláma et al., 2008) as an unknown. The ages calculated using only the low intensity curve and the combined curve were in both instances older than that for Plešovice, being 341 ± 0.96 and 343 ± 0.88 Ma respectively. The high intensity curve however, gave an age which was almost an exact match (337 ± 1.9 Ma). Without further experimentation, we can only speculate at this point that this outcome is potentially due to the smaller uncertainties on the higher primary beam intensity measurements.

Appendix D: Research Outputs

D.1 SIJARIRA MANUSCRIPT

U-Pb ages and provenance of zircons from the Neoproterozoic Sijarira Group, Western Zimbabwe - an Antarctica connection?

Sharad Master[a, b*], Sarah M. Glynn[b, c], Michael Wiedenbeck[c, b]

[a] Economic Geology Research Institute (EGRI);School of Geosciences, University of the Witwatersrand, Private Bag 3, W its 2050, Johannesburg, South Africa; *Corresponding Author; Email: sharad.master@wits.ac.za

[b] School of Geosciences, University of the Witwatersrand, Private Bag 3, W its 2050, Johannesburg, South Africa

[c] Deutsches GeoForschungsZentrum, Potsdam, Telegrafenberg, D-14473, Potsdam, Germany

Abstract

The Sijarira Group is a Precambrian unfossiliferous, unmetamorphosed redbed sequence, which unconformably overlies the Palaeoproterozoic Magondi Belt in western Zimbabwe. We performed SIMS U-Pb isotope dating of detrital zircons from a coarse-grained trough crossbedded sandstone, from the Chizarira Hills. Our data indicate that the Sijarira Group is derived from erosion of a distant late Mesoproterozoic (c. 1.05 Ga) terrain, with minor provenance from Neoproterozoic rocks. The vast majority (80%) of the zircons record ages between 1075 Ma and 835 Ma. The Sijarira Group cannot be regarded as a molasse of the nearby Pan-African Zambezi Belt, since it contains very few Neoproterozoic zircons, and the palaeocurrents were in general from E to W. We suggest that its provenance is from the erosion of a late Neoproterozoic collisional zone of the southern Mozambique Belt and Maud Belt of West Dronning Maud Land, Antarctica, to the east of the Zimbabwe

Craton. The c. 1075 to 1000 Ma detrital zircon population in the Sijarira sample could have been sourced from the HU Sverdrupfjella region, in the Maud Belt, where there are gneisses of that age range formed by late Mesoproterozoic arc collisions. The youngest Sijarira zircons may be derived from Neoproterozoic intrusive rocks from the Maud Belt, or they may be related to a 615 ± 30 Ma tectonic event recorded in eastern Zimbabwe. The lack of Pan-African zircons is due to a relative lack of Pan-African aged magmatism in West Dronning Maud Land and in the southern Mozambique Belt. Our new maximum age for the Sijarira Group of c. 632 M a indicates an Ediacaran depositional age. The Sijarira Group thus correlates in terms of age with other late Neoproterozoic to Palaeozoic post-Pan-African molasse basins surrounding the Kalahari Craton, such as the Okwa Group of central Botswana and the Nama basins of southwestern Africa.

Keywords

Ediacaran; redbeds; provenance; Maud Belt; Mozambique Belt

1. Introduction

The Sijarira Group is a non-fossiliferous redbed succession of sandstones, granulestones, conglomerates and shales, of continental fluviatile and shallow-marine origin, which outcrops in the Chizarira Hills and Hurungwe areas in western Zimbabwe. Although the unmetamorphosed Sijarira Group has not been dated, it overlies the Palaeoproterozoic Magondi mobile belt. It is aligned with, and has been regarded as a continuation of, the Sinclair-Ghanzi belt of early Neoproterozoic redbeds extending across Namibia and northern Botswana (Humphreys, 1969; Stagman et al., 1978).

The Sijarira Group was first recognized as a pre-Karoo sedimentary unit by Molyneaux (1903), and further reconnaissance of these beds was made by Molyneaux (1922). Outliers of the Sijarira Group were mapped in the Hwange (Wankie) area by Watson (1962) and Lockett (1979).The main outcrops of the Sijarira Group in the Chizarira Hills area were mapped by Chappell (1969) and Humphreys (1969). They subdivided the group into three subgroups and eight formations, having a total thickness of 660 m. The stratigraphically lowest Subgroup is the Lubu Subgroup (maximum thickness 250 m), which comprises the Sebungwe (37 m), Ruziruhuru (76 m) and Masumo (137 m) Formations. This is overlain by the Mcheni Subgroup (122 m), consisting of the Mbaruri (76 m) and Chizarira Hills (46 m) Formations. The uppermost Subgroup is the Sengwa Subgroup (291 m), consisting of the Siantangola (198 m), Masakesi (40 m) and Kazungwizi (53 m) formations. The lithologies consist of conglomerates, trough crossbedded and rippled sandstones, siltstones and mudstones which were deposited in fluvial, shoreline and shallow-water lacustrine or playa environments. The palaeocurrents, which had a wide spread in azimuths, were mainly east-to-west, with major modes at 250° and 350°, and minor modes at 150 ° and 45 ° (Chappell, 1969).

In the Hurungwe District of NW Zimbabwe, the Sijarira rocks were regarded as having been overthrust by the "Urungwe Klippe" (Stagman, 1962; Shackleton et al., 1966). Mapping by Harper (1970) and Mann (1970) has shown that the Sijarira Group rocks in this area have themselves been tectonically repeated in imbricate thrust stacks associated with the Urungwe Klippe. Mann (1970, 1979) subdivided the Sijarira Group into an 1170 m-thick southern facies with six formations and a 1314 m-thick northern facies with eight formations, including rocks from the Urungwe Klippe. The lithologies of the southern facies consist of

arenites, grits, greywackes, siltstones and shales which were deposited in fluvial, beach, estuarine and deltaic environments (Mann, 1970, 1979, 1982) . The palaeocurrents were generally from southeast-to-northwest (Mann, 1970, 1979). The basal unit in the southern facies, the Nyangadze Formation, was interpreted by Mann (1982) as being adeltaic deposit, in which a heavy mineral-rich band, interpreted as a palaeostrandline, contains concentrations of ilmenite-magnetite (12-58 wt %), garnet (5-18 wt %), epidote (2-8 wt %) and sphene (2-5 wt %). The northern facies lithologies consist of arenites, argillites, diamictites, orthoquartzites and stromatolitic and oolitic dolomites, which were deposited in shallow marine and glaciofluvial environments (Mann, 1970, 1979) . The orthoquartzites and dolomites of the northern facies were originally regarded by Stagman (1962) as being part of the Lomagundi Group, but their carbon isotope signature is totally different from that of the Lomagundi Group (Schidlowski et al., 1976). Although Mann (1970, 1979) placed the carbonate rocks of his "northern facies" into the Sijarira Group, this is at odds with the interpretation of the Urungwe Klippe as an allochthonous thrust sheet emplaced onto the Sijarira Group during Pan-African tectonism (e.g., Stagman, 1962; Shackleton et al., 1966; Treloar, 1986). Stagman et al. (1978) placed the sedimentary rocks of the Urungwe Klippe into the Tengwe River Group. This group consists of a sporadically developed basal arkose, covered by a 200 m-thick Calcareous Formation, consisting of basal limestones and marls overlain by dolostones. This is then overlain by a 300 m-thick Orthoquartzite Formation, which contains some shale intercalations. Unconformably overlying the Tengwe River Group there is a glacial diamictite, called the Msukwi River Diamictite, with striated and facetted pebbles (Molyneaux, 1922), which is overlain by banded shales, up to 100 m in thickness. Although Stagman et al. (1978) regarded this diamictite as being of Karoo age (i.e., Late Carboniferous), the fact that the diamictite is tectonised led Harper (1970), Mann (1970) and Bond (1981) to regard it as being of Neoproterozoic age, possibly related to the

Neoproterozoic glaciations found in the Katangan Rocks of the Lufilian Arc and Damara Orogen (Master and Wendorff, 2011). The tectonism which produced the thrusting in the Urungwe Klippe occurred during the late Neoproterozoic Zambezi Orogeny, between 850-450 Ma (Treloar, 1986; Hanson et al., 1994; Dirks et al., 1999; John et al., 2004).

On the basis of extant radiometric dating, the age of the Sijarira Group should be bracketed between 1211 ± 40 Ma (the recalculated age of the underlying Urungwe granite, Clifford et al., 1967), and the late Carboniferous, c. 320 Ma, age of the overlying Karoo beds (e.g., Riek, 1974; Chappell and Humphreys, 1981). If the youngest K-Ar mineral ages of biotite from the Urungwe granite are utilized, then the maximum age of the Sijarira Group is constrained to be c. 880 ± 40 Ma (Clifford et al., 1967). Despite this, the age of the Sijarira Group was erroneously reported as between 1345 and 1170 Ma, by Andrews-Speed and Unrug (1984), and by Fernandes et al. (2005).

2. Field occurrence and petrography of the Sijarira sandstone sample ZMB13/2

We conducted a reconnaissance traverse of the Sijarira Group, its Palaeoproterozoic basement, and the Karoo sedimentary cover in October 2013. We collected a sample of coarse-grained Sijarira Group sandstone at 17° 39’ 04.0” S; 27° 51’ 21.0” E, in the Chizarira Hills. Our sample ZMB13/2 comes from the Ruziruhuru Formation of the Lubu Subgroup (Chappell, 1969; Humphreys, 1969). The sandstone is coarse-grained and arkosic, with a pale pink colour and is characterized by the presence of trough crossbedding. It resembles fluviatile sandstones (facies St) that are commonly found associated with braided river environments (e.g., Miall, 1977).

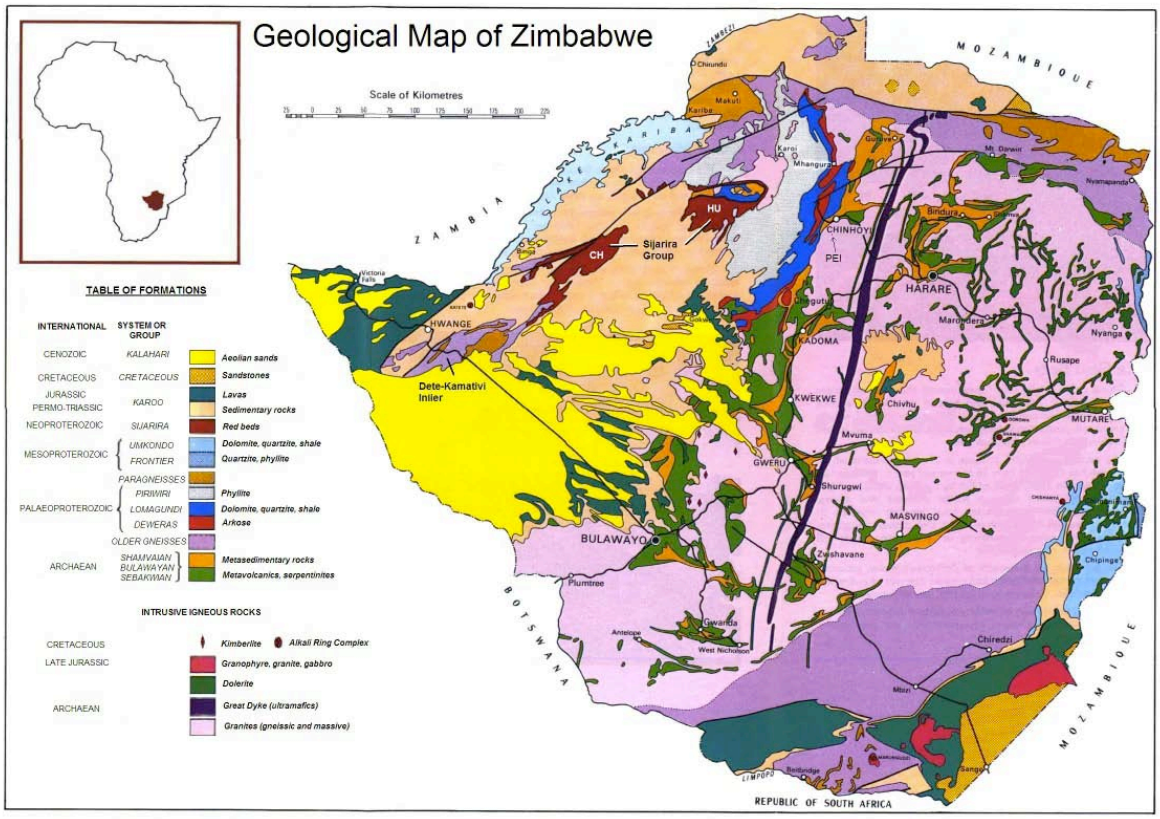

Figure 1: Geological map of Zimbabwe, showing the location of the Sijarira Group. Simplified and modified after Geological Survey of Zimbabwe (1994). CH = Chizarira Hills; HU = Hurungwe area; PEI = Portelet Estate Outlier.

The sandstone consists of a mixture of quartz, feldspar and lithic fragments cemented together by a fine-grained, maroon coloured matrix. The fragments range in composition from sub-rounded grains of (polycrystalline) quartz (Fig. 2b – left) to irregularly shaped chert fragments (Fig. 2b – right).

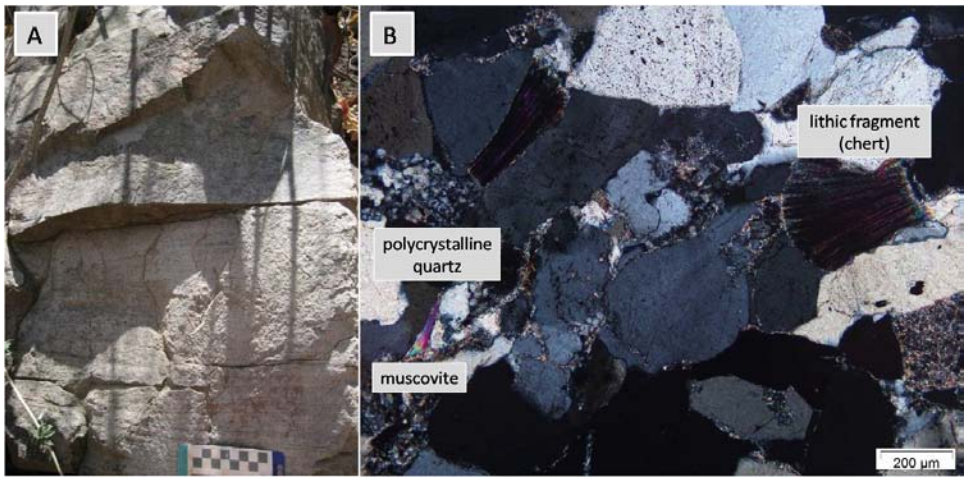

Figure 2: (A) Field photograph (with scale in cm), and (B) photomicrograph of sandstone sample Z MB 13/2 from the Sijarira Group.

3. Analytical Methods

After crushing and milling, zircons were extracted using standard heavy liquid preparation techniques. Once mounted, electron microprobe backscatter imaging (BSE), and cathodoluminescence (CL) imaging of the zircons were used to help in the selection of sample spots for U-Pb dating on the CAMECA 1280-HR SIMS instrument at the GFZ, Potsdam. Full details of the analytical protocols for U-Pb dating of zircons using the Potsdam instrument are given by Glynn et al. (2016).

4. Results

The zircon grains are for the most part sub-angular, with a small number still retaining their euhedral shape (such as the grain in Figure 3, which has been subjected to metasomatism, altering the rims and making them enriched in uranium). The data obtained from the Sijarira detrital zircons is presented in Table 1. The detrital zircon population ranges

in age from about 1991 to 631 Ma (Figures 3 and 4). The three youngest detrital zircon grains from the Sijarira sandstone are dated at 602.3 ± 28.2 Ma, 627.7 ± 7.8 Ma and 632.7 ±12.5 Ma, having a weighted mean age of 631.6 ± 4.4 Ma, which gives a maximum depositional age for the Sijarira Group. The two oldest zircon grains, which are slightly discordant, give ages of 1991.3 ± 6.3 Ma and 1746.9 ± 4.1 Ma, while the vast majority (80%) of the zircons record ages between 1075.3 ± 13.2 Ma and 834.7 ± 16.9 Ma, with a weighted mean average age of 1035.3 ± 2.8 Ma.

Table 1: SIMS U-Pb zircon data from Sijarira Quartzite sample Z MB 13/2

Spot	Comment	% $^{206}Pb_c$	µg/g U	µg/g Th	µg/g $^{*206}Pb$	$^{232}Th/^{238}U$ Meas	$^{207}Pb/^{206}Pb$ age (1)	± 1sd	$^{206}Pb/^{238}U$ age (1)	± 1sd	% Disc (2sd)	$^{*207}Pb/^{*206}Pb$	± 1sd	$^{*207}Pb/^{235}Pb$	± 1sd	$^{*206}Pb/^{238}Pb$	± 1sd	Error Correlation
Z MB 13/2 - Sijarira Quartzite (17° 39' 04.0" S; 27° 51' 21.0" E)																		
MB 13-2@1	rim	{0.02}	361	161	73	0.446	1038.4	9.9	1003.5	15.5	-3.6	0.07389	0.49	1.71595	1.74	0.1684	1.67	0.95890
MB 13-2@2	core	0.11	195	112	34	0.574	834.7	16.9	852.2	13.3	2.2	0.06690	0.82	1.30369	1.86	0.1413	1.67	0.89830
MB 13-2@3	c	0.07	324	111	68	0.343	1075.3	10.2	1068.9	16.5	-0.6	0.07526	0.51	1.87143	1.75	0.1804	1.67	0.95609
MB 13-2@4	c	{0.05}	113	28	23	0.245	1016.5	19.1	1055.4	16.3	4.1	0.07309	0.95	1.79262	1.92	0.1779	1.67	0.86958
MB 13-2@5	c	0.05	355	173	76	0.488	1033.4	10.1	1048.5	16.2	1.6	0.07371	0.50	1.79504	1.74	0.1766	1.67	0.95768
MB 13-2@6	c	0.01	2518	543	301	0.216	627.7	7.8	652.5	10.4	4.1	0.06067	0.37	0.89107	1.71	0.1065	1.67	0.97692
MB 13-2@7	c	{0.03}	285	142	59	0.496	1048.6	10.9	1017.6	15.7	-3.2	0.07426	0.54	1.75092	1.75	0.1710	1.67	0.95125
MB 13-2@8	c	0.03	1252	455	261	0.363	1040.0	5.0	1052.0	16.2	1.2	0.07395	0.25	1.80727	1.69	0.1773	1.67	0.98907
MB 13-2@9	c	0.15	341	160	70	0.470	1012.4	14.8	1023.7	15.8	1.2	0.07294	0.73	1.73097	1.82	0.1721	1.67	0.91535
MB 13-2@10	r	0.03	2543	95	483	0.038	1006.2	4.3	1041.5	16.1	3.8	0.07272	0.21	1.75818	1.69	0.1753	1.67	0.99213
MB 13-2@11	c	0.19	67	37	14	0.549	979.8	27.6	1005.7	15.7	2.9	0.07178	1.37	1.67095	2.17	0.1688	1.69	0.77712
MB 13-2@12	c	{0.04}	204	72	42	0.355	1060.2	12.9	1033.8	16.0	-2.7	0.07469	0.65	1.79137	1.79	0.1739	1.67	0.93281
MB 13-2@13	c	{0.10}	84	29	17	0.343	999.3	21.9	1025.9	16.0	2.9	0.07248	1.09	1.72385	2.00	0.1725	1.68	0.83948
MB 13-2@14	c	0.32	1018	329	121	0.323	632.7	12.5	633.7	10.1	0.2	0.06081	0.58	0.86616	1.77	0.1033	1.67	0.94420
MB 13-2@15	r	{0.03}	139	108	30	0.779	1033.0	22.3	1019.5	15.8	-1.4	0.07369	1.11	1.74096	2.01	0.1713	1.67	0.83216
MB 13-2@16	c	0.04	1059	905	400	0.855	1746.9	4.1	1620.2	24.1	-8.2	0.10688	0.23	4.21086	1.69	0.2857	1.68	0.99108
MB 13-2@17	c	{0.05}	270	109	52	0.404	998.2	13.3	961.5	14.9	-4.0	0.07243	0.66	1.60646	1.79	0.1609	1.67	0.93050
MB 13-2@18	c	{0.03}	236	92	49	0.391	1058.2	13.2	1041.4	16.1	-1.7	0.07462	0.66	1.80381	1.79	0.1753	1.67	0.93036
MB 13-2@19		{0.03}	157	115	35	0.733	1064.8	19.4	1039.8	16.1	-2.5	0.07486	0.97	1.80677	1.93	0.1750	1.67	0.86439
MB 13-2@20	c	0.06	320	131	65	0.408	1001.9	12.2	1024.7	15.8	2.5	0.07257	0.60	1.72387	1.78	0.1723	1.67	0.94061
MB 13-2@21	c	{0.03}	215	122	45	0.566	1060.8	16.7	1021.2	15.8	-4.0	0.07471	0.83	1.76830	1.87	0.1717	1.67	0.89502
MB 13-2@22		{0.06}	221	40	25	0.182	602.3	28.2	616.1	9.8	2.4	0.05996	1.32	0.82911	2.13	0.1003	1.68	0.78612
MB 13-2@23	c	0.87	647	107	241	0.165	1991.7	6.3	1796.8	26.3	-11.2	0.12242	0.35	5.42569	1.71	0.3214	1.67	0.97838
MB 13-2@24	c	{0.04}	192	58	38	0.305	1052.2	15.4	1030.1	15.9	-2.3	0.07440	0.77	1.77727	1.84	0.1733	1.67	0.90865
MB 13-2@25	c	0.21	147	66	28	0.450	1035.8	21.1	946.9	14.8	-9.2	0.07379	1.05	1.60984	1.98	0.1582	1.67	0.84722

Pb_c and Pb* indicate the common and radiogenic proportions respectively

{} indicate where no correction has been applied otherwise a value has been calculated using the present-day Stacey & Kramers common Pb value

(1) Corrected for common Pb

Errors are 1 sd

Positive numbers for % Disc, indicate reverse discordance

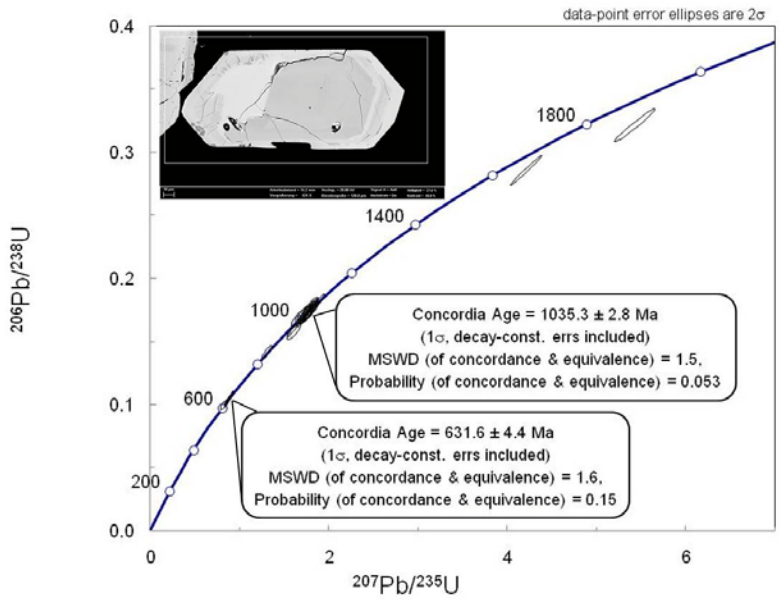

Figure 3: U-Pb Concordia diagram for zircons from sandstone ZMB13/2 from the Ruziruhuru Formation of the Sijarira Group. Inset (top left) shows a BSE image of a zircon grain having a deeply-embayed darker core, surrounded by a lighter euhedral overgrowth.

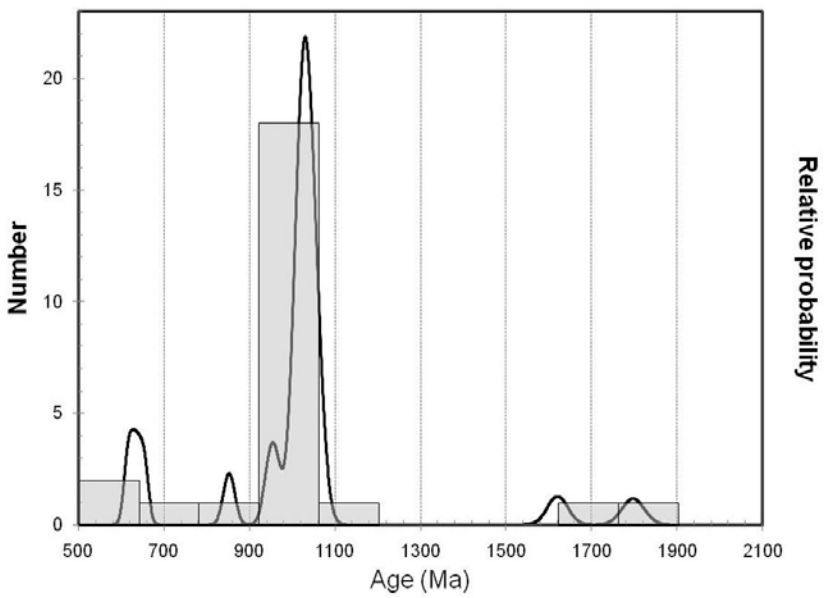

Figure 4: Relative probability distribution plot of U-Pb ages of detrital zircons from Sijarira sample ZMB13/2.

5. Discussion

Given that the Sijarira Group rests unconformably upon basement lithologies of the Magondi mobile belt, the most surprising thing about the age spectrum revealed by the detrital zircon population is the total lack of ages in the range of 2.2-1.96 Ga, which are characteristic of the Magondi Belt (Glynn et al., 2012, 2015; Master et al., 2013). Only one zircon, dated at 1991.3 ± 6.3 Ma is within the age range of metamorphism of the Magondi Belt, while the other Palaeoproterozoic zircon, dated as 1746.9 ± 4.1 Ma, is younger than the Magondi metamorphism (Treloar and Kramers, 1989; Munyanyiwa et al., 1995; Master et al., 2010).What is also totally unexpected is that the vast majority of the zircons record late Mesoproterozoic to early Neoproterozoic ages. Such ages are wholly unknown from the Magondi Belt or Zimbabwe Craton, and are also very scarce in the Mesoproterozoic plutons of the Choma-Kalomo Block, and in the Neoproterozoic Zambezi Belt to the north and northwest of the Zimbabwe Craton and Magondi Belt (Glynn et al., 2016).The source of these zircons, the only recorded instance of detrital zircons of this age within the region, is uncertain. Their ages are similar to, but mainly somewhat older than, the ages of pegmatites occurring in both the Choma-Kalomo Block and the Dete-Kamativi Inlier (Figure 1) which are between 1.03 and 0.95 Ga (Master et al., 2013; Glynn et al., 2016). Clifford et al. (1967) showed late Mesoproterozoic to early Neoproterozoic reworking of the Urungwe Granite at 1211 ± 40 Ma (recalculated Rb-Sr muscovite model age), and 937 ± 40 (K-Ar, muscovite) and 833 ± 40 Ma (K-Ar, biotite).Although the younger ages do overlap with some of the younger Sijarira detrital zircon ages, they do not represent ages of igneous events, just thermal resetting. The older Rb-Sr age of 1211 ± 40 Ma for the Urungwe Granite is within error of the c. 1.20-1.18 Ga age of the younger phase of the Choma-Kalomo Batholith (Hanson et al., 1988; Bulambo et al., 2004, 2006), suggesting a temporal and possibly tectonic link between thermal events in the western Magondi Belt, and arc-related

198 magmatism in the Choma-Kalomo Block. Van de Wel et al. (1998) recorded 1.02 Ga ages
199 from granites of the Tati granite-greenstone terrane of Botswana- but this event seems to be
200 of local significance, and is younger than most of the zircons recorded from the Sijarira
201 Group, which are between c. 1.07-1.03 Ga in age. Master et al. (1995) obtained a SHRIMP
202 U-Pb zircon age of 1034 ± 17 Ma for the Munwa Granophyre, from the Highbury impact
203 structure in the Magondi belt of Zimbabwe- but this is volumetrically very small, and could
204 not have been a source for the 1.07-1.05 Ga detrital zircons in the Sijarira sandstone sample.
205 The lack of local sources for the detrital zircon population in the Sijarira sandstone indicates
206 that their provenance lies farther afield than in the underlying Magondi Belt, or the adjacent
207 Archaean Zimbabwe Craton.
208
209 5.1. *Provenance of Sijarira detrital zircons from Antarctica?*
210
211 In considering the vexing question of the provenance of the Sijarira detrital
212 zircons, the sedimentology and palaeocurrent patterns of the Sijarira Group may provide
213 important clues. Palaeocurrent data obtained by Humphreys (1969), Chappell (1969), Harper
214 (1970), and Mann (1970, 1979, 1982) indicate that the main sediment supply was from the
215 southeast, with palaeocurrents trending towards the west and northwest. Furthermore, the
216 Sijarira sandstones contain abundant detrital garnets, sphene, and epidote, indicating
217 provenance from a metamorphic terrain (Mann, 1970, 1982). The obvious source of these
218 metamorphic detrital mineral components would appear to be the underlying Magondi Belt,
219 but the lack of detrital zircons of Magondi age seems to rule this out. In the Urungwe region,
220 the Magondi Belt basement below the Sijarira beds is only garnetiferous to the north of the
221 Sijarira outcrops (Wiles, 1961), while very few garnetiferous horizons are found to the
222 southeast, where the metamorphic grade is lower (Stagman, 1962), but where the

223 palaeocurrents indicate the sediments were transported from (Mann, 1970, 1979, 1982).The
224 Archaean granite-greenstone terrain of the Zimbabwe Craton, farther east, is characterized by
225 lower greenschist facies metamorphism (Saggerson and Turner, 1976), and is not a good
226 source for garnets. The Sijarira beds rest upon a peneplaned surface of granites or mica
227 schists of the Piriwiri Group (Stagman et al., 1978), implying low depositional gradients and
228 little topography, yet the sediments are coarse-grained- suggesting an uplifted, but distant,
229 source terrain. Stagman (1962) regarded the Sijarira redbeds as a "molasse formation
230 deposited in a post-orogenic basin, more or less synchronous with, but unaffected by, the
231 metamorphism that culminated in the emplacement of the Miami pegmatites in Cambrian
232 times." The Miami area in the northern Magondi Belt was affected by the Zambezi
233 metamorphism, with pegmatites dated at between 530 and 430 Ma (Clifford et al., 1967).
234 Main-phase collision, deformation and metamorphism, accompanied by voluminous granite
235 intrusion, took place in the Zambezi Belt and adjacent Lufilian Belt at about 550 Ma (John et
236 al., 2004; Naydenov et al., 2015; Milani et al., 2015). The lack of any detrital zircons of this
237 age in the Sijarira Group suggests that the Zambezi-Lufilian orogenic belt was not the source
238 of any significant sediment input into the Sijarira basin.
239
240 Viewed in the context of the entire Kalahari Craton, consisting of the Archaean
241 cores of the Zimbabwe Craton, Limpopo Belt, Kaapvaal Craton, and Grunehogna Block,
242 together with the Palaeoproterozoic Magondi Belt, and various accreted Mesoproterozoic
243 belts: Namaqua-Natal, Maud, and Mozambique belts (Jacobs et al., 2008), there does appear
244 to be one region which could serve as the source terrain for the Sijarira zircons. This is the
245 southern Mozambique Belt in Mozambique (Manhica et al., 2001; Koistinen et al., 2008), and
246 the Maud Belt of West Dronning Maud Land, Antarctica (Grantham et al., 2011). In this part
247 of the Kalahari Craton, Late Mesoproterozoic island arcs, dated at between c. 1.14 and 1.12

Ga, were formed by subduction of oceanic lithosphere, followed by intrusion of the Umkondo Large Igneous Province at c. 1.11 Ga, and then arc collisions between c. 1.08 and 1.03 Ga (Bauer et al., 2003; Bisnath and Frimmel, 2005; Board et al., 2005; Grantham et al., 2011). During the formation of the magmatic arcs, a retroarc foreland basin system developed on the adjacent Zimbabwe and Grunehogna Blocks, to produce the Umkondo foreland basin in Zimbabwe/Mozambique (Master, 2010, 2016), and the Ritscherflya basin on the Grunehogna Block in Antarctica (Moyes et al., 1995). Sedimentary rocks of the Umkondo and Ritscherflya basins were intruded by sills of the Umkondo Large Igneous Province (LIP), accompanied by outpouring of the Umkondo and Straumsnutane basalts respectively (Munyanyiwa, 1999; Krynauw et al., 1991). The Umkondo LIPS in both regions were overprinted at c. 1.08 Ga (Allsopp et al., 1989; Moyes et al., 1995) during the arc collision stage. Finally, during the Pan-African amalgamation of the Gondwana supercontinent in the late Neoproterozoic era, a collision between East and West Antarctica took place. This resulted in Pan-African c. 550 Ma structural and metamorphic overprinting of the Mesoproterozoic Maud Belt, and its continuation into southern Mozambique (Jacobs et al., 1998, 1999, 2003; Board et al., 2005; Grantham et al., 2011). In southern Mozambique, shear zones developed on the Zimbabwe Craton/Mozambique Belt boundary (Manhica et al., 2001), and the Chimanimani Mountains developed by thrusting of the Frontier Group quartzites and schists (representing the former passive margin of the Zimbabwe Craton), over the Umkondo Group, accompanied by regional metamorphism (Vail, 1966; Master, 2010, 2016).

We suggest that the Sijarira Group, despite being located on the western side of the Zimbabwe Craton, may in fact be a remnant of a Pan-African foreland basin resulting from a late Neoproterozoic collision in the southern Mozambique Belt and Maud Belt to the

273 east of the Zimbabwe Craton (Figure 5). This could explain the lack of Magondi aged
274 zircons, c. 2.06-1.96 Ga (Glynn et al., 2012; Master et al., 2015) in the Sijarira Group. The c.
275 1075 to 1000 Ma detrital zircon population in the Sijarira sample could have been sourced
276 from the HU Sverdrupfjella region, in the Maud Belt of West Dronning Maud Land,
277 Antarctica (Figure 5), where there are gneisses of that age range formed by late
278 Mesoproterozoic arc collisions in the Maud Belt (Board et al., 2005; Bisnath and Frimmel,
279 2005). The youngest Sijarira zircons (602.3 ± 28.2 Ma to 632.7 ±12.5 Ma)may be derived
280 from Neoproterozoic rocks from the Maud Belt, e.g., from intrusions that have yielded
281 garnet-whole rock Sm-Nd ages of 660-415 Ma in H.U. Sverdrupfjella (Moyes and
282 Groenewald, 1996), or mafic dykes from Heimefrontfjella (Figure 5) with an age of 586 ± 7
283 Ma (Bauer et al., 2009); or they may be related to a 615 ± 30 Ma tectonic event (biotite K/Ar
284 age) recorded from gneiss at Nyapanani Hill, Inyanga (Nyanga), in eastern Zimbabwe
285 (Snelling et al., 1964). The lack of Pan-African zircons is due to relative lack of Pan-African
286 aged magmatism in West Dronning Maud Land and in the southern Mozambique Belt- the
287 largest late Neoproterozoic intrusion in this region being the c. 100 km ^{2}518 ± 15 Ma
288 Brattskarvet suite in the Maud Belt (Moyes et al., 1993), in contrast to abundant Pan-African
289 c. 550 Ma magmatism associated with the Hook Batholith in the Lufilian-Zambezi Orogen,
290 which is exposed over an area of 12,000 km^2, and may have been up to 30,000 km^2 in area
291 (Milani et al., 2015).
292

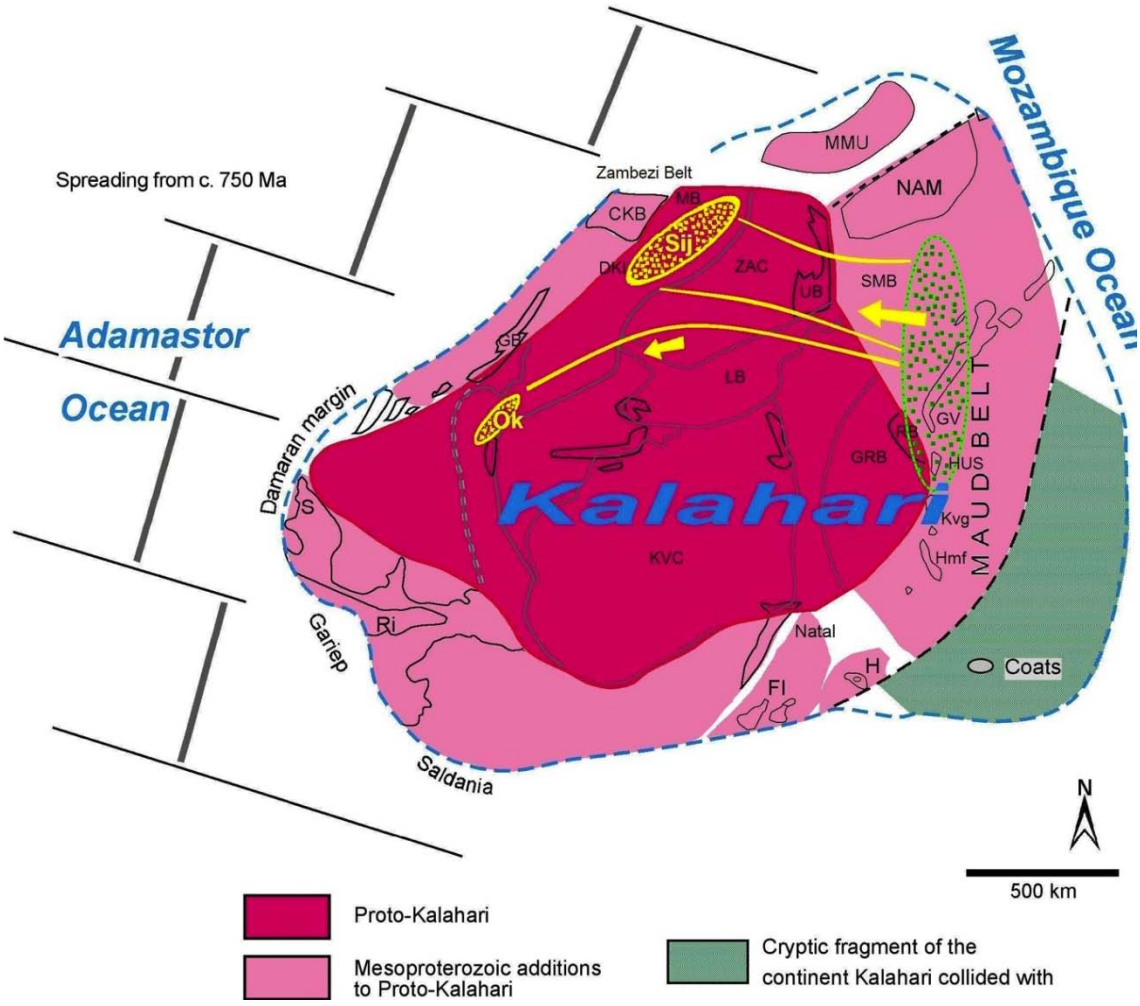

293

294 Figure 5: Late Neoproterozoic palaeogeography of the Kalahari Craton, showing the
295 Archaean and Palaeoproterozoic Proto-Kalahari core (bright pink), surrounded by
296 Mesoproterozoic Belts (pale pink), and the Neoproterozoic belt that collided to the east
297 (green), during the amalgamation of Gondwana (modified after Jacobs et al., 2008). The
298 possible source region for the Sijarira detrital zircons is shown in green stipple, while the
299 Sijarira (Sij) and Okwa (Ok) basins are shown in yellow stipples. Yellow arrows show
300 possible sediment dispersal paths, traversing the Umkondo Basin UB), Zimbabwe Archaean
301 Craton (ZAC), and Magondi Belt (MB). CKB = Choma-Kalomo Block; DK = Dete-Kamativi
302 Inlier; GB = Ghanzi Belt; S = Sinclair; Ri = Richtersveld; LB = Limpopo Belt; KVC =
303 Kaapvaal Craton; GRB = Grunehogna Block; FI = Falkland Islands; H = Haag nunataks;
304 HMf = Heimefrontfjella; KVg = Kirwanveggen; HUS = H.U. Sverdrupsfjella; RB =

Ritscherflya Basin; GV = Gjelsvikfjella; SMB = Southern Mozambique Belt; NAM = Nampula Block; MMU = Marupa-Malawi-Unango terrane.

Some support for an easterly derivation of the Sijarira Group comes from a small outlier of Sijarira-type redbeds south of Chinhoyi, around 80 km east of the most northeasterly outcrops of the Sijarira Group in the Hurungwe District. This outlier, called the Portelet Estate Outlier (Figure 1), consists of feldspathic sandstone, containing garnets, with intraformational shale clasts (Stagman, 1961). Sijarira-type redbeds may have been much more widespread on the Zimbabwe Craton, which has undergone a great deal of uplift and erosion in post-Miocene time (Lister, 1987; Moore et al., 2009). The Sijarira Group may have been preferentially preserved in fault blocks close to the rheological boundary between the Craton and the Choma-Kalomo Block (which represents a metacraton)(Glynn et al., 2016). The current outcrops of the Sijarira Group represent a small preserved remnant of a much larger basin. The craton had been uplifted and eroded prior to Karoo deposition, so that in the middle of the craton, the Karoo outliers of the Somabhula region SW of Gweru and the Featherstone Outlier rest directly upon Archaean granite and greenstone belt basement (Master, 1995).

The molasse-type sediments derived from the Antarctic Maud Belt and southern Mozambique Belt "by-passed" the Umkondo foreland basin, and traversed the Zimbabwe Archaean Craton and Magondi Mobile Belt, before being deposited in an epeiric craton-edge Sijarira basin. This is similar to how Mesoproterozoic Grenvillian-aged zircons dominate the detrital zircon record in Neoproterozoic to Palaeozoic Appalachian sedimentary basins in Laurentia (Eriksson et al., 2003; Cawood et al., 2007). The by-passing of the Craton and Magondi Belt may have been facilitated by the presence of a thin veneer of sedimentary

cover over the Craton- which was subsequently removed by erosion. Another problem with the detrital zircon record is bias, in terms of both how zircons are generated, and bias during analysis (since mainly the largest zircons are chosen, and cores are analyzed preferentially compared with narrow rims, which may be problematic to analyze) (Moecher and Samson, 2006). Thus the paucity of Pan-African ages can be explained if there were just a few or no igneous rocks being produced, since new zircon growth occurs mainly during anatectic events (Moecher and Samson, 2006).

5.2. *Implications of the Sijarira age for regional correlations*

The Sijarira Group, on the basis of its position near the northwestern margin of the Kalahari Craton, has been correlated in the past with the Sinclair and Ghanzi Group sedimentary rocks of Namibia and Botswana (Humphreys, 1969; Stagman et al., 1978). These rocks extend northeastwards for over a thousand km from central Namibia to northeast Botswana (Lehmann et al., 2015). The Ghanzi Group in Botswana has not been directly dated because it lacks suitable volcanic units. It unconformably overlies, and is therefore younger than, the 1106 ± 2 Ma Kgwebe Formation (Schwartz et al., 1996). This is confirmed by the presence of a group of detrital zircons dated at 1104 ± 16 Ma within rocks correlated with the Ghanzi Group, from borehole CKP4 in the Chobe area of northern Botswana (Kampunzu et al., 2000). Kampunzu et al. (2000) also found a detrital zircon as young as 1047 ± 24 Ma, which is the maximum age for the Ghanzi Group. Rocks of the Okwa Group, together with the underlying Ghanzi Group, have been affected by the Damara orogeny, and have been metamorphosed at about 530 Ma, and this age also provides a minimum age for the Ghanzi Group (Ramokate et al., 2000). Thus existing age constraints only allow us to bracket the age of the Ghanzi Group between about 1050 and 530 Ma. However, the lack of any glacial rocks

correlatable with those in the Neoproterozoic Damara Supergroup led Schwartz et al. (1996) to suggest that the Ghanzi Group was older than about 750 Ma. Recent geochronological results indicate that the earliest Neoproterozoic glaciation, the Surtian, took place in Central Africa at c. 710 Ma (Rooney et al., 2015), hence the Ghanzi Group would have be older than that. Ramokate et al. (2000) claimed to have dated a felsic rock from the Ghanzi-Chobe belt in NW Botswana, which gave a U-Pb zircon age of c. 750 Ma, but this age was never published. Master et al. (2012) suggested, on the basis of a negative carbon-isotope excursion, that the Ghanzi Group was deposited during the Bitter Springs Stage, at around 800-780 Ma. The negative carbon isotope excursion in the Ghanzi Group is similar to that found in the Tengwe River Group (Schidlowski et al., 1976; Stagman et al., 1978), and in the Makuti Group of the Zambezi Belt (Master, unpublished data). Geophysically the Ghanzi Group trends northeastwards from Botswana towards the Choma-Kalomo Block of southeastern Zambia (Lehmann et al., 2015) - where it may be represented by deformed sedimentary rocks that are younger than 1.28 Ga (Glynn et al., 2016).The Ghanzi Group is thus most likely to be much older than the Sijarira Group (by up to c. 150 Ma), and is not correlated with it. In terms of depositional age, and lithological sequence, the Sijarira Group correlates quite well with the Okwa Group of central Botswana, consisting of red conglomerates, sandstones and shales, which are dated at between 579.3 ± 11.6 Ma and c. 530 Ma (Ramokate et al., 2000). Ramokate et al. (2000) dated only five detrital zircons from the Okwa Group, which are too few to be representative, but their ages fall within the Palaeoproterozoic to Neoproterozoic age range obtained from the Sijarira Group. It is thus possible that the Okwa Group sedimentary rocks may also have been sourced from the same region as that proposed from the Sijarira zircons, i.e., from the collision zones on the east side of the Kalahari Craton (Figure 5).

Our new maximum age for the Sijarira Group of c. 632 Ma makes it very likely that it was deposited between 632 and 550 Ma (which represents the main phase of the Lufilian-Zambezi Orogeny, formed by the collision of the Kalahari and Congo Cratons; John et al., 2004; Naydenov et al., 2015). This new age constraint negates previous correlations suggesting a Mesoproterozoic or early Neoproterozoic age (Humphreys, 1969; Stagman et al., 1978), and supports the palaeomagnetically based correlations of Reid (1968), indicating a Latest Neoproterozoic(Ediacaran) age (i.e., 635-542 Ma, Knoll et al., 2006).It thus correlates in terms of age with other late Neoproterozoic to Palaeozoic post-Pan-African molasse basins surrounding the Kalahari Craton, including the Nama foreland basins adjacent to the Gariep and Damara Orogens (Gresse and Germs, 1993), the Okwa basin of central Botswana (Ramokate et al., 2000), the Natal Group of SE Africa (Thomas et al., 1992),and the Kundelungu Plateau in the Katanga Basin of D. R. Congo, related to the collision of the Kalahari and Congo Cratons (Master et al., 2005).

6. Acknowledgments

We acknowledge financial support from the South African National Research Foundation, the Geological Society of South Africa (Kent Fund), the Society of Economic Geologists (Tim Nutt Memorial Fund), and from the DST-NRF Centre of Excellence for Integrated Mineral and Energy Resource Analysis (CIMERA). The Carnegie Corporation (New York) is thanked for a Large Research Grant to SM. Additionally we would like to thank the German Ministry for Education and Research, as well as the Faculty of Science at the University of the Witwatersrand for financial support as part of a Helmholtz-South Africa SIMS initiative. Particular thanks go to Frédéric Couffignal and Uwe Dittmann at GFZ who respectively assisted greatly in the analysis and sample preparation. SM is grateful to the

School of Geosciences, and the Faculty of Science, University of the Witwatersrand, for granting sabbatical leave in 2016, during which part of this paper was written.

7. References

Allsopp, H.L., Kramers, J.D., Jones, D.L., Erlank, A.J., 1989. The age of the Umkondo Group, eastern Zimbabwe, and implications for palaeomagnetic correlations. South African Journal of Geology 92, 11−19.

Andrews-Speed, C.P., Unrug, R., 1984. Gold in the sedimentary cover of the Bangweulu Block, northern Zambia. In: Foster, R.P. (Eds.), Gold '82: The Geology, Geochemistry and Genesis of Gold Deposits. A.A. Balkema, Rotterdam, 222−236.

Bauer, W., Jacobs, J., Fanning, C.M., Schmidt, R., 2003. Late Meso-proterozoic arc and back-arc volcanism in the Heimefrontfjella (East Antarctica) and implications for the palaeogeography at the southeastern margin of the Kaapvaal–Grunehogna Craton. Gondwana Research 6, 449–465.

Bauer, W., Fielitz, W., Jacobs, J., Spaeth, G., 2009. Neoproterozoic mafic dykes of the Heimefrontfjella (East Antarctica). Polarforschung 79(1), 33 – 38.

Bisnath, A., Frimmel, H.E., 2005. Metamorphic evolution of the Maud Belt: P–T–t path for high-grade gneisses in Gjelsvikfjella, Dronning Maud Land, East Antarctica. Journal of African Earth Sciences 43, 505–524.

Board, W.S., Frimmel, H.E., Armstrong, R.A., 2005. Pan-African tectonism in the Western Maud Belt: P–T–t path for high-grade gneisses in the H.U. Sverdrupfjella, East Antarctica. Journal of Petrology 46(4), 671−699.

Bond, G., 1981. A possible Late Precambrian tillite from the Urungwe District, Zimbabwe. In: Hambrey, M.J. and Harland, W.B. (Eds.), Earth's Pre-Pleistocene Glacial Record. Cambridge University Press, Cambridge, 178−179.

Cawood, P.A., Nemchin, A.A., Strachan, R., Prave, A., Krabbendam, M., 2007. Sedimentary basin and detrital zircon record along East Laurentia and Baltica during assembly and breakup of Rodinia. Journal of the Geological Society, London 164, 257−275.

Chappell, J., 1969. The geology of the Eastern Portion of the Chizarira Game Reserve and adjacent country, Rhodesia. D.Phil. thesis (unpublished), Univ. College Rhodesia, Salisbury, Rhodesia (now University of Zimbabwe, Harare, Zimbabwe), 216 pp.

Chappell, J., Humphreys, M., 1981. Glacial sedimentation in the Lower Karoo, Mid-Zambezi Valley. In: M.J. Hambrey and W.B. Harland, (Eds.), Earth's Pre-Pleistocene Glacial Record. Cambridge University Press, Cambridge, 113−121.

Clifford, T.N., Rex, D.C., Snelling, N.J., 1967. Radiometric age data for the Urungwe and Miami granites of Rhodesia. Earth and Planetary Science Letters2, 5−12.

Dirks, P.H.G.M., Kröner, A., Jelsma, H.A., Sithole, T.A., Vinyu, M.L., 1999. Pb–Pb zircon dates from the Makuti gneisses; evidence for a crustal-scale Pan African shear zone in the Zambezi Belt, NW Zimbabwe. Journal of African Earth Sciences 28, 427–442.

Eriksson, K.A., Campbell, I.H., Palin, J.M., Allen, C.M., 2003. Predominance of Grenvillian magmatism recorded in detrital zircons from modern Appalachian rivers. Journal of Geology 111(6), 707−717.

Fernandes, C.J., Pulz, G.M., Kuyumjian, R.M., Pinho, F.E.C., 2005. Diferencasentre os depositos auriferous do Grupo Aguapei (Estado do M ato Grosso) e os classicos exemplos de ouro em conglomerados. Pesquisas em Geosciencias, Porto Allegre 32(1), 17−26.

452 Geological Survey of Zimbabwe (1994). Geological Map of Zimbabwe, 1:1,000,000 scale.
453 Geological Survey of Zimbabwe, Harare, Zimbabwe.
454 Glynn, S.M., Master, S., Armstrong, R.A., Hofmann, A., Bekker, A. 2012. N ew U-Pb
455 (SHRIMP) ages for the Palaeoproterozoic Magondi Supergroup, Zimbabwe. Abstracts
456 volume, 4th Annual Meeting of the Igneous and Metamorphic Studies Group,
457 University of the Witwatersrand, Johannesburg, South Africa.
458 Glynn, S.M., Wiedenbeck, M., Master, S., Frei, D., 2015. New U-Pb zircon geochronology of
459 the Choma-Kalomo Block (Zambia) and the Dete-Kamativi Inlier (Zimbabwe), with
460 implications for the extent of the Zimbabwe Craton. Abstracts volume, European
461 Geosciences Union (EGU) Annual Meeting, Vienna, Austria.
462 Glynn, S.M., Master, S., Wiedenbeck, M., Davis, D.W., Kramers, J.D., Belyanin, G., Frei, D.,
463 Oberthür, T., 2016 (under review). The Proterozoic Choma-Kalomo Block, SE
464 Zambia: exotic terrane, or a m etacratonic segment of the Zimbabwe Craton?
465 Precambrian Research.
466 Grantham, G.H., Manhica, A.D.S.T., Armstrong, R.A., Kruger, F.J., Loubser, M., 2011. New
467 SHRIMP, Rb/Sr and Sm/Nd isotope and whole rock chemical data from central
468 Mozambique and western Dronning Maud Land, Antarctica: Implications for the
469 nature of the eastern margin of the Kalahari Craton and the amalgamation of
470 Gondwana. Journal of African Earth Sciences59, 74−100.
471 Gresse, P.G., Germs, G.J.B., 1993. T he Nama Foreland Basin: sedimentation, major
472 unconformity bounded sequences and multisided active margin advance. Precambrian
473 Research 63, 247−272.
474 Hanson, R.E., Wilson, T.J., Brueckner, H.K., Onstott, T.C., Wardlaw, M.S., Johns, C.C.,
475 Hardcastle, K.C., 1988. Reconnaissance geochronology, tectothermal evolution, and

476 regional significance of the middle Proterozoic Choma-Kalomo block, southern
477 Zambia. Precambrian Research 42, 39−61.
478 Hanson, R.E., Wilson, T.J., Munyanyiwa, H., 1994. Geologic evolution of the
479 Neoproterozoic Zambezi Orogenic Belt in Zambia. Journal of African Earth Sciences
480 18, 135–150.
481 Harper, G., 1970. The structure and stratigraphy of the eastern portion of the Sijarira Group
482 and associated formations in the Lower Umniati River area, Rhodesia. Ph.D. thesis
483 (unpublished), University of London, London, U.K.
484 Humphreys, M., 1969. The geology of the Western Portion of the Chizarira Game Reserve
485 and adjacent country, Rhodesia. D.Phil. thesis (unpublished), University College of
486 Rhodesia, Salisbury, Rhodesia (now University of Zimbabwe, Harare, Zimbabwe),
487 297 pp.
488 Jacobs, J., Fanning, C.M., Henjes-Kunst, F., Olesch, M., Paech, H.J., 1998. Continuation of
489 the Mozambique Belt into East Antarctica: Grenville-age metamorphism and
490 polyphase Pan-African high-grade events in Central Dronning Maud Land. Journal of
491 Geology106, 385−406.
492 Jacobs, J., Hansen, B.T., Henjes-Kunst, F., Thomas, R.J., Weber, K., Bauer, W., Armstrong,
493 R.A., Cornell, D.H., 1999. New age constraints on the Proterozoic/lower Palaeozoic
494 evolution of Heimefrontfjella, East Antarctica, and its bearing on Rodinia/Gondwana
495 correlations. Terra Antarctica 6, 377−389.
496 Jacobs, J., Fanning, C.M., Bauer, W., 2003. Timing of Grenville-age vs. Pan-African
497 medium-to high grade metamorphism in western Dronning Maud Land (East
498 Antarctica). Precambrian Research125, 1–20.
499 Jacobs, J., Pisarevsky, S., Thomas, R.J., Becker, T., 2008. The Kalahari Craton during the
500 assembly and dispersal of Rodinia. Precambrian Research 160, 142–158.

John, T., Schenk, V., Mezger, K., Tembo, F., 2004. Timing and PT evolution of whiteschist metamorphism in the Lufilian arc-Zambezi belt orogen (Zambia): implications for the assembly of Gondwana. Journal of Geology 112, 71–90.

Kampunzu, A.B., Armstrong, R.A., Modisi, M.P., Mapeo, R.B.M., 2000. Ion microprobe U-Pb ages on detrital zircon grains from the Ghanzi Group: implications for the identification of a Kibaran-age crust in northwest Botswana. Journal of African Earth Sciences 30(3), 579−587.

Koistinen, T., Lehtonen, M.I., Fernando, S., Matola, R., 2008. Contribution to the structure at the eastern margin of the Archaean Zimbabwe craton, Mozambique. Geological Survey of Finland Special Papers 48, 121–144.

Knoll, A.H., Walter, M.R., Narbonne, G.Y., Christie-Blick, N., 2006. The Ediacaran Period: a new addition to the geological time scale. Lethaia 39, 13−30.

Krynauw, J.R., Watters, B.R., Hunter, D.R., Wilson, A.H., 1991. A review of the field relations, petrology and geochemistry of the Borgmassivet intrusions in the Grunehogna province, western Dronning Maud Land, Antarctica. In: Thomson, M.R.A., Crame, J.A. and Thomson, J.W. (Eds.), Geological Evolution of Antarctica. Cambridge University Press, Cambridge, 33−39.

Lehmann, J., Master, S., Rankin, W., Milani, L., Kinnaird, J.A., Naydenov, K.V., Saalmann, K., Kumar, M., 2015. New correlations and tectonic setting of the Kalahari Copperbelt in Namibia and Botswana. Ore Geology Reviews 71, 169−190.

Lister, L.A., 1987. The erosion surfaces of Zimbabwe. Zimbabwe Geological Survey Bulletin 90, 163 pp.

Manhica, A.D.S.T., Grantham, G.H., Armstrong, R.A., Guise, P.G., Kruger, F.J., 2001. Polyphase deformation and metamorphism at the Kalahari Craton-Mozambique Belt boundary. Geological Society London, Special Publications 184, 303−321.

526 Mann, A.G., 1970. The stratigraphy and structure of the Sijarira Group and associated
527 formations in the western portion of the Lower Umniati River area, Rhodesia. Ph.D.
528 thesis (unpublished), University of London, London, U.K.
529 Mann, A.G., 1979. S edimentological control of copper deposition in the Sijarira Group,
530 Western Umniati River area, Rhodesia. Special Publications Geological Society South
531 Africa 5, 219−227.
532 Mann, A.G., 1982. H eavy mineral sandstones of the Sijarira Group. Sedimentological
533 Division of the Geological Society South Africa, Rand Afrikaans University,
534 Abstracts volume, 107−110.
535 Master, S., 1995. A review and re-appraisal of ideas concerning the source of diamonds in the
536 Triassic Somabhula Gravels, Zimbabwe. In: Blenkinsop, T.G. and Tromp, P.L. (Eds.),
537 Sub-Saharan Economic Geology. Spec. Publ. Geol. Soc. Zimbabwe No. 3, A .A.
538 Balkema, Rotterdam, 161−176.
539 Master, S., 2010. The Zimbabwe-Antarctica link: a foreland basin model for the late
540 Mesoproterozoic Umkondo-Ritscherflya basin, prior to its Pan-African deformation.
541 Extended Abstracts Geological Survey Zimbabwe Centennial Conference Geological
542 Survey Zimbabwe and Geological Society Zimbabwe, Harare.
543 Master, S., 2016. The Chimanimani Mountains of Zimbabwe and Mozambique. A
544 spectacular mountain range formed during Gondwana amalgamation. In: Anhaeusser,
545 C.R., Viljoen, M.J. and Viljoen, R.P. (Eds.), Africa's Top Geological Sites. Struik
546 Nature, Cape Town, 39−43.
547 Master, S., Armstrong, R.A., Brandt, D., Ferraz, M.F.F., Gumede, T., Koeberl, C., Reimold,
548 W.U., Robertson, D.J., Woldai, T., Zeil, P., 1995. New geological, geophysical and
549 remote sensing data from the Highbury impact structure, Zimbabwe. Lunar and
550 Planetary Science XXVI, 903−904.

551 Master, S., Rainaud, C., Armstrong, R.A., Phillips, D., Robb, L.J., 2005. Provenance ages of
552 the Neoproterozoic Katanga Supergroup (Central African Copperbelt), with implica-
553 tions for basin evolution. Journal of African Earth Sciences 42(1−5), 41−60.
554 Master, S., Bekker, A., Hofmann, A., 2010. A review of the stratigraphy and geological
555 setting of the Palaeoproterozoic Magondi Supergroup, Zimbabwe: type locality for the
556 “Lomagundi” global carbon isotope excursion. Precambrian Research 182(4),
557 254−273.
558 Master, S., Wendorff, M., 2011. N eoproterozoic glaciogenic diamictites of the Katanga
559 Supergroup, Central Africa In: Arnaud, E., Halverson, G.P. and Shields-Zhou, G.
560 (Eds.), The Geological Record of Neoproterozoic Glaciations. Geological Society
561 (London), Memoirs 36, 173−184.
562 Master, S., Hendjala, F., Kasirye, S., 2012. Isotope chemostratigraphy and sedimentology of
563 the Neoproterozoic Kalahari Copperbelt (Botswana and Namibia): implications for
564 the ages of sedimentation and mineralization. Abstract, Namibia Copper Conference,
565 Geological Society of Namibia, Windhoek.
566 Master, S., Glynn, S., Frei, D., Davis, D., Oberthür, T., 2013. N ew U-Pb and Pb-Pb
567 geochronology of rocks and minerals from the Proterozoic Dete-Kamativi Inlier
568 (Zimbabwe) and Choma-Kalomo Block (Zambia): regional implications. Extended
569 Abstract, Geological Society of Zimbabwe Annual Summer Symposium, Victoria
570 Falls.
571 Master, S., Glynn, S., Wiedenbeck, M., 2015. The vanished orogeny: Geochronology of
572 Palaeoproterozoic “basement” gneisses of the Kariba and adjacent areas, western
573 Magondi Belt (Zimbabwe and Zambia). Abstracts volume, Geological Society
574 Zimbabwe Annual Summer Symposium, Kariba.

575 Miall, A.D., 1977. A review of the braided river depositional environment. Earth Science
576 Reviews 13, 1−62.
577 Milani, L., Lehmann, J., Naydenov, K., Saalmann, K., Kinnaird, J.K., Daly, J.S., Frei, D.,
578 Lobo-Guerrero Sanz, A., 2015. A-type magmatism in a syn-collisional setting: The
579 case of the Pan-African Hook Batholith in Central Zambia. Lithos 216−217, 46−72.
580 Moecher, D.P., Samson, D.P., 2006. Differential zircon fertility of source terranes and natural
581 bias in the detrital zircon record: Implications for sedimentary provenance analysis.
582 Earth and Planetary Science Letters 247(3−4), 252−266.
583 Molyneaux, A.J.C., 1903. The sedimentary deposits of Southern Rhodesia. Quarterly Journal
584 of the Geological Society, London 59, 266−290.
585 Molyneaux, A.J.C., 1922. A geological reconnaissance of the Sanyati Valley. Southern
586 Rhodesia Geological Survey Short Report 13, 10 pp.
587 Moore, A.E., Cotterill, F.P.D., Broderick, T.J., Plowes, P.D., 2009. Landscape evolution in
588 Zimbabwe from the Permian to present, with implications for kimberlite prospecting.
589 South African Journal of Geology112, 65−88.
590 Moyes, A.B., Groenewald, P.B., Brown, R.W., 1993. Isotopic constraints on the age and
591 origin of the Brattskarvet intrusive suite, Dronning Maud Land, Antarctica. Chemical
592 Geology (Isotope Geoscience Section) 106, 1993, 453−466.
593 Moyes, A.B., Krynauw, J.K., Barton, J.M., Jr., 1995. The age of the Ritscherflya Supergroup
594 and Borgmassivet Intrusions, Dronning Maud Land, Antarctica. Antarctic Science
595 7(1), 87−97.
596 Moyes, A.B., Groenewald, P.B., 1996. Isotopic constraints on Pan African Metamorphism in
597 Dronning Maud Land, Antarctica. Chemical Geology 129, 247−256.

598 Munyanyiwa, H., Kröner, A., Jaeckel, P., 1995. U–Pb and Pb–Pb single zircon ages for
599 charno-enderbites from the Magondi mobile belt, northwest Zimbabwe. South African
600 Journal of Geology 98, 52–57.
601 Munyanyiwa, H., 1999. Geochemical study of the Umkondo dolerites and lavas in the
602 Chimanimani and Chipinge Districts (eastern Zimbabwe) and their regional
603 implications. Journal of African Earth Sciences28, 349−365.
604 Naydenov, K., Lehmann, J., Saalmann, K., Kilani, L., Kinnaird, J.A., Charlesworth, G., Frei,
605 D., Rankin, W., 2015. New constraints on the Pan-African orogeny in Central
606 Zambia: A structural and geochronological study of the Hook Batholith and the
607 Mwembeshi Zone. Tectonophysics 637, 80−105.
608 Ramokate, L.V., Mapeo, R.B.M., Corfu, F., Kampunzu, A.B., 2000. Geology and regional
609 correlation of the Ghanzi-Makunda area, Western Botswana. Journal of African Earth
610 Sciences 30(3), 453−466.
611 Reid, A.B., 1968. A palaeomagnetic study of the Sijarira Group, Rhodesia. M. Phil. Thesis
612 (unpublished), University of London, London, U.K.
613 Riek, E.F., 1974. A fossil insect from the Dwyka Series of Rhodesia. Palaeontologica
614 Africana 17, 15−17.
615 Rooney, A.D., Strauss, J.V., Brandon, A.D., Macdonald, F.A., 2015. A Cryogenian
616 chronology: two long-lasting Neoproterozoic glaciations. Geology 43(5), 459−462.
617 Saggerson, E.P., Turner, L.M., 1976. A review of the distribution of metamorphism in the
618 ancient Rhodesian craton. Precambrian Research 3, 1−53.
619 Schidlowski, M., Eichmann, R., Junge, C.E., 1976. Carbon isotope geochemistry of the
620 Precambrian Lomagundi carbonate province. Geochimica et Cosmochimica Acta 40,
621 449–455.

622 Schwartz, M.O., Kwok, Y.Y., Davis, D.W., Akanyang, P., 1996. Geology, geochronology
623 and regional correlation of the Ghanzi ridge, Botswana. South African Journal of
624 Geology99, 245–50.
625 Shackleton, R.M., Vail, J.R., Wood, D.S., 1966. Preliminary report on the origin and
626 significance of the Urungwe Klippe, Rhodesia. 10th Annual Report, Research
627 Institute of African Geology, University of Leeds, 10−13.
628 Snelling, N.J., Hamilton, E., Rex, D., Hornung, G., Johnson, R.L., Slater, D., Vail, J.R., 1964.
629 Age determinations from the Mozambique and Zambezi Orogenic Belts, Central
630 Africa. Nature 201, 463−464.
631 Stagman, J.G., 1961. The geology of the country around Sinoia and Banket, Lomagundi
632 District. Geological Survey of Southern Rhodesia Bulletin49, 107pp.
633 Stagman, J.G., 1962. The geology of the Southern Urungwe District. Geological Survey of
634 Southern Rhodesia Bulletin 55, 82pp.
635 Stagman, J.G., Harrison, N.M., Broderick, T.J., Stocklmayer, V.R., 1978. An Outline of the
636 Geology of Rhodesia. Geological Survey of Rhodesia Bulletin 80, 126 pp.
637 Thomas, R.J., Marshall, C.G.A., Watkeys, M.K., Fitch, E.J., Miller, J.A., 1992. K-Ar and
638 $^{40}Ar/^{39}Ar$ dating of the Natal Group, Southeast Africa: a post Pan-African molasse?
639 Journal of African Earth Sciences 15(3−4), 453−471.
640 Treloar, P.J., 1986. Evolution of the Proterozoic Magondi and Zambezi mobile belts,
641 Zimbabwe. Journal of the Geological Society, London 143, 964−965.
642 Treloar, P.J., Kramers, J.D., 1989. Metamorphism and geochronology of granulites and
643 migmatitic granulites from the Magondi Mobile Belt, Zimbabwe. Precambrian
644 Research 45, 277−289.

645 Vail, J.R. 1966. Zones of progressive regional metamorphism across the western margin of
646 the Mozambique Belt in Rhodesia and Mozambique. Geological Magazine 103,
647 231−239.
648 Van de Wel, L., Barton, J.M., Kinny, P.D., 1998.evolution. South African Journal of
649 Geology 101(1), 67−72.
650 Watson, R.L.A., 1962. The Geology of the Kamativi and Lubimbi areas. Geological Survey
651 of Southern Rhodesia Bulletin 57, 42 pp.
652 Wiles, J.W., 1961. The geology of the Miami Mica Field. Bull. Geological Survey of
653 Southern Rhodesia Bulletin 51, 235 pp.

D.2 THESIS-RELATED CONFERENCE ABSTRACTS

CAG 2016: New age constraints on the Neoproterozoic Sijarira Group, in the Chizarira Hills, western Zimbabwe, with implications for regional correlations

Sharad Master[1,2], Sarah M. Glynn[2,3], Michael Wiedenbeck[3,2]
[1]Economic Geology Research Institute
[2]School of Geosciences, University of the Witwatersrand, Johannesburg, South Africa, sharad.master@wits.ac.za
[3]Helmholtz Zentrum Potsdam, Telegrafenberg, Potsdam, Germany

The Sijarira Group is a redbed sequence of continental fluviatile and shallow-marine origin, which outcrops in western Zimbabwe in the Chizarira Hills (where it is up to 660 m thick) and in the Hurungwe area (where it is overthrust by the "Urungwe klippe", which contains carbonate rocks and a glacial diamictite, of Neoproterozoic age). Although the unmetamorphosed Sijarira Group has not been dated, it overlies the Badze granite which has a (reset) Rb-Sr muscovite age of c. 1211 Ma. It is aligned with, and has been regarded as a continuation of, the Tsumis-Ghanzi belt of early Neoproterozoic redbeds extending across Namibia and northern Botswana.

We collected a sample of coarse-grained sandstone at 17° 39' 04.0" S; 27° 51' 21.0" E, in the Chizarira Hills. Our sample ZMB13/2 comes from the Ruziruhuru Formation of the Lubu Subgroup, overlying the basal conglomerates of the Sijarira Group. The sandstone is coarse-grained and arkosic, with a pale pink colour and is characterized by the presence of trough crossbedding. It resembles fluviatile sandstones that are commonly found associated with braided river environments. The sandstone consists of a mixture of quartz, feldspar and lithic fragments cemented together by a fine-grained, maroon coloured matrix. The fragments range in composition from sub-rounded grains of (polycrystalline) quartz to irregularly shaped chert fragments.

The detrital zircon grains from the sandstone are for the most part sub-angular, with a small number still retaining their euhedral shape. A total of 25 spots on 24 grains were measured for U/Pb isotope dating using the Cameca 1280-HR SIMS instrument at the Helmholtz Zentrum Potsdam. The two oldest detrital zircon grains, which are slightly discordant, give ages of c. 1.8 Ga, pointing to a source from the Magondi Belt, where the ages of metamorphism are between 2.0 and 1.8 Ga. The vast majority (80%) of the zircons record an age of c. 1035 Ma. The source of these zircons, the only recorded instance of detrital zircons of this age within the region, is uncertain, but their ages are similar to the ages of pegmatites occurring in both the Choma-Kalomo Block and the Dete-Kamativi Inlier. The three youngest detrital zircons from the Sijarira sandstone are dated at c. 632 Ma, which gives a maximum depositional age for the Sijarira Group. Our data indicate that the Sijarira Group is probably derived from erosion of a hitherto unknown late Mesoproterozoic (c. 1.05 Ga) pegmatite province intruded into the Palaeoproterozoic Magondi belt, with minor provenance from Neoproterozoic rocks. The origin of these pegmatites may be related to tectonic events in the Choma-Kalomo Block and Dete-Kamativi regions, along the northwestern edge of the Kalahari Craton. The Sijarira Group cannot be regarded as a molasse of the Pan-African Zambezi Belt, since it contains very few Neoproterozoic zircons, and the palaeocurrents were in general from E to W. Its former correlation with the Ghanzi Group of Botswana also cannot be sustained, since the Ghanzi Group has no glacial diamictites, and is probably pre-Sturtian (i.e., > c. 710 Ma) (Lehmann et al., 2015, Ore Geology Reviews, 71, 161-190), while the Sijarira Group is constrained to be < c. 632 Ma.

IMSG 2016: NEW U-Pb SIMS ZIRCON GEOCHRONOLOGY ON THE DETE-KAMATIVI INLIER (NW ZIMBABWE) AND THE CHOMA-KALOMO BLOCK, OF SE ZAMBIA

S.M. Glynn [1, 2], S. Master [1, 3], M. Wiedenbeck [2, 1], D. Davis [4], Frei, D [5], T. Oberthür [6]
[1]School of Geosciences, University of the Witwatersrand, Johannesburg, South Africa. sarahglynn22@gmail.com
[2]Helmholtz Zentrum Potsdam Deutsches GeoForschungsZentrum, Potsdam, Germany. Michael.Wiedenbeck@gfz-potsdam.de
[3]Economic Geology Research Institute. Sharad.Master@wits.ac.za
[4]Jack Satterly Geochronology Laboratory, University of Toronto, Toronto, Canada. dond@es.utoronto.ca
[5]Central Analytical Facility & Department of Earth Sciences, University of Stellenbosch, South Africa. dirkfrei@sun.ac.za
[6]Bundesanastalt für Geowissenschaften und Rohstoffe (BGR), Hannover, Germany. thomas.oberthuer@bgr.de

The Choma-Kalomo Block is a north-east trending, terrane located in southern Zambia. It is composed of a gneissic basement, overlain by a high-grade metamorphosed supracrustal metasedimentary sequence, which is intruded by granites and gneisses of the Choma-Kalomo Batholith, dated between ca. 1.37 and 1.18 Ga [1, 2]. The Dete-Kamativi Inlier likewise is composed of deformed and metamorphosed supracrustal sediments, with the exception that these have been divided into a set of four north-east trending formations [3].
Two models have been proposed to account for the current position of the Choma-Kalomo Block. The first model stipulated that the Choma-Kalomo Block, the Dete-Kamativi Inlier and the Kibara Belt in the DRC were once connected. For this to be valid both the Choma-Kalomo Block and Dete-Kamativi Inlier have to be considered as exotic terranes with respect to the surrounding Zimbabwe Craton and Palaeoproterozoic Magondi Belt [4]. However, our recent geochronological investigations of the Choma-Kalomo Block and Dete-Kamativi Inlier have demonstrated that the Kamativi region is floored by Archaean basement. From this we have concluded that the Zimbabwe Craton extends further west under the Magondi Belt than previously thought, and that the Dete-Kamativi Inlier is not an exotic terrane, thus refuting this first model.
The second model suggests that only the Choma-Kalomo Block is an exotic terrane, having become caught up between the Hook Batholith and the Magondi Belt, after rifting off of the Kibara Belt during the Pan-African Damara-Lufilian-Zambezi orogenic event. This implies no links between the Choma-Kalomo block and the Kamativi area prior to the Pan-African [2]. However, there are strong similarities between the Choma-Kalomo block and the Dete-Kamativi Inlier, particularly with both regions having abundant Palaeoproterozoic zircons. The Choma-Kalomo Block has until now been considered Mesoproterozoic in age, hence the claims it is exotic with respect to the neighbouring Archaean Zimbabwe Craton and Palaeoproterozoic Magondi Belt. However, our new U-Pb zircon ages in combination with information on the nature and age of Sn-bearing pegmatites in both the Choma-Kalomo Block and the Dete-Kamativi Inlier indicate that the Choma-Kalomo Block is not an exotic terrane. Rather we propose that the Choma-Kalomo Block is a metacratonic region belonging to the Zimbabwe Craton.

[1] Hanson *et al.,* (1988). *Precambrian Research*, 42, 39-61.
[2] Bulambo *et al*., (2004). Abstracts volume, 20th Colloquium of African Geology, France; Bulambo *et al*., (2006). Abstracts volume, 21st Colloquium of African Geology, Mozambique.
[3] Lockett (1979). The geology of the country around Dett: Geological Survey of Rhodesia, Bulletin, 85, 198 pp.
[4] Unrug (1992).International Geological Correlation Programme Project No 255, Bulletin-Newsletter, 4, 121-124.

GSZ Annual Summer Symposium 2015: Implications for the extent of the Zimbabwe Craton, from U-Pb zircon geochronology of the Dete-Kamativi Inlier (NW Zimbabwe) and the Choma-Kalomo Block, of SE Zambia.

S.M. Glynn[*, a, b], S. Master [a, c], M. Wiedenbeck [b, a], D. Davis [d], Frei, D [e], T. Oberthür [f]

[a] School of Geosciences, University of the Witwatersrand, Johannesburg, South Africa; [b] Helmholtz Zentrum Potsdam Deutsches GeoForschungsZentrum, Potsdam, Germany; [c] Economic Geology Research Institute; [d] Jack Satterly Geochronology Laboratory, University of Toronto, Toronto, Canada; [e] Central Analytical Facility & Department of Earth Sciences, University of Stellenbosch, South Africa; [f] Bundesanastalt für Geowissenschaften und Rohstoffe (BGR), Hannover, Germany.
[*]Corresponding author, email address: sarahglynn22@gmail.com

The Choma-Kalomo Block is a north-east trending, terrane located in southern Zambia. It is composed of a gneissic basement, overlain by a high-grade metamorphosed supracrustal metasedimentary sequence, which is intruded by granites and gneisses of the Choma-Kalomo Batholith, dated between ca. 1.37 and 1.18 Ga.

Two models have been proposed to account for the current position of the Choma-Kalomo Block. The first model stipulated that the Choma-Kalomo Block, the Dete-Kamativi Inlier and the Kibara Belt in the DRC were once connected. For this to be valid both the Choma-Kalomo Block and Dete-Kamativi Inlier have to be considered as exotic terranes with respect to the surrounding Zimbabwe Craton and Palaeoproterozoic Magondi Belt. However, our recent geochronological investigations of the Choma-Kalomo Block and Dete-Kamativi Inlier have demonstrated that the Kamativi region is floored by Archaean basement. From this we have concluded that the Zimbabwe Craton extends further west under the Magondi Belt than previously thought, and that the Dete-Kamativi Inlier is not an exotic terrane, thus refuting this first model.

The second model suggests that only the Choma-Kalomo Block is an exotic terrane, having become caught up between the Hook Batholith and the Magondi Belt, after rifting off of the Kibara Belt during the Pan-African Damara-Lufilian-Zambezi orogenic event. This implies no links between the Choma-Kalomo block and the Kamativi area prior to the Pan-African. However, there are strong similarities between the Choma-Kalomo block and the Dete-Kamativi Inlier, particularly with both regions having abundant Palaeoproterozoic zircons. The Choma-Kalomo Block has until now been considered Mesoproterozoic in age, hence the claims it is exotic with respect to the neighbouring Archaean Zimbabwe Craton and Palaeoproterozoic Magondi Belt. However, our new U-Pb zircon ages in combination with information on t he nature and age of Sn-bearing pegmatites in both the Choma-Kalomo Block and the Dete-Kamativi Inlier indicate that the Choma-Kalomo Block is not an exotic terrane. Rather we propose that the Choma-Kalomo Block is a metacratonic region belonging to the Zimbabwe Craton.

SAGA 2015: The Choma-Kalomo Block, SE Zambia: exotic terrane, or a metacratonic segment of the Zimbabwe Craton?

S. Master[1,2,3], S. Glynn[2,4,5], D. Frei[6], M. Wiedenbeck[5]

1. Economic Geology Research Institute
2. School of Geosciences, University of the Witwatersrand, Johannesburg, South Africa.
3. sharad.master@wits.ac.za
4. Sarahglynn22@gmail.com
5. SIMS Laboratory, Helmholtz Zentrum, Deutsche GeoForschungsZentrum, Potsdam, Germany
6. Central Analytical Facility & Dept. of Earth Sciences, University of Stellenbosch, South Africa.

SUMMARY

The Choma-Kalomo (C-K) Block is a Precambrian terrane in SE Zambia, composed of a high-grade metamorphosed gneissic basement intruded by Mesoproterozoic granites and gneisses of the C-K Batholith. The C-K Block is separated tectonically from Neoproterozoic terrains to the W and N, and it is covered by Mesozoic Karoo rocks to the SE, separating it from the Dete-Kamativi Inlier (DKI) of the Palaeoproterozoic Magondi Belt of Zimbabwe. Various tectonic models have been proposed to explain the presence of Sn and Ta-Nb-bearing quartz-muscovite pegmatites in the C-K Block, as well as in the DKI, and the Kibara Belt, with the C-K Block being regarded as an exotic terrane, caught up between the Congo and Kalahari Cratons during the Neoproterozoic Pan-African Zambezi Orogeny.

Our new U-Pb geochronological studies on zircons helps to constrain these models. We show that the CK Block and DKI were already together by 1030 Ma, and the two regions have a shared history since the Palaeoproterozoic. The emplacement of the C-K Batholith at 1.37 and 1.18 Ga may have caused decratonisation of the CK Block, by removal of the subcontinental lithospheric mantle. The CK Block is not an exotic terrane, but a metacratonic region of the Zimbabwe Craton.

Key words: Geochronology, zircons, Sn-Ta-Nb, Dete-Kamativi Inlier.

INTRODUCTION

The Choma-Kalomo (C-K) Block is a large expanse of Precambrian basement in the Southern Province of southeastern Zambia, characterized by NE-SW structural trends. It is flanked to the NW by the late Neoproterozoic (Pan-African) Hook Batholith, to the north by the Neoproterozoic Zambezi Belt, and to the SE and SW by sedimentary and volcanic rocks of the Permo-Triassic Karoo Supergroup of the Mid-Zambezi Basin, which separates it from the Palaeoproterozoic Magondi Belt of Zimbabwe and Botswana.

The C-K Block has a strongly deformed and metamorphosed basement consisting of a variety of granulitic and migmatitic gneisses which are mainly paragneisses of metasedimentary origin, in which there are linear metasedimentary schist belts (consisting of quartz – biotite ± muscovite ± garnet ± kyanite schists). This basement is intruded by a large composite granitic batholith, known as the Choma-Kalomo (C-K) Batholith, consisting of hornblende and biotite granites and granite-gneisses (Hanson et al., 1988). The basement rocks of the C-K Block are intruded by numerous quartz-muscovite pegmatites of several types. Of economic importance is a belt of pegmatites containing tin in the form of cassiterite, together with minor Ta, Nb and W, which constitute the “tin belt” of Southern Province (Legg, 1972).

Hanson et al. (1988) dated several phases of the composite C-K Batholith, and obtained U-Pb zircon ages of ca. 1.345 and ca. 1.20 Ga. They also obtained a Rb-Sr isochron age of ca. 1.23 Ga from what they considered a D2 shear zone in the granite gneiss. Bulambo et

al. (2004, 2006) did further SHRIMP U-Pb geochronology on the C-K Batholith, and were able to reproduce the two ages of granitic magmatism in this batholith, with better precision, at ca. 1.37 and ca. 1.18 Ga. Neither Hanson et al. (1988) nor Bulambo et al. (2004, 2006) dated any of the basement gneisses or schists intruded by the C-K Batholith.

Unrug (1992) proposed that the Choma-Kalomo block, the Kamativi Schist Belt of Zimbabwe, and the Kibara Belt of DRC were once connected (on the basis of containing tin pegmatites), and were displaced through 150-200 km sinistral movement along the Mwembeshi dislocation zone. The idea that the Choma-Kalomo block was part of the Kibaran belt was revived by Bulambo et al. (2004, 2006) who suggested that it is an exotic terrane, derived by rifting from the Kibaran Belt during Rodinia breakup, which was then caught up between the Congo and Kalahari Cratons during the Pan-African Damara-Lufilian-Zambezi orogenic event. Bulambo et al. (2004, 2006) argued the link based on the similarities of ages in the Kibaran belt and the Choma-Kalomo block, and the absence of 1.38 and 1.18 Ga granitoids in the Irumide Belt of eastern Zambia and the Ngamiland belt of Botswana.

If the Unrug (1992) argument was correct, then the Choma-Kalomo and Kamativi regions would both be exotic terranes with respect to the surrounding Zimbabwe Craton and Magondi Belt to the SE, and the Lufilian orogen to the NW. It would imply Pan-African tectonism in these two blocks to account for their present positions. However, geochronological investigations of the Choma-Kalomo Block by Cahen et al., (1984), Hanson *et al.* (1988), and Bulambo *et al.* (2004, 2006), and of the Kamativi area by Priem *et al.* (1971) and Master *et al.* (2013) show almost no Pan-African metamorphism in these regions. The Kamativi area is part of the Paleoproterozoic Magondi Belt (Master *et al.*, 2010). Furthermore, an Archaean age of 2.71 Ga for a granitic gneiss from the Kamativi area indicates that the basement there is part of the Zimbabwe Craton, which extended much further west under the Magondi Belt than previously thought (Master *et al.*, 2013; Glynn et al., 2015). Since the Kamativi belt is not an exotic terrane, but an integral part of the Magondi Belt, on the western flank of the Zimbabwe Craton, the Unrug (1992) model cannot be correct.

The model by Bulambo *et al.* (2004, 2006) which regards only the Choma-Kalomo block as an exotic terrane, caught up between the Hook batholith and the Magondi Belt during the Pan-African Damaran-Lufilian-Zambezi orogeny implies no links between the Choma-Kalomo block and the Kamativi area prior to the Pan-African orogeny, with the Choma-Kalomo block having an ancestry from the Kibara Belt, from which it was supposed to have rifted away prior to being caught up in the collision between the Congo and Kalahari Cratons (Bulambo *et al.* 2004, 2006). However, there is a strong similarity between the Choma-Kalomo block and the Kamativi belt, in terms of the nature and age of tin-bearing pegmatites in both areas. The tin-bearing pegmatites of the Choma-Kalomo block occur along regional NE-trending shear zones, with no associated granitic intrusions recognized, and their mineral associations include muscovite, tourmaline, cassiterite, tantalite, columbite and rare wolframite (Drysdall, 1967; Legg, 1972). Three types of pegmatite are recognised in the Choma-Kalomo area: (1) quartz-muscovite pegmatites, (2) quartz-muscovite-biotite-feldspar-tourmaline pegmatites, and (3) cassiterite-bearing quartz-muscovite and quartz-muscovite-feldspar pegmatites. Drysdall (1967) pointed out the great similarities between the pegmatites of the Choma-Kalomo area, and those of the Kamativi area, which also occur as three types: (1) quartz-feldspar-biotite-tourmaline-garnet pegmatites, (2) cassiterite-bearing quartz-feldspar-muscovite pegmatites, with accessory tantalite, columbite and amblygonite, and (3) tourmaline-bearing quartz pegmatites with cassiterite, wolframite and scheelite (Lockett, 1979).

The strongest argument for a link between the tin pegmatites of the Choma-Kalomo block and those of the Kamativi area comes from radiometric dating. Muscovite from the tin-bearing pegmatite at the Phoenix Mine

(situated at 16°49'S, 27°02'E, in the Choma-Kalomo block) was dated using both the Rb-Sr and K-Ar methods The (recalculated) ages are 1080 ± 31 Ma (Rb/Sr, Ri = 0.705), and 1060 ± 40 Ma (K/Ar)(Cahen et al. 1984). In the Kamativi area, the tin-bearing pegmatites were dated at 1025 ± 15 Ma (Rb-Sr isochron). Galena from the Elbas Mine in the Inyantue Formation of the Dete-Kamativi Inlier gave a near-concordant $^{207}Pb/^{206}Pb$ age of ~1.18 Ga (Master et al., 2013), which may be related to the coeval granitic plutonism in the Choma-Kalomo block, which has exactly the same age, 1.18 Ga, (Bulambo et al., 2004, 2006). Pb-Pb dating, using ID-TIMS on columbite and plagioclase, and LA-ICPMS on monazite, has produced new ages for the tin pegmatites at Kamativi, and their host rocks. A Pb-Pb isochron based on columbite and plagioclase gave an age of 1030 ± 9 Ma for a tin pegmatite (indistinguishable, within error, from the age of the Phoenix tin pegmatite in the C-K Block), while regression of the ages of two clusters of metamorphic monazite grains, probably derived from the country rocks invaded by the tin pegmatites, yielded ages of 1844 ± 9 Ma and 2028 ± 9 Ma (Master et al., 2013). Further studies were needed to help understand the age, affinity and ancestry of the C-K Block, and its relationship with the DKI.

METHOD AND RESULTS

We have done U-Pb geochronology on zircons from various rock units within the Choma-Kalomo Block, as well as in the adjacent Dete-Kamativi Inlier of Zimbabwe (Master et al., 2013; Glynn et al., 2015). Zircons were separated using standard techniques, and were examined using CL and BSE imaging. Selected spots, on identified cores and rims, were analysed using LA-ICPMS (Stellenbosch) and SIMS (Potsdam). Results were plotted on U-Pb Concordia diagrams, and only $^{207}Pb/^{206}Pb$ results that were less than ±10% discordant were used in age calculations. We have used our new geochronological data, together with additional existing data, to test the tectonic models that have been proposed for the formation of the Choma-Kalomo Block.

Our first sample is a metapelitic biotite-muscovite schist (Z9), just south of the C-K Batholith near Choma in Zambia. The detrital zircon ages fall into four separate clusters: ca. 3.39 Ga, ca. 2.7-2.6 Ga, ca. 2.1-1.7 Ga (with a peak at ca. 1.88 Ga), and 1.55 – 1.28 Ga (Figure 1).

The second sample (ZCK4C) is a semi-pelitic quartz-muscovite-tourmaline schist with crenulated cleavage from the Starfield Sn Mine at Masuku Mission in the CK Block, which has only Palaeoproterozoic detrital zircons, with two age clusters- around 2.03-2.02 Ga and 1.9-1.8 Ga, corresponding to the ages of granitic intrusion, and metamorphism, in the Magondi mobile belt on the western side of the Zimbabwe Archaean Craton. The third sample (ZCK13/2) is a quartz-plagioclase-orthopyroxene granulite, with some retrograde hornblende, which occurs as xenoliths within a 1.36 Ga granitic intrusion of the Choma-Kalomo batholith, and which contains zircon cores with Palaeoproterozoic (2.04 Ga) ages, and altered (metamorphosed/metasomatised) rims having ages of ca. 1.36 Ga, reflecting resetting during the granitic intrusion event.

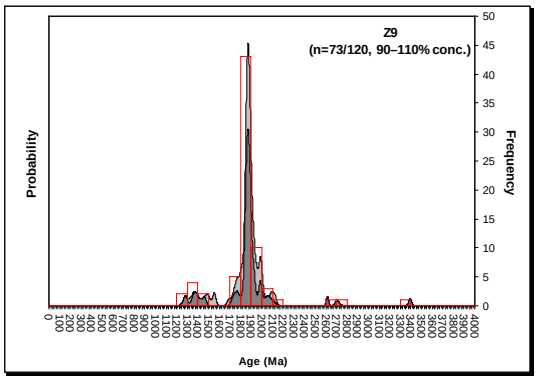

Figure 1: Histogram of ages of detrital zircons from biotite-muscovite pelitic schist Z9, from the Choma-Kalomo Block, Zambia.

The ages of the detrital zircon populations indicate the provenance of the sedimentary protolith of the schist that was dated. The ages in sample Z9 do not reflect derivation from the C-K batholith, whose older granites were dated at 1368 ± 10 Ma (Bulambo et al., 2004, 2006) to ca. 1345 Ma (Hanson et al., 1988), since there are only two zircon ages

(1368 and 1326 Ma) falling into that range, indicating that the batholith had not yet been fully exhumed and exposed at the time of sedimentation. The bulk of the detrital zircon ages are Palaeoproterozoic, with a huge peak, including the bulk of the zircons analysed, between 1.9 and 1.8 Ga. Some of the older Palaeoproterozoic ages correspond to ages of igneous events in the Magondi Belt of western Zimbabwe (Glynn et al., 2012; Master et al., 2013), while the large peak corresponds to the age of metamorphism in the Magondi Belt (between 2.0 and 1.8 Ga; Rb-Sr and Pb-Pb ages on granulites, Master et al., 2010; and U-Pb ages on monazites, Master et al., 2013). The oldest zircons, of Mesoarchaean (3394 Ma) and Neoarchaean (2709 – 2617 Ma) age, match closely the ages of Archaean rocks from the adjacent Zimbabwe craton, where the Sebakwe protocraton has ages between 3456 to ca. 3350 Ma (Horstwood et al., 1999), and the Upper Bulawayan greenstones have ages between 2.7 and 2.6 Ga (Blenkinsop et al., 1997). The Palaeoproterozoic zircon cores from ZDK13/2 and ZCK13/6 give ages in the range 2.04-2.02 Ga, which is the age of granitoids and granitoid gneisses in the Dete-Kamativi area (Master et al., 2013). By contrast, detrital zircons from the Nzilo Group in the Kibara Supergroup of D.R. Congo have age ranges from 3214 ± 7 Ma to 1329 ± 32 Ma (Kokonyangi et al., 2007). The bulk of the Kibaran detrital zircons (75%) have ages between 2434 ± 5 Ma and 1696 ± 18 Ma, with peaks at 2050 and 1850 Ma, and a significant Mesoproterozoic population (1499 ± 49 Ma to 1329 ± 32 Ma). The Kibaran detrital zircon population lacks zircons as old as the 3394 ± 13 Ma, or as young as 1278 ± 27 Ma (which are present in sample Z9), and it has peaks, such as at 2.05 Ga, which are absent in the Z9 population. Thus the histograms of ages from the Z9 sample and the Zimbabwe Craton (together with the Magondi Belt) match quite well, while there is a serious mismatch with the age histograms from the Kibaran Belt. Hence it is very unlikely that the C-K Block is derived from the Kibaran belt, and there is growing evidence that it may be a part of the Magondi Belt, on the western flank of the Zimbabwe Craton.

The matching of the ages of tin pegmatites of the C-K Block and those of the Kamativi area is a strong indication that the two regions were already juxtaposed at ca. 1.03 Ga. The fact that the schist Z9, with a maximum age of 1278 ± 27, is deformed, and so is the ca. 1.18 Ga phase of the C-K Batholith, indicates a post- 1.18 Ga deformation event- which is likely to be the Pan-African deformation event which juxtaposed the Hook Batholith to the west, and the Zambezi Belt to the north, with the C-K Block (Hanson et al., 1988).

CONCLUSIONS

The results of our new geochronological investigations of the Choma-Kalomo Block of southern Zambia, as well as of the Dete-Kamativi Inlier of Zimbabwe, indicate that the two regions have a similar history in the Palaeoproterozoic, with both regions having abundant zircons derived from the 2.04-1.8 Ga Magondi belt, and older Archaean detrital zircons derived from the Zimbabwe Archaean craton. The Choma-Kalomo Block has unique magmatism at ca. 1.38 and 1.18 Ga (different phases of the composite Choma-Kalomo Batholith). However, both areas again have great similarities in the late Mesoproterozoic to early Neoproterozoic eras, when both regions saw the emplacement of Sn and Ta-Nb bearing quartz-muscovite pegmatites, dated at around 1030 ± 30 Ma.

Our new data constrain tectonic models that have been proposed for the evolution of the Choma-Kalomo Block. They help to refute the notion that the C-K Block (by itself, or together with the Dete-Kamativi Inlier of Zimbabwe) was an exotic fragment of the Kibara Belt, which was caught up between the Congo and Kalahari Cratons during the Pan-African Zambezi Orogeny. Since both areas share similar zircons since the Palaeoproterozoic, it is suggested that the C-K block was part of the Magondi Belt, and hence originally part of the Zimbabwe Craton. It may have been decratonised by subcontinental lithospheric removal in the Mesoproterozoic, when Andean-type

magmatic arcs formed on the western edge of the Zimbabwe craton. The Choma-Kalomo Block is thus not an exotic terrane derived from the Kibara Belt, but is a metacratonic part of the Zimbabwe Craton.

ACKNOWLEDGMENTS

We are grateful to the following institutions for their support: Carnegie Corporation, NY, for Carnegie Large Research Grant to SM; National Research Foundation (South Africa) for Research Grant to SG; University of the Witwatersrand Faculty of Science for Travel Grant to SG; Society of Economic Geologists Tim Nutt Research Grant to SG; AEON funding for SG; GFZ support for SG, SM. SM thanks Jean-Paul Liegeois (ULB) for discussions. We thank Dan Harlov (GFZ) for sharing with us his expertise on zircon alteration textures.

REFERENCES

Blenkinsop, T.G., Martin, A., Jelsma, H.A. and Vinyu, M.L., 1997. The Zimbabwe Craton. In: de Wit, M.J. and Ashwal, L.D. (Eds.), Greenstone Belts. Oxford University Press, Oxford, 567-580.

Bulambo, M., De Waele, B., Kampunzu, A.B. and Tembo, F., 2004, SHRIMP U-Pb geochronology of the Choma-Kalomo block (Zambia) and geological implications: 20th Colloquium of African Geology, Orleans, France, 2-7 June 2004, Abstracts volume, p. 96.

Bulambo, M., De Waele, B., Kokonyangi, J., Johnson, S.P., Kampunzu, A.B. and Tembo, F., 2006, SHRIMP zircon U-Pb geochronology and geochemistry of the Choma-Kalomo Block granitoids (Zambia): geological implications: 21st Colloquium of African Geology (CAG21), Maputo, Mozambique, Abstracts.

Cahen, L., Snelling, N.J., Delhal, J., Vail, J.R., Bonhomme, M. and Ledent, D., 1984, Geochronology and Evolution of Africa: Clarendon, Oxford, 512 pp.

Drysdall, A.R., 1967, The tin belt of Southern Province. A summary report: Economic Report, Geological Survey of Zambia, 1.

Glynn, S.M, Master, S., Armstrong, R.A., Hofmann, A. and Bekker, A., 2012, New U-Pb (SHRIMP) ages for the Palaeoproterozoic Magondi Supergroup, Zimbabwe: Abstract, IMSG4, 4th Annual Meeting of the Igneous and Metamorphic Studies Group, 15-17 January 2012, University of the Witwatersrand, Johannesburg, South Africa.

Glynn, S.M., Wiedenbeck, M., Master, S. and Frei, D., 2015, New U-Pb zircon geochronology of the Choma-Kalomo Block (Zambia) and the Dete-Kamativi Inlier (Zimbabwe), with implications for the former extent of the Zimbabwe Craton: EGU Annual Meeting, Vienna, Abstracts.

Hanson, R.E., Wilson, T.J., Brueckner, H.K., Onstott, T.C., Wardlaw, M.S., Johns, C.C. and Hardcastle, K.C., 1988, Reconnaissance geochronology, tectonothermal evolution, and regional significance of the middle Proterozoic Choma-Kalomo block, southern Zambia: Precambrian Research, 42, 39-61.

Horstwood, M.S.A., Nesbitt, R.W., Noble, S.R. and Wilson, J.F., 1999, U-Pb zircon evidence for an extensive early Archean craton in Zimbabwe: A reassessment of the timing of craton formation, stabilization, and growth: Geology, 27, 707-710.

Kokonyangi, J.W., Kampunzu, A.B., Armstrong, R., Arima, M., Yoshida, M. and Okudaira, T., 2007, U-Pb SHRIMP dating of detrital zircons from the Nzilo Group (Kibaran Belt): Implications for the source of sediments and Mesoproterozoic evolution of Central Africa: Journal of Geology, 115, 99-113.

Legg, C.A., 1972, The tin belt of the Southern Province: Economic Report, Geological Survey of Zambia, 29, 58 pp.

Lockett, N.H., 1979, The geology of the country around Dett: Geological Survey of Rhodesia, Bulletin, 85, 198 pp.

Master, S., Bekker, A. and Hofmann, A., 2010, A review of the stratigraphy and geological setting of the Palaeoproterozoic Magondi Supergroup, Zimbabwe: type locality for the "Lomagundi" global carbon isotope excursion: Precambrian Research, 182(4), 254-273.

Master, S., Glynn, S., Frei, D., Davis, D. and Oberthür, T., 2013, New U-Pb and Pb-Pb geo-chronology of rocks and minerals from the Proterozoic Dete-Kamativi Inlier (Zimbabwe) and Choma-Kalomo Block (Zambia): regional implications: Geological Society of Zimbabwe Annual Summer Symposium, Victoria Falls, 28-30 November 2013.

Priem, H.N.A., Boelrijk, N.A.I.M., Verdurmen, E.A.Th. and Verschure, R.H., 1972, Isotopic dating in the Kamativi Tin Belt, Southern Rhodesia: Geologie en Mijnbouw, 50, 619–624.

Unrug, R., 1992, Kibaran terranes with cassiterite mineralization in the Zambezi Belt, Zambia and Zimbabwe. In: W. Pohl & J. Klerkx (Eds.), Metallogeny of the Kibara Belt, Central Africa. International Geological Correlation Programme Project No 255, Bulletin-Newsletter, 4, 121-124.

EGU 2015: New U-Pb zircon geochronology of the Choma-Kalomo Block (Zambia) and the Dete-Kamativi Inlier (Zimbabwe), with implications for the extent of the Zimbabwe Craton.

Glynn, S.M.[1, 3], Wiedenbeck, M.[1], Master, S.[2, 3,] Frei, D.[4]

[1]GeoForschungsZentrum, Potsdam, Germany; [2] Economic Geology Research Institute; [3]School of Geosciences, University of the Witwatersrand, Johannesburg, South Africa; [4]Central Analytical Facility & Dept. of Earth Sciences, University of Stellenbosch, South Africa sarahglynn22@gmail.com

The Choma-Kalomo Block is a north-east trending, Mesoproterozoic terrane located in southern Zambia. It is composed of as yet undated gneissic basement with a high-grade metamorphosed supracrustal metasedimentary sequence, which is intruded by hornblende granites and gneisses of the Choma-Kalomo Batholith, dated between ca. 1.37 and 1.18 Ga. Our new zircon U-Pb age data on metasedimentary rocks of the Choma-Kalomo Block identifies samples of different ages, with slightly different provenances. The oldest metasedimentary rock is a muscovite-biotite schist, which has only Palaeoproterozoic detrital zircons, the two age clusters around 2.03-2.02 Ga and 1.8-1.9 Ga, correspond to the ages of granitic intrusion, and metamorphism, in the Magondi Mobile Belt on the western side of the Archaean Zimbabwe Craton. The second sample is a garnetiferous paragneiss, which contains both Palaeoproterozoic (2.04 Ga), and Mesoproterozoic zircons, ca. 1.36 Ga, derived from the granites of the Choma-Kalomo Batholith. The third sample is a biotite-muscovite schist, in which the detrital zircon ages fall into four separate clusters: ca. 3.39 Ga, ca. 2.7-2.6 Ga, ca. 2.1-1.7 Ga (with a peak at ca. 1.18 Ga), and 1.55 – 1.28 Ga. The Archaean zircons in this sample are derived from the Zimbabwe Craton, while the Palaeoproterozoic samples come from the Magondi belt, and the youngest zircons come from both phases of the Choma-Kalomo Batholith.

A possible connection between the Choma-Kalomo Block and the Dete-Kamativi Inlier – some 150 km to the south-east in western Zimbabwe – has been proposed on the basis of similarities in the nature of their Sn-Ta-muscovite pegmatite mineralisation. The Dete-Kamativi Inlier, which is part of the Magondi Mobile Belt, is a window into Palaeoproterozoic north-east trending belts of deformed and metamorphosed supracrustal rocks. By dating localities which we suspect form the basement to the surrounding younger sediments, along with selected pegmatites from within the inlier itself; we have concluded that the Choma-Kalomo Block and Dete-Kamativi Inlier are, in fact, coeval. Preliminary results for a number of these granites and gneisses give ages between 2.05 and 2.02 Ga; correlating well with the 2.03-2.02 Ga ages of detrital zircons from the Choma-Kalomo Block.

While these basement rocks are not Archaean in age, we have identified Archaean aged zircons in both the Choma-Kalomo Block and the Dete-Kamativi Inlier, making them the Western most occurrences of Archaean granitoids, and implies that the Zimbabwe Craton extends much further west under the Magondi Belt than previously thought.

GSZ Annual Summer Symposium 2013: New U-Pb and Pb-Pb geochronology of rocks and minerals from the Proterozoic Dete-Kamativi Inlier (Zimbabwe) and Choma-Kalomo Block (Zambia): regional implications.

S. Master[1], S. Glynn[1,2], D. Frei[3], D. Davis[4] and T. Oberthür[5]

[1]EGRI, School of Geosciences, University of the Witwatersrand, Johannesburg, RSA, sharad.master@wits.ac.za; [2]GFZ, Potsdam, Germany; [3]University of Stellenbosch, Stellenbosch, RSA; [4]University of Toronto, Toronto, Canada; [5]BGR, Hannover, Germany.

The Dete-Kamativi Inlier is situated in western Zimbabwe, in a window of Precambrian rocks surrounded by late Palaeozoic, Mesozoic and Cenozoic rocks of the Karoo and Kalahari basins. It forms part of the Palaeoproterozoic Magondi Belt, which flanks the western part of the exposed Archaean Zimbabwe Craton (Lockett, 1979; Master et al., 2010). The only previous geochronological work in the Dete-Kamativi inlier was done by Priem et al. (1972). They obtained (recalculated) Rb-Sr whole-rock ages on granodioritic gneisses and intrusive granites of 2159 ± 100 Ma and 2000 ± 80 Ma, respectively. These poorly constrained ages reflect magmatic episodes on the western side of the Magondi basin pre- or syn-kinematic (granodioritic gneisses), as well as postkinematic (unfoliated granites), with respect to the Magondi Orogeny. The granodioritic gneisses probably represent a calc-alkaline magmatic arc, while the granites were interpreted as post-collisional crustal melts following granulite-facies metamorphism and migmatite formation (Master et al., 2010). U-Pb dating of paragneisses intersected in the Gweta borehole of NW Botswana showed a youngest detrital zircon age of 2125 ± 6 Ma, indicating a maximum depositional age for the sedimentary protolith (Mapeo et al., 2001). Majaule et al. (2001) obtained a TIMS U–Pb zircon age of 2039.2 ± 1.4 Ma for granitoids exposed at Kubu Island in Botswana, some 80 km SE of the Gweta borehole, indicating a southward extension of granitoids emplaced during the Magondi Orogeny.

Our new U-Pb ages on zircons were obtained using LA-ICP-MS. Detrital zircons from a leucogneiss (meta-arkose) (ZDK/9C) of the Malaputese Formation have ages ranging from 2254 ± 18 to 2796 ± 17 Ma, with a strong age peak at ca. 2.7 Ga. In terms of age and lithology, the correlation of the Malaputese Group with the Deweras Group (which has a maximum age of 2235 ± 32 Ma; Glynn et al., 2012), as suggested by Master et al. (2010), is confirmed. These rocks are slightly older than the Gweta paragneisses of NW Botswana. The detrital zircon population indicates a Neoarchaean, ca. 2.7 Ga provenance, with a lesser contribution from Palaeo-proterozoic sources. A foliated megacrystic K-feldspar-porphyritic granitoid (ZDK/2) is dated at ca. 2.03-2.04 Ga, similar in age to the Kubu Island granitoids from Botswana. A strongly foliated quartz-feldspar-biotite granitoid gneiss (ZDK/1) has complex inherited zircons, with ca. 3.2 Ga cores, new zircon growth at ca. 2.7 Ga, with latest (igneous or metamorphic?) overgrowths at 2.07 Ga. Finally, a highly deformed and migmatized biotitic granitoid gneiss (ZDK/11) gives a 2.71 Ga age; while another more mafic quartz-plagioclase-hornblende-biotite granodioritic gneiss (ZDK/12) from close to Kapami gives a 2.03 Ga age. These age data indicate the formation of an Andean-type magmatic arc on the western edge of the Zimbabwe Archaean craton at about 2.07-2.03 Ga, some 70-30 Ma prior to the onset of the Magondi Orogeny. The 2.71 Ga granitoid is also the westernmost occurrence of Archaean granitoids in Zimbabwe, and indicates that the Zimbabwe Archaean craton extended much further west under the Magondi Belt than previously thought.

The Choma-Kalomo (C-K) Block is a large expanse of Precambrian basement characterized by NE-SW structural trends which is present in southern Zambia. It is flanked to the NW by the late Neoproterozoic Hook Batholith, to the north by the Pan-African Zambezi Belt, and to the SE and SW by sedimentary and volcanic rocks of the Permo-Triassic Karoo Supergroup

of the Mid-Zambezi Basin, which separates it from the Palaeoproterozoic Magondi Belt of Zimbabwe and Botswana.

The C-K Block has a strongly deformed and metamorphosed basement consisting of a variety of granulitic and migmatitic gneisses which are mainly paragneisses of metasedimentary origin, in which there are linear metasedimentary schist belts (consisting of quartz – biotite ± muscovite ± garnet ± kyanite schists). This basement is intruded by a large composite granitic batholith, known as the Choma-Kalomo (C-K) Batholith, consisting of hornblende and biotite granites and granite-gneisses (Hanson et al., 1988). The basement rocks of the C-K Block are intruded by numerous quartz-muscovite pegmatites of several types. Of economic importance is a belt of pegmatites containing tin in the form of cassiterite, together with minor Ta, Nb and W, which constitute the "tin belt" of Southern Province (Legg, 1972).

Hanson et al. (1988) dated several phases of the composite C-K Batholith, and obtained U-Pb zircon ages of ca. 1.345 and ca. 1.20 Ga. They also obtained a Rb-Sr isochron age of ca. 1.23 Ga from what they considered a D2 shear zone in the granite gneiss. Bulambo et al. (2004, 2006) did further SHRIMP U-Pb geochronology on the C-K Batholith, and were able to reproduce the two ages of granitic magmatism in this batholith, with better precision, at ca. 1.37 and ca. 1.18 Ga. Neither Hanson et al. (1988) nor Bulambo et al. (2004, 2006) managed to date any of the basement gneisses or schists intruded by the C-K Batholith.

Bulambo et al. (2004, 2006) proposed a model which regards the C-K Block as an exotic terrane, caught up between the Hook batholith and the Magondi Belt during the Pan-African Damaran-Lufilian-Zambezi orogeny, and implying no links between the C-K Block and the Kamativi area prior to the Pan-African orogeny, with the C-K Block having an ancestry from the Kibaran Belt, from which it was supposed to have rifted away prior to being caught up in the collision between the Congo and Kalahari Cratons (Bulambo et al. 2004, 2006). However, there is a strong similarity between the C-K Block and the Kamativi belt, in terms of the nature and age of tin-bearing pegmatites in both areas. The tin-bearing pegmatites of the C-K Block occur along regional NE-trending shear zones, with no associated granitic intrusions recognized, and their mineral associations include muscovite, tourmaline, cassiterite, tantalite, columbite and rare wolframite (Legg, 1972). In the Kamativi area there are cassiterite-bearing quartz-feldspar-muscovite pegmatites, with accessory tantalite, columbite and amblygonite, and tourmaline-bearing quartz pegmatites with cassiterite, wolframite and scheelite (Watson, 1962; Rijks and van der Veen, 1972; Lockett, 1979).

A strong argument for a link between the tin pegmatites of the C-K Block and those of the Kamativi area comes from radiometric dating. Muscovite from the tin-bearing pegmatite at the Phoenix Mine (situated at 16°49'S, 27°02'E, in the C-K Block) was dated using both the Rb-Sr and K-Ar methods (Snelling et al., 1966). These ages were recalculated using updated decay constants as 1080 ± 31 Ma (Rb/Sr, Ri = 0.705), and 1060 ± 40 Ma (K/Ar), while in the Kamativi area, the tin-bearing pegmatites were dated at 1025 ± 15 Ma (Rb-Sr isochron) (Cahen et al., 1984). Galena from the Elbas Mine in the Inyantue Formation of the Dete-Kamativi Inlier was shown to have a near-concordant $^{207}Pb/^{206}Pb$ age of about 1.18 Ga (Master, 1991). This Pb mineralization event may be related to the coeval granitic plutonism in the C-K Block, which is dated at precisely the same age, 1.18 Ga (Bulambo et al., 2004, 2006).

Pb-Pb dating, using ID-TIMS on columbite and plagioclase, and LA-ICPMS on monazite, has produced new ages for the tin pegmatites at Kamativi, and their host rocks (Davis, 2012). A Pb-Pb isochron based on columbite and plagioclase gives an age of 1030 ± 9 Ma for a tin pegmatite (indistinguishable, within error, from the age of the Phoenix tin pegmatite in the C-K Block), while regression of the ages of two clusters of metamorphic monazite grains, probably derived from the country rocks invaded by the tin pegmatites, gives ages of 1844 ± 9 Ma and 2028 ± 9 Ma (Davis, 2012).

We have dated a series of detrital zircons (U-Pb, LA-ICPMS) from a biotite-muscovite schist (Z9), just south of the C-K Batholith near Choma in Zambia. The detrital zircon ages fall into four separate clusters: 3394 ± 13 Ma, 2709 ± 20 – 2617 ± 11 Ma, 2123 ± 13 – 1725 ± 18 Ma (with a huge peak at about 1880 Ma), and 1554 – 1278 ± 27 Ma. The ages of the detrital zircon populations indicate the ages in the provenance of the sedimentary protolith of the schist that was dated. The ages do not reflect derivation from the C-K batholith, whose older granites were dated at 1368 ± 10 Ma (Bulambo et al., 2004, 2006) to ca. 1345 Ma (Hanson et al., 1988), since there are only two zircon ages (1368 and 1326 Ma) falling into that range, indicating that the batholith had not yet been fully exhumed and exposed at the time of sedimentation. The bulk of the detrital zircon ages are Palaeoproterozoic, with a huge peak, including the bulk of the zircons analysed, between 1.8 and 1.9 Ga. Some of the older Palaeoproterozoic ages correspond to ages of igneous events in the Magondi Belt of western Zimbabwe (Glynn et al., 2012; Master et al., 2013), while the large peak corresponds to the age of metamorphism in the Magondi Belt (between 2.0 and 1.8 Ga; Rb-Sr and Pb-Pb ages on granulites, Master et al., 2010; and U-Pb ages on monazites, Davis et al., 2012). The oldest zircons, of Mesoarchaean (3394 ± 13 Ma) and Neoarchaean (2709 ± 20 – 2617 ± 11 Ma) age, match closely the ages of Archaean rocks from the adjacent Zimbabwe craton, where the Sebakwe protocraton has ages between 3456 to ca. 3350 Ma (Horstwood et al., 1999), and the Upper Bulawayan greenstones have ages between 2.7 and 2.6 Ga (Blenkinsop et al., 1997). By contrast, detrital zircons from the Nzilo Group in the Kibara Supergroup of D.R. Congo have age ranges from 3214 ± 7 Ma to 1329 ± 32 Ma (Kokonyangi et al., 2007). The bulk of the Kibaran detrital zircons (75%) have ages between 2434 ± 5 Ma and 1696 ± 18 Ma, with peaks at 2050 and 1850 Ma, and a significant Mesoproterozoic population (1499 ± 49 Ma to 1329 ± 32 Ma). The Kibaran detrital zircon population lacks zircons as old as the 3394 ± 13 Ma, or as young as 1278 ± 27 Ma (which are present in sample Z9), and it has peaks, such as at 2.05 Ga, which are absent in the Z9 population. Thus the histograms of ages from the Z9 sample and the Zimbabwe Craton (together with the Magondi Belt) match quite well, while there is a serious mismatch with the age histograms from the Kibaran Belt. Hence it is very unlikely that the C-K Block is derived from the Kibaran belt, and there is growing evidence that it may be a part of the Magondi Belt, on the western flank of the Zimbabwe Craton.

The matching of the ages of tin pegmatites of the C-K Block and those of the Kamativi area is a strong indication that the two regions were already juxtaposed at ca. 1.02 Ga. The fact that the schist Z9, with a maximum age of 1278 ± 27, is deformed, and so is the ca. 1.18 Ga phase of the C-K Batholith, indicates a post- 1.18 Ga deformation event- which is likely to be the Pan-African deformation event which juxtaposed the Hook Batholith to the west, and the Zambezi Belt to the north, with the C-K Block (Hanson et al., 1988).

The rocks of the Tara Outlier and the Sinakumbe Group on the C-K Block show similarities with the Sijarira Group on the Magondi Belt of western Zimbabwe, and if they are correlated, would serve as an "overlap" sequence deposited on both geological provinces. Further studies are under way to firm up the possible links between the C-K Block and the Magondi Belt- these include a study of the U-Pb ages of the basement gneisses in both regions, and of detrital zircons in the cover sequences in both areas, in addition to $^{40}Ar/^{36}Ar$ studies of micas from pegmatites, schists and gneisses.

Acknowledgements

We thank the Carnegie Corporation (New York) for a Large Research Grant to SM. The South African National Research Foundation is thanked for supporting SG through a student grant. We thank Jeremie Lehmann, Kalinn Neydanov and Lorenzo Milani for assistance with

sampling in the Choma-Kalomo Block, and we thank Rio Tinto Corporation for funding for the Zambian research, and for permission to publish some of that work.

References

Blenkinsop, T.G., Martin, A., Jelsma, H.A. & Vinyu, M.L. 1997. The Zimbabwe Craton. In: de Wit, M.J. and Ashwal, L.D. (Eds.), Greenstone Belts. *Oxford University Press*, Oxford, 567-580.

Bulambo, M., De Waele, B., Kampunzu, A.B. & Tembo, F. 2004. SHRIMP U-Pb geochronology of the Choma-Kalomo block (Zambia) and geological implications. Abstracts volume, 20th Colloquium of African Geology, Orleans, France, 2-7 June 2004 , p. 96.

Bulambo, M., De Waele, B., Kokonyangi, J., Johnson, S.P., Kampunzu, A.B. & Tembo, F. 2006. SHRIMP zircon U-Pb geochronology and geochemistry of the Choma-Kalomo Block granitoids (Zambia): geological implications. 21st Colloquium of African Geology (CAG21), Maputo, Mozambique, Abstracts.

Cahen, L., Snelling, N.J., Delhal, J., Vail, J.R., Bonhomme, M. & Ledent, D. 1984. Geochronology and Evolution of Africa. *Clarendon*, Oxford, 512 pp.

Davis, D. 2012. U-Pb geochronology of Columbite-Tantalite from the Kamativi Mine, Zimbabwe and from Abu Dabbab, Egypt. Unpublished Report, Department of Earth Sciences, University of Toronto, Canada, 15 pp.

Glynn, S.M, Master, S., Armstrong, R.A., Hofmann, A. & Bekker, A. 2012. New U-Pb (SHRIMP) ages for the Palaeoproterozoic Magondi Supergroup, Zimbabwe. Abstract, IMSG4, 4th Annual Meeting of the Igneous and Metamorphic Studies Group, 15-17 January 2012, University of the Witwatersrand, Johannesburg, South Africa.

Hanson, R.E., Wilson, T.J., Brueckner, H.K., Onstott, T.C., Wardlaw, M.S., Johns, C.C. & Hardcastle, K.C. 1988. Reconnaissance geochronology, tectonothermal evolution, and regional significance of the middle Proterozoic Choma-Kalomo block, southern Zambia. *Precambrian Research*, **42**, 39-61.

Horstwood, M.S.A., Nesbitt, R.W., Noble, S.R. & Wilson, J.F. 1999. U-Pb zircon evidence for an extensive early Archean craton in Zimbabwe: A reassessment of the timing of craton formation, stabilization, and growth. *Geology*, **27**, 707-710.

Kokonyangi, J.W., Kampunzu, A.B., Armstrong, R., Arima, M., Yoshida, M. & Okudaira, T. 2007. U-Pb SHRIMP dating of detrital zircons from the Nzilo Group (Kibaran Belt): Implications for the source of sediments and Mesoproterozoic evolution of Central Africa. *Journal of Geology*, **115**, 99-113.

Legg, C.A. 1972. The tin belt of the Southern Province. *Econ. Rep. Geol. Surv. Zambia*, **29**, 58 pp.

Lockett, N.H. 1979. The geology of the country around Dett. Bull. Geol. Surv. Rhodesia, 85, 198 pp.

Majaule, T., Hanson, R.E., Key, R.M., Singletary, S.J., Martin, M.W. & Bowring, S.A., 2001. The Magondi Belt in northeast Botswana: regional relations and new geochronological data from the Sua Pan area. *Journal of African Earth Sciences*, 32(2), 257-267.

Mapeo, R.B.M., Armstrong, R.A., Kampunzu, A.B., 2001. SHRIMP U-Pb zircon geochronology of gneisses from the Gweta borehole, NE Botswana: implications for the Palaeoproterozoic Magondi Belt in southern Africa. *Geological Magazine*, 138, 299-308.

Master, S. 1991. *The origin and controls on the distribution of copper and precious-metal mineralization at the Mangula and Norah mines, Mhangura, Zimbabwe*. Ph.D. thesis, Univ. Witwatersrand, Johannesburg, 385 pp.

Master, S., Bekker, A. & Hofmann, A. 2010. A review of the stratigraphy and geological setting of the Palaeoproterozoic Magondi Supergroup, Zimbabwe: type locality for the "Lomagundi" global carbon isotope excursion. *Precambrian Research*, 182(4), 254-273.

Master, S., Glynn, S. & Frei, D. 2013. New U-Pb zircon geochronology of the Palaeo-proterozoic Dete-Kamativi Inlier, Magondi Belt, Zimbabwe, and implications for the western boundary of the Archaean Zimbabwe Craton. Abstract, CAG24, 24th Colloqium of African Geology, Addis Ababa, Ethiopia, 8-14 January 2013.
Priem, H.N.A., Boelrijk, N.A.I.M., Verdurmen, E.A.Th. & Verschure, R.H. 1972. Isotopic dating in the Kamativi Tin Belt, Southern Rhodesia. *Geologie en Mijnbouw*, 50, 619–624.
Rijks, H.R.P. & van der Veen. A.H. 1972. The geology of the tin-bearing pegmatites in the eastern part of the Kamativi District, Rhodesia. *Mineralium Deposita*, 7, 383-395.
Watson, R.L.A. 1962. The geology of the Kamativi and Lubimbi areas. *Bull. geol. Surv. S. Rhod*., **57**, 42 pp.

BGSW7 2013: New U-Pb (SHRIMP) ages for the Palaeoproterozoic Magondi Supergroup, Zimbabwe

(1) **Glynn, S.M**, School of Geosciences, University of the Witwatersrand, Johannesburg, South Africa. GeoForshungsZentrum, Telegrafenberg, Potsdam, Germany, sarahg@gfz-potsdam.de
(2) **Master, S**, School of Geosciences, University of the Witwatersrand, Johannesburg, South Africa, sharad.master@wits.ac.za
(3) **Armstrong, R.A**, RSES, Australian National University, Canberra, Australia
(4) **Hofmann, A**, Department of Geology, University of Johannesburg, Johannesburg, South Africa
(5) **Bekker, A**, Department of Geological Sciences, University of Manitoba, Winnipeg, Canada

The Magondi Supergroup, composed of metasediments and minor volcanics makes up the bulk of the Magondi Belt, which is located on the western edge of the Zimbabwe Craton. The Magondi Supergroup is composed of three Groups: the Deweras, Lomagundi and Piriwiri. Of the three, the Lomagundi Group is significant in that it is the type locality for the "Lomagundi" global high $\delta^{13}C$ excursion in marine carbonates (Master *et al*., 2010), however its age is poorly established. In order to better constrain the timing of the excursion, zircons from the host sediments were analysed using the SHRIMP-RG facilities at the Australian National University in Canberra. Only zircons with ± 10% or less discordance were considered during our age evaluations.

DV 11/1 (a pyroclastic mafic agglomerate) and DV 11/2 (a metasediment) are both positioned near the base of the Deweras Group. Zircons from DV 11/1 are mainly Archaean in age, ranging from 2.5 to 2.8 Ga. The youngest detrital grain, dated at 2235 ± 32 Ma, provides a maximum age for the onset of Deweras sedimentation. The age distribution in DV 11/2 is bimodal, with peaks at 2.6 Ga and 2.8 Ga and a total absence of ages between 2.7 Ga and 2.8 Ga. The youngest Palaeoproterozoic zircon dated at 2171 ± 11 Ma is our best estimate for the maximum age of this unit.

Two samples from the Lomagundi Group (Z11/C–SKR2B and NC 1), a lithic tuff and felsic agglomerate, respectively, were analysed. Z11/C–SKR2B is composed of both a Palaeoproterozoic and an Archean population, with the youngest zircon providing a maximum age for the eruption of the tuff at 2070 ± 17 Ma. NC 1 yielded only a population between 2.6 and 2.8 Ga, as well as numerous younger discordant zircons.

All four of these samples reveal a distinct age peak at ca. 2.6 Ga. This age is interpreted to be due to xenocrystic zircons derived from the granite-greenstone basement (Leyshon and Tennick, 1988). In contrast, GD-Z/11-2A, a felsic tuff from the Piriwiri Group contains a large Palaeoproterozoic zircon population; the youngest of which yielded a 207/206 age of 2051 ± 9 Ma, thereby providing a maximum age estimate for the eruption of this unit. Interestingly, the Piriwiri sample also contains inherited grains as old as 3.3 Ga, which are likely to have been derived from the Zimbabwe Craton. This final observation suggests that the western margin of the Zimbabwe Craton can be extended some 50 km further to the northwest beyond where it has previously been established.

More data however is needed to confirm the ages presented here, because the majority of the ages have been constrained by only a handful of grains per sample.

References

Master S., Bekker A., Hofmann A. (2010) A review of the stratigraphy and geological setting of the Palaeoproterozoic Magondi Supergroup, Zimbabwe – type locality for the Lomagundi carbon isotope excursion. Precambrian Research, 182, 254-273.

Leyshon P.R., Tennick F.P. (1988) The Proterozoic Magondi mobile belt in Zimbabwe – a review. South African Journal of Geology, 91, 114-131.

DMG 2013: Refining the Margin of the Zimbabwe Craton: New U-Pb Zircon ages from the Dete-Kamativi Inlier, NW Zimbabwe

Glynn, S.M[1, 2]. Master, S[1, 3]. and Frei, D[4]
[1]School of Geosciences, University of the Witwatersrand, Johannesburg, South Africa [2]GeoForshungsZentrum, Telegrafenberg, Potsdam, Germany (sarahg@gfz-potsdam.de)
[1]Sharad.Master@Wits.ac.za; [3]EGRI
[4]Central Analytical Facility & Dept. of Earth Sciences, University of Stellenbosch, South Africa (Dirkfrei@sun.ac.za)

We have recovered zircons from a wide variety of sample materials collected from the Dete-Kamativi Inlier near the Zimbabwe-Zambia border. Laser ablation ICP-MS analyses of these samples both greatly refine the deformational history of the Dete-Kamativi Inlier as well as clarify key chronological relationships between the Zimbabwe Craton and basement units to the west below the Kalahari sands.

Data from two late, undeformed granites both yielded similar concordia intercept ages of 2.0 to 2.1 Ga. Though collected only 4 km from each other, the two granitic samples have distinctly different petrologies – which is also reflected by distinct differences between the inherited zircon populations. Zircons from sample Z DK-2 (coordinates 18°31'53"S 27°04'29"E) define tightly an age of 2.02 Ga, interpreted as the unit's crystallization age. In contrast, zircons from sample Z DK-1 (18° 33' 59"S 27°03'18"E) fail to define a precise magmatic age; rather the zircon population is dominated by older, commonly concordant components ranging between 2.6 and 3.3 Ga. The observed age spectrum for Z DK-1 is consistent with patterns observed further to the east and south in terrains clearly assigned to the Zimbabwe Craton.

Published zircon ages obtained from both outcrop and drill core samples from across central Botswana are dominated by ages similar to our 2.0 to 2.1 Ga population. It therefore seems that our study area occupies an important tectonic position between the Zimbabwe Craton and Palaeoproterozoic terrains forming the basement further to the west.

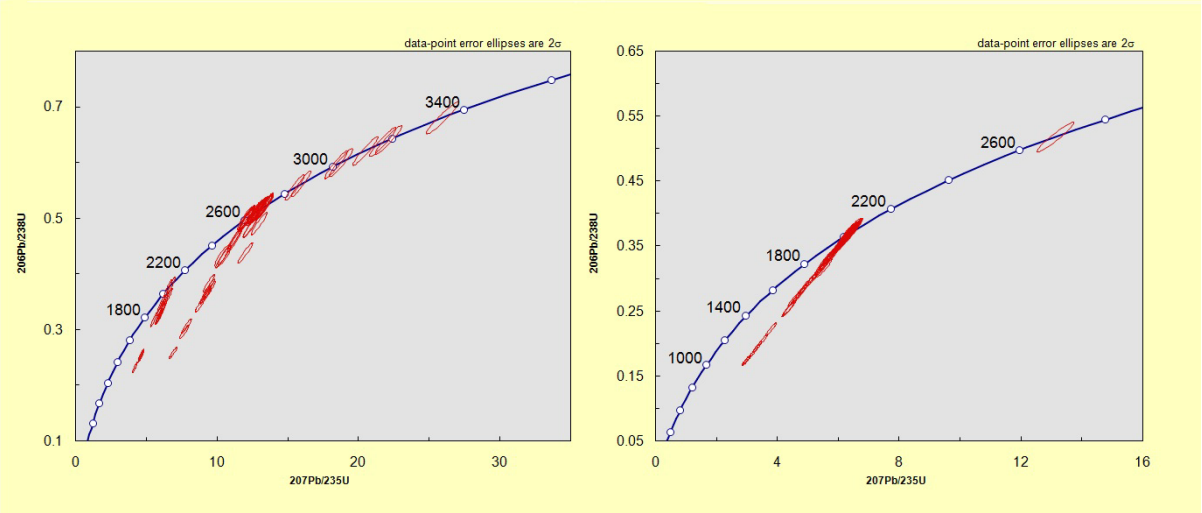

Laser Ablation ICP-MS results for the two granites, Z DK-1(left) and Z DK-2 (right).

CAG 2013: New U-Pb zircon geochronology of the Palaeoproterozoic Dete-Kamativi Inlier, Magondi Belt, Zimbabwe, and implications for the western boundary of the Archaean Zimbabwe Craton

Sharad Master[1,2], Sarah Glynn[2] and Dirk Frei[3]
[1]EGRI, [2]School of Geosciences, University of the Witwatersrand, Johannesburg, South Africa (sharad.master@wits.ac.za). [3]Central Analytical Facility & Dept. of Earth Sciences, University of Stellenbosch, South Africa.

The Dete-Kamativi Inlier is situated in western Zimbabwe, in a window of Precambrian rocks surrounded by late Palaeozoic, Mesozoic and Cenozoic rocks of the Karoo and Kalahari basins. It forms part of the Palaeoproterozoic Magondi Belt, which flanks the western part of the exposed Archaean Zimbabwe Craton (Lockett, 1979; Master et al., 2010). The only previous geochronological work in the Dete-Kamativi inlier was done by Priem et al. (1972). They obtained (recalculated) Rb-Sr whole-rock ages on granodioritic gneisses and unfoliated intrusive granites of 2159 ± 100 Ma and 2000 ± 80 Ma, respectively. These poorly constrained ages reflect magmatic episodes on the western side of the Magondi basin pre- or syn-kinematic (granodioritic gneisses), as well as postkinematic (unfoliated granites), with respect to the Magondi Orogeny. The granodioritic gneisses probably represent a calc-alkaline magmatic arc, while the granites were interpreted as post-collisional crustal melts following granulite-facies metamorphism and migmatite formation (Master et al., 2010). U-Pb dating of paragneisses intersected in the Gweta borehole of NW Botswana showed a youngest detrital zircon age of 2125 ± 6 Ma, indicating a maximum depositional age for the sedimentary protolith (Mapeo et al., 2001). Majaule et al. (2001) obtained a TIMS U–Pb zircon age of 2039.2 ± 1.4 Ma for granitoids exposed at Kubu Island in Botswana, some 80 km SE of the Gweta borehole, indicating a southward extension of granitoids emplaced during the Magondi Orogeny.

Our new U-Pb ages on zircons were obtained using LA-ICP-MS. Detrital zircons from a leucogneiss (meta-arkose) (ZDK/9C) of the Malaputese Formation have ages ranging from 2254 ± 18 to 2796 ± 17 Ma, with a strong age peak at c. 2.7 Ga. In terms of age and lithology, the correlation of the Malaputese Group with the Deweras Group (which has a maximum age of 2235 ± 32 Ma; Glynn et al., 2012), as suggested by Master et al. (2010), is confirmed. These rocks are slightly older than the Gweta paragneisses of NW Botswana. The detrital zircon population indicates a Neoarchaean, c. 2.7 Ga provenance, with a lesser contribution from Palaeoproterozoic sources. A foliated megacrystic K-feldspar-porphyritic granitoid (ZDK/2) is dated at c. 2.03-2.04 Ga, similar in age to the Kubu Island granitoids from Botswana. A strongly foliated qz-fsp-bt granitoid gneiss (ZDK/1) has complex inherited zircons, with c. 3.2 Ga cores, new zircon growth at c. 2.7 Ga, with latest (metamorphic?) overgrowths at 2.03 Ga. Finally, a highly deformed and migmatized biotitic granitoid gneiss (ZDK/11) gives a 2.7 Ga age; while another more mafic qz-plag-hbl-bt granodioritic gneiss (ZDK/12) from close to Kapami gives a 2.03 Ga age. These age data indicate the formation of an Andean-type magmatic arc on the western edge of the Zimbabwe Archaean craton at about 2.03 Ga, some 30 Ma prior to the onset of the Magondi Orogeny. The 2.7 Ga granitoid is also the westernmost occurrence of Archaean granitoids in Zimbabwe, and indicates that the Zimbabwe Archaean craton extended much further west under the Magondi Belt than previously thought.

References

Glynn, S.M., Master, S., Armstrong, R.A., Hofmann, A. & Bekker, A. 2012. New U-Pb (SHRIMP) ages for the Palaeoproterozoic Magondi Supergroup, Zimbabwe. Abstract, 4th Igneous & Metamorphic Studies Group Meeting, 15-17 Jan. 2012, Univ. Witwatersrand, Johannesburg, South Africa.

Lockett, N.H. 1979. The geology of the country around Dett. Bull. Geol. Surv. Rhodesia, 85, 198 pp.

Majaule, T. et al. 2001. The Magondi Belt in northeast Botswana: regional relations and new geochronological data from the Sua Pan area. Journal of African Earth Sciences, 32(2), 257–267.

Mapeo, R.B.M., et al. 2001. SHRIMP U-Pb zircon geochronology of gneisses from the Gweta borehole, NE Bots-wana: implications for the Palaeoproterozoic Magondi Belt in southern Africa. Geol. Mag., 138, 299–308.

Master, S., Bekker, A. & Hofmann, A. 2010. A review of the stratigraphy and geological setting of the Palaeoproterozoic Magondi Supergroup, Zimbabwe: type locality for the "Lomagundi" global carbon isotope excursion. Precambrian Research, 182(4), 254-273.

Priem, H.N.A., Boelrijk, N.A.I.M., Verdurmen, E.A.Th. & Verschure, R.H. 1972. Isotopic dating in the Kamativi Tin Belt, Southern Rhodesia. Geologie en Mijnbouw, 50, 619–624.

CFDW 2012: New U-Pb ages for the Palaeoproterozoic Magondi Supergroup, Zimbabwe

Glynn S.M.[1], Master S.[1, 2], Armstrong R.A.[3], Hofmann A.[4] and Bekker A.[5]

[1]*School of Geosciences, Univ. Witwatersrand, RSA* – sarahglynn22@gmail.com
[2]*EGRI* – sharad.master@wits.ac.za
[3]RSES, *Australian National University, Canberra, Australia*
[4]*Geology Department, Univ. Johannesburg, RSA*
[5]*Department Geol. Sci., Univ. Manitoba, Winnipeg, MB, Canada*

Keywords: Magondi, Lomagundi excursion, U-Pb geochronology.

The Palaeoproterozoic Magondi Supergroup is a metasedimentary succession with minor volcanic rocks, forming part of the Magondi Belt on the western edge of the Zimbabwe Craton (Figure 1a). It has been suggested in Master et al. (2010) that the belt extends through western Zimbabwe and northeast Botswana to include the Dete-Kamativi Inlier and the Matsitama Belt respectively. In the low-grade (greenschist to amphibolite facies) part of the Magondi Belt, there are three groups - the Deweras, Lomagundi and Piriwiri, while in the high grade parts of the belt, there are intrusive granitoids dated at about 2 Ga (Figure 1b).

The Lomagundi Group is the type locality for the "Lomagundi" global high $\delta^{13}C$ excursion in marine carbonates Master et al. (2010), but its age is very poorly constrained. This study aims at improving the geochronology of the Magondi Supergroup, for both local and global geologic and chemostratigraphic correlations.

The currently available geochronology for the Magondi Belt is sparse and in some instances no longer valid, due to large errors. There have been some newer studies such as McCourt et al. (2001) which have U-Pb dates but more still are needed to constrain both the timing of the deposition of the host sediments and consequently when the Lomagundi excursion occurred.

Zircons from five samples were analysed using the SHRIMP-RG facilities at the ANU in Canberra. Only zircons with ± 10% or less discordance are considered in the age calculations.

DV 11/1 is a pyroclastic mafic agglomerate (with mafic clasts in a chlorite-plagioclase-rich matrix), and DV 11/2 is an overlying wackestone, rich in mafic lithic clasts, both from the base of the Deweras Group. The zircons from DV 11/1 give mainly Archaean ages, ranging from 2580 ± 19 Ma to 2813 ± 23 Ma with an age peak of c. 2.63 Ga, reflecting derivation as xenocrysts from the underlying Neoarchaean terrains of the Zimbabwe Craton. The youngest zircon grain, dated at 2235 ± 32 Ma shows good igneous zoning, though it is not euhedral, and could be either indigenous or xenocrystic, giving a maximum age for the Deweras Group. The 67 zircons studied in DV 11/2 are mainly Neoarchaean, with a bimodal age distribution, with peaks around 2.64 Ga and 2.86 Ga, with a total absence of ages between 2.70 Ga and 2.80 Ga. There are only two Palaeoproterozoic zircons, with ages of 2439 ± 23 Ma and 2171 ± 11 Ma. The youngest age provides a maximum age for the wackestone, and for the rest of Deweras Group.

A lithic crystal tuff in the upper Lomagundi Sakurgwe Fm (Z11/C–SKR2B) contains a xenocrystic population of Palaeoproterozoic zircons ranging in age from 2070 to 2492 Ma, and an Archaean population ranging from 2604 to 2719 Ma. The youngest zircon age of 2070 ± 17 Ma provides a maximum age for the tuff. A felsic agglomerate from the Nyamakari "centre" within the Lomagundi Group (NC 1), consisting of an altered assemblage of alkali feldspar, quartz, carbonate and haematite, yielded only a xenocrystic zircon population dated at between 2615 and 2860 Ma, with a distinct peak at about 2635 Ma. There are numerous younger discordant zircons in this sample, which would yield upper intercept ages between about 2.1 and 2.2 Ga, but they are too discordant to yield reliable ages. A felsic crystal tuff from the Godzi "centre" in the Piriwiri Group (GD-Z/11-2A) contains many discordant zircons, and among the more concordant zircons it has a large xenocrystic population of Palaeoproterozoic zircons, ranging from 2051 to 2492 Ma, and numerous Archaean xenocrystic zircons with ages ranging from 2558 to 3339 Ma. The youngest peak in the age distribution is at 2115 Ma, however, the youngest zircon age of 2051 ± 9 Ma may provide a maximum age for the tuff.

These results indicate that the basal Deweras Group volcanics are younger than 2235 ± 32 Ma, while the rest of the Deweras Group is younger than 2171 ± 11 Ma. Volcanic tuff units in the upper parts of the Lomagundi and Piriwiri Groups indicate maximum ages of 2070 ± 17 Ma and 2051 ± 9 Ma respectively. Since all these age constraints are obtained from just one zircon grain in each sample, more data is needed to confirm them.

Additional work is currently underway to obtain more dates, not only for the main exposed part of the Magondi Belt but also for the Dete-Kamativi Inlier, in western Zimbabwe, where high-grade metamorphosed supracrustals of the Malaputese, Kamativi, and Tshontanda Formations are regarded as possible equivalents of the Deweras, Lomagundi and Piriwiri Groups (Master, 1991, Master et al., 2010).

References

Master, S., 1991. Stratigraphy, tectonic setting, and mineralization of the early Proterozoic Magondi Supergroup, Zimbabwe: a review. Econ. Geol. Res. Unit Inform. Circular: No. 238, Department of Geology, University of the Witwatersrand, Johannesburg, 75 pp.

Master, S., Bekker, A. and Hofmann, A., 2010. A review of the stratigraphy and geological setting of the Palaeoproterozoic Magondi Supergroup, Zimbabwe – type locality for the Lomagundi carbon isotope excursion. Precambrian Research, 182(4): 254-273.

McCourt, S., Hilliard, P., Armstrong, R.A. and Munyanyiwa, H., 2001. SHRIMP U-Pb zircon geochronology of the Hurungwe granite northwestern Zimbabwe: Age constraints on the timing of the Magondi orogeny and implications for the correlation between the Kheis and Magondi Belts. South African Journal of Geology, 104: 39-46.

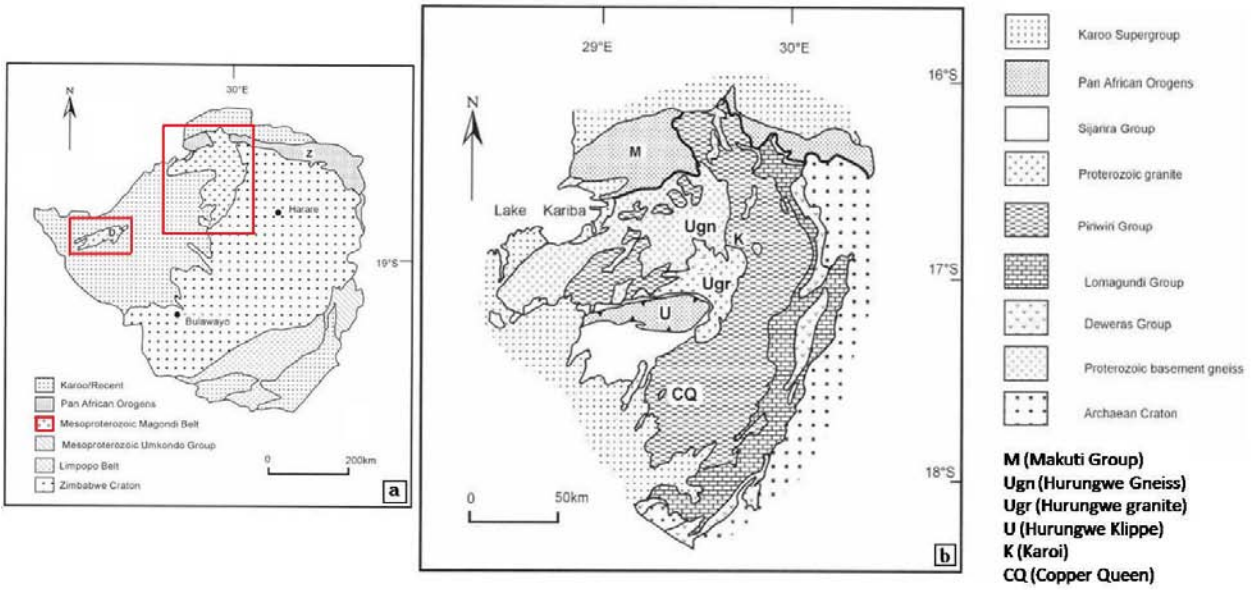

Fig. 1a – Geographical position of the Magondi Belt and the Dete-Kamativi Inlier in Zimbabwe. Fig. 1b – Main exposed part of the Magondi in NW Zimbabwe, modified after McCourt et al. (2001).

IMSG 2012: NEW U-Pb (SHRIMP) AGES FOR THE PALAEOPROTEROZOIC MAGONDI SUPERGROUP, ZIMBABWE

Glynn, S.M.[1,2] , Master, S.[1,3,4], Armstrong, R.A.[5], Hofmann, A.[6]and Bekker, A.[7]

[1]School of Geosciences, Univ. Witwatersrand, Johannesburg, RSA; [2]sarahglynn22@gmail.com; [3]EGRI; [4]sharad.master@wits.ac.za; [4]RSES, Australian National University, Canberra, Australia; [5]Dept. Geology, Univ. Johannesburg, Johannesburg, RSA; [6]Dept. Geol. Sci., Univ. Manitoba, Winnipeg, MB, Canada.

Keywords: Magondi, Zimbabwe, Palaeoproterozoic, Lomagundi excursion, U-Pb geochronology, SHRIMP.

The Palaeoproterozoic Magondi Supergroup is a metasedimentary succession with minor volcanic rocks, located in the Magondi Belt on the western side of the Zimbabwe Craton, in W Zimbabwe and NE Botswana [1]. In the low-grade (greenschist to amphibolite facies) part of the Magondi Belt, there are three groups- the Deweras, Lomagundi and Piriwiri, while in the high grade parts of the belt, there are intrusive granitoids dated at about 2 Ga. The Lomagundi Group is the type locality for the "Lomagundi" global high $\delta^{13}C$ excursion in marine carbonates [1], but its age is very poorly constrained. This study aims at improving the geochronology of the Magondi Supergroup, for both local and global geologic and chemostratigraphic correlations.

Zircons from 5 samples were analysed using the SHRIMP-RG facilities at the ANU in Canberra. Only zircons with ± 10% or less discordance are considered in the age calculations. DV11/1 is a pyroclastic mafic agglomerate (with mafic clasts in a chlorite-plagioclase-rich matrix), and DV 11/2 is an overlying wackestone, rich in mafic lithic clasts, both from the base of the Deweras Group. The zircons from DV11/1 give mainly Archaean ages, ranging from 2580 ± 19 Ma to 2813 ± 23 Ma with an age peak of c. 2.63 Ga, reflecting derivation as xenocrysts from the underlying Neoarchaean terrains of the Zimbabwe Craton. The youngest zircon grain, dated at 2235 ± 32 Ma shows good igneous zoning, though it is not euhedral, and could be either indigenous or xenocrystic, giving a maximum age for the Deweras Group. The 67 zircons studied in DV11/2 are mainly Neoarchaean, with a bimodal age distribution, with peaks around 2.64 Ga and 2.86 Ga, with a total absence of ages between 2.70 Ga and 2.80 Ga. There are only two Palaeoproterozoic zircons, with ages of 2439 ± 23 Ma and 2171 ± 11 Ma. The youngest age provides a maximum age for the wackestone, and for the rest of Deweras Group.

A lithic crystal tuff in the upper Lomagundi Sakurgwe Fm (Z11C-SKR2B) contains a xenocrystic population of Palaeoproterozoic zircons ranging in age from 2070 to 2492 Ma, and an Archaean population ranging from 2604 to 2719 Ma. The youngest zircon age of 2070 ± 17 Ma provides a maximum age for the tuff. A felsic agglomerate from the Nyamakari "centre" within the Lomagundi Group (NC1), consisting of an altered assemblage of alkali feldspar, quartz, carbonate and haematite, yielded only a xenocrystic zircon population dated at between 2615 and 2860 Ma, with a distinct peak at about 2635 Ma. There are numerous younger discordant zircons in this sample, which would yield upper intercept ages between about 2.1 and 2.2 Ga, but they are too discordant to yield reliable ages.

A felsic crystal tuff from the Godzi "centre" in the Piriwiri Group (GDZ/112B) contains many discordant zircons, and among the more concordant zircons it has a large xenocrystic population of Palaeoproterozoic zircons, ranging from 2051 to 2492 Ma, and numerous Archaean xenocrystic zircons with ages ranging from 2558 to 3339 Ma. The youngest peak in the age distribution is at 2115 Ma, however, the youngest zircon age of 2051 ± 9 Ma may provide a maximum age for the tuff.

Our results indicate that the basal Deweras Group volcanics are younger than 2235 ± 32 Ma, while the rest of the Deweras Group is younger than 2171 ± 11 Ma. Volcanic tuff units in the upper parts of the Lomagundi and Piriwiri Groups indicate maximum ages of 2070 ± 17 Ma and 2051 ± 9 Ma respectively. Since all these age constraints are obtained from just one zircon grain in each sample, more data is needed to confirm them.

Reference: [1] Master, S., Bekker, A. & Hofmann, A. (2010). Precambrian Research, 182, 254-273.

D.3 SIMS-RELATED CONFERENCE ABSTRACTS

MATW 2016: Performance Capabilities of the Cameca 1280-HR SIMS Instrument & its role in a virtual SIMS network

Sarah Glynn 1, 2 *
Michael Wiedenbeck 1
Frédéric Couffignal 1
Abiel Kidane 1, 3
Alexander Rocholl 1
Robert Trumbull 1

1. Helmholtz Zentrum Potsdam, Telegrafenberg, Potsdam, Germany
2. University of the Witwatersrand, Johannesburg, South Africa
3. Nelson Mandela Metropolitan University, Port Elizabeth, South Africa
Corresponding Author: sarahglynn22@gmail.com

Since December 2013 the Helmholtz Zentrum Potsdam has operated a 1280-HR instrument: the latest generation of Cameca large geometry ion microprobe. Here we report the observed performance of this tool, with particular emphasis on the determination of isotopic ratios on geomaterials.

The Potsdam group has already acquired extensive experience in the determination of $\delta^{18}O$ values in silicates, for which a single analysis requires *circa* 80 seconds of actual data acquisition. Running in full automatic mode and with the reference material(s) embedded within the grain mount, we are thus able to complete some 250 analyses in a 16 hour fully automated run. For such analyses we commonly achieve an analytical repeatability better than ± 0.15 ‰ (1sd), having recorded repeatabilities down to ± 0.092 ‰ (1sd, n = 100) in one suite of zircon analyses. A main consideration in $\delta^{18}O$ analyses with the 1280-HR is the need for careful sample preparation: on samples with as little as 5 µm topographic relief between silicate grains and epoxy embedding media we have observed charging problems despite using both a 35 nm gold coating and > 1 µA low energy electron flooding.

Thanks to the availability of a well characterized suite of tourmaline RMs, boron isotope analyses are already a well established application in the Potsdam SIMS facility. Here a single analysis involves 80 s of data acquisition, from which we can obtain a typical repeatability of ± 0.25 ‰ (1sd) and an overall analytical uncertainty of ± 0.9 ‰ based on a suite of four chemically distinct tourmaline RMs. We have also been able to analyze the boron isotopic compositions on areas as small as 3 µm with only a modest reduction in overall precision.

Large demand exists for U-Th-Pb age determinations, for which we currently have RMs only for zircon. For such work a single analysis commonly requires 12 to 15 minutes of data acquisition, meaning that a complete project typically involves *circa* 5 days of laboratory usage. Our zircon U-Pb protocol calls for the analysis of a quality control material during all analytical sessions. Here we often observe a ~1 % bias in the Pb/U results from the QCM as calibrated by the primary reference material. We conclude that under normal circumstances our inter-element results are reliable to better than 2 ‰ level. A key feature of the 1280-HR tool is the ability to conduct oxygen flooding during the analyses, which results in a 2x improvement in instrument sensitivity for Pb data acquisition. The technology behind the 1280-HR is sufficiently mature such that the main factor limiting analytical quality has, at least in some isotopic systems, become the interlaboratory bias observed during the "bulk" characterization of the reference materials.

The Potsdam 1280-HR is at the centre of a virtual SIMS network which is to be located in South Africa, and will provide the southern African Geosciences community with easier and more affordable access to this state-of-the-art technology.

Geoanalysis 2015: Performance Capabilities of the Cameca 1280-HR SIMS Instrument

Michael Wiedenbeck 1 *
Frédéric Couffignal 1
Sarah Glynn 1,2
Abiel Kidane 1,3
Alexander Rocholl 1
Robert Trumbull 1

1. Helmholtz Zentrum Potsdam, Telegrafenberg, Potsdam, Germany
2. University of the Witwatersrand, Johannesburg, South Africa
3. Nelson Mandela Metropolitan University, Port Elizabeth, South Africa
Corresponding Author: michael.wiedenbeck@gfz-potsdam.de

Since December 2013 the Helmholtz Zentrum Potsdam has operated a 1280-HR instrument: the latest generation of Cameca large geometry ion microprobe. Here we report the observed performance of this tool, with particular emphasis on the determination of isotopic ratios on geomaterials.

We have already acquired extensive experience in the determination of $\delta^{18}O$ values in silicates, for which a single analysis requires *circa* 80 seconds of actual data acquisition. Running in full automatic mode and with the reference material(s) embedded within the grain mount, we are thus able to complete some 250 analyses in a 24 hour cycle. For such analyses we typically achieve an analytical repeatability of ± 0.15 ‰ (1sd), though we have recorded repeatabilities down to ± 0.092 ‰ (1sd, n = 100) in one suite of zircon analyses. A main consideration in $\delta^{18}O$ analyses with the 1280-HR is the need for careful sample preparation: on samples with as little as 5 µm topographic relief between silicate grains and epoxy embedding media we have observed charging problems despite using both a 35 nm gold coating and > 1 µA of low energy electron flooding.

Thanks to the availability of a well characterized suite of tourmaline RMs, boron isotope analyses are already a well established application in the Potsdam SIMS facility. Here a single analysis involves 80 s of data acquisition, from which we can obtain a typical repeatability of ± 0.25 ‰ (1sd) and an overall analytical uncertainty of ± 0.9 ‰ based on a suite of four distinct tourmaline RMs. We have also been able to analyze the boron isotopic compositions on areas as small as 3 µm with only a modest reduction in overall precision.

Large demand exists for U-Th-Pb age determinations, for which we currently have RMs only for zircon. For such work a single analysis commonly requires 12 to 15 minutes of data acquisition, meaning that a complete project typically involves *circa* 5 days of laboratory usage. Our zircon U-Pb protocol calls for the analysis of a quality control material during all analytical sessions. Here we often observe a ~1 % bias in the Pb/U results from the QCM as calibrated by the primary reference material. We conclude that under normal circumstances our inter-element results are reliable at the ± 2 ‰ level. A key feature of the 1280-HR tool is the ability to conduct oxygen flooding during the analyses, which results in a 2x improvement in instrument sensitivity for Pb data acquisition.

The technology behind the 1280-HR is sufficiently mature such that the main factor limiting analytical quality has, at least in some isotopic systems, become the interlaboratory bias observed during the "bulk" characterization of the reference materials. A key limiting factor in the performance of the instrument itself is the constraint that only a single, 1-inch diameter sample may be in the secondary ion source at a time. This limitation often compels frequent sample exchanges in order to access calibration materials, thereby prohibiting extended automated runs.

Geoanalysis 2015: The Microanalytical Reference Materials Programme at the Potsdam SIMS Laboratory

A. Rocholl[1], M. Wiedenbeck[1], F. Couffignal[1], S. Glynn[1,2], A. Kidane[1,3], R. Alonso-Perez[4]

1: GFZ German Research Centre for Geosciences, Telegrafenberg, 14473 Potsdam, Germany
2: School of Geosciences, University of the Witwatersrand, Johannesburg, South Africa
3: Department of Geosciences, Nelson Mandela Metropolitan University, Port Elizabeth, South Africa
4: Harvard Mineralogical and Geological Museum, Cambridge, Massachusetts, USA

In November 2013 a CAMECA 1280-HR Secondary Ion Mass Spectrometer (SIMS) was installed at the Helmholtz Zentrum Potsdam. This state-of-the-art, large geometry instrument is optimized for both low-uncertainty isotope ratio determinations (e.g., $\delta^{13}C$, $\delta^{18}O$ and $\delta^{34}S$) as well as the quantification of low-abundance volatile elements in geological materials. SIMS technology, like most other microanalytical methods, is critically dependent upon the availability of high-quality reference materials in order to calibrate quantitative results. Unfortunately, few such materials are readily available, and for those phases for which well characterized RMs do exist these are in such limited supply that a direct traceability of results between laboratories is, in general, not possible.

A key consideration favoring Potsdam's investment in SIMS technology is the urgent need for new – and better characterized – microanalytical RMs for isotopic determinations. Thanks to its fine sampling size, SIMS is one of the most powerful methods for quantifying material heterogeneity, working at the sub-200 picogram scale for isotope ratio determinations on major elements. Analytical repeatabilities of ± 0.092 ‰ (1sd; n = 100) for $\delta^{18}O$ have been achieved on silicate materials using the Potsdam instrument.

Thanks to a close partnership with Mineralogical and Geological Museum at Harvard University, the Potsdam SIMS instrument has already begun evaluating the isotopic homogeneity of a broad suite of mineral phases. These starting materials, commonly large single crystals, have already undergone detailed studies of their major element contents, making them some of the best characterized and widely used geomaterials for calibrating EPMA analyses. If SIMS analyses detects little or no heterogeneity in the isotopic composition of a candidate material then "bulk" conventional isotopic determinations will be made by selected laboratories with established expertise in the given isotopic system. Our initial work focuses on developing $\delta^{11}B$ (tourmaline and mica), $\delta^{13}C$ (carbonates), $\delta^{18}O$ (silicates and carbonates), and $\delta^{34}S$ (sulphides) RMs that will then be made available to the global geoanalytical community. Other RM development work, and in particular the characterization of volatile element concentration in volcanic glasses, is also being planned.